UAB
Universitat Autònoma de Barcelona

TLAG of solution-derived REBCO superconducting films: ultrafast growth mechanism and influence of transient liquid composition

Lavinia Saltarelli

ADVERTIMENT. L'accés als continguts d'aquesta tesi queda condicionat a l'acceptació de les condicions d'ús establertes per la següent llicència Creative Commons: https://creativecommons.org/licenses/?lang=ca

ADVERTENCIA. El acceso a los contenidos de esta tesis queda condicionado a la aceptación de las condiciones de uso establecidas por la siguiente licencia Creative Commons: https://creativecommons.org/licenses/?lang=es

WARNING. The access to the contents of this doctoral thesis it is limited to the acceptance of the use conditions set by the following Creative Commons license: https://creativecommons.org/licenses/?lang=en

TLAG of solution-derived REBCO superconducting films: ultrafast growth mechanism and influence of transient liquid composition

A dissertation submitted for the degree of

DOCTOR OF PHILOSOPHY IN MATERIALS SCIENCE

by

Lavinia Saltarelli

Supervisors:

Prof. Teresa Puig Molina

Prof. Xavier Obradors Berenguer

Superconducting Materials and Large Scale Nanostructures Department (SUMAN)

Institut de Ciència de Materials de Barcelona (ICMAB-CSIC)

Doctorat en Ciència de Materials

Facultat de Ciències

Universitat Autònoma de Barcelona

April 2024

Lavinia Saltarelli
ICMAB-CSIC
Campus de la UAB, Bellaterra, Barcelona
lavinia.saltarelli@gmail.com

April 2024



This work is published under Creative Commons, CC BY-NC-ND 4.0
The material can be copied and reproduced, providing appropriate credit to the author. You may not use the whole or part of the material for any commercial purposes. No derivatives of the material are allowed under this license. The distribution of modified material requires the authors permission.

Memòria que porta per títol **"TLAG of solution-derived REBCO superconducting films: ultrafast growth mechanism and influence of transient liquid composition "** i presentada per aspirar al Grau de Doctor en Ciència de Materials per **Lavinia Saltarelli**

Autor:
Lavinia Saltarelli, M. Sc.

amb el vist i plau de: **Prof. Teresa Puig Molina**, Professora d'investigació del Institut de Ciències de Materials de Barcelona (ICMAB-CSIC) i **Prof. Xavier Obradors Berenguer**, Professor d'investigació del Institut de Ciències de Materials de Barcelona (ICMAB-CSIC).

I per a que així consti, signen el present certificat.

Directora:
Prof. Teresa Puig Molina

Director:
Prof. Xavier Obradors Berenguer

Bellaterra, abril de 2024

UNIVERSITAT AUTÒNOMA DE BARCELONA

Abstract

Departament de Ciències

Institut de Ciència de Materials de Barcelona (ICMAB-CSIC)

Doctor of Philosophy

TLAG of solution-derived REBCO superconducting films: ultrafast growth mechanism and influence of transient liquid composition

by Lavinia Saltarelli

The unparalleled feature of High Temperature Superconducting (HTS) materials of lossless electrical current conduction up to liquid nitrogen temperature and at high magnetic fields has encouraged research on $REBa_2Cu_3O_{7-\delta}$ (REBCO, RE= rare earth elements) systems to unravel the opportunities towards a plethora of different applications. Nonetheless, the excessive production costs of the commercialized HTS Coated Conductors (CCs) are impeding their worldwide spread. The work conducted in this thesis sets as an objective the reduction of the high cost/performance ratio of REBCO superconductors by coupling a cost-effective chemical solution deposition-based (CSD) methodology to the innovative transient liquid assisted growth (TLAG) process. The development of novel, robust chemical solutions led to the attainment of unprecedented chemical and microstructural homogeneity of films showing thickness of up to 2.7 μm, through implementation of two fundamental innovations. High-purity metal propionate powder precursors have been synthesized through facile and inexpensive one-pot methods. Additionally, the careful selection of an amine additive enhanced the rheological properties of the chemical precursor solution for YBCO and REBCO film fabrication. Variation of the (Ba:Cu) molar ratio of the initial chemical solution resulted in films of different transient liquid composition, enabling the in-depth analysis of the out-of-equilibrium kinetic mechanism of TLAG. Strict control of the processing parameters led to high-performance films exhibiting critical current density values up to 3 MA cm^{-2} and growth rates beyond 2000 nm s^{-1}. Advanced characterization techniques, such as *in-situ* synchrotron X-ray diffraction, shed light on the influence of transient liquid supersaturation, driving force towards YBCO nucleation and its successive epitaxial growth. These analyses have generated new and fundamental insights into the complex kinetic mechanism of TLAG.

Acknowledgements

This PhD thesis has been among the most challenging experiences I faced, but without any doubt I will cherish the highs, and also the lows, of the time spent in the labs, the conferences, the connections and the great friendships with so many incredible people.

First of all, I would like to express my gratitude to my two supervisors, Prof. Teresa Puig and Prof. Xavier Obradors, for granting me the opportunity of working on this extremely interesting project at the borders of chemistry and physics. You both believed in my capabilities from the very beginning, even when I had yet everything to prove. Teresa, thanks for all the amazing opportunities you put in my path, for the freedom I had to experiment in my first, real experience as a researcher and for pushing me to be a better, stricter, and meticulous scientist. Xavier, I cannot thank you enough for always being there for a discussion, for all the explanations, research works and the immense knowledge that you shared with me throughout the years.

Despite not being my supervisors, there are numerous people who contributed directly to this work who I would like to thank.
Prof. Susagna Ricart, who passionately followed closely all my chemical journey and supported it all the way through, even when it seemed complicated to find a solution, or when I started what we thought would be "small" side projects, just for the sake of curiosity.
Prof. Jordi Farjas, I cannot express how thankful I am for the enthusiasm with which you welcomed every one of my ideas, for all the scientific discussions, and for being always available to answer in detail any of my questions or doubts. I have learnt so much from every one of our conversations.
I would like to thank Dr. Daniel Sanchez for the live interest during our collaboration, for the scientific discussions and the amusing chats that got us through the long nights at ALBA Synchrotron. I truly enjoyed working alongside you.
Prof. Elies Molins, for the invaluable help with the structural investigation of the metal propionates I synthesized during this thesis. I believe it was a very fruitful collaboration, and I really want to thank you for the time you dedicated to it. I gained precious knowledge from all of our conversations and discussions, which I would have never thought I'd acquire at the beginning of my thesis. Watching you skilfully choose, mount, measure the single crystal samples and then discussing on the resulting structures was a great experience!

This entire work was conducted at Institut de Ciència de Materials de Barcelona (ICMAB-CSIC). I would like to acknowledge the financial support we received throughout the years: from Spanish Ministry of Science and Innovation through the "Severo Ochoa" Programme

for Centres of Excellence in R&D (CEX2019-000917-S and SEV-2015-0496), SUPEREN-ERTECH and SUMATE projects (PID2021-127297OB-C21 and RTI2018-095853-B-C21, co-financed by the European Regional Development Fund, MCIN/ AEI/ FEDER,UE) and PTI+ TransEner CSIC programme for Spanish NGEU. Also, the support from the European Union for ULTRASUPERTAPE project (ERC-2014-ADG-669504), IMPACT (ERC-2019-PoC-874964) and SMS-INKS (ERC-2022-PoC2-10108199), SUPERQUMAP project (Cost Action CA 21144), OPERA (Cost Action CA 20116), NANOCOHYBRI (cost Action CA 16218) and from the Catalan Government with 2021-SGR-00440, 2017-SGR-1519, and Catalan energy network XRE4S (2018 XARDI 00002). Personally, I thank the Spanish Ministry of Science and Innovation for the FPI Fellowship I was granted for the PhD thesis, PRE2019-090621.

Moreover, I would like to thank both Soleil Synchrotron and ALBA Synchrotron for granting us the opportunity of five beamtimes throughout the years in which this thesis has been carried out.
My gratitude goes to Dr. Cristian Mocuta, beamline scientist of DiffAbs Beamline at Soleil Synchrotron, for the precious time you devoted to all of our unconventional ideas. You were always enthusiastically ready with a brilliant solution, but what I really appreciated the most was how you would truly explain the details answering all the "whys". The synchrotron experiments with you were simply exciting!
On a similar note, my gratitude goes to Dr. Eduardo Solano, for receiving us at the NCD-SWEET Beamline at ALBA Synchrotron and working alongside us in developing a complicated system and elaborate experiments, even through the difficult pandemic times.

Great part of the work described in this thesis would not have been possible without the help of Anna Crespi, Xavier Campos and Joan Esquius from the XRD Service Laboratory at ICMAB. I cannot thank you all enough for being always ready to solve my problems and to explain how to improve the measurement conditions, for all of the "urgent" measurements you were always able to squeeze in, and for simply being such great people.
I would also like to acknowledge the work of Dr. Bernat Bozzo and Dr. Ferran Vallès, from the Low Temperatures Laboratory at ICMAB, who conducted the physical characterization of the samples.

Now, I would like to dedicate some words to my colleagues and friends.
I am incredibly thankful to have been able to share part of this journey with Dr. Kapil Gupta. Besides the impressive TEM analysis conducted on the films, which without any doubt was key to the optimization of the entire process, I truly enjoyed all the scientific discussions and personal chats we shared.
Additionally, my colleague Aiswarya for helping me demonstrate, at the beginning of her thesis, the high reproducibility of the physical properties of the films and for performing more detailed characterization of the superconducting properties.

Special thanks goes to Jordi Aguilar, who was so unbelievably talented in developing the program for the data analysis and treatment of the synchrotron data. You made the analysis of that complex data so much easier, and it was a real pleasure to work beside you, even through the (very) long night shifts at Soleil and ALBA Synchrotrons.
Mariona, for the incredible amount of work you perform that keeps everything inside our labs running smoothly. But mostly, for becoming a great friend outside of the labs with whom I truly enjoy spending time with, for all the chats, the drinks, and the support.
My first colleagues, who quickly became dear friends. Juri, thanks for the incredible amount of explanations you gave me at the very beginning of my thesis, thanks for all the (later, way too bitter) morning coffees and for all the discussions we had, which really helped me get an understanding of this complicated project. Artur, thanks for all the lunches, the bouldering, the fun times hiking around Cataluña, but mostly thanks for being a great friend.
Pedro, despite starting working with you later on in my thesis, I feel incredibly lucky that I could share science with you. I have to admit, every time you came to my office with and began a question with "In your opinion as a chemist..." I was nervous about what crazily brilliant idea you would soon test in one of the labs! I am grateful for the scientific discussions, for you always making me think a step further of what I would do on my own, for all your knowledge, but especially, I'm so grateful we built a great friendship out of the labs.
Silvia, you arrived at ICMAB when my motivation was far from peaking, but your great enthusiasm for the project pushed me to pursue new objectives. Thanks for teaching me a lot on thermal analysis, but mostly for being there and becoming my dear friend, for all the times shared in Barcelona and for not doubting in having calls, even from across the ocean, when it was most needed.
Jordi, from being my mentor when I was only a young Masters student, to becoming an amazing friend, the journey with you during these last years has been incredible. I am so thankful for the great friendship we have, for your amazing support, the long talks and for sharing the experience of growing together.
Gloria, Lucy, Dani, Sara, and Silvia, you've all been there with unparalleled support, some of you from the beginning, some who I had the pleasure to meet later on. Nonetheless, I am thankful for all the beers, dinners, hikes, parties, activities, the laughs and the cries we have shared during these years. You are all irreplaceable.
Last among my friends, but definitely not the least, Diana. We started this adventure together and ended it together, and I can just say that nothing of this would have been possible without you. Thank you for being one of the best people I have the incredible blessing to be able to call my friend.

Un grazie speciale alla mia famiglia, la roccia alla base di tutto. Ai miei genitori, per avermi dato l'immenso privilegio di poter scegliere sempre il mio cammino, anche quando sceglievo quello piú difficile. A mia madre, per spingermi sempre a far uscire la parte emozionale in

questo mondo che ci vuole ogni giorni di piú delle macchine fredde e performanti. A mio padre, per spingermi invece a tenere sempre la mente aperta e a cercare una spiegazione razionale delle cose, qualitá fondamentali che ho potuto apprezzare in questo mio primo approccio alla scienza, quella vera. A mio fratello, per esserci sempre con grande allegria, supporto e felicitá, da vicino e da lontano. Finalmente, a nonna Gic, che mi riempie il cuore (e la pancia) con tantissimo amore ogni volta che sono lí.

Contents

Abstract **v**

Acknowledgements **vii**

List of Abbreviations **xvii**

List of Journal Articles **xxi**

1 Conceptual Background **1**

1.1 Introduction and motivation 1

1.2 Fundamental Concepts 5

1.2.1 High Temperature Superconductors 5

1.2.1.1 REBCO crystal structure 7

1.2.2 Coated Conductors fabrication 8

1.2.2.1 Liquid mediated growth methodologies 10

1.2.3 TLAG-CSD approach 12

1.2.4 Notions on crystal growth from a melt 17

1.2.4.1 Formation of a melt 17

1.2.4.2 Crystallization from a melt: supersaturation 21

1.2.4.3 Nucleation and crystal growth 24

1.2.4.4 Solubility of Y and other RE in [Ba-Cu-O] melts 30

2 Synthesis of metal propionates: structural and thermal investigation of their suitability in REBCO precursor solutions **41**

2.1 Objectives 42

2.2 Synthesis and characterization of a series of metal propionate powders 44

2.2.1 General characterization 44

2.2.2 Structural investigation 47

2.3 Establishing compatibility of thermal behaviour and decomposition pathways 57
2.3.1 Decomposition of metal propionate powders 58
2.3.2 Metal propionate films decomposition 66
2.4 Conclusions 75

3 Metal-organic precursor solution and nanocrystalline precursor films for TLAG 77
3.1 Objectives 78
3.2 Development of novel YBCO precursor solution 79
3.2.1 Fundamental requirements of ideal precursor solution 79
3.2.2 Optimization process 82
3.2.3 Microstructural analysis of nanocrystalline films 91
3.2.4 Effects of amine additive excess 97
3.2.5 Rheology and chemical analysis of optimized solution 103
3.2.6 Thermal analysis of optimized solution 111
3.2.7 Effect of different storage methodologies on solution ageing 115
3.3 Variation of the RE for the preparation of REBCO precursor solutions 122
3.3.1 Analysis of REBCO precursor solutions rheological properties 122
3.3.2 Thermal behaviour of REBCO precursor solutions 124
3.3.3 Microstructural analysis of nanocrystalline films 127
3.4 Exploring amine additives as feasible alternatives for YBCO precursor solutions 131
3.4.1 Understanding complexation scenarios and their effect on the nanocrystalline films 131
3.4.1.1 Alkyl Amines 135
3.4.1.1.1 Ethylenediamine 135
3.4.1.1.2 Triethylamine 137
3.4.1.1.3 Triethanolamine 138
3.4.1.2 Aromatic Amines 139
3.4.1.2.1 Pyridine 140
3.4.1.2.2 Pyridine and MEA mixture 143
3.4.1.2.3 Pyridine-4-carbaldehyde 145
3.4.1.2.4 1-(Pyridin-2-yl)ethan-1-one 147
3.4.1.2.5 2,6-Dimethylpyridine 149
3.4.1.2.6 N-methylpyridine-2-amine 151
3.4.2 Rheological analysis of selected solutions with different amine additives 154
3.4.3 Thermal behaviour of solutions with new amine additives 157
3.4.4 Microstructural analysis of films deriving from solutions with different amine additives 162
3.5 Conclusions 164

4 Kinetic control of the TLAG process: intermediate phases and epitaxy development 167
4.1 Objectives . . . 168
4.2 Analysis of $BaCO_3$ elimination . . . 169
4.2.1 Heating ramp effect: reducing coarsening of secondary phases . . . 170
4.2.2 Consequences of increasing dwell time . . . 173
4.2.3 Result of base pressure variation on film microstructure . . . 176
4.2.4 Evaluation of $BaCO_3$ phase evolution during the low-P_{O_2} heating . . . 178
4.2.5 Challenges of $BaCO_3$ elimination on thick films . . . 182
4.2.6 Influence of copper content on the $BaCO_3$ elimination process . . . 184
4.3 Towards the growth of high-performance YBCO superconducting films . . . 188
4.3.1 Promoting c-axis YBCO nucleation in films of eutectic liquid composition . . . 188
4.3.2 Preliminary studies on TLAG of thick YBCO films . . . 202
4.4 TLAG from films of various liquid compositions: influence of supersaturation 209
4.4.1 Introductory considerations on liquid supersaturation . . . 209
4.4.2 Determining the effects of different liquid supersaturation on YBCO epitaxial nucleation . . . 215
4.4.2.1 Epitaxy and the contribution of secondary phases . . . 215
4.4.2.2 Morphological features of film surface . . . 222
4.5 TLAG of REBCO (RE = Sm, Gd, Yb) films . . . 228
4.6 TLAG of YBCO films deriving from solutions with different amine additives 233
4.7 Conclusions . . . 238

5 Understanding the kinetic mechanism of TLAG through *in-situ* XRD experiments 241
5.1 Objectives . . . 242
5.2 *In-situ* analysis of the $BaCO_3$ elimination . . . 245
5.2.1 *In-situ* Phase Transformation Process . . . 248
5.2.1.1 *In-situ* Phase Transformation on Binary and Ternary films . 250
5.2.1.2 *In-situ* Phase Transformation on ternary films of different liquid composition . . . 257
5.2.2 Elimination of $BaCO_3$ through an *ex-situ* quench process . . . 266
5.3 *In-situ* analysis of TLAG kinetic mechanism . . . 274
5.3.1 Promoting c-axis nucleation: growth in full-liquid regions . . . 274
5.3.2 Variations of the TLAG kinetic mechanism due to differences in transient liquid supersaturation . . . 280
5.3.2.1 Coarsening phenomena as a consequence of the *in-situ* phase transformation process . . . 281

5.3.2.2 YBCO nucleation from films of different composition varying in the state of nanocrystalline precursor phases 284
5.4 Challenges of growing thick films in *in-situ* conditions 290
5.5 Conclusions 298

6 General Conclusions **301**

A Experimental Methodologies **307**
A.1 Characterization techniques for metal propionate powders 308
A.2 YBCO precursor solution rheological and chemical characterization 309
A.2.1 Rheological Properties 309
A.2.2 Chemical Analysis 310
A.3 Thermal Analysis on Powders and Films 312
A.4 Thin Film Deposition and Pyrolysis 313
A.5 Thin Film Characterization 314
A.5.1 Structural Characterization 315
A.5.2 Microstructural Characterization 318
A.5.3 Electrical Characterization 321

B Appendix to Chapter 2 **323**
B.1 Experimental Section 323
B.1.1 Materials and General Details 323
B.1.2 Synthesis of metal propionates 324
B.1.3 Characterization of initial products 327

C Appendix to Chapter 3 **355**
C.1 Solution preparation procedure 355
C.1.1 Optimized YBCO solution 355
C.1.1.1 Rheological characterization 356
C.1.1.2 Supplementary Information 358
C.1.2 Optimized REBCO solution 358
C.1.3 Solutions with different amine additives 359
C.1.3.1 Supplementary Information 360

D Appendix to Chapter 4 **361**
D.1 Experimental set-up for TLAG P_{O_2}-*route* experiments 361
D.2 Data Acquisition and Treatment 365
D.2.1 Quenched Films 365
D.2.2 Grown Films of YBCO and other REBCO 368

D.2.2.1 Determination of secondary phase contribution 368
D.2.2.2 Surface morphology quality analysis 369
D.3 Supporting Information 373

E Appendix to Chapter 5 **377**
E.1 Experimental methodologies for *in-situ* synchrotron XRD experiments 377
E.1.1 Technical specifications and experimental set-up at DiffAbs and NCD-SWEET beamlines 377
E.1.2 Data acquisition and data treatment 381
E.2 Supplementary Information 387

Bibliography **389**

List of Abbreviations

YBCO	$YBa_2Cu_3O_{7-\delta}$
RE	Rare Earth element
REBCO	$REBa_2Cu_3O_{7-\delta}$
SmBCO	$SmBa_2Cu_3O_{7-\delta}$
GdBCO	$GdBa_2Cu_3O_{7-\delta}$
YbBCO	$YbBa_2Cu_3O_{7-\delta}$
HTS	High-temperature superconductors
CCs	Coated Conductors
PLD	Pulsed laser deposition
PVD	Physical Vapor Deposition
MOCVD	Metal organic chemical vapor deposition
TFA-MOD	Trifluoroacetate metal organic deposition
CSD	Chemical solution deposition
TLAG	Transient liquid assisted growth
SMES	Superconducting Magnetic Energy-Storage
FCLs	Fault Current Limiters
IBAD	Ion Beam-Assisted Deposition
RABiTS	Rolling-Assisted Biaxially Textured Substrate
YSZ	Yttria-Stabilized Zirconia
LMO	Lanthanum Manganite
APC	Artificial Pinning Center
MTG	Melt-Textured Growth
LPE	Liquid Phase Epitaxy
HLPE	Hybrid Liquid Phase Epitaxy
QLL	Quasi-Liquid Layer
ICP-AES	Inductively Coupled Plasma Atomic Emission Spectrometry
SRL-CP	Solute-Rich-Liquid Crystal-Pulling growth
ERC	European Research Council

SUMAN	Superconducting Materials and Functional Nanoengineered structures
SEM	Scanning electron microscopy
BSED	Back-scattered electron
RT	Room temperature
BM	Ball milling
SC	Single crystal
PXRD	Powder X-ray diffraction
Y_2O_3	Yttrium oxide
CuO	Copper oxide
$BaCO_3$	Barium carbonate
HProp	Propionic Acid
MeOH	Methanol
EA	Elemental Analysis
$Cu(Prop)_2$	Copper propionate
$Ba(Prop)_2$	Barium propionate
$Y(Prop)_3$	Yttrium propionate
$Ce(Prop)_3$	Cerium propionate
$Sm(Prop)_3$	Samarium propionate
$Gd(Prop)_2$	Gadolinium propionate
$Y(Prop)_3$	Ytterbium propionate
BaC_2O_4	Barium oxalate
MEA	Monoethanolamine
OM	Optical microscopy
TEM	Transmission electron microscopy
STEM-HAADF	High-angle annular dark field scanning transmission electron microscopy
EELS	Electron energy loss spectroscopy
HR-TEM	High-resolution transmission electron microscopy
STEM-EDX	Energy dispersive X-ray spectroscopy scanning transmission electron microscopy
XRD	X-ray diffraction
GIXRD	Grazing-incidence X-ray diffraction
FIB	Focused ion beam
NMR	Nuclear magnetic resonance
EPR	Electron paramagnetic resonance
FTIR-ATR	Fourier-transform Infrared Spectroscopy using attenuated total reflectance
TG-FTIR	Thermogravimetric analysis coupled to Fourier-transform

	infra-red spectroscopy
EGA	Evolved gas analysis
RE_2O_3	Rare earth oxide
En	Ethylenediamine
Et_3N	Triethylamine
TEA	Triethanolamine
Py	Pyridine
EWG	Electron withdrawing group
EDG	Electron donating group
Ar	Argon
T_E	$BaCuO_{2(s)}$-$CuO_{(s)}$ eutectic melting
T_P	YBCO peritectic melting
T_{ins}	YBCO instability line
FWHM	Full width at half maximum
P_{O_2}	Oxygen partial pressure
P_{CO_2}	Carbon dioxide partial pressure
(211)	Y_2BaCuO_5
(225)	$Y_2Cu_2O_5$
SFs	stacking faults

List of Journal Articles

Published journal articles:

1. Queraltó, A., Banchewski, J., Pacheco, A., Gupta, K., Saltarelli, L., Garcia, D., Alcalde, N., Mocuta, C., Ricart, S., Pino, F., Obradors, X., and Puig, T. Combinatorial Screening of Cuprate Superconductors by Drop-On-Demand Inkjet Printing, ***ACS Applied Materials & Interfaces*** 2021 13 (7), 9101-9112, DOI: 10.1021/acsami.0c18014

2. Barusco, P., Granados, X., Saltarelli, L., Fournier-Lupien, J.-H., Lacroix, C., Ben Saad, H., Sirois, F., Vlad, V.R., Calleja, A., Grosse, V., Puig, T., and Obradors, X., Chemical Solution Deposition of Insulating Yttria Nanolayers as Current Flow Diverter in Superconducting GdBa2Cu3O7-x Coated Conductors, ***ACS Omega*** 2022, DOI: 10.1021/acsomega.1c05352

3. Rasi, S., Queraltó, A., Banchewski, J., Saltarelli, L., Garcia, D., Pacheco, A., Gupta, K., Kethamkuzhi, A., Soler, L., Jareño, J., Ricart, S., Farjas, J., Roura-Grabulosa, P., Mocuta, C., Obradors, X., Puig, T. Kinetic Control of Ultrafast Transient Liquid Assisted Growth of Solution-Derived YBa2Cu3O7-x Superconducting Films, ***Advanced Science***, 2022, 9(32), 2203834., DOI: 10.1002/advs.202203834

4. Saltarelli, L., Gupta, K., Rasi, S., Kethamkuzhi, A., Queraltó, A., Garcia, D., Gutierrez, J., Farjas, J., Roura, P., Ricart, S., Obradors, X., Puig, T. Chemical and Microstructural Nanoscale Homogeneity in Superconducting YBa2Cu3O7-x Films Derived from Metal-Propionate Fluorine-free Solutions. ***ACS Applied Materials & Interfaces***, 2022, 14(43), 48582-48597, DOI: 10.1021/acsami.2c11414

5. Queraltó, A., Sieger, M., Gupta, K., Meledin, A., Barusco, P., Saltarelli, L., de Palau, M., Granados, X., Obradors, X., Puig, T. Transient liquid assisted growth of superconducting YBa2Cu3O7-x films based on pulsed laser deposition, ***Superconductor Science and Technology***, 2022, 36(2), 025003, DOI: 10.1088/1361-6668/acaad3

"Dai diamanti non nasce niente
dal letame nascono i fior"

Fabrizio De André

1

Conceptual Background

1.1 Introduction and motivation

Following decades of worldwide exploitation of fossil fuels, the scientific community is now confronted with the compelling need for a global transition towards renewable energy sources. Several solutions have been proposed and the development of novel functional materials with appealing properties has experienced an exponential boost, with opportunities for possible applications in clean energy production, harvesting, storage and transport. Concerning the latter point, superconducting materials are in the spotlight due to their distinguished characteristic of lossless electrical transport. Since 1911, when Kamerlingh Onnes discovered no electrical resistance in mercury below 4.2 K, it was clear that this would lead to numerous technological breakthroughs and a wide variety of possible features, as the same Onnes initially predicted. Nonetheless, the complete understanding of the phenomenon of superconductivity required several years of theoretical studies. A major contribution came from London and Shubnikov in the 1930s, who defined the magnetic behaviour in superconducting materials and made the fundamental distinction between type-I and type-II superconductors: the former displays mainly superficial current flow capacity and superconducting properties are lost at low fields, while the latter are able to transport bulk supercurrents up to high magnetic fields. It was in the 1950s when Abrikosov led to the full conception of the quantized vortices in the type II superconductors, opening the chase for superconducting materials with unprecedented properties.

The 30 years following that have seen the rise of numerous superconducting systems, with the predominance of niobium-based alloys due to their unmatched performance properties: NbTi,

Nb_3Sn, and Nb_3Ge, which respectively present critical temperature (T_c) at 9 K, 18 K, and 23.2 K [1, 2], could be successfully included in wire fabrication and, through their application in the production of magnetic coils, led to the irruption of superconducting materials on the market. These low-temperature superconductors (LTS) were prime competitors for medical purposes and in basic research facilities, where the coils are employed still nowadays in magnetic resonance imaging (MRI), nuclear magnetic resonance (NMR) devices, and in particle accelerators or high magnetic field laboratories. However, the need for expensive liquid helium-based refrigeration systems characteristic of these alloys has limited their widespread, and the hypothesis of the replacement of conventional electric technology centred on copper and iron by LTS was promptly discarded.

1986 was the revolutionary year, when Georg Bednorz and Alex Müller reported superconductivity at 30 K for the $Ba_xLa_{5-x}Cu_5O_{3-y}$ perovskite structure [3], awarded with the Nobel prize in Physics a year later. This marked the dawning of high temperature superconductors (HTS), resulting in the synthesis of various other perovskite compounds which exhibited superconducting behaviour at temperatures above liquid nitrogen (77 K). Among those, $YBa_2Cu_3O_{7-\delta}$ (YBCO) generated excitement in the superconducting community, increasing T_c to 93 K [4]. Soon, similar systems in which other rare earth elements (RE) substituted yttrium were developed, namely $REBa_2Cu_3O_{7-\delta}$ (REBCO), and several other compounds together with the record-breaking $Hg_2Ba_2Ca_2Cu_3O_x$ ($T_c = 130$ K), were announced [5].

During the following decades, the increase of global interest in HTS led to numerous research grants being awarded on this research topic and major discussions on the substitution of the commonly employed copper cables with HTS-based wires, especially following the successful inclusion of the $(Bi,Pb)_2Sr_2Ca_2Cu_3O_x$ (Bi-2223) and subsequently MgB_2 superconductors in multifilamentary wires [6–9]. These were obtained through the powder-in-tube (PIT) process, in which an external metallic tube (generally, silver, copper or bimetallic silver/stainless steel alloys) is containing the brittle ceramic superconductor sintered powders in its core [10]. Despite the innovation deriving from this fabrication method, it was not adaptable to most of the HTS materials, as these highly anisotropic systems require high textured growth structures to display high performances. This challenge was overcome by the development of the second generation tapes (2G), also known as coated conductors (CCs), in which the biaxially textured YBCO or REBCO superconductor layer is grown on a flexible metallic structure comprising buffer layers to reduce the lattice mismatch. The technological breakthrough generated by CCs laid the foundations to their entrance on the market [8, 11–13]. HTS layers are nowadays successfully produced with lengths of hundreds of meters and competitive properties ranging between 500-700 A/cm $\cdot$ width, making the major widespread of this technology a realistic feasibility and, together with it, the advance towards more sustainable solutions for energy harvesting and transportation [14–18].

Currently, the limiting factor towards a general use of CCs is the elevated production costs

of the available technology. Techniques such as Pulsed Laser Deposition (PLD) [17, 19, 20], Metal Organic Chemical Vapour Deposition (MOCVD) [21–23], Electron Beam Physical Vapor Deposition (EBPVD), metal evaporation (ME) [24–27], sputtering [28, 29] are amongst the most commonly employed for the production of the HTS layer, facing the downside of requiring expensive vacuum equipment and intrinsically slow diffusion kinetics. In the last decades, variations of such techniques were developed to improve the growth rates of the superconducting layer: in this framework, high rate PLD (PLD-HR) [30–33] and liquid-assisted PLD (PLD-LAP) [34] were the most appealing solutions [35]. Nonetheless, the emergence of chemical solution deposition (CSD) set the premise for a cost-effective option for the production of REBCO superconductors. This methodology utilizes inexpensive metal-organic chemical solutions whose metal cations components, following several annealing processes, lead to the formation of final superconducting material. The renowned trifluoroacetate metal-organic decomposition (TFA-MOD) route was the first to arise in the late '80s, and is still nowadays the CSD-based technique implemented in industrial processes [15, 36–45]. However, the solid-solid growth mechanism characteristic to the TFA-MOD route shows low growth rates (1-5 nm s^{-1}), with the additional disadvantage of liberating the highly toxic hydrofluoric acid (HF) as sole waste product. This has favoured the development of a more environmentally friendly CSD-based method through the complete elimination of fluorine from the system, thus developing fluorine-free metal-organic chemical solutions [46–50]. In this context, the combination of the cost-effectiveness of CSD with the fast crystallization kinetics of liquid-assisted growth processes have led to the development of the pioneering growth approach for REBCO systems deriving from fluorine-free chemical solutions in our research group, namely transient liquid assisted growth based on chemical solution deposition (TLAG-CSD). Unprecedented critical current density values in the range of 2-5 MA cm^{-2} and ultrafast growth rates beyond 100 nm s^{-1} were demonstrated through TLAG-CSD in the first years of its progress [51–55], showing its feasibility for industrial applications, given the compatibility of the CSD methodology with high-throughput and scalable deposition techniques.

Nonetheless, difficulties regarding the attainment of films of high thickness, indisputable requirement in the industrial fabrication of REBCO CCs, the comprehensive understanding of the TLAG mechanism and the nucleation control of the ultrafast growth demanded for further investigation and advance of the innovative TLAG-CSD approach. This led to the results presented in this thesis, in which a novel solution formulation was found pivotal for the achievement of several fundamental features the nanocrystalline precursor films must exhibit for an optimal epitaxial growth of YBCO through TLAG. Detailed analysis of this new growth method was conducted on transient liquid of different compositions, obtained through the simple variation of the stoichiometry of the initial chemical solution. This provided unprecedented and interesting insights on how liquid supersaturation is controlling the kinetic mechanism of TLAG.

The different topics discussed in this thesis will be, thus, presented in the following order:

- The remaining sections of the current **Chapter 1** will illustrate the fundamental concepts regarding superconductivity, the YBCO triple-perovskite structure and its global significance, current advances in HTS wire fabrication with a focus on melt-textured based processes, and state-of-the-art knowledge of TLAG.
- **Chapter 2** will explain the choice of employing synthetic procedures to prepare metal propionates of the cations needed for YBCO and REBCO growth through the TLAG-CSD approach, entering in detailed characterization techniques and a comprehensive study of their thermal behaviour to assess their compatibility with the proposed application.
- **Chapter 3** is devoted entirely to the novel solution formulation and optimization, covering the complete study which led to a profound understanding of the solution system and the role and behaviour of the amine additive employed to enhance its rheological properties. Solutions of various stoichiometries were employed in the preparation of films which will lead to transient liquids of different compositions during the growth of YBCO through TLAG. Moreover, variations of the optimized solution led to the possibility of tuning solution properties depending on the desired results through the use of a plethora of different amine additives or widening the possibilities to several RE other than the sole Y.
- **Chapter 4** analyzes the growth process of YBCO and other REBCO systems through TLAG, identifying the fundamental processing parameters that must be strictly controlled. The initial analysis of the elimination of the limiting phase of the process, barium carbonate, will evince the facile removal of this phase once governing the significant kinetic factors. Subsequently, the pivotal control of supersaturation in TLAG demonstrated the feasibility of high-performance films of different liquid composition, of increasing thickness and of various REBCO systems.
- **Chapter 5** examines the complex kinetic mechanism of TLAG through an analysis of the growth process using *in-situ* XRD experiments performed in synchrotron facilities. An evaluation of the complications arising from the challenging experimental methodology, possible solutions, and fundamental aspects of TLAG is presented, leading to meaningful knowledge on this ground-breaking growth process.

1.2 Fundamental Concepts

The current section has the aim of providing the reader with the theoretical background for a comprehensive understanding of the results presented in this thesis. Historical development and essential details on HTS and CCs fabrication will be illustrated, with a focus on the REBCO crystalline perovskite-type structure, being the superconducting compound of interest in the current work. An overview of the fundamental concepts on crystal growth from a melt is crucial since TLAG is, as evinced by its name, a liquid-assisted growth methodology. Finally, the kinetic mechanism of TLAG will be explained and the characteristic features of this innovative growth approach for REBCO superconductors will be presented.

1.2.1 High Temperature Superconductors

Besides offering unique opportunities towards the enhancement of the efficiency of electrical transport, superconducting materials may be employed in a wide variety of mechanical devices with superior performance to the conventional technologies, such as power cables, superconducting magnetic energy-storage (SMES) devices, transformers, fault current limiters (FCLs), equipment working at ultra-high magnetic fields (fusion reactors, particle accelerators, NMR) [9, 35], transport (motors, ships, levitating trains, electrical airplanes) [56] and thermoelectric technologies [57].

The initial enthusiasm generated by the discovery of superconductivity with the idea of implementing electric power and magnetic applications through the use of LTS such as NbTi or Nb_3Sn faded rapidly, despite these type of superconductors are still nowadays employed in the production of magnetic coils of unmatched performance for medical and scientific applications (MRI, particle accelerators, high-field magnets) [8]. The main reason was the low cost-effectiveness deriving from the liquid helium-based refrigeration system required for these materials, unattractive to industrial investors for its additionally complex implementation.

The announcement of HTS, starting with Bednorz and Müller in 1986 with the $Ba_xLa_{5-x}Cu_5O_{3-y}$ perovskite (T_c = 30 K) [3] and followed a year later by Wu *et al.* [4] with $YBa_2Cu_3O_{7-\delta}$ (YBCO) with T_c = 93 K, was the breakthrough the superconducting community awaited, and novel opportunities promptly unfolded. Such elevated critical temperatures were enabling the use of liquid nitrogen (boiling point at 77 K) as a coolant, with enormous difference cost- and abundance-wise compared to the previously required liquid helium.

For high magnetic field applications, the choice of a superconducting material relies on its performance under the externally applied magnetic field, measured as critical current density (J_c). HTS materials, which fall into the category of type-II superconductors, present distinct behaviour depending on the applied magnetic field (H), with the corresponding subdivision in normal, mixed (superconducting), and Meissner state according to the critical field values, as

displayed in the *H-T* phase diagram represented in Fig. 1.1. Below the value of lower critical field, H_{c_1}, the material is in the Meissner phase, experiencing screening currents on the surface which result in the complete expulsion of the magnetic field [58] and, thus, perfect diamagnetic behaviour. Between this critical field value and the upper critical field, H_{c_2}, the superconductor enters a mixed state, also known as Shubnikov phase: here, the magnetic field penetrates in the material in form of quantized flux lines (vortices) originating from circular superconducting currents which flow around the vortex core. The high values of H_{c_2} in type-II superconductors ($H_{c_2} \gg H_{c_1}$) are at the origin of the distinguished feature of this kind of materials of lossless transport of large currents, and capability of operating at high magnetic fields.

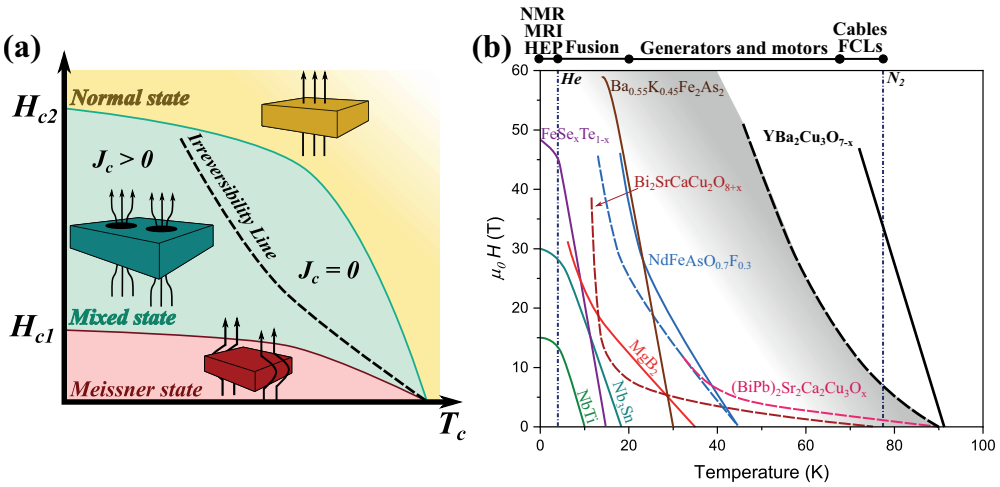


FIGURE 1.1: (a) Representation of the *H-T* dependency in type-II superconductors, displaying the different possible states corresponding to the applied magnetic field. Exemplary irreversibility field line (shown as black dashed line) is indicating the applied magnetic field above which loss of critical current density is exhibited. (b) Comparison of *H-T* values for several type-II superconductors (LTS and HTS), showing the upper critical fields, corresponding to H_{c_2} in (a) (solid lines), and irreversibility field lines, H_{irr} (dashed lines). Operating temperatures of liquid He and liquid N_2 are shown as dark blue dashed line, and major applications are indicated at the top of the graph, corresponding to their operating region. Adapted from [8, 35, 59].

For this to be valid, however, the vortices must remain pinned. When a current (J) is applied to the material, a Lorentz-like force (F_L) is generated and acts on the vortices similarly to a magnetic field acting on a moving charge [60], according to:

$$\vec{F}_L = \vec{J} x \vec{B} \tag{1.1}$$

The pinning force, (F_P), of the vortices is, conversely, acting against the F_L. The movement of the vortices caused by the F_L exhibits as a consequence energy dissipation. The maximum current density flowing in a superconductor displaying no dissipation of energy is defined as critical current density, J_c. At elevated values of applied magnetic fields and temperature, the inability of pinning the vortices results in $J_c = 0$ above the value of irreversibility field H_{irr} (dashed line in Fig. 1.1(a)). The upper boundary delimiting the region of lossless electrical transport of HTS in the region of the *H-T* phase diagram is, thus, defined by the value of H_{irr}. Fig. 1.1(b) reports both upper critical fields, H_{c_2} (as solid lines), and irreversibility fields, H_{irr} (dashed lines), of several type-II superconductors, including LTS and HTS compounds. From this graph, the reason behind the ferment of the superconducting community over YBCO is evident: the H_{irr} reaches liquid N_2 temperature in this cuprate-based HTS[1], marking a wide range of *H-T* in which high-field applications (above 10 T) are feasible.

1.2.1.1 REBCO crystal structure

HTS materials such as REBCO and other cuprates display highly anisotropic crystal structures. Representation of the YBCO unit cell is shown in Fig. 1.2. It crystallizes in a triple-perovskite structure composed by three ABX_3 pseudocubic cells: A are the Ba^{2+} or the Y^{3+} cations, with the former occupying the central position of the first and third pseudocubic cells, whereas the latter occupying the same position in the second cell. For the case of REBCO, RE^{3+} may be any rare earth element other than Ce, Tb, or Pr [60]. Conversely, B is the Cu^{2+}/Cu^{3+} cation, placed on the vertices. BaO planes are dividing the alternating CuO chains and the CuO_2 planes. Oxygen deficiency in the structure is a consequence of the presence of the former distribution. For example, in $YBa_2Cu_3O_{7-\delta}$, for values of δ between 0 and 1, the structure varies between presenting full oxygen doping or oxygen-deficient. A tetragonal structure is formed in the case of oxygen-deficiency ($\delta = 1$), with $a = b$, and the material showing no superconducting behaviour. Superconductivity arises in correspondence to oxygen incorporation in the structure, for $0 \leq \delta \leq 0.65$ [61], with a transition to an orthorhombic structure ($a \neq b$). The superconducting transition with maximum T_c value of 93 K in YBCO is achieved in the specific oxygen doping range of $\delta \approx 0.05$-0.07 [62]. The step of oxygen doping is of crucial importance during YBCO (or REBCO) fabrication for superconducting applications. In the optimally doped regime, the occupancy of the oxygen vacancies allows for the coexistence of the two different aforementioned orderings of the Cu-O bonds. Superconducting currents are able to flow along the stacked CuO_2 planes, which are provided with charge carrier density by the CuO chains, part of the charge reservoirs BaO-CuO-BaO structure. The origin of the high anisotropy of YBCO and other REBCO is found in the alternation of CuO_2 planes and CuO chains, with the critical current flowing in the former (*a-b* planes) surmounting the one in the c-axis direction. The unique feature of superconductivity along the CuO chains distinguishes

[1] $Bi_2Sr_2CaCu_2O_8$ (BSCCO) and $(Bi,Pb)_2Sr_2Ca_2Cu_3O_x$ both display values of H_{c_2} above 100 K and are not shown here.

REBCO from other HTS. Moreover, major drops in critical current density were observed at the grain boundaries of misoriented crystallites [63], thus making a high degree of epitaxy of YBCO a fundamental requirement for its application in CCs.

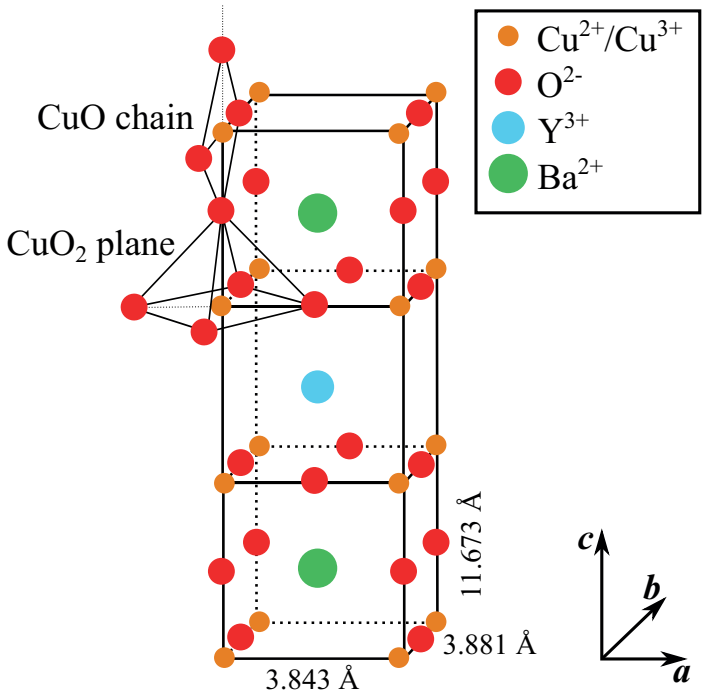


FIGURE 1.2: Representation of the crystalline structure of $YBa_2Cu_3O_{7-\delta}$ in its orthorhombic phase, which crystallizes in the *Pmmm* space group. CuO chains and CuO_2 planes are illustrated for clarity. Lattice parameters are obtained from the International Centre for Diffraction Database (ICDD) [64].

1.2.2 Coated Conductors fabrication

As mentioned above, the high anisotropy of YBCO and REBCO perovskite-like structures demanded for the development of methods to incorporate these materials in wire fabrication while ensuring their biaxial texture with low misalignment at the grain boundaries in order to prevent critical current percolation loss.

The powder-in-tube (PIT) approach of the 1st generation wire fabrication was only successful in the cases in which the superconducting behaviour of the compound employed is not influenced by grain misalignment. In this method, a powder of the superconducting material is inserted in an external tube of silver, copper or bimetallic silver/stainless steel alloys, and several rolling and annealing processes lead to the final multifilamentary wire [7, 10, 65].

The breakthrough towards the feasible use of YBCO and REBCO derived from the development of 2nd generation of superconducting wires and cables, namely Coated Conductors

(CCs), in which texture was successfully transferred to flexible metallic substrates of conventional thickness of $\approx 100\ \mu$m. The two deposition methods which are widely used to achieve this are ion beam-assisted deposition (IBAD) [66] and rolling-assisted biaxially textured substrate (RABiTS) [67]. Tapes produced through IBAD are obtained by substrate bombardment with an ion beam while simultaneously employing a physical vapor deposition (PVD) coating, allowing for a biaxial texture layer on top of a polycrystalline layer. These are composed by a hastelloy polycrystalline metallic substrate, covered with aluminum oxide (Al_2O_3) and yttria (Y_2O_3) on which biaxially textured buffer layers are deposited. Generally, the latter are magnesium oxide (MgO) or Y_2O_3-stabilized ZrO_2 (YSZ), topped with either lanthanum manganite ($LaMnO_3$, LMO) or cerium oxide (CeO_2) to ensure close lattice mismatch with the REBCO layer. In the case of CCs produced by RABiTS, the technique employs thermomechanical machinery to impart texture to NiW metallic substrates, followed by vapor deposition of buffer layers of Y_2O_3, YSZ and CeO_2, on which the REBCO layer is grown. A schematic representation of the typical Coated Conductor architecture is displayed in Fig. 1.3. The attainment of flexibility with the simultaneous low-lattice mismatch of the final buffer layer with the superconducting material of choice (generally, REBCO) enabled the commercial widespread of both methodologies and the feasibility of the use of YBCO and REBCO superconductors in applications.

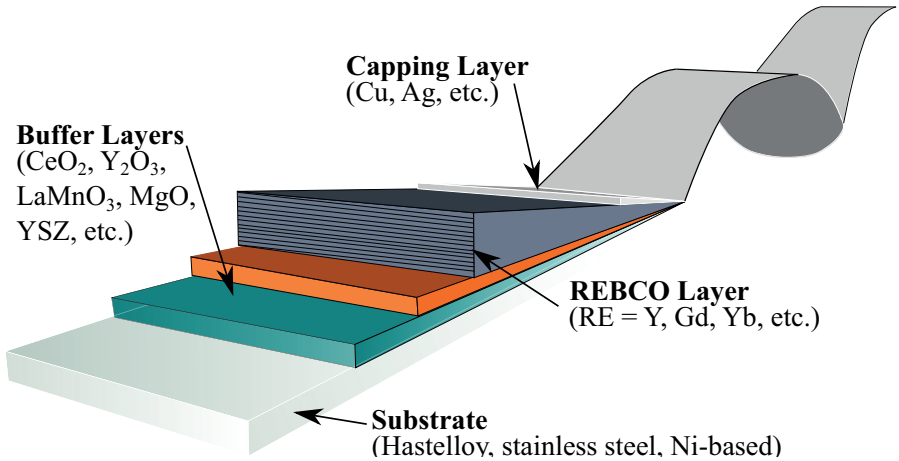


FIGURE 1.3: Schematic representation of the generic architecture of a Coated Conductor, showing the different composition of the layers.

The final REBCO layer is obtained through several deposition methods, with possibility of it being *in-situ*, if the growth occurs simultaneously to film deposition, or *ex-situ*, occurring separately. Most commonly used *in-situ* deposition techniques are MOCVD and PLD, while CSD approaches have gained popularity as promising *ex-situ* deposition technique for REBCO systems, generally employing the TFA-MOD route [40, 68] and Reactive Co-Evaporation and

Direct Reaction (RCE-DR), the latter established in the last decade [69]. The main drawback of the growth of REBCO through the aforementioned techniques is their low throughput, with growth rates generally limited below 10 nm s^{-1} due to the reduced atomic diffusivity in the vapor-solid or solid-solid reaction mechanisms these techniques rely on [35, 70, 71].
The necessity of increasing the rate of production, and thus reduce the cost, of the REBCO layer has promoted the development of liquid mediated growth processes, to favour the widespread of more commercially accessible HTS-based technologies.

1.2.2.1 Liquid mediated growth methodologies

Several solutions are behind the path towards the reduction of the current price of commercially available CCs. At present, companies have implemented strategies such as a general increase of J_c (possibly through introduction of artificial pinning centers, APC) [72], increase of the thickness of the REBCO film (and consequently, I_c) [15], and implementation of simultaneous multiple manufacturing methods (i.e. multi-lanes in roll-to-roll fabrication processes or multi-plumes in PLD) [73]. Nonetheless, the intrinsic characteristics of the employed low growth rate methodologies are inevitably limiting the improvement of the fabrication throughput. With the aim of enhancing this factor, the rate of the growth method itself must be significantly increased. This is where the utilization of liquid mediated growth techniques has opened novel possibilities and has captured the interest of industrial partners.
In liquid mediated growth methods, the diffusivity of the cation in the melt is fundamentally higher. In this direction, strong efforts were made in the last decade of the 1990s and early 2000s to determine the solubility of Y and other RE in the BaO-CuO melt through a wide variety of different liquid-based growth techniques [74–80], with the aim of understanding and developing methods to enhance the growth rates of such materials. Kursumovic *et al.* determined the yttrium diffusivity in a (3BaO:5CuO)[2] melt at 970 ºC to be as high as $4 \cdot 10^{-10} m^2 s^{-1}$ [77] through melt-textured growth (MTG). In this technique, employed to obtain bulk YBCO crystals, YBCO crystallization is carried out through formation of an incongruent melt of [Y_2BaCuO_5 ((211) phase) + liquid], which is then undercooled to temperatures below the peritectic one of YBCO. Thus, YBCO nucleates heterogenously given the presence of a seed crystal at higher temperature and its nucleation is driven by the supersaturation of such melt [74]. The potential feasibility of increased growth rates could be demonstrated through MTG techniques for YBCO, predicting growth rates of 200-800 nm s^{-1} for single crystals [81] and above 1000 nm s^{-1} for filaments [82].
The findings relative to the techniques presented up to this moment for the preparation of bulk YBCO crystals evidenced that the development of textured YBCO thin films for superconducting applications required for novel techniques with similar approaches. Liquid Phase Epitaxy (LPE), a technique earlier utilized for the production of composite semiconductor materials

[2] The (Ba:Cu) ratio is seen to have a great effect on the solubility of Y or RE in the melt. A detailed discussion regarding this topic will be provided later on in this chapter.

such as GaAS and InP, was thus adapted to the YBCO fabrication. As displayed in Fig. 1.4(a), this growth method relies on the use of a crucible containing a [BaO-CuO] melt at high temperature in which Y_2O_3 or YBCO are placed as a solute. A seed crystal is placed on a rotating holder[3] and put into contact with the melt, favouring YBCO growth through a temperature

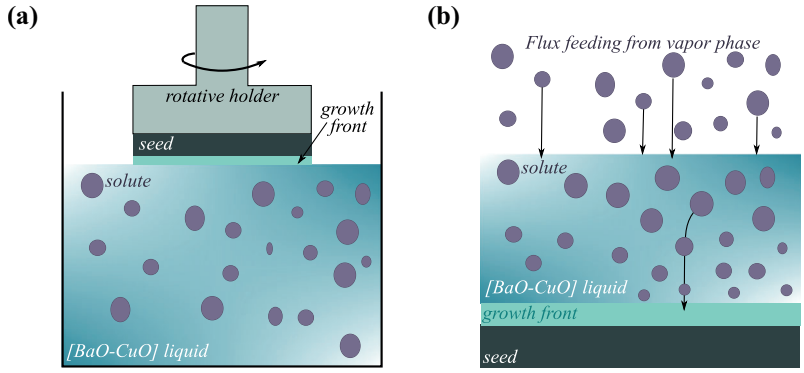


FIGURE 1.4: Representation of growth mechanism for the YBCO thin film through (a) LPE and (b) HLPE. The [BaO-CuO] melt obtained at high temperature is supersaturated with a solute, either YBCO or Y_2O_3 (containing Y). Heterogeneous nucleation and successive growth is obtained through a seed crystal. Adapted from [54].

gradient given the undercooling at the growth front, thus a variation in the supersaturation. Growth rates of up to 50 nm s^{-1} could be achieved through this technique [77, 79, 83]. However, strong limitations of this technique are: the highly corrosive nature of the melt, causing significant reactivity issues with the crucibles, the high processing temperatures, generally above 1000 ºC, and the complicated tuning of the melt supersaturation at the growth front. To surmount these difficulties, a variation of LPE, namely Hybrid Liquid Phase Epitaxy (HLPE), was successively developed. In this case, as visible in Fig. 1.4(b), a layer of the [BaO-CuO] melt is formed. Through PLD, an Y-rich solute is fed to it from a vapour phase. The greatest improvement is the possibility of controlling the supersaturation of the liquid through the regulation of the pulse frequency of the laser. YBCO was successfully grown through HLPE, with growth rates of 12-35 nm s^{-1} and displaying physical properties up to 1.2 MA cm^{-2} [80, 84].

Amongst other techniques employing a liquid-mediated growth in which the solute is fed from a flux through PLD or MOCVD, one may find Pulse-Laser Tri-Phase Epitaxy (TPE) [85, 86] and Vapor-Liquid-Solid (VLS) growth [87]. Recently, two novel techniques have emerged in the CCs fabrication scenario. In 2014, Moon *et al.* from SuNAM Co. Ltd [69] have developed the Reactive Co-Evaporation and Direct Reaction (RCE-DR) to fabricate GdBCO CCs through

[3] Rotation of the holder enhances the production of supersaturated liquid at the growth front due to convection.

a two-steps process which involves, first, fast co-evaporation of the precursor films in low T-P_{O_2} conditions, followed by annealing of the films at elevated temperature and high P_{O_2}. This emerged as the highest throughput method employed in the commercial framework. Lately, in 2021, Feighan *et al.* reported on the liquid-assisted processing (LAP)-PLD, a variation of the classical PLD which simultaneously overcomes the problem of both slow growth rates and inclusion of pinning centers. The key to this technique is the use of a non-stoichiometric target composition which generates a thin liquid layer during the PLD deposition and the REBCO film growth, enhancing the growth rate and enabling the self-assembly of APCs as fine nano-columns [34].

Despite all the aforementioned liquid-assisted techniques to be promising towards the enhancement of the CCs fabrication throughput, the use of ultrahigh vacuum methodologies (in the range 10^{-8}-10^{-12} bar) sets a serious challenge for a cost-wise reduction. Additionally, these techniques operate near thermodynamical equilibrium conditions, limiting the working windows to confined temperature ranges, employing growth temperatures close to 1000 ºC and through the disadvantageous use of corrosive melts for timely processes.

A breakthrough for feasible low-cost and high-throughput CCs fabrication derived from the work conducted in our research group, where the TLAG-CSD approach was developed [53]. This novel growth technique relies on the inexpensive CSD methodology coupled with the out-of-equilibrium growth kinetics of a transient liquid-assisted process, demonstrating the possibility of unprecedented growth rates beyond 1000 nm s^{-1} in a large window of high epitaxy and compatibility of APCs inclusion through the use of pre-formed nanoparticles[4]. A detailed explanation of the growth mechanism in TLAG will be given in the following section. Additionally, considering the liquid-assisted nature of the process, for a comprehensive understanding of the work conducted in this thesis, fundamental concepts on crystallization processes from a melt are believed to be necessary, and will be provided in the final part of this chapter.

1.2.3 TLAG-CSD approach

The theory at the origin of the innovative growth method of TLAG is the following: the global necessity for a cost-effective growth methodology for HTS[5] fabrication led to the implementation of an industrially suitable and scalable chemical solution deposition-based technique. This innovative method relies on an out-of-equilibrium, kinetically-driven liquid-assisted ultrafast growth process. The combination of these two key aspects makes TLAG competitive and appealing, given its use of inexpensive chemical solutions together with growth rates exceeding by factors 10-100 the reported values for commonly employed fabrication methods in the current industrial framework.

[4] This particular aspect will not be described in this work, as it is the focus of the PhD thesis of D. Garcia carried out during the same years as the present one.

[5] In the case of TLAG, YBCO and other REBCO have been implemented.

The TLAG-CSD approach may be summarized in four major points which, as demonstrated in the following chapters of this thesis, are each of fundamental importance for the attainment of high-performance YBCO (or other REBCO) superconducting films.

1. **Preparation of a metal-organic precursor solution:** metal-organic precursor salts of the three cations required for the formation of the final REBCO perovskite-type structure are mixed in an appropriate solvent (or mixture of solvents) in the desired concentration. The relation between high solution concentration and increased film thickness is renowned, and in order to reach more elevated concentration of the precursor solutions, additives may be employed. Solutions must be well dissolved to ensure the correct stoichiometry of the final REBCO is attained, and must ideally present long shelf-life, an appealing feature for the industrial implementation of any CSD-based method. Generally, the choice of employing commercially available metal-organic precursor salts for the preparation of the solution is preferred. However, throughout the work conducted in this thesis, the advantages of performing their synthesis in-house will be presented and thoroughly motivated (specifically, in Chapter 2).

2. **Deposition and pyrolysis:** the prepared chemical solution is deposited via spin-coating, ink-jet printing (IJP) or slot-die coating. Subsequently, it is placed in a tubular furnace for the first annealing, aimed at the decomposition of all organic matter to yield a homogeneous, nanocrystalline film composed by $BaCO_3$, CuO and Y_2O_3 (or RE_2O_3 for other tested RE). These phases are found in nanocrystalline form embedded in an amorphous matrix, and the films resulting from the pyrolysis process will be employed as precursors for the growth of YBCO or REBCO through TLAG. Deposition parameters and processing conditions of the annealing process have been optimized to promote the formation of the desired phases showing the optimal, reduced grain size which ensures a fast reaction in the following growth process.

3. **Elimination of $BaCO_3$ and growth of YBCO (or REBCO):** the growth process through TLAG requires the use of a high-temperature annealing ($\geq$ 800 ºC) and determined conditions of oxygen partial pressure. During this thermal treatment, which will be described in detail later on in this section, $BaCO_3$ must be eliminated in order for the reaction mechanism to proceed. Processing parameters must be correctly tuned to promote the epitaxial, c-axis nucleation of YBCO, necessary for the application proposed.

4. **Oxygenation process:** the final heat treatment is performed on the grown YBCO or REBCO film to induce oxygen incorporation in the structure and thus yield the structural transformation from tetragonal to orthorhombic, the one of interest due to it displaying superconducting properties.

Chapters 2 and 3 will present a detailed discussion on the synthesis of the metal-organic precursor salts and on the optimization of the metal-organic chemical solution, its deposition and

pyrolysis step. Despite Chapter 4 will be focusing on the growth of YBCO and three other REBCO systems through TLAG, an overview of the general reaction mechanism of this innovative growth process is required for a straightforward understanding of the reported findings, and is thus now presented[6].

As previously mentioned, the necessary, first step of the growth mechanism through TLAG is the elimination of $BaCO_3$. Since the publication of the first studies reporting the use of fluorine-free chemical solutions [46–50, 88], the formation of this precursor phase of barium led to the common belief in the superconducting community that its presence would completely hinder the formation of the final REBCO, due to its exceedingly high thermal stability [42, 89–91]. In powders, its decomposition occurs above 1000 ºC [92, 93], thermal conditions well above the processing temperature common to REBCO fabrication, given the peritectic temperature T_P of YBCO, for example, is found in the same range. Successively, however, the fundamental role of CuO in the elimination of $BaCO_3$ was revealed [94–96], demonstrating the prominent catalytic nature of copper in the reaction leads to the reduction of the processing temperature of several hundreds degrees through the mechanism:

$$BaCO_{3(s)} + CuO_{(s)} \rightarrow BaCuO_{2(s)} + CO_{2(g)} \tag{1.2}$$

The equation above accounts for thermal treatments performed in atmospheric conditions. Additionally, the determinant feature of reduced particle size was presented [97]: nanometric sized particles of precursor phases displayed a faster participation in the reaction scheme compared to the same particles in micrometric size, possibly explained through an increased cation diffusion during the reaction. This concept is at the base of the optimization of the pyrolysis process in TLAG-CSD towards the formation of the nanocrystalline precursor phases with reduced grain sizes for their successive high reactivity in the growth mechanism.

Therefore, the presence of CuO in the fabrication process of YBCO or REBCO films allows for the formation of a mixed oxide of barium and copper [98] which successively reacts, in the presence of copper oxide, to form a liquid phase of [Ba-Cu-O]. Detailed study of the binary system of (Ba-Cu-O) was fundamental for the progression of HTS fabrication, and works from Nevřiva *et al.* [94], Chu and Buchanan [99] and Lindemer *et al.* [95] resulted in the development of phase diagrams, illustrating the formation of melts in specific processing conditions (T-P_{O_2}, atmosphere, etc.). In TLAG, the mechanism of the [Ba-Cu-O] transient liquid formation is seen to assist the nucleation and the final growth of YBCO. TLAG is, thus, founded on the concept of kinetic preference towards [Ba-Cu-O] transient liquid formation in a region of the phase diagram in which, thermodynamically, YBCO is the expected equilibrium phase. The presence of a transient liquid is not predicted by classical thermodynamics, conferring to TLAG a characteristic out-of-equilibrium nature. Given the necessary overcoming of an

[6] For details regarding all experimental methodologies and characterization techniques employed in the bullet-point list above, refer to Appendix A.

energetic barrier, ΔG, for the formation of stable nuclei of a solid phase and its crystallization occurring following an induction period, the reaction pathway through a transient liquid is consistently faster as its formation is instantaneous[7]. A previous case study was reported for the fabrication of germanium nanowires, in which the generation of a liquid phase exhibited kinetic preference compared to crystallization in thermodynamic equilibrium conditions [100].

A schematic overview of TLAG is illustrated in Fig. 1.5, where the fundamental steps towards the final REBCO growth are observed. Upon heating of the nanocrystalline precursor film, the kinetically preferred [Ba-Cu-O] transient liquid is generated through melting of [$BaCuO_{2(s)}$ + $CuO_{(s)}$] (at high P_{O_2}) or [$BaCu_2O_{2(s)}$ + $Cu_2O_{(s)}$] (at reduced P_{O_2}). The $Y_2O_{3(s)}$ nanoparticles are stable and dispersed in the transient liquid until the conditions for their dissolution are met. This leads to yttrium supersaturating the liquid and diffusing towards the growth front in correspondence to the substrate-liquid interface. Here, nucleation of YBCO is favoured, and the kinetic control of the liquid supersaturation ensures the promotion of the c-axis orientation, which progresses its bottom-to-top growth.

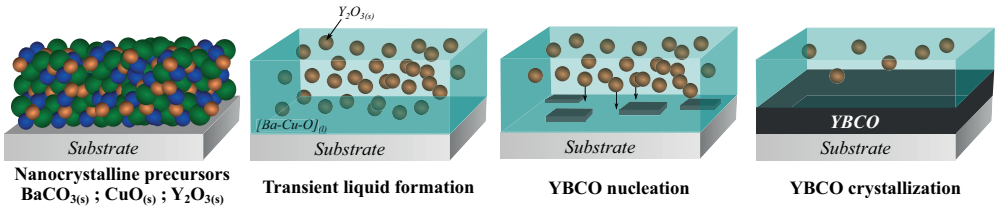


FIGURE 1.5: Schematic representation of the TLAG mechanism, illustrating the major steps occurring during this growth process.

A wide working window for c-axis nucleation is available for the growth of YBCO through TLAG, and is strictly correlated to the supersaturation conditions of the transient liquid. This region of the phase diagram may be reached through two different methodologies, namely TLAG routes, indicated as arrows in the phase diagram in Fig. 1.6. These are described as:

- ***TLAG T-route:*** YBCO crystallization is obtained through a fast heating at a constant, elevated P_{O_2} (blue arrow in Fig. 1.6). In this case, the elimination of $BaCO_3$ and the generation of the transient liquid are occurring concomitantly during the heating ramp.
- ***TLAG P_{O_2}-route:*** two-steps process which decouples the elimination of $BaCO_3$, occurring during the heating at reduced P_{O_2} until the attainment of the desired temperature, from the formation of the transient liquid and YBCO nucleation, promoted during a fast variation of the P_{O_2} of the system to reach the area of the phase diagram where c-axis nucleation is favoured. This is represented by two consecutive, red arrows in Fig. 1.6.

[7] A thorough discussion on the crystal growth from melts is object of the following section.

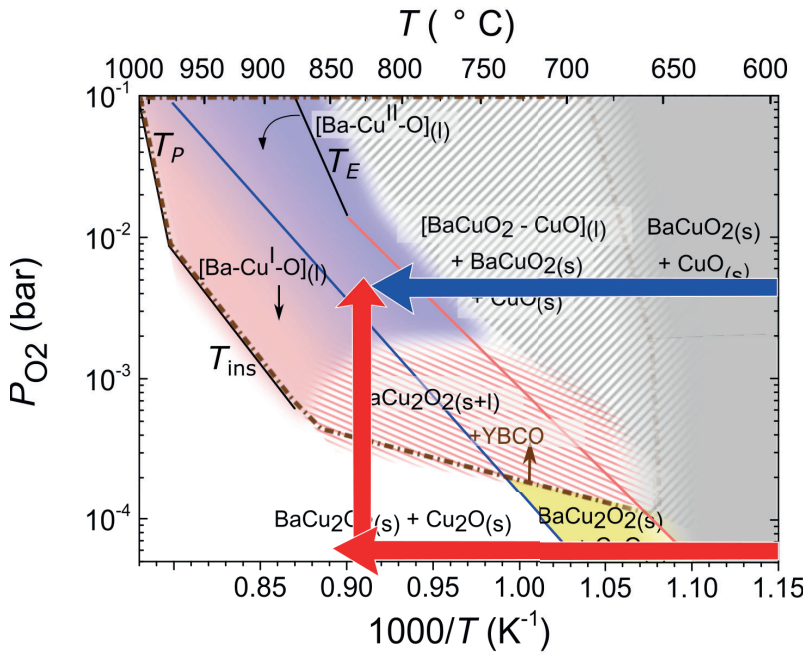


FIGURE 1.6: Possible routes employed for the growth of YBCO through TLAG, shown as arrows on the TLAG kinetic phase diagram indicating major areas of phase stability [101]. Blue arrow depicts the *TLAG T-route*, whereas the red arrows illustrate the two-steps process of *TLAG* P_{O_2}*-route*.

Comparably to other liquid-mediated growth approaches, the growth rates in TLAG are anticipated to be high. Y diffusivity in a [Ba-Cu-O] melt was demonstrated by Kursumovic *et al.* [77] to be $4 \cdot 10^{-10} m^2 s^{-1}$, two orders of magnitude higher than when studied in bulk ($8 \cdot 10^{-12} m^2 s^{-1}$). Indeed, the liquid-assisted nature of the process allows for ultrafast growth rates to be obtained: in the work conducted during this PhD thesis, YBCO growth at a unprecedented rate of over 2000 nm s^{-1} was demonstrated (see 5.3.1 and [101]), undoubted evidence of the high-throughput essence of TLAG.

For an exhaustive comprehension of the discussions regarding the experimental results on the growth of YBCO and other REBCO systems through TLAG, a thorough explanation of the cardinal aspects of crystal growth from melts is believed to be necessary, and is object of the following section.

1.2.4 Notions on crystal growth from a melt

The mechanism of crystal growth from a melt deriving from a solid phase (or several phases) may be viewed as a three steps process: initially, the solid is melted, generally through thermal annealing. Variations of the melt supersaturation conditions will be inducing the formation of the first nuclei of the final crystalline phase. When the conditions for stable nuclei precipitation are attained, crystal growth from the melt occurs. The growth mechanism employed in this thesis for the preparation of epitaxial REBCO films shows a parallelism with the latter description: as it was preliminarily presented above, and will be illustrated in detail in Chapters 4 and 5, the nanocrystalline phases of $BaCO_3$, CuO and Y_2O_3 are the solid precursors for the formation of the transient liquid. From the latter, REBCO nuclei are generated and the growth of the final perovskite-type crystal structure occurs. For this reason, a comprehensive discussion of the theoretical concepts at the foundation of the individual steps of the process of crystal growth from a melt are considered to be of fundamental interest for the complete understanding of the growth of REBCO films through TLAG, and are thus given in the following sections of the text. Finally, a literature overview regarding the complex property of solubility of RE in various [Ba-Cu-O] melts has the objective of giving insights into the parameters controlling supersaturation, envisioned to be of extreme importance for the interpretation of the experimental results provided in this thesis.

1.2.4.1 Formation of a melt

Melting of a crystalline matter may be regarded as a continuous, first order phase transition from an ordered solid phase to a liquid presenting no structural arrangement. This type of phase change involves, generally, a finite amount of latent heat: the system absorbs or releases a large amount of energy per volume, with the simultaneous addition of heat while the temperature of the system is kept unvaried. This results in a "mixed phase regime", where some parts of the solid have completed the phase transition prior to others. The melting point, T_m is defined as the point of critical temperature where the Gibbs free energy of the two states, solid and liquid, are both equal, $\Delta G = 0$.

The first conception of continuous melting was based on the theory of liquid-vapor critical point developed by Van der Waals in 1873. Here, two parameters are controlling the phase transition: the strength of long-range attraction between molecules, and the molecular size. However, the conventional model to describe the melting process derives from Frederick Lindemann (1910), who determined liquefaction of a solid to be initiated when the amplitude of atomic thermal vibrations are exceeding a fraction of the volume among atoms [102]. In this model, the average energy of the thermal vibration displays a correlation with the absolute temperature (T) through the equipartition theorem, according to:

$$m(2\pi\nu_E)^2\partial x^2 = k_B T \tag{1.3}$$

where m (atomic mass), ν_E (Einstein frequency), ∂x^2 (root-mean-square thermal average amplitude of vibration) are related to the absolute temperature (T) through the Boltzmann constant. In the assumption proposed by Lindemann, melting occurs when ∂x^2 reaches a critical fraction (c_L) of the nearest-neighbouring atomic spacing, a. Thus, the theorem may be rewritten as:

$$T_m = \frac{m(2\pi\nu)^2(c_L)^2a^2}{k_B} \tag{1.4}$$

A more modern vision of this theorem allows for the relation of T_m with characteristic properties of the bulk solid, through the equivalence of ν with the Debye frequency. Additionally, structural studies have revealed the crystalline ordering of a metal is directly correlated to the value of c_L, resulting in a difference between the melting of a bcc, fcc or hcp structure [103]. Nonetheless, Lindemann's criterion must be considered a non-exact model as the description is founded on harmonic forces of atomic vibrations, disregarding bond breakage during the phase transition, a necessary event for melting to occur. Moreover, the characteristics of the liquid are completely neglected, focusing exclusively on the nature of the solid. Despite these features, the clear description and the theoretical values of T_m closely matching experimentally determined ones have currently maintained a widespread use of this model [102, 103].
If considering Lindemann's description of the phenomenon of melting, however, it may be understood as a sudden and discontinuous phase change when the system reaches T_m. Contrarily, melting occurs over a thermal interval, and is thus referred to as *continuous melting*. Grain boundaries or any structural disorder in the solid may be at the origin of timely phase transitions from solid to liquid. Presence of impurities may shift the melting point given the varying concentration along the phase boundary between solid and liquid. Structural disorder (polycrystalline grains), conversely, combine the effect of grain boundary energy with the size of the grains to broaden an otherwise sharp transition.
Simultaneous to the derivation of the theory of melting by Lindemann, in the same year Tammann proposed that the melting is initiated at the surface of a crystal or solid, and surface melting controls the entire process [102]. Subsequently, this concept was reinforced by Stranski (1942), who determined that superheating is absent during a melting process [8] Frenken was the first to experimentally report on the role of the surface during the process of melting of Pb(110) in 1946: he determined that a crystal kept at homogeneous temperature (T) inevitably begins melting in correspondence of the surface as a result of reducing to zero the

[8] Superheating in a phase transition is generally linked to the generation of the new phase resulting from the elevated interfacial energy between the newly formed phase and the original one.

activation energy of the formation of a thin liquid layer [102–104], observing the formation of a solid-liquid interface on the (110) surface of Pb approximately 40 K below its expected T_m. Surface melting is, thus, a result of the wetting of the solid by its melt. It occurs when the surface energy of the solid-liquid-vapor interface is lower than that of the solid. As a consequence, a thin layer of the solid melts prior to the rest, at an inferior temperature than the bulk transition. This may be explained considering the lower strength of the bonds between superficial atoms which result in a reduced thermal stability of the most outer layers of a solid [105]. This concept is visually represented in Fig. 1.7, where the formation of a quasi-liquid layer (QLL) is obtained as the result of the reduction of the energy of the system (ΔG) and occurs at temperatures below the T_m of that specific solid. The formation of the QLL is in correspondence to a temperature known as wetting temperature (T_w): the QLL of thickness δ grows exponentially until reaching T_m, where the bulk transition occurs and complete melting of the crystal is observed.

Again, the criterion developed by Lindemann may be employed for the explanation of the QLL formation: surface atoms exhibit larger vibrational amplitudes if compared to the bulk atoms at the same temperature, given their reduced coordination. Therefore, these will attain the critical neighbouring distance at a temperature T below the one of the bulk transition T_m. The lower bond strength correlated to higher vibrational energy additionally clarifies the reason behind the earlier melting temperatures exhibited by grain boundaries, dislocations or other impurities.

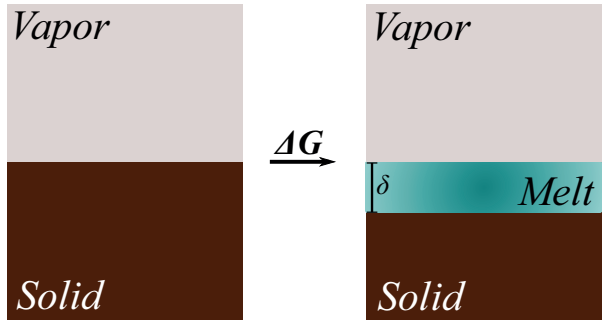


FIGURE 1.7: Schematic representation of the continuous melting process, starting from the formation of a quasi-liquid layer (QLL) of thickness δ occurring at the surface of a solid in contact with a vapor phase. The reduction in the energy of the system is initiating the process, which will successively generate the melting of the entire solid. Adapted from [103].

Up to this point, the considered models and theories are strictly describing ideally flat surfaces in crystal-like systems. However, a similar description may be applied in the case of nanometric systems, such as spherical nanoparticles, with the additional complication of size

effects and contributions linked to their curved nature[9]. Pawlow *et al.* first theorized, in 1909, the lowering of the melting point in a spherical particle due to size and effects related to the surface [106]. As displayed in Fig. 1.8, the melting in a spherical particle was demonstrate to follow a similar behaviour as the aforementioned for flat surfaces, initiating from an outer liquid layer (here, a continuous spherical one) of thickness δ, whose size is directly related to the curvature of the particle [107]. This layer is often denoted as liquid skin, giving name to the model [102]. From experimental studies on particle melting [108] the relation between T_m and particle size could be determined, according to:

$$T_m \propto \frac{1}{D} \tag{1.5}$$

where D is the diameter of the full particle. Thus, similar considerations to the discussion above regarding the reduced strength of bonds between surface atoms can be employed for the description of particle melting. Nonetheless, variations to this behaviour characteristic to particles have been observed in several studies.

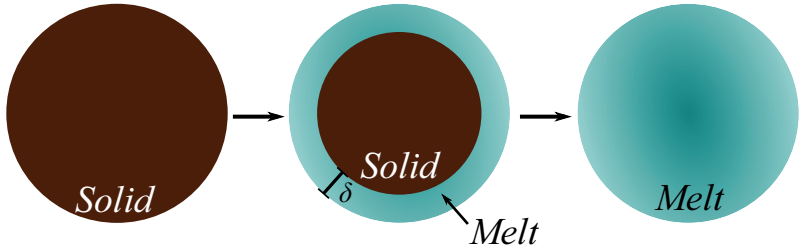


FIGURE 1.8: Schematic representation of the melting process in a spherical particle, initiated by the formation of a liquid skin of thickness δ, which increases until the full particle is found in liquid form. Adapted from [107].

In some cases, a critical size D_c, inferior to D, was determined, below which the particle sharply transforms into liquid [102]. However, the most interesting behaviour is the possible superheating of particles above T_m, attained through their insertion in a material displaying increased melting temperature [109] or through their inclusion in a matrix with corresponding epitaxial orientation [110].

These effects have been additionally observed in alloys of multiple phases [103]. The importance of size effect on variations of T_m, strictly controlled by surface melting phenomena, the relation between epitaxially oriented nanoparticles in the matrix of same texture, and the role of phase boundaries are all features which may be found in the films described in this thesis.

[9] The importance of this description is found in the model being a closer approximation to the situation of the nanocrystalline precursor phases in the pyrolyzed films employed for TLAG.

These may affect the reactivity of the phases towards the proceeding of the TLAG mechanism and must, thus, be considered.

1.2.4.2 Crystallization from a melt: supersaturation

Following the formation of a melt, the driving force towards the conclusive crystallization deriving from it may be obtained through consideration of the free energy of the liquid (initial phase) and the nucleated solid (final phase) [111]. Generally, this concept is described through difference in chemical potential of the two phases, according to:

$$\Delta\mu = \mu_L - \mu_S \tag{1.6}$$

This difference is, namely, the ***supersaturation*** of the liquid phase: with the system subjected to a specific temperature, this parameter measures the metastability of a solution in which the solute concentration is exceeding the one it can possibly dissolve. A more appropriate description of the supersaturation of a solution is given in the following equation:

$$\Delta\mu = k_B T log\left(\frac{C_\delta}{C_{eq}}\right) \tag{1.7}$$

where C_δ and C_{eq} are, respectively, the real and the equilibrium concentration of solute in the liquid. A different expression is provided by the definition of ***relative supersaturation*** (σ), as:

$$\sigma = \frac{C_\delta - C_{eq}}{C_{eq}} = \frac{C_\delta}{C_{eq}} - 1 \tag{1.8}$$

and thus, its correlation to $\Delta\mu$ may be expressed by the equation:

$$\Delta\mu = k_B T log\,(\sigma + 1) \tag{1.9}$$

Several processes are at the origin of crystallization from a supersaturated liquid. The schematic representation of a metastable zone in a diagram of concentration as a function of temperature is displayed in Fig. 1.9(a). Here, the curves *I* and *II* constitute, respectively, the boundaries towards the unsaturated system (stable liquid) and the phase of spontaneous nucleation (supersaturated solution). The region between the two lines is described as the **Ostwald-Meiers Regime**, and includes the *C-T* conditions for metastability of the solution. If a solution or liquid of composition A^I (placed at temperature T_3) is cooled to reach composition A (equivalent to a temperature of T_2), the intersection point of the solubility curve depicts the *C-T* equilibrium conditions between solid and solution at the given temperature.

Thermal reduction to the composition B results in no solid formation and the solution being supersaturated. A further temperature decrease, crossing the metastability boundary of line *II* will lead to a fast crystallization process. Following this description, the solution is described as *metastable* between the points A and B of the diagram. Maximum supercooling of the system may be expressed by relating the equations of thermal variation ($\Delta T_{max} = T_2 - T_1$) and of concentration difference ($\Delta c_{max} = c_{02} - c_{01}$) through the equation:

$$\Delta c_{max} \cong \Delta T_{max} \left(\frac{\partial c_0}{\partial T} \right) \tag{1.10}$$

However, crystallization may be also attained through continuous solvent evaporation from point A^{II} at a constant temperature of T_2, crossing the point A until the metastability boundary is reached, corresponding to the point C. The maximum variation of concentration will be, thus, described as $(\Delta c_{max})_T = c_{03} - c_{02}$, corresponding to a thermal variation of $\Delta T_{max} = T_3 - T_2$. When crossing to the metastable zone, from either temperature decrease of concentration increase, the formation of a critical nucleus requires a finite amount of time, generally referred to as *induction period of nucleation* (τ), defined as the time range from the achievement of supersaturation and the actual formation of the critical nucleus. Following this definition, the Ostwald-Meiers regime may be, thus, divided in two areas, separated by a dashed blue line in Fig. 1.9(a). In region identified as (1) in the diagram, ranging between the boundary of line *I* and the dashed line, no sudden nucleation occurs normally. When crossing the dashed line to the metastability boundary of line *II* (region (2) in the diagram), formation of a critical radius is attained and precipitation of stable nuclei may occur. The dependence of the *induction period of nucleation* on the supersaturation is represented in the plot in Fig. 1.9(b), and the general regions of supersaturation deriving from this description (referring to the diagram in Fig. 1.9(a)) may be identified as:

- **Region *AB*:** characterized by long τ, formation of stable nuclei is extremely rare;
- **Region *BC*:** a slight increase in supersaturation leads to a drop in τ, following the trend in Fig. 1.9(b);
- **Beyond point *C***: τ shows very reduced values, sudden precipitation of stable nuclei may occur.

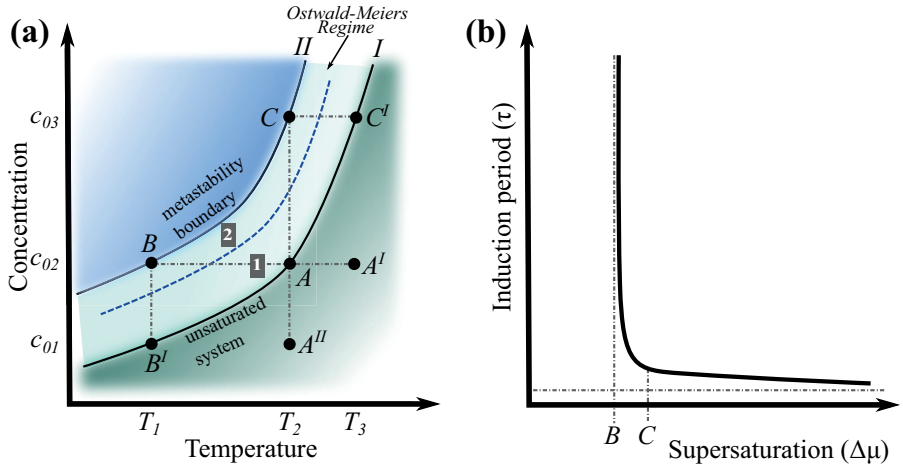


FIGURE 1.9: (a) Schematic representation of a diagram of concentration as a function of temperature, depicting the limits of the metastable zone for a liquid or solution, namely Ostwald-Meiers Regime. (b) Tendency of induction time (τ) as a function of the liquid supersaturation. Adapted from [111].

Consequently to understanding this theoretical model regarding the feasible methods of promotion of nucleation through variations of supersaturation, one may promptly envisage how both strategies have been employed in the fabrication of HTS, specifically of REBCO, in liquid-mediated growth processes. MTG is making use of supercooling below the peritectic temperature of YBCO to favour its crystallization from an incongruent melt composed by the (211) phase and [BaO-CuO] liquid [81], employing the thermal variation as driving force of the crystallization process. Conversely, as mentioned in the previous part of this section, in HLPE nucleation is promoted from a Y-rich vapor phase obtained through PLD, flux-fed to a previously stabilized liquid layer of [BaO-CuO], ensuring supersaturation tuning by the simple control of the pulse frequency [84].

In any of the fabrication methods described up to this point, control of supersaturation is demanding mainly due to the necessary tuning of the solute concentration. The advantage of the novel growth method of TLAG is the possibility of tuning liquid supersaturation either through processing parameters, such as final T-P_{O_2} conditions and heating ramps, or through the composition of the transient liquid: this innovative and simple approach allows for the preparation of films with specific amount of the precursor components of Y_2O_3, CuO and $BaCO_3$ which, through variations of the stoichiometry (i.e (Ba:Cu) molar ratio) of the initial chemical solutions, will lead to the formation of transient liquids exhibiting different properties. Thorough analysis of the growth of YBCO from transient liquids of different composition is one of the main objectives of this thesis, and a comprehensive evaluation of the influence of supersaturation on the epitaxial nucleation of YBCO from each liquid composition will be addressed in

Chapter 4. Nonetheless, several studies evinced the difficult nature of establishing the solubility of Y or other RE in the [Ba-Cu-O] melt, and a review of the most significant parameters controlling this factor is believed to be of significant importance. This will be, thus, provided in the final part of this section.

1.2.4.3 Nucleation and crystal growth

Subsequent to the description of the concept of melt supersaturation a further discussion regarding the formation of stable nuclei and the final crystal growth is now required.
All crystallization processes begin with a nucleation event and the following formation of a solid crystal, if the energetic conditions of the system are adequate. The generation of a nucleus of a new phase in the nutrient (which may be a liquid, melt or vapor) may occur exclusively for sufficiently high supersaturation conditions which allow crossing the metastability boundary towards stable nucleation, as observed in the aforementioned sections. The driving force of the crystallization process is the difference in free energy, ΔG. Given it is a first-order transition from the initial phase (nutrient) to the solid crystal (final phase), it is described as:

$$\Delta G = G_2 - G_1 \tag{1.11}$$

To fulfill the conditions for stable nucleation, the energy of the final phase (G_2) must be greater than the energy of the parent phase (G_1), thus $\Delta G < 0$ for the crystallization onset.
From classical thermodynamics, the equation above may be rewritten considering the free energy G to be described by the equation:

$$G = H - TS \tag{1.12}$$

with H, and S, respectively, the enthalpy, and entropy of the system. Considering $H = U + PV$ (with P and V being the system pressure and volume, respectively), eq. 1.11 may be thus be rewritten as:

$$\begin{aligned} \Delta G = G_2 - G_1 = U_2 + PV_2 - TS_2 - U_1 + PV_1 - TS_1 \\ \Delta G = \Delta UP\Delta V - T\Delta S \end{aligned} \tag{1.13}$$

In the case of solutions or melts, the expression for the change in free energy may be given considering a thermal difference, defining:

$$\Delta G = \Delta H - T\Delta S \tag{1.14}$$

in which the term ΔH is referring to the enthalpy of the melting or dissolution process, whereas ΔS represents the change of entropy in the system considered. However, ΔG may be also

written as:

$$\Delta G = nk_B T log\left(\frac{a}{a_0}\right)$$
$$\Delta G = nk_B T[log\left(\frac{f}{f_0}\right) + \left(log\frac{c}{c_0}\right)] \tag{1.15}$$

where a and a_0 are the activity of the supersaturated and saturated solutions, respectively. Correspondingly, f and f_0 are the activity coefficients, whereas c and c_0 are the concentrations of the solute in the supersaturated and in the saturated solutions. If supersaturation is low, $\frac{f}{f_0} = 1$, leading to:

$$\Delta G = nk_B T log\left(\frac{c}{c_0}\right) \tag{1.16}$$

The renowned relation between the free energy (thermodynamic potential), ΔF, and the chemical potential, μ, which reads:

$$\Delta G = \sum \Delta \mu_I n_i \tag{1.17}$$

leads to the final derivation of

$$\Delta \mu = k_B T log\left(\frac{c}{c_0}\right) \tag{1.18}$$

which is the expression for the ***supersaturation*** of the system, as previously defined in 1.2.4.2. It describes the change in chemical potential between the parent phase (liquid or melt) to the final solid phase (crystal) is the driving force of the crystallization process.

The process of nucleation may be divided in primary or secondary, depending on whether it is occurring spontaneously, namely ***homogeneous nucleation***, or if is promoted by the presence of external particles, defined as ***heterogeneous nucleation***. The latter is generally employed in industrial framework for the fabrication of functional materials based on the crystallization process [111].

The formation of a stable nucleus occurs when its size has attained a critical radius, r^*, which is required to surmount the free energy of formation, ΔG. The equation describing this reads:

$$\Delta G = 4\pi r^2 \gamma_s - \frac{4\pi}{3\nu} r^3 \Delta\mu \tag{1.19}$$

with the second term relative to the volume of the nucleus formed homogeneously, which may be defined as:

$$V = \frac{4\pi}{3} r^3 \tag{1.20}$$

divided by ν, the unit volume of one molecule, or unit cell if considering the nucleation of a YBCO stable nuclei. The first term of equation 1.19 is defining the energy term related to the surface of the formed nucleus. Being a positive term, with γ_s relative to the free energy of the

interface, it is describing the adverse situation of a new surface creation. As a result, ΔG must overcome the surface energy barrier for the formation of a stable nucleus of a finite volume to occur. Consequently, the expression for the critical nucleus radius, r^*, may be obtained through the identification of the maximum of eq. 1.19, setting $\partial(\Delta G)/\partial r = 0$:

$$r^* = \frac{2\gamma_s \nu}{\Delta\mu} \tag{1.21}$$

Therefore, by substituting r in eq. 1.19 with r^*, the energy required for the formation of a homogeneous nucleus is defined as:

$$\Delta G^*_{hom} = \frac{16\pi}{3}\frac{\gamma_s^3 \nu^2}{\Delta\mu^2} \tag{1.22}$$

relating the critical radius and energy barrier to the supersaturation through an inversely proportional correlation, described with this formulation for the first time by Gibbs in 1878. The term $\frac{16\pi}{3}$ is a shape factor characteristic for spherical nuclei, and will vary if the shape of the formed nucleus differs from a sphere in this model. An elevated concentration of the solute in the liquid, melt or solution may promote formation of stable nuclei due to its effect of lowering the energetic barrier. A simple, visual representation of the correlation of ΔG and critical nucleus radius, r^* is displayed in Fig. 1.10. For nucleus radius $r<r^*$, the nucleus is not stable and is dissolved in the liquid, melt or solution. Contrarily, for $r>r^*$, ΔG will decrease conferring stability to the nucleus, which will continue its growth.

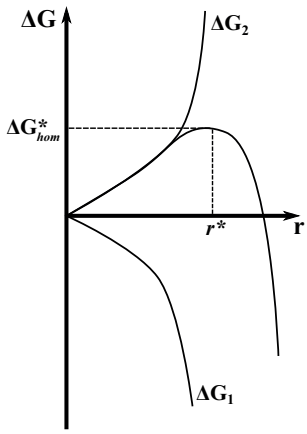


FIGURE 1.10: Formation of a nucleus is favoured once the critical radius r^* is reached, lowering the free energy of the system.

As previously stated, heterogeneous nucleation will occur in correspondence to external particles, which may include structural defects, interface between two phases or on a substrate. Considering the approximation of a liquid droplet, stable heterogeneous nuclei initiating their

formation on a solid surface will be forcefully induced to present the shape of a spherical segment, generally referred to as cap, as illustrated in Fig. 1.11. The cap with curvature radius r is formed with a characteristic angle θ with the surface, defined as wetting angle.

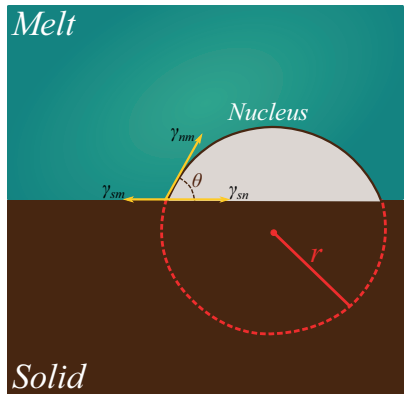


FIGURE 1.11: Schematic representation of the formation of a heterogeneous nucleus in contact with a solid surface, exhibiting the characteristic cap shape. The hypothetical formation of a homogeneous nucleus of radius r with the same curvature is represented as a dashed red line.

The relation between the free energy of formation of a homogeneous nucleus and a heterogeneous one accounts for a correction factor, $f(\theta)$ (being $0 < f(\theta) < 1$), which takes into account the geometrical differences of the two cases [111]. This correction factor may be expressed through:

$$f(\theta) = \frac{(1 - cos(\theta))^2 (2 + cos(\theta))}{4} \tag{1.23}$$

and the correlation between homogeneous and heterogeneous nucleation thus reads:

$$\Delta G^*_{het} = \Delta G^*_{hom} \cdot f(\theta) \tag{1.24}$$

The wetting angle is determined through the following expression, known as Young relation:

$$\gamma_{sm} = \gamma_{sn} + \gamma_{nm} cos(\theta) \tag{1.25}$$

which considers the three surface tensions acting simultaneously: γ_{sm} relative to the substrate-melt interface, γ_{sn} corresponding to the substrate-nucleus interface, and γ_{nm} relative to the nucleus-melt interface. Considering the equations above, $\Delta G^*_{het} < \Delta G^*_{hom}$ is always valid, and the curves of ΔG^* as a function of the critical radius in each of the two nucleation scenarios are illustrated in Fig. 1.12.

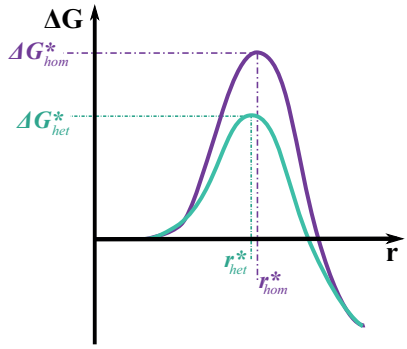


FIGURE 1.12: Competition between formation of stable homogeneous and heterogeneous nuclei. Adapted from [112].

Considering this relation for the growth of epitaxial YBCO or other REBCO, the growth of c-axis oriented grains is believed to be favoured over the spontaneous formation of homogeneous nuclei from the liquid layer. Nonetheless, if the supersaturation of the liquid system is elevated, competition between homogeneous nuclei (randomly-oriented grains) and heteroepitaxial grains displaying a/b-orientation (90º rotation compared to the epitaxial c-axis orientation, (h00) reflection), may occur, resulting in a mixed nucleation. Ichino *et. al* [113] were among the first to evaluate the tendency of ΔG^* as a function of supersaturation, depicted in Fig. 1.13, in which ΔG^*_{hom} is inserted (purple line) with the assumption of $f = 0.5$ (eq. 1.24). ΔG^*_{het} is favoured for lower values of $\Delta\mu$, promoting c-axis nucleation. If the supersaturation is increased, a competition between the free energy of formation of c-axis and a/b-axis orientations arises. When this barrier is overcome, a mixed homogeneous and heterogeneous nucleation is preferential. The general difference in the growth rate of the two competing epitaxial orientations, c-axis and a/b-axis, may be expressed through a Boltzmann-weighted probability function which described the various simultaneously acting nucleation rates for each nuclei orientation:

$$I = I_0 exp\left(\frac{-\Delta G^*_i}{k_B T}\right) \tag{1.26}$$

The growth in the direction of the a/b plane is normally greatly exceeding the one in the c direction [81].

Selection of the adequate substrate is pivotal given its fundamental effect on the nucleation at the growth front in TLAG, as previously indicated, given that a large mismatch between the YBCO lattice parameters and the ones of the chosen substrate may generate considerable strain effects.

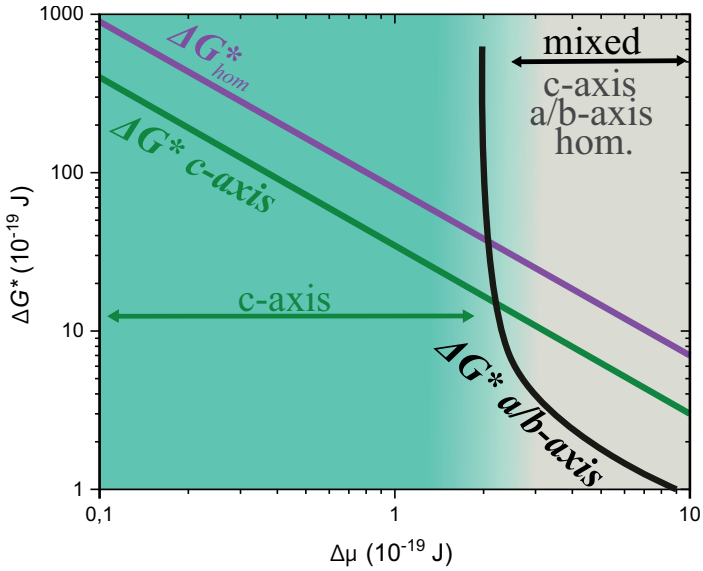


FIGURE 1.13: Free energy of formation ΔG^* as a function of supersaturation $\Delta\mu$ for the different types of orientations possible resulting from the nucleation of REBCO. Adapted from [113].

When considering heterogeneous nucleation (in this thesis, of c-axis oriented REBCO), the formed nucleus is subjected to an in-plane strain due to the lattice mismatch with the substrate. Consequently, an opposite strain is generated in the normal direction, generally due to the crystal structure adjustment to this deformation, referred to as Poisson effect. The nucleation energy barrier ΔG^*_{het} must, thus, include a factor which considers this effect:

$$\Delta G^*_{het,str} = \frac{16\pi\gamma_s^3}{3(\Delta G_v - \Delta G_{str})^2} f(\theta) \tag{1.27}$$

due to the presence of a strain energy density (G_{str}>0). The latter is described by the expression:

$$\Delta G^*_{str} = \Delta G^* \left(1 - \frac{\epsilon}{\psi}\right)^2 \left(1 - \frac{\eta\epsilon}{\Delta\mu}\right)^{-2} \tag{1.28}$$

with ϵ being the strain, ψ being the bond energy needed to be overcome to separate the first neighbouring atoms, and $\Delta\mu$ the supersaturation, as previously defined. The energy barrier in eq. 1.28 thus requires supersaturation conditions to exceed the strain energy per bond $n\epsilon$ for a stable nucleus to form. The expression $\Delta G^*_{str} > \Delta G^*$ is consistently fulfilled, given that a system subjected to greater strain requires a higher supersaturation for nucleation to occur if compared to a system in which no strain is present, as visually evinced in Fig. 1.14.

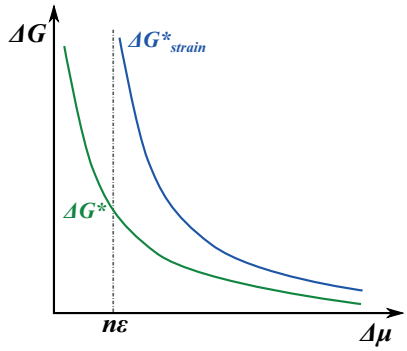


FIGURE 1.14: Correlation between energy barrier and supersaturation, considering the additional case of a system subjected to strain. Adapted from [114].

Moreover, parameters such as surface morphology and presence of defects must be carefully controlled to reduce the interfacial energy and, thus, ensure the desired nucleation.

The concepts provided up to this point are required for a comprehensive understanding of the TLAG mechanism and, thus, the experimental results presented in this thesis. The liquid-based nature of TLAG, relying on the kinetic preference of a transient liquid formation from which REBCO nuclei are generated through dissolution of the dispersed solid RE_2O_3 nanoparticles, finds a direct similarity in the theoretical concepts described in this section. Considering the fundamental role of melt supersaturation to the crystallization process, a final discussion regarding the solubility of Y and other RE in the [Ba-Cu-O] melt is required at this moment. The determination of this parameter has encountered great hindrances, as will be explained in the following subsection. Nonetheless, several authors have faced the complexity and contributed to widen the limited knowledge on this intricate topic. What follows is a literature overview of the latter, with the aim of providing a clear explanation of the concept of [Ba-Cu-O] melt supersaturation: from the data reported in literature, various calculations were carried out to unravel the trends of this parameter finding direct similarities with the growth of REBCO through TLAG described in this thesis.

1.2.4.4 Solubility of Y and other RE in [Ba-Cu-O] melts

The determination of Y and other RE solubility in melts of [Ba-Cu-O] has suffered from challenging experimental conditions, given the infamous corrosive nature of the melt, often presenting reactivity with the crucible employed for the analysis. Several of the values reported in literature are strictly dependent on the choice of the crucible material (often showing possible contamination of the melt through reactivity), atmosphere or growth methodology. The concepts and relations provided in the following portion of the text are, thus, an overview of

the general trends of Y (and other RE) solubility in [Ba-Cu-O] melts of different nature and the respective correlation of the supersaturation with various parameters (P_{O_2}, melt composition, choice of the RE). Relevant details of each set of presented data will be provided. Nevertheless, for the mentioned reasons, the reader is invited to set a focus on the overall tendencies described.

As presented earlier, the relative supersaturation, σ, of a melt may be described through the difference between the real and equilibrium concentration of the solute in the liquid (1.8). In TLAG, the nucleation of YBCO at the substrate-liquid interface is the result of the dissolution of the Y_2O_3 nanoparticles in the transient liquid and the migration of Y atoms towards the growth front. The driving force towards YBCO crystallization is thus the difference between the real, supersaturated Y concentration in the [Ba-Cu-O] transient liquid (C_δ) and its equilibrium concentration (C_{eq}).

Several studies have determined the solubility of Y, thus its C_{eq}, in melts of two compositions, specifically (3BaO:5CuO) and (3BaO:7CuO) [74, 79, 80]. No other melt compositions are found in literature for the case of yttrium, and the considerations that follow will thus take into account these two cases only. The tendency of C_{eq} of yttrium in the melts of the two compositions displayed in Fig. 1.15 is obtained from studies in air based on MTG [74], LPE [79] and HLPE [80]. The elevated temperature range is characteristic of these growth methodologies, but an extrapolation to a lower temperature interval for the (3BaO:5CuO) melt (shown as a dashed line in Fig. 1.15), closer approximation to the processing thermal conditions employed for the growth of YBCO through TLAG described in chapters 4 and 5, could be achieved from data in [80]. Therefore, in the range between 820 ºC and 900 ºC, C_{eq} will exhibit, respectively, values of 0.01 % and 0.06 %. A clear trend is observed: the composition with higher copper content, here (3BaO:7CuO), displays a generally increased Y solubility in the melt compared to the one with lower copper content, here (3BaO:5CuO), if considering the same temperature range.

These findings have been at the origin of the use of melt compositions with copper excess out of the stoichiometric ratio for YBCO formation, due to the considerable advantage of a straightforward lowering of the processing temperatures when selecting the same supersaturation conditions for the two melts, an extremely attractive aspect towards the implementation of industrial process of higher energetic efficiency. If considering the case of one composition exclusively, in contrast, one may promote the Y solubility in that melt through a simple temperature increase. The graph in Fig. 1.15 is thus giving an estimation of the equilibrium concentration, C_{eq}, of Y in melts of two compositions as a function of the temperature. Now, the major difficulty of estimating the value of real yttrium concentration in the system, specifically C_δ, has led to the hypothesis presented in previous studies conducted in our group [51]: the estimation of C_δ to be 10 % is obtained by extending the liquidus line from the region of the phase diagram relative to thermodynamic stability of Y_2O_3 + liquid, as visible in Fig. 1.16. Stoichiometric YBCO results from the dissolution of 17 % of yttrium, corresponding to the

full amount of this element present in the melt, an extremely rare phenomenon to occur.

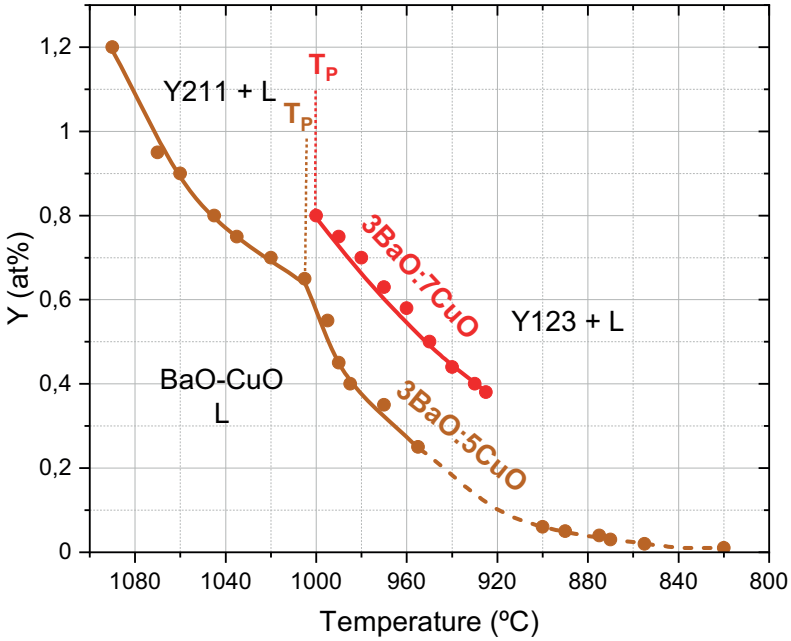


FIGURE 1.15: C_{eq} of yttrium as a function of temperature in melts of two compositions: (3BaO:5CuO) and (3BaO:7CuO), shown in brown and red, respectively. Data points are obtained from [74, 79, 80]. All these studies were conducted in air. The extrapolation of yttrium solubility to a lower temperature range is obtained from [80] exclusively for the former composition, and depicted as a dashed line.

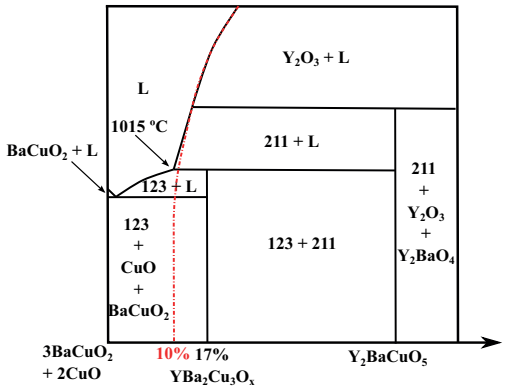


FIGURE 1.16: Extrapolation of the value of C_δ = 10 %, through the extension of the liquidus line of Y_2O_3 + liquid thermodynamic stability. Formation of $YBa_2Cu_3O_x$ is corresponding to the complete dissolution of all the Y present (17%). Phases are labelled as follows: 123 - $YBa_2Cu_3O_x$; 211 - Y_2BaCuO_5. Adapted from [115].

Therefore, by setting the value of C_δ to a fixed 10 %, the relation between supersaturation, $\Delta\mu$, and consequently relative supersaturation, σ, with the temperature can be straightforwardly calculated. The computed curves for both are shown in Fig. 1.17.

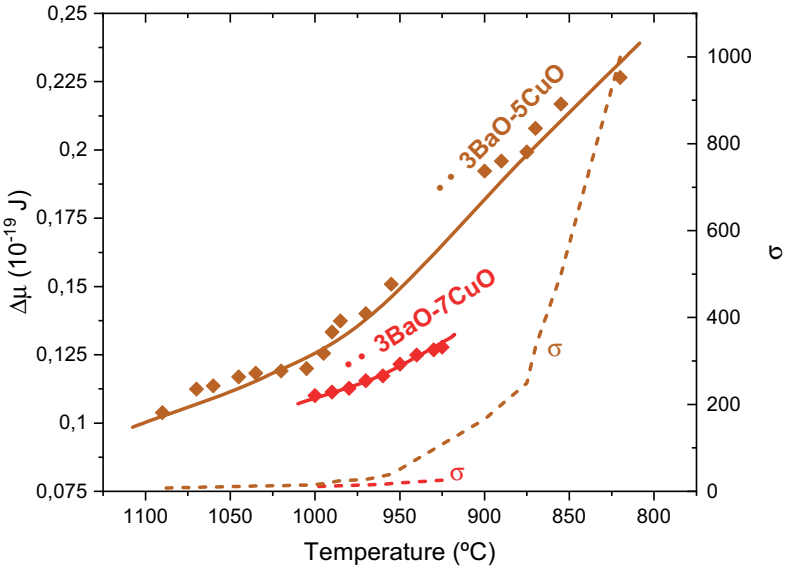


FIGURE 1.17: Curves of supersaturation, $\Delta\mu$ (solid lines), and relative supersaturation, σ (dashed lines), of yttrium in [Ba-Cu-O] melts of (3BaO:5CuO) and (3BaO:7CuO) compositions, shown in brown and red, respectively. Data points are calculated from equations 1.7 and 1.8, employing values of C_{eq} displayed in Fig. 1.15 and considering the hypothesis of a fixed C_δ = 10 %.

It is evident that $\Delta\mu$, and the directly related σ, follow an indirectly correlated tendency as the one displayed in the previous graph, Fig. 1.15, and are both lowered with the increase of the copper content of the specific composition analyzed. Nucleation may be, thus, favoured when considering the same thermal conditions for a composition with lower copper content: the strategy to promote nucleation at a constant temperature is to increase the concentration of the solute, which translates as Y solubility in the liquid. A higher supersaturation, displayed by the lower solubility of the composition with higher copper content, will thus be favourable towards the formation of stable nuclei which initiate the crystal growth from the melt by increasing the nucleation rate (eq. 1.26), if taking into account the same processing conditions. However, as displayed in Fig. 1.13, elevated supersaturation results in the nucleation of YBCO grains of mixed orientations, undesirable for the application proposed in this work.
Considering the same temperature range (950-1005 ºC, corresponding to the peritectic temperature of YBCO determined in these studies conducted in air) and the values of C_{eq} deriving from Fig. 1.15, the calculation of σ for each value of C_{eq} as a function of the variation of C_δ

(between 0.1 % and 10 %) is possible. The resulting curves of σ of Y in each of the two [Ba-Cu-O] melts considered, (3BaO:5CuO) and (3BaO:7CuO), are displayed in Fig. 1.18. At the lowest temperature (950 ºC), the C_{eq} of Y, thus its solubility, is doubled in the melt of higher copper content, leading to a maximum value of σ of 19 (when $C_\delta = 10$ % is selected). Contrarily, the relative supersaturation of Y in the melt of reduced copper content reaches a maximum value of 39 in the same conditions, over a factor 2 higher. However, it must be reminded that the hypothesized value of $C_\delta = 10$ % is employed in both liquids, in spite of unknown variations of this parameter when different melt compositions are employed. In general, the same trend is observed with the increase of temperature, as it is evident from the elevated values of C_{eq} exhibited by Y in the former melt. Nonetheless, as previously specified, with the aim of reducing the relative supersaturation inside the same system, an increase of temperature is required in order to promote Y solubility.

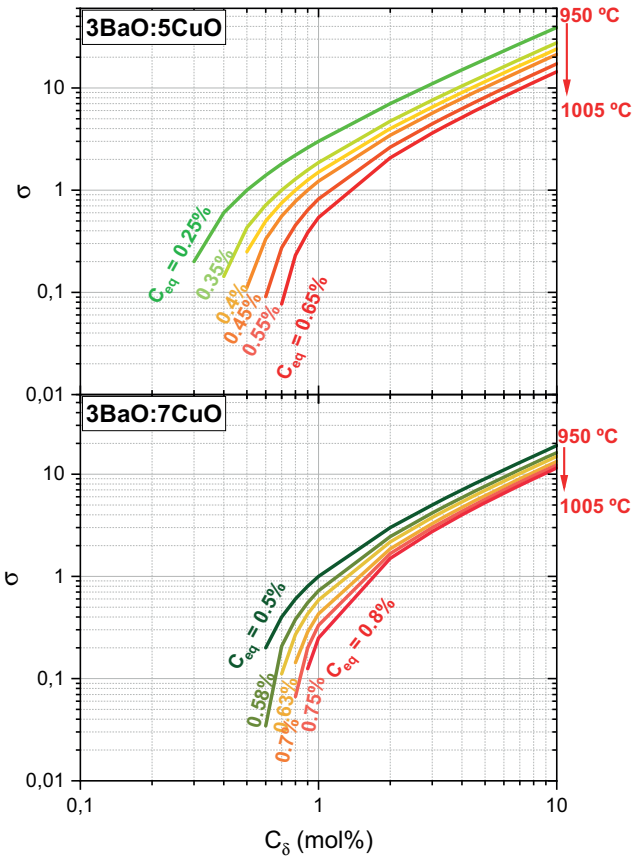


FIGURE 1.18: Calculation of the relative supersaturation σ of Y in [Ba-Cu-O] melts of compositions (3BaO:5CuO) and (3BaO:7CuO), in the temperature range 950-1005 ºC with a variation of C_δ between 0.1 % and 10 %. Corresponding values of C_{eq} are deriving from the indicated temperature range in Fig. 1.15, and are specified next to the relative curve.

Kuznesov *et al.* studied the solubility of Sm in [Ba-Cu-O] melts of various compositions in air, specifically (3BaO:4CuO), (3BaO:5CuO), (3BaO:7CuO), and (3BaO:9CuO) [78]. Despite Y being the RE of highest interest for the work described in this thesis, which is majorly regarding YBCO formation through TLAG, the following case study on Sm solubility may find a parallelism with the growth of YBCO from transient liquids of different (Ba:Cu) composition described in Chapters 4 and 5, and for this reason is discussed here. MTG was conducted in a temperature range 960 ºC and 1140 ºC, and a similar tendency to the aforementioned case of Y may be observed in the Sm solubility as a function of temperature graph in Fig. 1.19. Melt composition of highest copper content, here (3BaO:9CuO), is displaying the highest solubility of Sm in all of the tested temperatures, with a factor 4 increase if compared to the composition with lowest copper content, in this case (3BaO:4CuO).

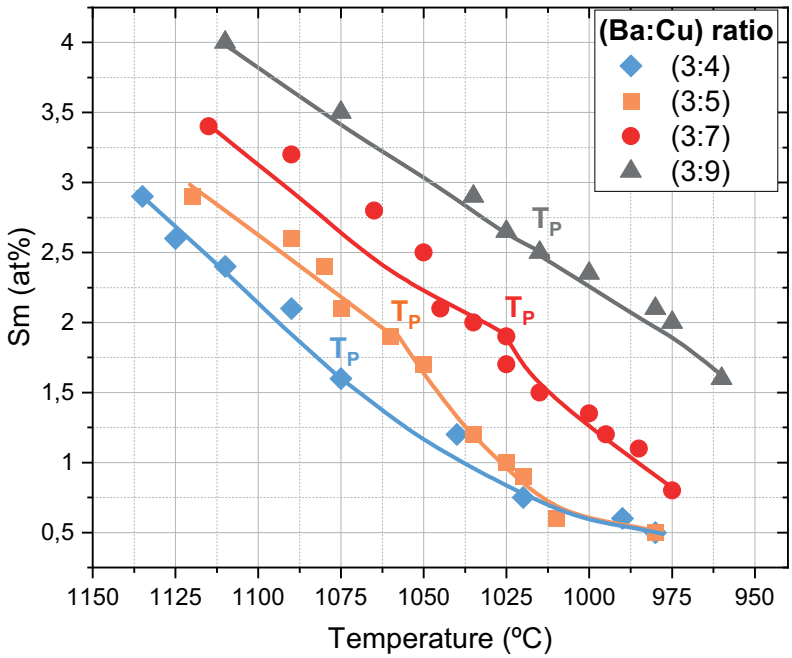


FIGURE 1.19: C_{eq} of samarium as a function of temperature in melts of four compositions: (3BaO:4CuO) (blue), (3BaO:5CuO) (orange), (3BaO:7CuO) (red), and (3BaO:9CuO) (grey). Study conducted through MTG in air. Adapted from [78].

By computing the relative supersaturation, σ, as a function of the variation of C_δ for each melt composition employing the values of C_{eq} obtained from the previous graph and with a variation of temperature, from the lowest value up to T_P corresponding to each melt composition in Fig. 1.19, as for the case of Y in Fig. 1.18, a similar trend is observed in Fig. 1.20. Sm solubility is low in melts of lower copper content (i.e. (3BaO:4CuO) and (3BaO:5CuO)).

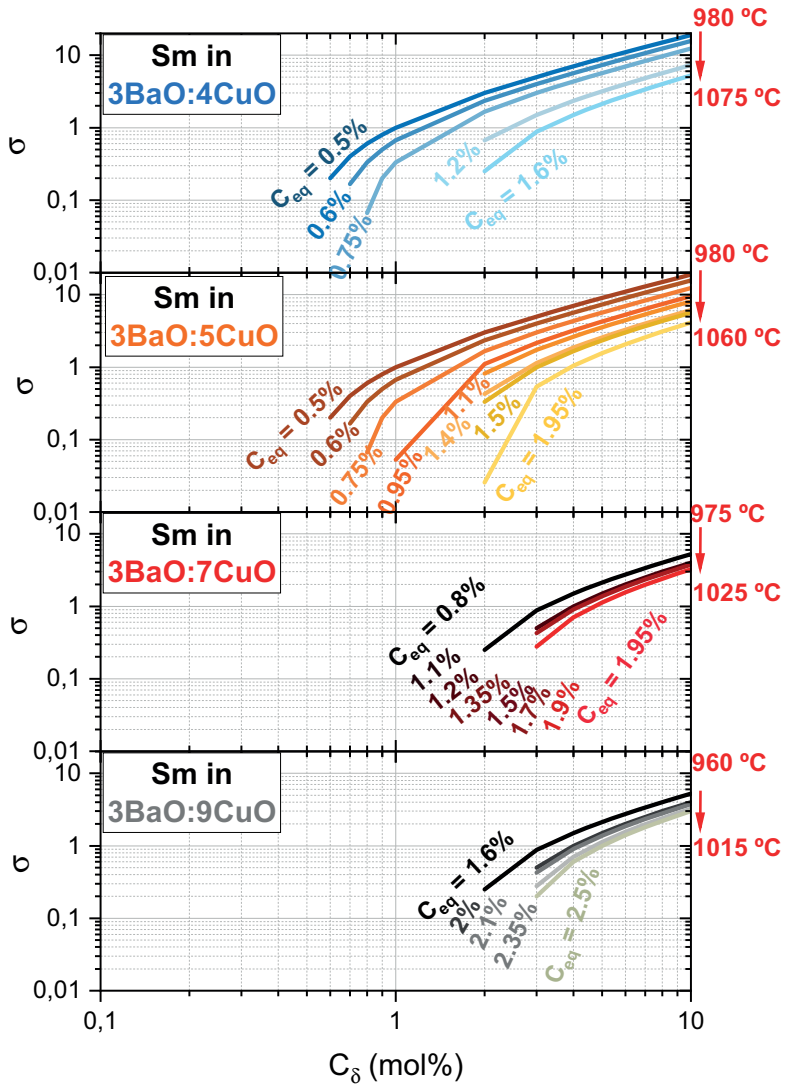


FIGURE 1.20: Calculation of the relative supersaturation σ of Sm in [Ba-Cu-O] melts of four compositions ((3BaO:4CuO), (3BaO:5CuO), (3BaO:7CuO), and (3BaO:9CuO)), with a variation of C_δ between 0.1 % and 10 %. The temperature is ranging between the lowest values and T_P for each melt composition in 1.19. Corresponding values of C_{eq} are indicated next to the relative curve.

This leads to high σ, given the inverse proportionality of these parameters. If Cu-rich compositions are considered, specifically (3BaO:7CuO) and (3BaO:9CuO), C_{eq} displays a general increase and a correspondent significant lowering of the relative supersaturation. This is evidently demonstrating the feasibility of an impressive modulation of the supersaturation by a simple change in the stoichiometry of the melt, a strategy that has been adopted in this thesis

for the growth of YBCO from transient liquids of compositions similar to the study presented here, and will be discussed in 4.4. If the focus is set on the curves corresponding to the lowest processing temperature selected for the two extreme cases, (3BaO:4CuO) and (3BaO:9CuO) melt compositions, one may observe a factor 3 increase in the value of C_{eq}, additionally being relative to a temperature 20 ºC lower in the latter case. This leads to an important decrease in σ, and a general possibility of employing lower processing temperatures for the nucleation of the final perovskite-type structure. In fact, the temperature range considered for each melt composition is observed to shift to higher values with the decrease of copper: interesting to notice how the highest temperature tested for the melt of (3BaO:4CuO) composition exhibits $C_{eq} = 1.6$ %, equivalent to the C_{eq} resulting for the lowest processing temperature in the case of a (3BaO:9CuO) melt. Again, clear evidence of the advantage of working with copper-rich melts for a noteworthy reduction of the fabrication temperature of the same material. If instead, the melt composition is kept constant, the relative supersaturation may be decreased through a raise in the thermal conditions which are seen to promote the solubility of Sm in the [Ba-Cu-O] melt. Nonetheless, it is important to remember that the studies taken into consideration here set the general objective of a reduction of the processing temperatures due to several reasons directly linked to the improvement of the fabrication method. In TLAG, the anticipated advantage of a thermal decrease correlated to an increase of copper content must necessarily be additionally resulting in high epitaxy, for the application proposed in this thesis. Therefore, a compromise must be found between liquid supersaturation and epitaxial nucleation from the liquid. Reminding the reader of the correlation between ΔG and melt supersaturation displayed in Fig. 1.13, the promotion of c-axis nucleation is obtained in REBCO systems through a decrease of the supersaturation and favouring heterogeneous nuclei to be formed. The choice of working with different compositions of the melt, obtained through copper content variation in the initial chemical solution, has thus, in this thesis, the objective of lowering the transient liquid supersaturation and encourage the epitaxially oriented (00l) nucleation and growth of the REBCO layer. This anticipated tendency will be correlated profusely to the experimental evidence reported in Chapter 4, specifically in 4.4.

As previously mentioned, the variation of the transient liquid composition is not the sole strategy employed in the growth of YBCO (or other REBCO) through TLAG to vary supersaturation. Tuning of the processing parameters, specifically T-P_{O_2}, results in a modification of the properties of the transient liquid and can be thus employed to control epitaxial nucleation of the superconducting material. Two works from the late '90s have studied the relation between the solubility of Y in the [Ba-Cu-O] melt at increasing T-P_{O_2} conditions. The first was conducted by Nakamura *et al.* in 1996 making use of a thermally equilibrated MgO rod dipped in the Y-Ba-Cu-O solution[10] to grow a single crystal which would be successively analyzed

[10]To be precise, the solution is exclusively composed by a [Ba-Cu-O] melt contained in a crucible made out of yttria. The corrosive nature of the melt, in contact with the crucible, will thus react to include yttrium in the solution.

by inductively coupled plasma atomic emission spectrometry (ICP-AES) [75]. The second, conversely, reported by Yao *et al.* in 1998, was performed employing the solute-rich-liquid crystal-pulling (SRL-CP) growth method [76], designed by the authors to overcome the generally low Y supersaturation and increase the growth rate of the single crystal. Both studies analyse the effect of an increase of P_{O_2} (specific values of 0.02 bar, 0.21 bar and 1 bar) and employ a melt composition of (3BaO:5CuO), thus no influence from variations of the compositions will be considered in this portion of the text. Fig. 1.21 displays the values of Y solubility (i.e. C_{eq}) in the [Ba-Cu-O] melt extrapolated from the aforementioned studies. The correlation of Y solubility with P_{O_2} is similar in both cases: however, the variation in the values of temperature is a direct cause of the characteristics of the growth method employed.

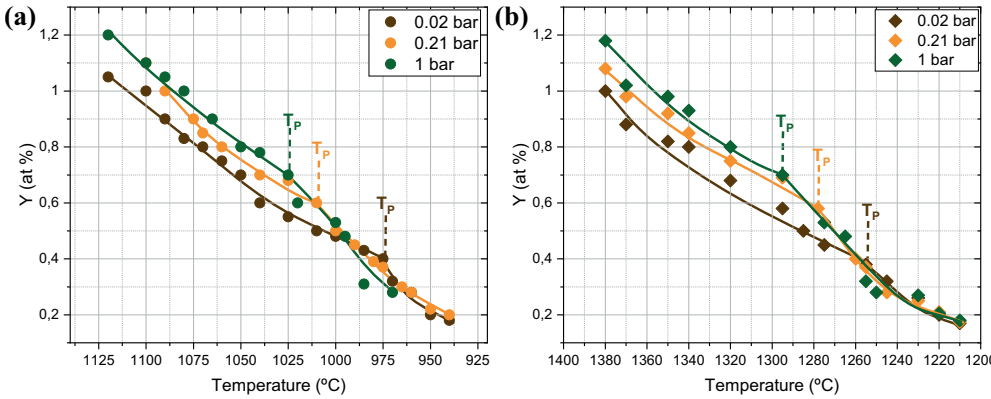


FIGURE 1.21: Y solubility in a melt of (3BaO:5CuO) composition for increasing P_{O_2} (0.02 bar, 0.21 bar and 1 bar) as a function of temperature. Data extrapolated from works of (a) Nakamura *et al.* [75] and (b) Yao *et al.* [76] The difference in the values of temperature derives from the growth method employed.

Two different tendencies are evident, and are similar from both works. When high temperatures are selected (above T_P), the solubility of Y is clearly enhanced when working at higher P_{O_2}. Selecting 1 bar of oxygen partial pressure will thus result in a lower supersaturation if compared to the utilization of the lower P_{O_2} values of 0.21 bar and 0.02 bar. However, for temperatures below 1300 ºC, in both cases a different trend is observed, with the overlapping of the data points leading to a more complex correlation between Y solubility in the melt and the oxygen partial pressure selected. This temperature region is the one of greatest interest for the work conducted in this thesis, given the selected growth temperatures for TLAG are below 900 ºC (all processing conditions will be thoroughly provided in Chapter 4). The absence of unambiguous data consequently leads to no direct conclusions deriving from literature regarding the correlation between these two parameters, and further studies are highly anticipated given the extreme interest in the community.

A final, interesting strategy to vary the supersaturation of the system is linked to the use of different RE, given that each display a characteristic solubility in the same [Ba-Cu-O] melt[11] Extrapolation of data from [74, 76, 79] regarding the RE solubility in a [Ba-Cu-O] melt employing, respectively, MTG, SRL-CP, and LPE growth methods (in air), lead to considerably appealing observations. The curves of RE solubility (C_{eq}) as a function of temperature for the cases of Yb, Y, Dy, Gd, Sm, and Nd are displayed in Fig. 1.22. The ionic radii of the RE^{3+} cations must be specified at this point: Yb^{3+} = 0.99 Å, Y^{3+} = 1.02 Å, Dy^{3+} = 1.03 Å, Gd^{3+} = 1.05 Å, Sm^{3+} = 1.08 Å, and Nd^{3+} = 1.12 Å. The increase of the RE^{3+} ionic radius is directly correlated to an increase in the RE solubility, with an inevitable increase in the processing temperature. However, as for the case of the data reported above regarding the correlation of supersaturation to P_{O_2}, two trends can be observed in the data relative to the RE dependency. For temperatures above 1020 ºC, the tendency suggests an increase of RE solubility when its ionic radius is higher, with the cases of Sm and Nd displaying more than a doublefold increase

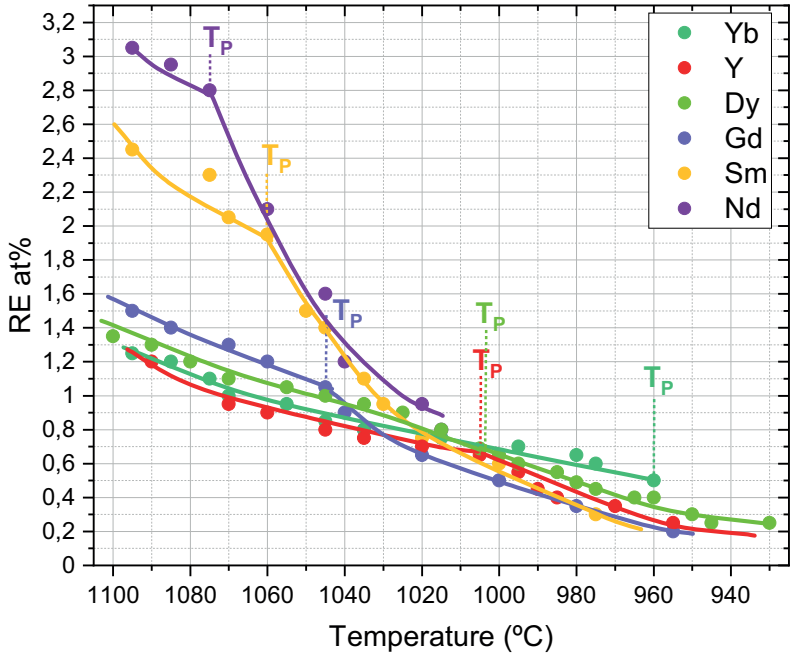


FIGURE 1.22: Solubility of RE in a (3BaO:5CuO) melt as a function of temperature for the cases of ytterbium (green), yttrium (red), dysprosium (light green), gadolinium (blue), samarium (yellow), and neodymium (purple). Data extrapolated from [74, 76, 79], all studies conducted in air.

in this parameter. This will result in a significant lowering of the supersaturation when these RE are employed, in contrast to the use of RE of smaller size. Nonetheless, the trend becomes

[11] Only a melt of (3BaO:5CuO) composition will be considered for this analysis.

unclear when focusing on the data points corresponding to temperatures below 1000 ºC, where an intersection between the data of each RE results in the case of Yb, the RE presenting smaller ionic radius, to display a significantly pronounced solubility, thus resulting in the lowest supersaturation in these conditions. It is evident that further investigation regarding the solubility of RE in melts of [Ba-Cu-O] must be conducted in order to have a more accurate determination of the correlation of RE solubility and its size. Specifically interesting for the advance of the CCs fabrication through TLAG is the correct identification of the tendency of the solubility of each RE for a lower temperature range, closer to the experimental working conditions. Hypothesis on the correlations of RE solubility and supersaturation of the transient liquid in the TLAG of REBCO (RE = Yb, Y, Sm, Gd) will be provided in 4.5, where a preliminary study of the growth of these different REBCO systems through TLAG is described.

In summary, the historical overview that led to the development of the TLAG-CSD methodology for YBCO fabrication has been provided in this chapter. The concepts of crystal growth from melts, and specifically Y or other RE solubility in [Ba-Cu-O] melts of various composition and in different processing conditions, have been provided, given these are cardinal points at the foundation of the liquid-assisted kinetic mechanism of TLAG. The delicate tuning of supersaturation is a challenging task which may be controlled through several parameters, as reported in this section of the text. For a comprehensive understanding of the experimental work reported in this thesis, the concepts and relations between the several processing parameters or melt compositions described here will be of significant importance, specifically when analysing the growth of REBCO through TLAG, object of chapters 4 and 5. A fine adjustment between the enhancement of the nucleation rate, generally linked to high melt supersaturation, and lowering the latter parameter to promote c-axis nucleation is required for the attainment of high-performance superconducting REBCO films, one of the major objectives of this thesis. The following chapters are devoted to present the novelties and progress that the experimental work performed during the years of this PhD thesis have generated for each step of the innovative TLAG-CSD methodology.

2

Synthesis of metal propionates: structural and thermal investigation of their suitability in REBCO precursor solutions

In this chapter, the development and optimization of synthetic routes for a series of metal propionate powders to be used as precursors in the metal-organic chemical solution employed in the preparation of REBCO superconducting films will be presented. Detailed characterization carried out through numerous techniques will lead to the determination of their high purity deriving from low-cost precursors and one-pot synthetic methods. A complete structural investigation will yield six previously unreported crystalline forms. To evaluate their compatibility in the REBCO precursor solutions, a comprehensive analysis of the thermal behaviour of the powders and films of each individual metal propionate was conducted. Profound understanding of the decomposition pathways provided detailed insight on the suitability of the synthesized products in the REBCO precursor solutions, subsequently subjected to the thermal treatments used for the fabrication of the final films. Additionally, the information in this chapter may find applicability for the preparation of any functional material that follows the metal-organic precursor decomposition pathway through CSD-based methodologies, yielding interesting possibilities for low-cost and high-throughput synthetic methods for the implementation of technologies based on various functional metal-oxides.

2.1 Objectives

The extensive overview on the history and progress of HTS fabrication presented in Chapter 1 has led to the conclusion that the production of REBCO CCs has faced numerous challenges since the dawning of their industrialization. Major obstacle to the widespread of this technology has been the feasibility of developing low-cost and high-throughput industrial processes based on the reel-to-reel configuration to obtain the biaxially textured REBCO superconducting layer [9, 13, 17, 18, 116]. CSD methodologies have promptly been considered the most promising candidates to reduce the production costs of the REBCO superconducting films [14, 15]: the metal cations contained in the inexpensive metal-organic chemical solutions employed in this technique are responsible for the formation of the final REBCO superconducting material following its deposition and several annealing processes. This process is commonly known as metal-organic decomposition (MOD), and found a widespread and early development through the route based on commercial fluorinated metal acetate precursors for the preparation of the REBCO precursor solutions, namely trifluoroacetate metal-organic decomposition (TFA-MOD) [36, 42, 117–119]. High-performance superconducting films could be obtained through this route, reaching usually critical current density (J_c) values in the range 4-5 MA/cm^2, although values up to 10 MA/cm^2 at 77 K in self-field [120] have also been demonstrated [121]. Consequently, despite TFA finds a preferential application in the industrial sector thus far [122], the inadequacy of its waste products (mainly the highly toxic hydrofluoric acid) and the slow growth rates intrinsic of the solid-solid reaction governing the growth process (below 1-5 nm/s) [35, 71, 123] are found as major drawbacks of this method. Considering the most recent regulations requiring sustainable chemical processes discouraging globally the use of fluorine-based chemical precursors and the low-throughput nature of REBCO fabrication through the TFA-MOD route, the development of novel chemical-based methods for this specific application was compelling. The complete elimination of fluorine from the system led to the development of fluorine-free solutions, widely acknowledged as encouraging precursor solutions for CSD-derived REBCO films. The most commonly employed precursors for solution preparation in this case are commercial metal acetates, generally dissolved in propionic acid (HProp) or mixture of solvents containing this acid. At times, the use of additives such as polymers or amines has been implemented to enhance certain rheological properties leading to more advantageous outcomes during film deposition and annealing. This substantial progress boosted the production of REBCO superconducting materials towards an environmentally-friendly alternative of the process which preserved the low-cost CSD-based methodology and the desired high-performance [46–50, 88]. Nonetheless, since the emergence of studies based on fluorine-free solutions, it was commonly believed that the inevitable formation of barium carbonate ($BaCO_3$) as the sole barium precursor phase for the REBCO growth would lead to significant hindrances, given its elevated thermal stability [42, 89–91]. $BaCO_3$ decomposition

temperature is found above 1000 ºC when analysed in powder form [92, 93]: this temperature is greatly beyond the processing temperature for REBCO superconductors, thus leading to the idea of its presence being a major complication to the material fabrication. Despite this, high-performance superconducting properties were obtained in YBCO films deriving from this type of precursor solutions through the use of the innovative growth process known as Transient Liquid Assisted Growth (TLAG) [53], demonstrating $BaCO_3$ is not a limitation to the growth of REBCO films. As sole CSD-based methodology with the unique assistance of a transient liquid to the growth mechanism, initial studies demonstrated unprecedented growth rates beyond 100 $nms^{-}1$ through TLAG. Despite showing additionally impressive values of critical current density of 5 MA/cm^2 at 77 K, this could be demonstrated on films of only 100 nm thickness of the final YBCO, given the metal-organic precursor solutions employed in the preparation of such films were developed through the use of commercial metal acetates, with limited solubility in the chosen media. Moreover, multideposition would face detrimental hindrance to the attainment of a homogeneous film after a fourfold or fivefold deposition, limiting the feasible thickness to 400-500 nm. For potential applications of TLAG in the industrial framework, the thickness of the films must be greatly enhanced without compromising the superconducting properties. Therefore, a novel solution formulation was pivotal to reach this competitive objective. The development of the latter will be discussed in the following chapter, entirely devoted to the precise optimization process which led to the achievement of a quadrupled increase of the film thickness, among other fundamental improvements to rheological properties of the precursor solutions.

One of the fundamental points of the novel solution formulation was the strategy of synthesizing metal propionate precursors of Y, Ba, and Cu prior to their use in the metal-organic precursor solution for the preparation of YBCO films. The inevitably incomplete conversion of metal acetates in propionic acid-based solvent mixtures, as widely used in literature, leads to the presence of undesired products in the YBCO precursor solution: mostly, non-reacted acetates, acetate-propionate mixtures, and acetic acid (deriving from the conversion reaction of metal acetate into metal propionate). Studies for the case of barium revealed the exclusive formation of a mixed complex of acetate and propionate also when the acetate of this metal is dissolved in excess of HProp [124, 125]. Considering the secondary products in solution, complications may arise in the decomposition of the metal-organic derivatives in the pyrolysis thermal treatment, resulting in major impediments to the preparation of the nanocrystalline precursor films facing obstacles such as crack formation or presence of undesired phases [126]. The use of pre-synthesized, high-purity metal propionate powders is believed to be of great benefit as the absence of any kind of secondary products in solution is anticipated to result in reproducible decomposition pathways to be followed.

Considering the widespread interest in the development of REBCO superconducting films, especially increased in the last decades [9, 122, 127–129], the initial optimization of the propionates of Y, Ba and Cu was then additionally extended to the ones of Ce, Sm, Gd, and Yb.

As a result, the preparation of different REBCO precursor solutions were studied in depth in this thesis, with the final objective of pursuing the fabrication of REBCO superconducting films through TLAG-CSD. Despite the use of the precursor of $Ce(Prop)_3$ is not described in the work conducted in this thesis, as it is not directly employed for the preparation of REBCO precursor solutions, yet it found application in the work conducted in a different project inside the group. Nonetheless, the optimization of the synthetic procedure, its full characterization and thermal behaviour will be reported here due to its possible interest, as it is common to use cerium oxide-based buffer layers in the fabrication of REBCO CCs given its reduced lattice mismatch, thus promoting the epitaxy of the superconducting layer [130, 131]. Moreover, the information presented in this chapter is believed to be of great significance for the application of these kind of precursors in any other CSD-based methodology which follows the MOD route, widening the perspective for any functional oxide material.

2.2 Synthesis and characterization of a series of metal propionate powders

2.2.1 General characterization

Propionates of copper ($Cu(Prop)_2$), yttrium ($Y(Prop)_3$), barium ($Ba(Prop)_2$), cerium ($Ce(Prop)_3$), samarium ($Sm(Prop)_3$), gadolinium ($Gd(Prop)_2$), and ytterbium ($Y(Prop)_3$) were obtained in powder form through simple, one-pot synthetic routes and employing low-cost oxide, carbonate or acetate precursors following the procedures described in the Experimental Section in B.1.2. The synthesis of all compounds resulted in high yields (between 68% and 96%) and high purity, corroborated by the accord between elemental analysis (EA) results and the theoretical values for each product, reported in B.1.2. The precise composition of each compound was established taking into account the EA in combination with the initial mass losses of the thermogravimetric analysis coupled to Fourier-transform Infrared Spectroscopy (TGA-FTIR), indicating possible coordination of H_2O molecules or solvent, and the results of the structural investigation. Specifically, for $Ba(Prop)_2$, $Sm(Prop)_3$, and $Gd(Prop)_2$, presence of residual solvent or H_2O detected by TGA-FTIR are absent in the determined single crystal structures that will be presented later in this section, indicating their loss is occurring during crystallization.

Fourier-transform Infrared Spectroscopy using attenuated total reflectance (FTIR-ATR) spectra were acquired for all of the synthesized compounds, and are displayed in Fig. B.1-B.7 (identification of the bands for individual metal propionates are shown). In all cases, the characteristic bands for propionate groups are identified: specifically, the vibrational modes relative to the aliphatic chains of the propionate ligands are present in the region between 2900-2800 cm^{-1}. The synthesis of $Sm(Prop)_3$ and $Yb(Prop)_3$ were the sole which employed the acetates

of these metals as precursors, and the FTIR-ATR spectra displayed in the following Fig. 2.1 are suggesting, within the detection limit of the technique, that full substitution of the acetate ligands by propionate ones was reached. Particularly important to determine this is the absence of the *C-C* stretching mode found at 1009 cm^{-1} for samarium acetate ($Sm(OAc)_3$) and at 1016 cm^{-1} for ytterbium acetate ($Yb(OAc)_3$), in addition to the lack of peaks due to the *COO* deformation bands (670 cm^{-1} for $Sm(OAc)_3$ and 675 cm^{-1} for $Yb(OAc)_3$) in the spectra relative to the propionate powders.

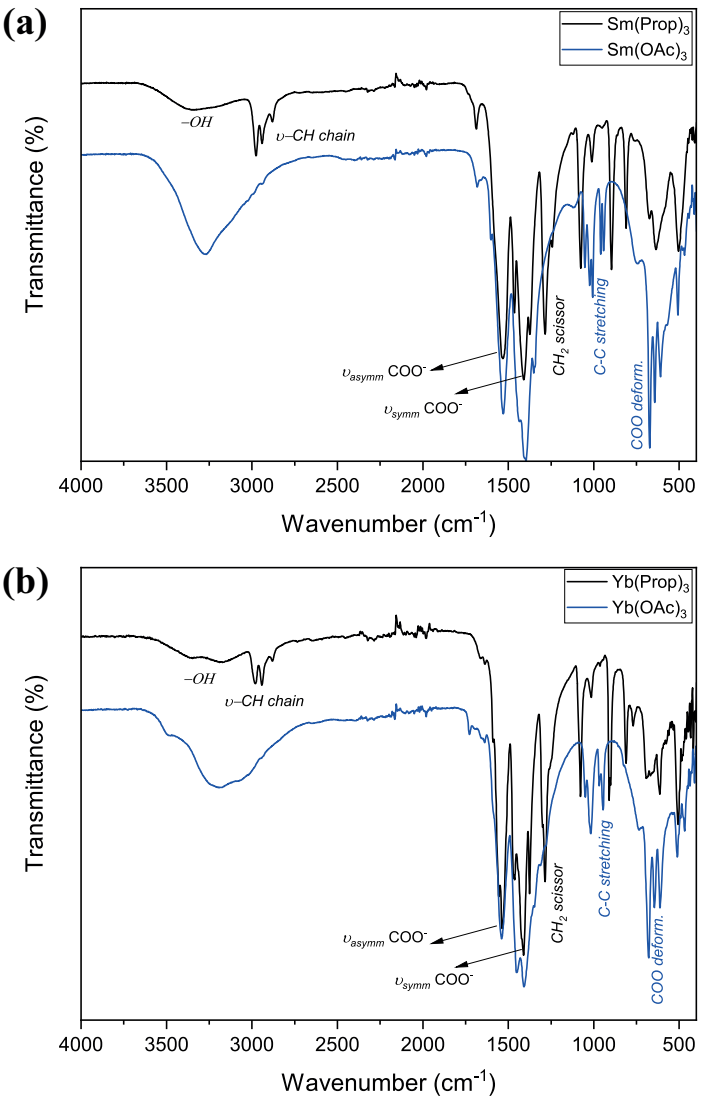


FIGURE 2.1: FTIR-ATR spectra measured for (a) $Sm(Prop)_3$, (b) $Yb(Prop)_3$ (black) compared to their respective acetate precursors (blue).

Examination of the powders through scanning electron microscopy (SEM) allowed for the determination of average grain sizes, showing a wide range of size distributions (Fig. B.8. In order to achieve final REBCO films of elevated thickness, high concentrations of the metal-organic chemical solutions employed for deposition are preferable, as this parameter is directly linked to the thickness of the film (more details will be given in the following chapter). Undoubtedly, saturated solutions may be obtained by enhancing the solubility of the precursors. As it will be observed in Chapter 3, the solubility of $Cu(Prop)_2$ is the most challenging in the system described in this thesis. The average grain size of 100 μm and the crystal-like shape of the as-synthesized powder has led to major complications towards a fast dissolution (Fig. 2.2(a)). Therefore, the solubility of this particular metal propionate was improved by drastically diminishing the grain size by means of mechanical grinding through ball milling (BM). Fig. 2.2 displays a comparison of the SEM images of the same powder of $Cu(Prop)_2$ before

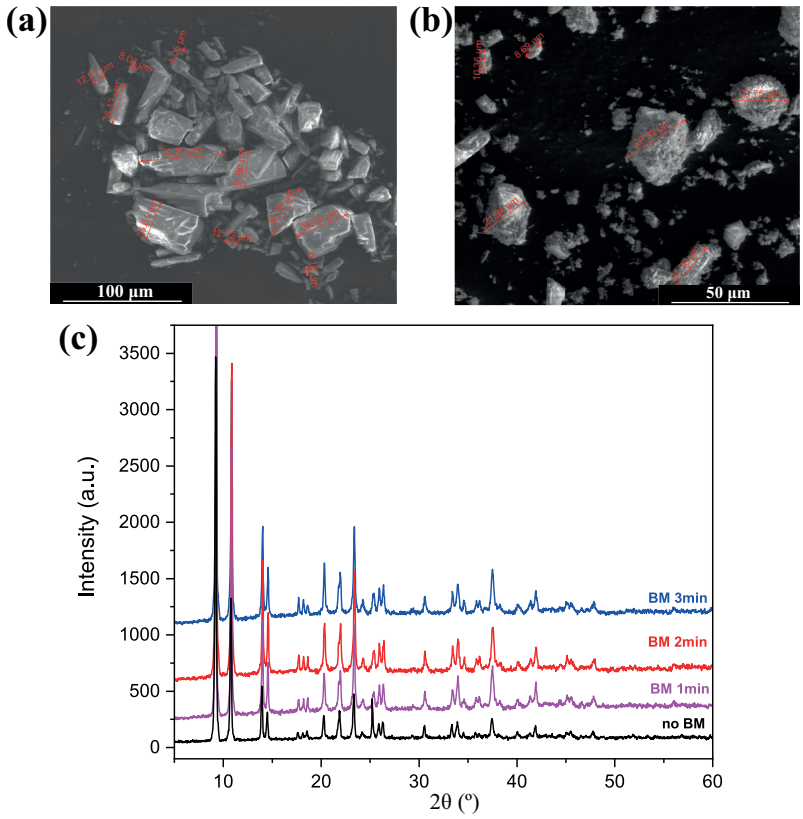


FIGURE 2.2: SEM images of $Cu(Prop)_2$ powder (a) as-synthesized and (b) after 1 minute of mechanical grinding at 650 rpm. (c) Comparison of XRD patterns of $Cu(Prop)_2$ powder as synthesized (black) and following increasing grinding times through ball milling (BM) going from a total of 1 to 3 minutes.

and after 1 minute of mechanical grinding at 650 rpm (respectively, Fig. 2.2 (a) and (b)). An average grain size of below 30 μm was obtained in this limited grinding time, and as shown in the X-Ray Diffraction (XRD) patterns in Fig. 2.2(c), no reactivity induced from the highly energetic grinding process could be observed up to a total grinding time of 3 minutes. The reduction of the grain size has been fundamental for a straightforward dissolution of this specific metal propionate precursor in the solvent mixture chosen for the metal-organic REBCO precursor solution, making higher concentrations feasible[1].

2.2.2 Structural investigation

With the objective of obtaining detailed structural information regarding the synthesized metal propionates, recrystallization of the powders through various crystallization methods was carried out, yielding suitable single crystals (SC) for all of the metal propionates. Understanding of the crystal structure of each metal propionate leads to achieving a higher degree of reproducibility of the decomposition of the organic matter during the pyrolysis thermal treatment: the growth of REBCO films through TLAG requires nanocrystalline precursor films, result of the pyrolysis process, which present a high nanoscale compositional homogeneity. Having knowledge of the crystal structure of the metal propionates is essential to control the decomposition mechanisms these will follow.
Two of the obtained crystal structures found matches in literature, specifically the cases of $Cu(Prop)_2$ and $Yb(Prop)_3$: the former corresponds to the one reported by Chung *et al.* [132], whereas the latter corresponds to the work of Bierke [133]. Comparisons of the acquired SC-XRD and the data from literature is displayed in Fig. B.9. No matches in literature could be found for the further six crystal structures obtained.
Crystallization of compounds of $Sm(Prop)_3$ and $Gd(Prop)_3$ occurs in a triclinic *P*-1 space group. Conversely, the cases of $Y(Prop)_3$ and $Ba(Prop)_3$ result in crystallization in the monoclinic *P*21/n space group. Crystal data and structure refinement for these compounds is displayed in Table 2.1, whereas bond lengths and torsion angles are reported in B.1.3.

Crystallization of gadolinium propionate through vapor diffusion of acetone in HProp displays two pairs of Gd(III) centers bearing $[GdO_8]$ and $[GdO_9]$ cores and coordination numbers 8 and 9, respectively (Fig. 2.3(a)). Crystal structures corresponding to pure gadolinium propionate were, up to now, not present in literature. The Gd(1) and Gd(3) exhibit two Gd-O bonds deriving from bidentate chelating propionate groups, two bridging propionate groups (bonded to Gd(2) and Gd(4)), and two oxygen atoms jointly bonded to a propionate group chelating a neighboring Gd center. Likewise, Gd(2) and Gd(4) centers are coordinating eight propionate ligands with coordination resembling the cases of the Gd(1) and Gd(3) centers, and a further oxygen atom relative to a HProp each (O11 and O27, respectively). The geometries of the

[1] As will be explained in detail in Chapter 3, the further addition of an amine compound as additive is the cardinal point which enabled a significant increase of solution concentration.

	$[Ba(Prop)_2] \cdot HProp$	$[Sm(Prop)_3(OH_2)]_n$	$[Gd(Prop)_3] \cdot HProp$	$[Y(Prop)_3(OH_2)_2]_n$
Empirical formula	$C_{39}H_{79}Ba_7O_{33}$	$C_9H_{17}O_7Sm$	$C_{21}H_{36}Gd_2O_{14}$	$C_9H_{19}O_8Y$
Formula weight	2037.40	387.57	413.50	344.14
Temperature (K)	294(2)	295(2)	295(2)	298(2)
Wavelength (Å)	0.71073	0.71073	0.71073	0.71073
Crystal system	Monoclinic	Triclinic	Triclinic	Monoclinic
Space group	*P*21/n	*P*-1	*P*-1	*P*21/n
Unit cell dimensions				
a (Å)	14.1996(18)	9.620(7)	12.794(8)	12.231(3)
b (Å)	16.142(2)	11.594(8)	13.055(9)	14.087(3)
c (Å)	30.554(4)	11.898(9)	20.780(13)	8.8837(18)
α(deg)	90	97.052(14)	75.855(12)	90
β(deg)	94.615(3)	92.512(14)	75.172(14)	97.219(4)
γ(deg)	90	102.805(13)	69.192(10)	90
V (Å)	6980.5(16)	1280.9(16)	3091(3)	1518.2(5)
Z	4	4	8	4
D_{calc} (Mg/m^3)	1.939	2.010	1.777	1.506
Absorption coefficient (mm^{-1})	3.961	4.604	4.312	3.866
F(000)	3876	756	1608	704
Crystal size (mm^3)	0.120x0.100x0.060	0.280x0.110x0.09	0.31x0.14x0.12	0.17x0.14x0.09
θ range for data collection (deg)	1.337 to 28.439	1.729 to 28.261	1.029 to 28.414	1.679 to 28.273
hkl ranges	-18≤h≤19 -21≤k≤21 -40≤l≤40	-12≤h≤12 -15≤k≤15 -15≤l≤15	-17≤h≤16 -17≤k≤17 -27≤l≤27	-16≤h≤16 -18≤k≤18 -11≤l≤11
Reflections collected	140781	34488	85834	32580
Independent reflections	17527	6292	15326	3758
Completeness to θ(%)	99.9	100.0	100.0	100.0
Absorption correction	Semi-empirical from equivalents	Semi-empirical from equivalents	Semi-empirical from equivalents	Semi-empirical from equivalents
Max. and min. transmission	1 and 0.707	1 and 0.31	1 and 0.163	1 and 0.485
Refinement method	Full-matrix least squares on $\|F\|^2$	Full-matrix least squares on $\|F\|^2$	Full-matrix least squares on $\|F\|^2$	Full-matrix least squares on $\|F\|^2$
Data / restraints / parameters	17527 / 653 / 767	6292 / 10 / 326	15326 / 86 / 683	3758 / 32 / 182
Goodness-of-fit on $\|F\|^2$	1.164	1.012	0.947	0.945
Final R indices [I>2sigma(I)]	$R_1 = 0.1130$ $wR_2 = 0.2679$	$R_1 = 0.0815$ $wR_2 = 0.1996$	$R_1 = 0.0711$ $wR_2 = 0.1551$	$R_1 = 0.0580$ $wR_2 = 0.1661$
R indices (all data)	$R_1 = 0.1933$ $wR_2 = 0.2986$	$R_1 = 0.1454$ $wR_2 = 0.2470$	$R_1 = 0.1775$ $wR_2 = 0.2006$	$R_1 = 0.0898$ $wR_2 = 0.1799$
Extinction coefficient	n/a	n/a	n/a	n/a
Largest diff. peak and hole (e · Å^{-3})	4.118 and -4.224	8.858 and -3.400	3.049 and -2.008	1.465 and -0.633

TABLE 2.1: Crystal data and structure refinement for $[Ba_7(Prop)_{14}(OH_2)_8]_n$, $[Sm_2(Prop)_6(OH_2)_2]_n$, $[Gd_2(Prop)_6 \cdot 2HProp]_n$, and $[Y(Prop)_3(OH_2)_2]_n$.

Gd centers are distorted triangular dodecahedron for Gd(1) and Gd(3), and muffin geometries for both Gd(2) and Gd(4) (S values reported in Table B.5). These are leading to a connectivity of polymeric 1D-chains through a mixture of $\mu_2 : \eta^2 : \eta^1$ (mixed bidentate chelating and bridging) and $\mu_2 : \eta^1 : \eta^1$ (bridging) coordination modes (Fig. 2.3(b)). The combination of bridging and bidentate chelating coordination of the propionate ligands is supported by the $\Delta\nu$ value calculated from the FTIR-ATR spectrum, reported in B.1.2.

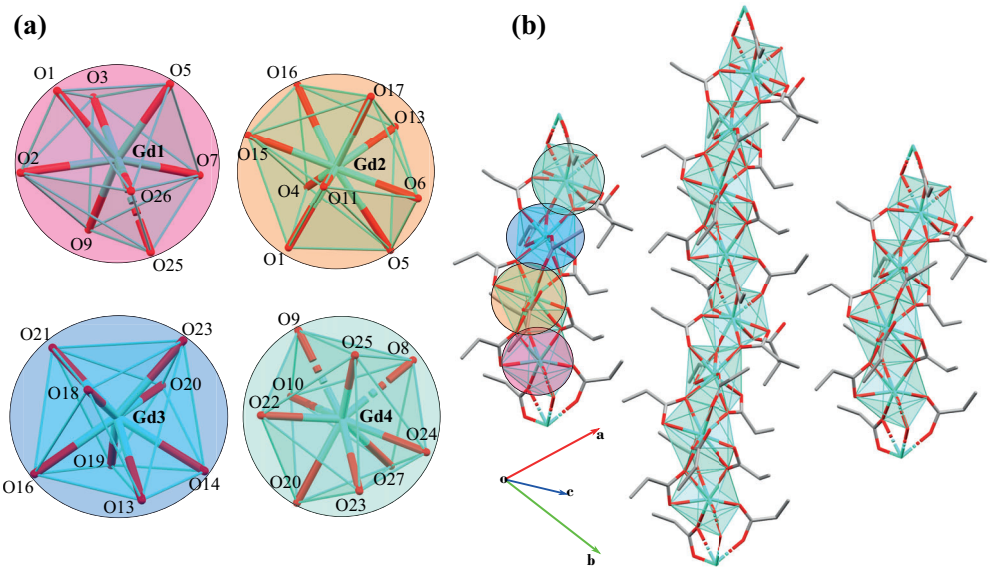


FIGURE 2.3: Representation of the (a) sequence of the crystallographically independent Gd(III) centers and (b) one-dimensional polymeric chains of $Gd(Prop)_3$.

Barium propionate exhibits seven Ba(II) centers which are crystallographically independent (Fig. 2.4) bearing one $[BaO_8]$ core, five $[BaO_9]$ cores and one $[BaO_10]$ core with coordination numbers 8, 9 and 10, respectively (Fig. 2.4(a)). Centers of coordination number 9 are Ba(1), Ba(3), Ba(4), Ba(5), and Ba(6), and these display two types of geometries: Ba(1), Ba(4) and Ba(5) a distorted hula-hoop geometry, whereas Ba(3) and Ba(6) a muffin geometry (S values reported in Table B.6). The latter Ba(II) centers show coordination to oxygen atoms deriving from two H_2O molecules (respectively, O4 and O6 for Ba(3) and O1 and O3 for Ba(6)) and several coordination modes combinations of the propionate ligands to the neighboring Ba(II) centers, including $\mu_2 : \eta^2 : \eta^1$, $\mu_4 : \eta^3 : \eta^2$, $\mu_3 : \eta^3 : \eta^2$, $\mu_3 : \eta^2 : \eta^2$, and $\mu_2 : \eta^2 : \eta^2$ (tritopic and ditopic oxygen atoms). Conversely, coordination to any H_2O molecule is absent in the cases of Ba(1) and Ba(4), which are instead showing Ba-O bonds exclusively relative to propionate ligands through a mixture of $\mu_2 : \eta^2 : \eta^1$, $\mu_3 : \eta^2 : \eta^2$, and $\mu_4 : \eta^3 : \eta^2$ connectivity with other Ba(II) centers (in particular, with Ba(1), Ba(2), Ba(3), Ba(4) and Ba(7) for Ba(3) and Ba(1), whereas with Ba(4), Ba(5), Ba(6) and Ba(7) for Ba(6)). Ba(5) is bonded

to a H_2O molecule through its oxygen atom (O5) and coordinated to Ba(1), Ba(2), Ba(4), Ba(6), and Ba(7) through combinations of $\mu_4 : \eta^3 : \eta^2$ and $\mu_3 : \eta^2 : \eta^2$ coordination modes deriving from the propionate groups. In contrast, Ba(2) exhibits a distorted tetradecahedron geometry (coordination number 10). The propionate ligands are arranged through $\mu_2 : \eta^2 : \eta^1$, $\mu_2 : \eta^2 : \eta^2$, $\mu_3 : \eta^2 : \eta^2$, and $\mu_4 : \eta^3 : \eta^2$, with a further Ba-O bond to a H_2O molecule (O7). Finally, Ba(7), with coordination number 8, bears a distorted hexagonal bipyramid geometry and displays coordination of the Ba(II) center through Ba-O deriving from two H_2O molecules (O2 and O5) in addition to a mixture of three coordination modes relative to the ligands: $\mu_2 : \eta^2 : \eta^1$, $\mu_2 : \eta^2 : \eta^2$, and $\mu_4 : \eta^3 : \eta^2$ with the neighboring Ba(1), Ba(2), Ba(3), Ba(4), Ba(5) and Ba(6).

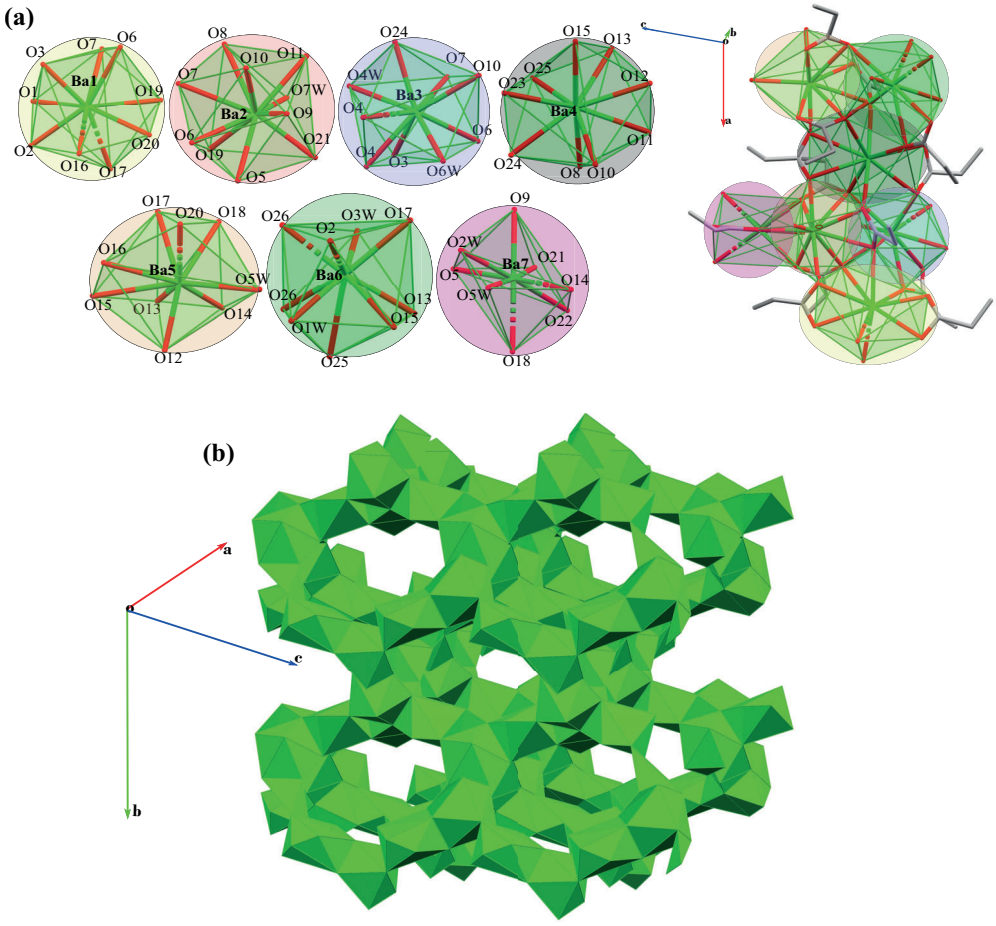


FIGURE 2.4: Representation of the (a) seven crystallographically independent Ba(II) centers in $Ba(Prop)_2$, displaying a distorted honeycomb 3D-lattice arrangement (b).

The different geometries of the crystallographically independent Ba(II) centers are leading

to the arrangement in a distorted honeycomb 3D-lattice (Fig. 2.4(b)). The crystal structure described here is the first case relative to a pure barium propionate compound which can be found in literature, considering that the sole previously described structure containing barium propionate, reported by Mos et al. [124], was a mixed complex of barium-acetato-propionate demonstrating no full substitution of the propionate ligands is reached when employing the acetate precursor of this metal.

The crystal structures obtained for $Y(Prop)_3$ and $Sm(Prop)_3$ are both yielding a 2D arrangement. Nasui *et al.* [134] reported a crystal structure relative to yttrium propionate, yet the one described in this thesis is a new polymorphic structure which displays several differences compared to the latter. The $[YO_9]$ core bears a muffin geometry with coordination number 9 (S values reported in Table B.7). The dimeric unit comprises two identical Y(III) centers, each showing connection to seven oxygen atoms relative to propionate groups and two H_2O molecules (O7 and O8 in Fig. 2.5(a)). The individual yttrium centres exhibit coordination to two propionate ligands through a $\mu_1 : \eta^1 : \eta^1$ (bidentate chelating) coordination mode, and to two with a mixed $\mu_2 : \eta^2 : \eta^1$ (bidentate chelating and bridging) coordination mode. The intramolecular and intermolecular H-bonds generated through the H_2O molecules, shown in Fig. 2.5(b), lead to the assembling of the dimeric units into a zig-zag 2D-sheet arrangement along the *bc* plane (Fig. 2.5(c)). The combination of coordination modes is in good agreement with the $\Delta\nu$ value reported in B.1.2, typical of a mixed bridging and bidentate chelating coordination of the propionate ligands.

A sole, further samarium propionate crystal structure is reported in literature [135], displaying an anhydrous structure and coordination of the samarium center to propionate ligands and HProp to yield a one-dimensional arrangement of polymeric chains. Conversely, the samarium propionate compound described in this thesis exhibits a $[SmO_9]$ core with coordination number 9 bearing a muffin geometry (S values reported in Table B.8). The two crystallographically independent Sm(III) centers are bonded through Sm-O to seven oxygen atoms relative to propionate groups and two H_2O molecules (O13 and O14 in Fig. 2.6(a)) for the case of Sm(1), whereas Sm(2) is bonded exclusively to propionate ligands. Two types of coordination modes are displayed by the propionate ligands, mixing $\mu_2 : \eta^2 : \eta^1$ and $\mu_2 : \eta^1 : \eta^1$. The former is a combination of bidentate chelating and bridging corresponding to the arrangement of the ligands between Sm(1)-Sm(1) and Sm(2)-Sm(2) centers, yielding the formation of 1D chains. The latter is relative to the bridging propionate groups which arrange the Sm(III) centers into distorted square lattice 2D-sheets along the *ab* plane, as shown in Fig. 2.6(b). This finding is in accord with the value of $\Delta\nu$ reported in B.1.2, corresponding to a mixed bridging and bidentate chelating coordination of the ligands.

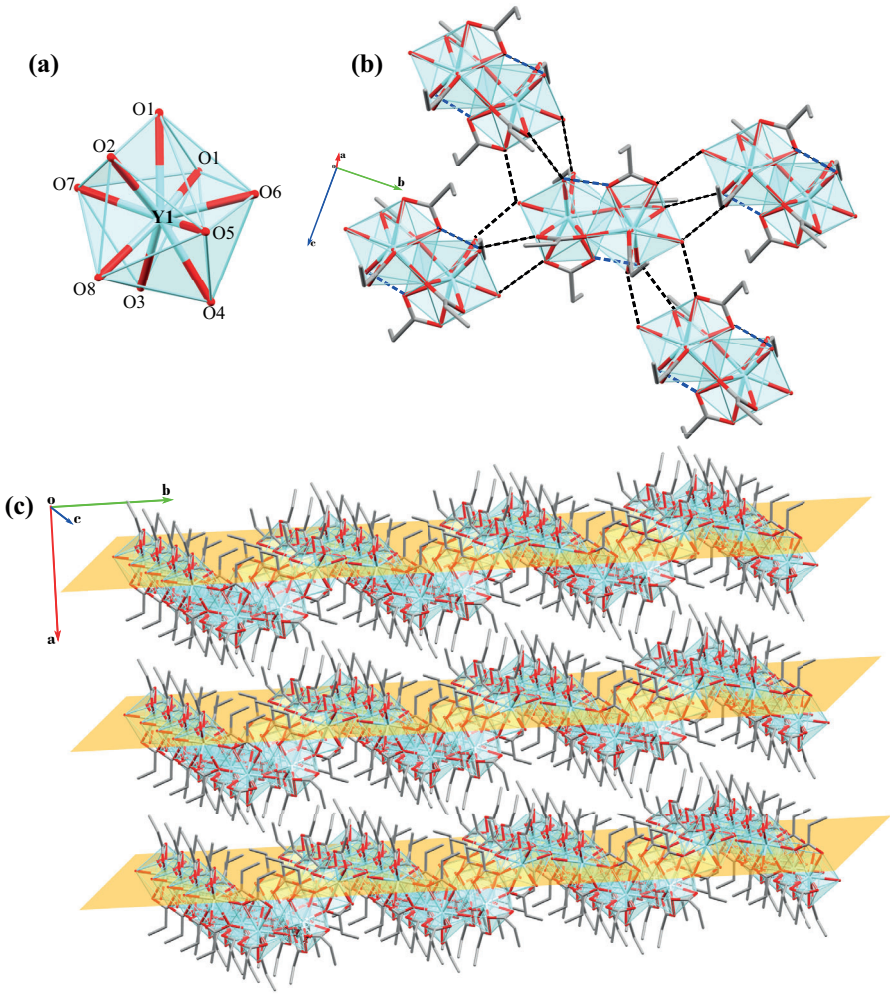


FIGURE 2.5: Representation of the (a) Y(III) core in the dimeric $Y(Prop)_3$ unit. (b) Intramolecular (blue dashed lines) and intermolecular H-bonds (black dashed lines) leading to the assembly of the dimers and (c) arrangement into the zig-zag 2D-sheets of $Y(Prop)_3$.

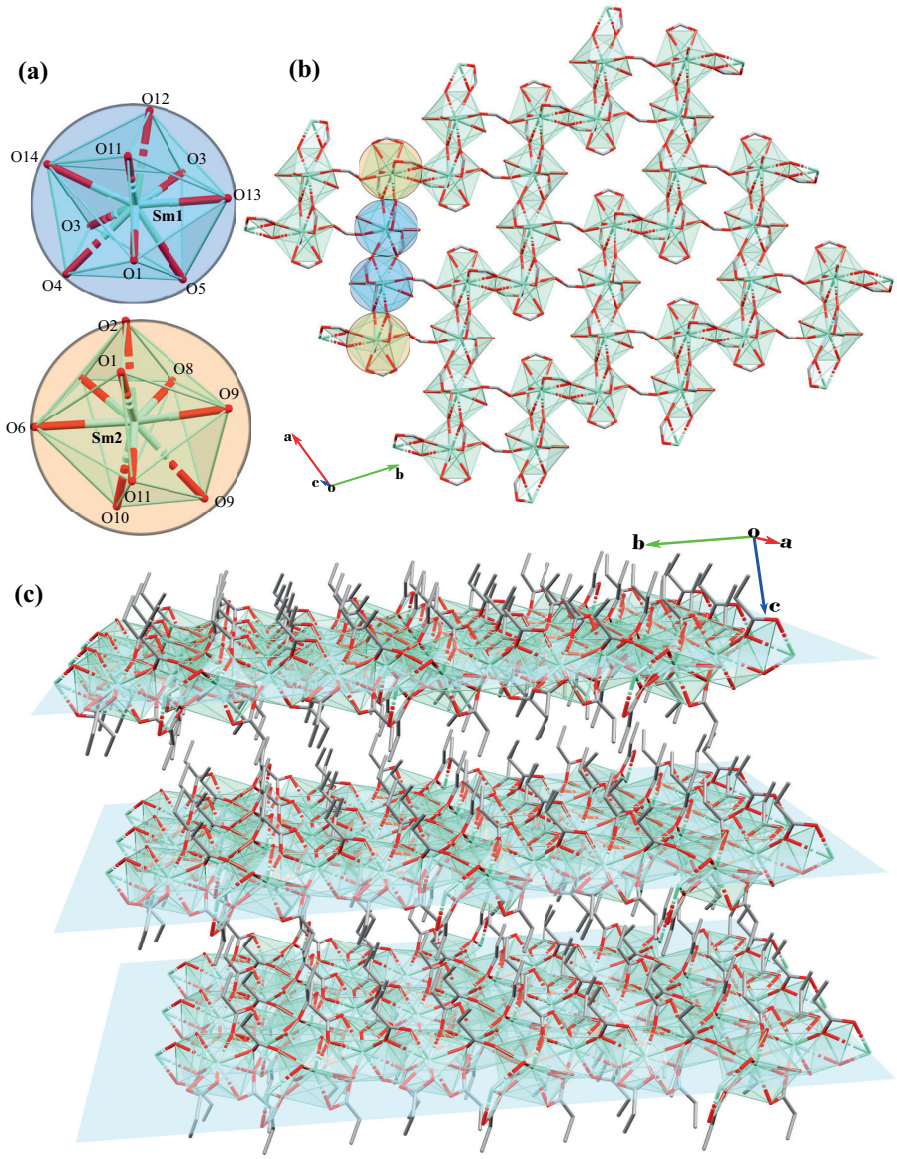


FIGURE 2.6: Representation of the (a) two crystallographically independent Sm(III) cores which are constituting the distorted square lattice 2D-sheets (b) and packing of the 2D-sheets of $Sm(Prop)_3$ in (c).

A visual overview of the different coordination modes of the propionate ligands is displayed in Fig. 2.7, where the bridging coordination along the $[1\bar{1}0]$ direction is evidently occurring alternatively between Sm(1) and Sm(2) centers.

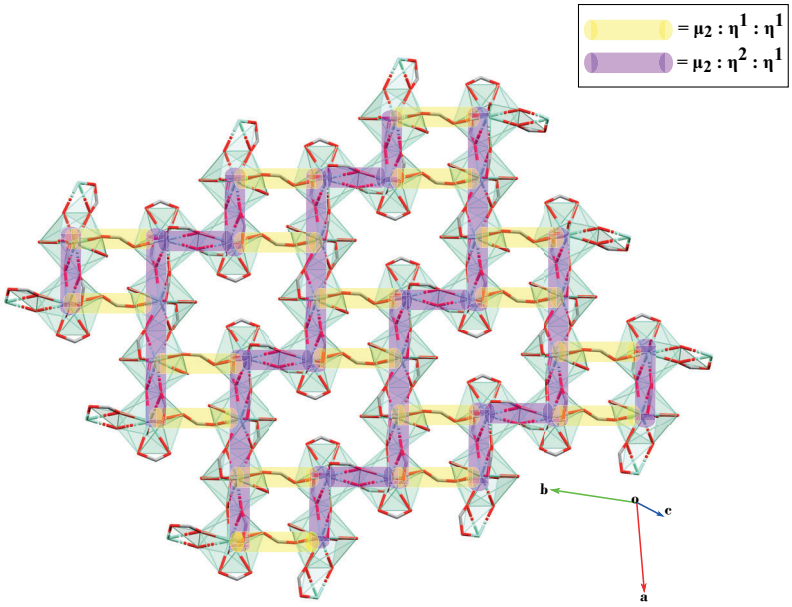


FIGURE 2.7: Different coordination modes of the propionate ligands forming the distorted square lattice 2D-sheets in the structure of $Sm(Prop)_3$.

A comparison between the measured Powder X-ray diffraction (PXRD) and the pattern calculated for the obtained single crystal structures of $Ba(Prop)_2$, $Sm(Prop)_3$, and $Gd(Prop)_3$ can be found in Fig. B.10, B.11, and B.12, respectively, and in Fig. B.13 for $Y(Prop)_3$, corroborating that the crystals selected to solve the crystal structures described above match the synthesized powders.

Two additional single crystal structures were obtained, specifically a second one for $Gd(Prop)_3$ and one for $Ce(Prop)_3$ when recrystallization was carried out by slow evaporation in MeOH. These are displaying a different structure when compared to the one exhibited by the PXRD relative to each compound (shown in Fig. B.14 and B.15, respectively). Nonetheless, both have found no match in literature, and are thus described here. Both structures crystallize in the monoclinic *P*21/c space group, and crystal data and structure refinement are reported in the following Table 2.2, whereas information on bond lengths and torsion angles, and S values can be found in B.1.3, and in Tables B.11 and B.12.

Gadolinium propionate single crystals resulting from slow evaporation in MeOH displays dimeric units formed by two identical Gd(III) centers bearing $[GdO_9]$ cores with coordination number 9 and a distorted muffin geometry (S values reported in Table B.11). For each gadolinium centre, two propionate ligands are exhibiting a $\mu_1 : \eta^1 : \eta^1$ (bidentate chelating) coordination mode, and two present a mixed $\mu_2 : \eta^2 : \eta^1$ (bidentate chelating and bridged) coordination mode. The two H_2O molecules in each Gd(III) center (O7 and O8) assemble the dimeric units in polymeric 1D-chains through inter- and intramolecular H-bonds, as displayed

in Fig. 2.8(b). The combination of coordination modes is in accordance with the value of $\Delta\nu$ reported in B.1.2, characteristic of a mixed bridging and bidentate chelating coordination of the ligands.

	$[Gd(Prop)_3(OH_2)_2]_n$	$[Ce(Prop)_3(OH_2)_3]_n$
Empirical formula	$C_9H_{19}GdO_8$	$C_9H_{21}O_9Ce$
Formula weight	412.49	413.38
Temperature (K)	294(2)	298(2)
Wavelength (Å)	0.71073	0.71073
Crystal system	Monoclinic	Monoclinic
Space group	*P*21/c	*P*21/c
Unit cell dimensions		
a (Å)	12.498(5)	10.404(5)
b (Å)	14.228(6)	15.347(7)
c (Å)	8.966(4)	20.967(9)
α(deg)	90	90
β(deg)	97.378(7)	103.163(7)
γ(deg)	90	90
V (Å)	1581.1(11)	3260(3)
Z	4	8
D_{calc} (Mg/m^3)	1.733	1.685
Absorption coefficient (mm^{-1})	4.219	2.825
F(000)	804	1640
Crystal size (mm^3)	0.16x0.15x0.07	0.18x0.14x0.12
θ range for data collection (deg)	1.643 to 28.444	1.660 to 29.097
hkl ranges	-12≤h≤11 0≤k≤19 0≤l≤16	-14≤h≤13 0≤k≤20 0≤l≤28
Reflections collected	36190	8615
Independent reflections	3963	8615
Completeness to θ(%)	100.0	100.0
Absorption correction	Semi-empirical from equivalents	Semi-empirical from equivalents
Max. and min. transmission	1 and 0.592	1 and 0.356
Refinement method	Full-matrix least squares on $\|F\|^2$	Full-matrix least squares on $\|F\|^2$
Data / restraints / parameters	3963 / 29 / 166	8615 / 0 / 349
Goodness-of-fit on $\|F\|^2$	1.086	0.834
Final R indices [I>2sigma(I)]	$R_1 = 0.0815$ $wR_2 = 0.2356$	$R_1 = 0.0758$ $wR_2 = 0.1473$
R indices (all data)	$R_1 = 0.1196$ $wR_2 = 0.2521$	$R_1 = 0.2896$ $wR_2 = 0.1898$
Largest diff. peak and hole ($e \cdot Å^{-3}$)	7.060 and -3.035	0.817 and -1.713

TABLE 2.2: Crystal data and structure refinement for $[Gd(Prop)_3(OH_2)_2]_n$ and $[Ce(Prop)_3(OH_2)_3]_n$.

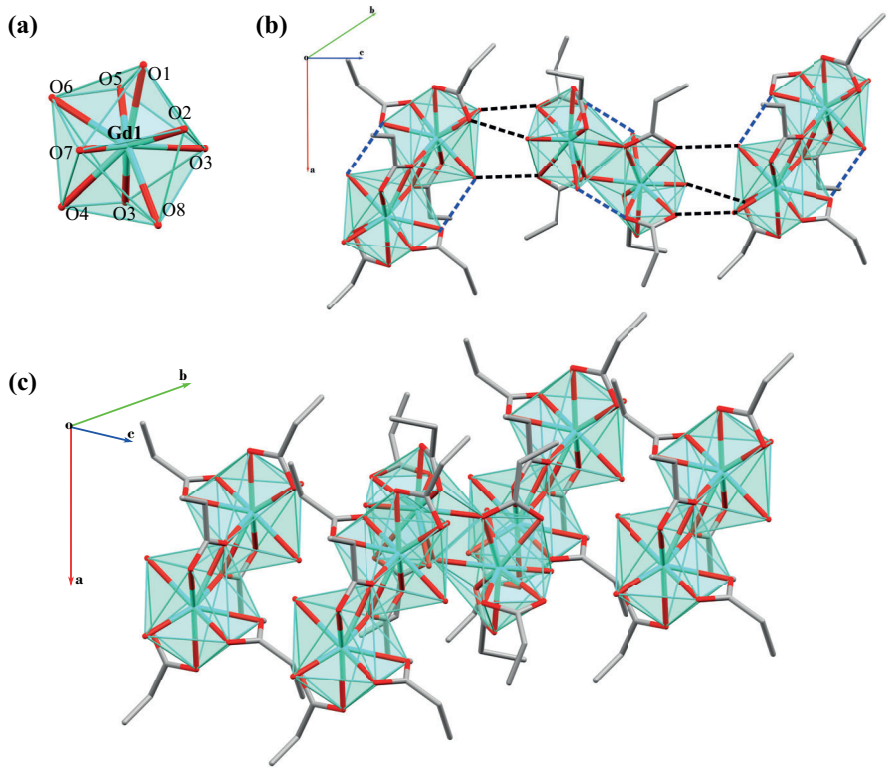


FIGURE 2.8: Representation of the (a) Gd (III) core in the dimeric $Gd(Prop)_3$ unit. (b) Intramolecular (blue dashed lines) and intermolecular H-bonds (black dashed lines) responsible for the formation of an array of polymeric 1D-chains, shown in (c).

Cerium propionate single crystals obtained through recrystallization in MeOH yield a novel, unreported crystal structure, in which the dimeric unit is formed by two crystallographically independent Ce(III) centers displaying $[CeO_9]$ and $[CeO_10]$ cores with coordination number 9 and 10 (Fig. 2.9(a)), bearing distorted muffin and sphenocorona geometries, respectively (S values reported in Table B.12). Ce(1) is connected to 10 O atoms deriving solely from propionate groups, whereas Ce(2) exhibits bonds to O atoms belonging to three H_2O molecules and 6 O atoms of propionate ligands. Two types of coordination modes are characteristic of the propionate ligands, mixing $\mu_2 : \eta^2 : \eta^1$ and $\mu_2 : \eta^1 : \eta^1$ coordination and assembling the dimeric units in polymeric 1D-chains. A further stabilization of the structure is due to the H_2O molecules present in between the chains, responsible for strong intermolecular H-bonds, as shown in Fig. 2.9(b). The combination of coordination modes is in accordance with the value of $\Delta\nu$ reported in B.1.2, typical of a mixed bridging and bidentate chelating coordination of the ligands.

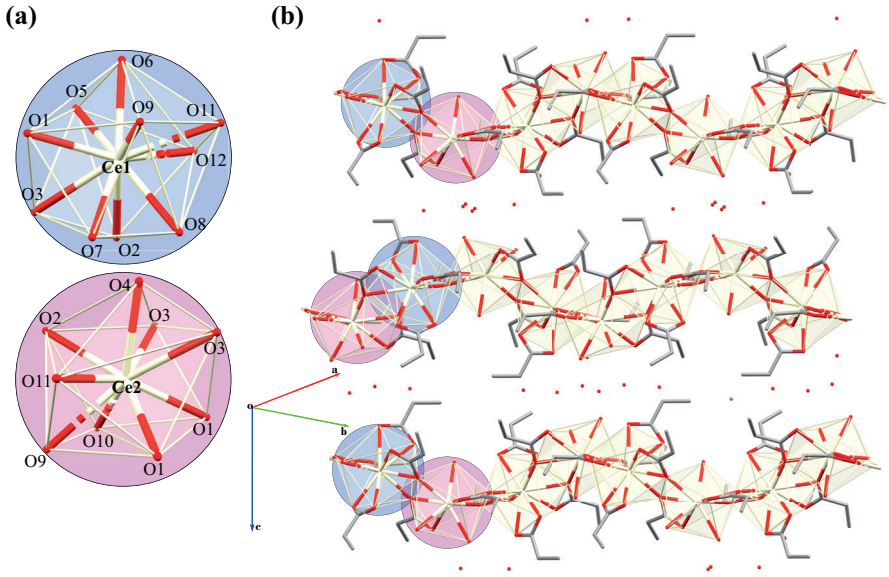


FIGURE 2.9: Representation of the (a) two crystallographically independent Ce (III) cores in the dimeric $Ce(Prop)_3$ unit, organizing the structure in (b) polymeric 1D-chains, stabilized by intermolecular H-bonds deriving from the crystallization H_2O molecules placed in between each chain. Hydrogen atoms are not shown for clarity.

2.3 Establishing compatibility of thermal behaviour and decomposition pathways

Subsequent to corroborating the high purity of the powder precursors, fundamental to avoid secondary products in the REBCO metal-organic precursor solution and ensure the achievement of elevated nanoscale homogeneity during the preparation of REBCO films, a complete study of the thermal behaviour of each metal propionate has been carried out. The decomposition of the propionate ligands has been analysed both for the powders, as an additional information regarding the absence of any undesired species, and in the form of films. Confirming the compatibility of these precursors in a thermal process that emulates the first annealing (pyrolysis) is of utmost importance towards the achievement of REBCO films with the desired nanocrystalline precursor phases for TLAG. The use of thermogravimetric analysis (TGA) coupled to an FTIR spectrometer (TG-FTIR) allows, through evolved gas analysis (EGA), to obtain relevant information regarding the volatiles evolved during the thermal treatment and thus, determine the decomposition pathways of each metal propionate.

2.3.1 Decomposition of metal propionate powders

The thermal behavior of all the metal propionate powder products was analyzed by comparing their decomposition pathway in inert conditions (N_2). With exception for the anhydrous $Cu(Prop)_2$, all powders display an initial mass loss below 150 ºC corresponding to dehydration and/or residual solvent elimination.

Earlier studies on the decomposition of calcium propionate [136] and of various lanthanide propionates by Grivel et al. [137] reported that the decomposition mechanism of salts deriving from carboxylic acids in an inert atmosphere generally yields symmetrical ketones (the length of the chain will depend on the substituent groups present) and carbon dioxide (CO_2): these are generated by a radical pathway through the recombination of the radical species which leads to the formation of the aforementioned symmetrical ketones. Nonetheless, in the case of metals which can experience redox reactions, the main volatile is the corresponding salt of the acid [138, 139].

The synthesized propionates of Y, Sm, Gd, and Yb described in this thesis follow a similar radical pathway mechanism, illustrated in eq. 2.1, and the results of the TG-FTIR are shown in Fig. 2.10. During the first mass loss at high temperatures, corresponding to 376 ºC, 356 ºC, and 371 ºC, for $Y(Prop)_3$, $Gd(Prop)_3$, and $Yb(Prop)_3$, respectively, the release of the symmetrical ketone 3-pentanone, CO_2, and the oxycarbonate species of the respective rare earth element is observed. The latter species are stable up to increased temperatures and are, instead, absent in the decomposition profile of the rest of the metal propionates precursors.

$$M_2(C_2H_5COO)_6 \longrightarrow \left[3C_2H_5\dot{C}O + 3C_2H_5^{\cdot} + O_2 + {}^{\cdot}OM + {}^{\cdot}COOM + 2CO_2\right] \longrightarrow$$
$$\longrightarrow M_2O_2CO_3 + 3C_2H_5COC_2H_5 + 2CO_2 \longrightarrow M_2O_3 + CO_2 \tag{2.1}$$

The last mass loss visible in the TG curves corresponds to the decomposition of the oxycarbonate to form the final rare earth sesquioxide by CO_2 release at the temperatures of 552 ºC, 426 ºC, and 439 ºC, for $Y(Prop)_3$, $Gd(Prop)_3$, and $Yb(Prop)_3$, respectively. The formation of Y_2O_3, Gd_2O_3, and Yb_2O_3 is confirmed by the masses of the final residues, which display a similar value if compared to the theoretical ones for a full conversion of the propionates to sesquioxides: 37.8% found for $Y(Prop)_3$ (expected 36.6%), 49.6% found for $Gd(Prop)_3$ (expected 47.8%), and 50.9% found for $Yb(Prop)_3$ (expected 50.2%). XRD patterns acquired for the final residue are further corroborating the formation of the sesquioxide, as shown in the following Fig. 2.11.

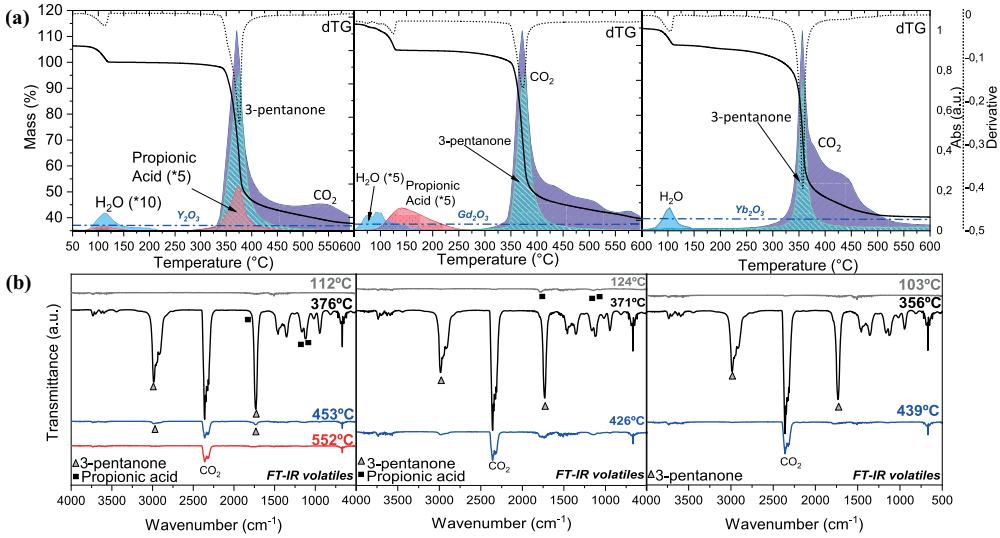


FIGURE 2.10: (a) From left to right, TGA decomposition curve (black) of $Y(Prop)_3$, $Gd(Prop)_3$, and $Yb(Prop)_3$ powders in inert conditions (N_2). The dotted line shows the TG derivative, whereas the gas evolution is shown as individual curves according to their thermal stability and elimination. The dashed and dotted blue line indicates the expected value for total decomposition to the relative sesquioxide of each RE. (b) FT-IR spectra corresponding to the main decomposition steps of $Y(Prop)_3$, $Gd(Prop)_3$, and $Yb(Prop)_3$ powder from each TGA in (a).

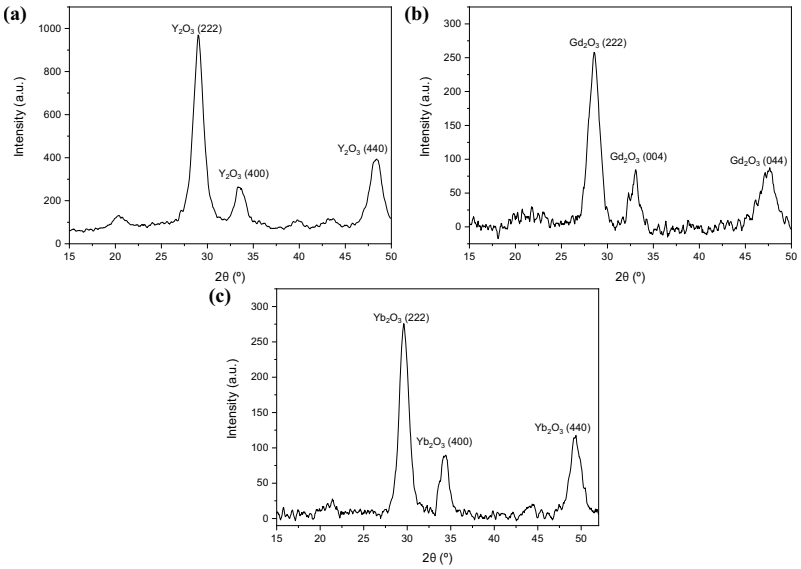


FIGURE 2.11: XRD of the final residue after the TG experiment for (a) $Y(Prop)_3$ showing the formation of Y_2O_3; (b) $Gd(Prop)_3$ showing the formation of Gd_2O_3; (c) $Yb(Prop)_3$ showing the formation of Yb_2O_3.

Nonetheless, $Sm(Prop)_3$ shows a mixed decomposition pathway, in which the volatiles typically evolved from a decomposition through radical pathway (eq. 2.1) are present together with the additional evolution of acetaldehyde and propionic acid, as shown from the EGA signals in Fig. 2.12(a). This is indicating that it is also following an oxidative mechanism as the one reported in equation 2.2, in which the degradative oxidation of the propionate groups to acetaldehyde, CO_2 and propionic acid is initiated by the presence of O_2.

$$M_2(C_2H_5COO)_6 \xrightarrow{[O_2]} 3C_2H_5COOH + 3CH_3COH + M_2O_2CO_3 + 2CO_2 \xrightarrow{[O_2]} M_2O_3 + CO_2 \tag{2.2}$$

In both of these mechanisms, the oxycarbonate species is formed and upon heating it finally decomposes through release of CO_2 to the sesquioxide, in this case Sm_2O_3, as suggested by the final residue mass percentage (49.7%, as compared to the expected 47.2% theoretical value), and confirmed by XRD analysis (Fig. 2.12(c)). The observed volatiles present in this thermal analysis conducted under a N_2 gas flow are possibly due to the presence of a residual O_2 content in the TGA furnace, which may trigger the second mechanism to be followed.
Differential scanning calorimetry (DSC) curves for all of the metal propionate powders registered during the thermal treatment are reported in Fig. 2.13. Similarities and differences of the DSC curves of the four compounds described to this moment must be considered, and are displayed in Fig. 2.13(a)-(d). A distinction must be made between the couples of compounds $Y(Prop)_3$ and $Yb(Prop)_3$, and $Gd(Prop)_3$ and $Sm(Prop)_3$. The latter are exhibiting an endothermic peak below 200 ºC successive to the dehydration step, which corresponds to the precursor melting, having no peak relative to this endothermic process to be observed in the dTG curve. Contrarily, no evidence of such a phenomenon is present in the DSC curves of $Y(Prop)_3$ and $Yb(Prop)_3$, in which the only mass loss prior to the propionate decomposition step is ascribed to the elimination of H_2O.
Differently from the above mentioned pathways, the decomposition of $Cu(Prop)_2$ is following a reductive mechanism (eq. 2.3) which yields acetaldehyde, CO, CO_2, 3-pentanone and propionic acid in a single mass loss and through a highly exothermic reaction, shown in Fig. 2.14. This is additionally confirmed in the DSC curve in Fig. 2.13(e) in which, in correspondence to the main decomposition step at temperatures ranging between 235 ºC and 280 ºC, an exothermic peak is found.

$$\begin{aligned} Cu(C_2H_5COO)_2 &\longrightarrow C_2H_5COOH + 3CH_3COH + CO + Cu \longrightarrow 2Cu + O_2 \\ &\longrightarrow 2Cu_2O + O_2 \longrightarrow 4CuO \end{aligned} \tag{2.3}$$

Thus, the full reduction to Cu (0) is promoted; however, the XRD of the final residue (Fig. 2.14(c)) shows an additional, partial oxidation to Cu_2O and CuO, corresponding to the slight

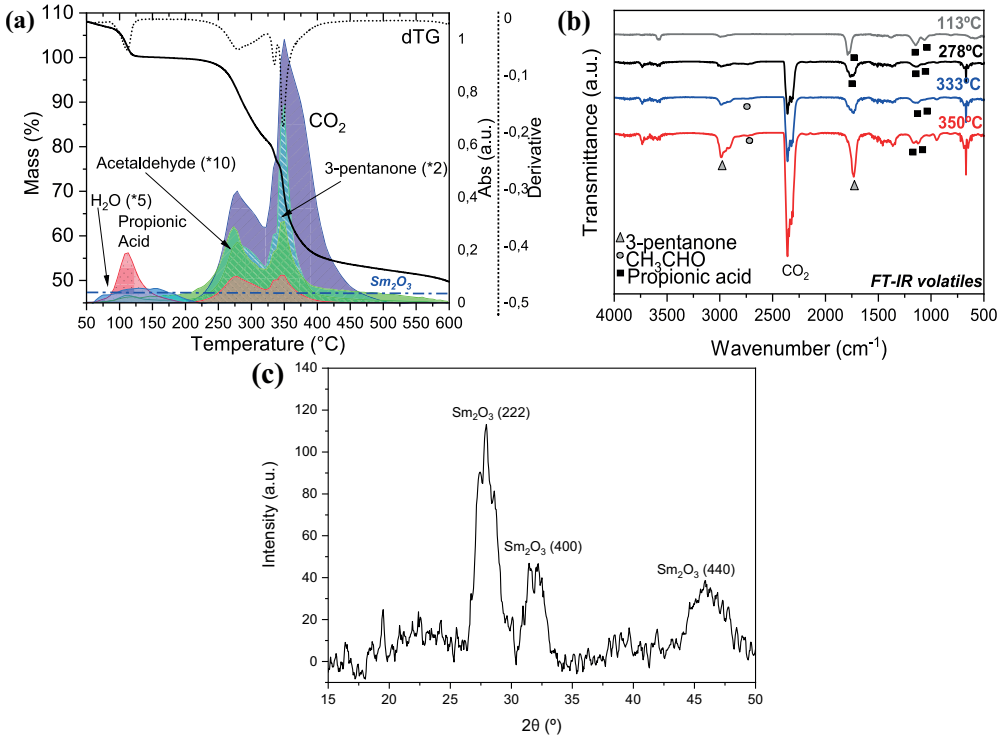


FIGURE 2.12: (a) TGA decomposition curve (black) of $Sm(Prop)_3$ powder in inert conditions (N_2). The dotted line shows the TG derivative, whereas the gas evolution is shown as individual curves according to their thermal stability and elimination. The dashed and dotted blue line indicates the expected value for total decomposition to Sm_2O_3. (b) FT-IR spectra corresponding to the main decomposition steps of $Sm(Prop)_3$ powder from TGA in (a). XRD of the final residue following the TGA experiment confirming the sole formation of Sm_2O_3 shown in (c).

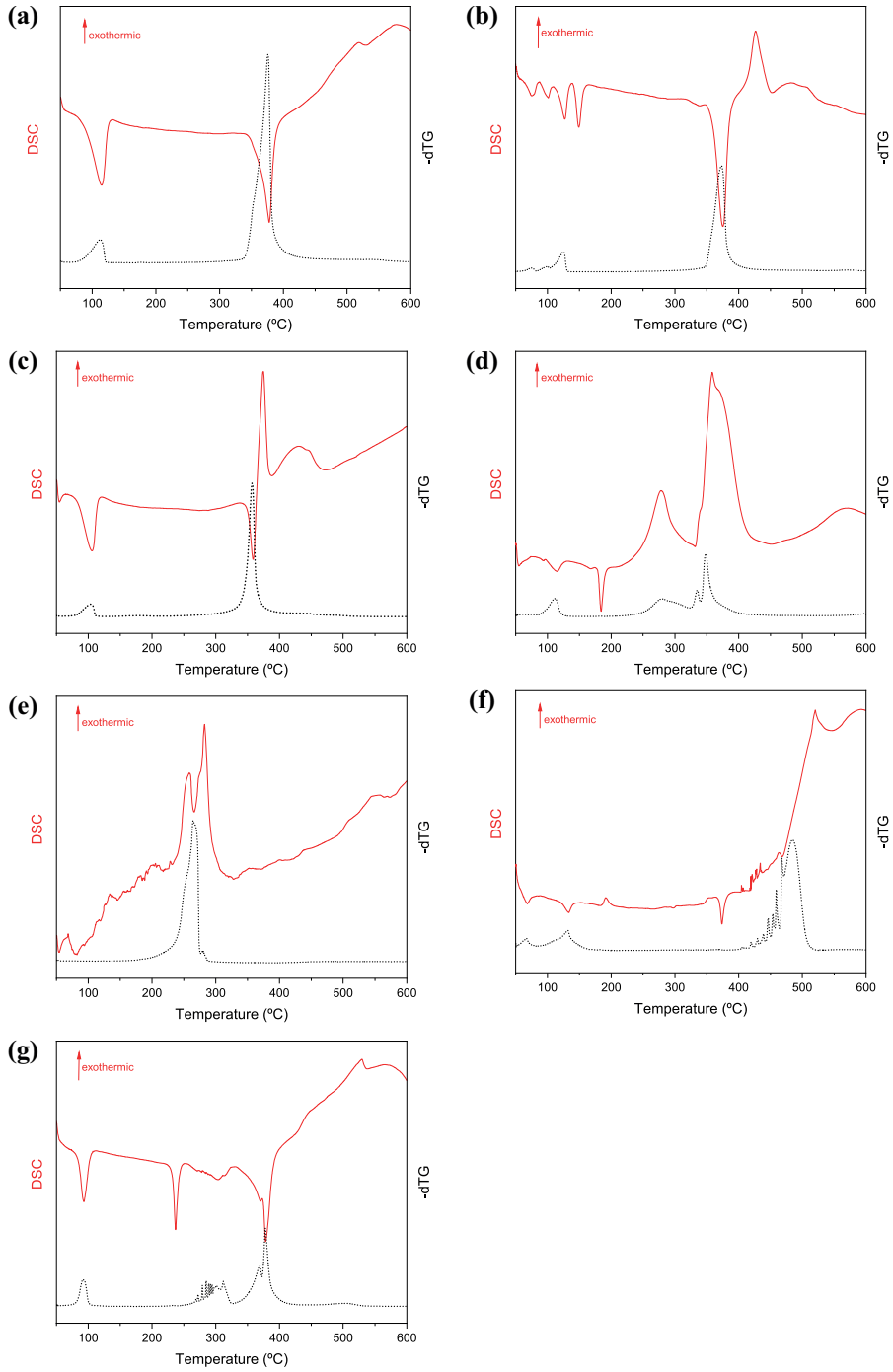


FIGURE 2.13: DSC and dTG curves for (a) $Y(Prop)_3$, (b) $Gd(Prop)_3$, (c) $Yb(Prop)_3$, (d) $Sm(Prop)_3$, (e) $Cu(Prop)_2$, (f) $Ba(Prop)_2$, (g) $Ce(Prop)_3$.

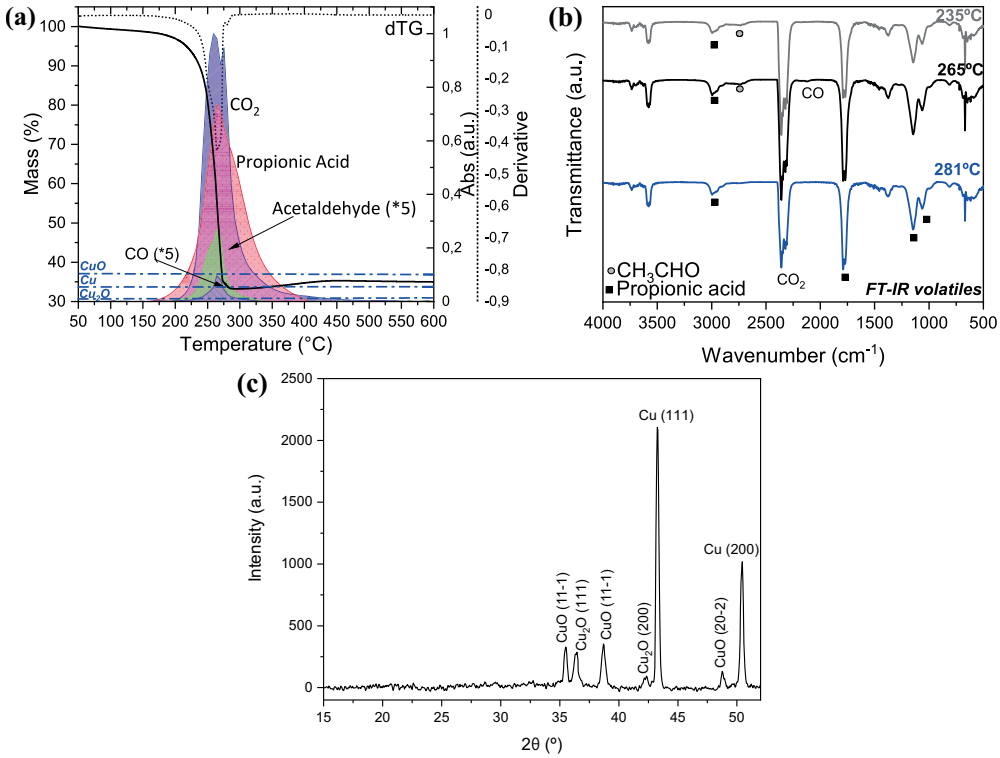


FIGURE 2.14: (a) TGA decomposition curve (black) of $Cu(Prop)_2$ powder in inert conditions (N_2). The dotted line shows the TG derivative, whereas the gas evolution is shown as individual curves according to their thermal stability and elimination. The dashed and dotted blue lines indicate the expected value for total decomposition to the oxides, CuO and Cu_2O, and metallic copper. (b) FT-IR spectra corresponding to the main decomposition steps of $Cu(Prop)_2$ powder from TGA in (a). XRD of the final residue following the TGA experiment confirming the formation of CuO, Cu_2O and metallic copper is shown in (c).

mass increase at temperatures above 400 ºC, possibly due to presence of residual O_2 in the TGA furnace. The discrepancy between the value of the mass of the final residue (34.8%) and the theoretical ones for Cu, Cu_2O and CuO (30.3%, 37.9%, and 34.1%, respectively) is due to the formation of a mixture of the three compounds in unknown proportion.

$Ba(Prop)_2$ decomposition in an inert atmosphere follows the radical path in eq. 2.4, exhibiting variations compared the previous cases described above. Following the initial dehydration and residual solvent elimination in the DSC curve in Fig. 2.13(f) an exothermic peak is observed, corresponding to a further crystallization of the product (192 ºC).

$$Ba(C_2H_5COO)_2 \longrightarrow \left[3C_2H_5\dot{C}O + 3C_2H_5^{\cdot}\right] \longrightarrow BaCO_3 + C_2H_5COC_2H_5 + CO_2 \tag{2.4}$$

$Ba(Prop)_2$ powder has a higher thermal stability compared to other precursors and the main decomposition step is observed at 485ºC. However, at 373ºC, before the final decomposition, an endothermic peak is present in the DSC curve with no corresponding peak in the dTG curve, thus related to the melting of the powder. The series of numerous sharp peaks due to the evolution of 3-pentanone gas bubbles through the melt, visible in the dTG in Fig. 2.15(a), are additionally confirming this process. The evolution of 3-pentanone derives from the recombination of the intermediate radical species, and the decomposition finally yields $BaCO_3$ with no evolution of CO_2 due to reaction stoichiometry, in contrast to the previously described metal propionates which followed this pathway. As oxides of barium are not thermodynamically stable at temperatures below 600 ºC, the carbonate is the expected phase and its formation is corroborated by the XRD of the final residue (Fig 2.15(c)) and its mass (69.5%), which is close to the expected theoretical value of 69.6% for $BaCO_3$ formation from $Ba(Prop)_2$.
In accordance with what observed in the studies of Kim *et al.* [140] and Roura *et al.* [141], the decomposition of the synthesized $Ce(Prop)_3$ occurs in three steps, as observed from the TG curve and the evolution of volatiles in Fig. 2.16. Similarly to the case of $Ba(Prop)_2$, melting of the powder occurs during the thermal treatment prior to the first, main decomposition step at 237 ºC, as visible from the DSC curve in Fig. 2.13(g), followed by evolution of volatiles from the melt and ending with the propionate decomposition. In the TG curve, three different mass loss steps are evident subsequent to the initial dehydration step at low temperatures. The three-step mechanism is reported in equation 2.5, and the first decomposition step corresponds to the loss of one propionate group, confirmed by the mass loss of this step being 16%, close to the expected value of 16.6%. The formation of the symmetrical ketone 3-pentanone, CO_2 and the mixed cerium propionate-hydroxide occurs during this step (eq. 2.5(i)). Cerium oxidation state is maintained in Ce^{+3}, given that its oxidation to Ce^{+4} is induced in the second main decomposition step (eq. 2.5(ii)), where the formation of cerium hydroxide through elimination of the two remaining propionate groups is occurring, confirmed by the evolution of 3-pentanone and CO_2. The last step yields cerium oxide following elimination of H_2O (eq. 2.5(iii)).

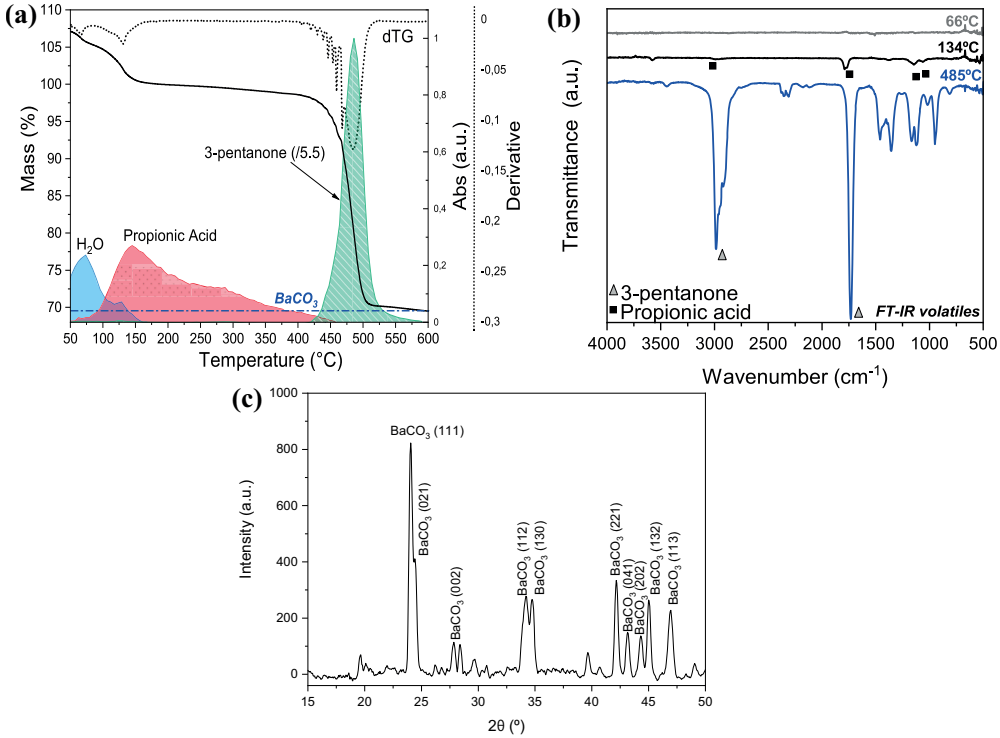


FIGURE 2.15: TGA decomposition curve (black) of $Ba(Prop)_2$ powder in inert conditions (N_2). The dotted line shows the TG derivative, whereas the gas evolution is shown as individual curves according to their thermal stability and elimination. The dashed and dotted blue line indicates the expected value for total decomposition to the $BaCO_3$. (b) FT-IR spectra corresponding to the main decomposition steps of $Ba(Prop)_2$ powder from TGA in (a). XRD of the final residue following the TGA experiment confirming the formation of $BaCO_3$ is shown in (c).

The resulting mass of 48.5% is in good agreement with the expected value of 47.5% for the formation of CeO_2, as it is also confirmed by the presence of reflections relative to CeO_2 in the XRD of the final residue Fig. 2.16(c).

$$\textbf{(i)}\quad Ce_2(C_2H_5COO)_6 \longrightarrow Ce_2(C_2H_5COO)_4(OH)_2 + C_2H_5COC_2H_5 + CO_2$$

$$\textbf{(ii)}\quad Ce_2(C_2H_5COO)_4(OH)_2 \longrightarrow 2Ce(OH)_4 + C_2H_5COC_2H_5 + CO_2$$

$$\textbf{(iii)}\quad 2Ce(OH)_4 \longrightarrow 2CeO_2 + 4H_2O \qquad (2.5)$$

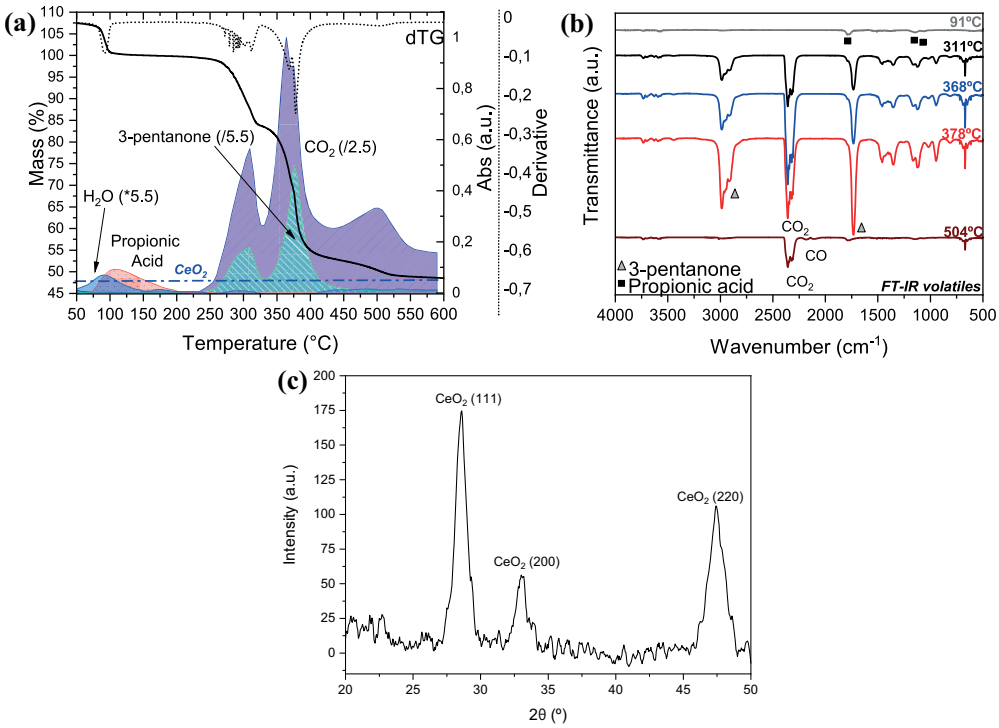


FIGURE 2.16: (a) TGA decomposition curve (black) of $Ce(Prop)_3$ powder in inert conditions (N_2). The dotted line shows the TG derivative, whereas the gas evolution is shown as individual curves according to their thermal stability and elimination. The dashed and dotted blue line indicates the expected value for total decomposition to CeO_2. (b) FT-IR spectra corresponding to the main decomposition steps of $Ce(Prop)_3$ powder from TGA in (a). XRD of the final residue following the TGA experiment confirming the sole formation of CeO_2 is shown in (c).

Therefore, the thermal analysis conducted on all of the synthesized metal propionates confirmed these display high purity and follow a thermal behavior through established decomposition pathways to yield the expected oxides or carbonates, marking a promising starting point for their use in the preparation of metal-organic precursor solutions for the fabrication of REBCO superconducting films through the TLAG-CSD approach.

2.3.2 Metal propionate films decomposition

To confirm the compatibility of the powder products as suitable precursors in the solvent mixture used for the preparation of the REBCO metal-organic precursor solutions, the decomposition of each metal propionate in the form of films has been analyzed. Details regarding the preparation of the solutions of each metal propionate and the deposition prior to the thermal analysis are reported in B.1.

Thermal decomposition of propionates of copper, yttrium, and barium have been extensively

studied by Rasi *et al.* [52, 125, 142, 143], considering how the various types of atmospheres may affect their thermal behaviour. However, it must be considered that solely acetates of the three metals dissolved in an excess of propionic acid were employed in said previous studies, and the resulting solution was used for deposition of the films. The use of acetate precursors is especially detrimental when considering the case of barium, as the complete conversion of acetate to propionate is never obtained, even in conditions of excess of propionic acid [124, 125]. Therefore, the use of metal acetates in the REBCO precursor solution, as previously specified, would lead to the inevitable presence of secondary products, such as mixed carboxylate species containing acetate and propionate ligands. The decomposition pathway of these compounds may not be compatible with the application proposed: a rapid gas evolution deriving from a large mass loss during the pyrolysis process is amongst the possible causes of crack formation in the REBCO precursor film [126]. Additionally, decomposition of secondary products may result in the formation of an undesired phase in the nanocrystalline precursor film: as it will be described in the following chapter, nucleation of the nanocrystalline phases must be strictly controlled during the pyrolysis process to yield films composed by the required $BaCO_3$ (preferably in its orthorhombic phase), CuO and Y_2O_3 and optimal microstructure for the growth of the final REBCO film through TLAG. For this reason, the metal propionate compounds described in this thesis are firstly synthesized as powders and, following the confirmation of their purity, dissolved in the chosen mixture of solvents in the correct stoichiometry for the formation of the corresponding REBCO film through annealing processes.

The analysis of thermal behaviour of films for the cases of $Cu(Prop)_2$, $Y(Prop)_3$, $Ba(Prop)_2$, and $Ce(Prop)_3$ will solely be carried out in the case of an oxidative atmosphere created by means of a flow of dry O_2. Fig. 2.17 displays the TG curves together with the evolved volatiles registered through EGA-FTIR for such films. As observed in previous studies [52, 125, 142, 143], in an oxidative atmosphere the decomposition of the propionate ligands occurs through an oxidative degradation (dismutation), evolving propionic acid, CO_2, and acetaldehyde in a one step process to yield CuO from the $Cu(Prop)_2$ film, Y_2O_3 from the $Y(Prop)_3$ film, $BaCO_3$ for the $Ba(Prop)_2$ film, and CeO_2 for the $Ce(Prop)_3$ film. The decomposition temperatures for $Cu(Prop)_2$ are in accordance to previously reported ones for solutions containing this metal propionate [2]: in the TG curve in Fig. 2.17(a), the sole decomposition step present for this film starts as early as 172ºC, with the major mass loss occurring at 220 ºC, and finally ends at 250ºC with the full oxidation of $Cu(Prop)_2$ to CuO. The decomposition of the film of $Y(Prop)_3$, shown in Fig. 2.17(b), displays a similar thermal behaviour as the one reported in the literature for similar systems [134, 142]. The oxidative degradation of the propionate groups happens in two steps: firstly, the mass loss observed at a temperature of 320 ºC leads to the formation of the oxycarbonate species ($Y_2O_2CO_3$), at temperatures ranging between 350 and 480 ºC,

[2] One must remember the use of metal acetates dissolved in solvent mixtures reported in previous studies. The individual synthesis of pure metal propionate powders prior to the dissolution in the REBCO precursor solution had not yet been reported until now for this specific application.

which then yields the final sesquioxide, Y_2O_3 at 500 ºC through CO_2 release. An equivalent decomposition mechanism is exhibited by a film deriving from a solution of $Ce(Prop)_3$ (Fig. 2.17(d)), which in dry O_2 decomposes through the evolution of the same volatiles, propionic acid, CO_2, and acetaldehyde, thus indicating its decomposition is following the degradative oxidation mechanism. It starts at 180 ºC and occurs through one major mass loss at 230 ºC to finally yield CeO_2. A focus on the thermal behaviour of the films of barium propionate must be now considered, given that EGA signals ascribed to methane (CH_4) and CO are additionally registered during the thermal treatment (Fig. 2.17(c)): these volatiles are deriving from the decomposition of acetaldehyde and the release of the intermediate species barium oxalate (BaC_2O_4).

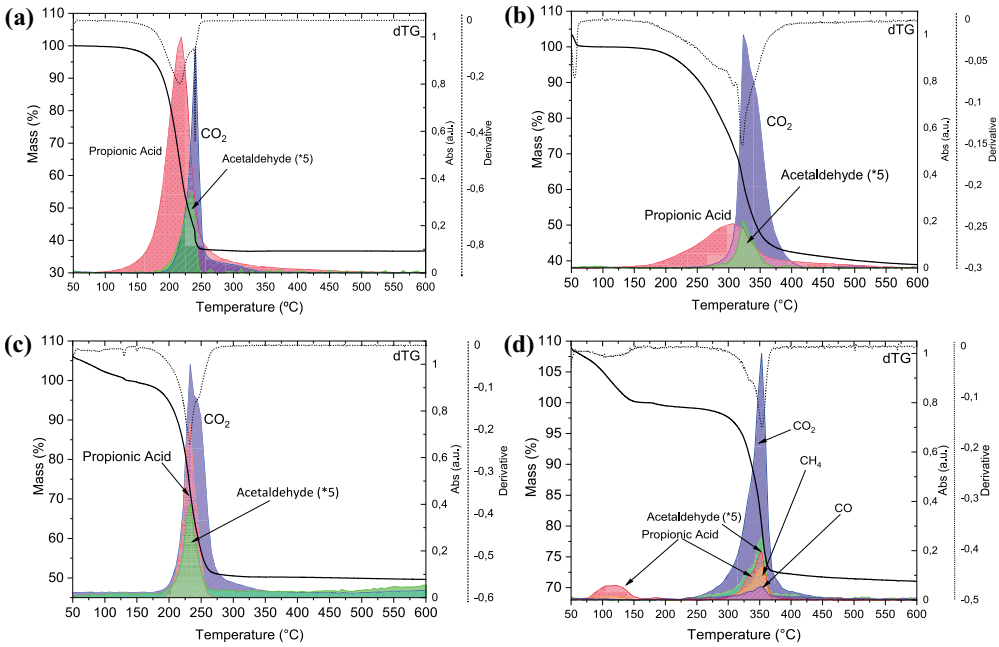


FIGURE 2.17: Decomposition of films of (a) $Cu(Prop)_2$, (b) $Y(Prop)_3$, (c) $Ba(Prop)_2$, and (d) $Ce(Prop)_3$ in oxidative atmosphere (dry O_2). The TG curves are shown as black solid lines, time derivative (dTG) as a black dotted line and EGA signals identified for each of the gases released during the process.

For the film of $Ba(Prop)_2$ obtained from the dissolution in HProp:MeOH (1:1) of the compound synthesized as described in B.1.2, the decomposition step differs from the case of a mixed carboxylate of acetate and propionate reported in [125]. Only one main mass loss is observed between 350ºC and 370ºC, presumably due to the sole presence of propionate groups. The detected volatiles, however, may be an indication of the formation of the oxalate species of barium (BaC_2O_4) in the final region of the decomposition process: BaC_2O_4 is known to

be a highly unstable species, and decomposes immediately following its formation, at temperatures between 330 ºC and 350ºC to yield $BaCO_3$ [125]. To effectively corroborate the presence of barium oxalate as part of the decomposition products of this system, a series of experiments in which films of solutions of different barium compounds were quenched at temperatures ranging between 300 ºC and 400 ºC. Three solutions were employed to fully compare the cases of the sole presence of barium acetate in solution, the presence of a mixed complex of barium acetate and propionate, and the sole presence of barium propionate. This was obtained by simply dissolving, respectively, commercial barium acetate ($Ba(OAc)_2$) in a mixture of acetic acid (HOAc) and methanol (1:1), commercial metal acetate in HProp:MeOH (1:1), and the synthesized $Ba(Prop)_2$ described in this thesis in the latter solvent mixture. The TG curves relative to the decomposition of the three films are displayed in Fig. 2.18(a), whereas the FTIR registered on films of each solution quenched at several, increasing temperatures are reported in Fig. 2.18(b). It is important to notice that the main mass loss step occurs at different temperatures for the three cases, being the case of only acetate the one with highest thermal stability displaying the main mass loss at 450 ºC, 100 ºC higher than the other two cases. The major decomposition step in the mixed propionate-acetate complex case occurs at similar temperature as the full-propionate case, presumably due to the decomposition of the propionate groups; however, at higher temperature, the former presents two consecutive, small mass losses, which are attributed to the decomposition of the acetate groups remaining in solution due to the incomplete conversion of acetate to propionate. This is confirmed by the evolution of formaldehyde during the thermal treatment of this film (Fig. 2.19(a)), characteristic gas evolved from the decomposition of an acetate. It is, indeed, the only aldehyde species evolved during the decomposition of a solution of $Ba(OAc)_2$, thus only acetate groups in solution, as evident from the EGA signals in Fig. 2.19(b). In oxidative atmosphere, the proposed mechanism in this case is the degradative oxidation of the acetate groups through evolution of acetic acid, formaldehyde and CO_2. From the FTIR spectra acquired following the quenches of the three films, the important difference to be noted is the prompt formation of BaC_2O_4 in the film relative to only propionate groups present, in which this species is visible starting from the film quenched at 320 ºC: here, the contribution of peaks deriving from the barium precursor is decreasing. Increasing the temperature to 340 ºC results in the complete absence of peaks relative to the precursor, and only peaks corresponding to the oxalate and the final carbonate are identified, suggesting the partial formation of the final product coexisting with the oxalate species. Given its formation happens at elevated temperature and taking into account the volatiles present at the moment of the oxalate formation, the origin of the oxalate species may be the oxidation of the remaining propionate groups by means of the evolved acetaldehyde. Finally, the EGA signal deriving from CO volatiles at 360 ºC in Fig. 2.17(c), is consistent with the complete transformation of the oxalate into the final carbonate. The absence of the oxalate peaks in the films deriving from a solution containing only acetate groups is a further confirmation of this hypothesis. Moreover, considering the two cases in which

propionates are present in solution, it is clear that, in both, the oxalate species is formed at a similar temperature, suggesting it is indeed deriving from the decomposition of the propionate groups, corresponding to the first mass loss in the sample of mixed propionate-acetate complex.

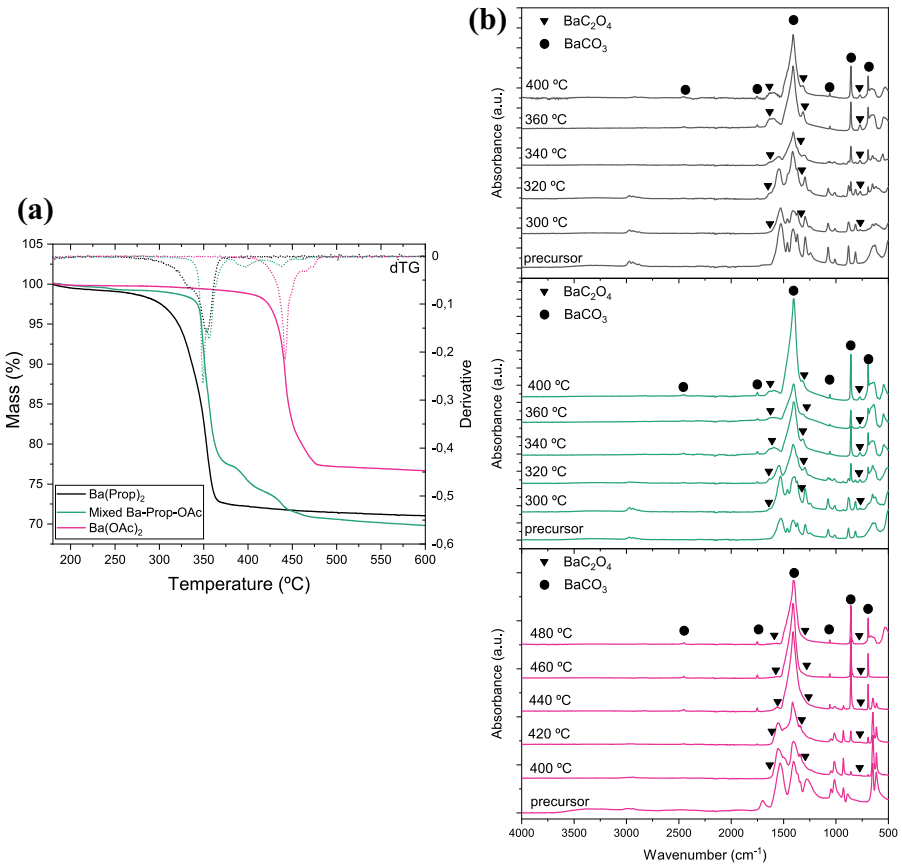


FIGURE 2.18: (a) Comparison of the thermal behavior of three solutions from different precursors of barium: a solution of$Ba(Prop)_2$ prepared using the precursor described in this chapter (black), being thus the case of only propionate groups in solution; a solution of $Ba(OAc)_2$ dissolved in HProp and MeOH (1:1), thus yielding the mixed propionate-acetate complex of barium (dark green); a solution of $Ba(OAc)_2$ dissolved in HOAc and MeOH (1:1), consisting in a solution in which only acetate groups are present (dark pink). (b) FTIR spectra registered on films of the same three samples in (a) following a series of quenches ranging between 300 ºC and 400 ºC, the temperature range where BaC_2O_4 is expected to be formed.

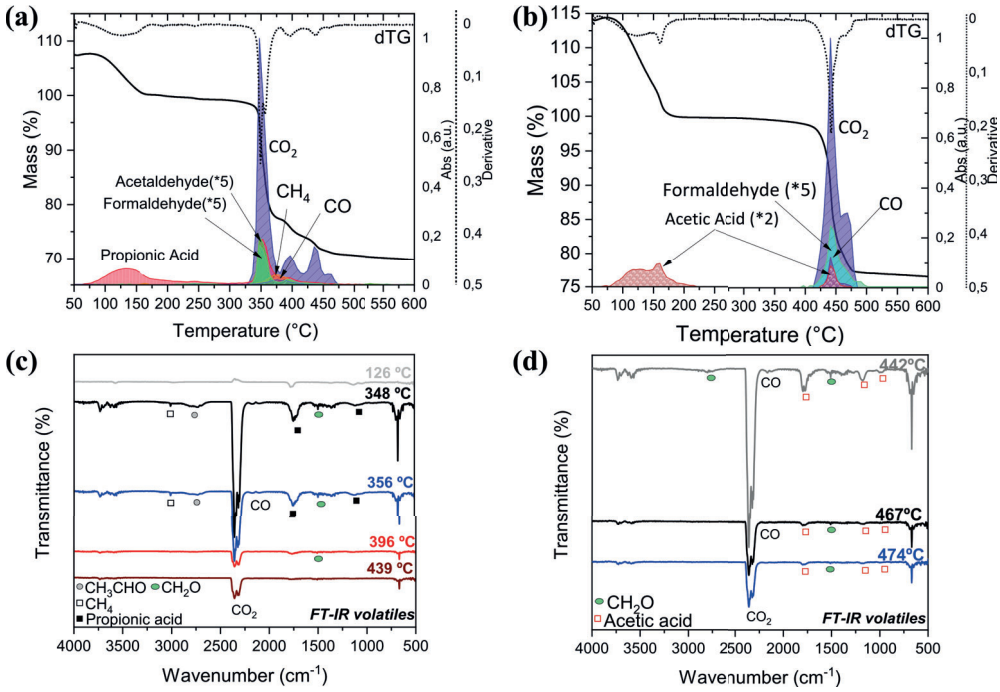


FIGURE 2.19: TG profile (solid black line), time derivative dTG (dotted black line) and gas evolution of a solution of (a) $Ba(OAc)_2$ in HProp:MeOH (1:1), yielding a solution in which both propionate and acetate groups are present and (b) $Ba(OAc)_2$ in HOAc:MeOH (1:1), yielding a solution only containing acetate groups. (c) and (d) are, respectively, the FTIR spectra registered in correspondence to the major mass losses in the TG curves in (a) and (b).

The analysis of the evolved gases from the three cases was crucial to confirm that the formation of barium oxalate is solely due to the decomposition of propionate groups. Despite barium oxalate is an intermediate product result of a secondary reaction, the corroboration of its presence during the decomposition pathway of $Ba(Prop)_2$ ensures an accurate understanding of the system, pivotal for the CSD-based application proposed in this thesis, and is of additional interest for its employment in various other functional systems prepared through the MOD methodology.

The formation of the final oxides for the films containing copper, yttrium and cerium propionates, and $BaCO_3$ was confirmed by XRD of films subjected to the pyrolysis process described in B.1, to demonstrate the solutions prepared through the use of these metal propionate precursors yield the desired phases in the same thermal treatment as the one employed for the preparation of the REBCO nanocrystalline precursor films. Following the annealing at 500ºC under a humid O_2 gas flow, the presence of oxides of copper, yttrium, and cerium and $BaCO_3$ is observed, as displayed in Fig. 2.20. Notice the difference in intensity of the XRD signals: given the different concentrations employed for each solution, due to solubility of each metal

propionate precursor in the solvent mixture, different thickness of the final films will be obtained.

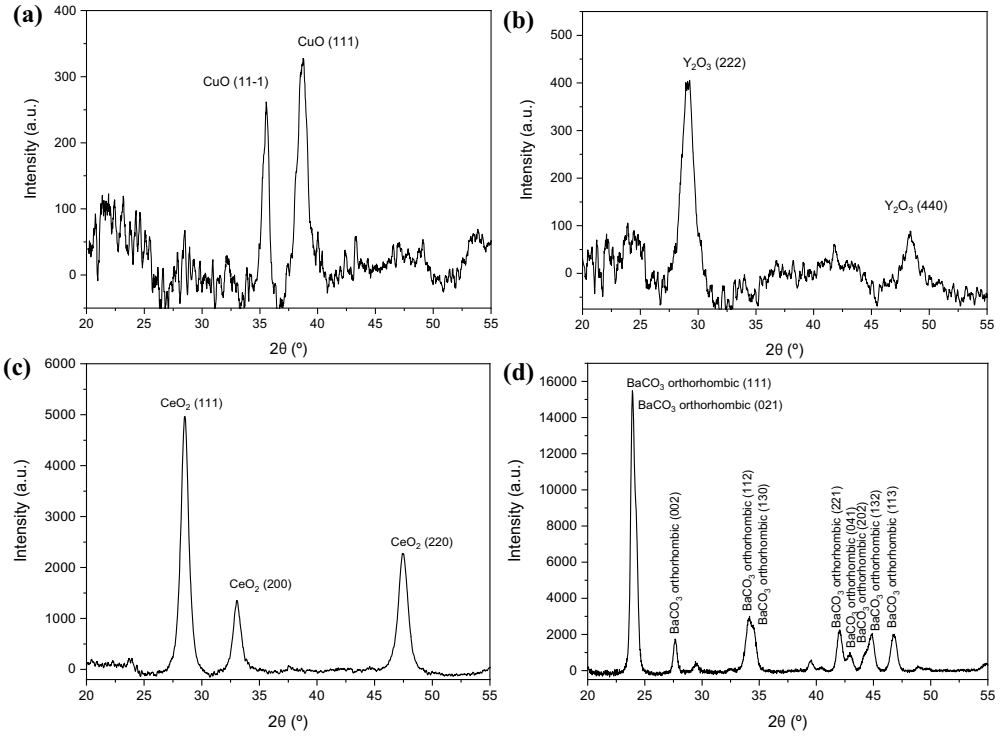


FIGURE 2.20: XRD patterns (measured in grazing incidence (GIXRD) geometry) of the final residue from the decomposition of films of (a) a solution of $Cu(Prop)_2$, (b) a solution of $Y(Prop)_3$, (c) a solution of $Ba(Prop)_2$, and (d) a solution of $Ce(Prop)_3$.

Ultimately, the same analysis of the thermal behaviour of films deriving from solutions of RE propionates (RE = Sm, Gd, Yb) has been conducted. However, in this case, decomposition in two oxidative atmospheres, dry and humid O_2, were studied and the comparison of the six TG curves may be found in Fig. 2.21(a). Films of each RE propionate which underwent thermal treatment in dry O_2 atmosphere (solid lines) display slightly higher decomposition temperature than the ones relative to films exposed to a humid O_2 flux (dashed lines). Different mechanisms are governing the decomposition in the two atmospheres considered, and this is at the origin of the variations in the decomposition temperatures.

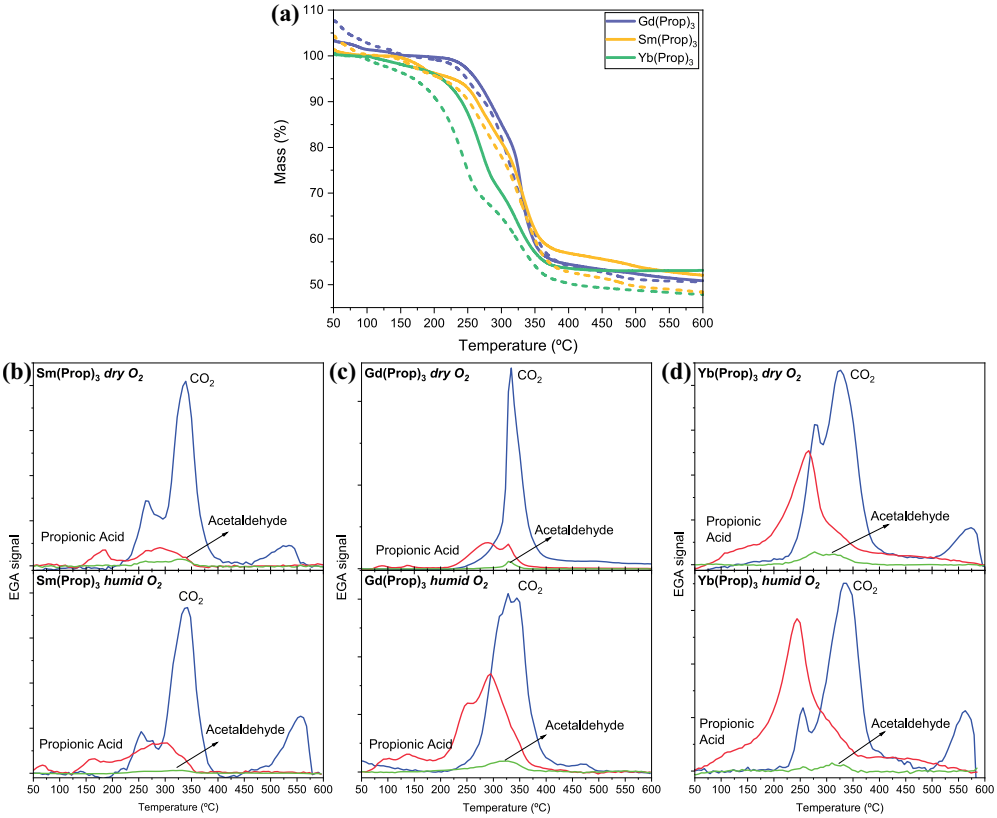


FIGURE 2.21: (a) TG curves for $Sm(Prop)_3$ (yellow), $Gd(Prop)_3$ (blue), and $Yb(Prop)_3$ (green), registered in dry O_2 (solid lines) and humid O_2 (dashed lines) flows. (b-d) Analysis of the evolved gases during the thermal treatment for $Sm(Prop)_3$, $Gd(Prop)_3$ and $Yb(Prop)_3$, respectively, comparing oxidative atmosphere created by means of a flux of dry O_2 (upper graphs) with the case of a humid O_2 flux (lower graphs).

In dry O_2, the oxidative degradation observed previously for the case of films of $Y(Prop)_3$ yields propionic acid, acetaldehyde and CO_2 displaying a one-step major mass loss to form the corresponding oxycarbonate of each RE element, and finally the sesquioxide by CO_2 elimination. Contrarily, when the films undergo an annealing in a humid O_2 flux, two mechanisms are competing: the hydrolysis and the oxidation mechanisms, with the former being favored at lower temperatures. Consequently, the decomposition initiates through the hydrolysis of the propionate ligands, releasing propionic acid and the sesquioxide of the RE through the mechanism shown in eq. 2.6(a). Nonetheless, hydrolysis is promptly superseded by the oxidation step when reaching more elevated temperatures, hence the CO_2, acetaldehyde, and propionic acid evolution which yield the oxycarbonate species of each RE. Finally, the final sesquioxide is formed through a further CO_2 release. The oxidation mechanism is impeding the advance

of the hydrolysis mechanism, considering that the former is thermodynamically favored compared to the latter when the temperature is increased. Fig. 2.21(b)-(d) displays the EGA signals acquired during the thermal treatment in both atmospheres for films of $Sm(Prop)_3$, $Gd(Prop)_3$, and $Yb(Prop)_3$. In a dry O_2 flux, the simultaneous release of propionic acid together with CO_2 and acetaldehyde is the evident demonstration that the decomposition is following an oxidative degradation of the propionate ligands as in eq. 2.6(b). This mechanism is in contrast to the one followed in the case of the experiments conducted in a humid O_2 flow, in which the presence of propionic acid prior to the release of any other gases is strong indication of an initial, independent decomposition step deriving from the hydrolysis mechanism.

$$\textbf{(a)}\quad M_2(C_2H_5COO)_6 \xrightarrow{[H_2O]} 6C_2H_5COOH + M_2O_3$$
$$\textbf{(b)}\quad M_2(C_2H_5COO)_6 \xrightarrow{[O_2]} 3C_2H_5COOH + 3CH_3COH + M_2O_2CO_3 + 2CO_2 \xrightarrow{[O_2]} M_2O_3 + CO_2 \qquad (2.6)$$

To demonstrate the formation of the sesquioxide of the three RE elements during the pyrolysis thermal treatment, XRD was measured in grazing incidence geometry (GIXRD) on the films resulting from spin-coating deposition of solution of each individual RE propionate which then were subjected to the thermal treatment described in the B.1. The presence of Sm_2O_3, Gd_2O_3, and Yb_2O_3 is pivotal for the application of the REBCO precursor films prepared through the deposition of the ternary RE-Ba-Cu precursor solution: in the films, these oxides found in nanoparticle form will successively dissolve, during the growth process through TLAG, in the transient liquid of [Ba-Cu-O] to initiate the nucleation of the final SmBCO, GdBCO, and YbBCO epitaxial films. As displayed in Fig. 2.22, the crystallization of the sesquioxide of each RE element is successfully demonstrated, confirming full compatibility of the powder precursors described throughout the entirety of this chapter for the preparation of REBCO films through the TLAG-CSD approach.

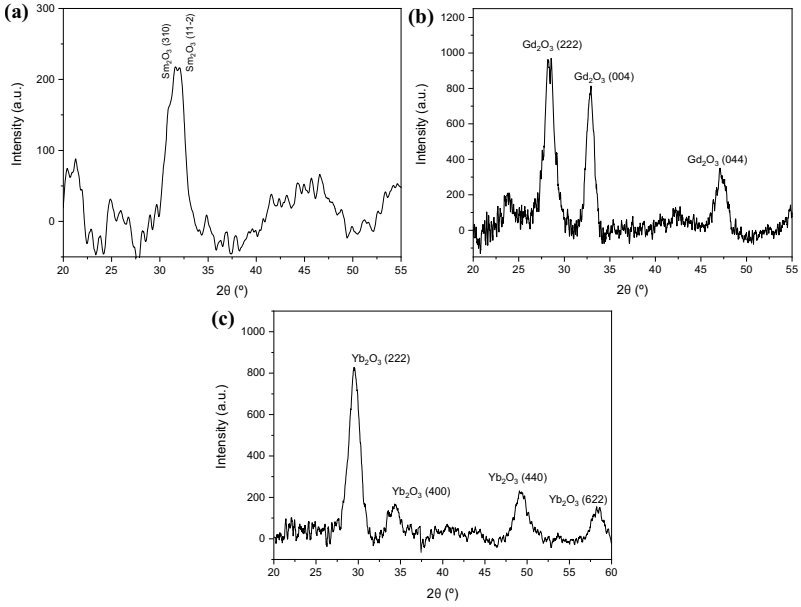


FIGURE 2.22: GIXRD acquired on the films resulting from the pyrolysis thermal treatment (conducted in a humid O_2 flow) deriving from (a) a solution of $Sm(Prop)_3$, (b) a solution of $Gd(Prop)_3$, and (c) a solution of $Yb(Prop)_3$.

2.4 Conclusions

The synthesis of a series of metal propionates has been developed and optimized and a detailed characterization led to confirming the feasibility of obtaining cost-effective and high purity powder precursors of copper, yttrium, barium, cerium, samarium, gadolinium, and ytterbium propionates for their use in the CSD of superconducting REBCO films, objective of the work described in this thesis. Crystal structures were obtained for all of the synthesized compounds through various crystallization techniques. Profound comprehension of the specific crystal structures is believed to be pivotal for a further control of the following decomposition pathways, at the base of the CSD methodology employed for the preparation of REBCO nanocrystalline precursor films which will finally yield the REBCO superconducting systems. Four novel crystal structures were obtained for the cases of $Ba(Prop)_2$, $Y(Prop)_3$, $Sm(Prop)_3$, and $Gd(Prop)_3$, and their characteristics could be correlated to their chemical properties. Also, a variation of the crystallization method resulted in two additional novel crystal structures for the cases of $Ce(Prop)_3$ and $Gd(Prop)_3$.

A complete analysis of the thermal behaviour for all of the synthesized products has been carried out and the decomposition pathways have been established for each individual metal propionate both for powders in inert atmosphere, and for films in an oxidative atmosphere. Employing metal propionates which have been previously synthesized and their purity has

been confirmed prior to their use in the REBCO metal-organic precursor solution is crucial for a consistent thermal decomposition: unwanted product mixtures derived from unreacted species that detrimentally vary the final, expected phase formation are avoided in such way, leading to a strict control of the microstructure and the nanoscale homogeneity of the REBCO nanocrystalline precursor films for TLAG.

Moreover, if desired, the metal propionate powders described in this chapter may be additionally employed as the non-fluorinated precursors in the low-fluorine TFA-MOD or in several functional materials prepared through CSD techniques which follow the MOD methodology, benefiting from the high-purity, low-cost and facile preparation methods of these presynthesized precursors.

However, in this thesis, the metal propionate powders reported in this chapter will find application as powder precursors for the preparation of a wide variety of metal-organic chemical solutions for the fabrication of REBCO films, following the essential demonstration of their chemical and thermal compatibility for the application proposed. A detailed study regarding said chemical solutions will be object of the following chapter.

3

Metal-organic precursor solution and nanocrystalline precursor films for TLAG

In this chapter, the YBCO precursor solution optimization process will be described. The initial objectives in section 3.1 and a further explanation in 3.2.1 will set the basis for the requirements the precursor solution has to meet, and explain how it should advance respect to the previous cases described in the group. The strategies for the optimization of the novel precursor solution will be then described in 3.2, with particular focus on the use of an amine additive and its effects on the nanocrystalline precursor films yielded by the first, low-temperature annealing (pyrolysis process), described in 3.2.3. A thorough microstructural analysis will also be described here, whereas the particular case of excess of amine additive will be subject of 3.2.4. The analysis of the chemical and physical properties of the novel YBCO precursor solution has been fundamental for an insightful understanding of the role of the amine additive, and two separate subsections will be dedicated to this: the first centered on the rheology and chemical analysis of the solution (3.2.5), whereas the second on the thermal behaviour of the different cases under study (3.2.6). Moreover, the way in which the solution is stored has been found to be of utmost importance to enhance its stability and shelf life, and the effects of this will be reported in section 3.2.7.

Finally, two different variations of the standard solution will be described: the first, in section 3.3, in which, the use of the corresponding RE propionates described in 2, led to the preparation of REBCO precursor solutions and nanocrystalline precursor films for the cases of SmBCO,

GdBCO and YbBCO; the second, object of section 3.4, in which the aim has been to explore a range of different amine additives possibly compatible with our system and evaluate their effect on the nanocrystalline precursor layers.

3.1 Objectives

Following the discussion in Chapter 1 and the further explanation in Chapter 2, one of the most important requirements for the application of REBCO superconducting films in the industrial framework is the possibility to obtain thick films without hindering the high physical performance of the superconducting material [144–146]. The current HTS market makes use of techniques such as Pulsed Laser Deposition (PLD) [17, 19, 20], Metal Organic Chemical Vapor Deposition (MOCVD) [21–23], Electron Beam Physical Vapor Deposition (EBPVD), metal evaporation (ME) [24–27], sputtering [28, 29] and trifluoroacetate metal-organic decomposition (TFA-MOD) through chemical solution deposition (CSD) [15, 36–45] for the growth of the HTS layer, principally based on expensive vacuum equipment and/or slow diffusion kinetics. Growth from a vapor phase consists in the deposition of RE, Ba and Cu adsorbed atoms on the growing interface, resulting in a growth rate directly affected by the atomic density. In vapor-based growth techniques, such as PLD, ME, sputtering, and MOCVD, control of supersaturation is determined by the difference between pressure of the adsorbed atoms at the growth front and that of equilibrium: it may be varied by changes in the deposition rate, oxygen pressure, and processing temperature, all parameters seen to influence the adsorbed atoms pressure at the growth front. Novel techniques to increase the growth rates have been developed in the last decade, with the two variations of PLD, high rate PLD (PLD-HR) [30–33] and liquid-assisted PLD (PLD-LAP) [34] showing the most promising results. Conversely, solid-solid growth mechanisms are governed by gas diffusion, where the elimination of the volatile gases is the limiting step for the nucleation of the desired REBCO. This mechanism is at the base of TFA-MOD, where supersaturation is strictly controlled through the variation of processing parameters (water pressure, oxygen pressure and temperature). Thorough control of the gas flow used for the growth process is, in this case, fundamental to ensure full evacuation and avoid gas stagnation at the film surface, which implies the complete hindrance of the reaction towards REBCO formation [35]. The techniques making use of vapor-based or solid-solid gas-mediated diffusion mechanisms result in low to mid-low growth rates: this is one of the major causes for the severe delay in the widespread of HTS-based technologies [71, 147], as their production is expensive and with low-throughput. In the scenario in which CSD is considered for the fabrication of the REBCO film, the development of a versatile and robust chemical solution but with higher throughput compared to TFA-MOD is of vital importance. The option of it being adaptable to various deposition techniques is pivotal, starting from the laboratory-based spin coating but imperatively expanding to industrially scalable approaches, i.e. slot die coating and inkjet printing. A fundamental requisite is the tunability of rheological

features of the chemical solution, with the concentration being top of the list. This parameter is strictly linked to the final thickness of the film when considering a single deposition method[1], therefore it is desirable to be able to adjust it to one's needs without compromising solution stability, reproducibility, or homogeneity of the final film. Moreover, following the global plead for greener chemical processes, as explained in Chapter 1, the following work is solely focused on the case of fluorine-free chemical solutions, completely eliminating fluorine from the process, and thus the toxic hydrofluoric acid (HF) generated as waste product of the TFA-MOD process.

Regarding the selection of precursors, an extensive discussion can be found in Chapter 2, where the choice of synthesizing metal propionates and therefore to disregard the use of commercial precursors has been thoroughly motivated. Here, the main objective is to report the ideas and experimental process which led to the optimization of a novel class of chemical solutions for the transient liquid assisted growth (TLAG) of high-performance YBCO films. As described in [51, 53], ultrafast growth rates of 100 nms^{-1} could be demonstrated through the use of an acetate-based fluorine-free chemical solution. This type of solution yielded YBCO superconducting films of high critical current densities, ranging between 3 and 5 MA cm^{-2} at 77K in self-field in films of 100 nm in thickness, also showing compatibility with the inclusion of preformed nanoparticles with the aim of enhancing the physical properties through artificial pinning centers (APCs) [55], demonstrating the enormous potential of the TLAG-CSD methodology at high-magnetic fields. However, the high-performance physical properties could be obtained exclusively on a thickness of 100 nm of final YBCO, mainly due to solubility limitations of the employed precursors in the chosen media; clearly, this called for the introduction of a novel solution which would enable higher thickness while maintaining the remarkable values of physical properties previously obtained, and thus progressing towards the demands for its industrial application. The process of development of a novel metal-organic fluorine-free precursor solution for the preparation of high-performance epitaxial REBCO films led to one European patent (European patent application no. PCT/EP2023/070988 filed on 28/07/2023) and a publication [148].

3.2 Development of novel YBCO precursor solution

3.2.1 Fundamental requirements of ideal precursor solution

In the previous section the general objectives were presented, considering how the solution has to be adapted to the demands of the industrial sector together with a progression from previous work performed in SUMAN group, inside the framework of the ERC Advanced Grant project, ULTRASUPERTAPE. Here, a discussion on the chemical and microstructural requirements

[1]The deposition method influences the final thickness *per se*, therefore the concentration of the solution must be adjusted to be optimal for a range of possible techniques

of the metal-organic precursor solution and the nanocrystalline precursor films that this yields will be carried out.

As explained in Chapter 1, one of the main objectives of the present work was to analyse the effects of altering the supersaturation of the transient liquid on the nucleation and epitaxial growth of YBCO, thus deepening the knowledge on the growth mechanism through the innovative TLAG process. The uncomplicated strategy adopted to obtain a tunable supersaturation of the transient liquid has been the preparation of chemical solutions of varying stoichiometry by changing the (Y:Ba:Cu) molar ratio, in which the name of each composition reflects the (Ba:Cu) molar ratio expected when the transient liquid is formed. Starting from the YBCO-stoichiometric mixture and increasing the copper content, the following range of compositions are considered in this thesis:

- **(2:3) composition**: (Y:Ba:Cu) proportion of 1:2:3, the exact stoichiometry for the formation of YBCO.
- **(3:6) composition**: (Y:Ba:Cu) proportion of 1:2:4, increasing the copper content from the stoichiometric case.
- **(3:7) composition**: (Y:Ba:Cu) proportion of 1:2:4.66, the Cu-rich mixture coinciding with the eutectic composition which showed most promising results in the previous studies in the group.
- **(4:11) composition**: (Y:Ba:Cu) proportion of 1:2:5.5, a composition with a large excess of copper respect to the YBCO stoichiometry. Copper-rich compositions have found widespread use in the growth of REBCO films through Liquid Phase Epitaxy (LPE) and Hybrid Liquid Phase Epitaxy (HLPE) [34, 84].
- **Y-rich (4:11) composition**: (Y:Ba:Cu) proportion of 1.35:2:5.5, namely an alternative to the (4:11) composition in which also the yttrium content is increased, creating a simultaneous excess of yttrium and copper. Yttrium- and copper-rich compositions showed the most promising results in coated conductor production through Reactive Co-Evaporation by Cyclic Deposition and Reaction (RCE-CDR). Its application in TLAG anticipates a higher contribution of solid yttria nanoparticles when the transient liquid with high copper excess is formed.

It can be noted how slight the modifications to the (Y:Ba:Cu) molar ratio are, therefore the first and most important requirement for the chemical solution is to reach complete dissolution, to ensure the correct stoichiometry desired for each composition. However simple this might seem, when working with chemical solutions one must consider the solubility limit of the powder precursors in the chosen mixture of solvents and how this might be an impediment to the accomplishment of a precursor solution for a specific composition. Following this consideration, a chemical solution which aims to be appealing for industrial applications must

imperatively be stable and have a prolonged shelf-life. It is necessary to point out that these are two aspects which are strictly correlated but the former does not directly imply the latter. If a stable solution is intended as one which does not present any solid precipitate, the fulfillment of this is not a direct proof that important changes in the solution's rheological properties have not occurred. In fact, the term **shelf-life** is defined differently, as *"the length of time a product may be stored without becoming unsuitable for use"*. Regarding this point, the storage methodology of the chemical solution is an extremely important factor, and various storage possibilities should be tested with the objective of maximising both the solution stability and its shelf-life. A thorough study concerning storage conditions for the chemical solutions used for TLAG-CSD described here may be found later on in this section (3.2.7). Moving on to the desired characteristics of the nanocrystalline layers obtained through the use of the metal-organic precursor solutions, the objective is set to accomplish thick, homogeneous and reproducible films which will be used as nanocrystalline precursor films for the TLAG process. Several fundamental aspects must be taken into consideration when optimising the chemical solution, as their achievement will provide the foundation for the growth process through TLAG. As explained in Chapter 1, TLAG is a non-equilibrium process kinetically controlled by the supersaturation of the transient liquid [53]. After its formation, it is the dissolution of the Y_2O_3 nanoparticles in the [Ba-Cu-O] liquid to cause its supersaturation and the following diffusion of Y atoms to the substrate-liquid interface favours nucleation of YBCO nuclei. This process occurs in time ranges of seconds, therefore, it is mandatory for the nanocrystalline phases in the precursor layers to be present in small sizes to ease their dissolution in the transient liquid, thus enhancing atomic mobility and assuring fast reactivity, enabling the ultrafast growth rates characteristic of the TLAG process. Moreover, the nanocrystalline precursor phases must be homogeneously distributed throughout the layer avoiding phase segregation, as this might lead to formation of secondary phases generated by local concentration of a given precursor phase. On a similar note, homogeneity is to be obtained also on the macroscale: major defects such as cracks or areas with distinct morphological features will be maintained as such after growth, hindering current percolation. An example of this is shown in Fig. 3.1, in which the Back Scattering Electron Detector (BSED) SEM image of a grown film clearly shows a variation of morphology resulting from the major defect present in the initial nanocrystalline precursor film. As discussed in Chapter 1, the films yielded by the pyrolysis process are a mixture of the three nanocrystalline precursor phases for YBCO, specifically Y_2O_3, CuO and $BaCO_3$, distributed in an amorphous matrix. Apart from the size of the phases, discussed above, it is essential that the formation of the $BaCO_3$ precursor leads to its orthorhombic phase. The extremely stable nature of $BaCO_3$ is no novelty in literature [92], and it is also considered one of the major challenges of the preparation of REBCO superconductors through the fluorine-free approach [42]. From previous studies, it could be demonstrated how adverse is the presence of monoclinic $BaCO_3$ as the only barium precursor to the epitaxial growth, being this phase stable up to temperatures of 900 ºC. Moreover, the formation of $BaCO_3$ monoclinic is usually

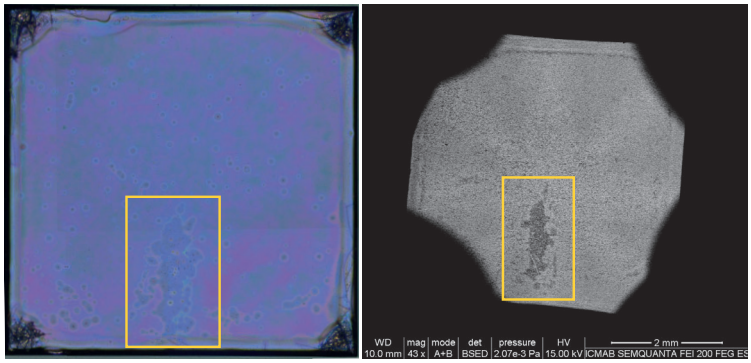


FIGURE 3.1: Major defect (highlighted by the yellow rectangle) present in the nanocrystalline precursor film (left) will generate an area of different morphology after the growth process, visible in the BSED SEM image on the right.

found to be linked to the presence of metallic Cu, which is known to be subject to strong coarsening phenomena [52, 91]. The presence of coarsened Cu(0) is highly undesirable given the extreme growth rates characterizing TLAG. The mandatory, initial reaction between $BaCO_3$ and the copper species to form the mixed barium-copper oxide would be strongly hindered in the case of large Cu(0) grains due to the slow reactivity, inevitably leading to insufficient and/or inhomogenoeus transient liquid generation. Thus, these phases would embody extremely unfavourable initial conditions for the TLAG process, and would lead to significant difficulties when trying to obtain high epitaxy. After considering all of the previous points, the last but also crucial requirement the precursor solution has to meet is its suitability for multideposition. As discussed above, the ultimate application of this kind of solutions would be in the industrial framework, where thickness enhancement is amongst the fundamental steps towards the delivery of HTS-based coated conductors (CCs) to the general market. Various strategies are adopted to do so, one of these being a multiple deposition of the precursor solution. Therefore, the ideal precursor solution should yield homogeneous films both when depositing single or multi-layers, especially considering the microstructure and phase homogeneity of the films.
Having set the aforementioned, necessary prerequisites for the YBCO precursor solution, the optimization process will be performed with close consideration of all the previously discussed points, and only precursor solutions which fulfill the entirety of the requirements will be adopted for TLAG-CSD.

3.2.2 Optimization process

Initially, the optimization of a novel solution employing the metal propionates synthesized as described in Chapter 2 was pondered without the inclusion of any additive. The reason behind this idea is the fact that, when including an additive of organic nature, there is an increase of the amount of carbon in solution (due to the chemical structure of the additive, as the most

widely used contain aliphatic chains of varying length) which might lead to difficulties in the decomposition of the metal-organic precursors during the pyrolysis process, which could result in carbon contamination in the grain-boundaries of the final YBCO film. This would imply detrimental consequences for the physical properties of the superconducting films [149]. Thus, trying to avoid such obstacle, the first step towards the novel fluorine-free solution formulation was the preparation of a saturated solution, as the main objective was the maximum enhancement possible of the final film thickness. Important to state that the first optimization effort was only focused on the (3:7) composition, then successively adapted to the other compositions. This preference is deduced from previous studies in our group which proved this stoichiometry to promote the epitaxial growth of YBCO through TLAG [51]. Thus, the following description of the optimization process will be concentrated on this specific composition, if not specified differently. The choice of solvents and the ratio of eventual mixtures are object of the same previous study: a mixture of propionic acid (HProp) and methanol (MeOH) in a ratio (1:1) was demonstrated to yield the best results as far as microstructure of the nanocrystalline precursor films is concerned. For this reason in the entirety of the present thesis this solvent mixture will be adopted, and any other solvent choice or mixture will be thoroughly detailed.

The first type of solution tested was obtained by simple addition of barium, copper and yttrium propionates to the solvent mixture, in a total concentration of 1 M in sum of metals. This was the maximum concentration possible without the involvement of any additive, given the limited solubility of the precursors in the chosen media. Specifically, the major difficulties are attributable to the complete dissolution of $Cu(Prop)_2$, not only for its anhydrous crystalline structure, but also as this precursor is the one added in majority in all of the compositions considered. Despite being stable during several months and allowing for the preparation of homogeneous, crack-free nanocrystalline precursor films, this type of solution resulted in layers of a thickness of merely 100 nm, as shown in Fig. 3.2. Bearing in mind the thickness enhancement requisite, it was a clear necessity to take into consideration the introduction of an additive, as a thickness of 100 nm per pyrolyzed layer would require a copious amount of multiple depositions, making the process not ideal for a future industrial application. Nevertheless, the system compelled for a careful selection of the additive to avoid its interference in the correct formation of the nanocrystalline precursor film. Preferably, the additive should aid the complete dissolution of the metal-organic precursors, enabling for higher concentrations to be obtained, and additionally favour the formation of homogeneous, low-porosity nanocrystalline precursor films with suitability for multi-deposition.

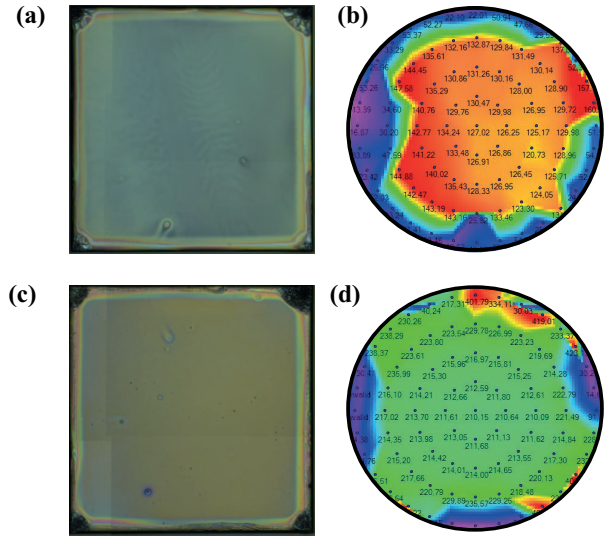


FIGURE 3.2: (a) OM image of a one-layered nanocrystalline precursor film obtained using a solution of 1 M with no additive. (b) Thickness measurement of the layer showed in (a), through reflectometry, with average thickness of 130 nm. (c) OM image of a nanocrystalline precursor film of two layers, obtained by multideposition of the same solution on the one-layered sample depicted in (a). (d) Thickness measurement of the film showed in (c), through reflectometry, indicating an average thickness of 210 nm.

Additionally, the additive should improve the mechanical properties of the film: the evolution of gases due to the decomposition of the organic ligands is at the origin of strong tensile stress and strain due to film shrinkage during the thermal treatment, possibly leading to cracking phenomena. Thus, the major chemical requirement for the additive was to promote $Cu(Prop)_2$ solubility in the mixture of solvents, possibly by means of complex formation. For this reason, amine compounds were promptly thought to be viable candidates, given their well-known ability to form complexes between the *N* atom and the metal centers, specifically favoured in the case of copper [150]. As previously stated, the chemical formula of the selected compound can play a fundamental role, as an excess of carbon in the solution may lead to a troublesome decomposition due to the excess of organic matter, possibly resulting in the formation of the undesired $BaCO_3$ monoclinic during the pyrolysis process, demonstrated to have detrimental effects on the epitaxial growth [52, 126]. Thus, short-chained aliphatic compounds are preferable. Another important feature is the compatibility of its thermal decomposition with the one of the metal-organic precursors employed: besides the decomposition of its organic matter to be limited to the temperature range of the pyrolysis process (with maximum temperature being 500 ºC), it must combine adequately in the elaborate metal-organic skeleton resulting in an augmented strain dissipation to prevent crack formation [126,

151, 152]. Hence, considering the listed limitations, the best fitting amine additive was monoethanolamine (MEA). This complies well with all the previous restrictions and presents the additional feature of containing an *-OH* functional group, making it an aminoalcohol: apart from possible complexation through the *N* atom of its $-NH_2$ functional group, it bears the possibility for further stabilization through H-bonds from the hydroxyl substituent.
As a starting point for the introduction of MEA in the precursor solution, a value of $5\%_{v/v}$ was added to a solution of 1 M concentration in sum of metals, to evaluate its effect compared to the case of no amine additive. Important to be noted, the extremely rapid dissolution of $Cu(Prop)_2$, suggesting an interaction between the amine and the copper precursor is occurring. The important loss of homogeneity of the nanocrystalline precursor films displayed in Fig. 3.3, showing a rough surface and numerous defects, is undoubtedly not optimal. However, on a positive note, one must consider the notable increase of thickness respect to the case in which no amine is used, doubling the previously obtained value. Regardless of the inhomogeneous morphology, the thickness improvement is suggesting this amine to be beneficial for the main objective proposed.

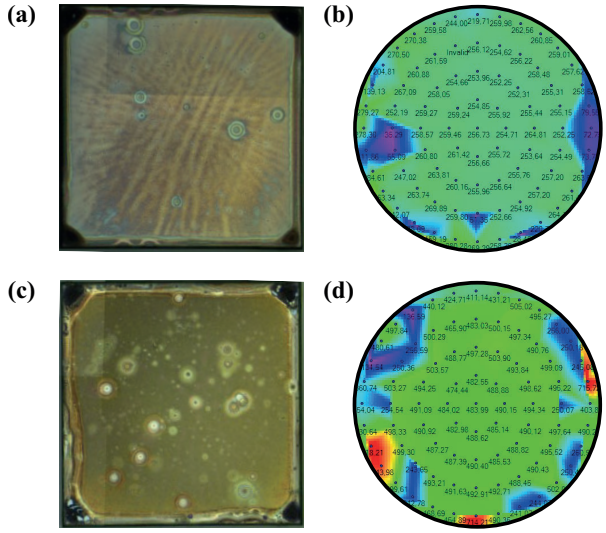


FIGURE 3.3: (a) OM image of a nanocrystalline precursor film obtained using a solution of 1 M with the addition of $5\%_{v/v}$ MEA. (b) Thickness measurement through reflectometry of the film showed in (a) with average thickness of 250 ± 50 nm. (c) OM image of a nanocrystalline precursor film of two layers, obtained by multideposition of the same solution on the one-layered film in (a). (d) Thickness measurement through reflectometry of the film showed in (c) indicating an average thickness of 480 ± 50 nm.

Therefore, taking into account the straightforward $Cu(Prop)_2$ dissolution as a distinct indication of being far from the saturated conditions in the case of the 1 M concentration when MEA is added, higher concentrations were tested. It was found that with the addition of the same

$\%_{v/v}$ of MEA, complete dissolution of the precursors could be achieved for concentrations up to 1.75 M. However, as showed in Fig. 3.4 , this solution results in deleterious consequences on the homogeneity of the nanocrystalline precursor films, yielding a completely cracked film when multideposition is attempted.

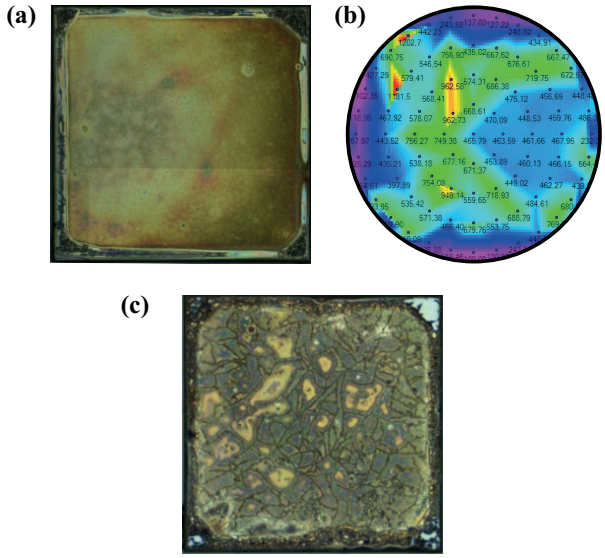


FIGURE 3.4: (a) OM image of a nanocrystalline precursor film obtained by deposition of a solution of 1.75 M with the addition of $5\%_{v/v}$ MEA. (b) Thickness measurement through reflectometry of the film showed in (a), with average thickness of 600 ± 50 nm. (c) OM image of a nanocrystalline precursor film of two layers, obtained by multideposition of the same solution on the one-layered film in (a). No thickness measurement is shown for the two-layered film, as a reliable value could not be obtained due to the high degree of inhomogeneity of the film.

Nonetheless, the remarkable value of 600 ± 50 nm thickness achieved for the first layer in Fig. 3.4 must not be overlooked, as it is again demonstrating the great potential of MEA for the aim of thickness increase. Finely adjusting the conditions was pivotal for the accomplishment of homogeneous nanocrystalline films for TLAG. Through a delicate fine-tuning process, the maximum concentration of 1.75 M could be maintained, with the finding that by using $4\%_{v/v}$ MEA highly homogeneous nanocrystalline films of 400 ± 50 nm thickness per layer could be obtained. Moreover, by multideposition of this solution, the homogeneous morphology of the film is preserved, yielding defect-free films of almost 1 μm thickness with only two depositions, as visible in Fig. 3.5.

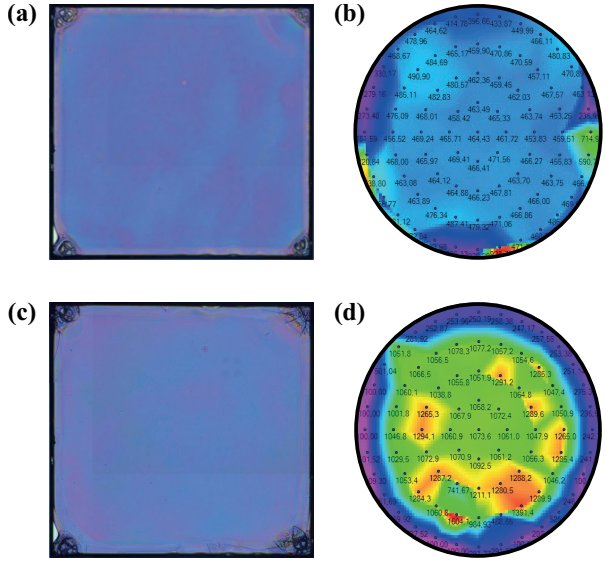


FIGURE 3.5: (a) OM image of a nanocrystalline precursor film obtained using a solution of 1.75 M with the addition of $4\%_{v/v}$ MEA. (b) Thickness measurement through reflectometry of the film showed in (a), with average thickness of 400 nm. (c) OM image of a nanocrystalline precursor film of two layers, obtained by multideposition of the same solution on the one-layered film in (a). (d) Thickness measurement of the two-layered film shown in (c), giving an average value of 1 μ m $\pm$ 50 nm.

An important feature was the possibility of obtaining complete dissolution of the metal propionate precursors for all the compositions listed in section 3.2.1, and through small variations of the $\%_{v/v}$ MEA, successful preparation of precursor solutions for the compositions considered was possible. The (Cu:MEA) molar ratio for each of the considered compositions listed in Table 3.1 is the result of a careful optimization process, with the aim of ensuring the achievement of highly homogeneous nanocrystalline precursor films: Fig. 3.6 shows two-layered films obtained from optimized solutions for each composition. As previously stated, the morphological homogeneity of the films is by far the sole requirement for this class of solutions. Thus, XRD analysis was carried out on these films and is shown in Fig. 3.6. The majority of $BaCO_3$ is found to be in the orthorhombic phase, while the copper and yttrium precursors crystallize as CuO and Y_2O_3, confirming these solutions are capable of forming the desired nanocrystalline precursor phases for TLAG, while simultaneously yielding defect-free films of high thickness.

Composition	(Cu:MEA) molar ratio	$\%_{v/v}$ MEA (for total concentration 1.75M, volume 5 mL)
(2:3)	1:0.8	4.3
(3:6)	1:0.66	4
(3:7)	1:0.61	4
(4:11)	1:0.6	4.1
Y-rich (4:11)	1:0.6	4.1

TABLE 3.1: Optimal (Cu:MEA) molar ratios for the compositions considered in this thesis, together with $\%_{v/v}$ for the concentration and volume of optimized solutions described in this section.

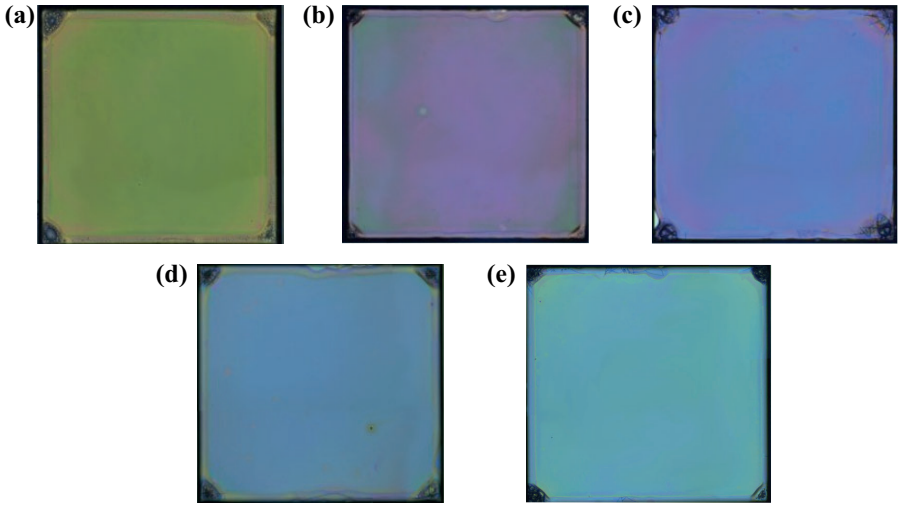


FIGURE 3.6: OM images of films deriving from optimized solutions of different compositions: (a) (2:3) composition solution of 1.75 M + 4.3$\%_{v/v}$ MEA; (b) (3:6) composition solution of 1.75 M + 4$\%_{v/v}$ MEA; (c) (3:7) composition solution of 1.75 M + 4$\%_{v/v}$ MEA; (d) (4:11) composition solution of 1.75 M + 4.1$\%_{v/v}$ MEA; (e) Y-rich (4:11) composition solution of 1.75 M + 4.1$\%_{v/v}$ MEA.

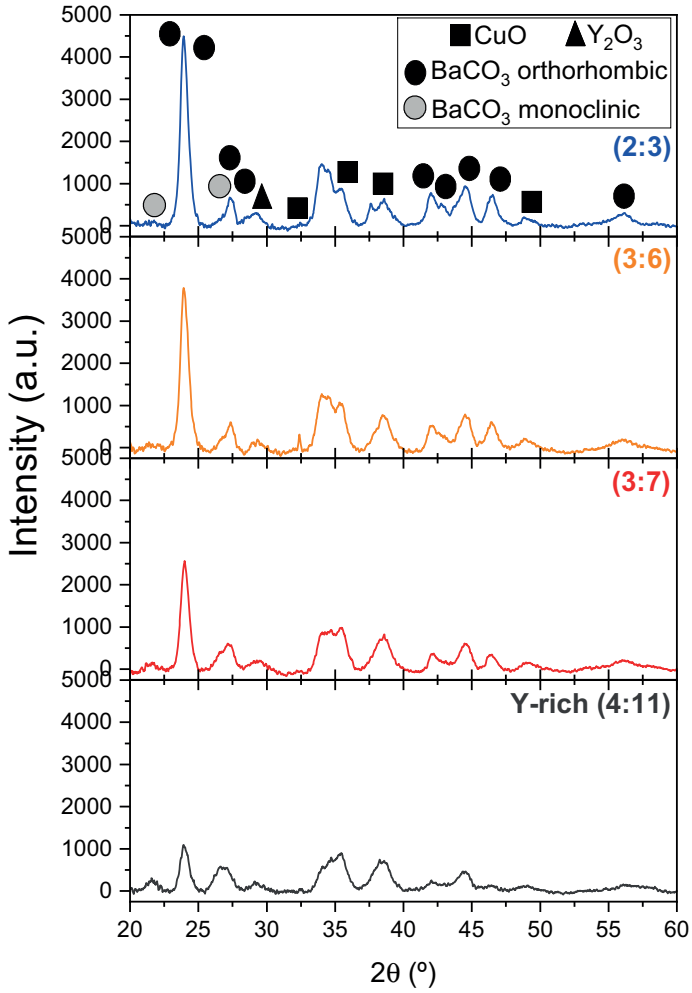


FIGURE 3.7: XRD analysis of nanocrystalline precursor films of various compositions, from top to bottom starting from the stoichiometric (2:3) composition and increasing the copper content to the Y-rich (4:11) composition.

Nonetheless, it must be noted that the (Cu:MEA) molar ratio is not stoichiometric: the amount of MEA would have to be increased to a 12.8%$_{v/v}$ MEA (for the (3:7) composition solution) if a complete complexation with copper is desired (detailed explanation of the possible complexation of MEA to the copper precursor will be given in 3.2.5). The precise optimization of the molar ratio is directly linked to the final aspect of the film resulting from the pyrolysis process. It is of utmost importance to stress that variations of only 0.2%$_{v/v}$ MEA can alter completely the morphology of the sample, as can be observed for the case of the (2:3) composition optimization process in Fig. 3.8. Cracking occurs in the cases in which not enough additive is employed, possibly due to a low mechanical resistance of the film: the elevated

amount of evolved gases as a result of the decomposition of the metal-organic precursors are mainly concentrated in one large mass loss step, as will be explained in detail in subsection 3.2.6. Insufficient use of MEA may thus lead to extreme strain, released by the formation of cracks. Conversely, major deposition defects which hinder the final homogeneous aspect of the film arise when an excessive content of MEA is employed, presumably as a result of excessive viscosity of the solution for the spin-coating parameters selected. Consequently, the optimization process enabled to achieve fully dissolved, reproducible and stable solutions for all the considered compositions which yield smooth, high-quality, crack-free, thick precursor films with a thickness of 400 nm for each single layer, with the desired nanocrystalline phases. Multi-deposition by spin coating as well as a thorough microstructural analysis to demonstrate suitability of these for the TLAG process will be object of the next subsection. However, it is relevant to specify that this class of solutions was additionally found to be compatible with ink-jet printing [153], through which combinatorial approaches led to a faster experimental optimization for high performance films [154–156], and with multi-layered depositions by slot die coating on metallic substrates, demonstrating the true possibility of application in the industrial framework.

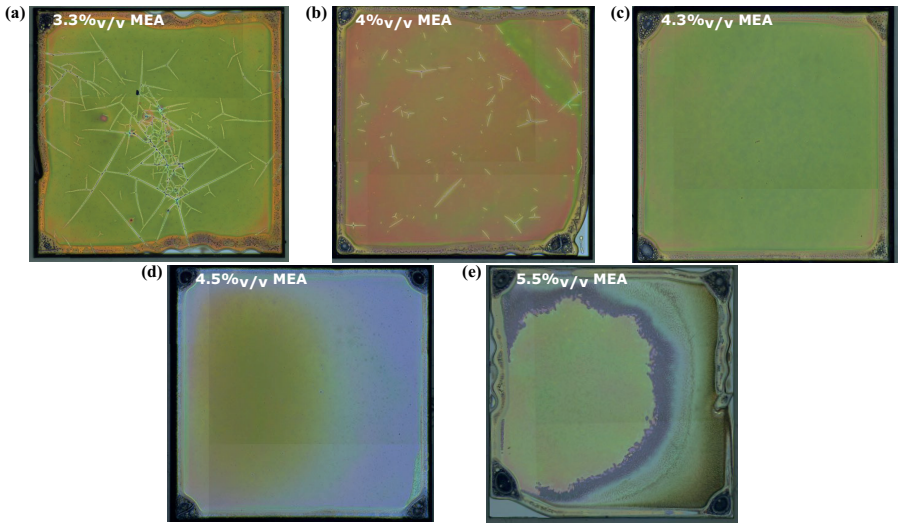


FIGURE 3.8: Optimization of (2:3) composition precursor solution, in which various $\%_{v/v}$ MEA were tested, fine-tuning the conditions previously found optimal for the (3:7) composition. (a)-(b)Appearance of cracks due to insufficient amine additive. (c) The value of 4.3$\%_{v/v}$ MEA is found to be optimal for this specific composition. (d) Defect during the deposition, possibly due to an elevated $\%_{v/v}$ MEA, effect increased detrimentally in (e).

3.2.3 Microstructural analysis of nanocrystalline films

Detailed microstructural analysis of various precursor films has been conducted through a variety of transmission electron microscopy (TEM) techniques. Characterization on two-layered films of (2:3), (3:7) and (4:11) compositions with optimized additive quantities, has revealed similar microstructural features. These present smooth surfaces while showing high thickness of each layer: around 470 nm for the (2:3) composition, 400 nm for the (3:7) composition and 320 nm for the (4:11) composition, displayed in Fig. 3.13, 3.11 and 3.14, respectively. The small variations in thickness values may be ascribed to different rheological properties of each solution: slight deviations will yield varying results during deposition, as will be studied further on in 3.2.5. Microstructural analysis of a two-layered, (3:7) composition film is displayed in Fig. 3.9. Low magnification cross-sectional high-angle annular dark field scanning transmission electron microscopy (STEM-HAADF) images show the smooth surface and

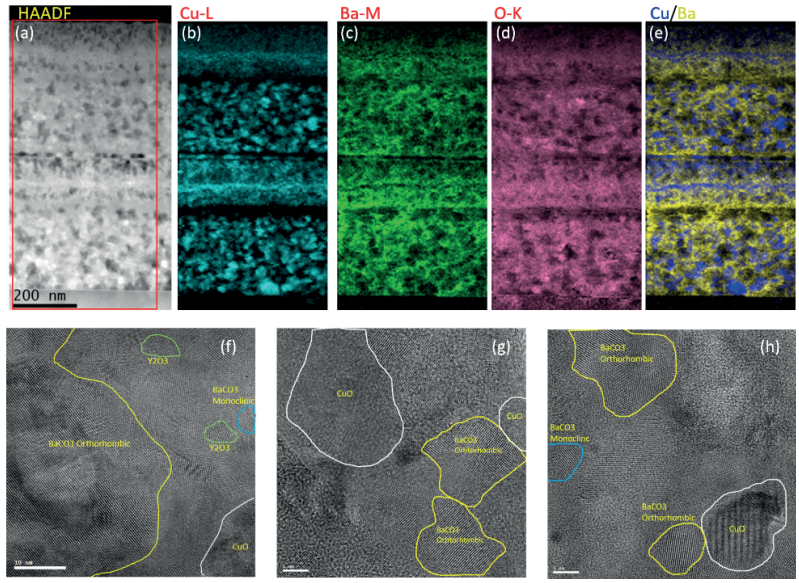


FIGURE 3.9: (a) STEM-HAADF image of a two-layered (3:7) precursor film deposited using the optimized solution. Elemental EELS maps of (b) Cu-L edge, (c) Ba-M edge, (d) O-K edge, (e) composite EELS map of Cu (blue) and Ba (yellow), from red rectangular region in (a). (f-h) HR-TEM images collected from different regions of the precursor film, displaying the individual sizes and the presence of all precursor phases in the same area, exhibiting a homogeneous distribution.

continuously homogeneous microstructure along the entire film. To precisely determine phase distribution, elemental analysis is performed through electron energy loss spectroscopy (EELS): elemental maps of $CuL_{2,3}$, $BaM_{4,5}$, and OK, reveal high nanoscale homogeneity, with CuO nanocrystals uniformly distributed within a $BaCO_3$ matrix, with no visible areas of phase

segregation or interfaces, establishing an ideal situation for the epitaxial growth of YBCO. A widespread characteristic of the TFA-MOD is, indeed, the formation of segregated CuO interlayers which tend to be found at the interface between two layers when films of multiple depositions are prepared, resulting in a major drawback for the successful nucleation of the final REBCO film [126]. The spatial distribution, crystalline state, and sizes of precursor phases could be determined through the analysis of high-resolution transmission electron microscopy (HR-TEM) images, shown in Fig. 3.9 (f-h). The three nanocrystalline precursor phases, namely $BaCO_3$, CuO, and Y_2O_3, can be undeniably identified in three different HR-TEM images taken from various regions of the film, validating the robustness and homogeneity resulting from this solution. Typical grain sizes of the nanocrystalline precursor phases vary between 10 nm and 30 nm for orthorhombic $BaCO_3$, 5 nm and 7 nm for monoclinic $BaCO_3$, 10 nm and 25 nm for CuO, and Y_2O_3 between 5 nm and 6 nm. In accordance with the theoretical principles of TLAG explained in Chapter 1, the reduced sizes measured here, together with the homogeneous distribution of the nanocrystalline precursors are considerably favouring a rapid and homogeneous transient liquid formation and facilitating atomic mobility, allowing to obtain highly epitaxial layers with ultrafast growth rates. Likewise, being $BaCO_3$ mainly present in the orthorhombic phase, it enables a direct reaction with the nanocrystalline CuO in the TLAG process, exhibiting no significant obstacle for its elimination, as it will be demonstrated in Chapter 4.

Additionally, energy dispersive X-ray spectroscopy (EDX) was used to conduct a complementary compositional analysis in which Y, Ba, and Cu STEM-EDX cross-sectional elemental maps confirm the uniform distribution of nanocrystalline phases.

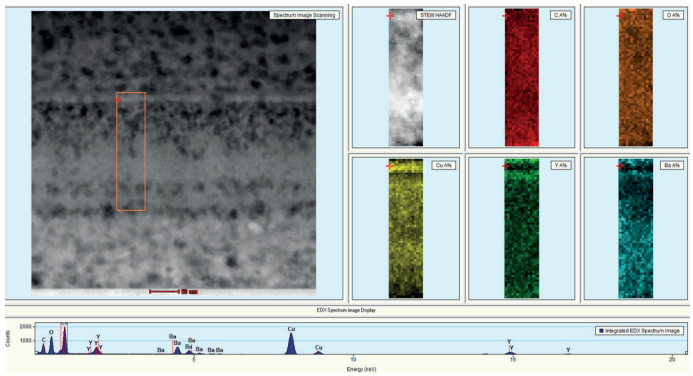


FIGURE 3.10: STEM-EDX cross-sectional elemental maps of Cu, Y, and Ba showing homogeneous distribution of these elements in a (3:7) composition nanocrystalline precursor film of two layers.

Regarding the possible effects of multideposition on the microstructure, Fig. 3.11 presents

(3:7) composition samples on which this aspect was analyzed: the cross-sectional STEM-HAADF images display a two-layered sample, a four-layered sample and an eight-layered sample, showing thickness of 800 nm, 1.5 μm and 2.7 μm, respectively. This demonstrates how remarkable thickness can be obtained without compromising the smooth surface or the general homogeneity of the film.

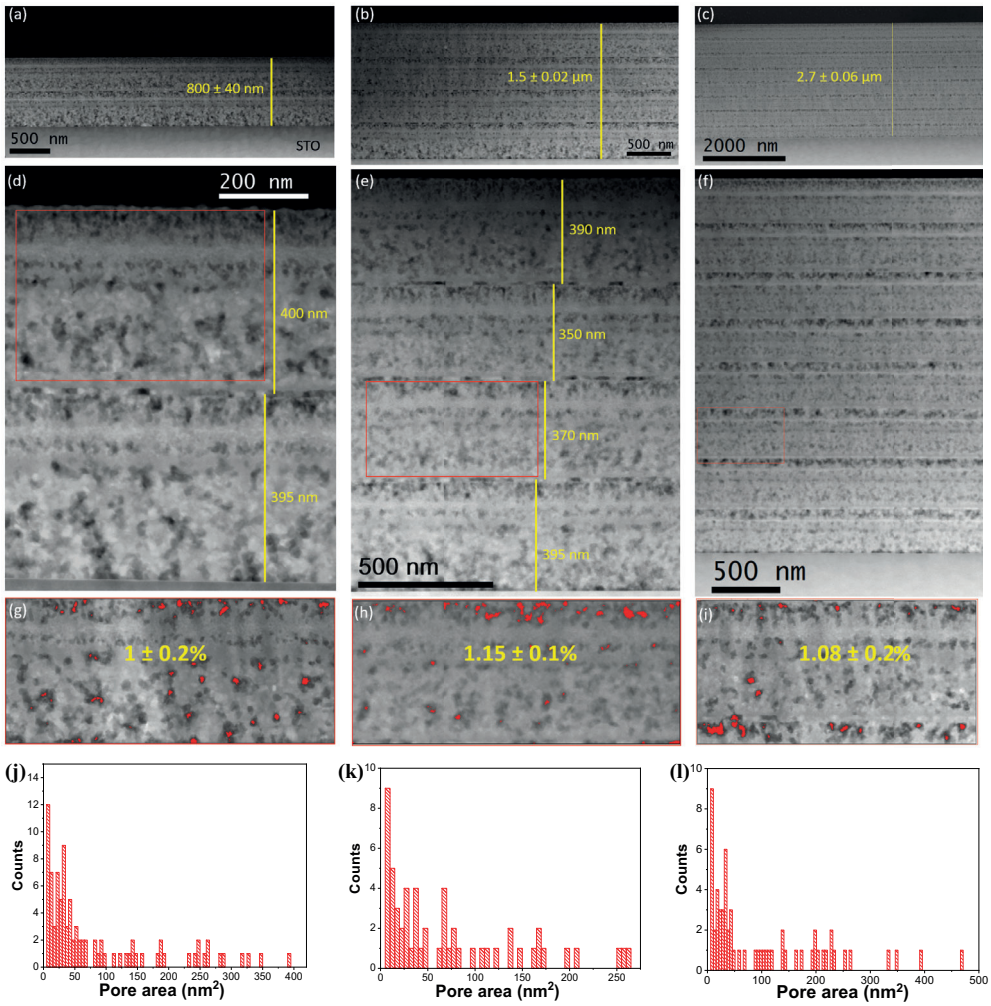


FIGURE 3.11: Cross-sectional low-magnification STEM-HAADF images of (3:7) composition nanocrystalline precursor films deriving from optimized solution of (a) two layers, (b) four layers, and (c) eight layers. Magnified STEM-HAADF images displaying similar thicknesses of individual layers for (d) two layers, (e) four layers, (f) eight layers, additionally showing the homogeneity of the microstructre regardless of the number of deposited layers. (g-i) Analysis of pore density using ImageJ software from the regions marked with red rectangles in (d-f), respectively; for quantification, pores are coloured in red. (j-l) Histograms of pore areas, employed for the calculation of average pore sizes.

Moreover, each layer shows similar thickness, again demonstrating the feasibility of this kind of solutions for the multideposition process: despite being eight layers the maximum number of multiple depositions tested, it clearly evidences no loss of homogeneity or significant differences in the nanocrystalline matrix, implying that the limit is yet to be reached. In Fig. 3.11(g-l), through the STEM-HAADF image analysis using the software ImageJ, estimated pore densities as low as $1.0 \pm 0.2\%$, $1.1 \pm 0.1\%$, and $1.1 \pm 0.2\%$ are determined for the multideposition films of two, four, and eight layers, respectively. Their low porosity is of great benefit to the fast reactivity of the TLAG process, favouring the reaction between $BaCO_3$ and CuO to form the transient liquid; however, such low porosity values are found to be the limit for successful gas transport, specifically out-diffusion of CO_2 or CO and diffusion of O_2, as lower values are shown to hinder the desired outcome of the decomposition process during the heat-treatment. Further analysis of this fundamental aspect will be presented in the following section. Nonetheless, a comparison with a sample prepared through the renowned TFA-MOD route is worth to be made at this moment. The porosity of two films prepared through the TFA-MOD process, one deposited by ink-jet printing and the second by spin-coating with multideposition, was analyzed and is displayed in Fig. 3.12.

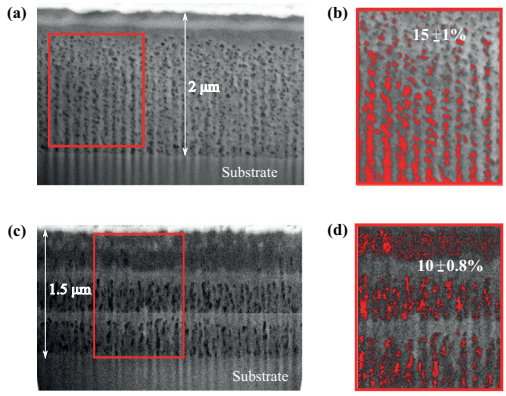


FIGURE 3.12: Cross-sectional SEM images of TFA-MOD films obtained by Focused Ion Beam (FIB) with (a) a single layer using ink-jet printing and (c) three layers using spin coating [126]. (b) and (d) show the pore density analysis using ImageJ from the red rectangular region in (a) and (c), respectively, where pores are coloured in red for quantification.

The porosity values are, respectively, $15 \pm 1\%$ and $10 \pm 0.8\%$, more than a factor 10 than the case of the optimized fluorine-free solutions discussed in this thesis.

The same analysis carried out for (3:7) composition was conducted on films of other compositions to assess whether all solutions are able to yield similar microstructural features, and results for the cases of (2:3) and (4:11) compositions are shown in the following Fig. 3.13, Fig. 3.14, respectively.

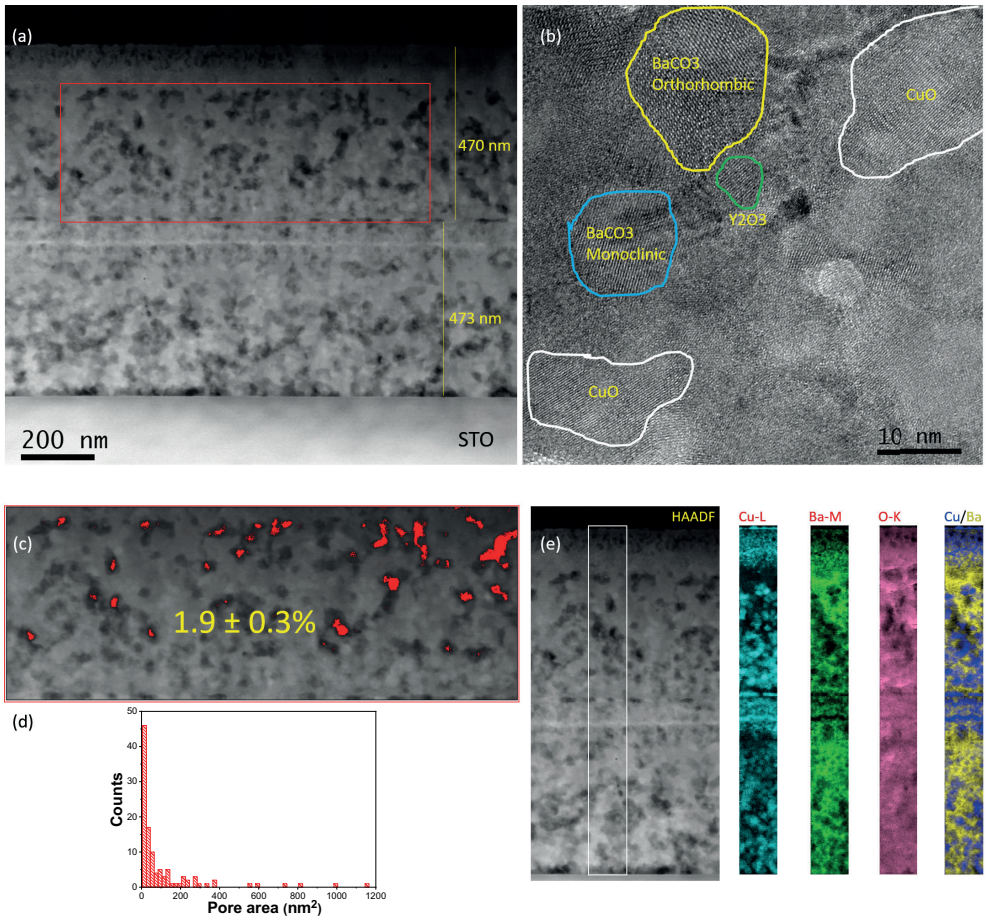


FIGURE 3.13: (a) Cross-sectional low magnification STEM-HAADF image of a two-layered precursor film deposited using the optimized solution for the (2:3) composition, confirming the smooth surface and similar thickness of each layer, being 470 nm *circa*, resulting in a total thickness of almost 1μm. (b) HR-TEM image displaying sizes and presence of nanocrystalline precursor phases in the same region, demonstrating the homogeneous distribution of the film. (c) Analysis of pore density from the red rectangular region in (a) using the software ImageJ; for quantification, pores are identified in red colour. (d) Histogram of pore area which serves to calculate average pore size. (e) Elemental EELS maps of Cu-L edge, Ba-M edge, O-K edge, and composite EELS map of Cu (blue)-Ba (yellow), again demonstrating the uniformity of phase distribution in the film.

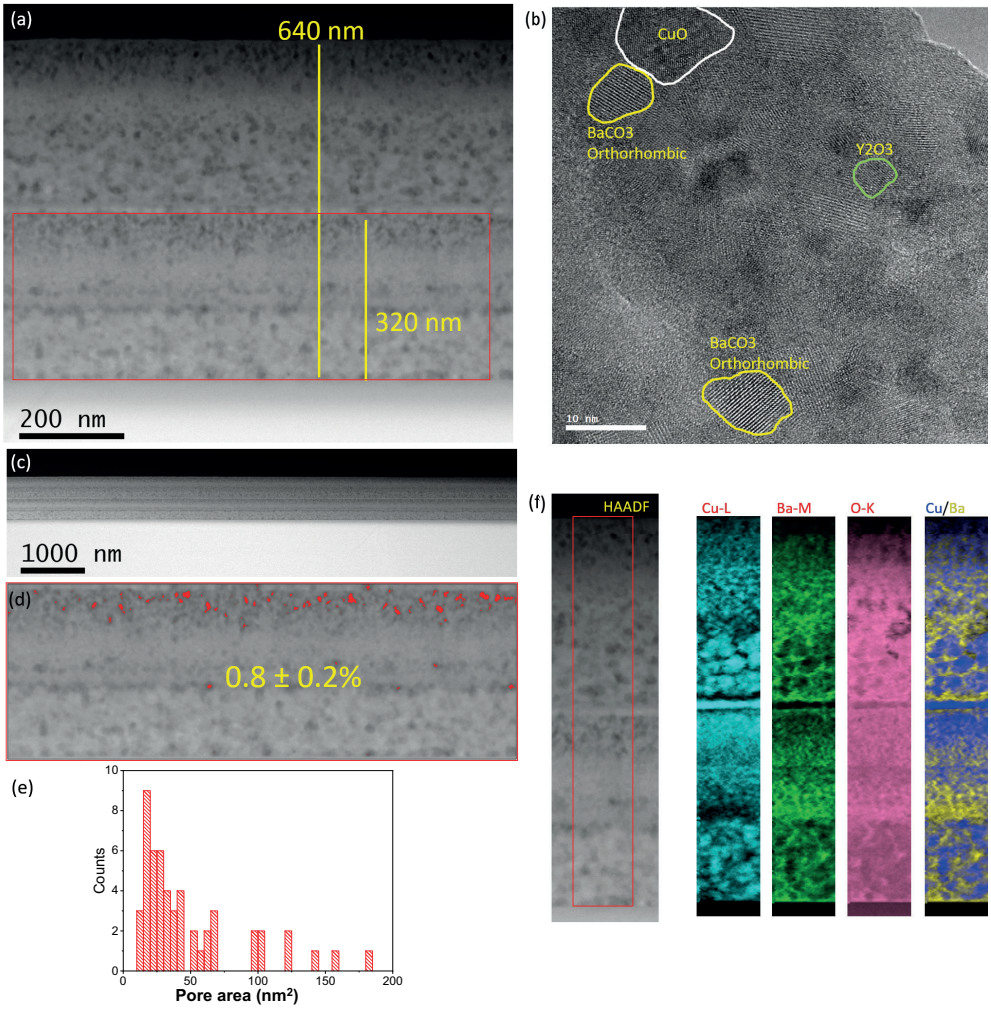


FIGURE 3.14: (a) Cross-sectional low magnification STEM-HAADF image of a two-layered (4:11) composition precursor film obtained through the use of the optimized solution, total thickness is around 640 nm, with each layer being 320 nm. (b) HR-TEM image in which the appearance of the three nanocrystalline precursor phases show the homogeneous distribution of the film. (c) Cross-sectional low magnification STEM-HAADF showing the remarkably flat and smooth surface of the entire film. (d) Pore density analysis using the software ImageJ obtained from the red rectangular region in (a), with pores coloured in red for quantification. (e) Histogram of pore area used to calculate the average pore size. (f) Elemental EELS maps of Cu-L edge, Ba-M edge, O-K edge, and composite EELS map of Cu (blue)-Ba (yellow).

The microstructural features of the films of the three compositions analysed here reveals the great similarities between the three cases. Size and distribution of the nanocrystalline precursor phases in the amorphous matrix are comparable, and the sole relevant distinction may

be identified in the porosity of the film, decreasing with the increase of the copper content of the composition: a (2:3) composition film exhibits a porosity of $1.9 \pm 0.3\%$ whereas in the copper-excess composition this value is reduced to $0.8 \pm 0.2\%$. Possibly, the discrepancy in the (Ba:Cu) ratio may lead to slight differences in the thermal behaviour of the chemical solution, with the varied gas evolution to result in a more dense or more porous film at the end of the pyrolysis process. Nonetheless, this disparity is not believed to significantly affect the following TLAG process, as the films of various compositions display the desired nanocrystalline phases in the small size ranges necessary for the fast reactivity to enable the ultrafast growth rates characteristic of TLAG.

3.2.4 Effects of amine additive excess

As discussed in the previous subsection, the nature and careful selection of the additive is crucial for the successful preparation of homogeneous and reproducible nanocrystalline precursor films, in the same way as the quantity employed. In Fig. 3.8, an example of the precise optimization of the amine content in solution is provided, in which it is evident how a mere variation of $0.2\%_{v/v}$ would be decisive for a positive or negative outcome.

With the greatest concerns being the complete dissolution of the metal-organic precursors and the possibility of reaching high concentrations, one would be prone to use a large quantity of additive, especially when this was proven to be extremely beneficial to the increase of $Cu(Prop)_2$ solubility, the precursor showing the greatest issues in the chosen media. To ensure an exhaustive knowledge of the effects of an amine additive excess, a (3:7) composition solution of concentration 1.75 M in total sum of metals and an $8\%_{v/v}$ MEA was prepared. The amine content in this case is doubled respect to the optimized solution, and the already fast dissolution observed in the latter case is, here, incredibly enhanced, reducing importantly the reaction time. However, a complete analysis of the effects on the nanocrystalline precursor films is mandatory.

Fig. 3.15 shows the OM image of a one-layered film prepared by using the solution with MEA excess. Indisputably, the quality of the film has declined: the homogeneity is completely lost and morphological irregularities are found throughout the entire surface. Moreover, the XRD pattern measured for this sample displays how adverse an amine excess is to the formation of the desired nanocrystalline phases: $BaCO_3$ is found only in its monoclinic phase and copper is majorly present as metallic Cu (Cu(0)). It is important to remind that the pyrolysis process is conducted at 1 atm in a 0.12 mL min^{-1} gas flow of humid O_2, employed to favour the hydrolysis and oxidation decomposition mechanism of the propionate ligands (see Chapter 2 for the detailed explanation of all decomposition mechanisms). The presence of the most reduced phase of copper is, thus, surprising.

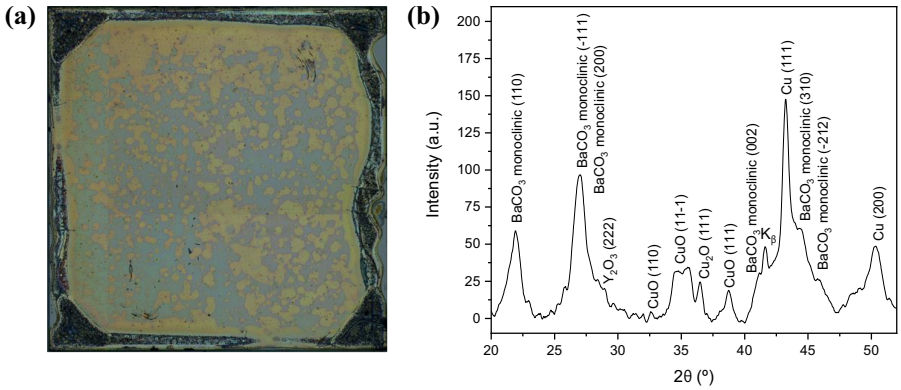


FIGURE 3.15: (a) OM image of a nanocrystalline precursor film obtained by a single deposition of a solution with excess of MEA (1.75 M + 8%$_{v/v}$ MEA), with the corresponding XRD pattern shown in (b).

It has been previously elucidated in detail in Chapter 1 how detrimental these phases are for the expected epitaxial nucleation and growth of YBCO through TLAG, as monoclinic $BaCO_3$ presents a prolonged thermal stability, beyond the preferred orthorhombic phase. Furthermore, the strong coarsening phenomena common for metallic Cu, which in this system is rarely re-oxidized, hinders the fast reactivity towards the homogeneous formation of the [Ba-Cu-O] transient liquid [52]. Detailed TEM analysis was carried out on the film obtained through the use of a solution with amine excess, and is shown in Fig 3.16. If the previously presented morphological features from the OM image and nanocrystalline phases from the XRD pattern suggested an adverse situation, the microstructural characteristics displayed in the cross-sectional low-magnification STEM-HAADF images are undoubtedly demonstrating the absolute contrast respect to the optimized conditions. Despite the thickness is almost 200 nm higher than the case with optimized MEA quantity, being one layer 580 nm thick, the microstructure confirms the presence of monoclinic $BaCO_3$ and metallic Cu, resembling certain films obtained when depositing acetate-based precursor solutions [91]. The metallic Cu grains vary considerably in size, ranging between 10 nm and 100 nm, again providing a general inhomogeneity in the nanocrystalline film which would yield detrimental results if subjected to the TLAG process. Moreover, the elemental EELS maps reveal a trend of phase segregation throughout the film: if analysing it from the substrate to the surface, the larger metallic Cu grains are isolated to the area closest to the substrate-film interface, successively followed by a monoclinic $BaCO_3$-rich region and finally two superficial, compact, separate layers of CuO and $BaCO_3$. The pore density analysis concluded the average pore size to be the minimal value of $0.49 \pm 0.15\%$, distributed in a non-homogeneous manner throughout the film, with the most superficial layer of CuO observed to be poreless.

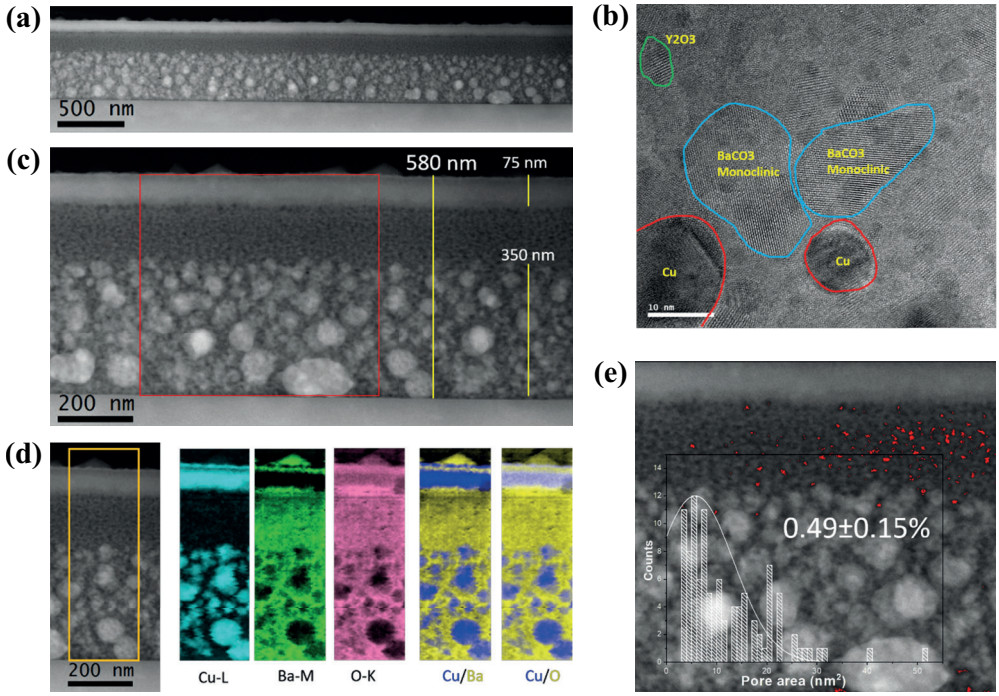


FIGURE 3.16: (a) Cross-sectional low-magnification STEM-HAADF image of a single layer film deriving from a solution with excess of MEA.(b) HR-TEM image proving the presence of metallic Cu and monoclinic $BaCO_3$. (c) Magnified STEM-HAADF image showing the thickness of the layer to be 580 ± 50 nm. (d) Elemental EELS maps of Cu-L edge, Ba-M edge, O-K edge, and composite EELS map of Cu (blue)-Ba (yellow), and Cu (blue)-O (yellow), confirming the metallic Cu nanoparticles. (e) Pore density analysis using ImageJ software from the red rectangular region in (c), where pores are coloured in red for quantification. Histograms of pore area are used to calculate the average pore sizes.

To precisely comprehend the phase formation, quenches at successive temperatures were performed during the thermal treatment, with XRD patterns from the resulting films presented in Fig. 3.17. The chosen temperatures to quench the films were 260 ºC, 300 ºC, 400 ºC and 500 ºC, in accordance with the major mass losses and individual precursor decomposition evinced from a previous study [52] and from the analysis reported in Chapter 2. The expected temperature for $Cu(Prop)_2$ complete decomposition in film is approximately 250ºC; nevertheless, before reaching 400 ºC there is an amorphous nature of the film showing no apparent formation of any crystalline phase ascribable to copper species. The straightforward deduction is, thus, that the decomposition of $Cu(Prop)_2$ does not coincide with its complete reduction to metallic Cu. The first crystallization occurs at 400 ºC, where the appearance of distinct peaks of Cu_2O are observed, indicating an initial reduction of Cu (II) to Cu (I).

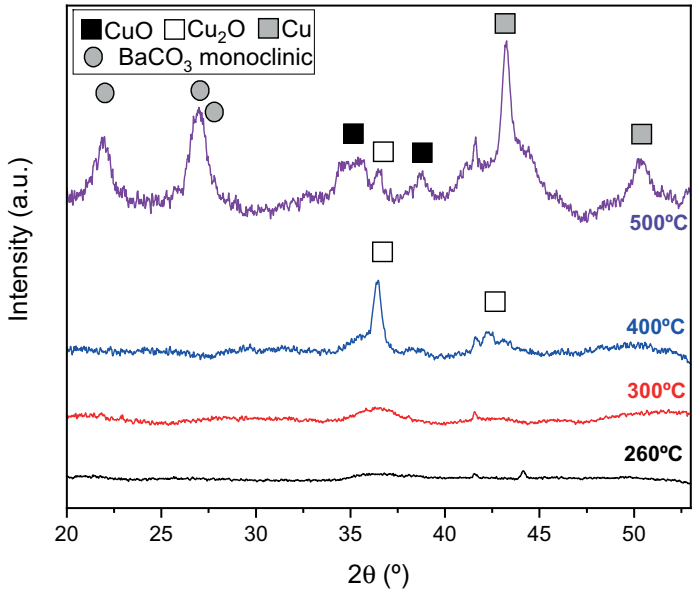


FIGURE 3.17: XRD analysis of films deriving from a solution with excess of MEA (1.75 M + 8%$_{v/v}$ MEA), quenched at various temperatures in order to fully understand the evolution of crystalline phases during the pyrolysis process.

The final quench performed at 500 ºC presents a minor part of the contribution from the copper precursor identifiable as CuO and Cu_2O, but the majority experienced a complete reduction to metallic Cu. Monoclinic $BaCO_3$ is also formed, with the intense peaks from this phase being the only result of $Ba(Prop)_2$ decomposition. The progression between the last two quenched films indicates that the reduction of Cu_2O to metallic Cu occurs at the final stage of the pyrolysis process. An explanation for the phase evolution observed during the pyrolysis process could be found in the microstructure that this film presents: the higher thickness and the extremely low porosity of the film may be causing a severely diminished gas transport. With the aim of favouring the hydrolysis and oxidation decomposition pathway of the metal-organic precursors, this specific thermal treatment is conducted in a flux of humid O_2, as explained in Chapter 2. The morphological and microstructural features of this particular film are believed to hinder the O_2 diffusion in the layer, and consequently hamper the elimination of CO_2 and CO from the lower part of the film: this temperature range coincides with the final decomposition of $Ba(Prop)_2$ and $Y(Prop)_3$, thus originating a strong release of CO_2 and CO. The amine additive, here in large excess compared to the films presented in the previous subsection, is additionally responsible for CO_2 and CO generation. If the elimination of CO is hindered due to the unfavourable microstructure, a strongly reducing atmosphere may be locally created, which would be responsible for the reduction of CuO to Cu_2O and, finally, to

metallic Cu, through the following reaction:

$$3CuO + 2CO \rightarrow Cu + Cu_2O + 2CO_2 \tag{3.1}$$

This is additionally proven by the presence of CuO solely in proximity of the surface, the area most exposed to the oxygen flux, whereas the large grains of metallic Cu (the most reduced phase) are found to be segregated in the most internal part of the film, close to the interface with the substrate, where the CO_2 and CO out-diffusion is supposedly most complicated. According to Fick's law of diffusion [157], the diffusion rate of a substance across a unit area, such as a film, is proportional to the concentration gradient. When increasing importantly the thickness of a film, the capability of the gas, in this case CO_2 and CO, to migrate towards the film surface and hence be eliminated is significantly reduced. In the specific case of MEA excess, the elevated thickness and the minimal porosity are both contributing to the impeded gas transport, resulting in the formation of undesired nanocrystalline phases.
Finally, the analysis of several STEM-HAADF images through the software ImageJ enabled an estimation of the pore density; additionally, the histograms displayed in Fig. 3.11,3.13, 3.14, and 3.16, allowed for calculations of the average pore sizes. A comparison of the pore density analysis and of the average pore size is displayed in Fig. 3.18, with various trends worth noting. Firstly, it is evident how, upon addition of MEA for the same (3:7) composition, a significant reduction of the pore density occurs, with the same result showed also for the average pore size. A film obtained from a solution with no additive has a porosity of $6.4 \pm 0.5\%$, whereas it is reduced to $1 \pm 0.2\%$ when optimal MEA quantity is added, and decreased to half this value when an excess of additive is employed. Let us now consider different compositions: there is a distinct decrease of porosity, again reflected in the average pore size, with the increase of the amount of copper in the composition, starting at almost 2% for the stoichiometric (2:3) composition and lowering to $0.8 \pm 0.2\%$ for the most Cu-rich (4:11) composition. However, in all cases of optimized additive content, the distribution of the pores is seen to be homogeneous, whereas when increasing the amount of MEA above the optimum value, this is found to be extremely inhomogeneous, displaying almost no porosity in the most superficial CuO layer and minimal pores presence in the most internal part of the film, along with small average sizes. Regardless of the case of MEA excess, which is undoubtedly the worst-case scenario, the low degree of porosity ranging between 1 and 2 % for the films deriving from optimized solutions is anticipated to be of great benefit to the epitaxial growth of YBCO through TLAG. This demonstrates the significant advantage of employing an additive, specifically MEA. Remarkable difference can be noted with the films in which no MEA is added in the solution, and the extreme case of films prepared through TFA-MOD [126], which present elevated porosity values of up to $15 \pm 1\%$.

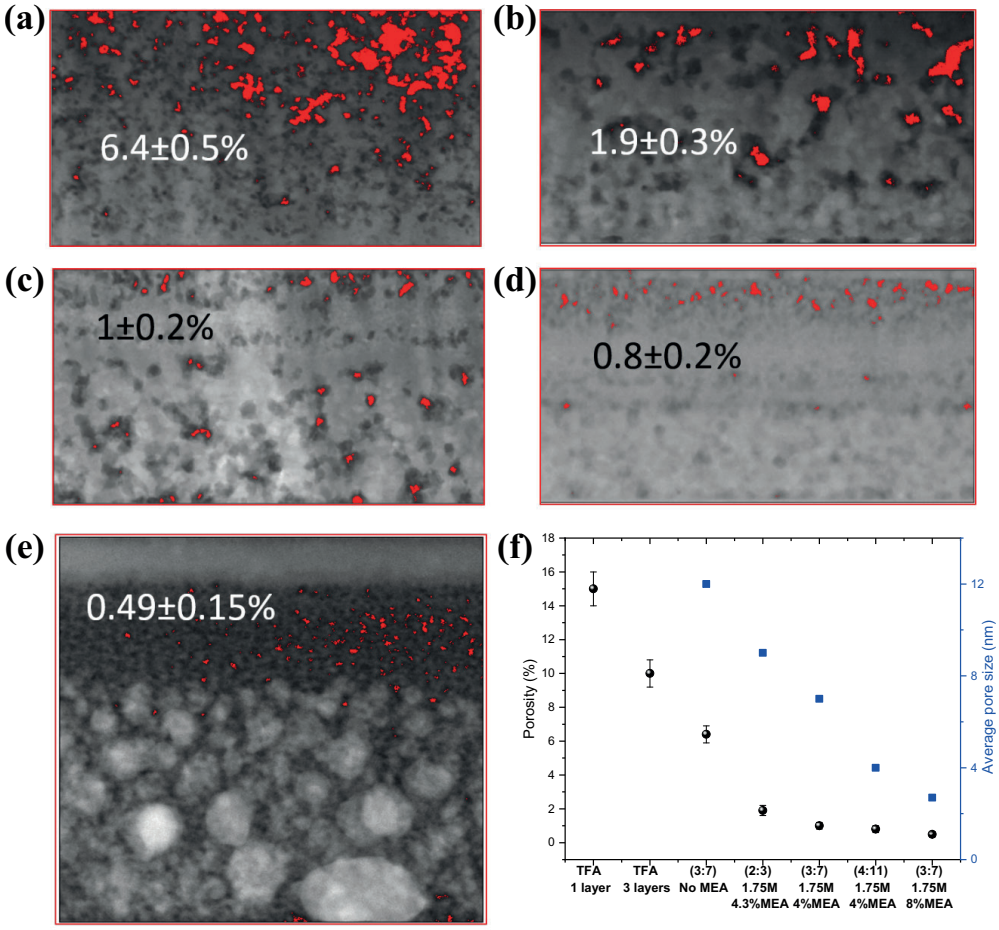


FIGURE 3.18: Estimation of pore density using image analysis of STEM-HAADF via ImageJ software for the cases of (a) no MEA, (3:7) composition, (b) 1.75 M + 4.3%$_{v/v}$ MEA, (2:3) composition, (c) 1.75 M + 4%$_{v/v}$ MEA, (3:7) composition (d) 1.75 M + 4.1%$_{v/v}$ MEA, (4:11) composition, and (e) 1.75 M + 8%$_{v/v}$ MEA, (3:7) composition, where pores are colored in red for quantification. (f) A plot showing the trend of porosity and average pore sizes for the samples in a-e.

Thus, the novel metal propionate-based solution developed and described in this chapter has enabled for an optimal degree of porosity to be obtained, which together with the homogeneous distribution of the three desired nanocrystalline precursor phases, set a promising basis for the epitaxial growth of these films through TLAG.

3.2.5 Rheology and chemical analysis of optimized solution

After having explored the effects of introducing an amine additive and how important the use of an optimal quantity is to the outcome of the nanocrystalline precursor films, it is of utmost importance to fully understand the role of MEA in the precursor solution. Hence, this subsection will be dedicated to a comprehensive analysis of the rheological and chemical properties of the novel precursor solution, with the aim of disentangling the correlation between the presence of the amine and the advantageous chemical and physical features of the solution. Let us consider, firstly, the rheological properties. Fig. 3.19 displays several viscosity measurements obtained from (2:3) and (3:7) composition solutions of 1 M and 1.75 M concentrations (total sum of metals), with increasing contents of MEA. The evident trend for both compositions and in both of the tested concentrations associates directly an increase of the MEA content in solution with an increase of the viscosity. Being both of those factors linked to the resulting thickness of the nanocrystalline precursor films, this tendency seems to avail the beneficial use of MEA to the purpose of increasing the final thickness. Nonetheless, as demonstrated in 3.2.4, a large excess of MEA is hindering the achievement of high-quality nanocrystalline films. Only a specific $\%_{v/v}$ MEA yields the desired features, thus compelling for a strict agreement between the rheological properties of the solution and the quality of the resulting films. Rheological properties of all solutions employed in this thesis, including solutions of different compositions and concentrations, are reported in Table C.1, Appendix C.

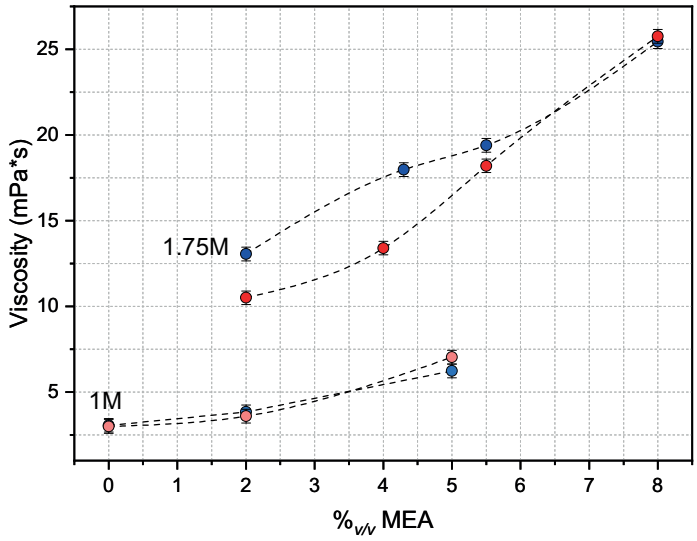


FIGURE 3.19: Viscosity measurements with varying quantity of MEA for solutions of (2:3) composition (shades of blue) and (3:7) composition (shades of red), with concentrations of 1 M and 1.75 M.

A further parameter which is considered important to control is the water content of the solutions. Several cases in CSD-related literature have shown that the water content in solution is strongly affecting the final epitaxy and quality of the YBCO film [158, 159], thus establishing a maximum threshold which ensures this parameter not to be altering the result: these are 1.5 wt% for full fluorine TFA-based solutions and 2 wt% for low fluorine TFA or fluorine-free solutions [51, 160]. For this reason, a continuous monitoring of the solution is necessary here, performed through the Karl-Fischer titration method [161].
Clearly, the novel class of solutions described in this thesis are inevitably subjected to Fischer esterification reaction, as a mixture in the ratio (1:1) of HProp and MeOH are used as solvents, producing H_2O as by-product of the reaction [162, 163]. When monitoring solutions with and without amine additive, an important difference is easily discernible, as shown in 3.20. The case of a solution without amine additive shows a rapid increase of the H_2Owt% over time, reaching the pre-established limit already by day 10 after its preparation. Conversely, despite starting from a higher H_2Owt% on day one, the solution which contains MEA in the optimized quantity displays a slower increase of the H_2Owt%, with a value close to the 2 wt% limit reached by day 28.

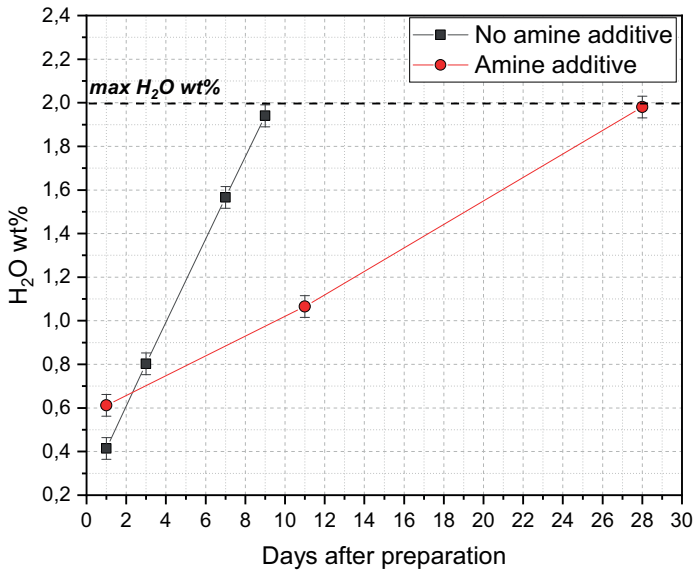


FIGURE 3.20: Evolution of H_2Owt% over time for (3:7) solutions with and without MEA, measured using Karl-Fischer titration method.

The evident difference in the tendency of H_2Owt% production in the two solutions can be ascribed to the presence of MEA as an additive. In fact, the mandatory first step of the Fischer esterification reaction is the protonation of the carbonyl group of the acid: the activation of the *C* atom of the carbonyl group is essential for the following nucleophilic attack performed by

the alcohol in order to form a tetrahedral intermediate which may then continue the renowned reaction mechanism (displayed in 3.21, for clarification) to form the ester and, as said, H_2O. When adding an amine to an acid, the deprotonation of the acid by the amine occurs, yielding a carboxylate, and preventing the first fundamental step of the reaction to take place; as a result, the whole reaction is impeded. As the optimized MEA quantity is certainly not close to be in stoichiometric ratio with the acid, being the latter in enormous excess, the reaction is only decelerated and not completely avoided. However, the addition of $4\%_{v/v}$ MEA is seen to raise the needed time to reach the maximum limit by a factor 3. At this moment, the maximum H_2Owt% considered is taken as a reference from previous studies [51]. Nonetheless, an extensive analysis of solution ageing, including its effects on the various rheological properties, one of which being the increasing water content, will be carried out in 3.2.7, where it will be determined whether the characteristics of aged solutions are truly influencing the epitaxial nucleation and physical properties of the final YBCO film.

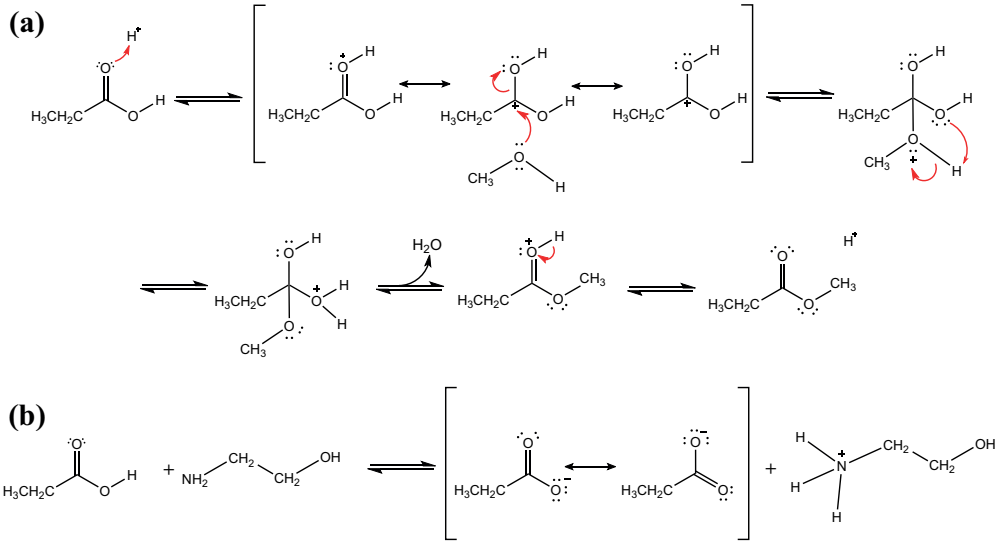


FIGURE 3.21: (a) Fischer esterification reaction mechanism for HProp and MeOH. Addition of an amine to an acid (in this case MEA to HProp) reacts through the mechanism in (b).

A comprehensive NMR analysis on the mixture of solvents was used to follow the evolution of the esterification reaction. Given the paramagnetic nature of copper (II) present in the precursor solution, this analysis had to be implemented solely on the solvents, disregarding the case of the ternary YBCO precursor solution. Nonetheless, it can be considered as an appropriate model for the case of the precursor solution: the esterification reaction is catalyzed by strong acids, high reaction temperatures or the presence of metals, given their renowned catalytic nature[164]. The analysis on the sole mixture of solvents is disregarding the latter factor, which may be the cause for a further acceleration of the esterification reaction rate.

Two solvent mixtures were prepared: one of HProp and MeOH, in a ratio (1:1), being this the solvent media for the solutions in which no amine additive is used, and the other of HProp and MeOH in the same ratio, with the addition of $4\%_{v/v}$, as in the case of optimized solutions. The NMR spectra were acquired immediately after preparation and, from the same solutions, stored as it would be done with precursor solutions, eight days from the preparation. A comparison between the spectra acquired on the different days is shown in Fig. 3.22 and 3.23, respectively, in which spectra of the solutions with MEA are displayed in dark red, while the ones from solutions without amine additive are represented in black. In the spectra of the as prepared solutions one can promptly acknowledge the main difference, as the peaks due to the methyl propionate (i.e. the ester formed from the esterification reaction between HProp and MeOH) are present in the mixture of solvents with no amine additive, whereas in the case with MEA none of the peaks due to this species are visible. This is suggesting that the esterification reaction is not initiated when the amine is added to the same solvent mixture, in accordance with the mechanisms proposed in Fig. 3.21. When the measurement on the same solutions is repeated eight days later, it can be noted that the peak of the ester has increased in the solution with no amine, and is now identified also in the solution with amine, though with an extremely low intensity. Through a simple correlation of the area of the peaks due to $-CH_3$ groups of the ester and of MeOH one can estimate the quantity of ester formed in each case. On day one, the solution without amine additive shows a 4% of ester respect to MeOH, and this quantity has been calculated to increase to 21% on day eight. Contrarily, the case in which MEA is present starts from a 0% on day one, as no peak from the ester is identified, and this value is raised to a mere 4% upon remeasurement on day eight. This conclusive data is corroborating the hypothesized mechanism and is proving that the production rate of H_2O due to Fischer esterification is strongly reduced in the cases where the amine is present in solution.

A further important feature to be examined is the reactivity of MEA in the chemical system considered in this thesis, with the aim of explaining the reason for which higher concentrations are enabled through the addition of this amine species, directly linked to the increase of solubility of $Cu(Prop)_2$. The initial hypothesis, considering the rapid dissolution of this precursor in solutions in which MEA is added, was the possible formation of a complex between the copper center and the MEA, aiding its solubility and stabilization in solution, resulting in high concentration solutions of endured stability. To confirm this assumption, Electron Paramagnetic Resonance (EPR) was used, as it can provide useful insight into the in-plane coordination, distinguishing various interactions between the electrons of the metal center, here Cu (II), and those of its surrounding nuclei. As for the previous techniques described, EPR spectra were acquired for two types of solutions. As the case under study is the possible complexation between $Cu(Prop)_2$ and the amine, this precursor is dissolved in one case in a mixture of HProp and MeOH in a (1:1) ratio to reach a total concentration of 1 M, whereas in the second case in the same mixture of solvents and total concentration with the addition of MEA in a (Cu:MEA)

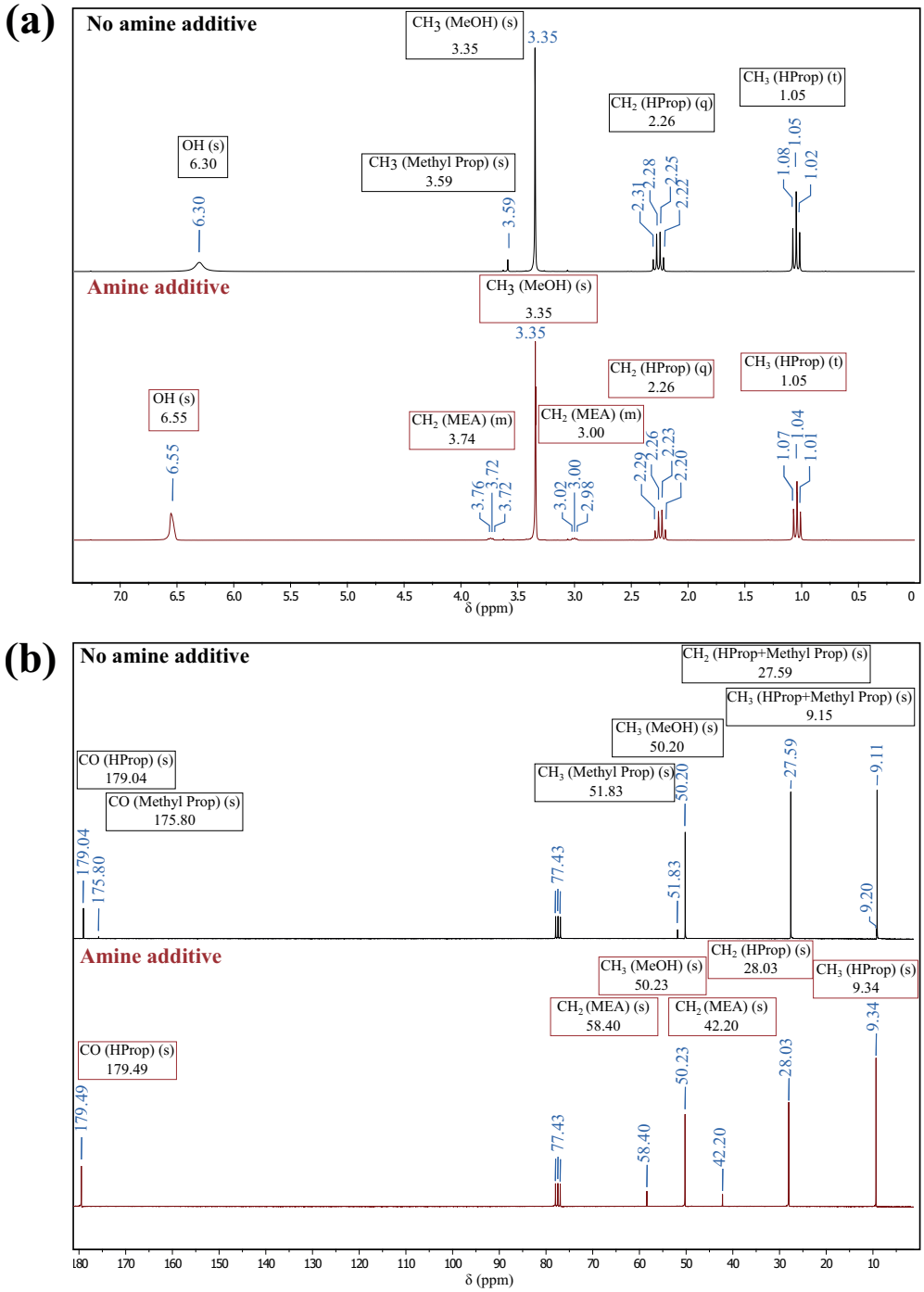


FIGURE 3.22: Comparison between the NMR spectra of mixture of HProp and MeOH in a 1:1 ratio (black) and the same mixture of solvents with the addition 4%$_{v/v}$ MEA (red) measured as prepared. Shown in (a) and (b) are, respectively, the comparisons between the ^{1}H spectra and ^{1}3C spectra.

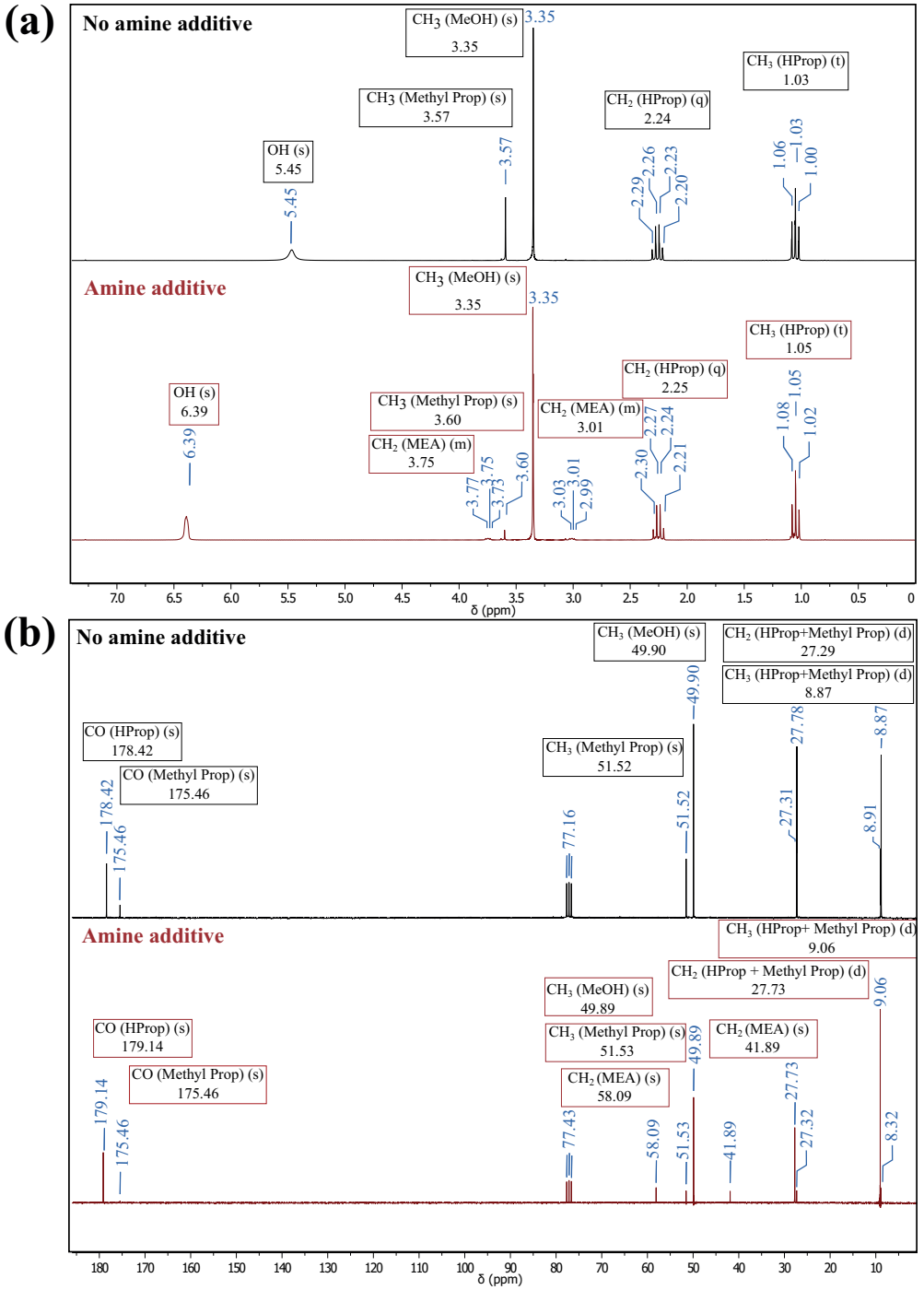


FIGURE 3.23: Comparison between the NMR spectra of mixture of HProp and MeOH in a 1:1 ratio (black) and the same mixture of solvents with the addition 4%$_{v/v}$ MEA (red) measured 8 days from preparation. Shown in (a) and (b) are, respectively, the comparisons between the ^{1}H spectra and ^{1}3C spectra.

molar ratio of (1:0.61). This is the molar ratio corresponding to an optimized solution of (3:7) composition. Hence, the single difference between the two analyzed solutions is the use of MEA. As observed in the EPR spectra in Fig. 3.24, the solution without amine additive yields a classic EPR spectrum expected from a Cu^{2+} octahedral elongated complex, with calculated values of $g_{II} = 2.358$ and $A_{II} = 141$ $cm^{-1}x10^{-4}$. A different situation is obtained for the solution in which MEA is employed, where the identification of two species contributing to the EPR spectra is suggested from the clear splitting of the bands. The calculation of the g_{II} and A_{II} factors give values of $g_{II} = 2.355$ and $A_{II} = 141.9$ $cm^{-1}x10^{-4}$ for the first species, comparable to the case with no MEA, and $g_{II} = 2.307$ and $A_{II} = 141.1$ $cm^{-1}x10^{-4}$ for the second species.

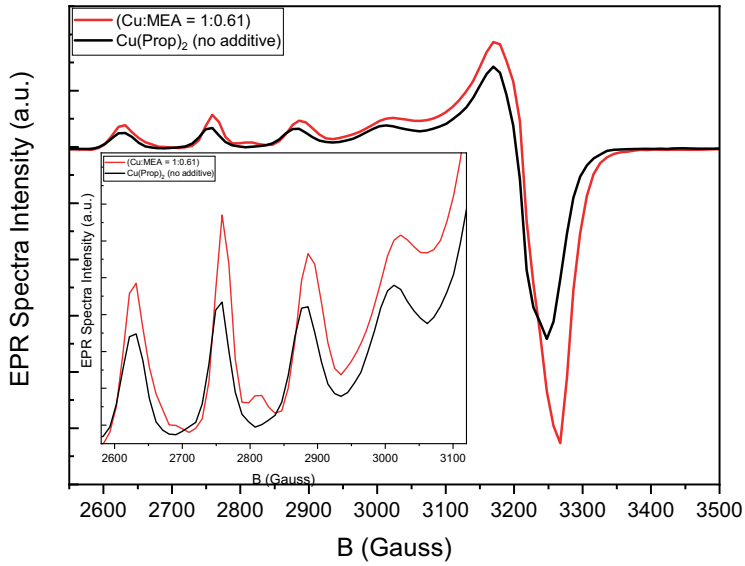


FIGURE 3.24: EPR spectra of a mixture of HProp and MeOH (1:1) and $Cu(Prop)_2$ without MEA (black), and with MEA (red). Inset shows the magnification of the main bands.

An adaptation of data from [165–167] allows for the construction of a graph that correlates these two values to a specific coordination arrangement for various copper complexes, shown in Fig. 3.25 for the solutions studied here. In accordance with the analysis of the EPR spectra, the in-plane coordination of the copper in the solution without amine additive is due to exclusively four oxygen atoms, only deriving from the $-(COO)^-$ groups of the propionate ligands, given the absence of any nitrogen in this solution. Conversely, the solution with MEA displays, as previously suggested by the EPR spectrum, the existence of two species simultaneously in solution: the first shows an in-plane coordination of the copper atom to four oxygen atoms, as in the previous case, and the second one in which the copper atom is subjected to an interaction with two oxygen atoms and two nitrogen atoms. This is the undeniable demonstration of the

formation of a complex with the MEA in the optimized solution. Given its possible coordination through both terminal groups, MEA is presumably forming a bidentally chelated complex with the copper center[2]. The contemporaneous existence of two species is thought to be due to the non-stoichiometric ratio between the amine and the $Cu(Prop)_2$. In fact, the (Cu:MEA) molar ratio required for a complete complexation of the copper precursor contained in a (3:7) composition solution would be (1:2), resulting in a $12.8\%_{v/v}$ MEA (when a 1.75 M solution is considered). Nonetheless, the analysis of the EPR spectrum relative to a solution with MEA excess (respect to the optimised quantity) is also displaying the presence of two species (C.2). It revealed values of $g_{II} = 2.358$ and $A_{II} = 145.3\ cm^{-1}x10^{-4}$ for the first species, again comparable to the case with no MEA, and $g_{II} = 2.277$ and $A_{II} = 166.9\ cm^{-1}x10^{-4}$ for the second species. The large discrepancy in the hyperfine coupling constant A_{II} presented by this solution may be due to a different orientation of the ligands relative to the equatorial plane, despite the coordination arrangement is still considered relative to two nitrogen atoms and two oxygen atoms. Density functional theory (DFT) models may be used to calculate the contribution of each ligand to the A_{II}, given the additivity relationship for equatorial ligands [168], and thus shed light on the difference in the coordination scenarios ascribed to varying $\%_{v/v}$ MEA. However, this analysis was out of the scope of the present work.

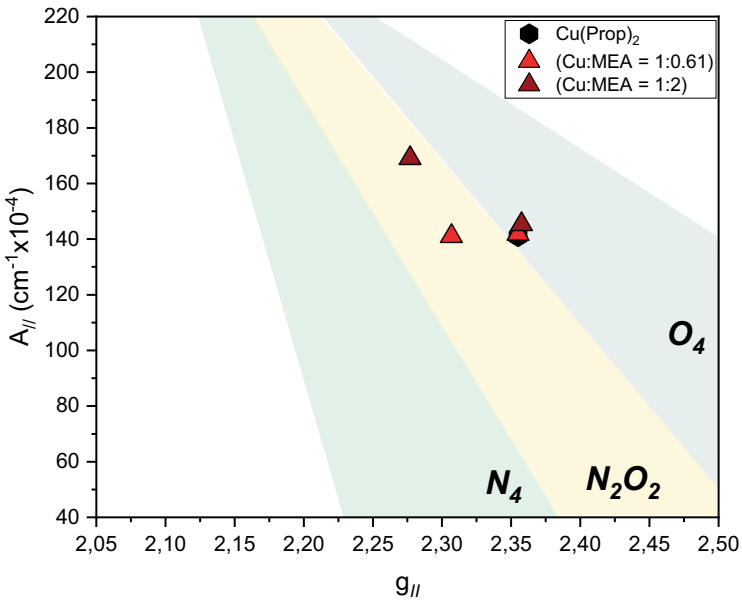


FIGURE 3.25: Correlation of the values of A_{II} and g_{II} to determine possible ranges corresponding to coordination arrangements for various copper complexes resulting from the solutions with and without amine additive. Adapted from [165–167].

[2]Trials to isolate and identify such complex have been carried out without success due to its elevated stability in the studied solution. Nonetheless, the hypothesis of the Cu-MEA complex being bidentate chelating is feasible.

The coordination arrangement exhibited by solutions in which MEA is added is, thus, a possible reason for the higher solubility of the copper precursor which enables for higher concentrations to be achieved, given the enhanced stability of this copper-amine complex respect to the sole $Cu(Prop)_2$. Although efforts have been made to crystallize said complex, only suitable single crystals of $Cu(Prop)_2$ could be obtained, further proof of the extremely stable nature of the Cu-MEA complex in the ternary solution, avoiding its precipitation and ensuring endured stability of the solutions.

3.2.6 Thermal analysis of optimized solution

Finally, to achieve a complete understanding of the novel fluorine-free solutions obtained through the optimization process described in section 3.2, a comprehensive thermogravimetric analysis coupled to infra-red spectroscopy (TG-FTIR) has been carried out. This technique allows to register the mass loss due to the decomposition of the components of the precursor solutions, here present as films deposited through drop coating, besides the *in-situ* analysis of the vibrational modes of the evolved volatiles, all while the films are subjected to the same heat treatment as in the pyrolysis process. Hence, this technique has been fundamental to acquire valuable information on which factors are determining the result of the thermal treatment and their correlation to the chemical and microstructural homogeneity of the nanocrystalline precursor films.

A detailed analysis of the individual metal propionates both in powder and in film is object of Chapter 2, and the thermal behaviour of the ternary solution is seen to concord with the decomposition mechanisms and temperatures of the individual metal-organic precursors. As described in Experimental Methodologies in Appendix A, the pyrolysis process is conducted in a humid O_2 atmosphere to favour the hydrolysis and oxidation decomposition mechanism (eq. 2.2) reaching a maximum temperature of 500 ºC. In the following analysis, the films will be subjected to the same atmosphere and thermal profile, and four kinds of solutions will be considered: two solutions without amine additive with a final concentration of 1 M in sum of metals, respectively of (2:3) and (3:7) compositions, and two optimized solutions in which MEA is employed, one for the (2:3) composition (1.75 M + 4.3$\%_{v/v}$ MEA) and one for the (3:7) composition (1.75 M + 4$\%_{v/v}$ MEA). For correct comparison between the cases with and without MEA, similar initial masses were used for the selected films, as it is renowned that different thickness values, meaning a high difference in the initial mass, may influence the decomposition temperatures due to variations in the evolution of the gases [52]. The scope of this section is not to unravel the decomposition mechanisms of ternary solutions, as this has been object of previous studies both for fluorinated [169, 170] and fluorine-free systems [52, 91]. As for the previous sections, the aim is, here, to comprehend the role of the amine additive and its effect on the decomposition profile of the ternary solution. The four solutions follow the hydrolysis and oxidation mechanism for the decomposition of the metal-organic precursors, as

expected in this atmosphere: the first mass loss is, evidently, only due to solvent evaporation, as corroborated by the sole evolution of HProp at temperatures below 150 ºC (no MeOH is present as the deposited films are placed on a heating plate at 70 ºC for 5 minutes before the thermal treatment). The metal organic precursor responsible for the first mass loss is $Cu(Prop)_2$, as its decomposition starts as early as 170 ºC and is seen to end before 250 ºC. This is, in general, the temperature range corresponding to the promotion of crack formation [91]. In this region an important mass loss may be observed, equivalent to 29% and 37% for the solutions without amine additive ((2:3) and (3:7) compositions, respectively) and 21% for the (2:3) composition with MEA and 33% for the (3:7) composition with MEA (Fig. 3.27 and Fig. 3.26). The considerable reduction of the mass loss when MEA is included in the solution compared to the case of no amine additive, where the major gas evolution is evidently concentrated in this temperature range, is implying that films from solutions with MEA are more robust against crack formation up to the films thickness studied. Amine-free solutions have displayed a disposition to generate cracks when the thickness is increased [126]. It is meaningful to remind that the formation of cracks is a mechanism of strain-release due to film shrinkage with thermal increase and an excessive volume of gas eliminated from the film at a given moment during the decomposition process. Nonetheless, thermogravimetric studies on the thermal stability of MEA in similar conditions revealed this compound to exhibit volitilization prior to effective decomposition, occurring in one mass loss around 150 ºC in specimens of MEA alone [171], contrarily to the elevated thermal stability of the widely employed TEA which decomposes at temperatures above 300 ºC. Nonetheless, given the complexation of MEA with copper from the $Cu(Prop)_2$ in this system, it is possible that decomposition of the linked amine ligands is here occurring in the same temperature range as the propionate ligands from this specific precursor. The enormous excess of the latter impedes the registration of a sufficient signal from the evolved volatiles deriving from the amine decomposition, complicating the identification of the temperature at which MEA is eliminated from the film. Nonetheless, the results reported in this section are a clear evidence of the extraordinary viscoelastic properties MEA conveys to the films, when used in the optimal quantity. The detected volatiles for the decomposition of $Cu(Prop)_2$ are deriving initially from the hydrolysis mechanism [143], thus only a signal from HProp is acquired, then replaced by the oxidation mechanism when higher temperatures are reached (220-300 ºC), generating mostly acetaldehyde, CO_2 and HProp from the beginning of the overlapping decomposition of $Ba(Prop)_2$ and $Y(Prop)_3$. For temperatures above 300 ºC and up to the final temperature of 500 ºC, the gas evolution may be ascribed to the oxidation of the intermediate decomposition products of yttrium and barium precursors, yttrium oxycarbonate ($Y_2O_2CO_3$) and barium oxalate (BaC_2O_4), which finally form the corresponding oxide and carbonate, respectively, through elimination of CO_2 [125, 142]. The mass of the final residues is in agreement with the values expected for dried precursor solutions, being 45% and 43% expected for, respectively, (2:3) and (3:7) composition solutions with optimized quantity of MEA, and in the cases without amine additive, 49% for the (2:3) composition and 47% for

the (3:7) composition. If comparing (2:3) and (3:7) compositions, another fact worth noting is the discrepancy between the initial mass loss due to solvent evaporation (below 160 ºC), being larger for the solution of (2:3) composition: given the higher viscosity of this solution, it will be probably hindering a complete drying of the deposited film, resulting in the HProp

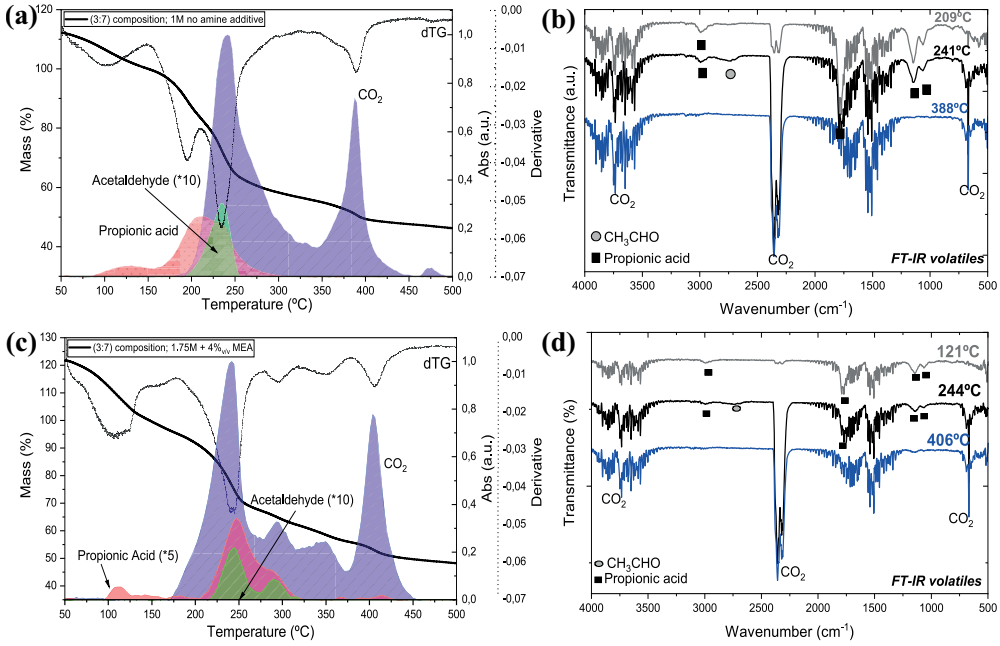


FIGURE 3.26: TG-FTIR analysis of (3:7) composition solutions (a)-(b) 1 M without amine additive and (c)-(d) 1.75 M + 4%$_{v/v}$ MEA measured in a humid O_2 flow. The TG and dTG profiles are displayed in (a) and (c), respectively, together with the gas evolution during the heat treatment. The FT-IR spectra corresponding to the temperatures where the mass losses are greatest is shown in (b) for the solution without MEA and (d) for the one with MEA.

evaporation to overlap with the same volatile deriving from the first hydrolysis path of the Cu(Prop)$_2$ decomposition. Moreover, the distinct (Ba:Cu) molar ratio in the two compositions considered in this thermogravimetric analysis are seen to affect the amount of CO_2 evolved: the (2:3) composition presents higher intensity peaks due to elimination of CO_2 in the temperature region ascribed to the decomposition of Ba(Prop)$_2$ (300-500 ºC), presumably as this composition is, in comparison, more rich in barium. Fig. 3.28 exhibits a comparison between the thermal behaviour of solutions with MEA and without any amine additive for both compositions and summarizes the important difference between the two cases. The solutions with amine additive are seen to follow a less abrupt mass loss and a general smoother decomposition profile respect to the ones in which no MEA is added.

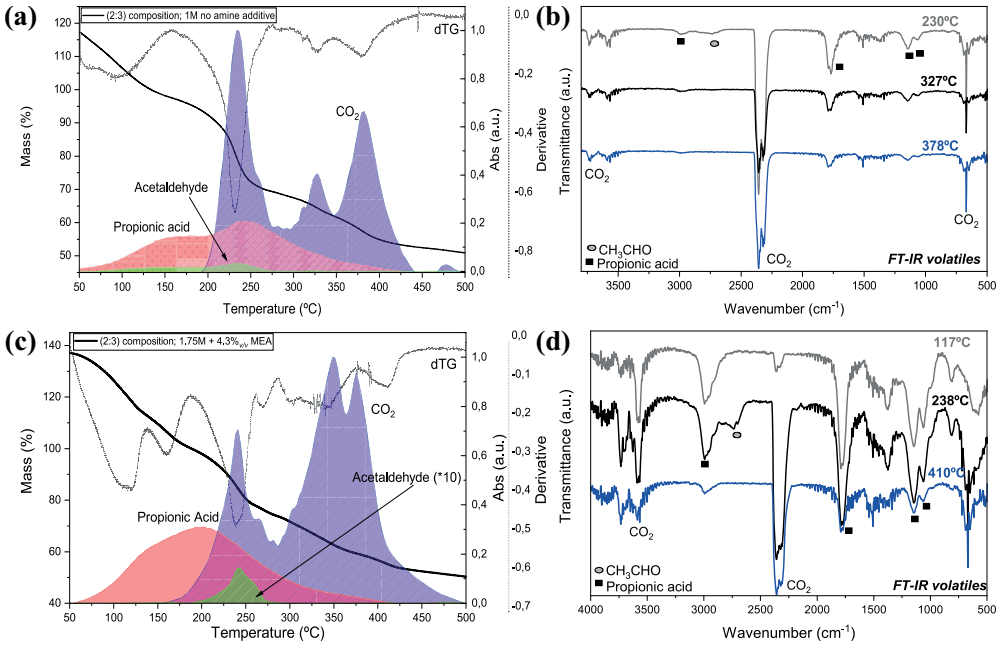


FIGURE 3.27: TG-FTIR analysis of (2:3) composition solutions (a)-(b) 1 M without amine additive and (c)-(d) 1.75 M + 4.3%$_{v/v}$ MEA measured in a humid O_2 flow. The TG and dTG profiles are displayed in (a) and (c), respectively, together with the gas evolution during the heat treatment. The FT-IR spectra corresponding to the temperatures where the mass losses are greatest is shown in (b) for the solution without MEA and (d) for the one with MEA.

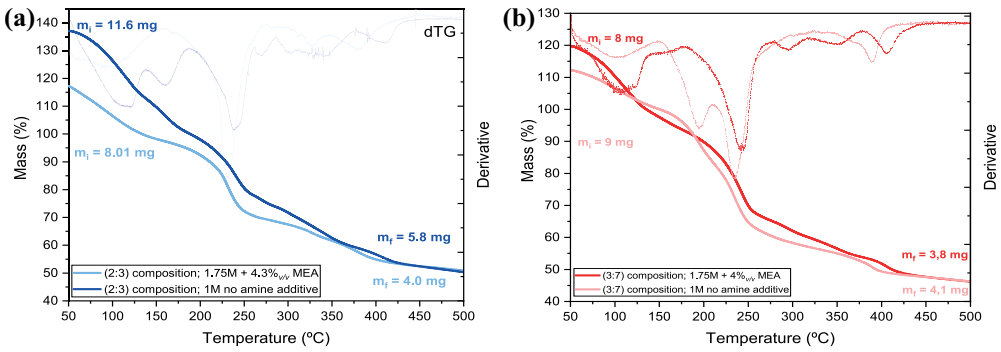


FIGURE 3.28: Comparison of TG and dTG of solutions with and without amine additive for (2:3) composition in (a) and for (3:7) composition in (b). Initial and final masses (m_i and m_f respectively) are displayed for a correct comparison of the samples, given the difference in concentration of the solutions.

The correlation between the characteristics of the TG curve and the robustness of the optimized solution towards avoiding formation of cracks on films of high thickness are suggesting

that the MEA is able to take part in the elaborate metal-organic skeleton in such manner to completely release strain originating from the decomposition of the propionate ligands of the metal propionate precursors. This is yet another evidence of the advantageous nature of MEA in the chemical solutions employed for TLAG-CSD.

3.2.7 Effect of different storage methodologies on solution ageing

Initially, the storage methodology chosen for the optimized solutions came from the knowledge acquired during previous studies [53, 55]: the idea of exposing the solution to air was the major concern, therefore vial caps with a silicon septum were employed. While this storage methodology was previously found to be satisfactory, during this thesis several problems have been encountered. A thorough study and a modification of the storage methodology for YBCO precursor solutions will be described in this subsection in detail. The following analysis has been conducted solely on (3:7) composition films, although the optimal storage methodology was then applied to all solutions with same results.

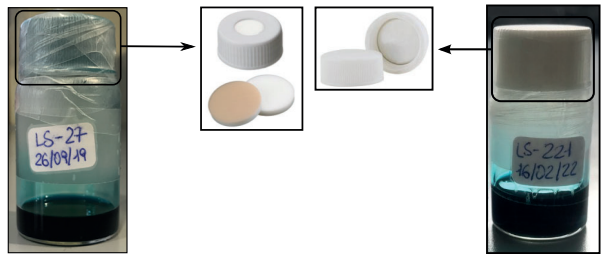


FIGURE 3.29: Types of vials and sealing caps employed during this thesis. On the left, a YBCO precursor solution stored in a vial with septum cap whereas a solution stored in a vial with a screw cap is shown on the right. The central insets present the appearance of each type of cap as an example.

Fig. 3.29 displays the two types of storage possibilities employed: the vials with septum caps (left) were used at the beginning of this study, later on superseded by the vials with screw caps (right) due to various reasons. Firstly, the septum and the cap are not sealed together, resulting in an untight storage. The septum was adopted to be able to take out an aliquot of solution without having to open the vial and exposing it to air (again, considering the hygroscopic nature of one of the solvents). However, when puncturing the septum, tears may occur resulting in pieces of the silicon septum falling in the solution, as shown in Fig. 3.30, where a large piece of septum is visible inside the vial. When solutions in which this problem was encountered were used for spin-coating deposition, the result led to films with numerous defects and ultimately, to the inclusion of Si particles in the films, confirmed by EDX (Fig. 3.30). As explained in 3.2.1, the homogeneous nature of the nanocrystalline precursor films is mandatory in order to obtain high performance films: such major particle inclusions determine impediment critical

current percolation, lowering importantly the physical properties of the films, as demonstrated in Fig. 3.31[3].

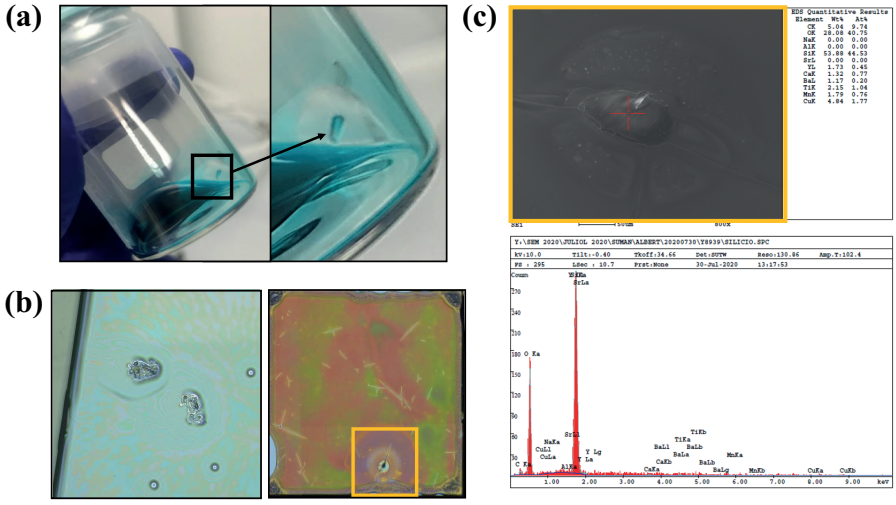


FIGURE 3.30: (a) Solution in which a piece of the septum is transferred inside the vial after puncturing it. (b) Deposition of such solution and example of the result after the pyrolysis process. (c) EDX of the large particle found in the nanocrystalline film of (b), indicated by an ochre square. Major contribution is identified as Si, as expected.

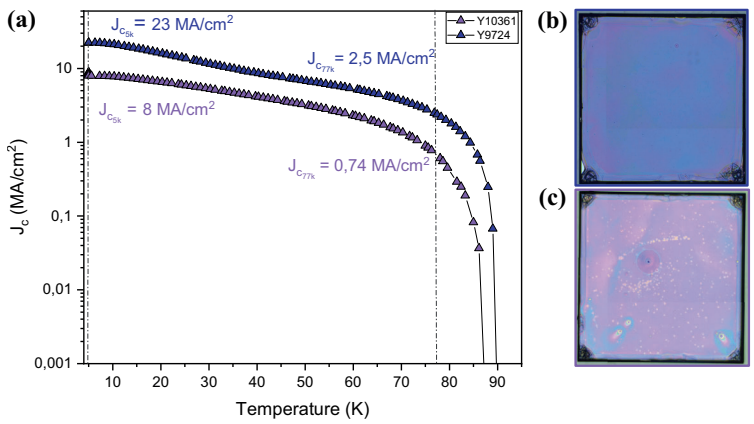


FIGURE 3.31: (a) Comparison of critical current density (J_c) curves with temperature for two grown films of (3:7) composition, coming from a fully homogeneous nanocrystalline precursor film (blue triangles, OM image in (b)) and one with Si inclusions due to septum pieces in solution (purple triangles, OM image in (c)). The clear decrease of J_c is ascribable to problems with current percolation due to the presence of the included particles.

[3] A standard profile result of optimization of TLAG processing parameters is used to compare the effect of defects on the physical properties. More information will be provided in detail in section 4.3.1 of the following Chapter.

When using screw cap vials, evidently, this will never occur as no puncturing of the septum is involved. Of course, a screw cap means the solution would be exposed to air during aliquot extractions. To avoid this, the sealed vial with the solution would be placed below an inverted funnel connected to a flow of Ar gas. After flowing several minutes, the area below the funnel is supposedly inert, making it safe to open the vial without risking the solution to come into contact with air. Besides the septum inclusion in solutions and films, the septum caps were found to be causing a second, meaningful complication. As previously stated, the septa and the caps are not produced with a sealing between the two parts: this, together with the fact that the septa were punctured numerous times for aliquot extractions, was inevitably favouring the evaporation of part of the solvents in the solution, causing its further concentration with time and, finally its precipitation. This effect could be completely avoided when the screw caps were introduced, as it is clearly demonstrated in Fig. 3.32. The level of the solution was marked following the last aliquot extraction and after a month, it is visible how the solution level has lowered for the case of the septum cap, whereas it was maintained identical when a screw cap is employed.

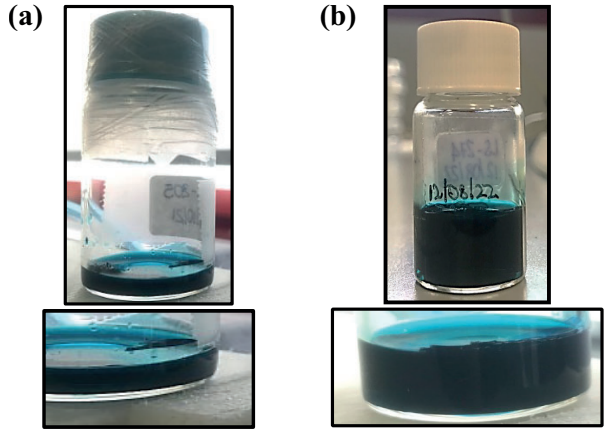


FIGURE 3.32: Solution level one month after the extraction of the last aliquot for solutions stored in a vial with (a) septum cap or (b) screw cap.

For solutions stored with the septum caps, the evaporation of the solvent and the following increase of the concentration of the solution has detrimental consequences: the solution stability is limited to a maximum of two months and the viscosity was demonstrated to vary significantly in the short time range of only a week. Solutions which were stored in vials with screw caps were found to be stable for over a year, and viscosity of several solutions was measured with time. Fig. 3.33 shows the comparison between these two cases. The volume of the solution (shown as label, in the case of the vials with screw cap) has an impact on the viscosity the solution exhibits. This may be due to the fact that even the slightest change (i.e. evaporation) on a reduced volume has an augmented effect: the solutions which display highest values

of viscosity are, indeed, the ones of lowest volume. In fact, a solution of 1 mL measured on day 66 shows the same viscosity as one measured on day 160 with a total volume of 3 mL. Thus, to maximize the stability of the solution, working with larger volumes is desirable to avoid such effects.

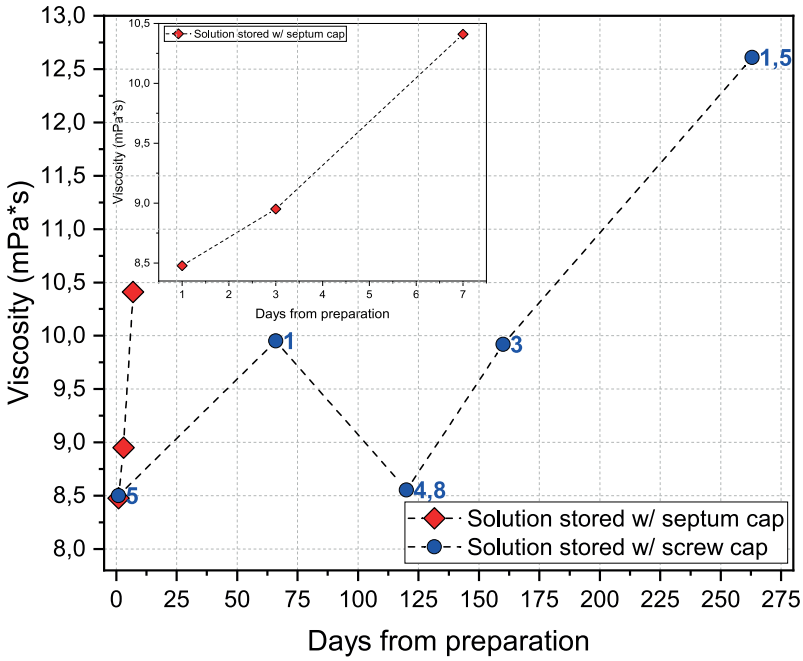


FIGURE 3.33: Viscosity of solutions stored through the two different methods. Solutions stored in vials with septum caps (red rhombi) are measured during one week, and the inset is showing the evolution. Solutions stored in vials with screw caps (blue circles) are measured up to 263 days, and the label to each measurement is indicating the total volume of the solution remaining in the vial when the measurement was performed.

The final, fundamental storage consequence that was investigated was the effect of the aged solutions on the outcome of the films after the thermal process of pyrolysis for both cases. Worth noting is the pre-established limit of H_2Owt% in previous studies [51, 91], which ensured the desired features of the nanocrystalline precursor films to be obtained. It was believed to be the increased H_2Owt% to drastically worsen the microstructural characteristics of the nanocrystalline film, thus setting the value of 2wt% as maximum threshold. Fig. 3.34 displays the measurement of H_2Owt% over time for both storage cases. It can be noted that the initial increasing trend is similar, demonstrating no significant variation due to choice of storage method. In correspondence to the day of water content measurements, all solutions were deposited through spin coating and the microstructure of the resulting nanocrystalline films investigated by means of XRD.

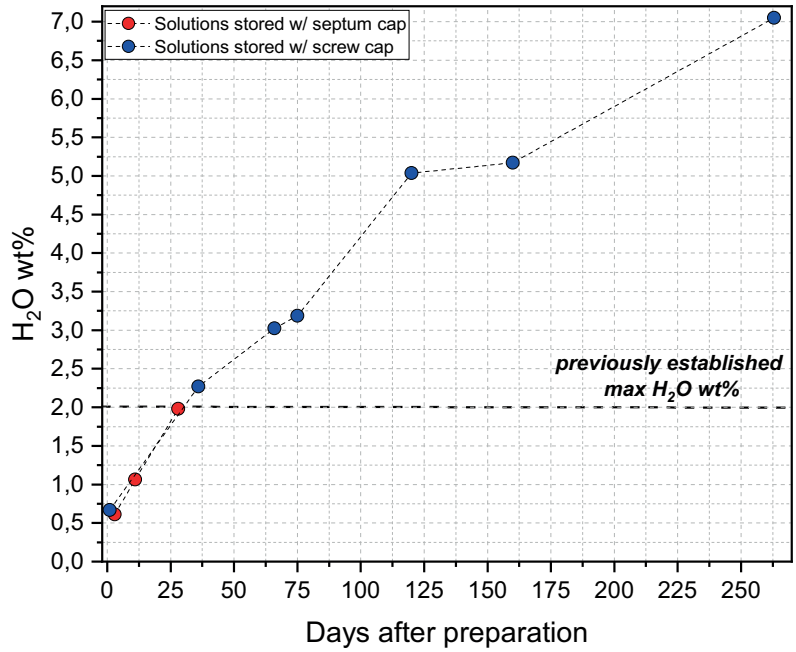


FIGURE 3.34: Water content in solutions stored in vials with septum cap (red circles) and with screw cap (blue circles).

Let us first consider the case of vials with septum cap. As said, solutions stored through this method are stable for up to two months. However, one can clearly observe from the OM images of the nanocrystalline precursor films in Fig. 3.35, that the morphological quality is worsening with the aging of the solution. Similarly, the microstructure is displaying a comparable trend: a 21-days-old solution favours the formation of detrimental, undesired crystalline phases. This implies the stability is not in accordance with the shelf-life of the solutions stored in this way, possibly being an unfavourable effect if the final objective is the application of these solutions in industrial framework where prolonged lifetime is advantageous cost-wise. When, instead, solutions stored in vials with screw caps are deposited and nanocrystalline precursor films are prepared from solutions up to 263 days old, one may immediately notice how the homogeneity of these is maintained (3.36). The desired nanocrystalline phases are displayed in all the films prepared through these solutions, despite the last one being more than 250 days old. Additionally, the increasing amount of water in solution seems to have no direct consequence on the achievement of the desired crystalline phases, in contrast to the aforementioned previous studies[51, 91]. This is once more stressing the crucial importance a correct storage methodology has on the success rate of the process, especially interesting for the establishment of CSD-based superconductors in industries.

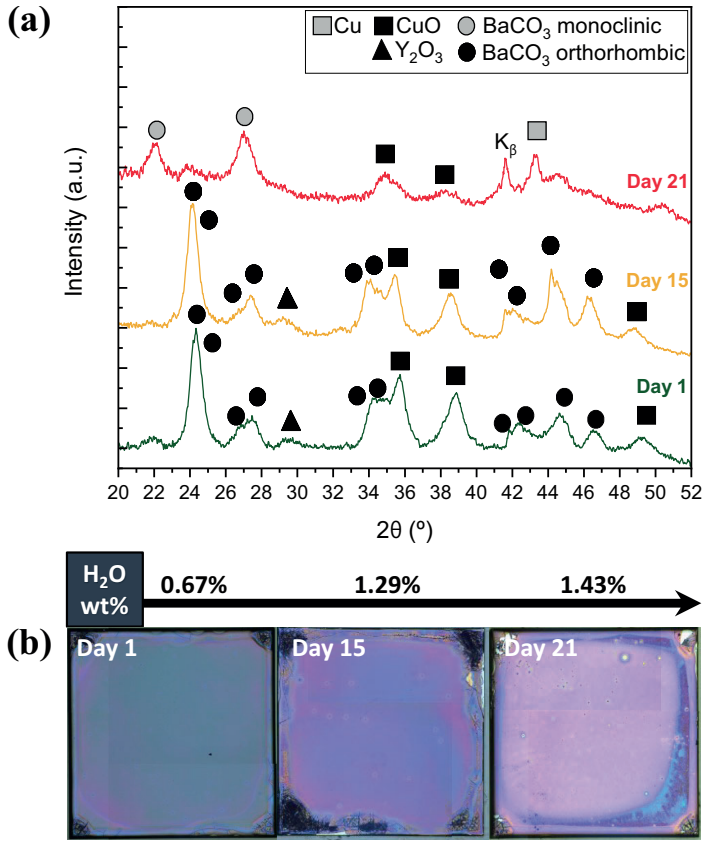


FIGURE 3.35: (a) XRD data acquired from nanocrystalline precursor films deriving from solutions 1, 15 and 21 days after their preparation, stored in vials with septum caps. (b) OM images of the nanocrystalline films in (a), with water content of the corresponding solution shown in the top part.

Finally, the physical properties of grown YBCO films deriving from aged solutions stored in vials with screw caps have been measured to identify a possible effect of the elevated water content on the epitaxy of the film. As shown in Fig. 3.37, the YBCO films display similar values of critical current density (J_c) and critical temperature (T_c), independently of the H_2Owt% the solution contains. This suggests there is no direct implication of the water content of the solution on the epitaxy of the final superconducting film. The initial desirable characteristics of the nanocrystalline precursor film are not to be overlooked, and any implication of the solution rheology that may lead to variations in the microstructure must be avoided.

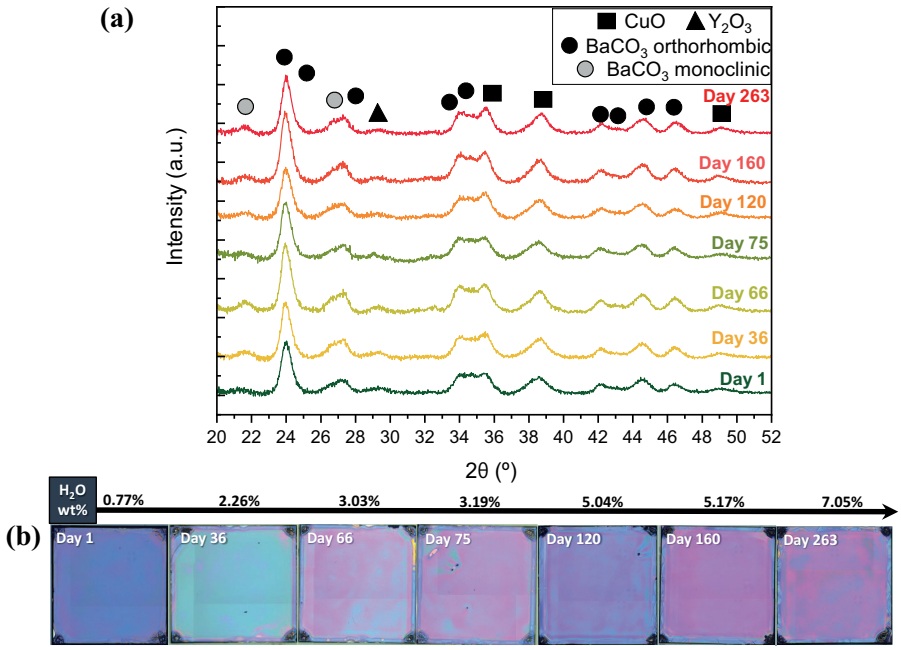


FIGURE 3.36: (a) XRD patterns from nanocrystalline films deposited with various solutions up to 263 days after their preparation, stored in vials with screw caps. (b) OM images of the same nanocrystalline precursor films displayed in (a), with water content of the corresponding solution shown in the top part.

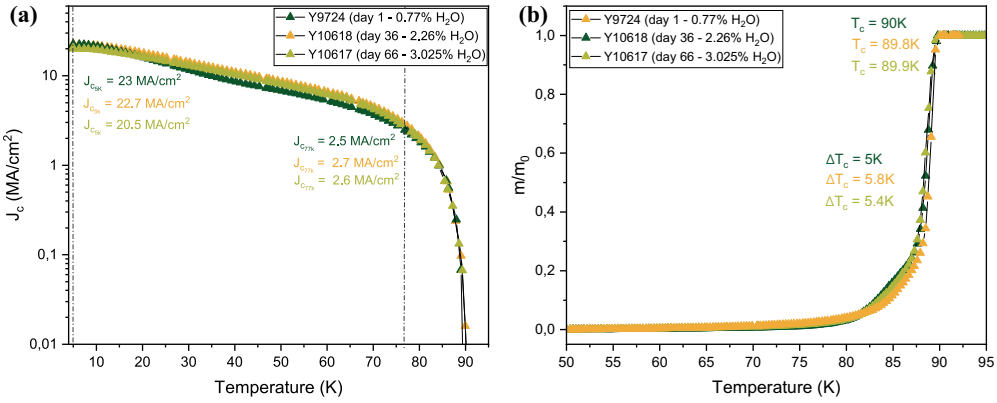


FIGURE 3.37: (a) Critical current density (J_c) versus temperature and (b) critical temperature (T_c) curves for grown films prepared using solutions of 1, 36 and 66 days old, demonstrating the high reproducibility of the process despite the long time after solution preparation or H_2Owt%. Growth processing conditions derive from a thorough optimization process on (3:7) composition films which may be found in 4.3.1.

Undoubtedly, the extensive analysis of rheological and chemical properties, and of thermal

behaviour may lead to the conclusion that the use of MEA is greatly beneficial considering various aspects: the promotion of the dissolution of metal propionate precursors, yielding possibility of increased concentration, the enhancement of the stability of the species in solution, and the improvement of the mechanical resistance of the films towards cracking phenomena. Moreover, the final study presented here depicts how the correct storage methodology may significantly prolong the shelf-life of the solutions, resulting in stability of over a year and demonstrating an unchanged outcome of the pyrolysis process on films deriving from solutions of over 250 days old. Accordingly, the great potential of the application of this kind of solutions for the preparation of YBCO superconducting films in the industrial framework is unquestionable.

3.3 Variation of the RE for the preparation of REBCO precursor solutions

As introduced in Chapter 1, the widespread interest developed in recent years for different REBCO systems originates from the variation of the irreversibility line for each RE perovskite, which leads to a plethora of achievable applications. When Sm or Gd are used as substitutes for Y, a wider range of magnetic field applications are possible due to their intrinsically elevated irreversibility line, resulting in higher critical temperature (T_c) values compared to YBCO. The characteristic effect of enhanced flux pinning phenomena are consequently increasing the possible critical current density (J_c) values [120, 172–174]. Contrarily, the use of Yb is significantly interesting when considering the possible reduction of processing temperatures towards the implementation of industrial methods with higher energetic efficiency. The YbBCO optimal nucleation conditions are found at reduced processing temperatures compared to YBCO, again due to an intrinsic difference in the irreversibility line presented from this system [127, 175]. Moreover, in the specific case of the growth of REBCO films through the TLAG-CSD approach described in this thesis, a variation of the RE will imply its different solubility in the transient liquid, and consequently different supersaturation conditions, possibly resulting in tunable growth rate. In this section, the optimized solution for the case of YBCO, which has proven to yield optimal nanocrystalline precursor films for TLAG, will be adapted to a variation of the RE. The possible effects on the rheology of the solutions or on the microstructure of the nanocrystalline precursor films will be investigated.

3.3.1 Analysis of REBCO precursor solutions rheological properties

Following the same preparation procedure explained in detail in Appendix C.1, optimized for the case of the YBCO precursor solution, REBCO precursor solutions could be obtained for the cases of RE = Sm, Gd, and Yb. Subsequent to corroborating the high purity of the RE propionates of Sm, Gd and Yb and their thermal compatibility with TLAG heat treatments (Chapter

2), the use of the different RE precursors entailed no difficulty to the successful preparation of such REBCO precursor solutions. The entire analysis was conducted on (3:7) composition solutions only, disregarding any change in stoichiometry to avoid additional effects due to this parameter.

Rheological properties of the REBCO precursor solutions considered in this section are displayed in the following Table 3.2. One can promptly notice how similar the values of viscosity are for all the solutions considered, showing no direct impact of the change of RE propionate precursor on this specific rheological property. However, discrepant values are found for the contact angle that these solutions exhibit: YBCO and GdBCO precursor solutions are $19.4° \pm 0.1°$ and $19.1° \pm 0.1°$, respectively, in contrast to the lower values of $12.3° \pm 0.1°$ for SmBCO and $13.2° \pm 0.1°$ for YbBCO. This is suggesting a different wettability of these solutions on the substrates of choice, which may eventually lead to differences in their deposition and, possibly, the final thickness of the resulting films. An additional slight variation is encountered in the initial water content values: as explained in 3.2.5, this parameter is, in our system, a combination of the H_2O produced due to Fischer esterification reaction and the coordinated H_2O from the metal propionate precursors. As $Ba(Prop)_2$ and $Cu(Prop)_2$ are identical in the four solutions considered here, the main contribution to this value will be due to the H_2O contained in each RE propionate. From the TGA experiments performed on the powders in Chapter 2, the Gd precursor is known to display less H_2O compared to the rest, thus explaining the difference in the H_2Owt% in this solution.

REBCO precursor solution	Concentration (M)	Water content on day of preparation (wt%)	Viscosity (mPa·s)	Contact Angle (°)
YBCO	1.5M + 3.4%$_{v/v}$ MEA	0.65 ± 0.06	8.68 ± 0.05	19.4 ± 0.1
SmBCO	1.5M + 3.4%$_{v/v}$ MEA	0.66 ± 0.06	8.96 ± 0.05	12.3 ± 0.1
GdBCO	1.5M + 3.4%$_{v/v}$ MEA	0.43 ± 0.06	8.94 ± 0.05	19.1± 0.1
YbBCO	1.5M + 3.4%$_{v/v}$ MEA	0.60 ± 0.06	8.66 ± 0.05	13.2 ± 0.1

TABLE 3.2: Rheological properties of REBCO precursor solutions, showing the values of an optimized YBCO precursor solution as reference. Water content, viscosity and contact angle reported here are measured on the day of the preparation of the solution to confirm reproducibility of the rheological properties and of the measurements.

The evolution of the latter parameter over the first month after the preparation of each solution has been monitored through Karl Fischer titration method and is displayed in Fig. 3.38. Apart from the aforementioned differences in the initial value, one may observe the general trends to be similar. By normalizing to the value of H_2Owt% on day one, the individual effect of the RE may be assessed. Y, Sm and Yb solutions show resembling behaviour, with the

case of the solution with Yb displaying the slowest rate of increase. For what concerns the Gd solution, instead, it presents the highest rate of H_2O production, possibly due to a major catalytic effect of this particular cation for Fischer esterification.

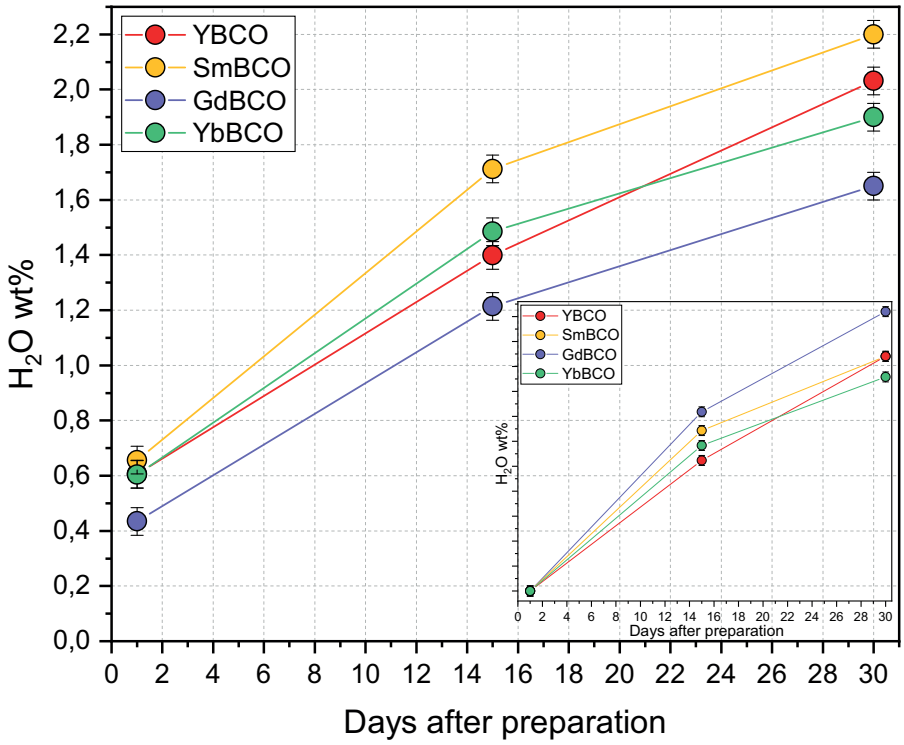


FIGURE 3.38: Evolution of H_2O wt% with time over the first month after solution preparation. Inset: same curves normalized to the value of the first measurement (day 1).

Overall, changing the RE from Y to Sm, Gd, or Yb seems to imply no significant impact or variation to the optimized solution rheology, as all the examined properties are maintained in acceptable ranges for the desired application; nevertheless, possible effects on the nanocrystalline precursor films due to these minor differences will be considered later on in this section.

3.3.2 Thermal behaviour of REBCO precursor solutions

Prior to the deposition of the REBCO precursor solutions and the heat treatment to yield nanocrystalline films, a thorough thermal analysis on films deriving from these solutions was mandatory to confirm their decomposition pathway is compatible with the pyrolysis process. As previously performed on the optimized YBCO precursor solution (3.2.6), the three REBCO precursor solutions underwent TG experiments in a humid O_2 atmosphere to promote the hydrolysis and oxidation decomposition mechanism of the metal propionate precursors. A

comparison of all solutions is displayed in Fig. 3.39, with the YBCO case included as reference. As explained in Experimental Methodologies (Appendix A), the films for TG processes are deposited through drop coating: the higher mass presented by the YBCO solution may be due to a different volume employed during the deposition of this specific solution. However, it lies within a reasonable difference for its comparison with the other solutions, and no effects due to elevated thickness are observed, other than a larger, low-temperature mass loss

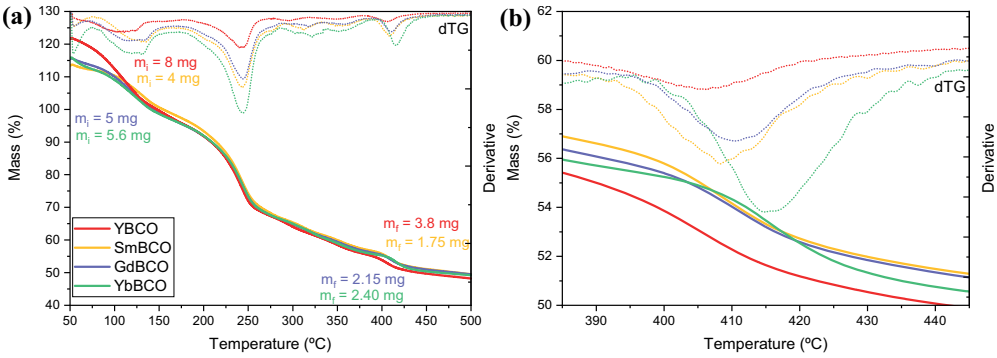


FIGURE 3.39: (a) Comparison of TG curves (solid lines) for solutions of YBCO (red), SmBCO (ochre), GdBCO (blue) and YbBCO (green), shown with the corresponding time derivative (dTG) curves (dotted lines, same colours). Initial and final masses of each solution are indicated, again in the corresponding colour. The final decomposition step corresponding to the conversion of the oxycarbonate to the sesquioxide is displayed in (b), enlarged.

given by solvent evaporation. The major decomposition processes occur in the same temperature ranges suggesting the REBCO precursor solutions are indeed exhibiting similar thermal behaviour as the optimized YBCO one. The analysis of the evolved gases through EGA-FTIR allows for the identification of the same species during the thermal treatment, and confirms the three REBCO precursor solutions are following the decomposition mechanism already identified for the YBCO solution, as Fig. 3.40 is corroborating. The first mass loss (below 150 ºC) is solely relative to solvent evaporation, as confirmed by the characteristic bands observed in the FTIR spectra of all examined solutions. Given the high viscosity of the optimized solutions, a complete drying of the solvent is not reached in the drying step before the TG experiment. At 240 ºC the first relevant precursor-originated mass loss is observed: the majority is ascribable to $Cu(Prop)_2$, which starts its decomposition already barely below 200 ºC. Nonetheless, it is overlapping with the beginning of the RE propionate decomposition, giving rise to the largest evolution of CO_2 of the whole thermal process, in addition to HProp and acetaldehyde. Considering the humid O_2 atmosphere, the decomposition is initially uniquely due to hydrolysis, releasing HProp, then immediately superseded by the oxidation of the propionate groups to form CuO and the respective RE oxycarbonate, at this stage. The following, reduced gas release found at 300 ºC, is corresponding to the inception of $Ba(Prop)_2$ oxidation: as explained

in Chapter 2, this precursor displays thermal stability up to temperatures ranging between

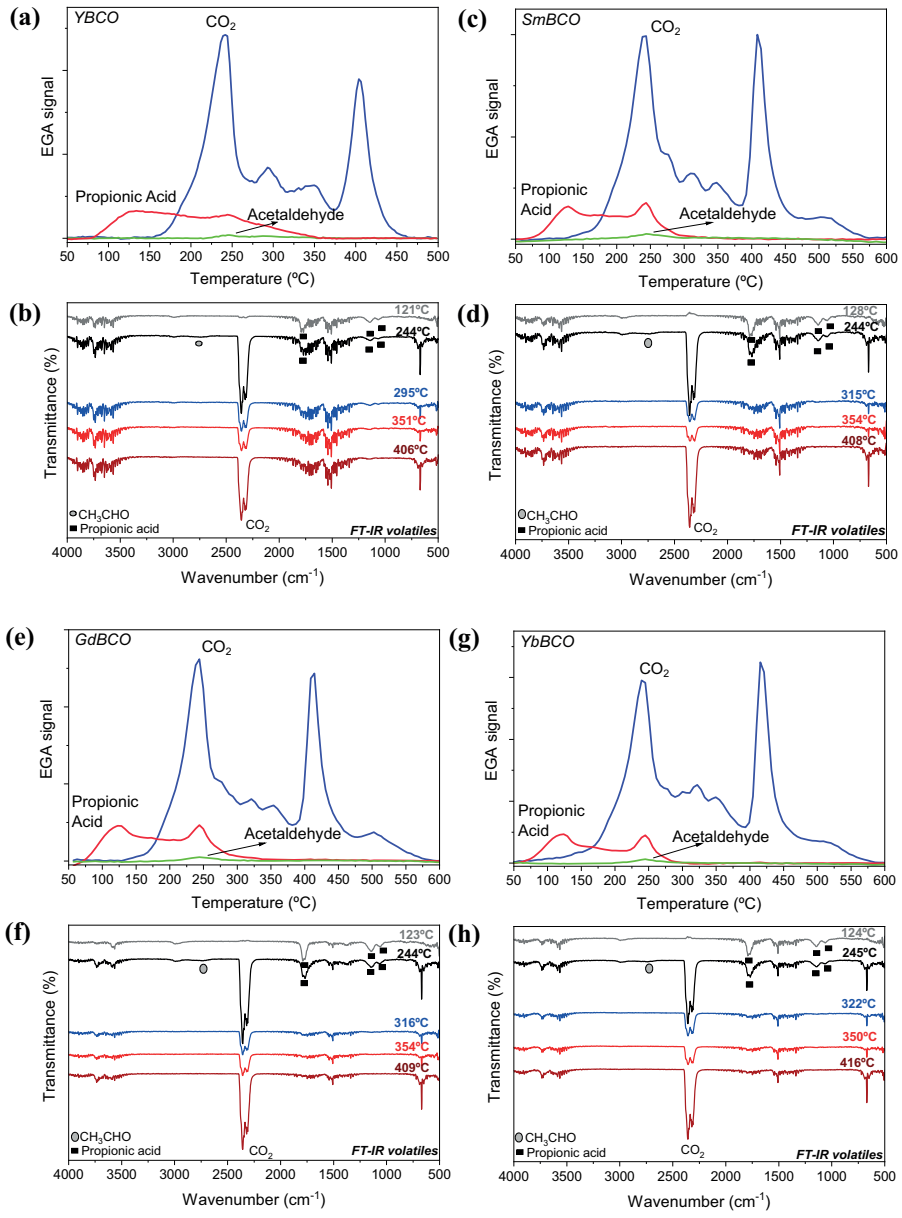


FIGURE 3.40: EGA-FTIR data of the gases released due to precursor decomposition during the thermal process, together with FTIR spectra corresponding to the most significant mass losses for (a)-(b) YBCO, (c)-(d) SmBCO, (e)-(f) GdBCO, and (g)-(h) YbBCO.

280 ºC and 300 ºC. In all the analyzed solutions, the last mass loss is related to a pronounced release of CO_2 found at 400 ºC approximately, and mainly due to two concomitant breakdown

processes: the intermediate species of barium oxalate (BaC_2O_4) decomposes to the final product $BaCO_3$ and the sesquioxide of each RE (RE_2O_3) is formed, both through an elimination of CO_2 (details reported in 2.3.2). Worth noting the temperature shift of this last mass loss in accordance with the different RE following the atomic number in the order Y<Sm<Gd<Yb, easily identified in the shift in the peak positions of the time derivative (dTG) curves, relative to the exact decomposition temperature. Given the similar film masses, this effect is presumably due to the varying thermal stability and temperature of formation of each RE_2O_3. The masses of the final residues of the TG experiment are in good agreement with the theoretical ones (45%) for the formation of the nanocrystalline precursor phases of RE_2O_3, $BaCO_3$ and CuO, final confirmation of the adequacy of these precursor solutions to the thermal processes employed in the TLAG-CSD process.

3.3.3 Microstructural analysis of nanocrystalline films

As previously stated, the formation of the nanocrystalline precursor phases of CuO, $BaCO_3$ and the respective RE_2O_3 is pivotal for the proper epitaxial growth of the REBCO film through TLAG. However, these must be present with reduced grain sizes and must be necessarily distributed homogeneously throughout the entire film. Similarly to the case of the YBCO precursor films, a comprehensive microstructural analysis conducted through XRD and TEM was carried out to validate that the characteristics presented by the films of the three REBCO systems considered are suitable for their application in the TLAG process.

The deposition via spin-coating of precursor solutions of SmBCO, GdBCO and YbBCO and the following heat treatment (pyrolysis) yielded homogeneous films in all cases, as displayed in the OM images in Fig. 3.41, where the YBCO case is shown as reference. The desired nanocrystalline precursor phases are obtained, as proven through the respective XRD data. In order to asses the nanoscale homogeneity in the microstructure of the films, various TEM techniques have been employed. All films display congruent features, with smooth surfaces and elevated thickness obtained through a double-fold deposition, between 630 ± 10 nm and 680 ± 10 nm (Fig. 3.42). Similarly to what observed in the case of multideposited precursor films of YBCO in 3.11, the preparation of two-layered films has no repercussion on the general homogeneity; although in this case no more than double-fold depositions have been tested, these characteristics suggest several more deposition processes are possible, paving the way towards the fabrication of thick REBCO films.

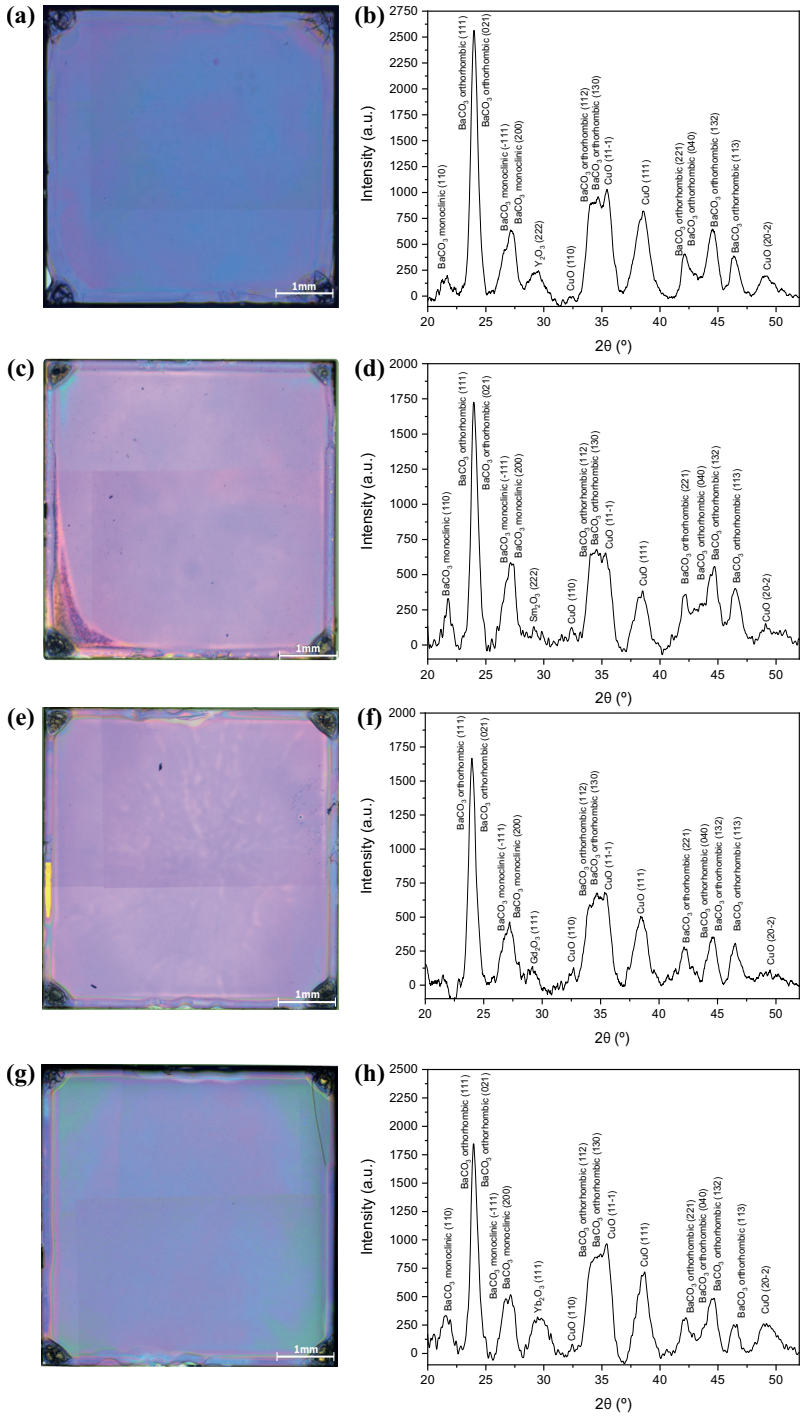


FIGURE 3.41: (a), (c), (e), (g) OM images of the nanocrystalline precursor films of YBCO, SmBCO, GdBCO and YbBCO, respectively. (b), (d), (f), (g) GIXRD measurements of the respective films in (a), (c), (e), and (g).

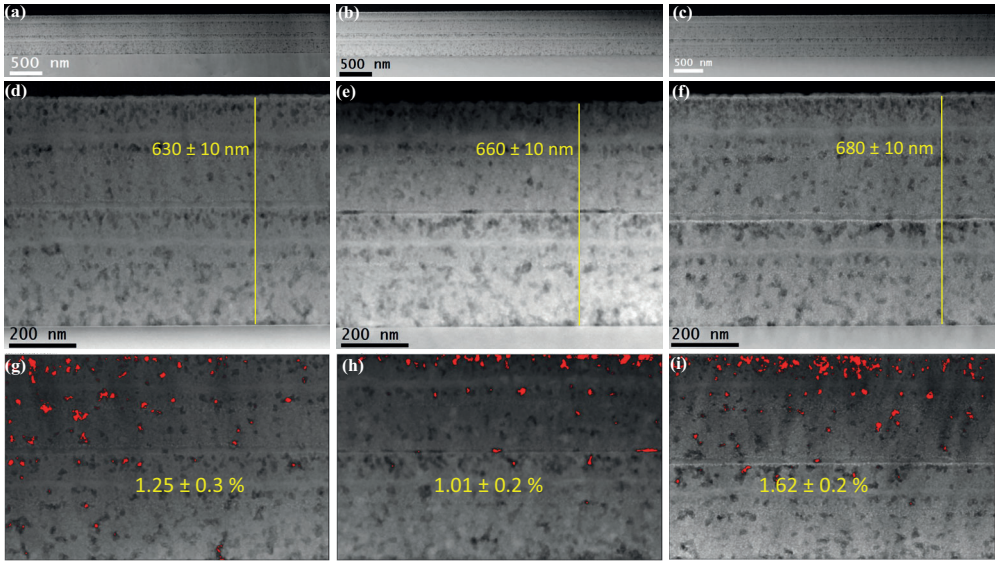


FIGURE 3.42: Cross-sectional low-magnification STEM-HAADF images of nanocrystalline precursor film deposited using a 1.5M + 3.4%$_{v/v}$ MEA solution for the cases of (a) SmBCO, (b) GdBCO and (c) YbBCO. Total thicknesses of the two-layered films are determined through magnified STEM-HAADF images shown in (d), (e), and (f) for the cases of SmBCO, GdBCO and YbBCO, respectively. (g)-(i) Pore density analysis through the use of the software ImageJ, with pores displayed in red for their quantification.

Porosity of the films has been determined through the analysis of the STEM-HAADF images, with the use of the software ImageJ. The estimations of pore density result in $1.23 \pm 0.3\%$ for SmBCO, $1.01 \pm 0.2\%$ for GdBCO, and $1.62 \pm 0.2\%$ for YbBCO, consistent to the value of $1 \pm 0.2\%$ found for two-layered YBCO precursor films, considered to be ideal for the TLAG process. Such reduced values of porosity are believed to importantly augment the reactivity of the nanocrystalline precursor phases towards the transient liquid formation. A second, crucial feature which was proven to enhance the growth rates is the presence of the nanocrystalline precursor phases in small sizes. As explained in Chapter 1, being TLAG a liquid-assisted process in which the rates of nucleation and growth of the final REBCO nuclei are governed by the RE_2O_3 solid nanoparticle dissolution in the transient liquid, when these are presenting a small grain size, the easiness for their dissolution will be incremented importantly. HR-TEM was the technique through which spatial distribution, crystalline state, and typical sizes of the nanocrystalline precursor phases could be established for films of the three REBCO systems considered in this thesis. Fig. 3.43 proves the identification of all the nanocrystalline phases relative to each REBCO system under study. Typical sizes for CuO nanoparticles vary between 10 and 30 nm. As shown in the XRD data in Fig. 3.41, $BaCO_3$ is present in both its orthorhombic and its monoclinic phase: here, it is noticeable how the orthorhombic phase is in

majority, presenting grain sizes in the range 15-40 nm, whereas the least common monoclinic phase shows grains of 10-15 nm typical diameters.

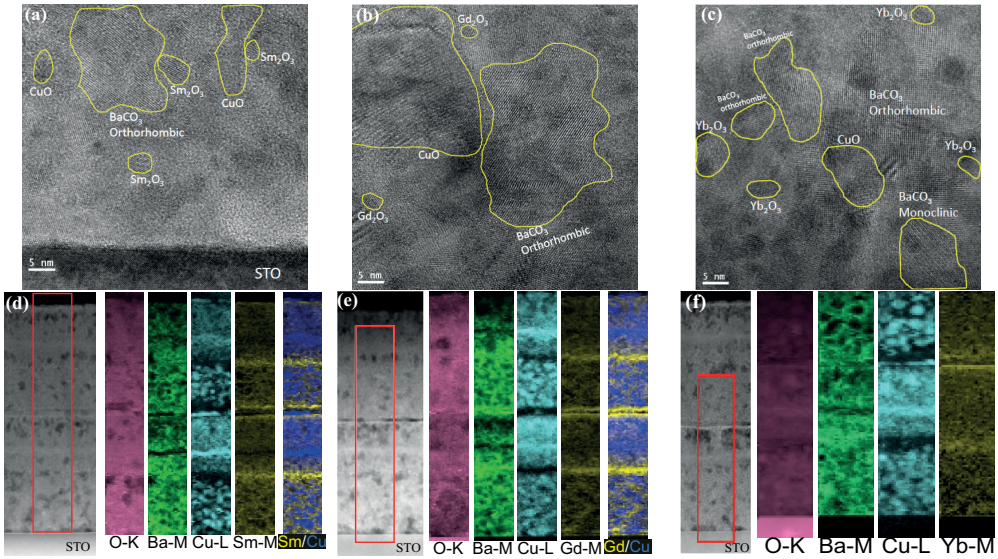


FIGURE 3.43: HR-TEM images collected from (a) SmBCO, (b) GdBCO, and (c) YbBCO precursor films: the individual sizes and the presence of all precursor phases in the same area are evidence of a homogeneous distribution of the chemical solutions employed. STEM-HAADF images of (d) SmBCO, (e) GdBCO, and (f) YbBCO two-layered films deriving from $1.5\text{M} + 3.4\%_{v/v}$ MEA solution. Elemental EELS maps of O-K edge (pink), Ba-M edge (light green), Cu-L edge (light blue), RE (Sm-M, Gd-M, and Yb-M) edge (yellow) and composite EELS map of Cu (blue) and RE (yellow), from red rectangular regions in (d), (e) and (f).

Ultimately, the RE oxides have extremely reduced diameters, being Sm_2O_3 of 3-7 nm, Gd_2O_3 of 3-5 nm, and Yb_2O_3 of 5-6 nm. These characteristic nanoparticle sizes are in good agreement with the aforementioned preference for enabling fast reactivity in the TLAG process. Additionally, employing EELS, the acquisition of elemental maps for $CuL_{2,3}$ edge, $BaM_{4,5}$ edge, OK edge and RE (Sm-M, Gd-M, and Yb-M) edge was possible, which evinced the uniform distribution of the phases, final proof of the high homogeneous nature of these films. Despite small segregations of the RE_2O_3 of only 15 nm of maximum thickness are observed, these are not seen to hinder the distribution of the phases uniformly also in the rest of the film.

The overall outcome of the pyrolysis process regarding both macroscopical and nanoscale homogeneity of the films described in this section corroborates their suitability for the following TLAG process to prepare epitaxial films of each of the REBCO systems. The results concerning the epitaxial growth of films of varying RE will be discussed in Chapter 4, specifically in 4.5.

3.4 Exploring amine additives as feasible alternatives for YBCO precursor solutions

The final section of this Chapter will be devoted to answering the following question: are different amines other than MEA compatible with our system and how do their chemical properties affect the solution and the resulting nanocrystalline films? Besides the search for the possible introduction of a new amine additive which might lead to a precursor solution with varying rheological properties, the focus of this investigation was additionally set on disentangling two fundamental processes in solution formulation: firstly, the overcoming of difficulties due to chemical and rheological properties (such as dissolution and stabilization of the metal-organic precursors) different from the second one, the enhancement of the mechanical and viscoelastic features of the films during the pyrolysis thermal treatment.
Initially, as explained in 3.2, a careful selection of the additive led to the exclusion of various possible amine compounds due to strict restrictions on several parameters which are crucial to obtain the desired favourable outcome. In the work described in this section, an assortment of amines of various nature were selected, each with distinct chemical features which were thought to possibly aid the achievement of the final goal: YBCO precursor solutions which yield thick, homogeneous nanocrystalline precursor films. Following the reason at the basis of the introduction of MEA in the solution, the central objective is the possibility of reaching even higher thickness than the ones described in 3.2.3, opening new paths towards the thickness enhancement for future industrial applications of TLAG-CSD.
It must be noted that, as for the case of REBCO precursor solutions, this entire study was conducted solely on solutions of (3:7) composition, with no change in the choice of solvents or the ratio of the mixture, and performing no modification of the thermal profile of the pyrolysis process. All these parameters were maintained constant to avoid additional information which, at this moment, was not of interest, being the only focus the effect of each new amine additive involved. It is, however, anticipated that every one of these parameters may be varied in a future continuation of this study to further improve the results and, thus, move towards the applicability of a plethora of additives for this specific solution system.

3.4.1 Understanding complexation scenarios and their effect on the nanocrystalline films

Among the various possible compounds the amine family may offer, a first, general distinction must be made, as displayed in the following scheme in Fig. 3.44, between alkyl amines and aromatic amines. As several amines from these two groups have been tested, giving a simple definition of each may be relevant at this moment.
Alkyl amines are all of those amines in which the substituent groups bonded to the *-N* atom

are of aliphatic nature. Differently, **aromatic amines** are those organic compounds which have a benzene ring bonded to the *-N* atom. This may occur in such a way in which the *-N* atom

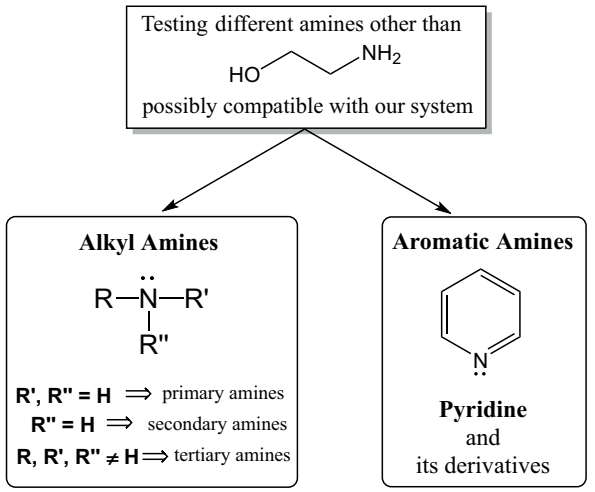


FIGURE 3.44: Schematic representation of the types of amines inside this large family of compounds.

is bonded to a *-C* of the six-membered aromatic ring (i.e. aniline) or, as in the case of pyridine, having the *-N* atom substituting one of the *-C* atoms of the aromatic ring. These two families of compounds consist in a vast number of possible amines which may serve for the purpose proposed here. However, as this study was intended as a preliminary screening of the behaviour of various amines, relating it to their chemical structure and reactivity, a limited selection was mandatory. Several points were considered, as for the initial choice of MEA, as requirements for the amine additive:

- the eventual formation of a complex with $Cu(Prop)_2$ to aid its dissolution aiming for higher concentration of the solutions and, thus, higher thickness of the nanocrystalline precursor films;
- compatibility with the thermal profile of the pyrolysis process, with its full decomposition to be reached before the end of the process;
- it must be a constituent of the film in a way to maintain the elevated thickness and, at the same time, avoid cracking through dissipation of the strain generated by the evolution of volatiles;
- it must favour the hydrolysis and oxidation decomposition mechanism of the metal propionate precursors, thus avoid the formation of undesired crystalline phases, such as

metallic Cu or monoclinic $BaCO_3$, generated by a strongly reducing local atmosphere inside the film

Table 3.3 displays the amine additives selected considering the aforementioned requirements, together with the chemical properties of each, showing MEA as reference.

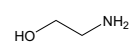
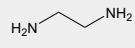
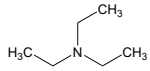
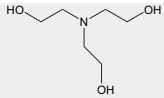
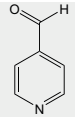
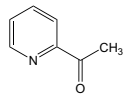
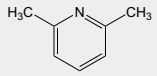
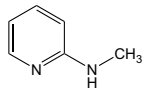
Name	Structure	Type of amine	Boiling point (ºC)	Density (g/mL)	Viscosity at 25º C (mPa·s)	pKa
Monoethanolamine (**MEA**)		Alkyl amine (primary), amino alcohol	170	1.012	18.95	9.5
Ethylenediamine (**En**)		Alkyl amine (primary), diamine	116	0.898	1.54	pKa_1 = 10.712 pKa_2 = 7.564
Triethylamine (**Et_3N**)		Alkyl amine (tertiary)	89	0.727	0.347	10.78
Triethanolamine (**TEA**)		Alkyl amine (tertiary), amino alcohol	335	1.124	590.5	7.76
Pyridine (**Py**)		Aromatic amine	115	0.982	0.879	5.23
Pyridine-4-carbaldehyde (**4-Formylpyridine**)		Aromatic amine	72	1.137	Not available	4.72
1-(Pyridin-2-yl)ethan-1-one (**2-Acetylpyridine**)		Aromatic amine	189	1.08	Not available	2.64
2,6-Dimethylpyridine (**2,6-Lutidine**)		Aromatic amine	144	0.925	0.93	6.60
N-methylpyridine-2-amine (**2-(Methylamino) Pyridine**)		Aromatic amine	200	1.052	Not available	6.73

TABLE 3.3: List of the amines considered for the study described in this section, with chemical properties of interest for their application as additives in the YBCO precursor solution. For additional simplification, their chemical structure is provided.

A short discussion on the characteristics of each amine and the possible complexation it may bear is of great interest to better understand the implications on the solution.

Amongst the alkyl amines, three compounds were chosen to conduct this preliminary study: ethylendiamine (En), triethylamine (Et_3N) and triethanolamine (TEA).

It might be observed that En is the diamine corresponding to MEA, where the *-OH* group is

substituted by a second $-NH_2$. In this case, a complexation through chelation is likely, and En is commonly considered a bidentate chelating agent. This primary amine has a relatively low boiling point (116 ºC) and approximately a factor 12 lower viscosity respect to MEA. Values of pKa are in the same range as MEA, indicating it has similar basicity. Et_3N presents the lowest boiling point of all alkyl amines tested and an extremely low viscosity. This tertiary amine may show major difficulty towards complex formation due to steric hindrance.

TEA, on the contrary, presents the highest boiling point of all of the tested amines, including the aromatic compounds. Additionally, its exceptionally elevated viscosity may result in highly viscous solutions, a further complication when employed for deposition techniques. Showing less basic character than the rest of the chosen alkyl amines, this tertiary amino alcohol may encounter serious steric hindrance complications: however, the terminal -*OH* groups may favour eventual stabilization through hydrogen bonds. Also, TEA was found to facilitate the formation of coordination polymers with a variety of metal cations [176, 177].

Regarding aromatic amines, it is widespread knowledge that Py generates strong σ-bonds with various transition metals due to the simplicity of the sp^2 lone pair of the -*N* atom to occupy a vacant orbital belonging to the metal[178]. Therefore, it was chosen as the first candidate of the aromatic amines class, despite its rather low viscosity value if compared to MEA. With Py being the building block, a series of Py derivatives have been tested, with various functional groups which are responsible for strong variations of the chemical reactivity. The chosen aromatic amines are: 4-Formylpyridine, 2-Acetylpyridine, 2,6-Lutidine and 2-(Methylamino)Pyridine. For sake of clarity, a brief, generic explanation on properties of functional groups is provided (summarized from [178]). An electron withdrawing group (EWG) is any functional group which attracts electrons from the -*C* atom it is bonded to, making it electron deficient and thus more reactive to an electrophilic attack. Examples of EWG are $-NO_2$, -*CN*, -*CHO*, -*COR*. Aldehydes are, generally, stronger EWG than ketones as the former generate a stronger stabilization through mesomeric effect (-M). Contrarily, an electron donating group (EDG) is any functional group which donates electrons to its neighbouring -*C* via a lone pair which leads to stabilization through a mesomeric effect (+M). The increase in electron density makes the carbon centers more reactive to a nucleophilic attack. Functional groups such as -*OH*, $-NH_2$ and NR_2 are some examples of EDG.

4-Formylpyridine has a formyl group at the *para* position respect to the -*N* atom which generates a further mesomeric effect (-M) if compared to the Py alone, due to the strong electron withdrawing character of this substituent.

The acetyl group from 2-Acetylpyridine, found at the *ortho* position, exhibits a less intense electron withdrawing character, giving rise to weaker stabilization through mesomeric effect (-M). However, complexation through the -*N* atom may be hindered by the positioning and dimensions of the acetyl group in this case.

Similar consequence is observed in the case of the 2,6-Lutidine, where the access to the -*N*

atom is subject to steric hindrance due to the two methyl groups, making it a worse nucleophile compared to Py, reflected in its higher pKa value.
The EDG $-NH$ in the 2-(Methylamino)pyridine bears possibility of stabilization through mesomeric effects; this compound may form complexes through chelation betweeen the two *-N* atoms of the *-N-C-N* bond.
Now that a general assessment of the chemical properties and reactivity of each of the chosen amines has been made, the effects of their use in the YBCO precursor solution and the result of the pyrolysis process will be described.

3.4.1.1 Alkyl Amines

For what concerns the alkyl amines, initial tests on solutions conceived the use of each amine in the same (Cu:amine) molar ratio as the optimized one for MEA, (Cu:MEA)=(1:0.61). Certainly this molar ratio is not expected to be optimal in each of the cases, yet it was taken as starting point to collect initial information regarding the differences between the specific amine tested and MEA. For alkyl amines, only solutions of concentration of 1.5 M in sum of metal salts have been prepared. The individual results for each new amine additive will be described separately.

3.4.1.1.1 Ethylenediamine

This additive has been tested in previous studies in the TFA system and was found incompatible due to precipitation of the solution following its addition[42]. Initial trials on the system described in this thesis using the molar ratio (Cu:En)=(1:0.61) have led to no dissolution of the metal propionate precursors. To obtain a fully dissolved solution with no signs of precipitates, the molar ratio of (Cu:En)=(1:2) had to be reached (corresponding to a $12\%_{v/v}$ En). Once $Cu(Prop)_2$ was added to a solution with this molar ratio, the colour changed promptly to a dark purple, suggesting a difference in the coordination scenario amongst the amine and this precursor respect to the otherwise bright blue solutions resulting from MEA addition.

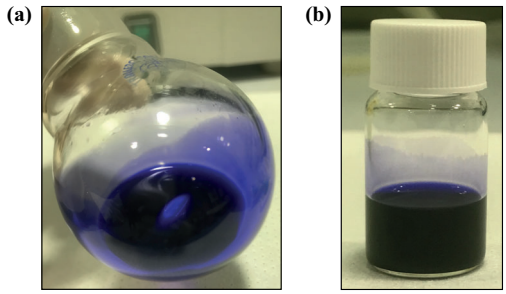


FIGURE 3.45: Colour of the solution resulting from the addition of $Cu(Prop)_2$ with the presence of En in (a) the flask during solution preparation and (b) the final solution. The sudden shift to dark purple suggests coordination between the amine and the metal propionate precursor.

This change of colour solely occurred when the molar ratio (Cu:En)=(1:2) was reached, coinciding with this value being the minimum for a complete dissolution. Presumably, a bidentate chelating coordination of En is necessary in order to favour the solubility of $Cu(Prop)_2$ in solution in these specific conditions. More information regarding the nature of the eventual Cu-En complex formed will be given in 3.4.2. This solution appeared to present a high viscosity, which was then experimented at the moment of deposition. The resulting nanocrystalline precursor films, displayed in Fig. 3.46, indeed present what seems to be a rough surface with important border effects which are likely due to the rheology of this solution. The thickness of a two-layered film results in a higher value than one deriving from an optimized solution

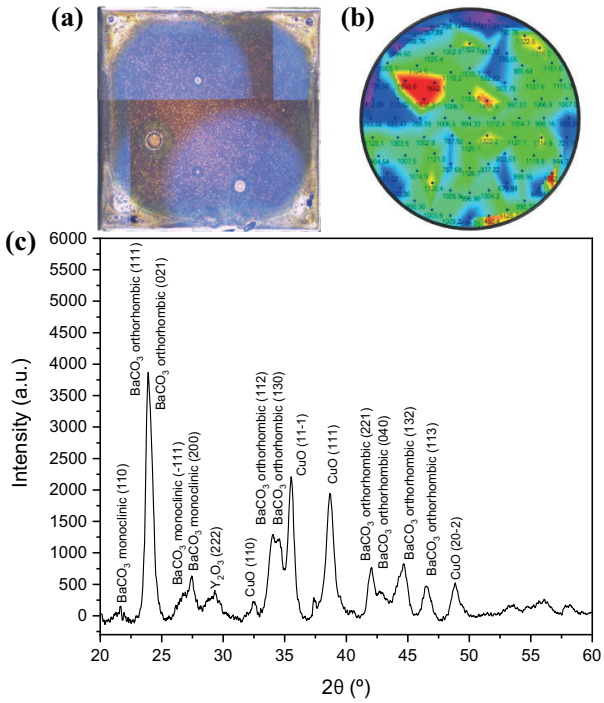


FIGURE 3.46: (a) OM image of a two-layered film obtained from a solution of 1.5 M with the addition of En. (b) Measurement of thickness of the film in (a) by reflectometry. (c) XRD data acquired from the sample in (a) showing the presence of the desired nanocrystalline phases of $BaCO_3$, CuO and Y_2O_3.

with MEA, being over 1200 ± 50 nm. Most importantly, the XRD data acquired from this film presents the desired nanocrystalline phases, with $BaCO_3$ found majorly in its preferred orthorhombic phase. Despite the non ideal aspect of the film, observed in the OM image, these results can be considered promising for the application of this amine in the preparation of YBCO precursor solutions for TLAG-CSD.

3.4.1.1.2 Triethylamine

Similarly to the case of En, when Et_3N is employed, molar ratios below (Cu:Et_3N)=(1:2) are insufficient to obtain a complete dissolution of the metal propionate precursors. Therefore, through the addition of 12.7%$_{v/v}$ Et_3N a fully dissolved, homogeneous and stable YBCO precursor solution could be achieved. The considerable amount of amine needed in this case may be necessary due to the high steric hindrance which makes the *-N* atom less accessible for coordination.

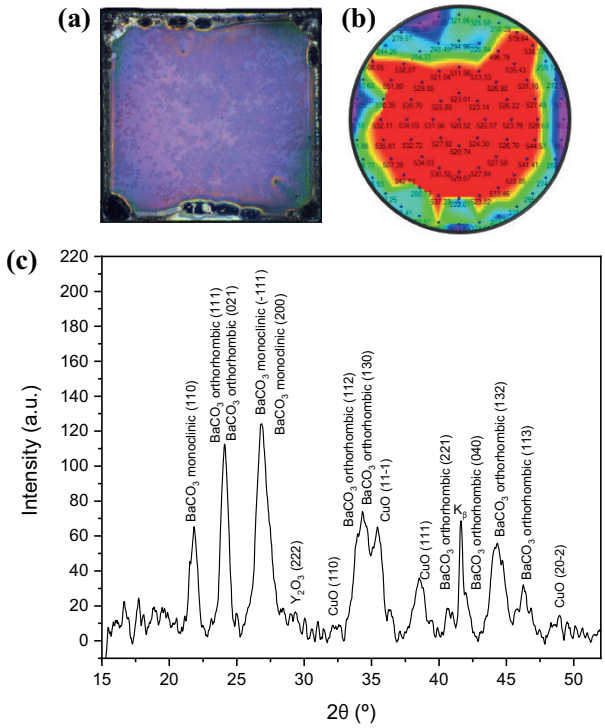


FIGURE 3.47: (a) OM image of a two-layered film obtained from a solution of 1.5 M with the addition of Et_3N. (b) Measurement of thickness of the sample in (a) through reflectometry, showing average thickness of 520 ± 50 nm. (c) XRD data acquired from the film in (a) showing the presence of the desired nanocrystalline phases of CuO, Y_2O_3 and $BaCO_3$, however with a higher contribution from the monoclinic phase of the latter.

The outcome of the use of this kind of solution for the preparation of nanocrystalline films may be found in Fig. 3.47. Despite the moderately homogeneous film obtained, the thickness of a double-fold deposition is just above 500 nm, merely 100 nm more than what may obtained with just one layer of a solution in which MEA is employed. Moreover, the nanocrystalline phases identified in the XRD pattern are showing the presence of a high contribution of monoclinic $BaCO_3$, unpreferable given its elevated thermal stability[52, 126]. The combination of

these results are indicating that this particular amine is not a suitable additive in this specific system, especially when considering the enhancement of the thickness as the major objective.

3.4.1.1.3 Triethanolamine

The case of TEA is extremely different from the aforementioned alkyl amines. Starting with a molar ratio of (Cu:TEA)=(1:0.61), corresponding to an $8\%_{v/v}$ TEA, successive to $Cu(Prop)_2$ addition a prompt and complete precipitation of a sky blue solid occurs (Fig. 3.48). The inevitable achievement of this solid may be the result of the formation of a coordination polymer with the precursors of $Ba(Prop)_2$ and $Cu(Prop)_2$ present until the moment. Moreover, the XRD data obtained from the dried powder results in a different pattern than the ones exhibited by the metal propionate precursors, suggesting the formation of a different species (Fig. C.3).

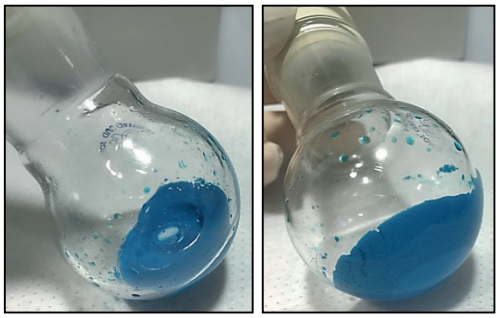


FIGURE 3.48: Precipitate obtained during the preparation of a solution with $8\%_{v/v}$ TEA.

Following this outcome, a lower molar ratio was believed to be more adequate, thus (Cu:TEA) = (1:0.15), corresponding to $2\%_{v/v}$ TEA was employed. It is important to stress that, despite such low quantity of additive involved, a fully dissolved and stable solution could be obtained, supposedly aided by the hydrogen bond interactions through the three terminal -*OH* groups of the aliphatic chains. After deposition and pyrolysis, a homogeneous film was achieved. Nonetheless, the thickness of each layer is merely 330 ± 50 nm and, additionally, the nanocrystalline phases obtained are a mixture of monoclinic $BaCO_3$, metallic Cu and a small contribution of CuO. This unfavourable situation resembles the case of excess of MEA, and the effects of having such nanocrystalline phases have been explained in detail in 3.2.4. Several studies have used TEA as an additive for precursor solutions for CSD applications [43, 47, 53]. However, all of these studies used metal acetates as precursors and one a water-based solution. These conditions may be optimal for the use of TEA as an additive, but seem detrimental in the solution preparation procedure employed for the present study. A potential interpretation of the reason for the formation of the undesired phases may be that in this system there is a preference for TEA to form coordination polymers with one or more of the metals employed. The thermal stability of such compounds has not been investigated but it may be shifting the

decomposition of the precursors at different temperatures and thus, favouring the nucleation of the observed crystalline phases respect to the desired ones.

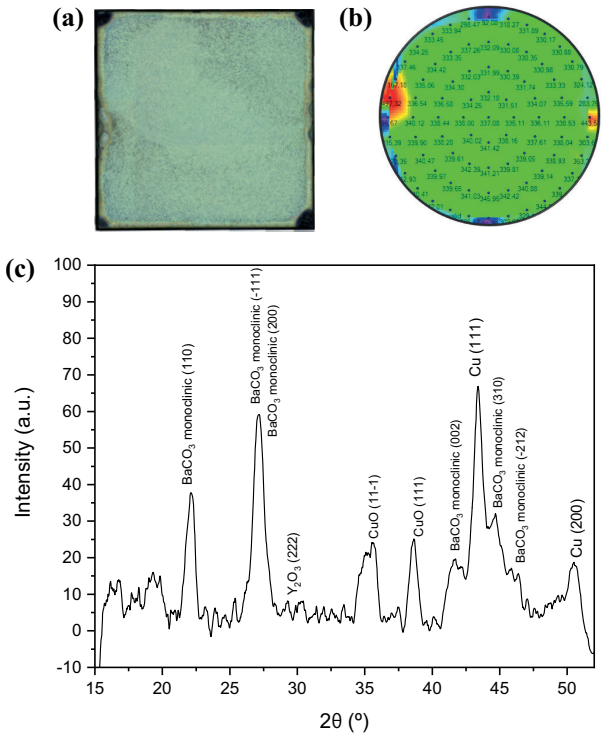


FIGURE 3.49: (a) OM image of a nanocrystalline film of one layer obtained from the deposition of a solution of 1.5 M + 2%$_{v/v}$ TEA. (b) Measurement of the thickness of the film shown in (a) through reflectometry. (c) XRD pattern acquired from the film in (a), showing the presence of the undesired phases of monoclinic $BaCO_3$, Cu(0) and CuO.

Despite the trials performed with TEA, in these specific conditions it seems to yield incompatible results and thus, its use as additive will be discarded. However, based on the various studies in which TEA led to successful results, possibly a variation of the solvents or a different thermal profile may generate a positive outcome, making TEA adequate for its use in the CSD of YBCO precursor solutions.

3.4.1.2 Aromatic Amines

Regarding aromatic amines, an initial optimization using Py in solution has led to the discovery, as will be explained later in detail, that a molar ratio lower than the optimal for MEA would produce the most suitable results. Here, various concentrations were tested, mainly due to the extremely elevated capacity of Py and its derivatives to aid in the dissolution of the

metal propionate precursors, specifically of $Cu(Prop)_2$. Again, each amine will be assessed separately.

3.4.1.2.1 Pyridine

In previous studies, Pyridine (Py) was applied to fluorine-free metal-organic solutions for the preparation of YBCO, employing mostly acetylacetonate and acetate metal precursors[88, 179, 180]: Py was used as a solvent, generally mixed with HProp, and only concentrations of 1.5 M or below have been tested. Contrarily, in the findings described here, Py was strictly used as an additive to enhance the solubility of the metal propionate precursors. Firstly, the optimal molar ratio for MEA was tested. Thus, a solution of 1.5 M + 4.4%$_{v/v}$ Py was prepared: the extremely rapid dissolution of all powder precursors was doubtlessly suggesting a possibly strong coordination, hypothesizing the feasibility of lower molar ratios. Employing this solution for deposition resulted in films of high homogeneity, as displayed the OM image in Fig. 3.50.

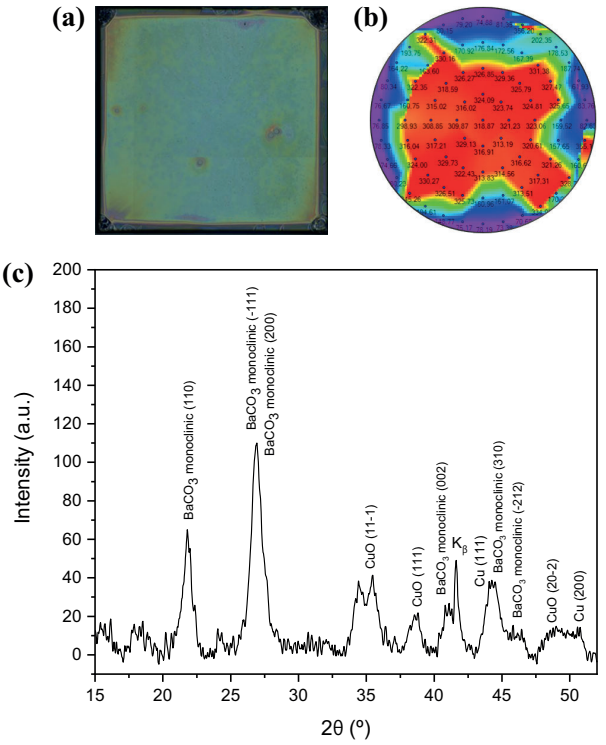


FIGURE 3.50: (a) OM image of a one-layered film obtained by depositing a solution of 1.5 M + 4.4%$_{v/v}$ Py, with (Cu:Py)=(1:0.61). (b) Thickness measurement through reflectometry revealing a thickness of 330 ± 50 nm for the sample in (a). XRD data shown in (c), which identifies the presence of detrimental crystalline phases for the application of such film in the TLAG process.

However, the thickness of only 330 ± 50 nm per layer and the undesired nanocrystalline

monoclinic phase of $BaCO_3$ are deleterious for the application of these films in the TLAG process. Being conscious of the great potential of Py towards an increase of the concentration of the YBCO precursor solutions, given its propensity to form stable complexes with copper[181], a lower molar ratio was tested, specifically (Cu:Py) = (1:0.41). In this way, a solution of 1.5 M + 3%$_{v/v}$ Py was prepared encountering no major difficulty for the dissolution of the metal propionate precursors and showing an extremely rapid dissolution, suggesting the solubility limit is far from these conditions. After pyrolysis, this kind of solution results in two-layered films of approximately 560 ± 50 nm with a less homogeneous aspect shown in the OM image. Nonetheless, the XRD pattern is showing an improvement towards the desired phases, as the contribution of orthorhombic $BaCO_3$ has importantly increased respect to the previous film, and no peaks suggesting the presence of Cu(0) can be identified.

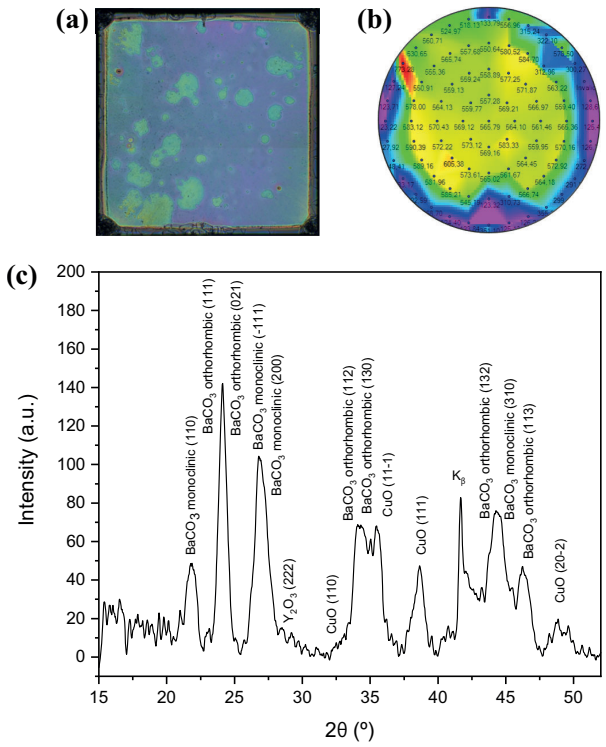


FIGURE 3.51: (a) OM image of a two-layered film deriving from the multi-deposition of a solution of 1.5 M + 3%$_{v/v}$ Py, with (Cu:Py)=(1:0.41). (b) Thickness of film displayed in (a), measured through reflectometry. (c) XRD data from film in (a), showing the improvement towards the desired crystalline phases respect to the film prepared with the solution with higher Py content in 3.50.

Following this result and anticipating the promising possibilities Py may offer towards an increase of the concentration, and thus thickness, the molar ratio of (Cu:Py)=(1:0.41) was

maintained while the concentration was raised up to the maximum 3 M in total sum of metals. Such elevated concentration is expected to yield films of elevated thickness, and effectively this was the case, as shown in Fig. 3.52. One layer deposited through this solution results in a thickness of over 750 nm, almost doubling the value obtained for the optimized solution with MEA. Nonetheless, the film is completely cracked and, thus, unusable for the TLAG process. In an attempt to avoid the detrimental cracking of the films deriving from this kind of solution, the total concentration was lowered to 2.8 M, 2.3 M and 2 M. The appearance of cracks was, alas, not prevented, as it may be observed in the OM images in Fig. 3.52; nonetheless, very valuable information was comprehended when analyzing the XRD data relative to such films. The three films deriving from the solutions with higher concentrations (3 M, 2.8 M and 2.3 M) which result in destructive cracking, are showing impressive thickness values ranging between 1000 nm and 700 nm per layer as well as the sole presence of the desired nanocrystalline phases in XRD: $BaCO_3$ orthorhombic in majority, CuO and Y_2O_3. Contrarily, despite having a thickness of 500 ± 50 nm with only scarce cracking phenomena, the film obtained from the solution of 2 M shows the unique presence of the undesired monoclinic crystalline phase of $BaCO_3$, together with a mixture of CuO and Cu_2O, and Y_2O_3. Based on the experience with the films with MEA excess, the excessive cracking displayed by the films of high thickness is the necessary mechanism of strain release due to the elevated gas evolution deriving from the decomposition of the precursors. The amount of released volatiles is, in these cases, far beyond the capability of the film to maintain its skeletal integrity. However, the formation of cracks allows for a complete elimination of the gases resulting from the decomposition of the metal propionates and thus the nucleation of the desired crystalline phases following the thermal process. Different situation is shown by the film deriving from the 2 M solution: the lower thickness of the film, meaning lower amount of gas to be eliminated, enables the achievement of an almost crack-free film. However, the small cracks present are insufficient for a complete elimination of the evolved volatiles where, presumably, as previously seen for the extreme case of films with MEA excess, the trapped CO_2 may be reduced to CO and create a localized, reducing atmosphere, favouring the formation of the unwanted phase of monoclinic $BaCO_3$ and partial reduction of CuO to Cu_2O.

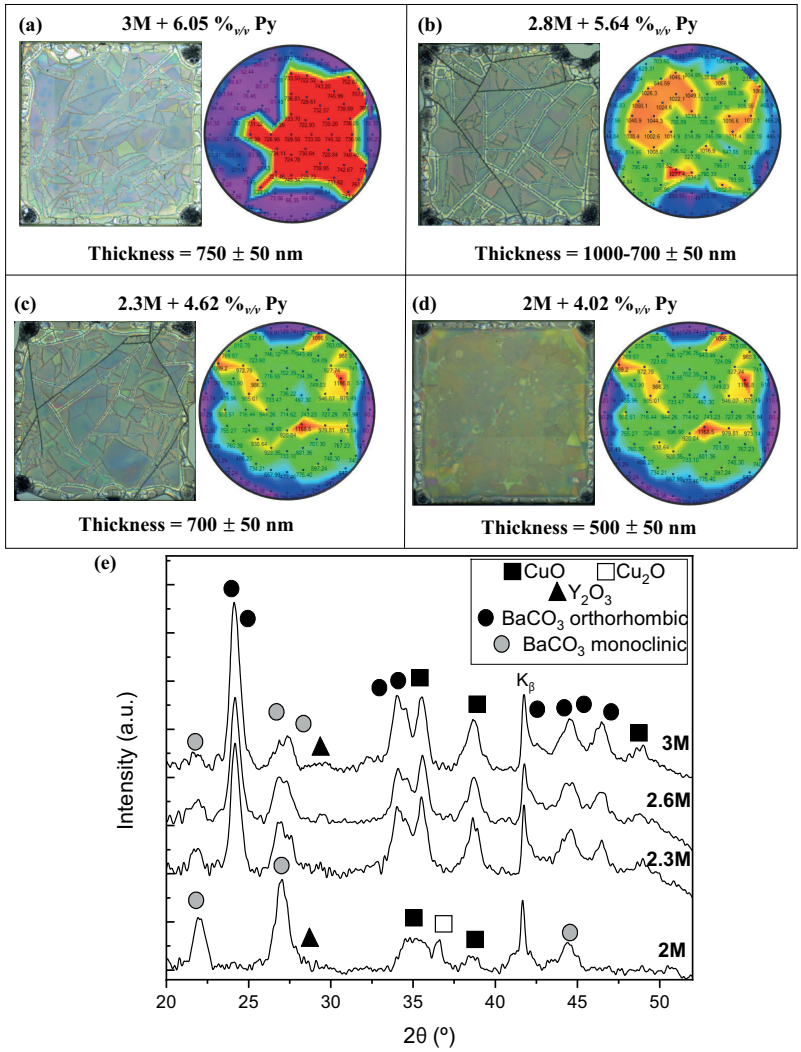


FIGURE 3.52: Testing solutions of various concentrations with the molar ratio (Cu:Py) = (1:0.41). (a)-(d) show OM image and respective thickness measurement through reflectometry of one-layered films deriving from solutions of 3 M + 6.05%$_{v/v}$ Py, 2.8 M + 5.64%$_{v/v}$ Py, 2.3 M + 4.62%$_{v/v}$ Py, 2 M + 4.02%$_{v/v}$ Py, respectively. (e) XRD data for the four films showed in (a)-(d).

3.4.1.2.2 Pyridine and MEA mixture

The employment of Py has demonstrated the possibility of reaching unprecedented concentrations of the solutions, given the easiness of this aromatic amine to form a complex with copper and aiding the dissolution of $Cu(Prop)_2$. However, Py alone is not conferring sufficiently strong mechanical properties towards the elimination of great quantity of gas during the

pyrolysis process. Therefore, to ensure a more robust skeletal integrity, the idea of using a mixture of MEA and Py was tested, believing that MEA would grant the elasticity and resistance against cracking which had been previously observed in films obtained during the optimization of the solutions with this amine additive. The optimized molar ratios of both additives were preserved, being (Cu:MEA) = (1:0.61) and (Cu:Py) = (1:0.41), and final concentrations of 2.5 M and 2 M were tested, encountering no difficulties for the complete dissolution of the powder precursors during solution preparation. Films resulting from these solutions are displayed in Fig. 3.53. It may be observed that in both cases the first layer shows a homogeneous aspect

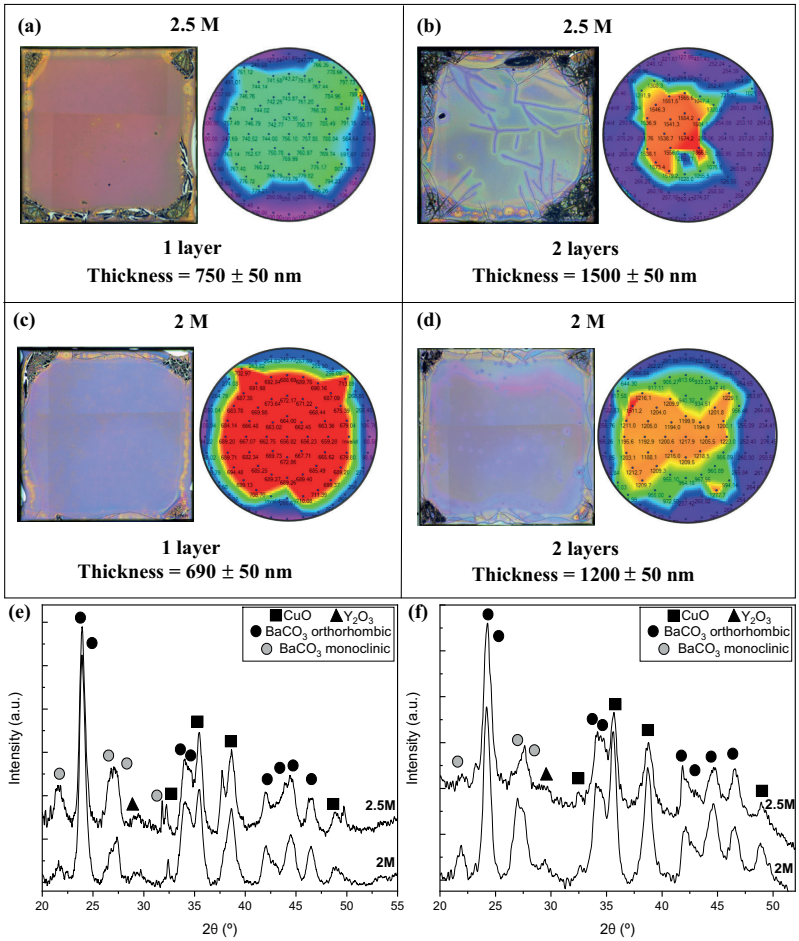


FIGURE 3.53: OM image and thickness measurement obtained through reflectometry of films deriving from solutions of (a)-(b) 2.5 M and (c)-(d) 2 M, with the addition of MEA and Py in molar ratios (Cu:MEA) = (1:0.61) and (Cu:Py) = (1:0.41). Films of one layer are shown in (a) and (c), and the multideposition of two layers is object of (b) and (d) for each solution. XRD data of the films in (a)-(d) are shown in (e) for the one-layered films and in (f) for the two-layered films.

and impressive thickness values, being 750 ± 50 nm and 690 ± 50 nm for the 2.5 M and for the 2 M solution, respectively. Nonetheless, when adding a second layer, the 2.5 M solution yields a cracked film whereas the 2 M solution ensures the achievement of a homogeneous one. Thickness values are, respectively, 1500 ± 50 and 1200 ± 50, demonstrating the great potential of this mixture of additives towards the thickness enhancement. The nanocrystalline phases formed are in agreement with the expected ones for an optimized solution with MEA in all cases, confirming the success of these kind of solutions; however, the case of two-layered film from the 2.5 M solution is, again, resembling what previously observed for the Py alone, requiring formation of cracks due the great stress coming from the evolution of the volatiles. Possibly, by varying the heat treatment profile, this effect may be reduced or completely eliminated: however, it is of utmost importance to ensure the correct formation of the desired phases also when a different heating ramp is employed, and a comprehensive microstructural analysis is suggested. Nonetheless, the films from the solution of 2 M fulfill all the requirements for their application in the TLAG process and are, moreover, demonstrating that an important increase of the thickness is feasible through the use of the mixture of MEA and Py, without hampering the homogeneous nature of the film or the formation of the appropriate crystalline phases in the chosen experimental conditions. A microstructural analysis of such films through TEM will be described in 3.4.4.

3.4.1.2.3 Pyridine-4-carbaldehyde

Pyridine-4-carbaldehyde (4-Formylpyridine) was initially tested in the same molar ratio as the optimized solution with MEA, (Cu:4-Formylpyridine) = (1:0.61), to investigate whether the lower molar ratio was more appropriate for Py but not for its derivatives. Due to the high solubilizing capability of this aromatic amine, a solution of 1.5 M + 4.4%$_{v/v}$ 4-Formylpiridine was successfully prepared, showing an extremely fast dissolution for all the metal propionate precursors. The deposition of such solution and its pyrolysis yields films of 420 ± 50 nm which, however, present cracking along the entire surface (Fig. 3.54). Moreover, the phases identified in XRD are found to be the undesired $BaCO_3$ monoclinic, a mixture of CuO and Cu(0), and Y_2O_3. Being this unfavourable result similar to the case of Py when the same, excessive molar ratio is employed, it was lowered to (Cu:4-Formylpyridine) = (1:0.41). The concentration of the solutions was increased to 2.6 M and 2 M encountering no difficulty whatsoever for the dissolution of the powder precursors, demonstrating the great potential of this amine in the possible complex formation, as anticipated in 3.4.1. Through the use of these solutions, films of elevated thickness were obtained, being 900 ± 50 nm and 820 ± 50 nm deriving from the 2.6 M and the 2 M solutions, respectively.

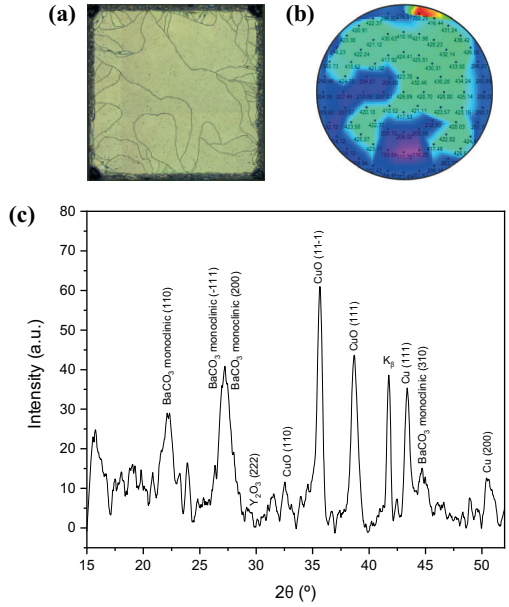


FIGURE 3.54: (a) OM image of a one-layered film deposited using a solution of 1.5 M + 4.4%$_{v/v}$ 4-Formylpyridine, displaying cracks. (b) Thickness measurement through reflectometry and (c) XRD data from the film in (a).

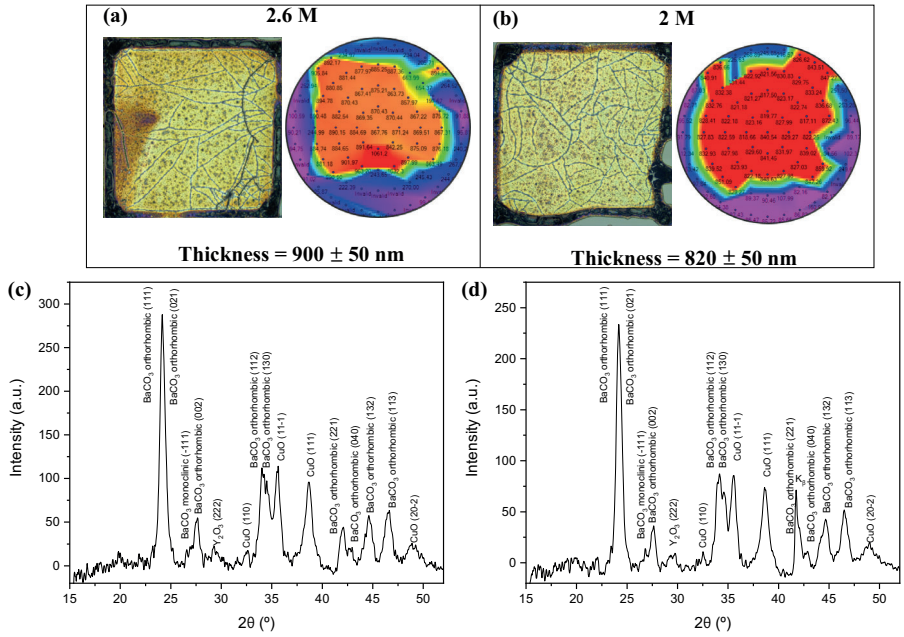
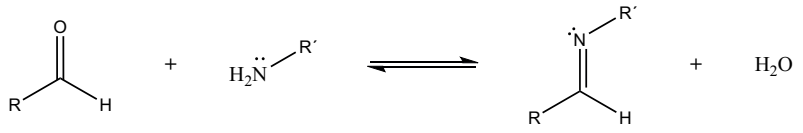


FIGURE 3.55: OM image and thickness measurements (obtained through reflectometry) of films deposited using solutions of (a) 2.6 M + 5.95%$_{v/v}$ 4-Formylpyridine and (b) 2M + 4.57%$_{v/v}$ 4-Formylpyridine. (c)-(d) XRD data respective to each film in (a) and (b).

Despite both films displaying the necessary nanocrystalline phases for TLAG, the surface appears inhomogeneous and with substantial cracking. In the defined conditions of the thermal profile used, a smooth, crack-free film is unattainable; nonetheless, the possibilities of thickness enhancement through the use of this aromatic amine are such that variations in the deposition parameters or in the heat treatment should be implemented in order to maximize the chances of a positive outcome.

An important comment must be made regarding the reason for which a mixture with MEA was not considered for 4-Formylpyridine. A common reaction of aldehydes when mixed with an amine is the formation of an imine releasing H_2O, according to the following generic reaction mechanism, adapted from [182]:



(3.2)

The formation of the imine would result in an increase in the water content of the solution, additional to the one given by Fischer esterification, together with the presence of yet another species in solution which may hamper the correct decomposition of the precursors in the pyrolysis process. Taking these motivations into account, the idea of using a mixture of 4-Formylpyridine and MEA was discarded.

3.4.1.2.4 1-(Pyridin-2-yl)ethan-1-one

For the aromatic additive 1-(Pyridin-2-yl)ethan-1-one (2-Acetylpyridine), considering the previous results for Py and for 4-Formylpyridine, the molar ratio of (Cu:2-Acetylpyridine) = (1:0.41) was tested. The initial concentration of the solution with the sole addition of 2-Acetylpyridine was 1.5 M, and a fast dissolution was observed for the three powder precursors, suggesting a favourable interaction with this amine additive. After pyrolysis, the resulting film shows a rough surface and a low thickness, being one layer only 350 ± 50 nm. Nonetheless, the desired nanocrystalline phases are identified in the XRD pattern of this film, suggesting the correct decomposition pathway was followed.

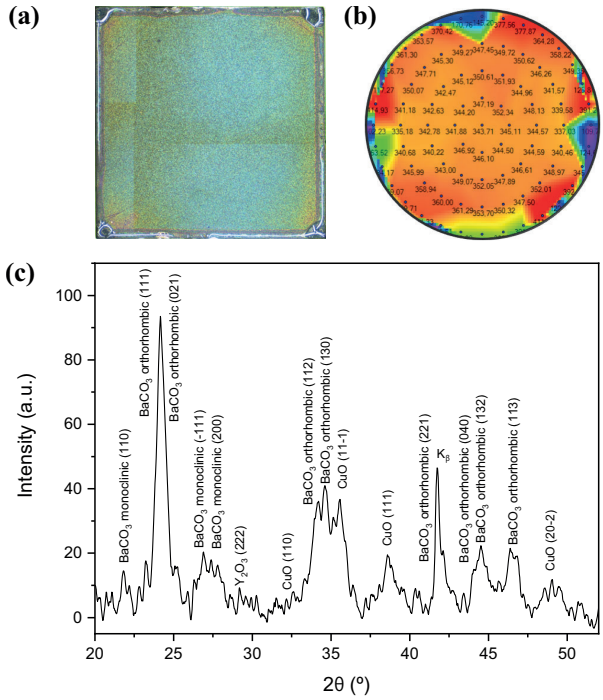


FIGURE 3.56: (a) OM image of film deriving from the deposition and pyrolysis of a solution of 1.5 M + 4.1%$_{v/v}$ 2-Acetylpyridine, with its respective reflectometry thickness measurement displayed in (b) and XRD pattern displayed in (c).

With the aim of enhancing the thickness from the latter, unsatisfactory result, 2-Acetylpyridine was tested in a mixture with MEA, using both optimal molar ratios as implemented for the case of Py, specifically (Cu:MEA)=(1:0.61) and (Cu:2-Acetylpyridine) = (1:0.41). It must be noted that also ketones may react with amines according to the reaction described in 3.2 to form imines; thus, the formation of the imine between the acetyl group of this Py derivative and MEA may occur. However, the decision to test this combination was taken as higher concentration than 1.5 M could not be obtained if employing the 2-Acetylpyridine alone. The preparation of solutions with this mixture may additionally serve as further information regarding which crystalline phases are promoted from such initial conditions. Through the use of the optimal molar ratios for the two amine additives, solutions of total concentration of 2.6 M and 2 M were successfully prepared. No precipitation of any solid was observed, suggesting that if imine formation is occurring, this species is stable in solution. Deposition of these solutions result in the impressive thickness of almost 1 μm in both cases, and the desired nanocrystalline phases optimal for TLAG were identified in both XRD patterns (Fig. 3.57). Nevertheless, the homogeneity of the films is non-existent, displaying extreme crack formation and rough surfaces. Despite this detrimental result, the appearance of the desired crystalline phases is an indication of fulfillment of the expected decomposition pathway; as observed

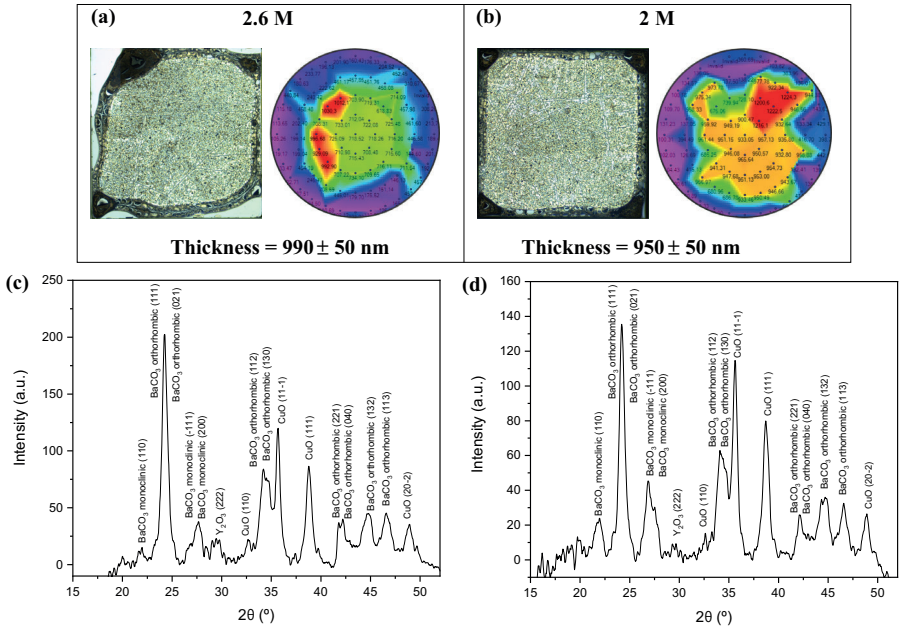


FIGURE 3.57: OM images and thickness measurements ontained through reflectometry of films deriving from solutions of (a) 2.6 M and (b) 2 M with a mixture of MEA and 2-Acetylpyridine as additives in the optimal molar ratios. (c)-(d) XRD patterns measured on films displayed in (a) and (b), respectively.

previously for the case of Py, the cracking is the inevitable mechanism to release the strain in the film during decomposition of the precursors. Bearing in mind the impressive thickness value obtained through the use of this kind of solutions with only one deposition, an optimization of various parameters may be worthwhile: a comprehensive study of the rheological properties may allow for a deeper understanding of which parameters are the most appropriate to change to ensure an improvement towards more homogeneous films.

3.4.1.2.5 2,6-Dimethylpyridine

2,6-Dimethylpyridine (2,6-Lutidine) was firstly used as a single additive in a solution of total concentration 1.5 M and employing the optimal molar ratio used for the other Py derivatives, (Cu:2,6-Lutidine) = (1:0.41). This aromatic amine granted a fast dissolution of the powder precursors, and the deposition of this solution resulted in a relatively homogeneous film, with the presence of minor defects but no cracking phenomena observed. Nonetheless, the thickness of one layer is merely 300 ± 50 nm, around 100 nm lower than in the case of the optimized solution with MEA. An additional negative feature is the presence of the monoclinic phase of $BaCO_3$ in great majority, together with CuO and Y_2O_3. Films with these characteristics are not ideal for their use in the TLAG process.

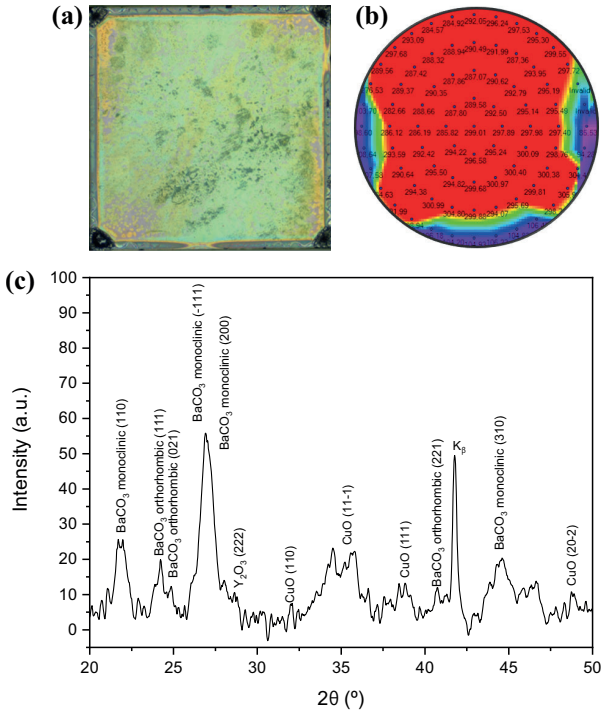


FIGURE 3.58: (a) OM image, (b) thickness measurement through reflectometry and (c) XRD pattern of a film obtained through deposition of a solution of 1.5 M + 4.24%$_{v/v}$ 2,6-Lutidine.

Considering the latter result, this aromatic amine was tested in a mixture with MEA with the aim of enhancing the thickness and, expectedly, maintain a crack-free film. Higher concentrations of the solution could be reached, specifically 2.6 M and 2 M, keeping the optimal molar ratios of (Cu:2,6-Lutidine) = (1:0.41) and (Cu:MEA) = (1:0.61). A full dissolution of the precursors was obtained in both cases, yielding stable solutions; their deposition and the successive heat treatment resulted in homogeneous and defect-free films, as displayed in Fig. 3.59. The high thickness of the films, specifically being 850 ± 50 nm for the solution of 2.6 M and 480 ± 50 nm for the 2 M solution (single layer depositions), are the additional result of the beneficial effect of the mixture of MEA and 2,6-Lutidine: the former was demonstrated to increase the elasticity and resistance of the films and the latter enabled higher concentrations to be reached. Nonetheless, it must be noted that the desired crystalline phases are exhibited only by the film deriving from the 2 M solution. The film deposited with the use of the solution of highest concentration appears to favour the formation of the detrimental phases of monoclinic $BaCO_3$ together with Cu(0) as major copper contribution. Presumably, the extremely elevated thickness of this film, together with the fact that MEA is successfully maintaining its structural integrity, avoids the formation of cracks but, contemporarily, is trapping the evolved volatiles inside the film. As previously explained in 3.2.4, the confinement of gases in the film matrix

may lead to the formation of a localized reducing atmosphere which may favour the nucleation of the monoclinic phase of $BaCO_3$ together with the full reduction of CuO to Cu(0).

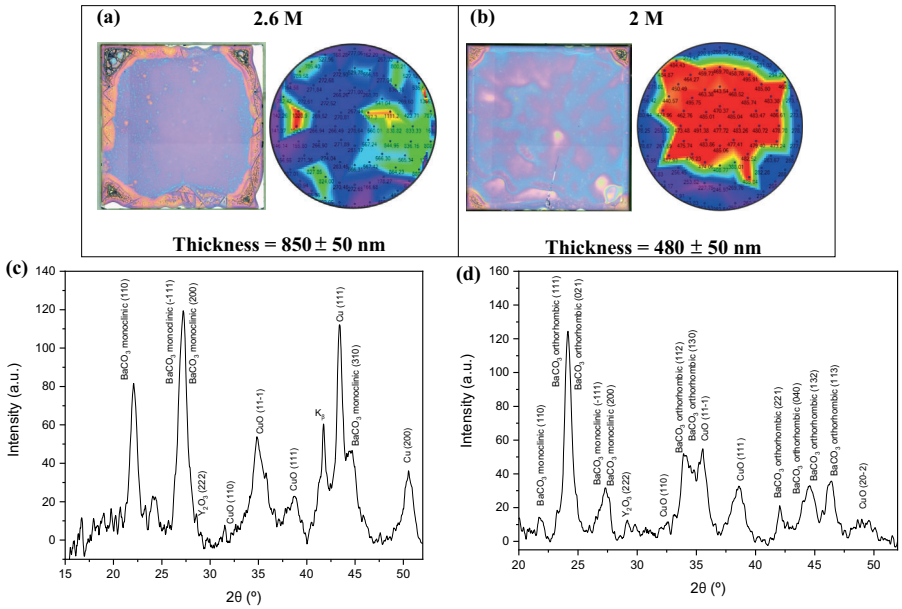


FIGURE 3.59: OM images and reflectometry thickness measurements of films obtained through the deposition of solutions of (a) 2.6 M and (b) 2 M with a mixture of MEA and 2,6-Lutidine using the optimal molar ratios. (c)-(d) XRD data acquired from the films displayed in (a) and (b), respectively.

On the contrary, the thickness of the film deriving from the 2 M solution is believed to be optimal to successfully eliminate the gases due to precursor decomposition without hindering its homogeneity. However, one must take into account the difference of concentration between 2 M and 2.6 M: a solution of intermediate concentration may be found which may still yield films of the desired characteristics for TLAG with a higher thickness than the film deriving from the 2 M solution, making the implementation of further experiments with this kind of solutions of great interest.

3.4.1.2.6 N-methylpyridine-2-amine

With the final aromatic amine tested, N-methylpyridine-2-amine (2-(Methylamino)Pyridine), the optimal molar ratio obtained from the previous additives has been employed in a solution of 1.5 M concentration. Using the ratio (Cu:2-(Methylamino)Pyridine) = (1:0.41), an extremely fast dissolution of the metal propionate precursors was experienced, suggesting a strong interaction between the copper and the amine. Nonetheless, the film obtained by its deposition shows a non homogeneous surface with major morphological defects, a reduced thickness of only 280 ± 50 nm and the crystalline phases with a strong contribution of monoclinic $BaCO_3$.

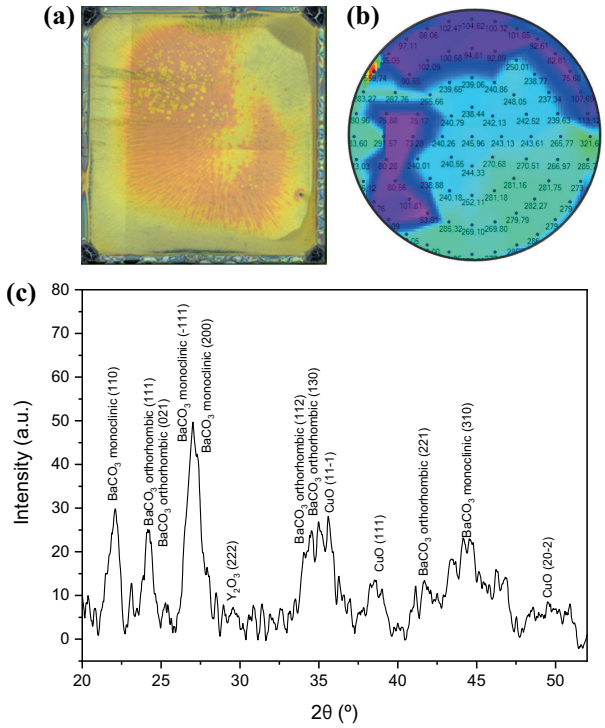


FIGURE 3.60: (a) OM image and (b) thickness measurement through reflectometry of a film obtained by deposition of a 1.5 M + 4.48%$_{v/v}$ 2-(Methylamino)Pyridine solution. (c) XRD data obtained from the film in (a).

Given this uninteresting outcome for the application proposed and the impossibility of obtaining a higher concentration with this aromatic amine alone, a mixture with MEA was implemented. Again, as for the previous cases, the optimal molar ratios have not been varied. However, in this case, a higher concentration than 1.5 M was not achieved, possibly due to a competition between complexation capabilities of the two additives or an insufficient complexation between the aromatic amine and $Cu(Prop)_2$, which in the previous cases was expected to aid the achievement of a complete dissolution. Despite that, deposition of this solution resulted in a highly homogeneous film with a final thickness of 560 ± 50 nm, increased if compared to the case of MEA alone. The XRD pattern acquired for this film allows for the identification of uniquely the desired nanocrystalline phases, with $BaCO_3$ orthorhombic being in great majority, together with reflections relative to CuO and Y_2O_3 (Fig. 3.61).

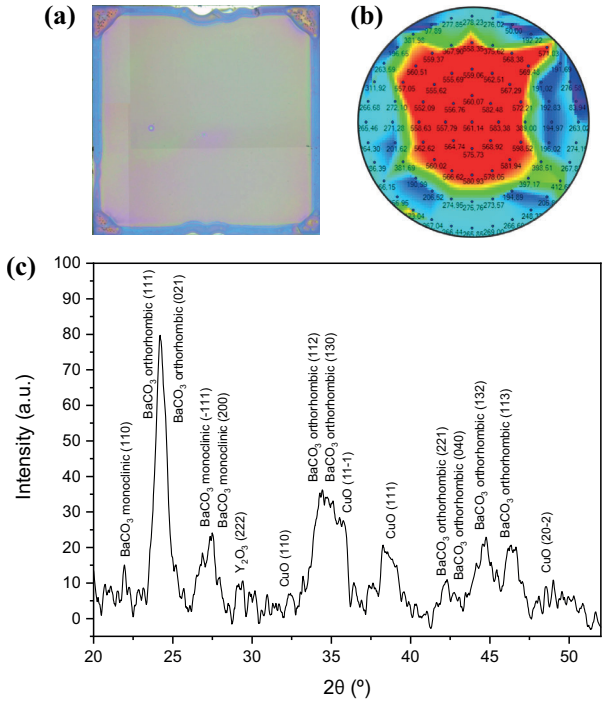


FIGURE 3.61: (a) OM image and (b) thickness measurement through reflectometry of a film obtained by deposition of a 1.5 M solution with a mixture of amine additives in the molar ratios (Cu:2-(Methylamino)Pyridine) = (1:0.41) and (Cu:MEA) = (1:0.61). (c) XRD data obtained from the film in (a).

The positive outcome resulting from the use of the mixture of MEA and 2-(Methylamino) Pyridine is showing great potential for its application in the TLAG process; however, for a further enhancement of thickness, solution parameters may be varied in order to augment the possibility of higher concentrations to be reached, for example the choice of solvents or their mixture ratio.

As a general observation following this preliminary study on the effect of various amine additives, it may be concluded that, amongst the tested compounds, aromatic amines are generally favouring the coordination of copper in the $Cu(Prop)_2$ precursor, aiding its solubility in the media, whereas alkyl amines are presenting a mixed behaviour. Further experimental studies should be conducted and a comprehensive analysis of the rheology of these solutions and their thermal behaviour in the pyrolysis process jointly with a detailed microstructural analysis of the nanocrystalline films through TEM techniques are mandatory to obtain the complete information required for their successful optimization. Substantially due to time limitations during this thesis work, such information was retrieved solely on a selection of exemplary solutions

chosen among the aforementioned cases. To have representation from each of the two classes of amines tested, an additive from the group of alkyl amines and a second one from the aromatic amines were considered for further trials, being En the representative of the alkyl amines and Py the one for the aromatic amines. The following two subsections will be devoted to a detailed analysis of the chemical and thermal properties of these solutions and a microstructural analysis of films through TEM techniques.

3.4.2 Rheological analysis of selected solutions with different amine additives

An overview of the rheological properties of each of the selected solutions may be found in Table 3.4, where an optimized solution with MEA is shown as reference values. It may be noted that the solution with En has the same concentration as the one with MEA, whereas for the solution with Py, the concentration of 2.3 M was chosen and for the case of the MEA-Py mixture, both concentrations of 2.5 M and 2 M were analyzed. The water content on the day of preparation is, thus, a very similar value for the solutions with MEA and En, given their identical concentration, but increases in the rest of the cases. As specified in 3.2.5, the

Amine of choice	Concentration (M)	(Cu:amine) molar ratio	Water content on day of preparation (wt%)	Viscosity (mPa·s)	Contact Angle (º)
Monoethanolamine	1.5M + 3.4%$_{v/v}$ MEA	(1:0.61)	0.65 ± 0.06	8.68 ± 0.05	19.4 ± 0.1
Ethylenediamine	1.5M + 12%$_{v/v}$ en	(1:2)	0.64 ± 0.06	20.42 ± 0.05	27.5 ± 0.1
Pyridine	2.3M + 4.62%$_{v/v}$ Py	(1:0.41)	0.89 ± 0.06	22.68 ± 0.05	29.5 ± 0.1
Mixture of Monoethanolamine and Pyridine	2.5M + 5.66%$_{v/v}$ MEA + 5.04%$_{v/v}$ Py	(Cu:MEA = 1:0.61) (Cu:Py = 1:0.41)	0.91 ± 0.06	76.19 ± 0.05	42.1 ± 0.1
Mixture of Monoethanolamine and Pyridine	2M + 4.53%$_{v/v}$ MEA + 4.02%$_{v/v}$ Py	(Cu:MEA = 1:0.61) (Cu:Py = 1:0.41)	0.87 ± 0.06	31.64 ± 0.05	28.9 ± 0.1

TABLE 3.4: Rheological properties of a series of solutions with different amine additives, selected from the preliminary study, with the data from the optimized solution with MEA shown in the first entry as reference. The parameters that have been taken into account are the optimal (Cu:amine) molar ratio, water content, viscosity and contact angle. All of these have been measured on the day of preparation of the solution to ensure reproducibility of the measurements.

H_2Owt% at this moment is a combination of the H_2O released from the inevitable Fischer esterification reaction and the one relative to the metal propionate precursors: with an increase

of the concentration, meaning an increase in the employed quantity of each powder precursor, a more elevated value of this parameter is to be expected. Viscosity and contact angle measurements reveal a huge increase respect to the case of MEA for the solution with En and the ones with Py and Py-MEA mixture. In the former case it may be solely attributed to the elevated quantity of the new additive introduced, as the concentration is kept constant. The latter, instead, may suffer from a double contribution of the high concentrations and the use of the additives. The rheology of the extreme case of the 2.5 M solution with MEA and Py, which displays high values of viscosity of almost 80 mPa·s and contact angle of 42º, provides an explanation to the quality loss and cracking of the films prepared through its multideposition (3.4.1.2.1).

To fully understand the complexation scenario of each of the solutions in Table 3.4, EPR measurements were performed similarly to the case of MEA described in 3.2.5. To confirm the assumed formation of a complex between the amine of choice and the Cu center belonging to $Cu(Prop)_2$, this powder precursor is dissolved in the same solvent mixture used for the preparation of solutions (HProp and MeOH in a 1:1 proportion), with the addition of each amine in its optimal (Cu:amine) molar ratio. The hypothesis of the presence of a Cu-amine complex was formulated following the possibility of dissolving the least soluble $Cu(Prop)_2$ to form solutions of endured stability and with extremely high concentrations. Again, the EPR spectrum of the optimized case with MEA will be used as benchmark, analyzing possible variations between its coordination mode and the one presented by the other amine additives.

In Fig. 3.62, the EPR spectra of all solutions analyzed are displayed. The three solutions in which new amines are tested are showing a different behaviour respect to the case of a solution with MEA. The identification, in the latter case, of two contributions due to the presence of different species is not possible in the solutions in which either En, Py or the mixture MEA-Py are involved.

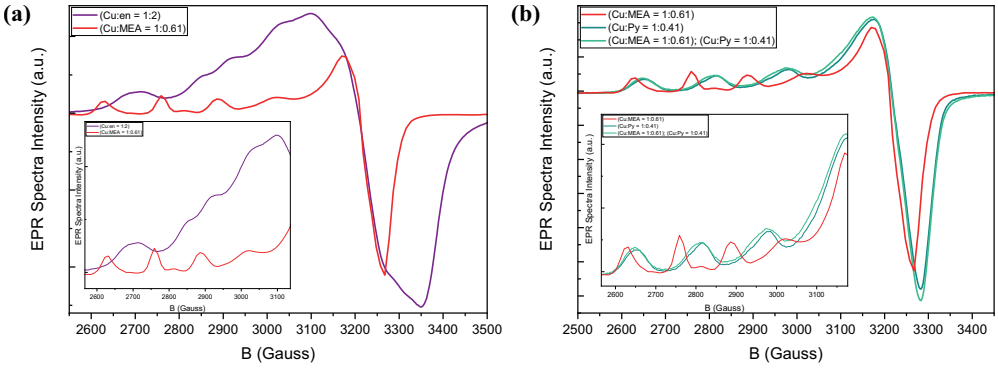


FIGURE 3.62: (a) EPR spectrum of a solution of 1.5 M + 12%$_{v/v}$ En, using optimal (Cu:En) molar ratio of (1:2) (purple). (b) EPR spectra of the solutions with Py (dark aquamarine) and MEA-Py (light aquamarine). The EPR spectrum of an optimized solution with MEA (red) is shown in both cases for sake of comparison.

The optimized solution with En is exhibiting a completely opposed situation than the case of MEA, suggesting a dissimilar coordination with the metal center. The analysis of the spectra led to the determination of the g_{II} and A_{II} factors, being in this case $g_{II} = 2.289$ and $A_{II} = 110.1\ cm^{-1}x10^{-4}$. Through the use of the adapted data from [165–167], the correlation of the calculated factors could provide information regarding the coordination of this specific amine with the $Cu(Prop)_2$ (Fig. 3.63). As it was expected for En, given its bidentate nature and its ability of being a strong chelating agent, the in-plane coordination is given exclusively by four -*N* atoms. This is a confirmation of the bidentate chelation of two En per Cu^{2+}, a coordination arrangement which was also hypothesized for MEA (being the ligands in this case two -*N* atoms and two -*O*).

The EPR analysis of solutions with Py and with the mixture MEA-Py is indicating a further variation from the case of MEA alone. The interesting fact is the identical appearance of both spectra, disregarding the employment of MEA in the solution. No evidence of a contemporaneous concomitance of two species is visible in the EPR spectra of the solution with the MEA-Py mixture. Moreover, the calculated values for g_{II} are 2.285 and 2.282 and A_{II} are $171.8\ cm^{-1}x10^{-4}$ and $172.7\ cm^{-1}x10^{-4}$ for the Py and MEA-Py solutions, respectively. Such comparable values are strongly suggesting that Py is responsible for the major contribution to the coordination with the copper center. Indeed, the coordination through its lone pair and the possibility of stabilization through resonance on the aromatic ring would certainly provide a stronger complexation capability in conditions of a hypothetical competition with MEA. These findings are reflected in the correlation between g_{II} and A_{II}, which are resulting in adjacent points corresponding to the complexation through two -*N* atoms and two -*O* atoms. Presumably, the two -*N* atoms are relative to Py ligands, whereas -*O* ones may be due to the $-(COO)^-$ groups of the propionate ligands. In fact, if this contribution was due to coordination with MEA through the oxygen of the terminal -*OH* functional group, a major difference should have been exhibited by the EPR spectra of the two solutions, as one is lacking this additive. Considering this plausible explanation, the simple addition of MEA to the solution changes completely the outcome of the pyrolysis process, yielding crack-free films only when this additive is employed. Based on the previous experience with the optimized solution with MEA, supposedly its role in this solution goes beyond the complexation with the copper precursor and is strictly linked to the mechanical properties of the film, making it more elastic and resistant towards the appearance of cracks.

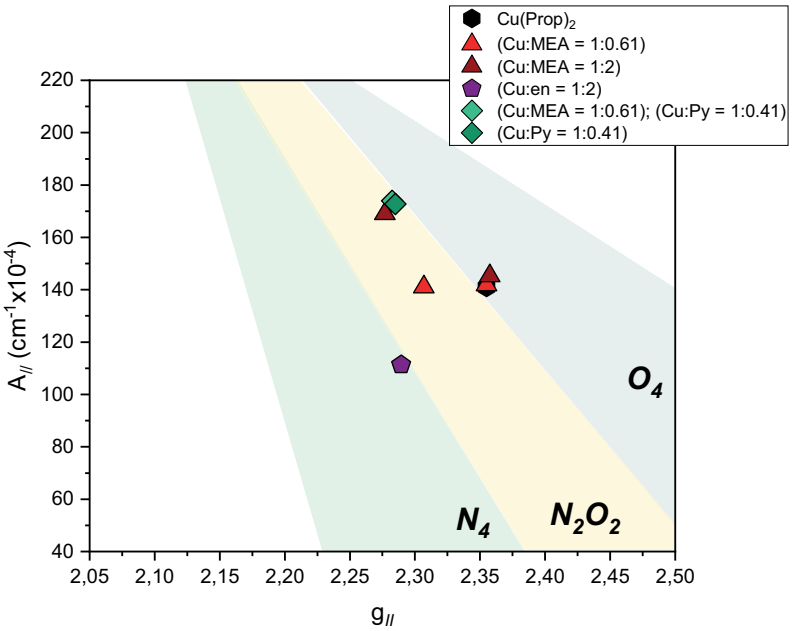


FIGURE 3.63: Coordination arrangements between each amine additive described in this subsection and the Cu center. The data for the cases of $Cu(Prop)_2$ optimized MEA (1:0.61), and MEA excess (1:2) are indicated for completion. Data adapted from [165–167].

As established for the case of MEA, through this analysis the formation of complexes of various nature between the copper precursor and the relative amine additive was corroborated. The appearance of such coordination species is allowing for an important increase of the concentration of the solutions, which results in films of elevated thickness; additionally, these solutions present endured stability of several months given the strong complexation with $Cu(Prop)_2$ which avoids its precipitation, a rapidly occurring phenomenon when no additive is employed.

3.4.3 Thermal behaviour of solutions with new amine additives

To determine the compatibility of the solutions with En, Py and MEA-Py with the thermal profile employed during the pyrolysis process and the effect of each amine on the decomposition, TG experiments coupled to EGA-FTIR were carried out. As this heat treatment is conducted in a humid O_2 atmosphere, as specified in Chapter 2, the anticipated decomposition pathway followed by the films will be the hydrolysis and oxidation of the metal propionate precursors. The main expected volatiles will be, initially, HProp, result of the hydrolysis of the propionate groups, then superseded by their oxidation when higher temperatures are reached, coinciding with CO_2, HProp and acetaldehyde elimination (detailed description of the full mechanism

may be found in Chapter 2). In Fig. 3.64, the TG profile together with the analysis of the evolved volatiles is reported for an optimized solution with En. The TG curve evidences a

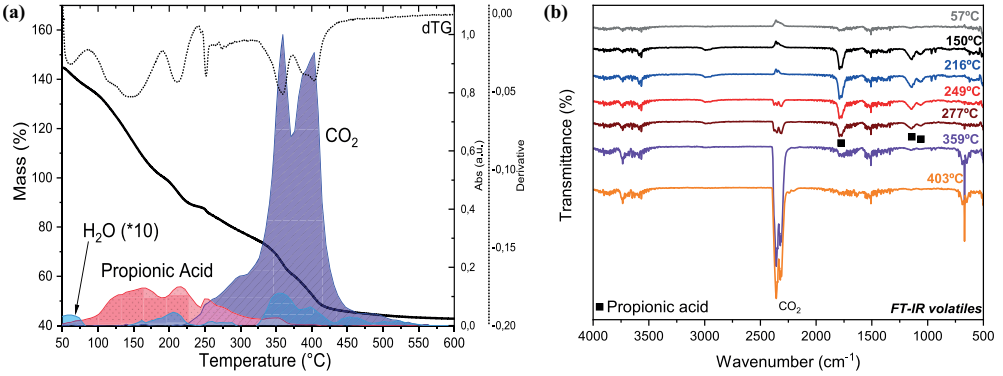


FIGURE 3.64: (a) TG curve, time derivative (dTG) and evolved volatiles obtained through EGA-FTIR registered in a humid O_2 flow relative to the decomposition process of a film deriving from an optimized solution with En. (b) FTIR spectra corresponding to the major mass losses observed in the TG curve, with identification of the detected volatile and indication of the temperature matching each spectrum.

roughly continuous mass loss up to over 400 ºC. Mass losses below 150 ºC are expected to be due to solvent evaporation, and the release of HProp is be an indication of the occurrence of this process. However, no evidence of the successive oxidation of the propionate groups may be found when the temperature is increased: no acetaldehyde is released during the entire thermal treatment and significant evolution of CO_2 only occurs at temperatures above 325 ºC. Moreover, the characteristic temperatures for the decomposition of each individual metal propionate determined in 3.2.6 are not followed here. Presumably, a different decomposition pathway is leading to the formation of the desired crystalline phases. Peaks attributable to En or species resulting from its decomposition, other than the identified ones, could not be detected. This may be due to different reasons, one of these being a possible oxidation of En through a radical path [183]. The FTIR spectra corresponding to each main mass loss (coinciding with the peaks at specific temperatures in the time derivative dTG curve), are confirming the sole presence of HProp, CO_2 and H_2O. The collected information is insufficient to exactly determine and propose a decomposition pathway for the metal propionate precursors in this film. Additional data regarding the intermediate species formed during the process would be extremely beneficial: their identification would be supposedly possible, for example, by performing quenches at the temperatures corresponding to the major mass losses followed by FTIR and XRD characterization of the film at that moment. Due to time constraints, this determination was regrettably not possible, and establishing the novel decomposition pathway is pending. Nonetheless, the comparison with the TG curve exhibited by an optimized solution

with MEA, displayed in Fig. 3.65, depicts the enormous difference in the decomposition profile followed by this kind of solution: as solutions with En are resulting in nanocrystalline precursor films with the desired phases for the TLAG process, it may be of great interest to deepen the lacking knowledge regarding their decomposition mechanisms. The mass of the final residue, however, must be carefully taken into consideration: being 36% the theoretical value for a dried precursor solution of 1.5 M + 12%$_{v/v}$ En, the resulting 44% is implying an 8% discrepancy. One of the most common difficulties when employing organic additives in solution is their complete elimination during the pyrolysis process: residual organic matter is detrimental if this is remaining as carbon contamination in the grain boundaries of the final YBCO, reducing importantly the physical properties of such superconducting films [149]. The possibility of this occurring to films obtained through optimized solutions with En cannot be discarded at this moment, and whether its consequence may be observed in the grown films will be addressed in Chapter 4.

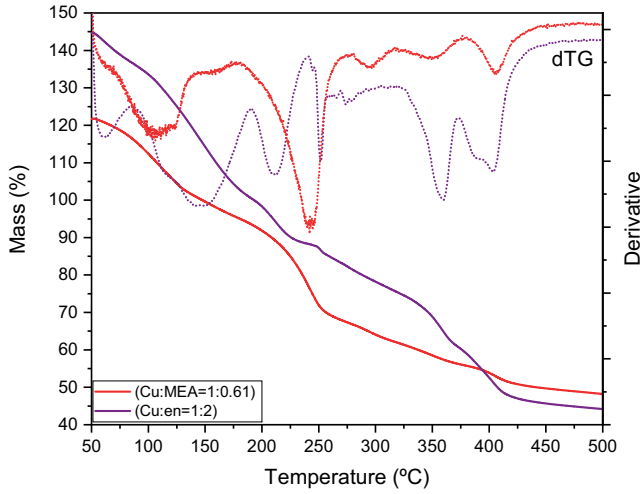


FIGURE 3.65: Comparison of TG and time derivative (dTG) curves for optimized solutions with En (purple) and MEA (red) registered in a humid O_2 flow following the thermal profile of the pyrolysis process.

For what concerns solutions with Py and the mixture MEA-Py, Fig. 3.66 shows the TG curves and the data from the coupled EGA-FTIR for both cases. The two solutions are following the expected hydrolysis and oxidation decomposition pathway, as it can be confirmed by the evolution of the characteristic volatiles. Contrarily to what observed in the solution with En, here a signal of Py could be detected: in both solutions, its appearance below 200 ºC indicates that the degradation of this additive is occurring prior to any major decomposition step, recalling that Cu(Prop)$_2$ is the first one taking place between 200 ºC and 250ºC. Moreover, as demonstrated in depth in [126], the appearance of cracks is enhanced close to the temperature

of 240 ºC. It is easily noticed how, in the TG curve relative to the film with Py alone, the greatest mass loss (72.8% of the total) is occurring uniquely in one step which comprises solvent evaporation overlapped by the initial decomposition of the propionate groups. Films obtained by deposition of solutions with Py alone resulted in inevitable cracking, as shown in Fig. 3.52, and the reason for this may now be clarified after examining this TG curve.

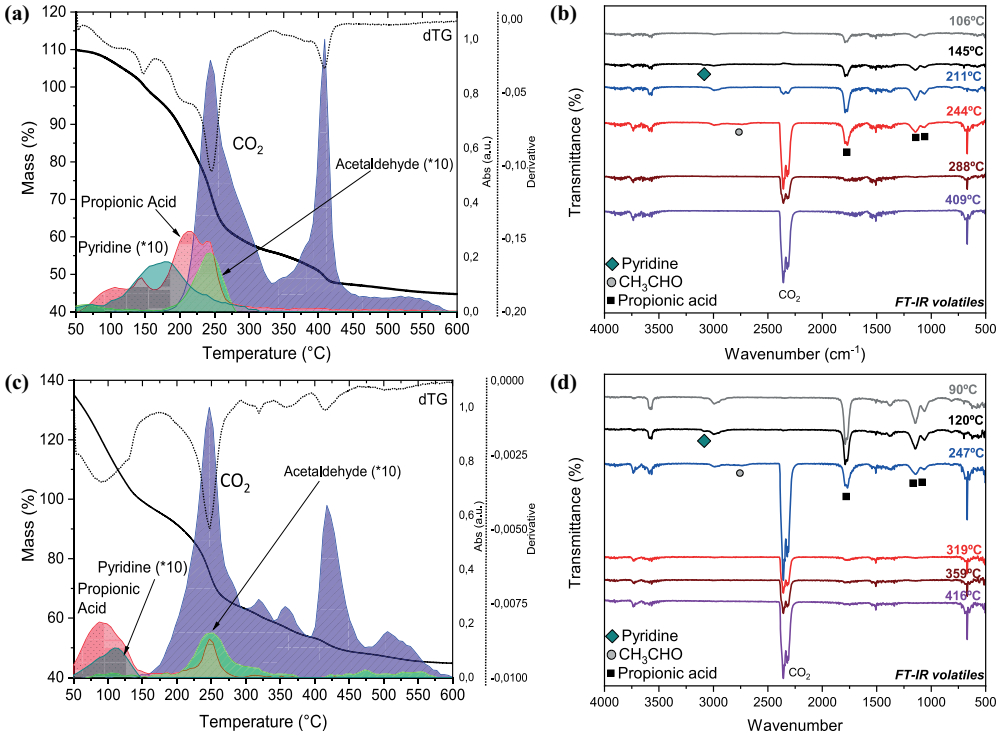


FIGURE 3.66: TG and time derivative (dTG) curves together with the evolution of the detected volatiles for a solution of (a) 2.3 M + 4.62%$_{v/v}$ Py and (b) 2 M + 4.53%$_{v/v}$ MEA + 4.02%$_{v/v}$ Py, registered in a humid O_2 flow. (c)-(d) FTIR spectra corresponding to the major mass losses of the TG curves in (a) and (b), respectively, allow for the identification of the evolved volatiles. Corresponding temperature of each spectrum is specified.

Despite the unfavourable morphological features, these films are yielding the desired crystalline phases for TLAG, and the mass of the final residue of the TG experiment is in good agreement with the theoretical value, being the former 43.8% and the latter 44.7%. A different situation is exhibited by the TG curve of the solution in which the mixture of MEA and Py is employed. The detection of Py is, once again, during the solvent evaporation step, confirming its complete evolution before the initiation of any degradative process. Nonetheless, the evaporation of the solvents and the first major mass loss occur in two easily discernible steps, resulting in a less drastic mass loss over the same temperature range. This TG curve seems to

follow thoroughly the thermal behaviour of a film deriving from the optimized solution with MEA. The successive gas evolution is attributable to the oxidation of the propionate groups of barium and yttrium precursors: the former decomposing through the oxalate intermediate to $BaCO_3$ and the latter yielding the final sesquioxide through the oxycarbonate, both by release of CO_2 (described in detail in Chapter 2). The formation of these crystalline phases, preferred for the application of these films in the TLAG process, was previously confirmed by XRD (Fig. 3.53) and is additionally proven by the mass of the final residue (44% compared to the 40.3% of the theoretical value). A comparison of the TG and time derivative (dTG) curves of the films deriving from the solutions with Py and MEA-Py with the case of the optimized solution with MEA is displayed in Fig. 3.67. The almost identical thermal behaviour between both solutions containing MEA is clearly evinced: the slight shift towards higher temperatures relative to the film of MEA-Py may be due to the higher film thickness. Similarly, the higher initial mass loss from solvent evaporation may be given by the high viscosity of the solution, which, additionally to the elevated film thickness, may hinder a complete drying of the film performed on a pre-heated heating plate before the TG experiment. These TG curves are decisive proof of the beneficial nature of MEA in solutions. The film deriving from the solution with Py alone, as mentioned before, exhibits a large mass loss concomitant to the temperature range where crack formation is favoured and is, in fact, matching the morphological outcome

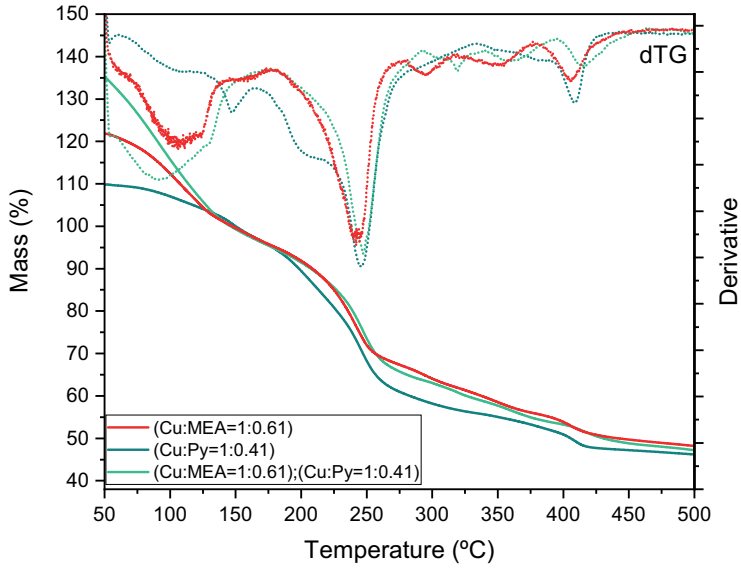


FIGURE 3.67: Comparison of TG and time derivative (dTG) curves for optimized solutions with Py (dark aquamarine), mixture of MEA and Py (light aquamarine) and MEA (red) registered in a humid O_2 flow following the thermal profile of the pyrolysis process.

of the pyrolysis process. When MEA is added in the solution, the mass losses in the TG

curve are less pronounced: it is believed MEA is enhancing the elastic properties of the film, granting major resistance towards crack formation result of the inevitable gas evolution during the thermal treatment. This is effectively reflected in the smooth morphology obtained from the films containing the mixture of MEA and Py, despite their thickness is as elevated as the case of Py alone. Hence, the addition of MEA in the solution is necessary to ensure a high-quality morphology, whereas the inclusion of Py allows for an important increase of the concentration of the solution, which finally results in films of enhanced thickness.

3.4.4 Microstructural analysis of films deriving from solutions with different amine additives

The previous subsections validated the compatibility of different amine additives other than MEA for their application in the YBCO precursor solutions used for TLAG-CSD. Films resulting from the depositions of such solutions display the presence of the desired crystalline phases, confirmed through XRD measurements. Through a variety of TEM techniques, a comprehensive microstructural analysis is carried out to assure the sizes, homogeneity and distribution of the crystalline phases is in accordance with the strict requirements necessary for a highly epitaxial growth through TLAG.

Alas, the rough surface presented by the films deriving from optimized solutions with En hinders the preparation of TEM lamellae through conventional methods. Thus, the analysis of their microstructure through TEM had to be discarded for the moment.

Films obtained from solutions with the mixture of MEA and Py display a homogeneous and smooth surface, thus presenting no difficulties for their TEM analysis. Therefore, the microstructure of a film of one layer obtained from a solution of 2.5 M + 5.66%$_{v/v}$ MEA + 5.04%$_{v/v}$ Py was studied. The film presents a smooth surface and an elevated thickness, as observed for the previously analyzed films obtained from optimized solutions with MEA in 3.2.3. However, given the high concentration obtained through Py addition, the thickness of this one-layered film is 760 ± 10 nm, almost double of a single layer of an optimized solution with MEA, as observed in the cross-sectional STEM-HAADF image in Fig. 3.68. Through the analysis of these images employing the software ImageJ, the porosity of the film could be determined: the estimation of the pore density results in $2.5 \pm 0.15\%$. The increased porosity may be due to the result of the pronounced gas evolution during decomposition of the metal propionate precursors on such an extreme thickness, as well as to the presence of Py in solution. Moreover, the porosity is varying throughout the film, with the top portion presenting a more dense and compact aspect. This may be an indication of a non homogeneous distribution of the crystalline phases. Thus, to evaluate this, EELS was employed to acquire elemental maps for $CuL_{2,3}$ edge, $BaM_{4,5}$ edge and OK edge. These are evidencing a similar situation already observed in the films from solutions with MEA, with high homogeneity maintained throughout the whole layer. Nonetheless, the sole presence of Ba is found in the area of the

film which appeared more dense, implying a slight Ba-rich segregation.

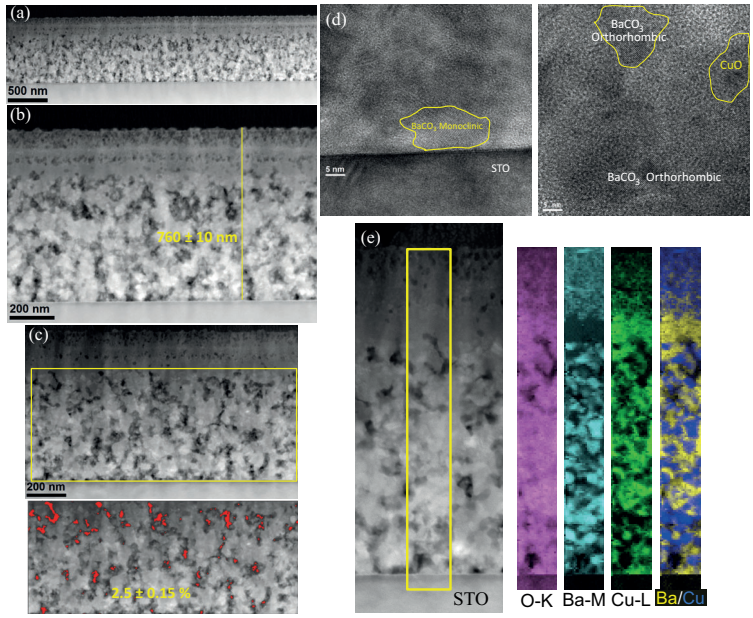


FIGURE 3.68: (a) Cross-sectional STEM-HAADF of a one-layered film deriving from a solution with MEA and Py in optimal (Cu:amine) molar ratios. Thickness of the film is determined in (b) to be 760 ± 10 nm. (c) Analysis of the STEM-HAADF image through software ImageJ results in a value of porosity of $2.5 \pm 0.15\%$. (d) HR-TEM images identifying the nanocrystalline phases of CuO and $BaCO_3$. (e) EELS elemental maps for $CuL_{2,3}$ edge, $BaM_{4,5}$ edge and OK edge demonstrate the homogeneous distribution of the phases throughout the entire film.

Considering its reduced thickness, it is not expected to hamper the homogeneous formation of the transient liquid. However, a possible effect of this will be assessed later on the grown films in Chapter 4. As previously explained in 3.2.3, the importance of small sized crystalline phases for a fast reactivity in the TLAG process requires their precise determination through HR-TEM, which can provide relevant information regarding their typical sizes, spatial distribution and crystalline state. CuO nanoparticles present typical diameters of 24 nm. The XRD in Fig. 3.53 confirms $BaCO_3$ is present in both its orthorhombic and its monoclinic phase, with the former being the major contribution. In the HR-TEM images, this is clearly evidenced, with average grain sizes of 32 nm for the orthorhombic phase and 15 nm for the monoclinic phase. The latter shows coarsening effects in the grains which are found closer to the substrate-film interface. Possibly, given the elevated thickness of the film, the area near the substrate may be subjected to a more challenging elimination of volatiles: this may create a reducing atmosphere, as previously observed in the extreme case of films with MEA excess in 3.2.4, where the combination of this with a severely reduced porosity favoured the formation

of large grains of $BaCO_3$ monoclinic and the full reduction of CuO to Cu(0). In this film, however, the generally adequate porosity is facilitating the gas evolution, resulting in only a minor coarsening effect. Nonetheless, in films presenting such increased thickness, porosity is a parameter which must be strictly controlled if the nucleation of unfavourable phases wants to be avoided.

The presented microstructural analysis revealed that films obtained through the deposition of optimized solutions with the combination of MEA and Py are showing the required features for their application of TLAG. The high nanoscale homogeneity conferred by MEA together with the extremely elevated thickness of the film given by the possibility of increasing the concentration of solutions due to Py inclusion is enabling a further thickness enhancement respect to films of optimized solutions of MEA alone, promoting TLAG-CSD towards an even more successful industrial application.

3.5 Conclusions

A comprehensive analysis of various precursor solution systems has been provided in this chapter. The full optimization process for the YBCO precursor solution, which has led to the introduction of an amine additive, was thoroughly described. The amine additive, MEA, was demonstrated to enhance the concentration and stability of solutions, and the final thickness of the films while ensuring a high homogeneity on the macroscale and on the nanoscale, yielding the desired microstructural characteristics for their successive application in the TLAG process. The process of multideposition of this solution confirmed its great potential for its use in the industrial framework, as films of up to 2.7μm through an eight-fold deposition were successfully prepared, without consequences due to the process on the homogeneous nature of the films. A detailed microstructural analysis through a variety of TEM techniques demonstrated the films were fulfilling all of the appointed requirements and evidences the extremely beneficial nature of the amine additive for the objective proposed. Different techniques were used to shed light on the role of MEA in solution, and the vast information retrieved from rheological, NMR, EPR, and TG-FTIR analyses allowed for a complete understanding of the complex chemical system.

The knowledge obtained through the optimization of the YBCO solution could be further extended to three REBCO systems, by employing the pre-synthesized metal propionates of samarium, gadolinium and ytterbium described in Chapter 2. The effect of the change of the RE was assessed, showing no evidence of significant variations either on the chemical properties of the solutions or on the microstructural features of the nanocrystalline films.

A preliminary study on the feasibility of introducing novel amines as additives for the YBCO precursor solutions led to the analysis of the effect of eight new amine compounds, three alkyl amines and five aromatic amines. The compatibility of each in solution has been tested and the effect on the outcome of the nanocrystalline films investigated. The initial experiments

resulted in the selection of solutions with one amine additive from each of the two families, specifically ethylenediamine for the alkyl amines and pyridine (in a mixture with MEA) for the aromatic amines. The optimised solutions of both cases underwent an extensive study of their chemical properties and thermal behaviour to seek compatibility with the TLAG-CSD process. In both cases, the decomposition of the metal-organic solutions containing these amine additives resulted in films composed by the desired nanocrystalline phases after the pyrolysis process, setting a promising foundation for the following TLAG process. Moreover, the case of the mixture of MEA and Py demonstrated the feasibility for an important thickness enhancement, leading to the thickness of one layer being the equivalent to two layers of the optimised solution with MEA only. This result is especially interesting when considering the future implementation of TLAG in industrial framework: the thickness of the film may be precisely tuned only through small variations of the chemical properties of the precursor solution. Finally, microstructural analysis on one of these cases confirmed the presence of the favourable features for TLAG.

The result of the use of all aforementioned solutions on the final epitaxial films obtained through the TLAG process will be discussed in the following Chapter 4.

4

Kinetic control of the TLAG process: intermediate phases and epitaxy development

In the current chapter the effort towards a full optimization of the TLAG process will be described. The high morphological and microstructural reproducibility of the nanocrystalline precursor films with optimal characteristics described in the previous chapter allowed for a thorough analysis of the several parameters controlling the complicated TLAG process, revealing the fundamental ones requiring a precise adjustment. As mentioned in Chapter 1, the complete elimination of the barium precursor phase, $BaCO_3$, is mandatory, being this the limiting step for the transient liquid formation. For this reason, a comprehensive analysis of this initial step is relevant towards the optimization of high-performance superconducting YBCO films, and will be object of the entire first section: here, various kinetic parameters will be taken into consideration with the aim of obtaining the optimal crystalline phases which favour a straightforward formation of the transient liquid. TLAG was then performed on a large variety of films, starting with an initial optimization focused on the (3:7) liquid composition, followed by investigation on films of different thickness, and successively pursuing the understanding of the effect of a variation in the transient liquid composition, considering the change in the supersaturation as the copper content is increased from the stoichiometric case. Finally, preliminary results on the growth of films deriving from variations of the standard solution will be presented, described in 4.5 and 4.6, showing possible strategies for novel solution

formulation, including different amine additives and other RE systems, yet resulting in high-performance superconducting films and opportunities of TLAG, respectively, for modulation of film characteristics and beyond the sole YBCO system.

4.1 Objectives

One of the most considerable challenges for the fabrication of HTS is the possibility of increasing the film thickness while maintaining high-performance physical properties. In the framework of the ERC project, unprecedented critical current density (J_c) values could be obtained through TLAG on films of 90 nm thickness [53], demonstrating the feasibility of this innovative method for a possible future industrial application if the thickness of the films can be increased without compromising the superconducting properties. Through the optimised chemical solution described in Chapter 3, homogeneous pyrolyzed films of up to $2.7 \pm 50\,\mu$m thickness were achieved, suggesting a promising foundation for the following TLAG process. Nonetheless, the initial optimization of YBCO growth through TLAG was carried out exclusively on films of (3:7) composition which underwent a double multideposition process (800 ± 50 nm after pyrolysis process) and consisting in a final YBCO thickness of 450 ± 50 nm, then extended to other specific cases.

As explained in detail in Chapter 1, two routes are possible for TLAG of YBCO films. The Temperature Route (*T-route*) consists in heating the films employing fast heating ramps at a constant oxygen partial pressure (P_{O_2}) until the desired temperature is reached. In this case, the elimination of $BaCO_3$ and the transient liquid formation are observed consecutively while heating, and the elevated heating ramps are beneficial to minimize the nucleation of thermodynamically favoured secondary phases. Contrarily, the Oxygen Partial Pressure Route (P_{O_2}-*route*) advantageously decouples the elimination of $BaCO_3$ from the transient liquid formation and YBCO nucleation step. This is achieved by performing the heating at low P_{O_2} below the YBCO instability line (T_{ins}), thus in an area of the *T*-P_{O_2} phase diagram where YBCO is not expected as a crystalline phase. During this step, the elimination of $BaCO_3$ *via* its reaction with CuO yields the formation of the mixed Ba-Cu oxide $BaCu_2O_2$ and Cu_2O, the crystalline precursor phases for the formation of the transient liquid through this growth route. Successively, a rapid variation of the P_{O_2} of the system is performed, crossing several orders of magnitude of P_{O_2} in a time range of seconds during which the transient liquid formation and, subsequently, YBCO nucleation from the liquid are occurring. A schematic representation of both routes may be found in Chapter 1 (Fig. 1.6). The expected reaction path for TLAG P_{O_2}-*route* is expressed by the following equation:

$$\begin{aligned} BaCO_{3(s)} + CuO_{(s)} + Y_2O_{3(s)} \rightarrow BaCu_2O_{2(s)} + Cu_2O_{(s)} + Y_2O_{3(s)} \rightarrow \\ \rightarrow [Ba - Cu^{(I/II)-O}]_{(l)} + Y_2O_{3(s)} \rightarrow YBa_2Cu_3O_{7-\delta} \end{aligned} \tag{4.1}$$

Formation of the solid phases in the upper line of eq. 4.1 is depicting the reactions occurring during the low-P_{O_2} step, at P_{O_2} values ranging between 10^{-5} bar and 10^{-6} bar. The lower line, is instead referring to the rapid pressure change in which YBCO is nucleating and growing from the [Ba-Cu-O] transient liquid, where copper may show different oxidation state depending on the specific processing conditions. It must be taken into account that equation 4.1 is, here, not stoichiometrically balanced. It is solely describing a general mechanism without considering the specific transient liquid composition. Nonetheless, for compositions with copper excess, the final step should result in the formation of stoichiometric YBCO together with copper oxide (CuO and/or Cu_2O, once again depending on the growth conditions) given its overabundance in these compositions. Ideally, in optimally selected T-P_{O_2} conditions, copper oxide grains will be expelled to the surface of the film through pushing effects characteristic of a high c-axis nucleation, thus not impeding current percolation. In this thesis, experiments regarding only the P_{O_2}-*route* were carried out and the entirety of the current chapter will be focused on the optimization of the growth of YBCO (and, partially, other REBCO systems) through the latter route of TLAG with the aim of understanding the thermodynamic and kinetic parameters controlling the process. Special focus will be given to the role of liquid supersaturation, with a detailed analysis of TLAG from films of five different liquid compositions seeking a comprehensive understanding of the effect of supersaturation in the growth from a transient liquid.

4.2 Analysis of $BaCO_3$ elimination

One of the most renowned drawbacks initially considered for the growth of YBCO through CSD-based methodologies employing fluorine-free metal-organic chemical solutions is the formation of $BaCO_3$ as the barium precursor phase [89, 90]. It was considered undesirable given its exceedingly high thermal stability, possibly hindering the entire growth process [42, 91]. In powders, its decomposition temperature is found above 1000 ºC [92, 93], thus beyond the processing temperature for YBCO superconductors, implying a major complication to the material fabrication. However, it was demonstrated that, in sintered oxide powders of (Ba-Cu-Y) ternary systems, the decomposition temperature of $BaCO_3$ could be reduced up to 200 ºC, given the catalytic effect of CuO and Y_2O_3 phases and through the use of slow heating rates of $dT / dt = 1$ ºC/min [93]. Nonetheless, through the use of TLAG, it was previously and thoroughly demonstrated the presence of this phase not to be an obstacle for the growth of high-performance YBCO films [51–54, 101]. However, the referenced previous work conducted in SUMAN group was carried out on films deriving from a commercial metal-acetates-based chemical solution which led to different microstructural features of the nanocrystalline precursor films for TLAG: besides the lower thickness, a fundamental characteristic was found to be the higher porosity of these films, ranging between 5 and 17 % [51], especially beneficial as

the elimination of $BaCO_3$ is obtained through CO_2 out-diffusion. Given the contrasting microstructure exhibited by the films described in this thesis, a thorough analysis regarding exclusively the $BaCO_3$ elimination step was necessary, as the elevated thickness and the extremely reduced porosity compared to previous cases may result in a complication to the success of this step of the process. If not otherwise specified, the following results are regarding two-layered (3:7) composition pyrolyzed films, presenting a thickness of 800 ± 50 nm and estimated pore density of $1.0 \pm 0.2\%$ prior to the thermal treatment.

4.2.1 Heating ramp effect: reducing coarsening of secondary phases

Throughout the experimental work performed during the years of this PhD thesis, the growth furnace employed to realize TLAG P_{O_2}*-route* experiments was improved in several ways. Certainly, the most important modification of the set-up has been the possibility of significantly increasing the heating rate of the thermal profile, and a detailed description of both the set-up and the strategy used to accomplish this may be found in Appendix D. Fig. 4.1 shows a

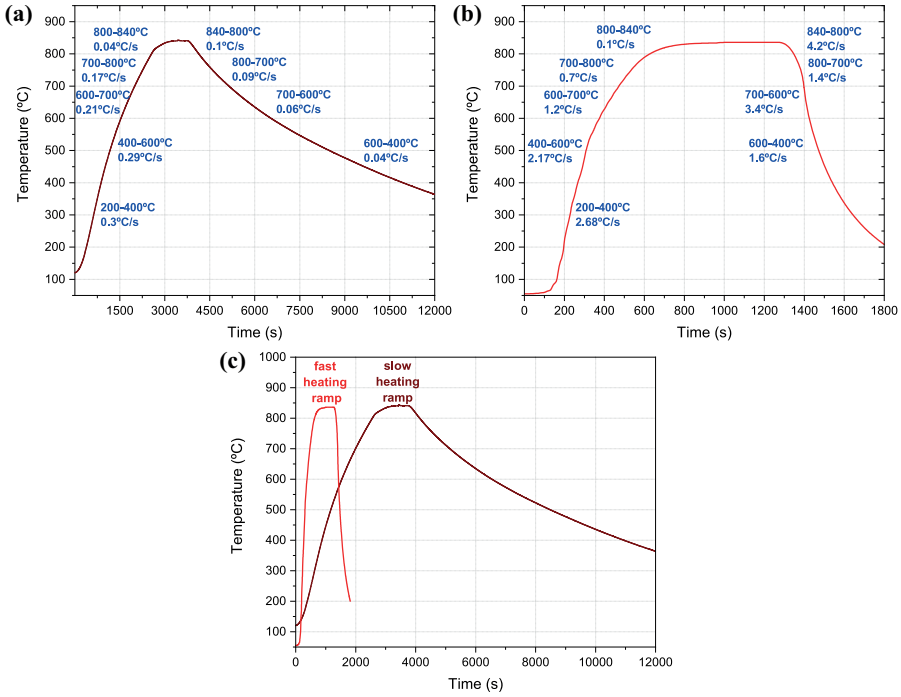


FIGURE 4.1: Thermal profiles of (a) standard slow heating ramp (average heating rate is $dT / dt = 0.2$ °C s^{-1}) and (b) standard fast heating ramp (average heating rate is $dT / dt = 1.4$ °C s^{-1}), with maximum $T_{set} = 835$ °C in both cases. Linear fits were used to determine the heating rate (dT / dt), calculated on several temperature ranges (of 200 °C or lower) due to the non-linearity of the heating profile. (c) Comparison of the two thermal profiles in (a) and (b), showing the impressive reduction of the total processing time when the fast heating ramp is employed.

comparison between the two standard thermal profiles employed: a slow heating ramp with an average heating rate of $dT / dt = 0.2$ ºC s^{-1}, opposed to the case of a fast heating ramp in which the average heating rate is $dT / dt = 1.4$ ºC s^{-1}, as indicated in Table 4.1.

Type of heating ramp	Average (dT/dt) Heating (ºC/s)	Total time Heating (min)	Average (dT/dt) Cooling (ºC/s)	Total time Cooling (min)
Slow	0.2	58	0.07	150
Fast	1.4	15	2.7	9

TABLE 4.1: Comparison between slow and fast heating ramp parameters, indicating the great differences between average heating and cooling rates, and total time of both processes for the standard heating ramps shown in Fig. 4.1.

By implementing the fast heating ramp, the total heating time could be reduced by a factor 4 and, more impressively, the total cooling time by a factor 16. This was anticipated to be extremely beneficial as the films would be exposed to increased temperatures for shorter time ranges, reducing the coarsening of the precursor phases during heating.

To confirm the feasibility of a complete elimination of $BaCO_3$ in the films described in this thesis, quench processes were performed, consisting of carrying out solely the first step of the TLAG P_{O_2}-*route* experiment. Thus, the film is heated at low P_{O_2} until the desired temperature is reached and then cooled down as rapidly as possible at the same, constant P_{O_2}. This allowed to identify the crystalline phases of the film[1] at the moment prior to executing the fast P_{O_2} variation, and decide whether the crystalline phases are favourable for a straightforward formation of the transient liquid in the following step of an eventual growth process. The processing conditions chosen for a standard quench process, result of initial optimization trials, are the following: a base pressure ($P_{O_{2,base}}$) of 10^{-5} bar and a set temperature (T_{set}) of 835 ºC. Several kinetic parameters will be varied in the subsequently reported results with the aim of determining the optimal conditions for $BaCO_3$ elimination in this process. As indicated by the processing times of heating and cooling shown in Table 4.1, the set-up employed for the experiments with slow heating ramp was limiting a rapid execution of the cooling, and possible effects of this on the microstructure will, thus, have to be considered.

Fig. 4.2 displays the grazing-incidence XRD (GIXRD) patterns of two films which underwent quench processes through the use of the aforementioned heating ramps. Evident differences

[1] Determination of the crystalline phases after the quench process was obtained through grazing-incidence XRD (GIXRD) measurements. Details regarding the specific measurement conditions are presented in Appendix D.

may be observed in the resulting XRD patterns, the most striking being the presence of reflections corresponding to numerous phases in the quenched film when using a ramp of 0.2 ºC s^{-1} (Fig. 4.2(a)).

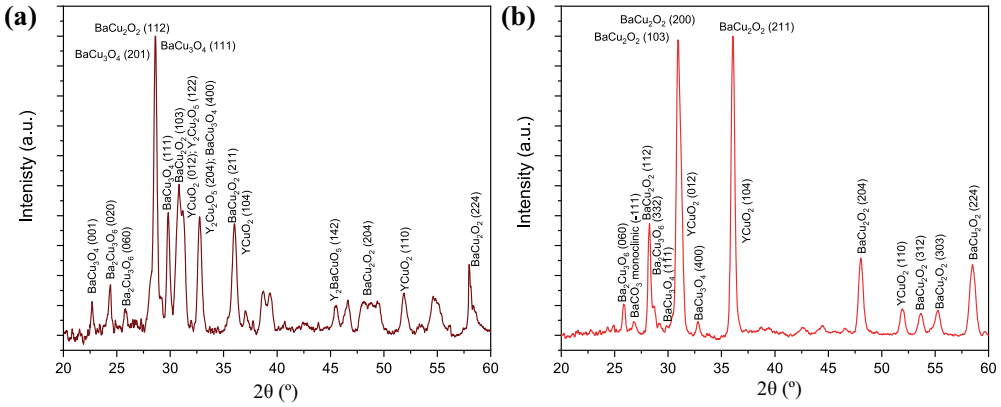


FIGURE 4.2: GIXRD of two (3:7) composition films subjected to quench processes at $P_{O_{2,base}} = 10^{-5}$ bar heated to $T_{set} = 835$ ºC with (a) a slow heating ramp (average heating rate of $dT/dt = 0.2$ ºC s^{-1}) and (b) a fast heating ramp (average heating rate of $dT/dt = 1.4$ ºC s^{-1}).

The film quenched through the use of the slow heating ramp exhibits the desired majoritarian phase, $BaCu_2O_2$, found amongst a mixture of various others: the mixed oxides of yttrium and copper, $YCuO_2$ and $Y_2Cu_2O_5$, the Y_2BaCuO_5 ((211) phase), its presence being extremely undesirable at this moment of the process, and the Ba-Cu mixed oxide $BaCu_3O_4$. In the second film, which was subjected to a quench process using an average heating rate of 1.4 ºC s^{-1}, $BaCu_2O_2$ is indisputably the principal contribution observed, together with only minor peaks due to $YCuO_2$ and $BaCu_3O_4$. The variation of intensity deriving from contributions of additional and undesired secondary phases may find an explanation in the extreme discrepancy between the heating rates employed. Films subjected to a slow heating ramp would experience temperatures above 600 ºC for over two hours considering heating and cooling, favouring greatly grain coalescence once the first nuclei are formed. The possibility of these phases to be enlarged by the extremely slow cooling process is, indeed, very high, despite the cooling not being relevant for the successive step of the TLAG process. The presence of $Y_2Cu_2O_5$, only visible in the case of this specific quench process, is an indication of the transformation from the Cu(I) to Cu(II) oxidation state mixed oxide due to the fact that, during the slow cooling, the system is crossing several areas of the phase diagram slowly enough to allow for their transformation. Moreover, the dual presence of both phases of Y-Cu mixed oxide suggests that also the slow heating is playing a role in the formation of large grains of $YCuO_2$ phase, favoured at higher temperatures [184]. A further indication of important coarsening effects when the slow heating ramp is employed is the intensity of the peaks of the $BaCu_3O_4$ phase, which displays

a stronger contribution if compared to the same phase in the film quenched with increased heating rate. Likewise, the Debye-Scherrer crystallite size for $BaCu_2O_2$ grains is in the range of 44 nm for the films quenched by heating at 1.4 ºC s^{-1}, and up to 70 nm for the films heated at 0.2 ºC s^{-1}. Despite being the desired crystalline phase, its coarsening is not ideal towards a fast reaction in the successive step of the process: the presence of large grains prolongs their melting and hinders the straightforward formation of the transient liquid. It must be specified that an insignificant contribution from $BaCO_3$ monoclinic is present in the film quenched with fast heating ramp, contrarily to the case of slow heating, in which no contribution from any of the barium carbonate precursor phases can be identified. For the given film thickness and microstructure, the elimination of $BaCO_3$ is, here, kinetically controlled by the heating rate and the fast heating ramp is allowing for the complete removal of the orthorhombic phase of $BaCO_3$, but not for its monoclinic one. This is in accordance with other works, in which the monoclinic phase of $BaCO_3$ is notably showing higher thermal stability at reduced oxygen partial pressures [52, 93]. Despite this minor contribution from $BaCO_3$ monoclinic, the combination of $BaCu_2O_2$ being the majoritarian phase with smaller grain size and the absence of detrimental and coarsened secondary phases is an indication that the use of the fast heating ramp is anticipated to be advantageous towards a successful growth of YBCO through TLAG in this particular route and for these particular films. From this starting point, the effects of different kinetic parameters, such as dwell times, set temperature, and base pressure, will be modulated with the aim of demonstrating the complete elimination of $BaCO_3$ is possible in this kind of system, additionally for different film thickness. The use of the slow heating ramp is thus discarded, given the unfavourable abundance of coarsened secondary phases and the non-exclusive formation of the $BaCu_2O_2$ mixed oxide. Moreover, the poor epitaxy and low-performance physical properties demonstrated from the growth of YBCO films employing the slow heating ramp confirmed its unfavourable application in the TLAG process.

4.2.2 Consequences of increasing dwell time

As shown in Fig. 4.2(b), the elevated heating rate employed results in a remaining contribution from the monoclinic phase of $BaCO_3$, and despite it being only minor, its presence is not desirable in the following step of the process. In fact, the rapid P_{O_2} variation results in the transformation of the solid $BaCu_2O_2$ and Cu_2O phases into the [Ba-Cu-O] transient liquid: a large amount of $BaCO_3$ present at this moment would necessarily require its reaction to form $BaCu_2O_2$ first, which will then follow the expected mechanism. However, the change in P_{O_2} is occurring in a time range of seconds, and any solid transformation deflecting from the TLAG mechanism will inevitably complicate and slow down YBCO nucleation. As a result, if $BaCO_3$ is reacting during the P_{O_2} jump, the transient liquid formation will be inhomogeneous throughout the film and possibly shifted at higher P_{O_2} values, consequently initiating the Y_2O_3 dissolution and YBCO nucleation at unfavourable P_{O_2} conditions for full c-axis growth. This

issue will be thoroughly discussed later on in this chapter and in Chapter 5, regarding *in-situ* XRD experiments on the TLAG P_{O_2}*-route* process, in which the particular set-up conditions are shown to affect the elimination of $BaCO_3$ in specific cases and a detailed analysis of the consequence of this on the transient liquid formation will be presented. Here, to ensure the complete elimination of $BaCO_3$ during the low-P_{O_2} heating, different kinetic parameters were analysed, beginning with the implementation of various dwell times after reaching T_{set}. Fig. 4.3 displays the GIXRD acquired on three films quenched at the same T_{set} of 835 ºC (at constant $P_{O_{2,base}} = 10^{-5}$ bar) which were subjected to dwells of 0, 2 and 5 minutes once the T_{set} was reached. It is evident that formation of the majoritarian crystalline phase of $BaCu_2O_2$ is comparable in the three experiments, displaying no variation in intensity or broadness of the peaks, thus suggesting no relevant differences in its grain size or crystallinity. However,

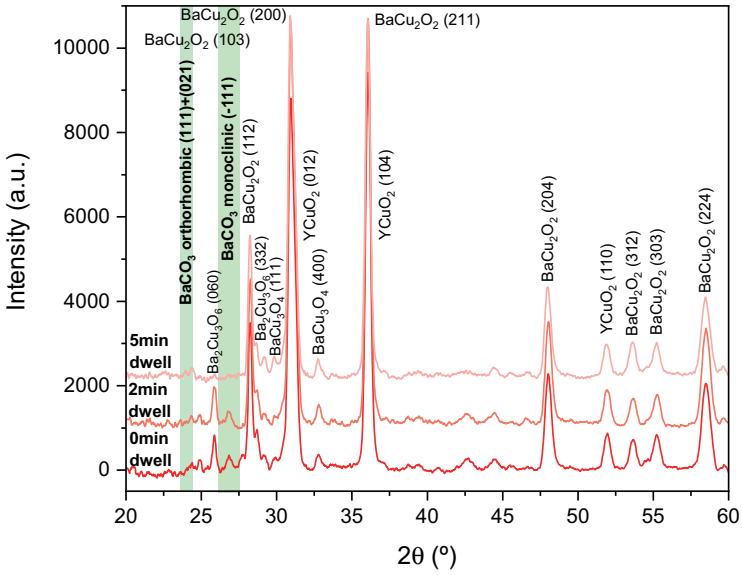


FIGURE 4.3: GIXRD of three films subjected to quench processes with increasing dwell times of 0, 2 and 5 minutes duration once the T_{set} = 835 ºC was reached. 2θ ranges relative to peaks of $BaCO_3$ phases are highlighted in dark and light green, corresponding to the orthorhombic and the monoclinic phases, respectively.

shifting the focus on the elimination of $BaCO_3$, one can observe how the films from experiments with 0 and 2 minutes dwell times are both showing the presence of peaks relative to this phases. Contrarily, an increase of the dwell time to 5 minutes is sufficient to eliminate completely all contributions deriving from $BaCO_3$, indicating the elimination of this phase may be kinetically controlled through longer dwell time. Considering the same heating rate, film thickness and microstructure, the process of $BaCO_3$ elimination is regulated by CO_2 outdiffusion: as the porosity of these kind of films is as low as $1.0 \pm 0.2\%$, gas removal may be

more demanding and short dwell times are not sufficient for it to reach completion. Fig. 4.4 displays a focus of the 2θ range corresponding to the $BaCO_3$ peak positions in the previously shown GIXRD of the three films discussed here. The integration of the peaks relative to the barium precursor phases allows for an understanding of the elimination of $BaCO_3$ as a function of the dwell time employed. As prime consideration, it must be noted that, despite the film quenched with no dwell shows the presence of minor peaks deriving from both $BaCO_3$ orthorhombic and monoclinic phases, their contribution is reduced to below 5% and below 15% for the orthorhombic phase and the monoclinic phase, respectively, if compared to the initial values after the pyrolysis process (taken as 100%).

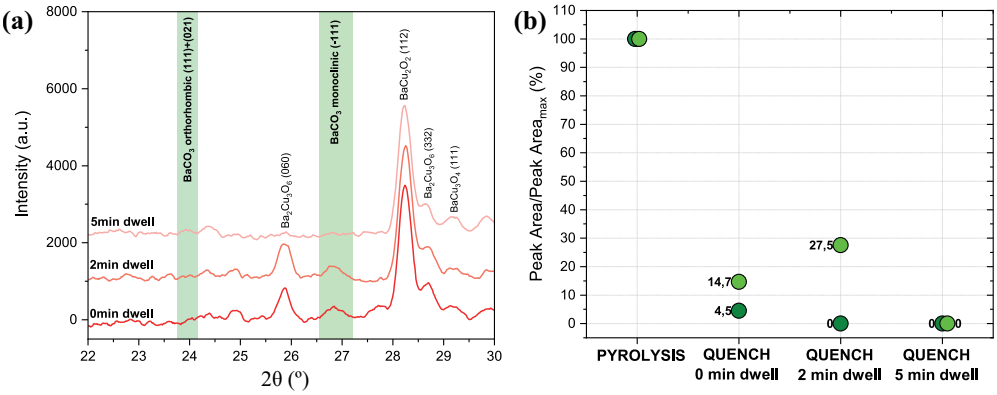


FIGURE 4.4: (a) Zoom in on the 2θ range corresponding to the $BaCO_3$ peak positions from the GIXRD of the three films quenched with $dT\,/\,dt = 1.4$ ºC s^{-1} to 835 ºC at $P_{O_{2,base}} = 10^{-5}$ bar shown in Fig. 4.3. (b) Representation of the percentile peak area reduction relative to the $BaCO_3$ orthorhombic (dark green) and monoclinic (light green) phases after quench considering the maximum value to be the one resulting from the pyrolysis process.

When analysing the dwell time effect on the peak area relative to each phase, the film quenched without performing any dwell displays similar contribution from both orthorhombic and monoclinic phase of $BaCO_3$. Given the high heating rate, a complete elimination in this case is not reached due to the fast kinetics of the process which preclude a total CO_2 evacuation. If the dwell time is increased to 2 minutes, the orthorhombic phase of $BaCO_3$ is completely removed, whereas an increase in the peak area of the monoclinic phase is observed here. This may be due to the partial amorphous nature of the nanocrystalline precursor films: in the HR-TEM images in Fig. 3.9 it is clear how the nanocrystalline phases of $BaCO_3$, CuO and Y_2O_3 are embedded in an amorphous matrix. Upon heating during the quench process, crystallization of amorphous phases may occur as the temperature is increased[2]. This is the case of the monoclinic phase of $BaCO_3$, which displays higher crystallinity when the film is subjected

[2]Crystallization of the precursor phases, especially $BaCO_3$, will be clearly observed during the low-P_{O_2} heating performed in *in-situ* XRD experiments at synchrotron facilities, reported in Chapter 5.

to a higher temperature for a longer time range. Finally, the film quenched with a 5 minute dwell confirms the possibility of a complete removal of both $BaCO_3$ phases, demonstrating the kinetics of the process may be modulated and a complete CO_2 evacuation is possible in the system described here, through a simple increase of the time at which the film is maintained at the same, elevated temperature.

4.2.3 Result of base pressure variation on film microstructure

The modification of a second processing parameter was examined and the GIXRD of two films quenched employing different $P_{O_{2,base}}$ are displayed in Fig. 4.5, with the tested values of base pressure being $P_{O_{2,base}} = 10^{-5}$ bar and $P_{O_{2,base}} = 10^{-6}$ bar. A dwell of 5 minutes was implemented in both cases, as previously demonstrated to be optimal for complete $BaCO_3$ elimination at $P_{O_{2,base}} = 10^{-5}$ bar. As for previously reported results, the same heating rate of $dT / dt = 1.4$ °C s^{-1} was employed and both films were heated at a final T_{set} of 835 °C. Despite the formation of comparable crystalline species, noticeable variations between the resulting XRD patterns are observed, with the film quenched at lower base pressure generally displaying broader and less intense peaks of the majoritarian solid phase of $BaCu_2O_2$. Moreover, despite no orthorhombic $BaCO_3$ is present, a contribution deriving from the monoclinic is visible, demonstrating that the complete removal of CO_2, and as a result, $BaCO_3$, is not fully achieved in these conditions. Apart form the kinetic control of the process through heating rate and dwell time, an explanation for this result may additionally be found in the thermodynamic equilibrium lines for gas solid-reactions relative to O_2/CO_2 [95]. Both the oxygen partial pressure (P_{O_2}) and the carbon dioxide partial pressures (P_{CO_2}) play key roles in the elimination of $BaCO_3$, however through opposed effects. Specific P_{O_2} conditions will determine the oxidation state of copper in the system, thus regulating the formation of Cu_2O or CuO, and $BaCu_2O_2$ or $BaCuO_2$. As stated, the working conditions in TLAG P_{O_2}*-route* are fixed at low oxygen partial pressures during the heating, therefore only the reduced phases of copper will be formed.

Contrarily, P_{CO_2} is directly linked to the speed and equilibrium of the conversion reaction of $BaCO_3$ into either BaO, $BaCu_2O_2$ or $BaCuO_2$ (again, the latter is not present in this specific growth route). This parameter may be strongly affected by a local CO_2 build-up generated by complicated gas evacuation (generally caused by poor gas flow or small furnace sizes and geometries). In the particular furnace set-up used for the experiments in this chapter (Fig. D.1), the large volume of the sample environment is sufficient for complete gas evacuation, as demonstrated from the results described in this section, avoiding detrimental CO_2 accumulation in proximity of the film surface.

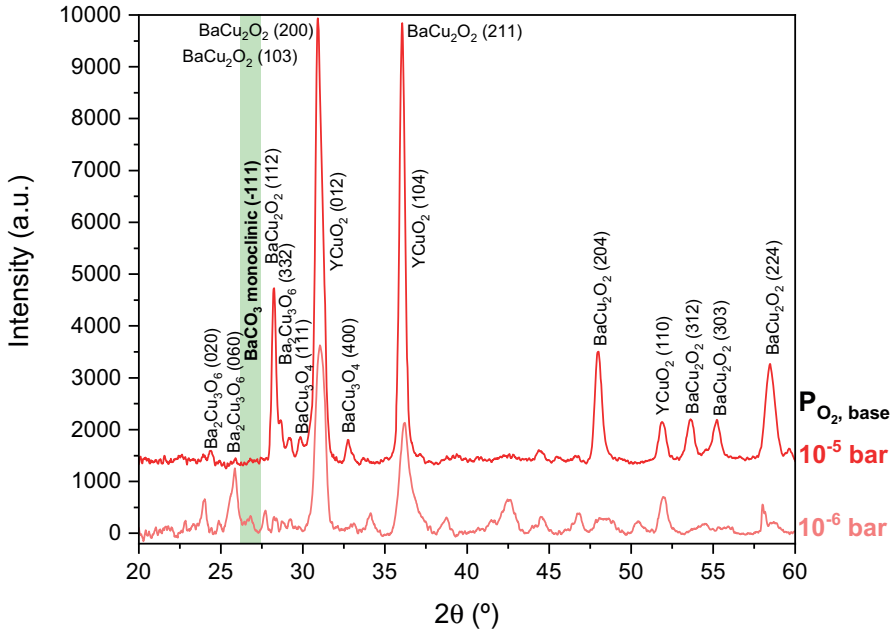


FIGURE 4.5: GIXRD of two films quenched at 835 ºC employing the same heating ramp (dT / dt = 1.4 ºC s^{-1}), comparing the effect of different base pressures: $P_{O_{2,base}} = 10^{-5}$ bar and $P_{O_{2,base}} = 10^{-6}$ bar (indicated on the right side of the graph). In both experiments, a dwell of 5 minutes was performed when the T_{set} was reached.

Nonetheless, two general mechanisms are competing when P_{O_2}, and consequently, P_{CO_2}, are varied:

$$BaCO_3 + Cu_2O \leftrightarrow BaCu_2O_2 + CO_2 \tag{4.2}$$

$$BaCO_3 \leftrightarrow BaO + CO_2 \tag{4.3}$$

Considering the same T_{set} = 835ºC, as visible in Fig. 4.6, the decomposition of $BaCO_3$ shifts towards the mechanism in equation 4.3 when the P_{CO_2} is lower, which is directly correlated to a decrease of P_{O_2}. In this case, an eventual accumulation of CO_2 inside the film, which may be occurring due to the reduced porosity, will move the equilibrium of the reaction to the left side, stabilizing $BaCO_3$ and delaying its elimination.

Taking into account the presence of the remaining, detrimental $BaCO_3$ monoclinic phase and the broader aspect of the peaks relative to the other crystalline phases in the film, thus suggesting lower crystallinity, the $P_{O_{2,base}}$ of 10^{-5} bar was selected as most suitable option for the optimization of the TLAG process. This is mainly due to the requisite of a film composed by the crystalline phases of $BaCu_2O_2$ and Cu_2O with small grain sizes, necessary for the fast reactivity towards the generation of the transient liquid. The extreme rates of nucleation and growth achieved through the transient liquid are hindered when large crystallites are present,

as these experience prolonged melting and are, thus, limiting the velocity of the second step of the growth process.

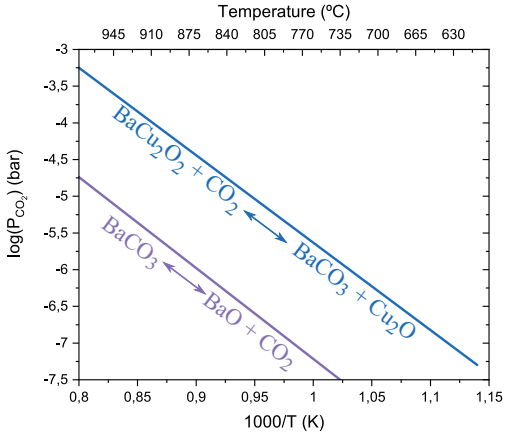


FIGURE 4.6: Thermodynamic equilibrium lines of CO_2 gas-solid reactions as a function of P_{CO_2} for equilibrium reactions of $BaCO_3$ to $BaCu_2O_2$ (blue solid line, when copper is present in the system) and to BaO (lilac solid line, relative to the sole $BaCO_3$ decomposition). Plot adapted from [95].

4.2.4 Evaluation of $BaCO_3$ phase evolution during the low-P_{O_2} heating

With the aim of a better understanding of the $BaCO_3$ elimination process, quenches at various T_{set} were performed to follow the evolution of this phase in the low-P_{O_2} heating, with the first chosen temperature to be as low as 760 ºC, a second intermediate one of 835 ºC and a final, elevated one of 900 ºC. Besides revealing information on the thermal behaviour of the barium precursor phase in the studied system, these experiments are interesting for the application of TLAG P_{O_2}-*route* for the growth of other REBCO systems: the T_{set} will be especially crucial in the case of the YbBCO system, which displays characteristic nucleation temperatures even 100 ºC lower than the YBCO case [127, 175], particularly appealing when considering higher energetic efficiency of industrial fabrication processes of CCs.

Fig. 4.7 displays the GIXRD of the three films quenched with increasing T_{set}. Important to specify that no dwell was performed in any of those experiments, as the objective was to observe the evolution of the phases of $BaCO_3$ to understand its mechanism in this system, and not exclusively reach a complete elimination in each process. Similarly to the previously investigated cases, all films exhibit comparable reflections relative, in majority, to the desired mixed oxide of barium and copper ($BaCu_2O_2$). However, the quench at 760 ºC yields an elevated contribution of the orthorhombic phase of $BaCO_3$, with an additional minor one deriving from its monoclinic phase (a focus on the 2θ region where the principal peaks of $BaCO_3$ are

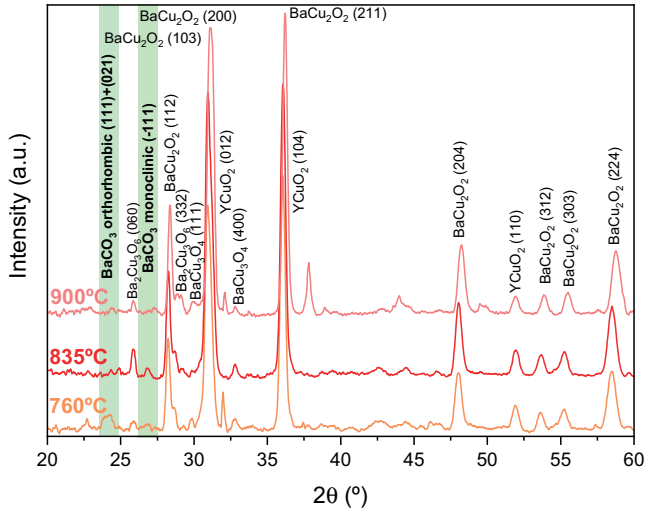


FIGURE 4.7: GIXRD of three films quenched with increasing T_{set} of 760 ºC, 835 ºC and 900 ºC. 2θ ranges where $BaCO_3$ peaks appear are highlighted in dark and light green, respectively for the orthorhombic and monoclinic phase. Processing parameters are chosen considering the optimal ones resulting from the previously described experiments: $P_{O_{2,base}} = 10^{-5}$ bar and average heating rate of 1.4 ºC s^{-1}. No dwell was performed in any of those experiments.

found is shown in Fig. 4.8(a) for a straightforward visual identification). Undoubtedly, a final temperature of 760 ºC is excessively low to fully eliminate the barium precursor phase from the film. Nonetheless, its elimination process has already initiated at this temperature: the integration of the peaks relative to $BaCO_3$, reported as percentile compared to each of their maximum values obtained after the pyrolysis process, have reduced to almost 11% and 22% for orthorhombic and monoclinic phases, respectively (Fig. 4.8(b)). When considering the GIXRD relative to the film quenched at T_{set} = 835 ºC, it is evident how the orthorhombic contribution has been drastically reduced, suggesting its elimination to be almost complete. However, an intensity increase of the monoclinic peak implies a thermally induced crystallization is occurring, possibly deriving from an amorphous portion of the initial film. Finally, reflections relative to both $BaCO_3$ phases disappear completely when the T_{set} of 900 ºC is reached. The corroboration of the evolution of the percentile contribution of both phases as a function of the T_{set} is represented in Fig. 4.8(b). Here, the monotonic decrease of the orthorhombic phase is directly correlated to the temperature increase, whereas the monoclinic phase exhibits a slight increase at intermediate temperatures, to result in a null contribution of the two concomitant with the most elevated T_{set} tested.

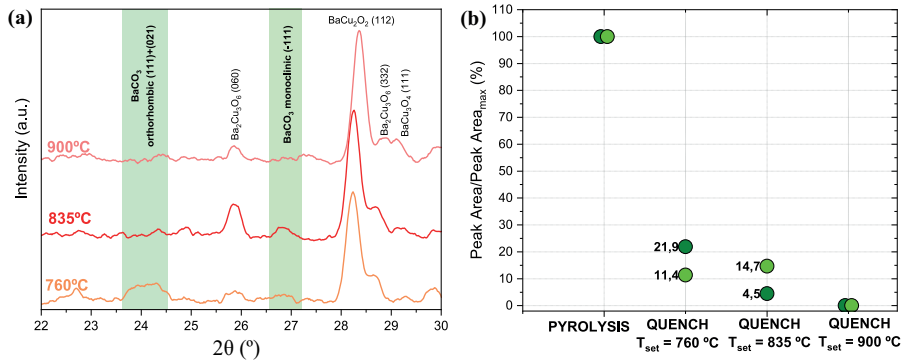


FIGURE 4.8: (a) Zoom of the 2θ range corresponding to the $BaCO_3$ peak positions from the GIXRD of the three films quenched with $dT / dt = 1.4$ ºC s^{-1} to different T_{set} at $P_{O_{2,base}} = 10^{-5}$ bar shown in Fig. 4.7. (b) Representation of the peak area reduction relative to the $BaCO_3$ orthorhombic (dark green) and monoclinic (light green) phases as a percentage normalized to the value from the GIXRD resulting from the pyrolysis process. Solely the quench processes at 760 ºC and 835 ºC data points are labelled with the percentage value, as the last experiment yields a film free of any $BaCO_3$ phase.

To investigate the possible crystallization process and further gather insight on the mechanism of $BaCO_3$ elimination in these films during the low-P_{O_2} heating, TGA experiments coupled to MS and FTIR have been performed, and the results are reported in Fig. 4.9. Since the elimination of $BaCO_3$ is obtained through CO_2 out-diffusion exclusively, this is the only volatile species registered with EGA throughout the thermal treatment. The MS spectrum in Fig. 4.9(a) is evidently showing the release of CO_2 ($m/z = 44$) is occurring in two consecutive stages, the first being at $T = 576$ ºC and the second at $T = 772$ ºC. The elimination of the barium precursor phase in this film may thus be described by two independent processes: a partial elimination at temperatures below 600 ºC, which is presumably corresponding to a phase with lower thermal stability, outlived by a second phase enduring until higher temperatures. The second decomposition peak above 770 ºC is decisively demonstrating the elimination of $BaCO_3$ can be completed in such a thermal treatment at reduced oxygen partial pressures.
The identification of the phases responsible for each decomposition step of the MS spectrum was possible through the additional acquisition of FTIR on the same film throughout the TGA experiment, and Fig. 4.9(b) displays the comparison between the spectrum acquired from the film prior to the heat treatment and the one acquired at 640 ºC (an intermediate temperature between the two peaks obtained in the MS spectrum). The broad peak shown in the spectrum after pyrolysis is the total contribution of both phases of $BaCO_3$[3], whereas at 640 ºC the contribution deriving from the orthorhombic phase is reduced almost completely, only displaying a

[3] As shown in the XRD data of the (3:7) composition films after pyrolysis reported in Fig. 3.7, $BaCO_3$ is present as a mixture of its orthorhombic and its monoclinic phases, with the former in majority compared to the latter, additionally confirmed through TEM analysis.

sharp peak relative, thus, to the monoclinic phase. Consequently, the first decomposition peak in the MS spectrum can be certainly attributed to the complete elimination of the orthorhombic phase successively followed by the monoclinic one, as expected at higher temperatures given its increased thermal stability at low P_{O_2} [95]. These results are, indeed, in good accordance with the phase evolution of $BaCO_3$ observed in the quenches performed at increasing temperatures shown in Fig. 4.7.

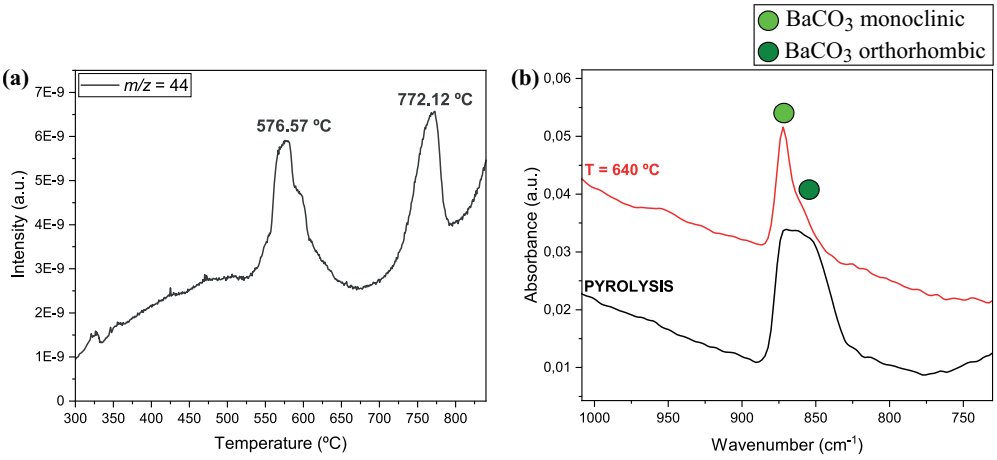


FIGURE 4.9: (a) TGA-MS registered during a low-P_{O_2} heating of a two-layered (3:7) composition film, showing the release of CO_2 ($m/z = 44$) is occurring through independent processes at two different temperatures. (b) TGA-FTIR was acquired on the same film: here, the spectra of the film before the low-P_{O_2} heating (after pyrolysis, black line) and at 640 ºC (red line) during the thermal treatment are represented, with the temperature value being chosen in between the two decomposition steps observed in the MS spectrum. The peaks relative to $BaCO_3$ monoclinic and orthorhombic are indicated, respectively, with a light green and a dark green solid circle.

The results reported to this moment are successfully demonstrating that the process of $BaCO_3$ elimination in the films described in this thesis during the first step of the P_{O_2}-*route* is kinetically-driven. Simple tuning of the processing parameters allows for a complete removal of this phase, confirming that the presence of $BaCO_3$ as the sole nanocrystalline precursor phase of barium is not a limitation for the fabrication of YBCO through CSD-based methodologies. More specifically to this work, these findings are establishing encouraging foundations for the growth of epitaxial YBCO films through TLAG P_{O_2}-*route*.

4.2.5 Challenges of $BaCO_3$ elimination on thick films

With the aim of boosting the industrial fabrication of YBCO (and in general, REBCO) superconducting films, high-performance physical properties should be demonstrated on films of elevated thickness through the use of the TLAG-CSD methodology. Investigating the possibility of $BaCO_3$ elimination in thick films has thus been of utmost importance to this goal. Consequently, quench processes were carried out on films of (3:7) composition with a threefold and fourfold increase of the thickness compared to the ones described in the previous subsections: specifically, six-layered and eight-layered films, with thickness of 2200 ± 50 nm and 2700 ± 50 nm, respectively (prior to the low-P_{O_2} heating). Previous studies evinced that the process of $BaCO_3$ elimination is strictly controlled by the thermally activated process of CO_2 out-diffusion [52]: the processing temperature is, therefore, playing a key role in the elimination of the barium precursor phase, as it was also observed in 4.7. The temperature required for a complete CO_2 evolution is higher when the thickness of the film is significantly increased, given that the volume through which this volatile species must diffuse is raised.

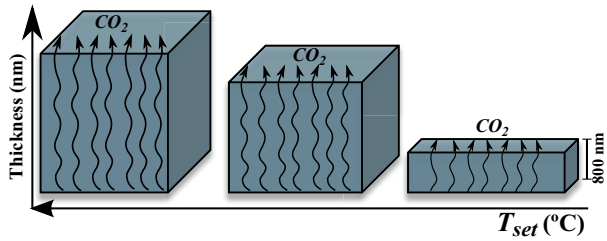


FIGURE 4.10: Schematic representation of CO_2 out-diffusion as a function of thickness with a general correlation to the T_{set}. The thickness values examined in this subsection are represented in scale, taking as a reference the thickness of a two-layered film (800 ± 50 nm), considered the standard.

Fig. 4.11 displays the quenches performed on films of elevated thickness evaluated for their successive growth through TLAG P_{O_2}-*route*. If comparing to the thickness of a two-layered film (800 ± 50 nm after pyrolysis), widely employed throughout this thesis as standard thickness for optimization of processing conditions, the factor three and four increase in this parameter requires the processing temperature to be raised. The minimum T_{set} tested for the quench processes reported in this subsection is, thus, 860 ºC. In both of the films employed, the majority of $BaCO_3$ is eliminated by performing a dwell of 5 minutes once the T_{set} is reached, similarly to what previously observed for films of lower thickness (4.2.2). The six-layered film displays complete removal of the orthorhombic phase, and a remaining minor contribution deriving from the monoclinic phase of the barium precursor. The unprecedentedly examined extreme thickness of the eight-layered film required a fine adjustment of the processing temperature, and quench processes with two consecutive T_{set} were implemented. A temperature

of 860 ºC is not sufficient to eliminate $BaCO_3$ in this specific case, and the contribution of this species is solely corresponding to its orthorhombic phase. Considering the previously reported phase evolution, the simultaneous presence of remaining orthorhombic $BaCO_3$ and absence of monoclinic suggests the film might be in the final moment of the first decomposition step observed in the MS spectrum in Fig. 4.9(a). Upon temperature increase to T_{set} = 870 ºC, the orthorhombic phase is completely eliminated and a minor contribution from the monoclinic one is now visible, indicating that the mechanism of $BaCO_3$ elimination is not affected by the considerable increase in film thickness.

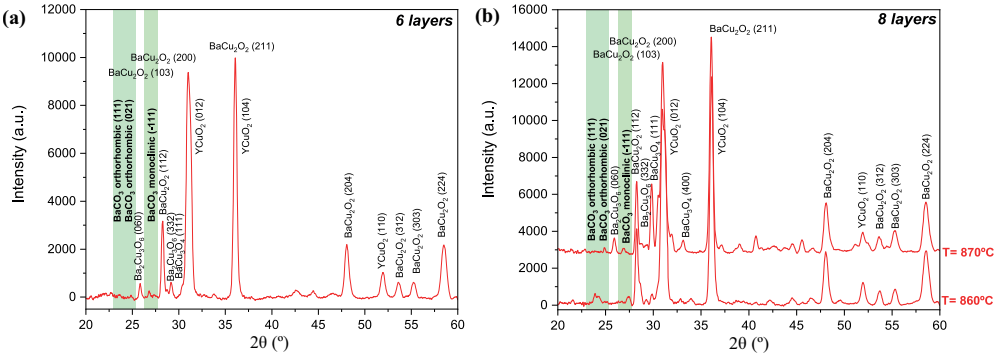


FIGURE 4.11: GIXRD of two thick films quenched at $P_{O_{2,base}} = 10^{-5}$ bar employing an average heating rate of 1.4 ºC s^{-1}: (a) six-layered film quenched at a T_{set} = 860 ºC and (b) two eight-layered films quenched at T_{set} = 860 ºC and T_{set} = 870 ºC. In both plots, the 2θ ranges corresponding to $BaCO_3$ phases are indicated by highlighted regions, respectively dark green for the orthorhombic phase and light green for the monoclinic one.

A focus on the 2θ range corresponding to the $BaCO_3$ peak positions from the GIXRD of the quenches performed on the eight-layered films is reported in Fig. 4.12(a), here shown together with the GIXRD after the pyrolysis process. Despite at T_{set} = 860 ºC $BaCO_3$ orthorhombic is remaining in the film, the enormous reduction of the peak relative to this phase is clearly evident if compared to the same peak after the first thermal treatment. The integration of these peaks reveals the quench process at this temperature eliminates orthorhombic $BaCO_3$ to below 10%. A 10 ºC increase in the final temperature of the process is thus sufficient to completely remove the contribution of this phase. For what concerns the monoclinic phase, an increase directly linked to the increase in temperature is observed, as anticipated from the results previously described. The microstructural analysis reported in 3.2.3 revealed the nanocrystalline phases of $BaCO_3$, CuO and Y_2O_3 are embedded in an amorphous matrix. The temperature increase may consequently favour crystallization of, possibly, part of the $BaCO_3$ monoclinic which was initially found as amorphous, augmenting its contribution to roughly 10% when the temperature of the process is increased from 860 ºC to 870 ºC. It is assumed that this minor

monoclinic $BaCO_3$ contribution can be completely removed with an adequate fine-tuning of the T_{set}, presumably possible through a subsequent 5-10 ºC increase.

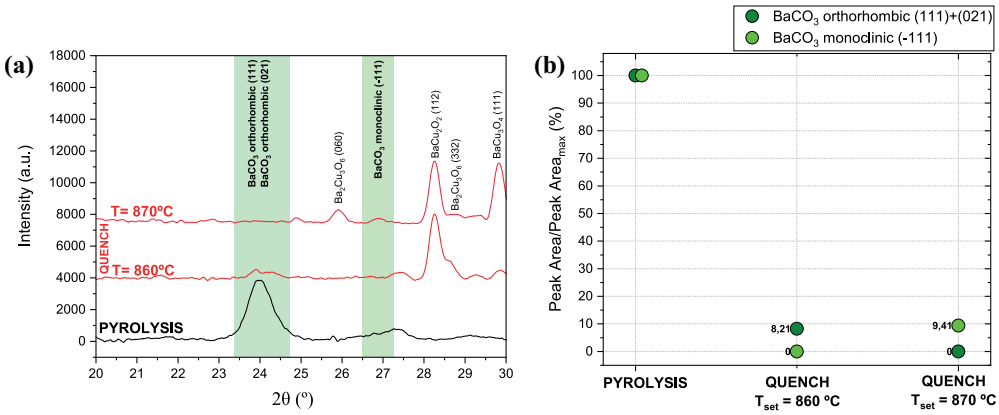


FIGURE 4.12: (a) Zoom on the 2θ range corresponding to the $BaCO_3$ peak positions from the GIXRD of the quench processes performed on the eight-layered films from Fig. 4.11. GIXRD corresponding to the films following the quench processes are shown in red, with the corresponding T_{set} indicated. For comparison, the GIXRD of the film after pyrolysis is also reported (black), to evince the reduction of the $BaCO_3$ phase. (b) Reduction of the contributions of $BaCO_3$ phases subsequent to the quench processes, as a percentage normalized to the peak area of the GIXRD after pyrolysis.

Overall, the quench processes described in this subsection have demonstrated the feasibility of a significant thickness increase for the successive TLAG, with the aim of proving the viability of this innovative growth method in future industrial applications. In previous preliminary studies on TLAG of thick films, a complete $BaCO_3$ removal was demonstrated on films of up to 800 nm thickness [55] deriving from a metal acetates-based chemical solution. In this thesis, this parameter has been duplicated and, through an uncomplicated optimization of the processing temperature, the full elimination of $BaCO_3$ can be achieved, regardless of the chosen film thickness.

4.2.6 Influence of copper content on the $BaCO_3$ elimination process

In Chapter 1, several strategies adopted throughout the decades with the objective of tuning the melt supersaturation, resulting in the possibility of widening the c-axis nucleation window of processing conditions and, additionally, lowering the temperatures of the YBCO (or other REBCO systems) manufacturing processes, have been presented and described in detail. An appealing one, which also constituted one of the main objectives of this work, is the possibility of tuning the transient liquid composition by a simple variation of the copper content of the initial metal-organic chemical solution. Through the preparation of films with copper

excess respect to the stoichiometric amount necessary to form YBCO the supersaturation of the transient liquid is changed, consequently altering the optimal epitaxial nucleation conditions. Moreover, studies on the Ba-Cu binary system evidenced the catalytic role of CuO in the elimination of $BaCO_3$ for the successive reaction towards the formation of a mixed oxide of barium and copper [96]. To ensure the complete elimination of the barium precursor phase during the low-P_{O_2} heating of the TLAG and additionally obtain information regarding the possible influence of the copper content in this system, four films of each of the considered compositions have been subjected to a standard quench process ($P_{O_{2,base}} = 10^{-5}$, heating to T_{set} = 835 ºC at dT / dt = 1.4 ºC s^{-1}, 5 minutes dwell when the final temperature is reached). A comparison between the GIXRD of each film after pyrolysis and after the quench process is reported in Fig. 4.13. A primary consideration must be made before analysing the outcome of the quench process. After pyrolysis, there is a correlation between the crystallinity exhibited by the phases in each film and the liquid composition: films with lower copper content, specifically the stoichiometric (2:3) composition and the one with lowest copper excess, (3:6) composition, display a general increased intensity and sharp aspect of the peaks, significantly pronounced for the $BaCO_3$ phases. Contrarily, the compositions with copper excess, (3:7) and Y-rich (4:11) compositions, are characterized by XRD patterns with broad, low-intensity peaks of the barium precursor phase. An explanation for this feature is found in the same composition of the films: a wide variation of the copper content results in a presumable shift of the $BaCO_3$ nucleation to higher temperatures. As the optimised pyrolysis thermal profile is the same, this leads to the films with higher copper content to have an increased amorphous character respect to the ones with low copper content, which have crystallised sufficiently throughout the duration of the thermal treatment. The microstructural features of the nanocrystalline precursor films are of extreme importance to the success of the TLAG process and the effects of these discrepancies will be taken into account in section 4.4, where the growth of YBCO from different transient liquids will be investigated.

A relationship between the crystallinity of the nanocrystalline precursor film and the success of the quench process concerning complete $BaCO_3$ elimination can be perceived from the GIXRD in Fig. 4.13. Despite the majoritarian phase formed after quench is the expected mixed oxide of $BaCu_2O_2$ in the four cases considered, films of compositions with lower copper content are displaying a major impediment towards the full removal of the barium precursor phases. A contrasting outcome is obtained for films of the eutectic and the composition with highest copper excess, where a complete elimination of all $BaCO_3$ phases is achieved.

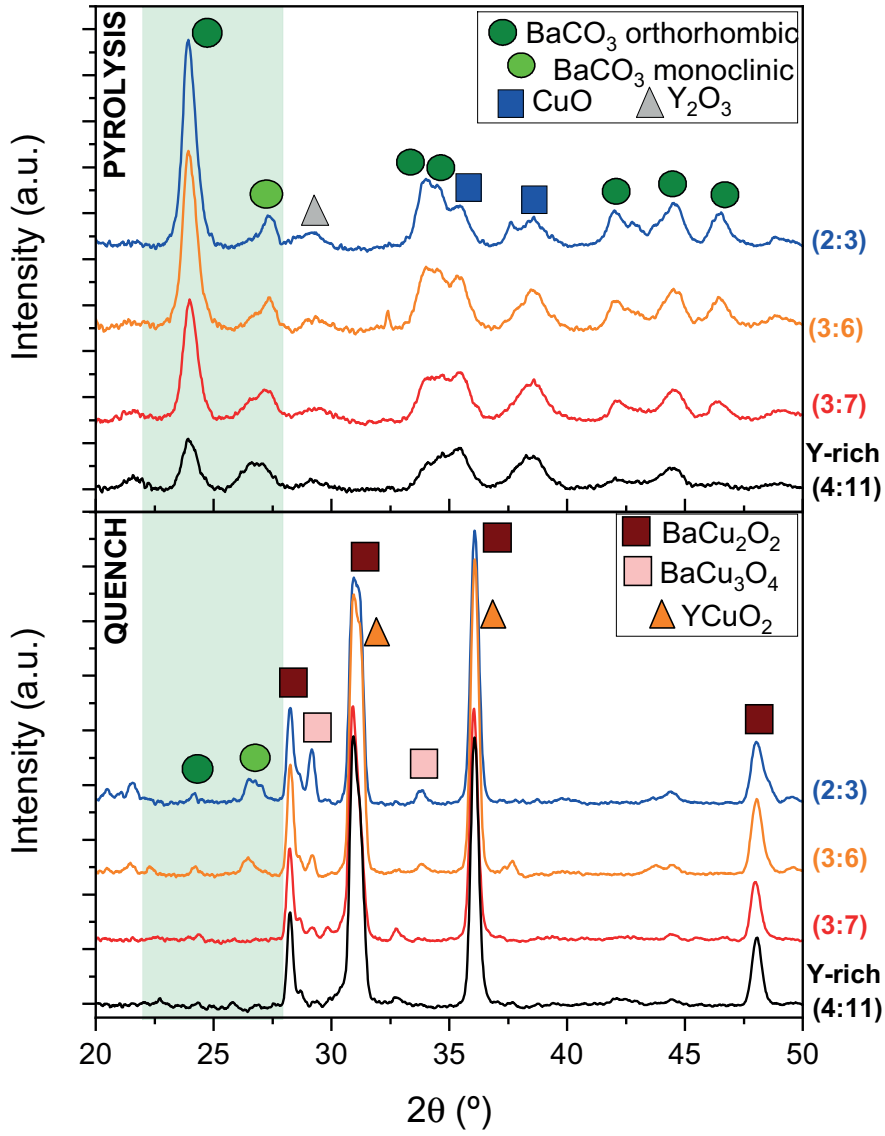


FIGURE 4.13: Comparison between GIXRD of films of the various liquid compositions (indicated next to each of the corresponding plots) considered in this thesis after pyrolysis (upper panel) and after the quench process (lower panel), performed at $P_{O_2,base} = 10^{-5}$ bar, heating until $T_{set} = 835$ ºC with an average heating rate of $dT/dt = 1.4$ ºC s^{-1} and a dwell of 5 minutes before the fast cooling of the system. All of the films represented here are 800 ± 50 nm thick (twofold deposition) prior to the heat treatment.

The integration of the peaks relative to $BaCO_3$ resulting from the low-P_{O_2} heating is related to the copper content of each composition in Fig. 4.14. The contribution of $BaCO_3$ phases is especially elevated for copper contents of 3 and 4 molar concentrations (respectively, (2:3) and

(3:6) compositions), with the monoclinic phase in great majority compared to the orthorhombic one. This may be deriving from a combination of two effects. The initially elevated crystalline character of $BaCO_3$ phases after pyrolysis implies a higher thermal stability, hindering the complete removal of these phases at the selected processing conditions. Additionally and most importantly, the lower copper contents of these compositions denotes a higher (Ba:Cu) ratio compared to the one of the films with copper excess, producing an impairment in the catalytic effect of CuO towards its reaction with $BaCO_3$ to form $BaCu_2O_2$.

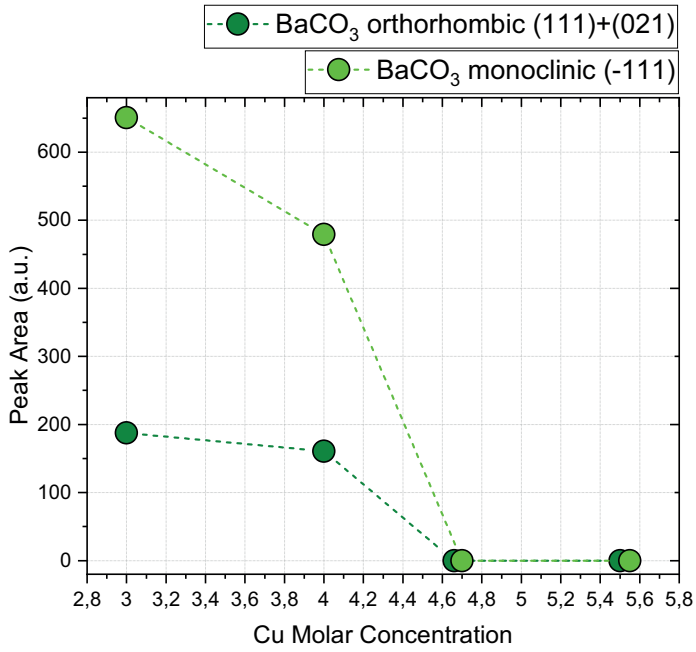


FIGURE 4.14: Peak area as a function of the copper content (molar concentration) obtained through the integration of the $BaCO_3$ orthorhombic (dark green) and monoclinic (light green) peaks in the GIXRD of the films of the four compositions after quench displayed in Fig. 4.13.

The chosen processing temperature for the quench of films of these compositions seems, thus, not to be sufficient for $BaCO_3$ full elimination, suggesting both these compositions require the implementation of higher T_{set}. Nonetheless, considering both the ideal reduction of the processing temperatures for HTS fabrication processes and the likelihood of coarsening of solid phases directly linked to an excessive temperature, the use of compositions with a copper excess seems to be beneficial when analysing strictly the process of $BaCO_3$ elimination up to this point. In fact, (3:7) composition and Y-rich (4:11) composition are showing a null contribution deriving from both $BaCO_3$ phases in the quench process performed. A combination of the catalytic effect of CuO, here in large excess, and the higher amorphous character of the initial nanocrystalline films are presumably facilitating its complete removal in the case of films

of the latter compositions.
The delicate control of $BaCO_3$ elimination and how it may affect, together with the differences in transient liquid supersaturation, the epitaxial nucleation of YBCO in TLAG P_{O_2}-*route* will be thoroughly discussed in the following section of this chapter, concerning growth processes performed at ICMAB in the set-up described in Appendix D, and in Chapter 5 (specifically in 5.3.2) focused on YBCO growth through TLAG P_{O_2}-*route* performed at synchrotron facilities which allowed to follow the phase evolution through *in-situ* XRD experiments.

4.3 Towards the growth of high-performance YBCO superconducting films

Subsequent to the detailed analysis of $BaCO_3$ elimination in the specific set-up used for TLAG P_{O_2}-*route* at ICMAB, illustrated exhaustively in Appendix D, a thorough investigation of the following step, the liquid-assisted nucleation and growth of YBCO, was carried out. The growth furnace described in D.1 was designed in-house and became operative coinciding with the start of this thesis. As a consequence, no previous information regarding the processing parameters to favour c-axis nucleation of YBCO in this set-up was available, and an initial evaluation of those with the aim of optimizing the growth process was mandatory. The optimization was solely focused on films of (3:7) composition, disregarding momentarily the growth from different transient liquids in order to avoid further complications due to the unknown effect of varying liquid supersaturation. Additionally, the repercussions of increasing film thickness on the achievement of high c-axis YBCO orientation were investigated as preliminary study on the fabrication of thick YBCO films of high-performance through TLAG P_{O_2}-*route*. The final analysis centered on the influence of tuning the liquid supersaturation on the c-axis oriented nucleation of YBCO, achieved through the growth of films of different transient liquid compositions, will be presented in the following section, where a comprehensive review considering the tendencies resulting from variations of liquid supersaturation will lead to a broader understanding of the kinetic parameters governing TLAG.

4.3.1 Promoting c-axis YBCO nucleation in films of eutectic liquid composition

Similarly to the analysis presented in section 4.2, the optimization of the YBCO growth step of the process was executed while studying the effect of the heating ramp. As explained in Appendix D, the set-up was limited at first to a slow heating ramp with an average heating rate of $dT / dt = 0.2$ ºC s^{-1}, not adjustable differently due to furnace specifications. Further on in the project the set-up was modified to ensure tunability of this parameter, leading to the achievement of films matching the microstructural requirements of the solid precursor phases

for an optimal growth of YBCO through TLAG following the low-P_{O_2} heating. The entire optimization process that follows was conducted on films of (3:7) composition and displaying a thickness of 800 ± 50 nm prior to TLAG, yielding final YBCO films with thickness in the range of 400-500 nm. Any variation to this parameter will be thoroughly specified, when introduced.

The extensive, initial optimization was focused on the variation of the processing parameters of T_{set} and final oxygen partial pressure ($P_{O_{2,final}}$), and a large set of those have been tested. Previous knowledge allowed for the selection of these parameters to a confined region. The establishment of the TLAG kinetic phase diagrams for films deriving from the previously employed metal acetates-based chemical solution has determined the optimal c-axis nucleation window for TLAG: this coincides with the regions where the formation of the [Ba-Cu-O] transient liquid occurs and the system surpasses the free energy barrier (ΔG_i) of the nucleation of YBCO solid phase from the melt [54, 101]. The P_{O_2}*-route* kinetic phase diagram derived from previous studies using acetate solutions is shown in Fig. 4.15, and represents the regions of melting and phase formation observed in this system.

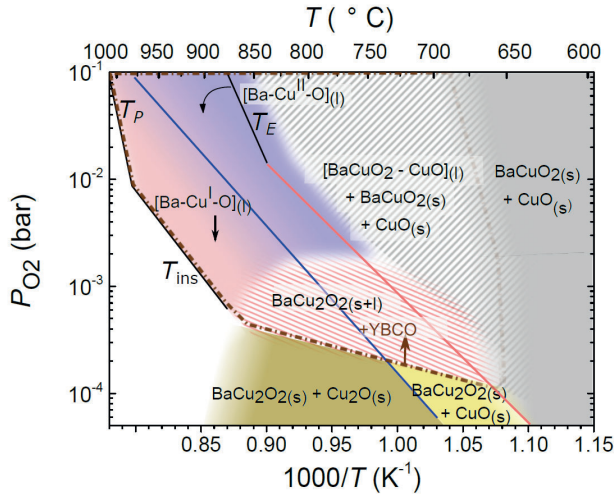


FIGURE 4.15: Representation of the TLAG P_{O_2}*-route* constructed by Rasi *et al.* [101] from the phase evolution observed during *in-situ* XRD experiments at SOLEIL Synchrotron facility. Striped lines are corresponding to regions of coexistence of solid phases and liquid. The pink to blue shaded area represents the *T*-P_{O_2} conditions for full [Ba-Cu-O] liquid formation, with a colour gradient corresponding to the change in copper oxidation state. Solid lines are referring to: $CuO_{(s)}$-$Cu_2O_{(s)}$ (blue line) [185]; $BaCuO_{2(s)}$-$BaCu_2O_{2(s)}$ (red line) [95]; eutectic melting of $BaCuO_{2(s)}$-$CuO_{(s)}$ (T_E) [186]; peritectic melting of YBCO (T_P) [187]; YBCO instability line (T_{ins}) [188].

It is important to notice the several blurry transitions between different regions of coexisting

phases. This is mainly due to the insufficient number of experiments, limiting the precise determination of these transitions. Nonetheless, this diagram greatly aided in the identification and establishment of the preliminary processing conditions employed in the experimental work performed in this thesis. Additionally, it is significant to remind this is a kinetic phase diagram, obtained from previous experiments carried out at synchrotron facilities: heating ramps of 4.5 $^{o}Cs^{-1}$ were employed at $P_{O_{2,base}} = 0.01$ mbar ($P_{TOT,base} = 0.05$ mbar) and pressure jumps of time ranges of several seconds (larger times than the ones used in the growth furnace at ICMAB employed for the experiments described in this chapter). Solid lines are taken from literature (see figure caption for references), and the YBCO instability line (T_{ins}) and peritectic line (T_P) are setting the upper boundaries for YBCO formation. No stable YBCO nucleation is observed at T-P_{O_2} values below T_{ins} [188] where instead the solid phases of $BaCu_2O_2$ and Cu_2O are favoured[4], allowing for the first step of the TLAG P_{O_2}-*route* to be performed as explained in the previous section. At temperatures greater than T_P, incongruous melting of YBCO to the Y_2BaCuO_5 (211) phase + liquid is observed [187].

YBCO growth with high c-axis orientation was reported in previous studies in a window of processing conditions corresponding to the full-liquid regions of the kinetic phase diagram [51, 54, 101]. Therefore, the optimization process described in this subsection has been carried out employing T_{set} values ranging between 815 ºC and 850 ºC and $P_{O_{2,final}}$ between 1 mbar and 6.7 mbar. The solid points on the kinetic phase diagrams displayed in Fig. 4.16 refer to the exact T-P_{O_2} conditions selected for each sample part of the optimization process.

To assess epitaxial quality of the resulting films, analysis of the 2D-XRD patterns acquired with a Bruker-AXS D8 Advance diffractometer equipped with general area detector diffraction system (GADDS) for each sample shown in this figure has been carried out. A procedure for the integration of the peaks relative to each phase observed in the 2D-XRD was followed in order to obtain the contribution of each secondary phase to the epitaxy of the film. Complete description of the measurement conditions for grown films and the method of peak integration can be found in the Appendices, specifically in A.5.1 and D.2.2.1, respectively. This analysis led to obtaining the resulting contributions of secondary phases as a percentage normalized to the epitaxial YBCO (005) reflection, allowing for their straightforward quantification and simplifying the optimization process. As a reminder for the reader, these values are not an indication of the volume percentage of each phase in the sample but only a ratio between integrated areas of the corresponding reflections observed in the 2D-XRD patterns. Initial deductions can be made from Fig. 4.16, in which the contributions of randomly-oriented YBCO grains, (103), and of the Y_2BaCuO_5 (211) secondary phase are represented as a colour map corresponding to each condition of T-$P_{O_{2,final}}$ tested. One may immediately perceive a major difference between the two cases: there is a predominance of the two analysed phases in most of the tested conditions when employing the slow heating ramp, obtaining percentage values

[4] In the binary BaO-CuO system, at temperatures beyond the T_{ins} and reduced P_{O_2}, $BaCu_2O_{2(s)}$ melting occurs [187].

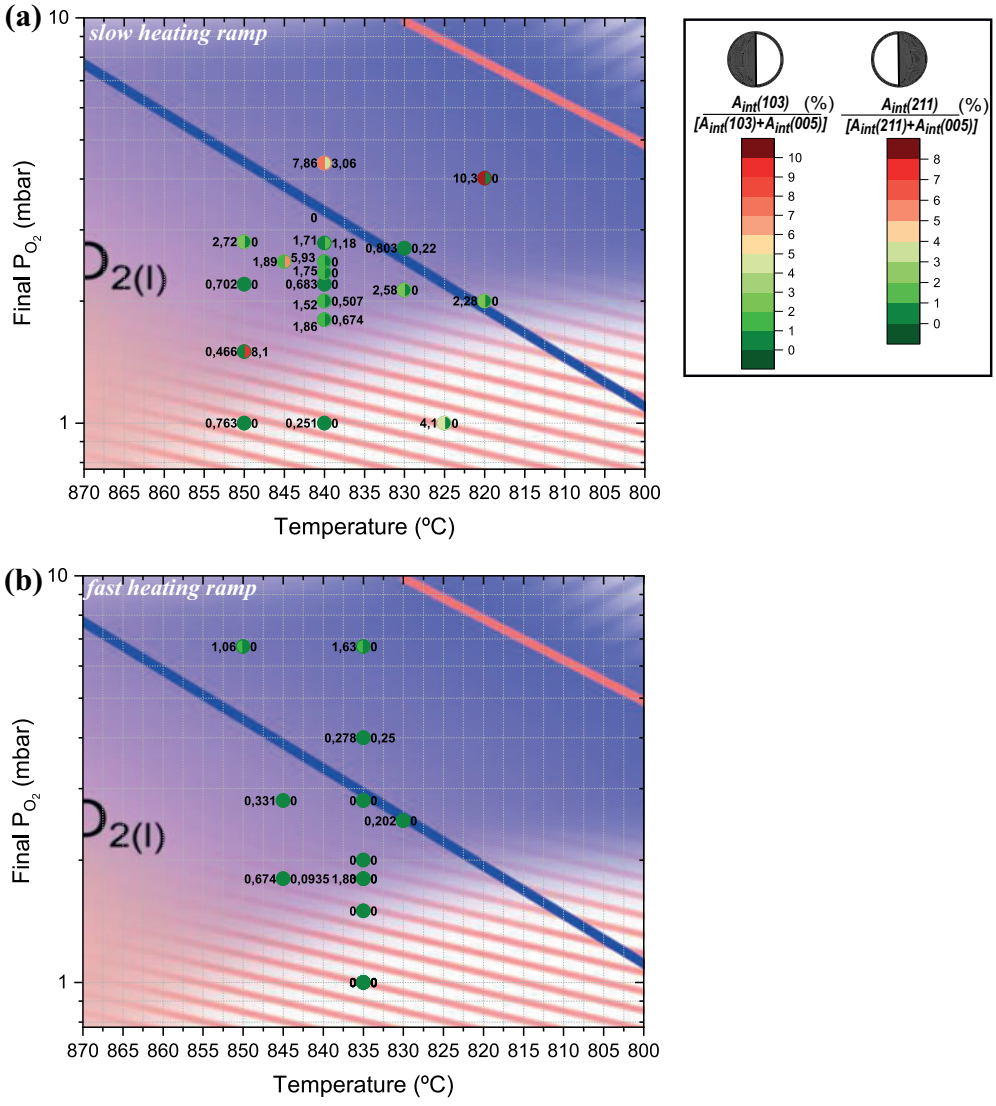


FIGURE 4.16: Optimization process for TLAG P_{O_2}*-route* of (3:7) composition films through the use of (a) a slow heating ramp (average heating rate dT / dt = 0.2 ºC s^{-1}) and (b) a fast heating ramp (average heating rate dT / dt = 1.4 ºC s^{-1}). The position of each single point is corresponding to the T-$P_{O_{2,final}}$ conditions, whereas the colour map is relative to the contributions of randomly-oriented YBCO grains (left side of the full circle) and (211) secondary phase (right side of the full circle) to the epitaxy of the film (see legend on the right side). The labels next to each point are indicating the percentage of the respective contribution, obtained through integration of the corresponding peaks in the 2D-XRD patterns of every film.

of up to 10 % and 8 % for the (103) and (211) phases, respectively. Contrarily, in all of the growth conditions of T-P_{O_2} tested using the fast heating ramp (average heating rate of 1.4 ºC

s^{-1}), the contributions relative to these phases are consistently below 2 %, with the most elevated ones corresponding to the highest value of $P_{O_{2,final}}$ tested (6.7 mbar). The origin of this outcome may be interpreted additionally considering the comparison presented earlier in this chapter regarding films quenched with the use of these two different heating ramps (Fig. 4.2). When employing a slow heating ramp, despite the elimination of $BaCO_3$ is ensured, one is probably facing important coarsening effects. The enlarged grains present at the end of the low-P_{O_2} heating are undesirable for the successive P_{O_2} jump. A potential explanation for this may be found in the following hypothesis. While the pressure is changed rapidly in the system to reach the $P_{O_{2,final}}$, the transient liquid is formed: however, larger grains present longer melting times compared to smaller grains of the same phase, postponing their participation in the formation of the transient liquid. The result is an insufficient or inhomogeneous transient liquid generation: areas of the film will be presenting full liquid composition opposed to the contemporary presence of undissolved, solid phases in other regions of the film. This unideal situation will result in nucleation conditions which are far from the optimal ones for a fully epitaxial layer to be grown: as a consequence, secondary phases or misoriented YBCO grains can be easily formed. Nonetheless, the use of both heating ramps coincide in yielding a region of confined T-P_{O_2} conditions in which the contributions of both phases are low (< 2 %), specifically for the T_{set} of 835 ºC. The films grown through heating at 0.2 ºC s^{-1}, however, show a more reduced range of $P_{O_{2,final}}$ values with low secondary phases contributions, ranging from 1 mbar to 2.8 mbar, with several processing conditions resulting in values of (103) contribution close to 2 %. Contrarily, this situation is observed for films grown through the fast heating ramp only at $P_{O_{2,final}} = 6.7$ mbar, and the same range of optimal processing conditions is enlarged up to final pressure of 4 mbar.

Fig. 4.17 considers solely the contributions of said phases from films obtained selecting this optimal processing temperature ($T_{set} = 835$ ºC) and observes the effect of an increase in $P_{O_{2,final}}$ for the two different heating ramps. Exclusively one set of processing conditions is adequate to reduce entirely the (103) contribution in the case of the $dT / dt = 0.2$ ºC s^{-1} heating ramp, corresponding with $P_{O_{2,final}} = 2.8$ mbar. Four $P_{O_{2,final}}$ conditions are instead displaying no presence of the (211) secondary phase (1, 2.2, 2.4 and 2.5 mbar). The majority of the tested conditions are resulting in a significant percentage for both of the analysed phases. Apart from the highest $P_{O_{2,final}}$ value tested (in the case of the slow heating ramp, this value coincides with 4 mbar), there appears to be no evident trend linking the increase of P_{O_2} with a predominant amount of secondary phases. Possibly, the aforementioned coarsening effects occurring during the low-P_{O_2} heating are fundamentally limiting the success of the transient liquid formation and thus increasing the propensity towards nucleation of secondary phases or higher degree of YBCO misorientation. Moreover, the resulting epitaxy may be intrinsically affected as the grain size of the precursor phases may additionally not be reproducible.

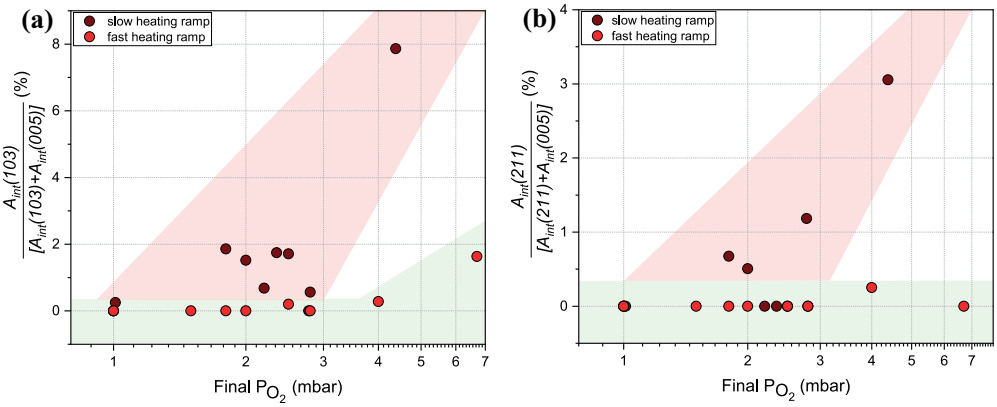


FIGURE 4.17: Contribution of (a) YBCO misoriented grains (103) and (b) (211) secondary phase to the epitaxy of the films considering the increase of $P_{O_{2,final}}$ for films grown at a constant T_{set} employing the slow heating ramp (burgundy full circles) and the fast heating ramp (red full circles). Shaded areas highlight the resulting contributions of majority of films from heating at 0.2 ºC s^{-1} (red) and at 1.4 ºC s^{-1} (green).

Contrarily, in the case of the films grown through the use of the fast heating ramp, the contributions of (103) and (211) are close to 0 % in all of the tested conditions, demonstrating an important improvement to the epitaxial nucleation and the possibility of a wider range of processing conditions resulting in high c-axis YBCO. A slight increase in the (103) contribution may be observed at $P_{O_{2,final}} = 6.7$ mbar. As discussed in Chapter 1, specifically in the section regarding Y solubility in [Ba-Cu-O] melts in 1.2.4.4, the supersaturation of a (3BaO:5CuO) melt at high P_{O_2} was hypothesized to be lower, given the improved solubility in this case at elevated temperatures. The lack of accurate data in a temperature range closer to the processing conditions employed in the TLAG experiments described here only allow for an assumption to be provided. The non-optimal increased formation of misoriented YBCO grains when elevated $P_{O_{2,final}}$ is selected is an indication of a possible increase of liquid supersaturation for elevated final pressure, with the consequence of mixed nucleation [113].

A complementary straightforward consequence of these considerations is observed in the resulting critical current values of the films grown in the aforementioned conditions, as evidenced in Fig. 4.18. A clear division is noticeable regarding the J_c values of the films grown employing the fast and the slow heating ramp, the former leading to generally incremented values respect to the latter. This anticipated outcome is a direct consequence of the increased epitaxy of the films grown through the use of the fast heating ramp, which results in the reduced presence of misorientation and (211) secondary phase. In all of the tested conditions, the J_c at 5 K is above 15 MA cm^{-2}, whereas solely in two cases when the slow heating ramp was employed such increased J_c values could be reached. Nonetheless, these two optimal conditions display lower maximum critical current density than several of the ones grown through the use of the

fast heating ramp.

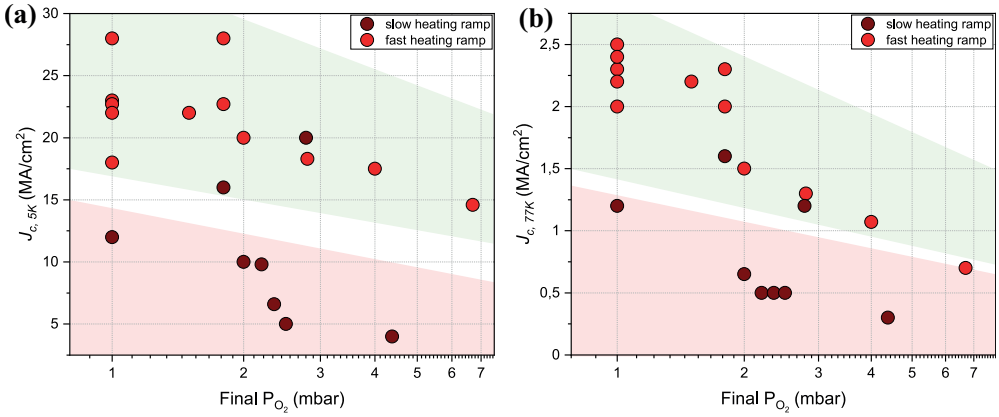


FIGURE 4.18: Values of J_c at (a) 5 K and (b) 77 K for the films shown in Fig. 4.17, increasing P_{O_2} at the constant T_{set} of 835 ºC, employing the slow heating ramp (burgundy full circles) and the fast heating ramp (red full circles).

Comparing the effect of the presence of YBCO misoriented grains and (211) on the epitaxy and thus on the resulting physical properties (J_c measured at 5 K) of films grown through TLAG using the two heating ramps described in this Chapter (Fig. 4.19), it is evident how the general increase in the window of possible conditions for full c-axis nucleation and growth of YBCO through heating at 1.4 ºC s^{-1} leads to enhanced J_c values. For films grown through the use of the slow heating ramp, as previously stated, only two conditions are leading to physical properties comparable to the fast heating ramp. Nonetheless, it must be noted how the contribution of (103) grains is significantly decreasing J_c only in specific films, suggesting other parameters may be responsible for current percolation impediment. Considering now the (211) secondary phase, a similar situation is observed here, with the films heated at 0.2 ºC s^{-1} again displaying only two cases with high-performance physical properties. However, several films showing no contribution of this phase are resulting in reduced J_c, again suggesting as for the presence of (103) grains that the physical properties are influenced by additional variables.

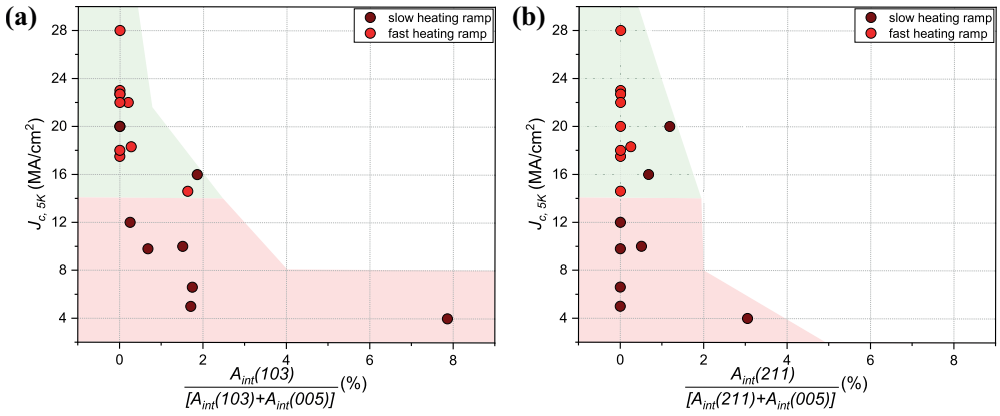


FIGURE 4.19: Effect of presence of (a) YBCO (103) grains and (b) (211) secondary phase on the J_c (measured at 5 K) for films grown through TLAG using the slow heating ramp (burgundy full circles) and the fast heating ramp (red full circles).

The extensive analysis of all the different processing conditions tested employing both heating ramps led to the selection of the optimal growth conditions, based on the enhanced critical current density value exhibited by the film obtained from such process. Firstly, as previously observed for the quenched films in 4.2.1, $dT\,/\,dt = 1.4$ ºC s^{-1} is the ideal heating rate amongst the two tested. Excellent epitaxy is obtained when performing the P_{O_2} jump at $T_{set} = 835$ ºC, from $P_{O_{2,base}} = 10^{-5}$ bar to $P_{O_{2,final}} = 1$ mbar, as shown in Fig. 4.20, where a comparison with a film grown in the same processing conditions but heating at $dT\,/\,dt = 0.2$ ºC s^{-1} is reported. Evidently, the presence of YBCO (103) grains in the film grown using the slow heating ramp is noticeable in the 2D-XRD image and in the granular surface morphology in the SEM image. Conversely, highly epitaxial YBCO reflections may be observed in the 2D-XRD image relative to the film grown with the fast heating ramp. Moreover, this shows a flat YBCO layer with the CuO deriving from the copper excess intrinsic of the (3:7) composition found as superficial precipitates. This is the exemplary surface morphology when copper-rich compositions are considered: the excess of copper must be ideally expelled to the surface to ensure it is not impeding current percolation by sectioning the continuity of the YBCO epitaxial film. This is characteristic to liquid-assisted growth methodologies and the ultrafast growth rates typical in TLAG enable the CuO to be pushed to the film surface. The YBCO film should be formed as a continuous layer, with no evident porosity or areas presenting bad wetting. From this moment on, films exhibiting these morphological features will be described as having a flat surface.

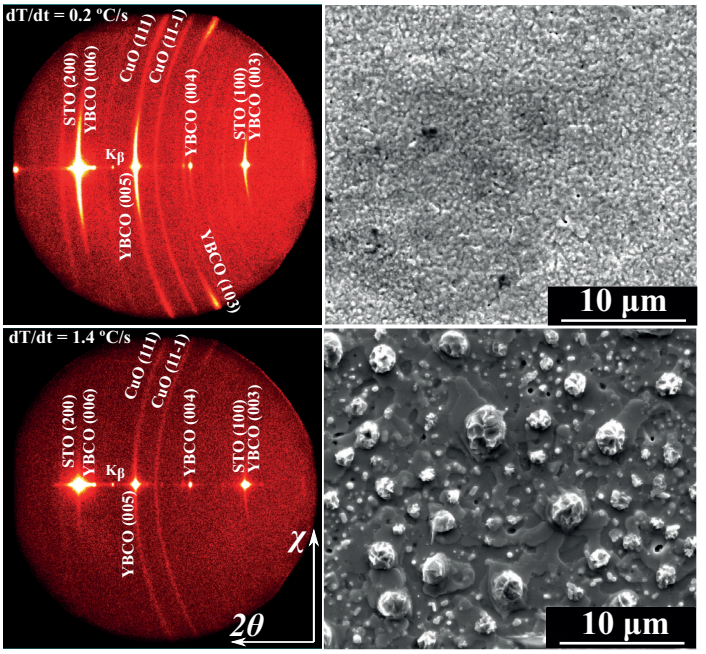


FIGURE 4.20: 2D-XRD images acquired from GADDS and corresponding SEM image for two films grown through the same processing conditions (T_{set} = 835 ºC and final $P_{O_{2,final}}$ = 1 mbar) using the slow heating ramp (upper panels) and the fast heating ramp (lower panels). Identification of the crystalline phases is indicated in proximity of the relative reflection.

The integration in χ of the YBCO (005) peak from the 2D-XRD for the two cases reveals an increased breadth for the film grown through the slow heating ramp, suggesting major misalignment of the (00l) reflection (Fig. 4.21(a)), as opposed to the film grown with the fast heating ramp, which displays a narrower peak: the full width at half maximum (FWHM) can be reduced from 0.88º to 0.63º when increasing the heating rate, indicating the c-axis orientation of YBCO is improved. Consequently, when comparing the physical properties relative to the two films, the latter is displaying J_c values which are doubled respect to the former, at both 5 K and 77 K.

Considering now exclusively the films resulting from the optimized growth conditions with average heating rate of $dT / dt = 1.4$ °C s^{-1} displayed in Fig. 4.17 and 4.18, an assessment of the reproducibility of TLAG has been carried out by repeating the growth in the same processing conditions for eight films. The samples represented here were prepared over a time frame of 8 months from deposition of different batches of the metal-organic precursor solution. Moreover, independent thermal treatments (pyrolysis and growth processes) were employed for each film.

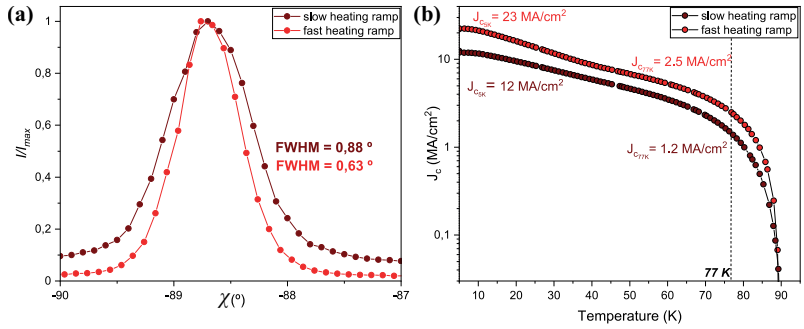


FIGURE 4.21: (a) Integration in χ of the YBCO (005) peak of the 2D-XRD shown in Fig. 4.20, comparing the case of the slow heating ramp (burgundy) and the fast heating ramp (red). (b) $J_c(T)$ curves for the same films considered in (a), demonstrating the great enhancement of the physical properties when the fast heating ramp is employed.

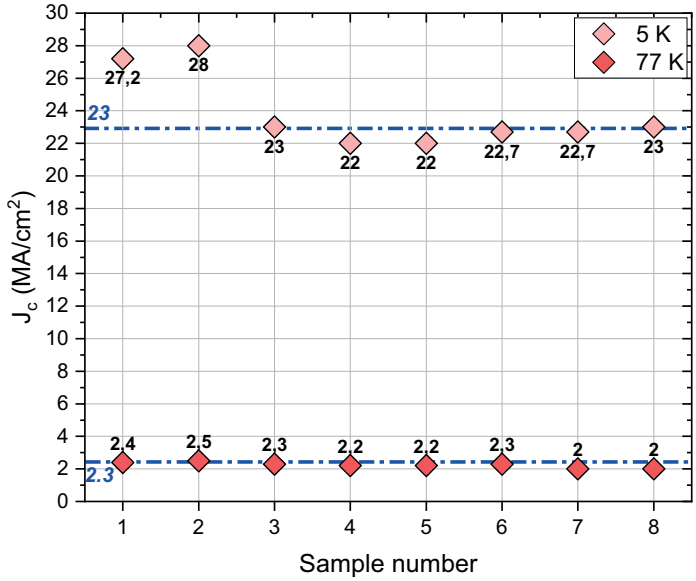


FIGURE 4.22: Evaluation of reproducibility of the TLAG process for eight films grown in the same, optimal processing conditions: heating to T_{set} = 835 ºC at 1.4 ºC s^{-1} and $P_{O_{2,final}}$ = 1 mbar. The films are obtained from deposition of different batches of the metal-organic chemical solution, proving the use of the CSD methodology coupled to TLAG P_{O_2}*-route* can yield highly reproducibile results.

The critical current density values are ranging between 22 and 28 MA cm^{-2} at 5 K and between 2 and 2.5 MA cm^{-2} at 77 K, demonstrating the high reproducibility of the growth process as well as the entire TLAG-CSD approach employing the chemical solutions described in this thesis.

The correlation between J_c values and presence of YBCO (103) grains and (211) secondary phase displayed in Fig. 4.19 suggests that the heating ramp is an extremely relevant parameter, and the reduced physical properties resulting from the use of a slow heating ramp during the growth process are a demonstration of this effect. The proposed explanation provided thus far was finally evaluated and corroborated through TEM analysis, which aided in the understanding of the causes behind the difficult J_c enhancement in the case of films grown through the slow heating ramp. Here, an extensive comparison of the microstructure of films grown employing both heating rates was performed.

As previously reported in this section, the growth of YBCO through TLAG P_{O_2}*-route* employing the two heating ramps can yield highly epitaxial films of high-performance when optimal processing conditions are selected in each specific case. The low magnification STEM-HAADF images shown in Fig. 4.23 are indeed demonstrating this, given it displays two epitaxial YBCO films obtained through the use of slow and fast heating ramp, respectively 4.23(a) and (b). However, the causes behind the differences in quality of the epitaxy, as seen from the previously presented results deriving from XRD analysis, will now be assessed.

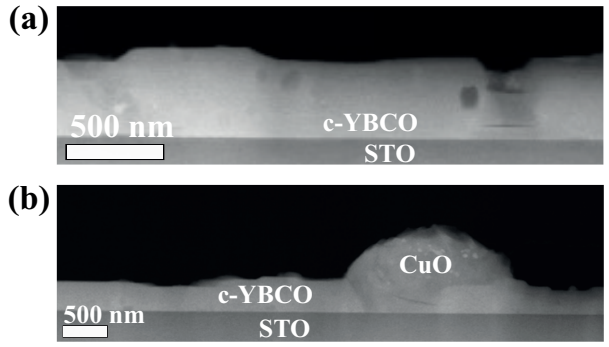


FIGURE 4.23: Low magnification STEM-HAADF image for two epitaxial YBCO films grown employing optimised processing conditions for each of the two heating ramps studied in this section: (a) slow heating ramp and (b) fast heating ramp.

Comparable, homogeneous thickness of 400-450 nm is exhibited by both films, with the image corresponding to the fast heating ramp depicting the presence of a large grain of CuO pushed to the film surface, as desirable for the growth from eutectic liquid composition.

Nonetheless, a first, major distinction between the two cases, previously identified in the XRD analysis, is the major formation of secondary phases (identifiable as darker circles) in the film grown heating at low rates. Moreover, interruption of the YBCO film may be observed. This is clearly evidenced by the intermediate magnification cross-sectional STEM-HAADF image shown in Fig. 4.24, where the latter case displays a rough surface, non homogeneous thickness of the c-axis YBCO and large grains of secondary phases (over 100 nm in diameter) distributed throughout the film. Conversely, a highly epitaxial orientation, homogeneous thickness and

smooth surface is exhibited by the film grown employing the fast heating ramp. These findings are in line with the previously reported results for the slow heating ramp, demonstrating the preferential grain coalescence during the thermal treatment in such conditions.

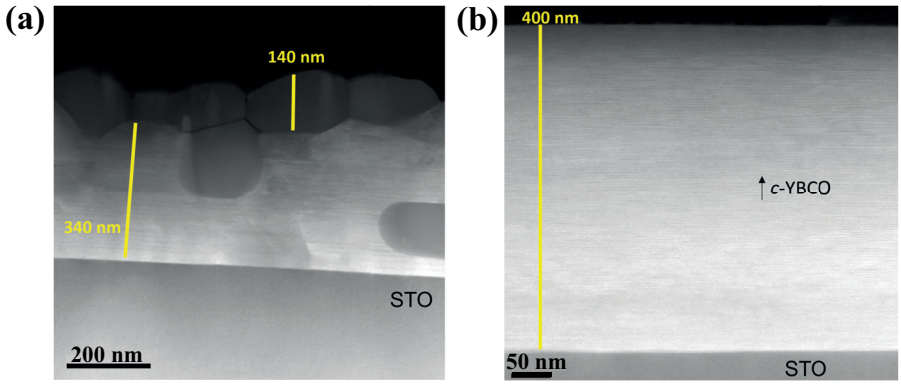


FIGURE 4.24: Intermediate magnification cross-sectional STEM-HAADF images of two films grown through heating at (a) 0.2 ºC s^{-1} and (b) 1.4 ºC s^{-1}. The improvement towards the reduction of formation and coarsening of secondary phases when increasing the heating rate is clearly discernible.

Identification of the secondary phases was possible availing EDX mapping, and the STEM-HAADF images in Fig. 4.25 display the detrimental situation of the distribution of secondary phases in a film obtained through the growth with slow heating rate: big CuO and Cu_2O grains are trapped in the inferior region of the film close to the interface with the STO substrate, together with a large grain of the $Y_2Cu_2O_5$ (225) secondary phase. This is further corroborating the outcome of the quench process described in the previous section, in which the formation and coarsening of this phase in the GIXRD of quenched films with slow heating ramp was believed to be originated by the long heating and, especially, cooling times of the thermal treatment. Moreover, the aggregation of these phases is such that the c-axis YBCO is completely interrupted in this section of the film, generating major impediment to critical current percolation. Additionally, the defect landscape of such films comprises lattice bending close to these grains, as in the image shown in Fig. 4.25(b), where the large barium- and copper-rich crystallite (possibly, $BaCu_3O_4$) is creating such a distortion in the YBCO lattice.

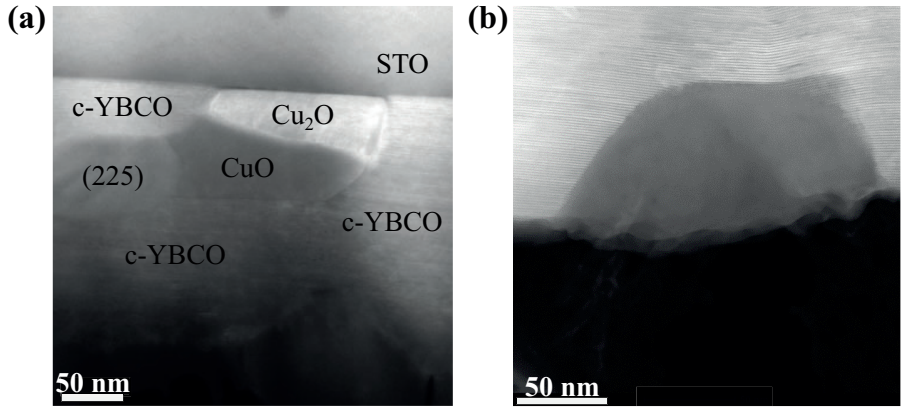


FIGURE 4.25: Intermediate magnification cross-sectional STEM-HAADF images of two areas of a film grown through the use of the slow heating ramp. (a) The epitaxial YBCO film (c-YBCO) discontinuity caused by the presence of largely coarsened (225), CuO and Cu_2O grains. (b) Bending of c-YBCO around the borders of a barium- and copper-rich secondary phase.

Likewise, this defect is perceptible in the YBCO surrounding the grains of two secondary phases displayed in Fig. 4.26, where EDX maps of the Y K-edge, Ba L-edge, Cu K-edge and O K-edge allowed for the identification of the (211) and (225) in two different regions of the film. Several approaches of YBCO growth through CSD-based methodologies take advantage of the common formation of secondary phases in nanoparticle sizes (generally ranging between 5 and 20 nm in diameter). Defects generated during the crystallization of YBCO in the growth process, defined as natural pinning centers, are believed to be beneficial as these may additionally generate secondary defects in the microstructure due to nanostrain effects [8, 189–191]. However, the secondary phases embedded in the films grown through the slow heating ramp exhibit typical diameters of over 150-200 nm, which will provoke limited current percolation. Nonetheless, in the TEM analysis of TLAG films reported in previous studies, an elevated presence of $YBa_2Cu_4O_8$ intergrowths, generally termed 248 stacking faults (SFs), was found to be characteristic of the growth through this method [54]. Such defects are know to be at the origin of an increase of strain at the local scale (nanostrain), and have been demonstrated to additionally induce a local Cooper pair suppression, beneficial to vortex pinning [40, 190]. The presence of long 248 SFs is also confirmed in the films described in this thesis, as is clearly evidenced in the HR-TEM image in Fig. 4.27, and are observed in the films grown through the use of both heating ramps.

Finally, despite the achievement of high c-axis YBCO in films grown through the use of both heating ramps, the quality of films obtained through slow heating rate is evidently worsened by the formation of large grains of secondary phases as a result of coarsening phenomena due to the prolonged times the films are exposed to elevated temperature during the growth process.

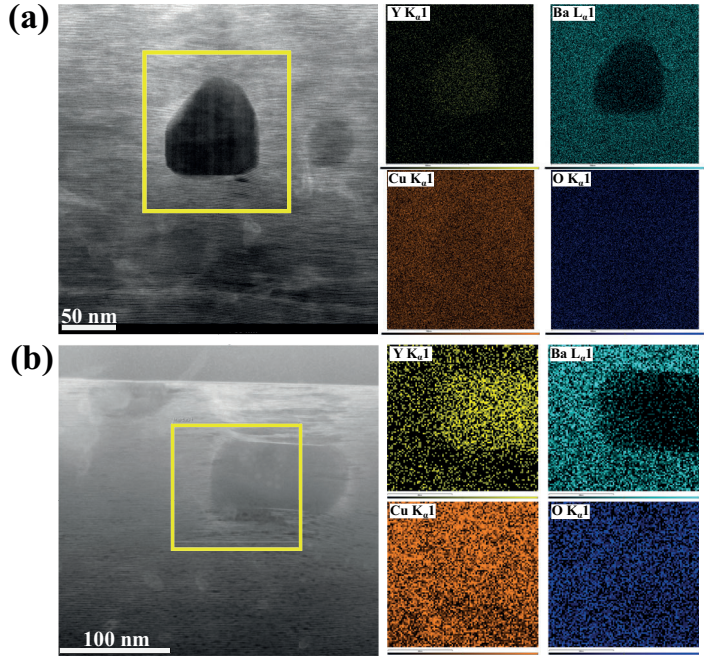


FIGURE 4.26: Analysis of two different regions of a film heated at 0.2 ºC s^{-1} through EDX mapping of the area highlighted by a yellow square in the cross-sectional STEM-HAADF images for secondary phase identification. Y K-edge, Ba L-edge, Cu K-edge and O K-edge maps confirm the grain in (a) to be (211) and the one in (b) the (225) secondary phase.

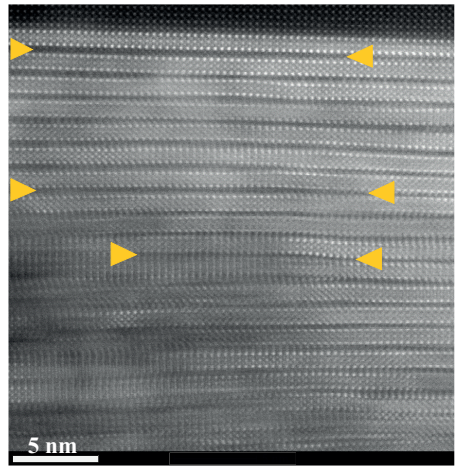


FIGURE 4.27: HR-TEM image of an epitaxial YBCO film grown through TLAG in which the long 248 intergrowths are visible throughout the entire thickness, indicated by yellow arrows.

Considering the entirety of the results presented in this subsection, one may conclude that

the increase of the heating ramp from an average heating rate of 0.2 °C s^{-1} to 1.4 °C s^{-1} enables the elimination of a wide portion of these undesired phases, and the simultaneous reduction of the size of the ones which are present. Moreover, the characteristic effect of the liquid-assisted growth promotes pushing effects of the copper precipitates to the film surface, an additional feature which avoids hindrance to current percolation and allows for high-performance superconducting films to be obtained. The drop in physical properties displayed by the majority of the films grown at 0.2 °C s^{-1} may thus be ascribed to the strong coarsening resulting from the prolonged heating time needed to reach the T_{set}. Prior to performing the P_{O_2} jump, the film displays large, crystalline grains of $BaCu_2O_2$ and Cu_2O besides a variety of other secondary phases. Moving to the following step during the P_{O_2} variation, their inevitably slow melting will consequently result in the formation of the [Ba-Cu-O] transient liquid inhomogeneously throughout the film: this is anticipated to modify detrimentally the supersaturation conditions[5], favouring competing mechanisms between secondary phases grain coalescence and YBCO nucleation.

4.3.2 Preliminary studies on TLAG of thick YBCO films

Following the attainment of high-performance films with high reproducibility through TLAG-CSD on a thickness of 400 nm and considering the great industrial interest for thick films of competitive performance, the implementation of the growth of YBCO films of higher thickness was carried out, employing both the slow and the fast heating ramp.

TLAG of thick films with the slow heating ramp was conducted on films of three and four layers, resulting in, respectively, 600 ± 50 nm and 800 ± 50 nm of final YBCO. A film of two layers is used as reference for comparison with an optimised case. The selected processing conditions in this case were: heating at a constant $P_{O_{2,base}}$ of 10^{-5} bar to T_{set} = 835 °C, with an average heating rate of $dT/dt = 0.2$ °C s^{-1} and performing a P_{O_2} jump to the final value of 1.8 mbar once the desired temperature is reached[6]. The 2D-XRD images acquired with GADDS, the corresponding integrated XRD patterns and SEM images relative to such films are displayed in Fig. 4.28. The two-layered film evidently displays high epitaxy and optimal surface morphology, with the CuO excess found as superficial precipitates. No apparent presence of secondary phases is visible in the integrated XRD, suggesting the ideal nucleation conditions were accomplished for the growth of this film. When increasing film thickness, despite the optimal surface morphology is maintained, a loss of epitaxy is observed, especially for the film of four layers: the 2D-image displays lower degree of textured YBCO reflections, indication of a certain degree of misorientation around the c-axis, and the integrated XRD patterns

[5] In theoretically ideal TLAG conditions, supersaturation is given by the dissolution of a certain amount of solid yttria nanoparticles in the [Ba-Cu-O] transient liquid. If a large part of yttrium is involved in the formation of other solid phases, the supersaturation will be additionally varied.

[6] These processing conditions were found to yield high epitaxy and elevated critical current density in the two-layered films grown through the use of the slow heating ramp.

are showing a higher contribution of the YBCO misoriented grains (103). Moreoever, the appearance of peaks due to additional secondary phases, such as the (211) phase and the mixed oxide of yttrium and copper (225), are suggesting further optimization is needed for films of such thickness in order to reduce their contributions towards the enhancement of current percolation. An increase in the T_{set} may be found beneficial when increasing the thickness with the aim of favouring c-axis nucleation, given the supersaturation conditions of the transient liquid formed in these processing conditions appear to be excessive for a favoured c-axis nucleation. As described in 1.2.4.4, a possibility of decreasing the supersaturation in the same melt composition is a thermal increase, as this results in a higher Y solubility.

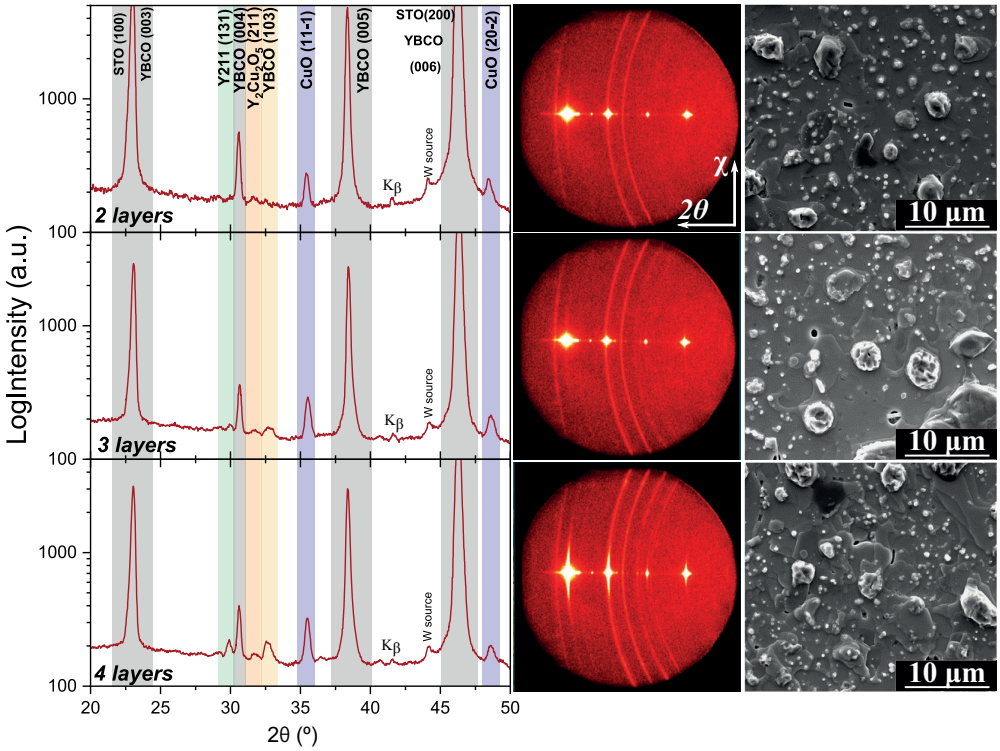


FIGURE 4.28: Comparison between the films of different thickness grown through TLAG P_{O_2}-*route* employing the slow heating ramp ($dT / dt = 0.2$ °C s^{-1}). From top to bottom: two-, three- and four- layered films, leading to 400 ± 50 nm, 600 ± 50 nm, and 800 ± 50 nm of final YBCO, respectively. (Left) Integration in χ of the 2D-XRD acquired from GADDS (centre). Peak identification is indicated in the top panel of the former, and shaded areas are extended to the lower panels. (Right) Surface morphology relative to each film.

Conversely, the investigation of thick films grown through the use of the fast heating ramp was implemented with more elevated thickness values: specifically four-, six-, and eight-layered films were employed, corresponding to 800 ± 50 nm, 1100 ± 50 nm, and 1400 ±

50 nm of final YBCO. Considering that the thickness was here doubled to the previous case and taking into account the inadequate processing conditions for the thicker film heated at 0.2 ºC s^{-1}, incremental T_{set} were selected correlated to the thickness increase. Starting from the optimised processing conditions for the films of two layers, with T_{set} = 835 ºC, the temperature was increased to 850 ºC, 860 ºC and 880 ºC for the four-, six-, and eight-layered films, respectively. These desired temperatures were reached by heating at 1.4 ºC s^{-1} at a constant $P_{O_{2,base}} = 10^{-5}$ bar, followed by the P_{O_2} jump to the final value of 1 mbar. Given the preliminary nature of this study, only the parameter of growth temperature was varied, selecting the optimal values of the others from the optimization of the two-layered films reported in 4.3.1. The 2D-XRD images with the respective integrated XRD patterns and surface morphology analysis of said films are displayed in Fig. 4.29.

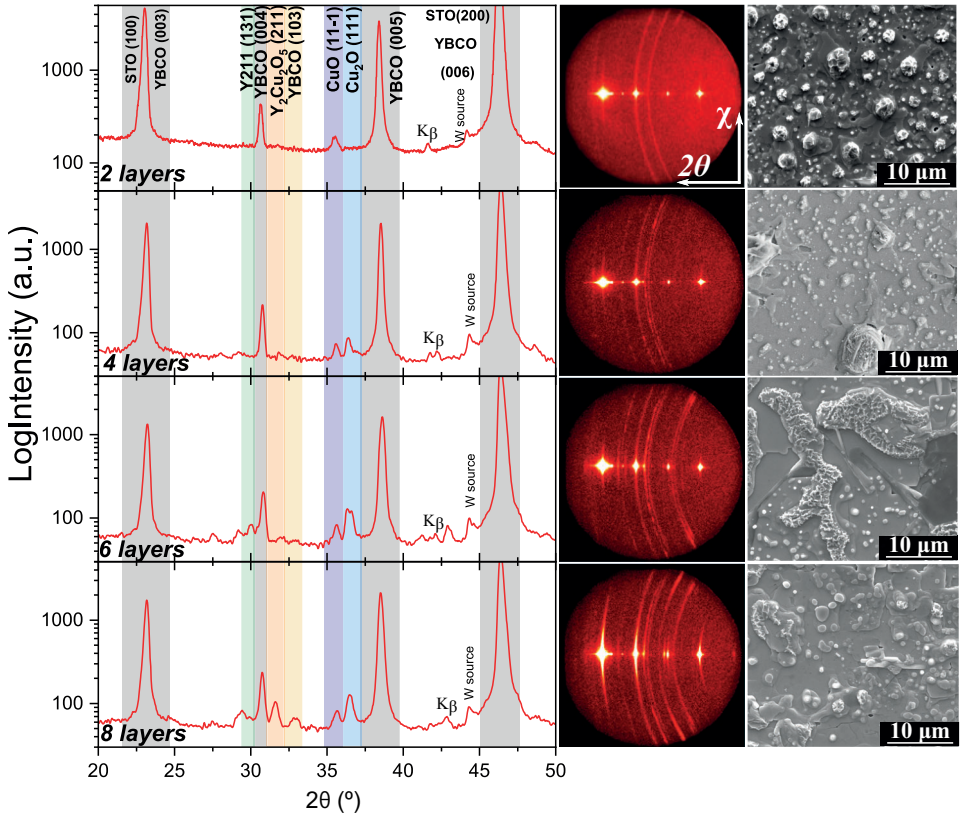


FIGURE 4.29: Analysis of the outcome of TLAG P_{O_2}*-route* on films of different thickness grown through the use of the fast heating ramp (dT / dt = 1.4 ºC s^{-1}). From top to bottom: two-, four-, six-, and eight-layered films, leading to 400 ± 50 nm, 800 ± 50 nm, 1100 ± 50 nm, and 1400 ± 50 nm of final YBCO. (Left) Integration in χ of the 2D-XRD patterns together with the corresponding 2D image (centre). Peak identification is indicated in the top panel, and shaded areas are extended to the lower panels. (Right) Surface morphology displayed by SEM images relative to each film.

Similarly to the case of the films grown employing the slow heating ramp, as the thickness of the film is increased a slight degree of c-axis misorientation is observed. Nonetheless, epitaxial YBCO was obtained up to a thickness of 1400 ± 50 nm of final YBCO. An equivalent trend is also observed for what concerns the presence of secondary phases, again predominant in the films of higher thickness: the films of six and eight layers are exhibiting some contributions from the (211) and the (225) secondary phases. Moreover, the 2D-XRD relative to these are showing the simultaneous presence of CuO and Cu_2O, the oxides of copper of two oxidation states: the latter is formed given the extremely elevated processing temperatures selected for the TLAG process, and is partially oxidised to the former upon cooling, when crossing the $CuO_{(s)}$-$Cu_2O_{(s)}$ line in the phase diagram (Fig. 4.15) [95, 185]. The morphological features are optimal for the two- four- and eight-layered films, displaying a flat surface on which the copper oxide excess is found as segregated precipitates. Contrarily, the six-layered film is evidencing the formation of copper oxide as dendritic-like structures (confirmed by EDX, Fig. D.12). Nonetheless, the unfavourable feature encountered in the films of highest thickness is the formation of microcracks, indicated by arrows in Fig. 4.30. Possibly, the elevated thickness may be provoking extreme in-plane tensile stress, either during the growth or during the post-annealing oxygenation process. Further investigation is necessary in order to determine at which point of the process the microcracking is occurring, given that the results presented here are only the product of preliminary tests. Nonetheless, depending on the depth of the formed cracks, these may be causing an important drop in the physical properties of such films due to major current percolation impediment.

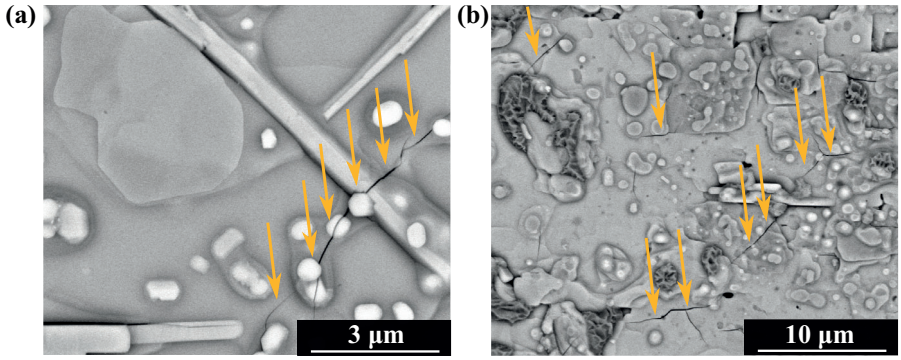


FIGURE 4.30: Back-scattered electrons (BSED) SEM images of films of (a) six and (b) eight layers grown through TLAG P_{O_2}-*route* employing the fast heating ramp, displaying the formation of microcracks (indicated with yellow arrows).

Finally, the measurement of the physical properties for the thick films grown in the two variations of processing conditions described above may be found in the following Fig. 4.31.

The case of the slow heating ramp results in similar physical properties for the two- and three-layered films, possibly due to the combination of similar thickness and use of optimised processing conditions. The thickness increase to four layers sees a decrease by more than half on the final J_c values, both at 5 K and 77 K. This may be likely caused by the decreased texture of the grown YBCO film, evident from the ring intensity around the (00l) diffraction spots of YBCO in the 2D-XRD image in Fig. 4.28. For the films grown through the use of the fast heating ramp, a main enhancement of the physical properties is possible on films of four layers, yielding 800 ± 50 nm of final YBCO with critical current density values of 19 MA cm^{-2} at 5 K and 2 MA cm^{-2} at 77 K, almost equalling the outcome of the optimised two-layered films while doubling their thickness. However, once again an important drop in J_c values is experienced when increasing the thickness to the six- and eight-layered films. The lower degree of epitaxy of these films together with the presence of microcracking, shown in Fig. 4.30, may be considered to be the cause of the reduction of the physical performance.

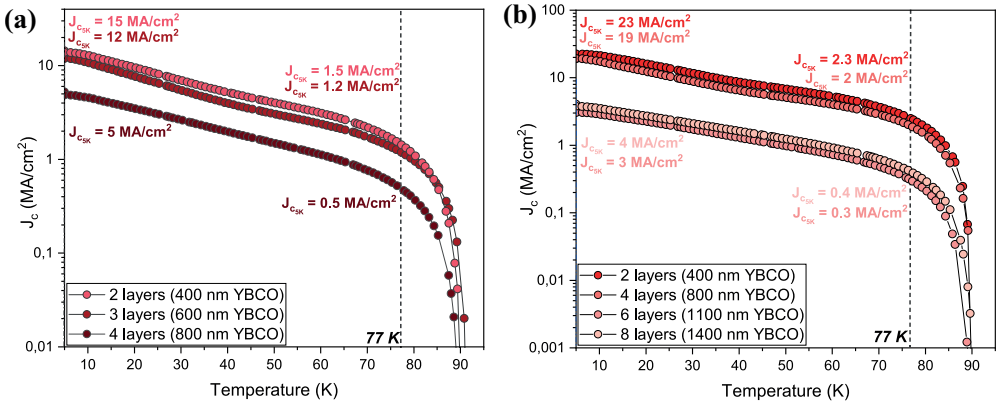


FIGURE 4.31: J_c as a function of temperature for the films of different thickness grown in TLAG P_{O_2}*-route* employing (a) the slow heating ramp (average heating rate $dT / dt = 0.2$ ºC s^{-1}) and (b) the fast heating ramp (average heating rate $dT / dt = 1.4$ ºC s^{-1}). Other processing parameters are specified for each case earlier in the text.

Given the high-performance exhibited by the film of four layers, TEM analysis was carried out to investigate the microstructure, with the resulting images displayed in Fig. 4.32. The high homogeneity of the thickness of epitaxial YBCO, being 750 ± 50 nm, is evident from the cross-sectional STEM-HAADF image in Fig. 4.32(a). The film displays a smooth surface with minor presence of secondary phases. The most superficial region of the film, approximately 80-90 nm thickness from the surface (darker upper segment of the film), is the sole portion where a high defect density is found. Through STEM-EDX elemental maps, secondary phases of (211), (225) can be identified, as displayed in Fig. D.13. Nonetheless, their small size and low distribution are again believed to be of no hindrance to the superconducting performance, as proven by the high J_c value exhibited by this film. However, minor presence of a Ba-Ti-O

reactivity phase with the STO substrate, possibly $BaTiO_3$, is found, with the probably origin being the renowned highly corrosive nature of the transient liquid. Despite here being only found in small amount, the presence of reactivity phases with the substrate may be enhanced when increasing the growth temperature. However, these can be straightforwardly avoided through the use of buffer layers. The high epitaxy is evidenced by the HR-TEM image shown in Fig. 4.32(b), where the c-axis oriented YBCO is displayed. Moreover, as previously found typical in TLAG YBCO films [54], long 248 intergrowths are present close to the interface with the substrate (Fig. 4.32(c)). As previously stated, the presence of these SFs is beneficial due to the nanostrain causing an increase of the vortex pinning.

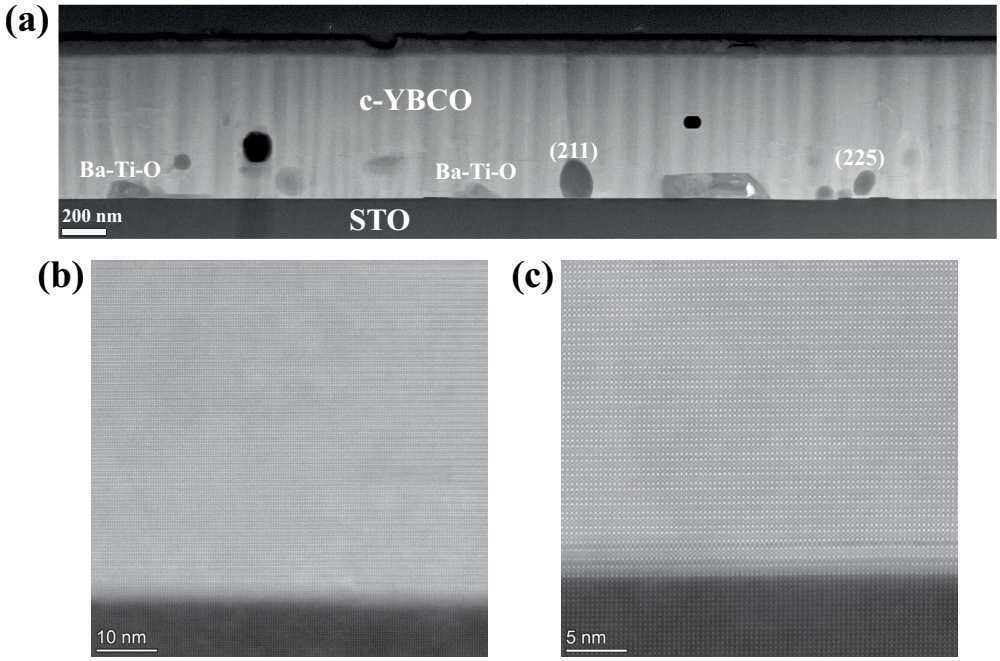


FIGURE 4.32: (a) Low magnification cross-sectional STEM-HAADF image of a four-layered film grown through TLAG P_{O_2}*-route*. High thickness homogeneity of the highly epitaxial YBCO film are evident, in addition to the presence of twin boundaries in the entire film thickness. Secondary phases labels are placed in proximity of the corresponding grain. (b) HR-TEM image displaying the defect-free c-axis oriented YBCO grown on the STO substrate. (c) Evidence of the presence of 248 intergrowths close to the substrate-film interface, showing a distortion of the lattice.

The values of critical current (I_c) for all of the thick films analysed in this subsection are displayed as a function of film thickness in the plot in Fig. 4.33. A great improvement is observed when considering the films of two and four layers grown through the use of the fast heating ramp if compared to the ones in which the slow heating ramp is employed: the I_c is

doubled for the two-layered films and, more impressively, almost quadruplicated for the case of the four-layered one. This promising outcome is certainly demonstrating the fundamental role played by kinetic parameters in the growth through TLAG. As previously reported and evident in the comparison of the TEM images of the films grown employing the two heating ramps, the increase of the average heating rate is substantially reducing the coarsening effects responsible for the crystallization of large grains which are supposed to then lead to an insufficient or inhomogeneous transient liquid formation. This is inevitably hindering the uniform nucleation of epitaxial YBCO and promoting secondary phases which coarsen and coalesce to large grains causing major impediments to current percolation. Films of higher thickness (six and eight layers) are displaying reduced I_c values for the several reasons reported previously, with the feasibility of an enhancement through further optimization of the processing conditions.

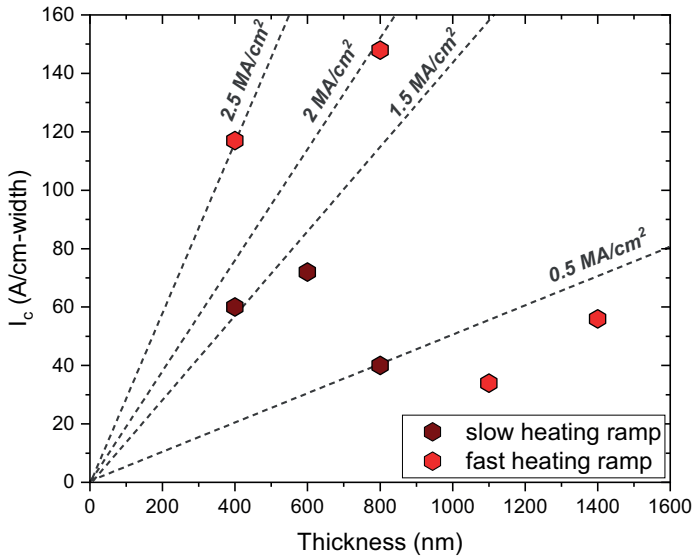


FIGURE 4.33: Plot showing I_c values as a function of final YBCO thickness for films grown through TLAG P_{O_2} - route employing the two heating ramps described in this section.

Nonetheless, this initial investigation regarding the effect of film thickness increase has yielded encouraging results towards the demonstration of the relevance of TLAG-CSD in the industrial framework. The elimination of $BaCO_3$ was confirmed not to be a limitation when elevated thickness was considered, as described in 4.2.5, contrary to general knowledge. High-performance physical properties are additionally demonstrated on YBCO films of almost 1 μm thickness, undoubtedly boosting the suitability of the TLAG-CSD approach developed in this thesis towards the commercial sector.

4.4 TLAG from films of various liquid compositions: influence of supersaturation

The growth optimization on the eutectic composition object of the previous section evinced the importance of controlling kinetic parameters such as the heating rate and the combination of T_{set} and $P_{O_{2,final}}$ to, respectively, reduce the coarsening of secondary phases and improve the epitaxy by tuning supersaturation of the melt. In the current section, a detailed analysis of the influence of varying the transient liquid supersaturation through the growth of films of different liquid composition will be presented.

As previously described in detail in Chapter 1, the innovation at the basis of the TLAG process is the kinetic preference to form a [Ba-Cu-O] transient liquid in non-equilibrium conditions, specifically in regions of the phase diagram where YBCO is the predicted stable phase. Yttrium is found in the liquid as dispersed crystalline Y_2O_3 nanoparticles, resulting from the pyrolysis process. The driving force of TLAG is the Y supersaturation in the transient liquid following the dissolution of the yttria nanoparticles. The atomic mobility of the yttrium atoms is enhanced by the liquid assistance to the process, favouring the Y migration towards the substrate-to-liquid interface which acts as nucleation front of YBCO nuclei and induces its epitaxial growth, if the processing conditions are selected correctly. However, as evidenced in 1.2.4.4, only limited knowledge is available in literature regarding the Y solubility in the [Ba-Cu-O] melt (C_{eq}), and thus its correlation to supersaturation, deriving from several studies obtained in equilibrium conditions. The attainment of the even more relevant data regarding the real concentration of Y (C_{delta}) in the kinetic conditions characteristic to TLAG is yet to be acquired. Generally, the Y supersaturation may be controlled through changes in several processing parameters (T_{set}, $P_{O_{2,final}}$, heating rate), as seen in the previous sections, or in liquid composition: in this thesis, its variation was achieved through the straightforward tuning of the stoichiometry of the metal-organic precursor solution, directly correlated to the composition of the resulting transient liquid. To reach a comprehensive understanding of the TLAG mechanism and the fundamental role played by the modification of the supersaturation deriving from modifications of the transient liquid composition, the effects of growth from films of various compositions will be analysed, starting with some initial considerations regarding the formation of the [Ba-Cu-O] transient liquid.

4.4.1 Introductory considerations on liquid supersaturation

Several studies were the object of extensive analysis of the mechanism controlling the melting of BaO-CuO mixtures, both in film and powder form, especially following the discovery of superconducting behaviour in $La_{x-2}Sr_xCuO_{4-y}$ (LSCO) and YBCO systems [186, 192–194], given the great interest in understanding the growth of the newly discovered materials from such melts. It is renowned that the crystalline state of the studied sample strongly affects

the temperature at which thermally-controlled phenomena (i.e. melting) occur. Specifically, investigation of BaO-CuO mixtures deriving from grinded powders exhibit higher melting temperature compared to the case of films obtained through CSD methods [94, 186, 194]. The latter case displays characteristic melting temperatures up to 150 ºC lower than the past studies on powders, demonstrated at first from films of metal-trimethylacetates and metal-hydroxide based precursor solutions [99] and corroborated in the last decade on solutions of metal-acetate precursors [195]. The effort of all these studies has led to the construction of a pseudo-binary phase diagram of the $BaCuO_2$-CuO system through the analysis of quenches of said mixtures in a variety of gas atmospheres. A schematic model may be found in Fig. 4.34, in which the mol% of CuO of the four liquid compositions considered in this thesis have been indicated. In the mentioned studies, given that $BaCO_3$ decomposition is the limiting step for the formation of $BaCuO_2$, this latter phase is present at lower temperatures in solid form together with CuO if the carbonate elimination had began or was completed at the specific quenching temperature. T_E is indicating the eutectic line, determining the melting onset temperature. The (3:7) composition is the sole to show congruent melting at the eutectic point, where the (Ba:Cu) ratio corresponds to **3**(BaO):**7**(CuO). For compositions with lower copper content, specifically the stoichiometric (2:3) composition and the first investigated with copper excess respect to that, the (3:6) composition, the BaO-CuO mixture melts partially and displays the presence of crystalline $BaCuO_2$ until the liquidus temperature, T_L. Contrarily, the (4:11) composition shows the presence of solid CuO after partial melting, given its characteristically elevated copper excess. Above T_L in all cases, the homogeneous melt of $BaCuO_2$-CuO is generated. It was demonstrated that copper-rich melts promote higher yttrium equilibrium concentration in the melt, with the result of decreasing the corresponding supersaturation (as described in 1.2.4.4). Therefore, the use of compositions with great copper excess was explored in this thesis, following investigations on other REBCO systems [34, 68, 78], as a further possible approach to reduce the optimal processing temperature for c-axis YBCO growth, particularly interesting when considering the feasibility of TLAG in more energetically efficient industrial processes. A variation of the (4:11) composition, namely Y-rich (4:11) composition, is additionally employed in the following investigation of the influence of liquid supersaturation reported in this section. The (Y:Ba:Cu) molar ratio in this specific composition is (1.35:2:5.5), thus allowing for the formation of the same 4(BaO):11(CuO) transient liquid but with a higher solid component due to the added yttrium content compared to the other compositions.

Nonetheless, it must be taken into account that the aforementioned studies employed for the adaptation of the pseudo-binary phase diagram have been carried out through thermogravimetric analysis conducted with slow heating rates (below 0.15 ºC s^{-1}) and on samples with highly different features compared to the films described in this thesis work. The optimization of the fast heating ramp on the eutectic composition films described in the previous subsection demonstrated that the increase in the heating rate to 1.4 ºC s^{-1} is optimal to preserve small

nanocrystalline precursor grain sizes, fundamental to favour the fast reactivity during the transient liquid formation and the YBCO growth from it. The entire study regarding the influence of supersaturation on the epitaxial growth of YBCO from different liquid compositions will, thus, be performed through the sole use of the fast heating ramp (average heating rate of $dT/dt = 1.4$ °C s^{-1}) in TLAG P_{O_2}-*route* experiments.

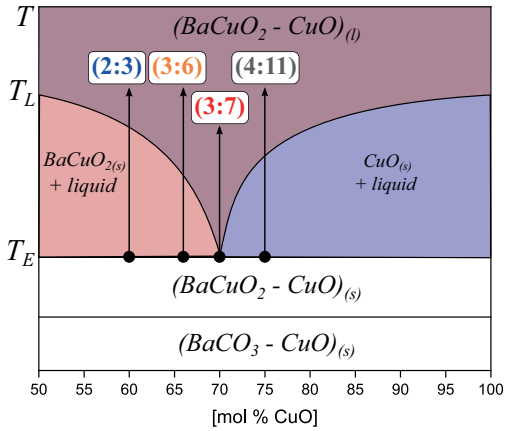


FIGURE 4.34: Schematic representation of the $BaCuO_2$-CuO phase diagram adapted from [94, 99], to include the liquid compositions described in this thesis. Ratios of Ba and Cu for each liquid composition are specified as (Ba:Cu), corresponding to each mol% of CuO indicated with arrows on the phase diagram. Specific eutectic and liquid formation temperatures are depending on various processing parameters (atmosphere, grain size of precursor phases, sample type).

Following the optimization of TLAG P_{O_2}-*route* on films of (3:7) composition, the initial investigation on the growth of films of the five different transient liquids considered in this thesis work was conducted adopting the optimal processing conditions determined for the eutectic mixture (heating to $T_{set} = 835$ °C at a constant $P_{O_{2,base}} = 10^{-5}$ bar, performing a pressure jump to $P_{O_{2,final}} = 1$ mbar). It must be specified that all films described in this section are exhibiting an approximate thickness of 800 ± 50 nm prior to the TLAG process (result of twofold deposition and pyrolysis process), yielding final YBCO in the range of 400-500 nm. No variation of this parameter has been investigated in films of different liquid compositions, given that the understanding of the influence of supersaturation to the epitaxial nucleation of YBCO was the prime objective of this section.

Fig. 4.35 reports the 2D-XRD images acquired from GADDS and the corresponding surface morphology of films of all compositions. Clearly, the eutectic composition is discerning between optimal c-axis nucleation conditions, with the two compositions with higher copper excess displaying similarly high epitaxy, in contrast to the low-copper content ones which are exhibiting strong contributions of misorientation around the c-axis (rings are visible around the (00l) diffraction spots). Moreover, the optimal film surface showing flat and continuous

c-axis YBCO with the copper excess nucleated as superficial CuO grains is solely exhibited by the copper rich (3:7) and the two (4:11) compositions. The least copper rich ones are displaying a highly granular surface, coinciding with misoriented YBCO nucleation: in the extreme case of the (2:3) composition, the formation of large grains of YBCO (103) is denoting the non-optimal supersaturation conditions, enhanced by the inadequate growth parameters. Despite the stoichiometry of the (3:6) composition is more copper-rich, surface analysis shows no presence of CuO precipitates: these are possibly trapped inside the film and a misorientation of the c-axis YBCO is appreciable.

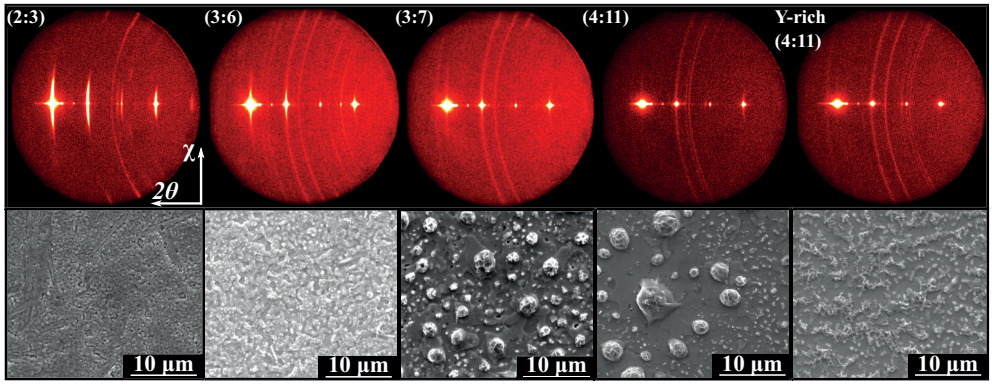


FIGURE 4.35: XRD and SEM results from the initial testing through TLAG P_{O_2}*-route* process on films of different transient liquids. Copper is increased in the stoichiometry of the liquid going from left to right (exact composition identified on the upper-left of each panel). 2D-XRD images are shown in the upper panels and surface morphology analysis through SEM in the lower panels. Films are grown at a $T_s$et = 835 ºC at a constant base $P_{O_2} = 10^{-5}$ bar, performing a pressure jump to a final P_{O_2} of 1 mbar.

and, depending on size and distribution, may be disrupting importantly current percolation.

A comparison of the rocking curves (ω-scans) measured on the five films is displayed in Fig. 4.36. The correlation between elevated copper content of the liquid composition and high epitaxial texture of the film is evident, with the eutectic composition yielding a film with $\Delta\omega$ = 0.18º and the (4:11) and Y-rich (4:11) composition films both resulting in a value of 0.19º. Previous studies in the group reported values of $\Delta\omega < 0.6$º to be linked to improved current percolation [54], suggesting the extremely low ones reported here for the copper-rich films to be promising towards high-performance physical properties, similar to the state-of-the-art YBCO grown on single crystalline substrates through conventional methods. As anticipated from the 2D-XRD images showing higher misorientation of YBCO in the compositions with lower copper content, the relative rocking curves have a similarly broader FWHM ($\Delta\omega$ =

0.31° and $\Delta\omega = 0.30°$ for the (2:3) and for the (3:6) composition, respectively), suggesting the elevated supersaturation in these liquids is promoting mixed nucleation.

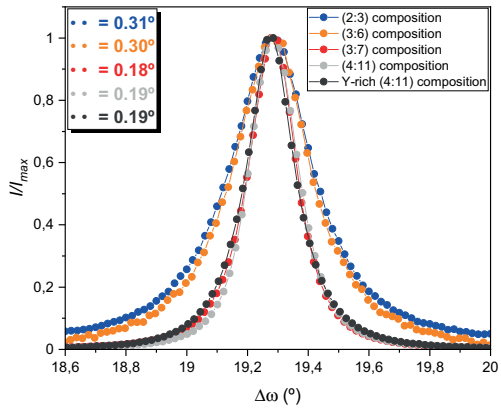


FIGURE 4.36: Rocking curves relative to the grown films of the five transient liquid compositions displayed in Fig. 4.35. Values of $\Delta\omega$ are indicated in the inset, using the same colour as the plotted curves.

The analysis of the physical properties measured on these films follows a foreseeable, comparable trend (Fig. 4.37). J_c values measured at 5 K on such films are plotted as a function of $\Delta\omega$, and the great enhancement of current percolation is tangible when considering the copper-rich compositions characterised by lower $\Delta\omega$ values. Compositions with lower copper content are, instead, displaying a decrease in J_c by more than half together with more elevated $\Delta\omega$. Accordingly, the comparison of the T_c curves is further demonstrating the improved outcome of the eutectic composition and the compositions with larger copper excess, which display critical temperatures above 90 K and sharp transitions distinguished by reduced ΔT_c values, strong indication of optimal oxygen doping and no phenomena linked to current percolation hindrances (such as presence of large secondary phases, reactivity phases or C accumulation in the YBCO grain boundaries). Contrarily, the T_c relative to the stoichiometric (2:3) and the (3:6) composition are showing critical temperatures below 90 K in addition to broader transitions, indicative of phenomena linked to suppression of superconducting properties. This correlation is characteristic to the measurement of these properties through SQUID magnetometry (details on the measurement may be found in A.5.3), as it measures the flux penetration in the superconducting film. Any hindrance to current percolation will be evident due to the broadening of such transitions.

J_c, T_c and ΔT_c values for each film object of this initial investigation are reported in the following Table 4.2.

The reported preliminary results suggest the supersaturation of the liquid in the same processing conditions is crucially controlling the conversion of homogeneous to heterogeneous

nucleation, giving rise to homogeneously nucleated YBCO when the supersaturation is high (compositions with lower copper content) transformed to highly epitaxial YBCO when the liquid supersaturation is lowered (eutectic and copper-excess compositions). As previously mentioned in 1.2.4.4, in the case of the reported studies on Y solubility in [Ba-Cu-O] melts, two melt compositions were tested, namely (3BaO:5CuO) and (3BaO:7CuO) [74, 79, 80].

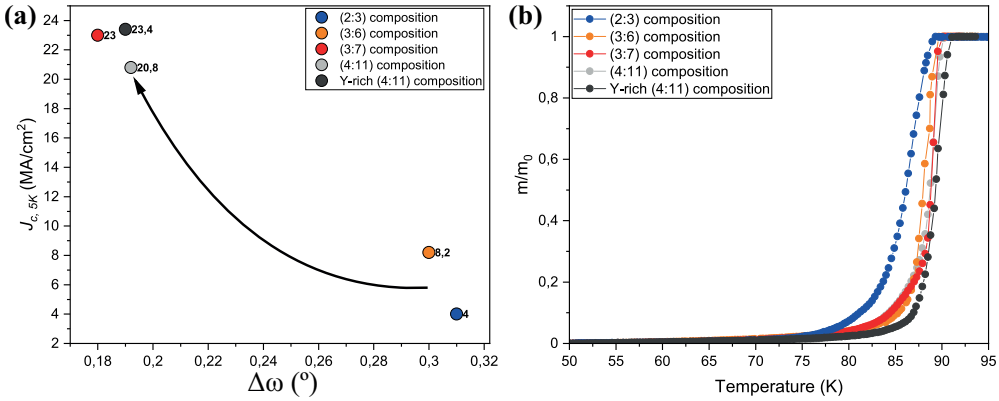


FIGURE 4.37: (a) J_c values measured at 5 K reported as a function of the $\Delta\omega$ obtained from the rocking curves of samples of the five liquid compositions, showing the increase by more than double directly correlated to the increase in copper content in the precursor solution stoichiometry. (b) Comparison of the T_c curves measured on the same films as in (a).

Liquid Composition	J_c 5K (MA/cm^2)	J_c 77K (MA/cm^2)	T_c (K)	ΔT_c (K)
(2:3)	4.0	0.4	89.3	7.0
(3:6)	8.2	0.9	89.6	6.0
(3:7)	23.0	2.5	90.0	5.0
(4:11)	20.8	2.0	90.3	5.0
Y-rich (4:11)	23.4	2.3	91.0	4.4

TABLE 4.2: Physical properties of films of the five compositions grown employing the processing conditions resulting from the optimization process conducted for the (3:7) composition described in 4.3.1.

Substantial decrease in supersaturation could be achieved when increasing the copper content of the melt. When analysing the solubility of samarium in [Ba-Cu-O] melts of four compositions [78], specifically (3BaO:4CuO), (3BaO:5CuO), (3BaO:7CuO), and (3BaO:9CuO), which straightforwardly finds a parallelism with the study of different liquid compositions carried out in this thesis for the case of Y, the trend was increasingly evident. The increase in the copper content of the melt composition results in an important increase in the solubility of the RE in the melt, when the same processing conditions are considered. Thus, with a simple increase of the copper content, lower supersaturation may be reached, previously linked to a favoured nucleation of c-axis REBCO [113].
With the aim of understanding the parameters controlling the nucleation and growth of YBCO through TLAG from different supersaturation conditions, a wide variety of growth profiles have been tested on films of the five liquid compositions and several contributions to the final epitaxy will be taken into account to identify possible tendencies correlated to liquid supersaturation. A final evaluation of these contributions will clearly elucidate the crucial parameters determining high-performance film properties.

4.4.2 Determining the effects of different liquid supersaturation on YBCO epitaxial nucleation

A total of 57 samples of the five different liquid compositions have been grown through TLAG P_{O_2}-*route* employing a large set of processing conditions. Considering the optimization previously performed on (3:7) composition films, the tested temperature ranged from 825 ºC to 850 ºC and the $P_{O_{2,final}}$ values extended over the range 1-7 mbar. The first step of the process was unvaried for all experiments, given the use of the fast heating ramp (average heating rate $\mathrm{d}T$ / $\mathrm{d}t$ = 1.4 ºC s^{-1}) and the $P_{O_{2,base}} = 10^{-5}$ bar were previously demonstrated to yield optimal crystalline precursor phases for the formation of the transient liquid. Thorough characterization of all films has been carried out, specifically through various XRD techniques, SEM analysis to evaluate surface morphology and TEM analysis to inspect microstructural features, and physical properties to determine their superconducting performance. Correlations between the results of all of the former characterization techniques have been analysed to fully evaluate the outcome of varying supersaturation on the epitaxy, and discussions will be regarding two main subjects: the contribution of secondary phases and the morphological characteristics of film surface. The data analysis methods employed for the results described in this subsection are thoroughly explained in Appendix D, specifically in D.2.2.

4.4.2.1 Epitaxy and the contribution of secondary phases

This first portion of the analysis will be exclusively devoted to the investigation of how the supersaturation of each specific liquid composition affects the epitaxy of YBCO and the eventual promotion towards nucleation of secondary phases.

A perceptible tendency may be observed when comparing the contribution of the epitaxial texture ($\Delta\omega$) to the critical current density, showing a comparable trend at both 5 K and 77 K (Fig. 4.38). Similarly to the preliminary results from a single set of growth conditions (Fig. 4.36), the films of compositions with lower copper content exhibit here larger values of $\Delta\omega$, suggesting worsening of the texture in films of these liquid compositions. Possibly, the elevated supersaturation conditions are unfavourable for full c-axis orientation and are thus lying in the region of mixed nucleation (Fig. 1.13). The low epitaxy hinders current percolation, inevitably leading to a general drop in the values of J_c for both (2:3) and (3:6) compositions. Conversely, the compositions more rich in copper result in higher epitaxial nucleation and, thus, generally more elevated values of critical current density. However, despite this trend, one may observe a significant overlapping of the $\Delta\omega$ values of all compositions around the range 0.25-0.30º in which the J_c is strongly increased only in the films of copper-excess.

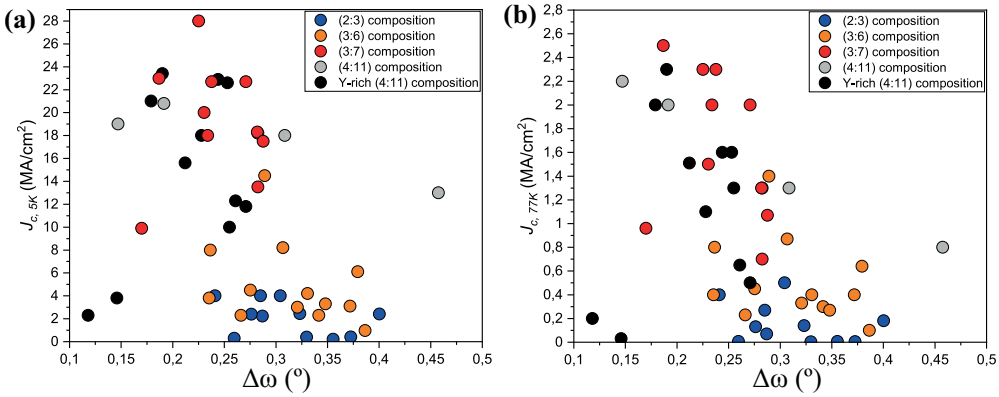


FIGURE 4.38: J_c values measured at (a) 5 K and (b) 77 K as a function of the $\Delta\omega$ values obtained from the rocking curves of the films of the five liquid compositions grown in all of the tested processing conditions in TLAG P_{O_2}*-route*.

This result is clearly demonstrating the texture is an important parameter, but by no means the sole contribution to the improvement or deterioration of the physical properties. Therefore, a complete analysis of the correlation of several possible parameters to the high-performance of the films considering the differences in supersaturation is necessary to be able to precisely control the nucleation conditions regardless of the transient liquid composition.

A detailed analysis of the 2D-XRD patterns of the films of the five liquid compositions grown in all of the tested conditions was carried out. Integration in χ of the peaks relative to phases judged as a disruption to the full epitaxy allowed for a quantification of the contribution (as a percentage) of the individual phase to the epitaxial moiety. Details regarding the evaluation of the secondary phases and the method followed for integration may be found in D.2.2.1. The phases considered to be of major relevance towards the worsening of the epitaxial film quality are: a/b-grains and homogeneously nucleated YBCO grains (random orientation, (103)), and

the secondary phases of (211) and (225). In Fig. 4.39 the contribution of each one of the listed phases to the YBCO (005) peak is represented for each individual liquid composition as a colour map on the TLAG kinetic phase diagram, with each point indicating the particular set of (T, $P_{O_{2,final}}$) conditions selected. Several considerations are to be made, dividing the focus on the phases deriving from a mixed homogeneous and heterogeneous nucleation, namely misoriented YBCO (103) and a/b-grains (respectively, (a) and (d) in Fig. 4.39), from the secondary phases of (211) and (225) (Fig. 4.39 (b) and (d), respectively). The contributions of randomly-oriented YBCO (103) and a/b-grains are predominant in the compositions characterized by low copper content, specifically important in films of (2:3) composition grown at elevated $P_{O_{2,final}}$ in all of the tested temperatures, where values of the contribution of the latter phase to the epitaxy close to 70% are reached[7]. Supersaturation increases with the T_{set} and the $P_{O_{2,final}}$ [113]: for same processing conditions, the supersaturation is higher in liquid compositions with low copper content, thus favouring the emergence of a/b-oriented YBCO and misoriented grains due to the competing homogeneous-heterogeneous nucleation. Films of copper-rich compositions exhibit null contributions deriving from a/b-grains in all of the tested conditions, demonstrating the decrease in supersaturation through tuning of the transient liquid composition is successfully promoting the c-axis growth. Nonetheless, the (4:11) and Y-rich (4:11) compositions display the highest presence of secondary phases. Evidently, Y-rich (411) composition greatly favours the nucleation of (225) grains, given the large excess of copper and, additionally, of yttrium intrinsic to the stoichiometry, and is found to be indirectly correlated to the T_{set}. Nonetheless, this phase is present in the other compositions as well, with the sole exception being the eutectic one. Formation of secondary phases is presumably favoured in the compositions of lower copper content due to the non-ideal nucleation conditions for c-axis YBCO: as explained in 4.2.6, the initial hindrance to the elimination of $BaCO_3$ is an additional parameter negatively affecting the full formation of the transient liquid. Besides favouring homogeneous nucleation of YBCO, the possible inhomogeneities in the transient liquid layer will lead to competition between growth of specific secondary phase and YBCO, as a result of localized elevated concentrations of a particular metal cation. For what concerns the contribution of the (211) secondary phase (Fig. 4.39(b)), the sole composition presenting significant formation of such crystalline phase is, again, the Y-rich (4:11) composition in several of the tested growth conditions. Promotion of the nucleation of such phase has been previously reported in YBCO growth from Y-rich melts, which resulted in a mixture of YBCO and (211) in the cases of melt-textured techniques [196–202] and zone melting processed specimens [203, 204]. The (211) phase is at times intentionally included in epitaxial YBCO samples as it was proven to enhance critical current densities due to pinning effects [197, 203].

[7] A reminder for the reader, these values are employed as a straightforward quantification of the contribution of a specific phase to the epitaxy, but are not indicating the volume fraction of the analyzed phase. For more information regarding the calculations leading to the attainment of these values, please see D.2.2.1

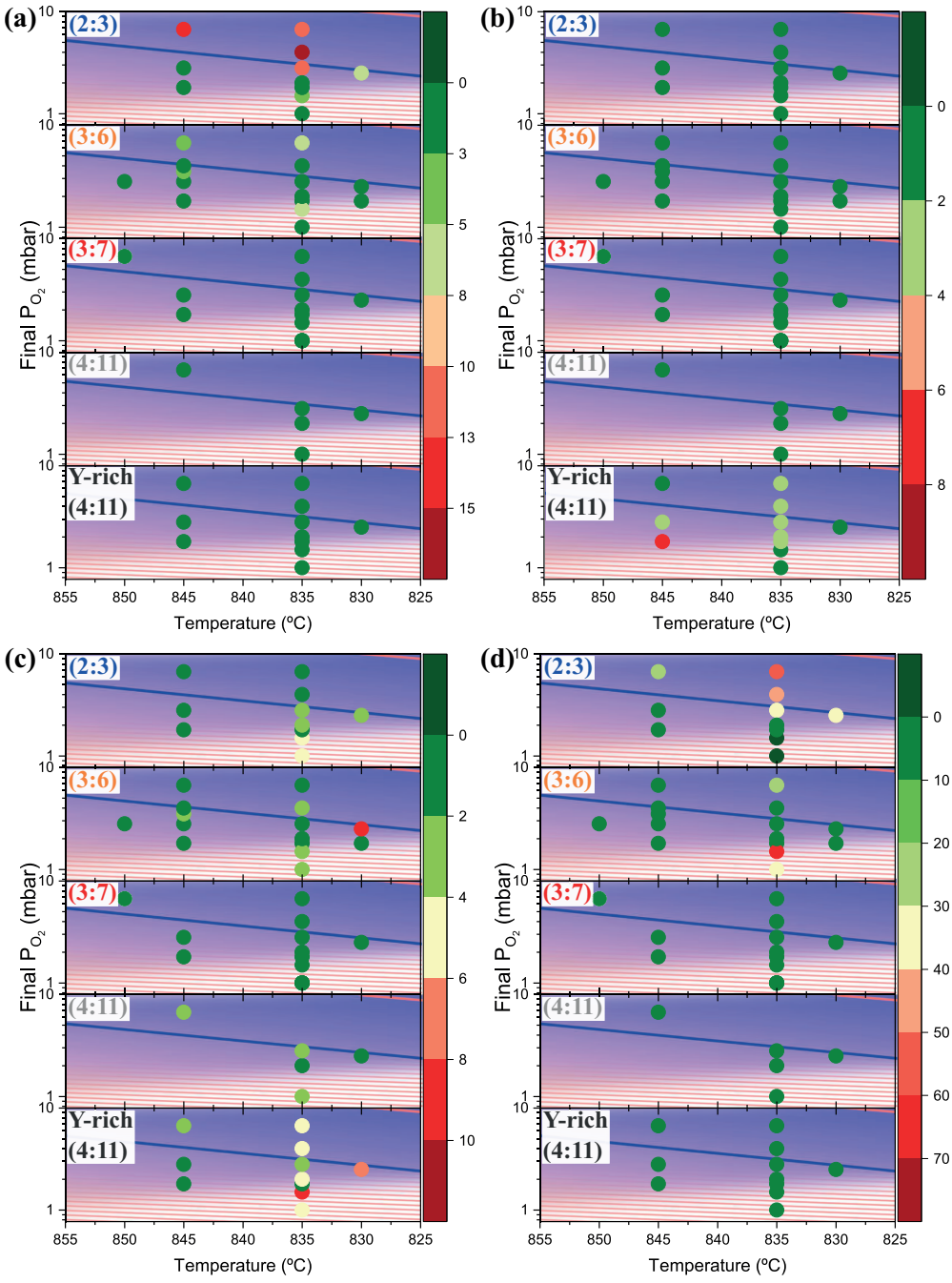


FIGURE 4.39: Contributions of individual secondary phase to the epitaxy of the film represented as colour maps on the TLAG kinetic phase diagram for each of the five transient liquid compositions. The points correspond to the specific conditions of T_{set} and $P_{O_{2,final}}$ in which each film is grown. Contributions of (a) randomly-oriented YBCO (103), (b) (211) secondary phase, (c) (225) secondary phase, and (d) a/b-grains are considered for this analysis, with respect to the YBCO (005) peak. The liquid composition is indicated in top-left of each panel. For easier visual understanding, the scale is adapted according to the maximum intensity of each phase.

However, as reported in 4.2.1, when employing the slow heating ramp large coarsened nuclei of this phase were demonstrated to be at the origin of critical current percolation impediment. For the films described here, a further analysis to unravel possible correlation between the presence of these secondary phases and the physical properties of the YBCO film was conducted through TEM studies, and will be presented further on in the text.

An overview of the contribution of each of the phases considered to be disrupting the epitaxy of the films to the J_c (measured at 5 K) may be found in Fig. 4.40. Similarly to the previous discussion, a distinction between contributions from misoriented or homogeneously nucleated YBCO grains and other secondary phases may be made. Observing the dependence of J_c

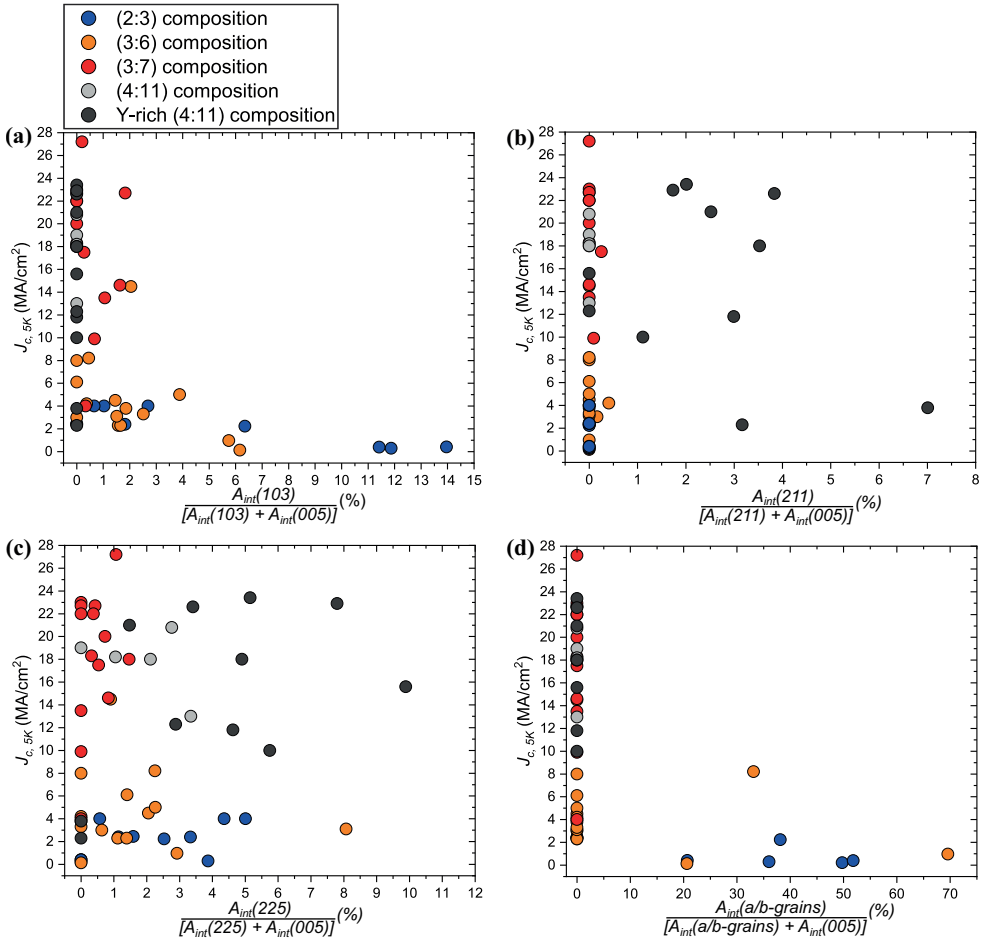


FIGURE 4.40: J_c (measured at 5 K) dependence on the contribution of (a) YBCO (103) grains, (b) (211) secondary phase, (c) (225) secondary phase, and (d) a/b-grains for the films of the five liquid compositions grown in the processing conditions shown in Fig. 4.39.

on the presence of YBCO (103) and a/b-grains, it is evident that the increased presence

of these phases is leading to a significant drop in the physical properties. In line with the results presented until now, this is principally found in the films of compositions with low copper content, where the elevated supersaturation conditions intrinsic to the transient liquid are unfavourable for the nucleation of the sole c-axis orientation of YBCO in the processing conditions tested. No contributions from these phases are displayed by the films of copper-rich compositions, leading to values of $J_{c,5K}$ of up to 28 MA cm^{-2}. Liquid supersaturation in these compositions seems to be optimal for the promotion of c-axis oriented stable YBCO nuclei. Nonetheless, when considering the contributions of (211) and (225) secondary phases, previously determined to be more significant in the compositions with larger copper-excess, no specific correlation to the physical properties can be observed linked to the increase or decrease of the secondary phases in question. Hypothetically, these phases are exhibiting such small grain sizes as to avoid the disruption of the film, thus creating no hindrances to current percolation. Moreover, if present in the appropriate size range, these may act as natural pinning centers and enhance physical properties through defect generation in the YBCO lattice, demonstrated to increase vortex pinning [8, 189–191].

Microstructural analysis through TEM confirms this hypothesis. The cross-sectional STEM-HAADF image shows the film displays homogeneous thickness of the epitaxial YBCO layer with the presence of a large grain of CuO on the film surface (Fig. 4.41(a)). Considering its size, the superficial position is desirable to avoid hindrances to current percolation, and as previously mentioned, is indicative of a rapid heterogeneous nucleation consequently pushing these grains to the surface. Nonetheless, despite several grains of secondary phases are observed inside the film, their reduced sizes ($\leq$ 100 nm) are not limiting the physical properties through current blockage. Through the acquisition of STEM-EDX elemental maps acquired for Ba L-edge, Y K-edge, Cu K-edge, and O K-edge, the identification of these secondary phases is possible. As expected due to the liquid composition of this film, the secondary phases are predominantly yttrium- and copper-rich, possibly identifiable with the mixed oxide $Y_2Cu_2O_5$. The additional minor presence of grains composed by barium and copper suggest the formation of the mixed oxide of these elements. Epitaxial YBCO grown through TLAG is characterized by (248) intergrowths, as observed in Fig. 4.41(b), and in this film, these are majorly present in the upper portion. However, the growth of highly epitaxial YBCO is obtained, as displayed in Fig. 4.41(c). The absence of a direct correlation between the prevailing presence of secondary phases of (211) and (225) in films of Y-rich (4:11) liquid composition and an expected decrease in the physical properties finds thus an explanation in the TEM images presented here. Despite the formation of several grains of the aforementioned secondary phases, the superconducting properties of the films of this composition display high-performance given the reduced size of these grains which are not an obstacle to current percolation or present no major disruption of the highly epitaxial grown YBCO.

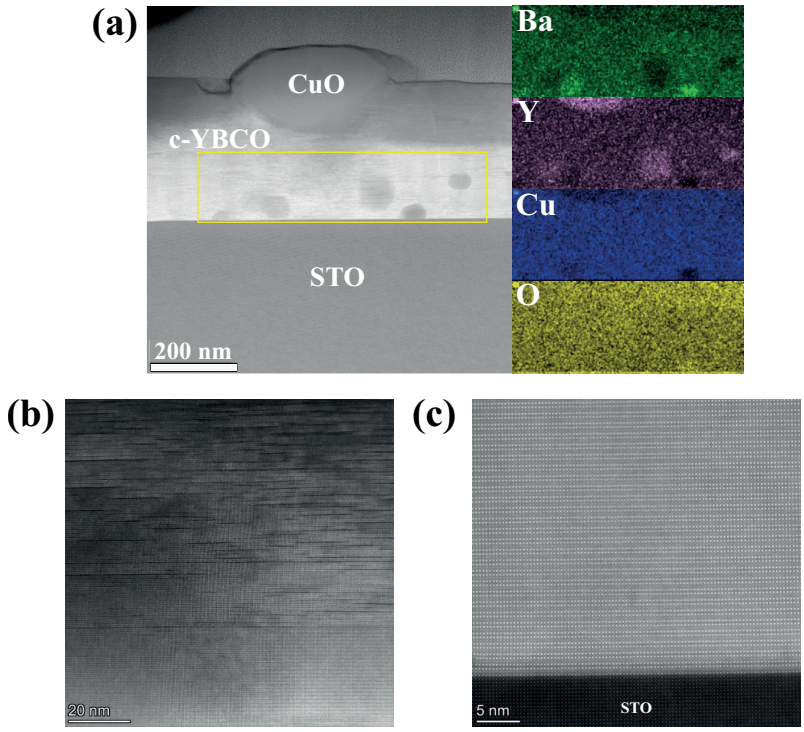


FIGURE 4.41: (a) Cross-sectional STEM-HAADF image of a film of Y-rich (4:11) composition grown through TLAG P_{O_2}-*route* heating to a T_{set} = 835 ºC with the use of the fast heating ramp at a $P_{O_{2,base}}$ = 0.01 mbar and performing a pressure jump to $P_{O_{2,final}}$ = 1 mbar. STEM-EDX elemental maps are acquired on the region of the film indicated by a yellow rectangle for Ba L-edge, Y K-edge, Cu K-edge, and O K-edge, and allow for the identification of the secondary phases. (b) Evidence of the formation of long (248) intergrowths, distorting the YBCO lattice. (c) HR-TEM displaying the growth of highly-epitaxial YBCO. Darker area is corresponding to the substrate (STO) single crystal lattice.

Let us now consider the overall correlations of physical properties to the presence or absence of the phases considered in this analysis. The most determinant cases are the ones of complete absence of the analysed phase: if considering each individual composition, J_c values are increasing when the contribution of the phase is close to zero. However, if considering the global trend on the films of all the compositions studied, the low-copper content ones are yielding films of decisively lower performance compared to the copper-rich films. This tendency is visually distinguished in Fig. 4.42, where critical current density values are plotted as a function of the copper content in each liquid composition. (2:3) and (3:6) composition films exhibit maximum J_c values of 4 MA cm^{-2} and 14.5 MA cm^{-2}, respectively. In contrast, besides the higher maximum J_c values, films deriving from the eutectic liquid composition and the ones

with copper excess display critical current densities in a range of more elevated values, with the lowest-performing cases coinciding with the leading ones from the compositions with less copper.

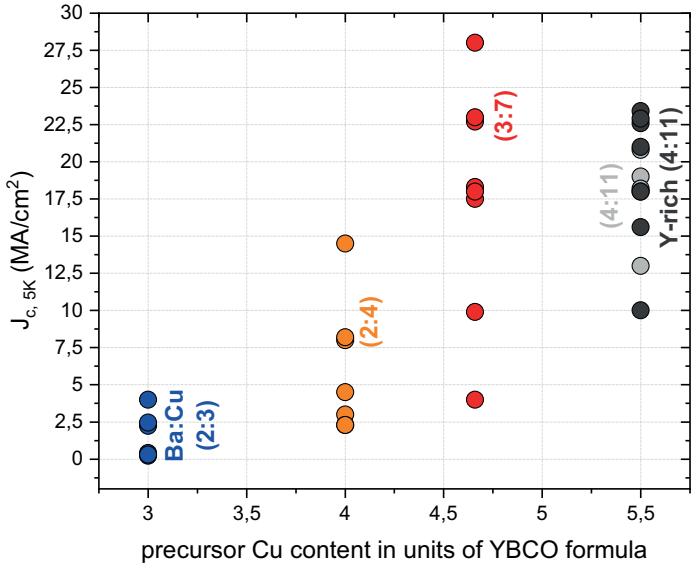


FIGURE 4.42: Values of J_c measured at 5 K as a function of the copper content in each liquid composition, relative to films grown through TLAG P_{O_2}*-route* described in this subsection.

Therefore, taking into account the best-performing films for each composition where the presence of phases disrupting the epitaxial YBCO film is nonexistent or close to zero, further parameters must be affecting the physical properties and seem to have a significant relation between these and the specific transient liquid composition. In light of this, the final analysis conducted on the films of different compositions described in this subsection has been a thorough examination of the surface morphology from SEM images.

4.4.2.2 Morphological features of film surface

With the objective of attaining a complete evaluation, a system of classification of morphological features observed in the SEM images has been developed. Firstly, a distinction between "ideal surface morphology" and "contributions to current blockage" was made, and a definition of each is now given. As illustrated in 4.2.1, "ideal surface morphology" is linked to highly epitaxial YBCO, expected to be smooth and continuously homogeneous, with the possibility of terrace-like steps characteristic of the liquid-assisted growth process. If the film under examination is deriving from a copper-rich composition, precipitates of copper oxide are to be found as protrusions on the film surface in order to avoid hindering current percolation through the c-axis YBCO. Conversely, "contributions to current blockage" are all of the phenomena

linked to a disruption of the film continuity, such as dewetting, presence of grains deriving from substrate-liquid reactivity (usually, needle-like formations), granular morphology which is generally linked to a higher contribution of misoriented YBCO, and a/b-grains, which are typically visible given their 90º orientation respect to the epitaxial film surface. Detailed explanation of how these features were classified is given in Appendix D, specifically D.2.2.2. Representative cases of surface morphology from films of the five liquid compositions in several processing conditions are shown in the following Fig. 4.43, where the mentioned typical features may be observed.

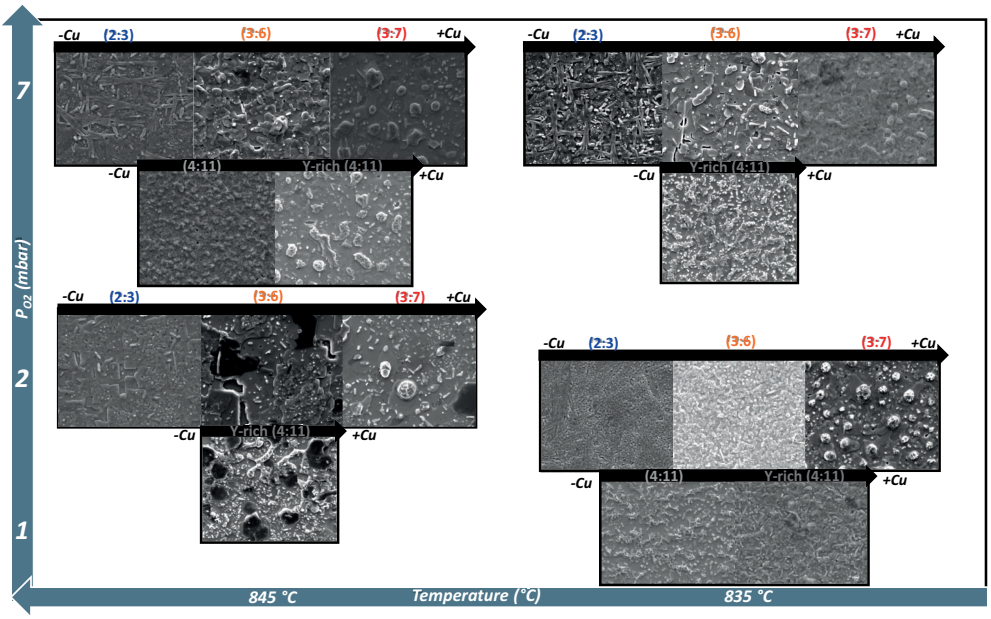


FIGURE 4.43: SEM images of used for the analysis of surface morphological features of films of the five liquid compositions grown through TLAG P_{O_2}*-route*, represented on a *T*-P_{O_2} diagram with corresponding processing conditions.

One may notice how the compositions more rich in copper present a smooth surface with the precipitates due to the excess of copper found as superficial precipitates, and in some cases of the (4:11) or Y-rich (4:11) compositions, as dendritic-like structures. Major features considered to be hindering current percolation are most commonly visible in the films of lower copper content liquids, which are exhibiting granular morphology and dewetting phenomena, the latter mainly found in proximity of large grains of secondary phases or misoriented YBCO.

Following this evaluation, a method to visually represent an overview of this qualitative analysis had to be established. Considering the concomitant use of machine-learning based algorithms in the group for the study of several parameters linked to the TLAG-CSD approach

[156], categorical variables were chosen for the representation of these morphological features. In this context, a binary model (0,1) was employed: when one of these surface characteristics was present in the film, it was indicated with a 1, whereas a 0 was assigned to the complete absence of such features. Through the use of this model, plots showing the correlation between the two distinguished morphological categories as a function of $P_{O_{2,final}}$ could be built considering the two (constant) processing temperatures of 835 ºC and 845 ºC. The results are displayed in Fig. 4.44. In these plots, the quantification of presence or absence is visibly identifiable and several considerations may be made. The stoichiometric (2:3) composition shows, at both of the tested T_{set}, complete absence of a smooth surface and a persistent presence of phenomena contributing to current blockage in all of the selected $P_{O_{2,final}}$ conditions. The elevated supersaturation intrinsic to this liquid composition is never successfully lowered enough to promote full c-axis nucleation through variations of the processing conditions, resulting in films with generally granular morphology at low $P_{O_{,final}}$ and more elevated contributions due to misorientation and homogeneous nucleation, with the addition of dewetting, when this processing parameter is increased. This may be suggesting a different trend than what observed in the studies of Y solubility as a function of P_{O_2} reported in Chapter 1, specifically in 1.2.4.4, where an increase of the latter parameter, at elevated temperatures, was linked to an increased Y solubility in the melt, and thus a lowering of the supersaturation. Again, these studies were performed in conditions of thermodynamical equilibrium, far from the out-of-equilibrium conditions characteristic of TLAG. Here, the films of (2:3) composition, a liquid which displays an intrinsically high supersaturation deriving from its stoichiometry, seems to show an increase of the supersaturation when the $P_{O_{,final}}$ final is increased.

Similar trend is observed in the films of (3:6) composition grown at low T_{set}, which nonetheless show an improvement at lower $P_{O_{2,final}}$ conditions with the increase of temperature to 845 ºC. This is anticipated by the data displayed in Fig. 1.15, in which the supersaturation when considering one single melt composition may be importantly lowered through an increase in temperature, as the Y solubility in the melt is enhanced. Nonetheless, with a $P_{O_{2,final}}$ increase, there seems to be a direct correlation to the liquid supersaturation, with the result of worsening the nucleation conditions for c-axis YBCO. However, these results are suggesting the intrinsically elevated supersaturation for these compositions at the selected T-$P_{O_{2,final}}$ conditions are still excessive for the promotion of full c-axis nucleation: the formation of misoriented and homogeneously nucleated YBCO in these films in addition to the fast growth rates typical of TLAG are favouring the presence of secondary phases and other morphological phenomena responsible for the impediment of critical current percolation, resulting in the general drop in physical performances demonstrated in Fig. 4.42.

The eutectic composition is instead characterised by optimal surface morphology in all of the tested growth conditions, with only exception being the film grown at lower temperature (835 ºC) and at the highest final $P_{O_{2,final}}$ tested (6.7 mbar): here, a highly granular morphology and the absence of CuO precipitates on the surface of the film are indicating lower c-axis oriented

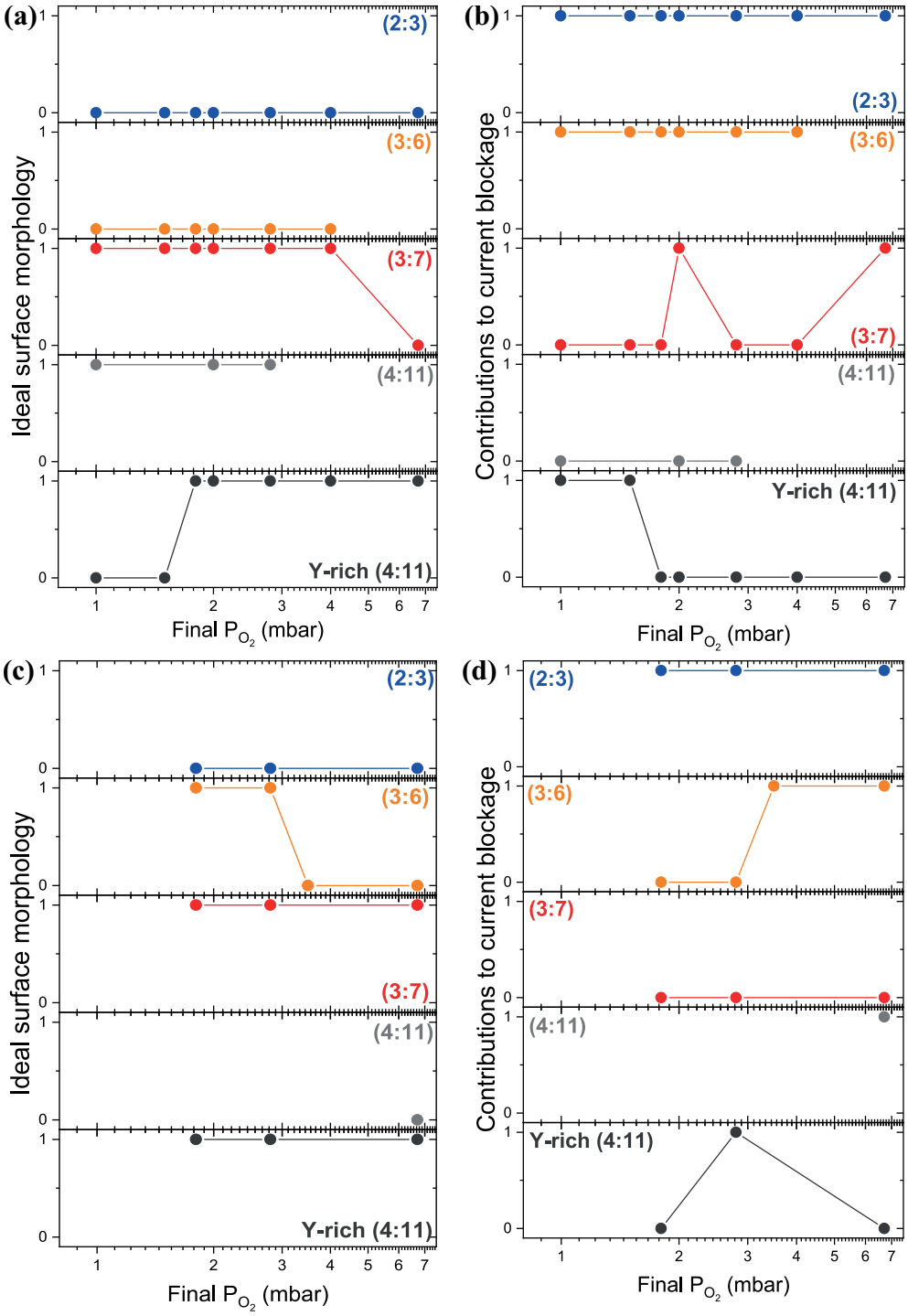


FIGURE 4.44: Representation of the surface morphology analysis quantified through the use of categorical variables following a binary model (0 = absence; 1 = presence). Ideal surface morphology and contributions to current blockage (as defined in the text) are displayed for films grown at (a),(b) 835ºC and (c),(d) 845 ºC as a function of $P_{O_{2,final}}$.

YBCO resulting from the increase in supersaturation directly correlated to the extreme increase in P_{O_2}. The tendency of supersaturation with P_{O_2} variation is therefore an extremely relevant one, and further investigation to fully evaluate the Y (or other RE) solubility with the increase of this parameter is essential, especially in the working temperature range of TLAG.
The low supersaturation characteristic of the liquid composition with highest copper excess, the (4:11), is favouring the formation of highly epitaxial films with optimal surface morphology and complete absence of any phenomena linked to current impediment in all of the selected $P_{O_{2,final}}$ values at 835 ºC. Contrarily, in the only film of this composition tested at a higher temperature, the combination of additionally elevated P_{O_2} is leading to a rough surface with no copper oxide precipitates present, strong indication of an increased supersaturation of the liquid and thus, promotion of homogeneous YBCO nucleation. The presence of higher solid portion in the transient liquid of Y-rich (4:11) composition (thus higher supersaturation compared to the case of (4:11) composition) seems instead to be detrimental for the achievement of optimal surface morphology when low T_{set} and low $P_{O_{2,final}}$ (coinciding with low supersaturation due to processing conditions) are selected. However, the increase of the latter parameter at the constant, low T_{set} = 835 ºC seems to be beneficial for an improvement towards an ideally smooth epitaxial YBCO surface with protrusion of CuO precipitates. Additionally, the increase in T_{set} to 845 ºC provides optimal conditions for films with smooth surfaces to be obtained, presumably due to an enhancement of the Y solubility in the liquid (thus lowering of the supersaturation), with only one condition of $P_{O_{2,final}}$ (2.8 mbar) showing dewetting phenomena contiguous to visible grains of secondary phases.

Finally, a brief discussion is required after analysing the factors at the origin of the correlation between the supersaturation of the transient liquid and the resulting physical performance of the films, influenced by the contributions of secondary phases and misoriented or homogeneous nucleation to the c-axis YBCO. Undoubtedly, this is a multi-parameter problem: several, different factors are to be favourably controlled in order to enhance the final physical performance of the superconducting films. Additionally, small contributions of these are at the origin of important decrease in the physical properties, requiring a precise tuning of the supersaturation through processing parameters for each liquid composition. As shown in Fig. 4.38, the texture of the epitaxial YBCO film is a fundamental parameter to be controlled, and the decrease of the $\Delta\omega$ obtained from the rocking curves is directly linked to the increase of the physical properties of the film, if other parameters are not affecting the outcome. However, it is evident that for compositions of lower copper content, even when $\Delta\omega$ values were reduced, no improvement to the performance of the films could be achieved, suggesting other variables to be playing an important role. In the tested processing conditions, however, the high supersaturation of the melts deriving from the (2:3) and (3:6) compositions are greatly favouring the homogeneous nucleation of YBCO, together with the presence of misoriented grains. Tuning the growth parameters of T_{set} and $P_{O_{2,final}}$ is not leading to a sufficient lowering of the intrinsically high

supersaturation of these liquid compositions. Moreover, as reported in 4.2.6, the incomplete elimination of $BaCO_3$ in the first step of TLAG, the low-P_{O_2} heating, may additionally result in an inhomogeneous formation of the transient liquid, from which stable nuclei of secondary phases may arise. This is further reflected in the highly defective surface morphology observed for the films of these compositions, which exhibit granular morphology characteristic of poor epitaxy. Due to the extreme growth rates of TLAG, in proximity of secondary phases or large misoriented YBCO grains, dewetting phenomena are present, again a contribution to current percolation impediment and the plausible cause of a general drop in the physical properties of such films. To overcome such complications, higher processing temperatures are believed to be beneficial for (2:3) and (3:6) composition films for two main reasons: firstly, the elimination of $BaCO_3$ would reach completion if higher T_{set} were employed, leading to the full layer involved in the transient liquid formation. Secondly, considering the elevated percentage of homogeneously nucleated YBCO determined in the tested processing conditions, it is assumable that with higher temperature the supersaturation conditions would be shifted towards heterogeneous nucleation, favouring the c-axis orientation of YBCO. However, through the use of copper-rich liquid compositions, a general lowering of the supersaturation of the [Ba-Cu-O] transient liquid is obtained, directly correlated to the attainment of highly epitaxial films at lower temperature processing conditions, where the compositions of lower copper content display mixed nucleation. Additionally, considering one of the future objectives is to facilitate the industrial application of the TLAG-CSD approach, higher processing temperatures are generally undesirable, especially due to the global transition to more energetically efficient processes for CCs production. For this reason, films deriving from the eutectic and the copper-excess liquid compositions are more appealing towards the use in the industrial framework, given the wide high epitaxy window found at lower temperatures. The lower supersaturation characteristic of the transient liquids of these compositions are determining excellent heterogeneous nucleation in a wide region of P_{O_2} values together with the possibility of maintaining a reduced temperature of the growth process. High-performance films are obtained in several T-P_{O_2} conditions in films of (3:7), (4:11) and Y-rich (4:11) compositions, demonstrating that a careful control of the transient liquid supersaturation contributes to the achievement of full c-axis YBCO nucleation with negligible presence of secondary phases and optimal surface morphology. Moreover, the optimization of the kinetic parameter of the heating ramp results in the reduction of coarsening phenomena: despite the films of Y-rich (4:11) composition experience the formation of significant amounts of (211) and (225) secondary phases, their small grain sizes were proven to be of no obstruction to current percolation and high critical current densities were obtained in several growth conditions from the transient liquid of this specific stoichiometry.

In Chapter 3, the investigation of different variations to the optimised solution for YBCO film fabrication have been motivated and presented. In section 3.3, various RE metal propionate precursors have been employed for the preparation of precursor solutions of the SmBCO, GdBCO and YbBCO systems. Contrarily, section 3.4 was entirely devoted to an implementation of not previously introduced amine compounds as additives for the YBCO precursor solution. In both of the presented cases, metal-organic solutions with desired rheological and chemical features were obtained, and those led to the preparation of homogeneous nanocrystalline precursor films with the required microstructural characteristics for their growth through TLAG. In the following two sections, the preliminary results deriving from the application of such films in TLAG P_{O_2}*-route* will be presented, demonstrating the feasibility of TLAG for REBCO systems other than YBCO and additionally the prospect of having a wide range of chemical solutions to choose from depending on the deposition or film requirements.

4.5 TLAG of REBCO (RE = Sm, Gd, Yb) films

Initial testing on REBCO (RE = Sm, Gd, Yb) films deriving from metal-organic chemical solutions in which the $Y(Prop)_3$ precursor has been substituted with $Sm(Prop)_3$, $Gd(Prop)_3$, and $Yb(Prop)_3$, as described in detail in 3.3, led to interesting considerations for a possible implementation of TLAG to the fabrication of various REBCO systems. Following the literature analysis reported in 1.2.4.4, the change of RE is directly correlated to a substantial variation of the supersaturation conditions of the system, given each RE presents characteristic solubility in the same [Ba-Cu-O] melt [74, 76, 79]. Despite the information in the range of processing conditions close to TLAG is at the moment unavailable, the anticipated difference in RE solubility is considered an appealing strategy to vary the supersaturation, and thus promote the c-axis nucleation in the same [Ba-Cu-O] liquid composition[8]. As previously stated, the significance of varying the RE is the broad variety of possible applications of each REBCO superconductor. Considering YBCO as a reference, if Y is substituted with Sm or Gd, their use in a wider range of magnetic field values may be implemented due to their fundamentally higher irreversibility line which, in the specific case of these REBCO systems, yields higher critical temperature values compared to YBCO. This property is demonstrated to enhance significantly flux pinning phenomena and, consequently, critical current density values [120, 172–174]. Contrarily, the use of Yb instead of Y finds great relevance towards the reduction of processing temperatures, particularly interesting when implementing industrial methods with higher energetic efficiency. This important feature is the result of YbBCO optimal nucleation conditions being significantly lower than YBCO, again due to an intrinsic difference in the solubility of this RE in the transient liquid, varying importantly the supersaturation of the system [127, 175]. Additionally, among the approaches employed to enlarge the high epitaxy window and, thus,

[8] In this section, only films of (3:7) composition have been considered.

the processing conditions, solutions with RE mixtures have been optimised with encouraging outcomes, the most common system being $Y_{0.7}Gd_{0.3}Ba_2Cu_3O_{7-\delta}$ ((Y,Gd)123) [205, 206]. Given the different solubility of each RE in the [Ba-Cu-O] transient liquid, with the general tendency yet to be accurately determined (see 1.2.4.4, specifically Fig. 1.22), even more compelling in the out-of-equilibrium TLAG conditions, the processing conditions had to be chosen specifically depending on each REBCO film. Due to time constraints, and being this solely an initial testing with a proof-of-concept objective, a small number of T-P_{O_2} conditions were tested for each case. Fig. 4.45 reports a comparison between the optimal result achieved for each REBCO, considering YBCO as the "standard criterion". The low-P_{O_2} heating was performed for all films at $P_{O_{2,base}} = 10^{-5}$ bar, with average heating rate of $dT / dt = 1.4$ ºC s^{-1}, and finally performing a pressure jump to $P_{O_{2,final}} = 1.8$ mbar. With SmBCO and GdBCO systems displaying higher RE solubility at higher temperatures in 1.22, it was anticipated that a lower supersaturation, and thus higher c-axis nucleation, would be achieved for higher temperatures if compared to the case of YBCO. Therefore, these films were grown selecting the same processing temperature of $T_{set} = 870$ ºC, approximately 30 ºC higher than the optimal one for YBCO. From the GADDS 2D-XRD images, it is clear how both these films show a highly epitaxial orientation of REBCO, with narrow spots corresponding to the (00l) reflections. No presence of secondary phases is observed in the corresponding integrated XRD patterns, other than peaks from copper oxides CuO and Cu_2O, expected given the intrinsic copper excess of these films[9]. In the case of SmBCO, a minor contribution from a mixed oxide of barium and copper phase is observed, preventable with a more extensive tuning of the growth conditions. Optimal surface morphology is obtained for the case of GdBCO, which is displaying a highly smooth surface, indication of a high c-axis orientation, with, in addition, the copper excess in form of oxide precipitates successfully pushed to the film surface. As determined in section 4.3, nucleation conditions in films of (3:7) composition must ensure the expulsion of the intrinsic copper excess (due to the stoichiometry of the transient liquid) to the film surface to avoid current percolation impediment and, thus, ensuring high-performance films. For what concerns SmBCO, the flat surface is disrupted by several pores. Small, superficial grains of CuO are visible, together with larger grains of a solid phase of barium and copper species (confirmed by EDX shown in Fig. D.14). These features are an indication of non-optimal c-axis nucleation conditions, especially complex when considering SmBCO, given the similar atomic radii of Sm and Ba (2.59 Å and 2.78 Å, respectively) which commonly allows for Sm/Ba substitution in the perovskite-type structure [174]. Nonetheless, the high epitaxy displayed by this film is demonstrating the feasibility of TLAG for the growth of this REBCO system, once the processing parameters will be correctly controlled.

[9] A reminder for the reader: the study of REBCO films has been exclusively conducted employing solutions of (3:7) composition to avoid further complications originated by variation of the supersaturation conditions, given the limited knowledge regarding RE solubility in the [Ba-Cu-O] transient liquid

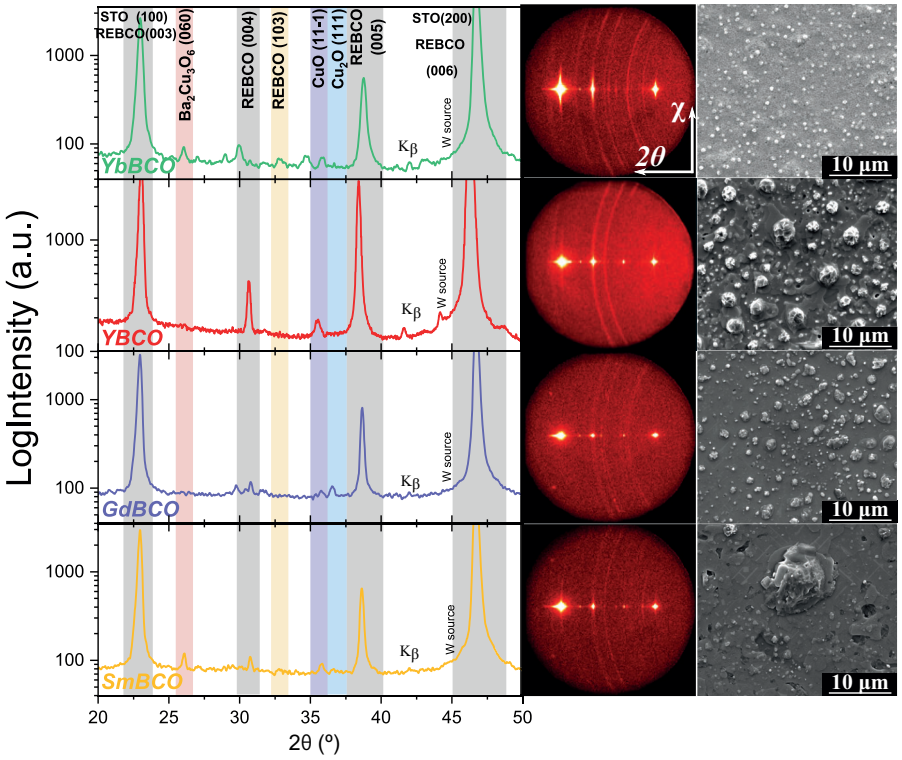


FIGURE 4.45: Comparison between the films of different REBCO systems grown through TLAG P_{O_2}*-route*. From top to bottom, following the increasing ionic radius of the RE: YbBCO, YBCO, GdBCO, SmBCO. (Left) Integration in χ of the 2D-XRD (center). Peak identification is indicated in the top panel of the integrated XRD, and shaded areas are extended to all the lower panels. (Right) Surface morphology displayed by the SEM images relative to each film.

Conversely, the selected temperature for the TLAG process on the film of YbBCO was set to $T_{set} = 785$ ºC, significantly lower than the YBCO case, due to the lower peritectic temperature of YbBCO respect to the one of the YBCO system. Moreover, according to the data presented in Fig. 1.22, the solubility of Yb in the [Ba-Cu-O] melt at low temperatures is seen to be higher than the one presented by Y, with the consequence of a lower liquid supersaturation, directly linked to higher c-axis YbBCO nucleation [113]. However, a consideration regarding the process must be made at this point. As presented in section 4.2, the complete elimination of $BaCO_3$ is mandatory before performing the pressure jump, given the removal of this species is the limiting step of the reaction. In the YBCO films quenched at various, increasing temperatures (Fig. 4.7), it is evident how, at a $T_{set} = 760$ ºC, $BaCO_3$ is still showing an important contribution in the film. Therefore, performing the pressure jump from such unfavourable initial conditions implies an additional complication towards the epitaxial nucleation, as the

remaining $BaCO_3$ must react to form $BaCu_2O_2$ in order for this phase to participate in the transient liquid generation. This is possibly varying considerably the supersaturation conditions of this liquid, and leads to a slight misorientation around the c-axis of the final YbBCO. An important contribution due to secondary phases is additionally evident in the integrated 2D-XRD pattern. However, the SEM image displays a rather smooth surface morphology with presence of CuO grains, indicating the supersaturation conditions to be close to the optimal for high c-axis nucleation and a possible improvement is anticipated with further optimization of the processing parameters.

Fig. 4.46 evidences the variations in the rocking curves (ω-scans) presented by the four REBCO films considered in this section. As explained above, the GdBCO film results in high epitaxy after the TLAG process, yielding a rocking curve with $\Delta\omega = 0.17º$, comparable with the value registered for the YBCO case in the optimised growth conditions ($\Delta\omega = 0.18º$). SmBCO film presents a broader rocking curve, with $\Delta\omega = 0.38º$, demonstrating the misorientation observed in the XRD patterns is significantly contributing to a reduction of the epitaxial texture. However, the most unfavourable outcome is obtained for the YbBCO film, in which substantial misorientation around the c-axis YbBCO results in an elevated value of $\Delta\omega = 0.50º$.

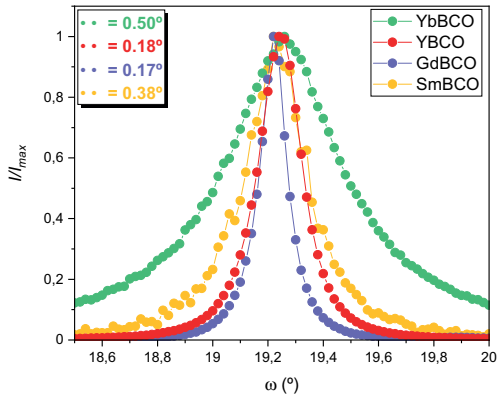


FIGURE 4.46: Rocking curves of the four REBCO systems grown through TLAG P_{O_2}*-route* described in this section. Values of $\Delta\omega$ are indicated in the inset with corresponding colour as the rocking curve relative to each film.

Considering these results, the liquid supersaturation is supposed to be optimal for the cases of GdBCO and YBCO at the selected processing conditions. The necessary increase in temperature going from YBCO to GdBCO seems to be in accordance with the trend observed in the data deriving from literature reported in Fig. 1.22 at higher temperatures: the increased ionic radius of the RE results in its higher solubility in the [Ba-Cu-O] melt of the same composition, and the consequent lowering of the liquid supersaturation results in high c-axis nucleation. Conversely, the supersaturation conditions in the cases of SmBCO and YbBCO appear to be too elevated for the promotion of a fully epitaxial nucleation. Following the trend observed in

Fig. 1.22, Sm solubility in the [Ba-Cu-O] melt is highly enhanced when higher temperatures are selected. The degree of misorientation observed in the 2D-XRD of the film of this REBCO system is suggesting an increase in the growth temperature would be beneficial towards lowering of the supersaturation, and the subsequent improvement of the epitaxial texture. Similarly, the misorientation in the film of YbBCO is indicating the nucleation to be originated from excessive supersaturation conditions. The promotion of c-axis YbBCO nucleation requires for a decrease of the supersaturation, obtained through enhancement of the Yb solubility in the transient liquid. This may be attained through either a slight thermal increase at the same $P_{O_{2,final}}$ or through a decrease of the latter parameter (based on the correlation between supersaturation and $P_{O_{2,final}}$ observed in TLAG films of YBCO described in the previous sections). Overall, given the proof-of-concept nature of this study and the limited time dedicated to the optimization, the presented results are considered satisfactory and highly epitaxial REBCO films are anticipated through minor tuning of the growth conditions.

Finally, physical properties measured on these films confirm the need for further efforts towards a more accurate optimization of TLAG for the REBCO systems analysed here (Fig. 4.47), as was previously carried out for YBCO films which, here, display the highest critical current density values of the four REBCO systems considered. Despite the values of J_c

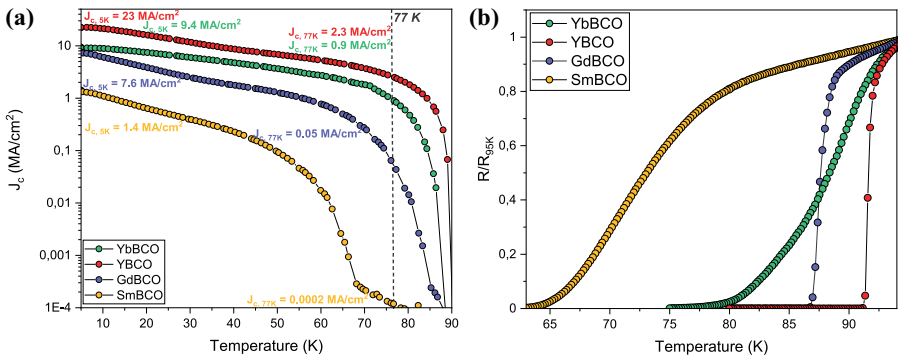


FIGURE 4.47: (a) J_c curves as a function of temperature measured through SQUID magnetometry at 5 K and 77 K for the films of the four REBCO systems grown through TLAG described in this section. (b) T_c curves from resistivity as a function of temperature for the same films in (a), obtained through the Van der Pauw method normalized to each value at 95 K.

registered for YbBCO are promising, exhibiting 9.4 MA cm^{-2} and 0.9 MA cm^{-2} at 5 K and 77 K, respectively, the other REBCO systems present lowering of the physical performance. The GdBCO film additionally exhibits high J_c at 5 K, with a value of 7.6 MA cm^{-2}, however followed by an extreme drop to null values at 77 K. Similarly, the extreme case of SmBCO displays null values at both temperatures. This effect is believed to be caused by an inadequate oxygenation process following the growth, presumably yielding a low degree of oxygen doping in the REBCO structure. An additional indication of this is the exceptionally broad

transitions displayed from the T_c curves from resistivity obtained through the Van der Pauw method, shown in Fig. 4.47(b), reflecting an inhomogeneous oxygen distribution within the samples [207]. Complications during the oxygen in-diffusion process are common in REBCO systems, and several efforts are being made to understand the kinetics of the oxygen diffusion process, especially important for CCs fabrication [208, 209].
The preliminary results obtained for the three REBCO systems other than YBCO implemented in this thesis are demonstrating true feasibility of the application of TLAG to the fabrication of REBCO superconducting films. Moreover, the preparation of such films through the deposition of the optimised solution in which the in-house synthesized metal propionates of Sm, Gd and Yb were employed proves that the entire TLAG-CSD approach may be extended to other systems with favourable outcomes. Nonetheless, further optimization of the processing conditions for each REBCO system should be carried out to ensure the achievement of high-performance properties comparable to the in-depth studied case of YBCO.

4.6 TLAG of YBCO films deriving from solutions with different amine additives

In Chapter 3, specifically in section 3.4, a vast analysis of possible amine additives to substitute MEA in the metal-organic chemical solution employed for the CSD of YBCO superconducting films has been presented, assessing the effect of the chemical properties on the complexation achievable with the metal propionate precursors in solution. Despite several amine compounds showed interesting results, a major focus was set on two cases: ethylenediamine (En) and the mixture of MEA with pyridine (Py), each of them being a promising representative of the two families of amine compounds tested (aliphatic and aromatic, respectively).
In this subsection, an analysis of the growth of these films through TLAG P_{O_2}*-route* will be presented. Similarly to the case of the films deriving from the optimised solution with MEA, the initial stage of this study was to ensure the complete elimination of $BaCO_3$ during the low-P_{O_2} heating. Therefore, a quench process for each film has been carried out and the resulting GIXRD are displayed in Fig. 4.48. In both films from solutions with En and MEA-Py mixture, only a minor contribution from $BaCO_3$ phases is visible, with the latter film showing exclusively a small peak from the monoclinic phase. This may be due to the small microstructural variations observed in the TEM of this film after pyrolysis (Fig. 3.68): the grain size of $BaCO_3$ was found to be larger in average compared to the films from optimised solutions with MEA, presumably due to the doubled thickness after pyrolysis of one layer in this case, which may lead to variations in the decomposition temperature of the metal-organic precursors during the thermal treatment. Nonetheless, the full elimination of the barium precursor phase is believed to be possible in such film through the selection of a moderately higher processing temperature.
For the film deriving from the solution with En, the extremely elevated thickness (estimated

1200 ± 50 nm), is believed to be the reason behind $BaCO_3$ still being present in the film, in spite of the orthorhombic and monoclinic contributions to be negligible. The rough

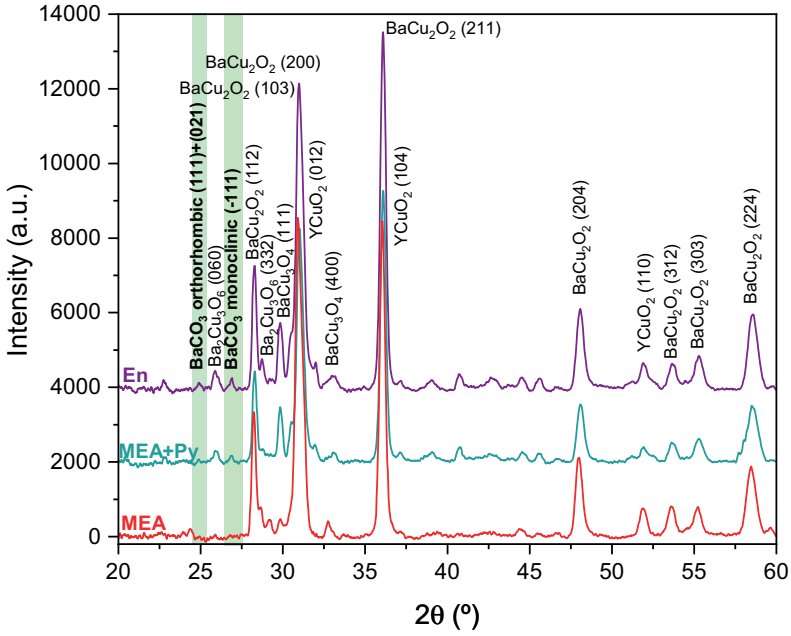


FIGURE 4.48: GIXRD of films deriving from solutions with different amine additives following the quench process: mixture of MEA and Py (aquamarine solid line) and En (purple solid line). Optimised solution with MEA is shown as reference for this comparison (red solid line). The processing conditions for the three films are identical: T_{set} = 835 ºC, with average heating rate of dT / dt = 1.4 ºC s^{-1} and $P_{O_{2,base}} = 10^{-5}$ bar. $BaCO_3$ orthorhombic and monoclinic principal contributions are identified by highlighted areas corresponding to their 2θ peak positions, respectively dark green and light green.

surface of this particular film does not allow for TEM analysis to be conducted through conventional sample preparation methods, and microstructural analysis of the nanocrystalline precursor film prior to TLAG is at the moment pending. Despite $BaCO_3$ is present in both films, the insignificant contributions are believed not to be a hindrance to the growth of YBCO through TLAG, especially given the fact that the majoritarian crystalline phase present in both quenched films is the desired mixed oxide of $BaCu_2O_2$, with comparable crystallinity to the optimised case of a film prepared from a solution with MEA.

Fig. 4.49 displays the results of TLAG P_{O_2}-*route* on the films from solutions with different amine additives mentioned up to now. Undoubtedly evident from the 2D-XRD images, all the

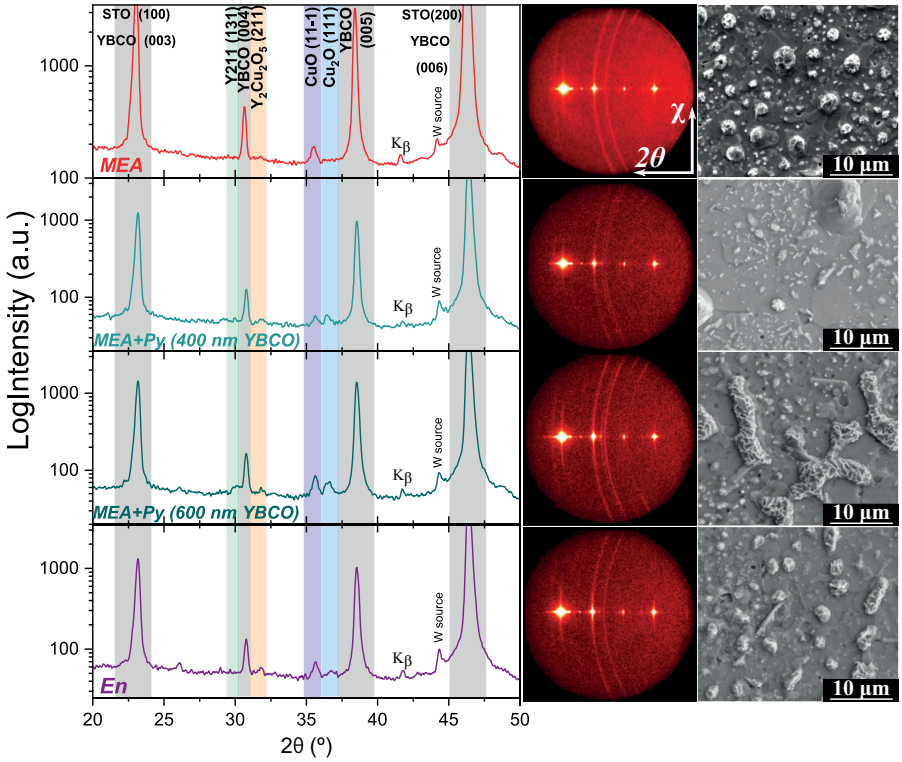


FIGURE 4.49: Comparison between the YBCO films obtained from solutions of different amine additives grown through TLAG P_{O_2}*-route*. From top to bottom, films from solutions with: MEA (shown for reference purposes), mixture of MEA and Py (1 layer of a solution of 2 M concentration in sum of metal salts, reaching a final thickness of 400 nm of YBCO after growth), mixture of MEA and Py (1 layer of a solution of 2.5 M concentration in sum of metal salts, reaching a final thickness of 600 nm of YBCO after growth), En. 2D-XRD images acquired from GADDS (center) and corresponding integration in χ (left). Peak identification is indicated in the top panel of the integrated XRD, and shaded areas are extended to all lower panels. (Right) Surface morphology displayed by SEM images relative to each film.

films lead to a highly epitaxial orientation of YBCO, and the presence of secondary phases is exclusively relative to reflections of CuO and Cu_2O species, expected given excess of copper contained in the eutectic transient liquid composition of these films. Moreover, the SEM images are showing optimal surface morphology features. Comparing the obtained results to the film deriving from an optimised solution with MEA as a reference of the ideal surface morphology, exhibiting the characteristic flat surface of the c-axis YBCO and superficial CuO precipitates, the films from solutions with MEA-Py mixture and En display similar quality. In the case of the film of higher thickness prepared from a solution with MEA-Py, the CuO on the surface is present as dendritic-like structures, previously observed in films of (4:11) composition. This unusual shape may be caused by different parameters governing the nucleation

process of CuO in films of such composition due to the copper excess, which are resembling the situation in the film described here, given its elevated thickness and minor microstructural deviations from the optimal case with MEA.

Texture analysis to determine out-of-plane tilt of the c-axis oriented YBCO was carried out and the rocking curves (ω-scans) of the four cases are reported in Fig. 4.50. The film prepared through a solution with MEA-Py mixture of 2 M concentration in sum of metal salts yields a similar final YBCO thickness to a film obtained with the optimised solution with MEA only: given the optimal processing conditions for the growth of the latter case were selected here, one may observe how comparable values of $\Delta\omega$ are achieved (respectively, 0.17º and 0.18º), indicating highly epitaxial YBCO.

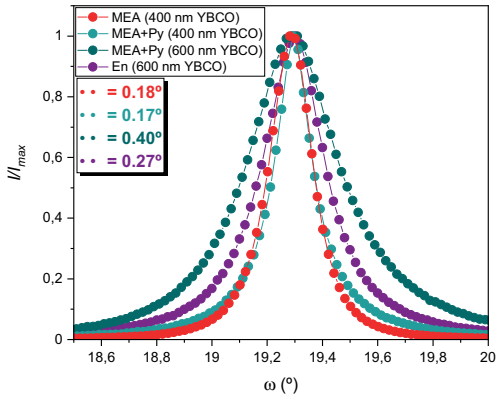


FIGURE 4.50: Rocking curves of the films deriving from solutions with different amine additives (optimised solution with MEA shown as reference) grown through TLAG P_{O_2}*-route* described in this subsection. Values of $\Delta\omega$ are indicated in the inset, in the colour corresponding to the rocking curve relative to each film.

Contrarily, the epitaxy of the thicker films, specifically the ones deriving from the solution with MEA-Py mixture and from the solution with En, present broader rocking curves resulting in larger $\Delta\omega$ values, being 0.40º and 0.27º respectively. While the latter is in line with previously reported $\Delta\omega$ values for high-performance YBCO films, the lower epitaxy of the former may be ascribed to the fact that the processing conditions must be adjusted to the more elevated thickness of this specific film, here favouring a mixed homogeneous and heterogeneous YBCO nucleation. Further, straightforward optimization of the processing conditions is believed to lead to a film exhibiting full c-axis YBCO orientation, given no exceptional complications were encountered in the growth of such film.

Physical properties have been measured on all of the above mentioned films, and the J_c and T_c curves as functions of temperature are shown in Fig. 4.51. Despite the J_c curves showing lower values compared to the reference film obtained from deposition of an optimised solution with MEA only, the physical properties exhibited by the films studied in this subsection are

found to be encouraging for the possible implementation of metal-organic solutions of various chemical characteristics for the fabrication of epitaxial YBCO films. Higher values of J_c are assumed to be readily obtained following a thorough optimization of the growth conditions, according to the corresponding film characteristics. Nonetheless, the T_c curves are showing superconducting transition to occur at 90 K or over for all of the films and sharp transitions with ΔT_c values consistently below 7 K. The T_c values close to the reported 90-92 K for YBCO [4] are demonstrating the feasibility of these kind of solutions for the epitaxial growth of high-performance YBCO through TLAG. Moreover, such elevated T_c values are a demonstration of no carbon contamination on the grain boundaries of the grown YBCO, confirming no hindrance to the full decomposition of all organic matter is occurring during the pyrolysis process regardless of the new additive employed.

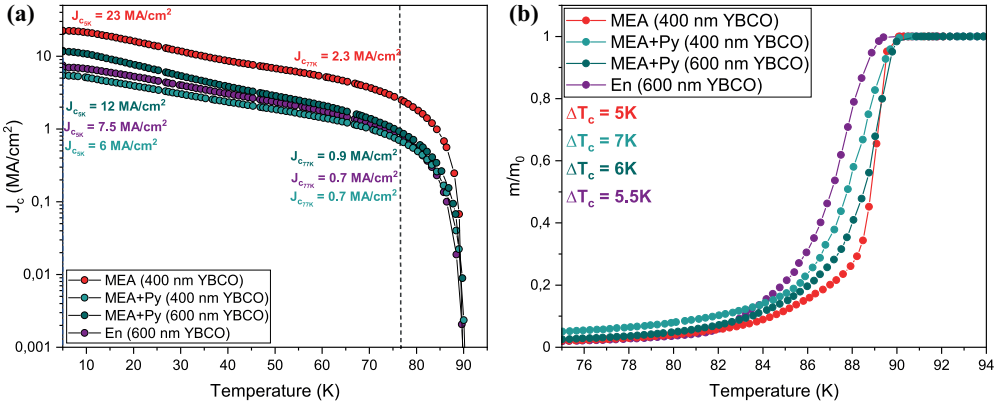


FIGURE 4.51: (a) J_c and (b) T_c curves for the films deriving from solutions with different amine additives, showing the curves of the grown film from the optimised solution with MEA as a reference case. Values of J_c at 5 K and 77 K are indicated on the plot in (a), in the same colour corresponding to the curve relative to each film, similarly for the values of ΔT_c indicated on the plot in (b).

The preliminary results reported in this subsection are demonstrating the great potential of the TLAG-CSD methodology for the growth of epitaxial YBCO films, with possibility of tuning the chemical and rheological properties of the precursor solution according to the requirements of either deposition technique or desired film characteristics. In this thesis, a variety of amine additives has been tested and only two compounds have been considered for the application to the final step of the growth through TLAG. Through the implementation of these new amine additives, the thickness of the film was successfully enhanced resulting in highly epitaxial YBCO films and maintaining competitive physical performance. Moreover, the different amine additives provide variations to the solution rheology, which are anticipated to be the foundation towards the development of a large selection of solution possibilities and attainment of a plethora of optimized precursor solutions for the growth of YBCO through TLAG.

However, further experimental work on this topic is believed to be of significant impact and several other amine compounds may be implemented with successful outcome.

4.7 Conclusions

A complete analysis of several parameters controlling the growth of YBCO through TLAG has been conducted in this chapter. An initial, detailed investigation regrading the widely supposed complicated elimination of $BaCO_3$ from the films described in this thesis was reported. Despite the presence of this phase was demonstrated not to be of any limitation towards its elimination in previously studied films through TLAG, the significant microstructural differences presented by the films developed employing the novel metal-organic chemical solution (object of Chapter 3) compared to former cases resulted in the mandatory examination of this process. $BaCO_3$ was successfully eliminated from films of different thickness and different liquid compositions following a careful optimization process which consisted in the tuning of kinetic parameters, observed to be useful in the regulation of the kinetically-controlled CO_2 out-diffusion through which the barium precursor phase can be removed. Insights on the mechanism of $BaCO_3$ elimination were given, and the feasibility of its removal in all of the films presented here has been demonstrated, showing the first step of TLAG P_{O_2}*-route* is yielding the desired crystalline phases of $BaCu_2O_2$ and Cu_2O with optimal microstructural features for the successive [Ba-Cu-O] transient liquid formation.

The optimization of TLAG P_{O_2}*-route* on films of eutectic compositions led to the understanding of how kinetic parameters are controlling the epitaxial nucleation of YBCO: regulation of the heating rate, achievable through an important modification of the experimental set-up, resulted crucial to reduce the coarsening and coalescence of grains of secondary phases. The presence of these in YBCO films grown through the use of a slow heating ramp are seen to detrimentally decrease the superconducting properties, and a major enhancement of the possible window of processing parameters resulting in c-axis YBCO nucleation (and thus, physical properties) is demonstrated when the heating rate is increased from 0.2 ºC s^{-1} to 1.4 ºC s^{-1}. Additionally, initial investigations on TLAG of thick films resulted in the achievement of high-performance films of almost 1 μm, boosting the possibilities of application of TLAG-CSD to the industrial framework.

Further knowledge regarding the complicated control of liquid supersaturation has been obtained from the vast analysis of films of different compositions grown through TLAG P_{O_2}*-route*. The generally high supersaturation of (2:3) and (3:6) liquid compositions resulted in the promotion of mixed homogeneous and heterogeneous YBCO nucleation in all of the tested conditions, suggesting the necessity for higher processing temperatures to be achieved. The addition of higher amounts of copper to the stoichiometry of the initial metal-organic chemical solution yields liquid compositions of greater copper excess, namely (3:7), (4:11) and Y-rich

(4:11) compositions. The intrinsically lower supersaturation conditions are here greatly favouring full c-axis YBCO nucleation and growth in the majority of the tested processing conditions. Nonetheless, a comprehensive analysis of the contribution of secondary phases and of the surface morphology of all films was pivotal to deeply understand the growth mechanism from these various liquid compositions, shining new light on the relevance of liquid supersaturation in the innovative growth of YBCO through TLAG.

Finally, preliminary studies of TLAG on films deriving from variations of the optimized solution with MEA were tested with promising results. The growth of three REBCO systems other than YBCO, specifically SmBCO, GdBCO and YbBCO, led to the achievement of epitaxial films with good surface morphology. Further optimization of the growth parameters is needed to improve the physical performance of such films. Nonetheless, the reported results are setting an encouraging foundation for the application of TLAG to other highly interesting REBCO systems, widening the possibilities of TLAG for CCs fabrication. The growth of YBCO from films deriving from solutions with different amine additives (respectively, En and a mixture of MEA and Py) resulted in highly epitaxial films with good physical properties and optimal film morphology, demonstrating the feasibility of a wide variety of metal-organic chemical solutions to select from, according to deposition requirements or microstructural preferences of the final films. The introduction of new amines has led to the attainment of an important thickness increase: the enhanced solubility of the metal propionate powder precursors resulting from the improved coordination between the $Cu(Prop)_2$ and the newly employed amine compounds allowed for higher concentrations of the precursor solutions to be reached, as explained in 3.4. This led, in the specific case of the mixture of MEA and Py for example, to thickness of one layer being the same as the thickness resulting from a doublefold deposition deriving from a solution with MEA only. The highly epitaxial YBCO obtained from the growth of the films in which new amine additives have been employed sets a promising foundation for the increase of film thickness through modulation of solution properties, especially interesting for industrial applications or when different deposition methods are implemented, each demanding predefined requirements.

5

Understanding the kinetic mechanism of TLAG through in-situ XRD experiments

The previous chapter demonstrated the unquestionable potential of TLAG for the attainment of reproducible, high-performance superconducting films through this innovative, high-throughput method based on the inexpensive chemical solutions described in Chapter 3. Exemplary epitaxy and elevated J_c values could be obtained for films of different compositions of the transient liquid and films of different thickness. The sole use of *ex-situ* techniques allowed for assumptions and trends to be observed and postulated. The entirety of the present chapter, contrarily, will be devoted exclusively to unravelling the mechanisms occurring during the TLAG process by means of a detailed analysis of numerous *in-situ* XRD experiments carried out during the time of this PhD thesis. Two synchrotron facilities hosted a total of five beamtimes in which the experiments were conducted: three stays at the DiffAbs Beamline at SOLEIL Synchrotron in Saint-Aubin, France, under the guidance of Beamline Scientist Dr. Cristian Mocuta, and two stays at the NCD-Sweet Beamline at ALBA Synchrotron in Cerdanyola del Vallès, Spain, with the support of Beamline Scientist Dr. Eduardo Solano. The development of a custom-made set-up aided in recreating the experimental conditions of the standard *ex-situ* experiments performed at ICMAB, and it was upgraded during the years according to the complications encountered. The strategies to overcome eventual difficulties and understand the complex kinetic mechanisms at the base of TLAG will be carefully explained,

yielding valuable, novel, and detailed knowledge for a further optimization of YBCO growth through the TLAG-CSD approach.

5.1 Objectives

Several of the cardinal points that have to be fulfilled in order to grow highly epitaxial YBCO films through the TLAG process have been previously explained in Chapter 4. Through the fulfillment of those and a thorough optimization of the processing conditions, the resulting films displayed epitaxial texture and competitive physical properties.
The great advantage of *in-situ* XRD experiments is the possibility of observing the phase transformation during the entire growth process, clearly evidencing which of those are governing the process and which processing parameters are the most relevant. From the description of the TLAG mechanism in Chapter 1, it is evident how the complete elimination of $BaCO_3$ is necessary for the epitaxial growth, as its removal *via* its reaction with CuO to yield solid phases of $BaCu_2O_2$ and Cu_2O is the limiting step prior to the formation of the transient liquid. Some considerations must be made before entering the detailed analysis of the *in-situ* experiments. The initial microstructural characteristics of the films resulting from the pyrolysis process have been found optimal for the *ex-situ* growth through TLAG in the tubular furnace described in Chapter 4, in which the large volume of the sample environment in the furnace is avoiding stagnation of evolved gases, facilitating CO_2 exchange and thus the elimination of $BaCO_3$. Contrarily, the reduced volume of the conduction-type Anton-Paar furnace employed in the *in-situ* set-up has previously been linked to unfavourable gas flow conditions [52]. This may compel for novel experimental strategies to be adopted in order to overcome the effects arising from this problem. A schematic representation and full description of the custom-made experimental set-up employed in the *in-situ* XRD experiments performed in the two synchrotron facilities may be found in Appendix E. The processing conditions adopted throughout all *in-situ* experiments are the result of a set of experimental trials (not discussed here) which led to the determination of the following:

- A **heating ramp** of 4.5 ºC s^{-1} (300 ºC min^{-1}) has been used in the majority of the *in-situ* experiments. This is higher than the heating ramp of the optimal *ex-situ* conditions, which was limited to an average of 1.4 ºC s^{-1} due to the furnace heating capacity. The fast heating ramp results beneficial to avoid coarsening effects during the heating, maintaining the small sizes of the nanocrystalline phases and ensuring fast reactivity in the TLAG process. If not specified otherwise, this is the selected value.

- A **gas flow** of 500 mL min^{-1} employed during the pressure jump step has shown improvement in YBCO epitaxy respect to more reduced values tested. This was the maximum gas flow possible with the combination of mass-flows available in the experimental set-up.

- Setting the **final total pressure** (P_{TOT}) of the experiment to elevated values has resulted in majorly c-axis YBCO, contrarily to the cases of lower values which, instead, favoured homogeneous nucleation. As explained in the description of the experimental set-up in Appendix E, in this growth system, differently from the one employed at ICMAB for growth processes (described in D.1), the $P_{TOT} \neq P_{O_2}$, therefore the use of mass-flows ensured the desired P_{O_2} corresponding to each value of P_{TOT} selected in the experiments. A P_{TOT} of 32, 35 or 100 mbar was employed in the experiments described in this chapter, and the exact value will be specified when relevant.

- The value of the **move** valve set to 100% ensures the fastest pressure jump possible in the custom-made set-up. The importance of a fast transition between low- and high-pressure systems is pivotal, as this step coincides with the transient liquid formation. Being TLAG a kinetically-driven process, if the system crosses slowly areas of the phase diagram in which solid secondary phases are thermodynamically preferred, it is possible for those to be formed preferentially, thus hindering the correct formation of the transient liquid and, consequently, of highly epitaxial YBCO film. Further studies resulting from the variation of the opening of the move valve are anticipated to be of great interest, however were not the object of the experiments described in this thesis.

Regarding the acquisition time of the experiments, mainly two ranges have been employed. Initially, a 2D-XRD frame was acquired every 100 ms during the entire experiment. Despite this being the favoured option when analyzing the behaviour of the precursor phases in the first step of the process (low-pressure heating), given their low intensities, it was clear that during the nucleation and growth of YBCO (during the pressure jump) valuable information was being lost due to the ultrafast nature of the growth process. For this reason, in collaboration with Beamline Scientist Dr. Cristian Mocuta of DiffAbs Beamline at SOLEIL Synchrotron, experiments with ultrafast acquisition times were implemented, reducing this time to only 2 ms per frame. This allowed for the unprecedented following of the processes occurring during the pressure jump, when the precursor phases react to form the transient liquid and YBCO nucleation and growth takes place. A complete description of how the data presented in this chapter was acquired and the methods used for its analysis is reported in E.1.2.
One must consider that the development and adaptation of the experimental conditions required for the *in-situ* growth of YBCO through the TLAG P_{O_2}-*route* was particularly demanding. In the initial beamtime runs during the time of this thesis, the vacuum set-up was carried dismounted to the beamline and assembled there prior to the experiments. The Anton-Paar furnace was provided by the beamline, thus no previous optimization of the thermal profiles could be implemented given the short, valuable time available for *in-situ* experiments. The work conducted in previous theses had already evidenced a complicated control of the pressure jump in the *in-situ* experimental set-up [51, 52, 54], and the experiments described in this chapter are no difference. Large variations in the selected temperature and the step of the

pressure jump have been observed throughout the various beamtime runs, and are believed to be linked to the slight modifications in the assembling of the vacuum system: after every set of experiments, novel information would lead to the implementation of changes in the set-up, thought to overcome experimental difficulties encountered during the *in-situ* experiments. However, owing to the entrance of gas in the confined sample environment at the time of the pressure jump, a different thermal response from the Anton-Paar inductive furnace was observed. In some cases, overshoots of up to 20 ºC were occurring during the pressure variation, whereas in others, the entrance of gas coincided with a drop in temperature and the following oscillation to establish the initially determined T_{set}. Some examples of such thermal profiles are shown in the following Fig. 5.1.

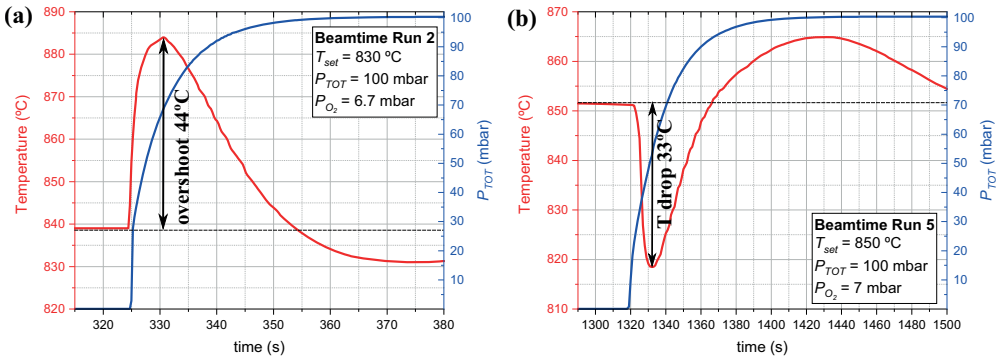


FIGURE 5.1: Examples of the thermal profiles of experiments deriving from the (a) second and (b) fifth beamtime runs carried out throughout this thesis work. In both experiments the P_{TOT} was set to 100 mbar and the P_{O_2} approximately 7 mbar. The differences in the set-up configuration resulted in a large overshoot in the former case, and a drop in temperature in the latter one at the time of the pressure jump.

As previously stated, the moment of the pressure jump is corresponding to the formation of the transient liquid and the initiation of YBCO nucleation and its successive growth. Uncontrolled variations of the processing conditions and irreproducibility of this delicate step resulted in pressure jumps of various speeds: reaching the desired final pressure in a long time range is inevitably worsening the epitaxial nucleation. Nonetheless, at the time, no further set-up optimization was allowed, and attempts to deal with the complications arising from this were made in several ways. The realization that the strict control of the processing conditions was not ensured led to the construction of a movable rack through a project in collaboration with ALBA Synchrotron (PTI+TransEner CSIC programme for Spanish NGEU). This allows for the set-up to be mounted and optimized prior to beamtime experiments to fully control the system and overcome any possible difficulty previously encountered. However, during the time of this thesis, only initial experimental trials could be carried out with this system, and a complete control of the processing conditions was still under process. At present, further

work is being conducted to implement reproducible growth processes with successful outcome. Nevertheless, interesting results were obtained from the *in-situ* experiments carried out during the five beamtime runs of this thesis, and are believed to be a valuable contribution towards a deeper knowledge on TLAG mechanisms and kinetics.
As explained in Chapter 4, the TLAG P_{O_2}*-route* displays the advantageous possibility of decoupling the elimination of $BaCO_3$ from the growth of YBCO. As the former is identified as the limiting step of the whole process, with its incomplete elimination shown to hinder the epitaxial growth of YBCO and favouring its homogeneous nucleation, a special focus on this step will be made. Therefore, the following section will be concentrating solely on the process of $BaCO_3$ elimination. Comparisons between the cases of Binary (Ba-Cu-O) and Ternary (Y-Ba-Cu-O) films of (3:7) composition will be presented[1], followed by the analysis of how to promote c-axis nucleation in the system described. Having determined the optimal conditions for the *in-situ* experiments regarding the first step of the process in the case of films of (3:7) composition and an assessment on the growth rate, the rest of the chapter will be devoted to understanding the growth kinetics of films of different compositions and an evaluation of the influence of varying the transient liquid supersaturation on the final epitaxy of YBCO will be given. The final section will consider the consequences of increasing film thickness on the growth of YBCO in the set-up for the *in-situ* XRD experiments.

5.2 *In-situ* analysis of the $BaCO_3$ elimination

The analysis described in detail in 4.2 clarified how a complete understanding of the parameters controlling the initial step of the process is mandatory. The possibility of an *in-situ* study of the $BaCO_3$ elimination process is highly advantageous to attain comprehensive information regarding the removal of this phase and the proceeding of the TLAG mechanism.
Similar experimental conditions were employed for the TLAG of YBCO in the work of former PhD theses in the group [51, 52, 54, 55]. However, in these cases the nanocrystalline precursor films used for the TLAG process were deriving from metal acetate-based solutions which presented a different microstructure with lower thickness and a higher distribution of pores than the one displayed by the films described in the current work. Rasi *et al.* [91] had previously shown how the different microstructure in these kind of films would affect the elimination of $BaCO_3$, with the films showing a more compact aspect presenting a major delay in the reaction of $BaCO_3$ with CuO to form the intermediate of $BaCu_2O_2$[2]. A similarity with the films resulting from the novel chemical solution developed during this PhD thesis may be found, as

[1] As for the results shown in the previous chapters, the (3:7) composition is referred to as the standard case, and several studies will be carried out exclusively on films of this composition.

[2] In the case of this particular study, the difference in microstructure was resulting from solution ageing and an increased water content in the solution. In 3.2.7 it was demonstrated how the ageing in the solutions developed in this thesis is not leading to any significant microstructural variations, showing in addition that the novel solution formulation is effectively solving this problem.

these show high thickness (800 nm after pyrolysis) and unprecedentedly low porosity (in the range of 1-2 %).

As presented in Chapter 4, YBCO growth through TLAG P_{O_2}*-route* is divided in two steps, allowing for the elimination of $BaCO_3$ and the formation of the transient liquid from which YBCO nuclei are generated to occur in two separate and consecutive moments. Initial testing of TLAG P_{O_2}*-route* in the *in-situ* XRD experiments revealed serious difficulties towards the elimination of $BaCO_3$. Fig. 5.2 presents a comparison of the I(2θ) diffractograms plotted with temperature between a standard film prepared through CSD (Fig. 5.2(a)), as the entirety of the samples described in this thesis, and a YBCO precursor film prepared through PLD (Fig. 5.2(b)), which results in the absence of $BaCO_3$, possibly aiding towards a faster kinetic mechanism for the formation of YBCO [210]. Both films were grown with the same processing conditions: low-pressure heating ($P_{TOT,base}$ = 0.05 mbar, $P_{O_{2,base}}$ = 0.01 mbar) until T_{set} = 860ºC with heating rate of 4.5 ºC s^{-1}, and reaching $P_{O_{2,final}}$ = 1 mbar ($P_{TOT,final}$ = 5 mbar) through the pressure jump. These experiments have been carried out to corroborate that the complication towards the epitaxial growth is a result of the difficult elimination of $BaCO_3$ in the set-up employed for the *in-situ* XRD experiments, given that the sole difference between the initial microstructure of these films is the presence of the latter phase. In both cases, the first I(2θ) diffractogram represented coincides with the last frame acquired prior to the pressure jump, indicated in both figures as a blue dashed line. The time corresponding to the temperature increase is additionally indicated. The film prepared by CSD is showing a large time range (almost 18 minutes) after the change in pressure in which this precursor species is still present and, consequently, YBCO nucleation and growth is impeded as the transient liquid formation is not occurring or is highly insufficient. Only the successive thermal increase allowed for a diminished $BaCO_3$ contribution and, as a result, the increase of the peak relative to YBCO.

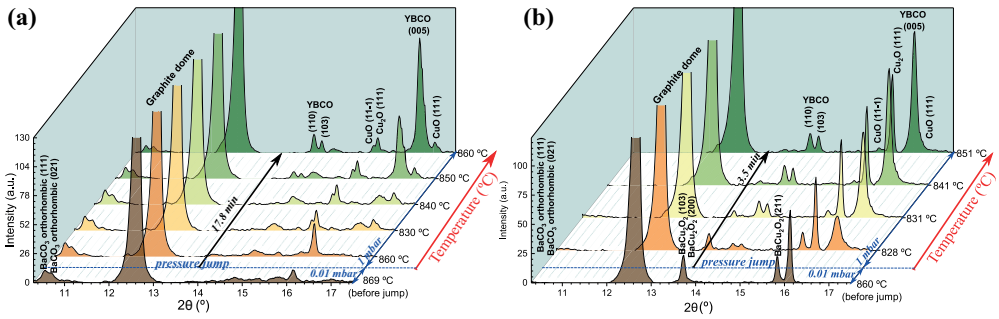


FIGURE 5.2: I(2θ) obtained through the integration in χ of the acquired 2D-XRD images, represented here as evolution of temperature for (a) a standard film prepared through CSD and (b) a film prepared through PLD. The first I(2θ) diffractogram is corresponding, in both cases, to the 2D-XRD image acquired prior to the pressure jump (represented as a blue dashed line). P_{O_2} values are represented on the z axis, and the total time of the temperature increase is indicated on the graph. Identification of the peaks is indicated in correspondence to each 2θ position.

Contrarily, the film prepared by PLD, lacking $BaCO_3$ in all of the I(2θ) scans considered, shows immediate and straightforward growth of YBCO during the diffractograms following the pressure change (in a total time of 3.5 min), prior to which the solid precursor phases for the transient liquid formation ($BaCu_2O_2$ and Cu_2O) are observed. In the former case, no trace of the mixed oxide of barium and copper is visible, as the constant contribution of $BaCO_3$ is suggesting the formation of this phase through its reaction with CuO is impeded. This result is clearly evidencing that the difficulty encountered in the case of the CSD films for the elimination of $BaCO_3$ is having a detrimental effect on the formation of epitaxial YBCO in the set-up configuration employed for *in-situ* XRD experiments. As explained in detail in 4.2, the elimination of this phase is strictly controlled by CO_2 out-diffusion. In a large tubular furnace as the one employed for the growth processes at ICMAB, the evolution of this volatile is not impeded, and the reaction can reach completion by simple tuning of processing parameters. In the case of the Anton-Paar inductive furnace employed in the set-up for *in-situ* XRD experiments, the reduced volume and geometry of it is believed to be hindering the complete removal of CO_2 due to poor gas evacuation, and thus the proceeding of the reaction towards the full elimination of the barium precursor phase. With the main objective being the detailed analysis of the kinetic mechanisms governing the TLAG process, the development of a method to enhance $BaCO_3$ elimination was mandatory, given that no major modifications of the set-up could be implemented at the time. Two main strategies were proposed to face this problem, and will be described in detail in the following subsections:

- ***In-situ* phase transformation process**: in order to increase the likelihood of the system to eliminate $BaCO_3$, successive to the heating at low pressure to the determined set temperature, the P_{O_2} of the system is changed to 0.1 mbar. This value is below the YBCO instability line, thus avoiding its formation. The gas renewal due to the variation of pressure is believed to be aiding the elimination of residual $BaCO_3$ which could not be removed completely during the heating by favouring the evacuation of accumulated CO_2. The possible causes behind the difficult $BaCO_3$ elimination will be explained in detail in the corresponding subsection.
- **Elimination of $BaCO_3$ through an *ex-situ* quench process**: previous elimination of $BaCO_3$ through a quench process performed *ex-situ* in the growth furnace at ICMAB as described in Chapter 4. The resulting films are stored in vacuum containers and brought to the synchrotron facility to be employed in *in-situ* conditions having eliminated the barium precursor phase prior to the experiment[3].

Benefits and drawbacks of each strategy will be discussed in the following subsections, and the resulting repercussions on the TLAG process due to the use of films deriving from both cases will be analyzed and discussed in the successive sections.

[3]Details regarding the procedure of *ex-situ* quench and storage in vacuum containers can be found in D.2.1.

5.2.1 *In-situ* Phase Transformation Process

One of the strategies towards the enhancement of $BaCO_3$ elimination in TLAG P_{O_2}-*route* was the employment of a four-steps process which may be subdivided into two main parts: the process here denominated as *In-situ* Phase Transformation Process (steps 1 and 2), with a following standard TLAG P_{O_2}-*route* process (steps 3 and 4). A schematic overview of the combination of the two is represented in Fig. 5.3, and it is divided in the following points:

1. **Heating at low pressure**: the film is heated with a rate of $dT / dt = 4.5$ °C s^{-1} to $T_{set} =$ 850 °C at a constant pressure of $P_{TOT,base} = 0.05$ bar, corresponding to $P_{O_{2,base}} = 0.01$ mbar.

2. **Pressure jump to $P_{TOT,final} = 35$ mbar, $P_{O_{2,final}} = 0.1$ mbar**: rapid change (≤ 20 s) in the pressure of the system to reach $P_{TOT,final} = 35$ mbar, corresponding to $P_{O_{2,final}} = 0.1$ mbar, a value below the YBCO instability line. This step was introduced to favour the elimination of residual $BaCO_3$, expected due to the gas renewal inside the *in-situ* furnace as a result of the pressure increase, contemporarily ensuring no YBCO formation. A dwell is performed at this *T-P* conditions, followed by cooling of the system.

3. **Second heating at low pressure**: following the elimination of $BaCO_3$ from the previous steps, the system is now composed by the desired precursor phases for the TLAG process. This heating is, therefore, the same low-pressure heating of a standard growth process, with the use of a heating rate of $dT / dt = 4.5$ °C s^{-1} to the desired set temperature (in the scheme, 850 °C is chosen as an example). However, the fact that the system underwent a previous thermal process must not be disregarded, and possible coarsening effects must be considered.

4. **Pressure jump to final YBCO growth conditions**: rapid change in the oxygen partial pressure of the system to reach the desired, final pressure value for YBCO nucleation and growth. Here, $P_{O_{2,final}} = 7$ mbar is chosen as an example ($P_{TOT,final} = 100$ mbar), as this combination of $P_{TOT,final}$ and $P_{O_{2,final}}$ was found to be favouring high epitaxy. However, several final temperature and pressure conditions were tested, and will be evaluated in section 5.3.

In this subsection, only steps 1 and 2 of the scheme displayed in Fig. 5.3 will be discussed, being these the processing conditions of the *in-situ* phase transformation process. As explained in Chapter 1, the elimination of $BaCO_3$ and reaction with CuO at low P_{O_2} yields the mixed species of $BaCu_2O_2$ together with Cu_2O [95], given the reduction of Cu(II) to Cu(I) when crossing the Cu(II)/Cu(I) reduction line upon heating [95, 185]. When performing step 2, the system ends in the area of the kinetic phase diagram where both these phases are favoured in their solid form. The mixed oxide of barium and copper is unstable at atmospheric conditions and it reacts promptly with CO_2 to form $BaCO_3$, thus it is optimal to avoid air exposure of

the films once steps 1 and 2 are completed. The entire *in-situ* phase transformation process was conducted at the reduced pressure of 0.05 mbar ($P_{O_{2,base}}$ = 0.01 mbar), as is evidenced by the values of P_{O_2} shown in Fig. 5.3. However, a clarification must be made regarding the reason for which the P_{O_2} value was lowered again in step 3, instead of increasing it to the final, desired value directly after step 2, avoiding a second heating and possible coarsening effects. The experimental set-up allows solely for one pressure setting prior to the experiment.

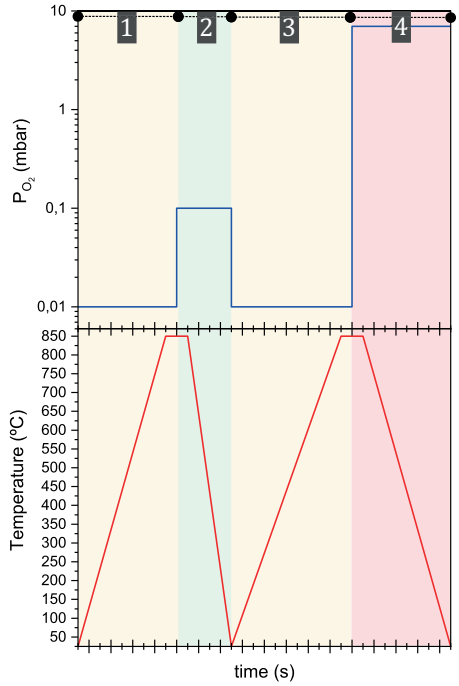


FIGURE 5.3: Schematic overview of the *in-situ* phase transformation process. In the upper and lower panels, respectively, the P_{O_2} and temperature profiles are displayed. The pressure jumps (steps 1 to 2 and 3 to 4) are represented in this scheme as an instantaneous change, however as observed in Fig. 5.1, these occur over a time range between 9 and 45 seconds, depending on the $P_{TOT,final}$ selected.

The combination of mass-flows responsible for the exact mixture of N_2 and air resulting in the desired P_{O_2} is controlled remotely from the control room; contrarily, the needle valves which are allowing for the precise control of the total gas flow (and thus the total pressure) can only be operated manually and this must be done by physically entering the experimental hutch. Therefore, if step 3 was to be avoided, the hutch had to be opened to enter and adjust the valves to the final pressure of the growth process, followed by the mandatory safety procedures before the experiment could be resumed. This would mean several minutes of the film undergoing a dwell at the constant temperature of 850 ºC and 0.1 mbar, also a highly probable cause

of coarsening phenomena. Moreover, the reproducibility regarding the time needed for this pressure adjustment would be impossible to determine, being it operator-dependent. For these reasons, it was decided to proceed to a fast cooling of the system after the pressure jump at 0.1 mbar, adjust the final pressure with the system being at low temperature, and finally perform steps 3 and 4.

5.2.1.1 *In-situ* Phase Transformation on Binary and Ternary films

As a starting point to understand the mechanisms at the basis of $BaCO_3$ elimination, binary (Ba-Cu-O) and ternary (Y-Ba-Cu-O) films of (3:7) composition were employed. The analysis of binary films finds its relevance given the elevated complexity of the system: an initial focus on the case of nanocrystalline films only composed by $BaCO_3$ and CuO is thought to aid in the understanding of the system kinetics, then widened to the complete ternary system. Binary and ternary films described here are obtained by deposition of solutions containing the same amount of barium and copper precursors in the (Ba:Cu) molar ratio corresponding to a (3:7) composition, to ensure precise comparability.

A consideration on the microstructure of the nanocrystalline precursor films must be made before analyzing their phase evolution in the *in-situ* process. The comparison between the integrated 2D-XRD scans of a binary and a ternary film after pyrolysis is displaying a major difference in the crystallinity of the phases, with the crystalline character of the binary being higher than the ternary one, as evidenced by the sharp, intense peaks in Fig. 5.4. This may find an explanation in the step of decomposition of the metal-organic precursors during the pyrolysis. Despite the decomposition temperatures being similar, as demonstrated previously in the work of Rasi *et al.* [91], the crystallization of the phases is detected at different temperatures: a binary film yields the formation of CuO, simultaneously to the initial presence of $BaCO_3$ orthorhombic, at temperatures below 350 ºC, contrarily to a ternary film in which this phase is observed at higher temperature. Thus, as both films undergo an identical thermal process with maximum temperature of 500 ºC, the higher nucleation temperature observed in the ternary will result in lower crystalline aspect of the nanocrystalline phases. The grains of CuO and $BaCO_3$ formed earlier for the binary films will be subjected to coarsening effects and crystallization throughout the thermal increase in the final part of the heating ramp followed in the pyrolysis process.

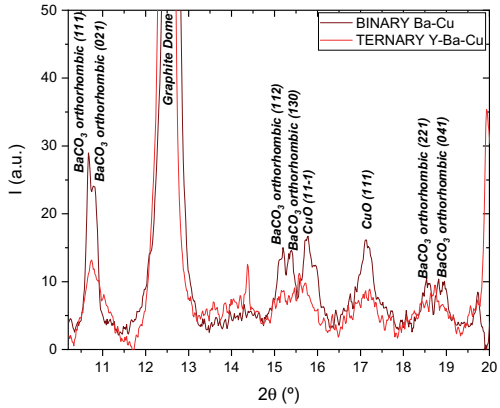


FIGURE 5.4: Integrated 2D-XRD scan of binary (burgundy) and ternary (red) nanocrystalline precursor films prior to the *in-situ* process. The curves are obtained through integration in χ of the acquired 2D-XRD images with an acquisition time of 1 s.

The different crystalline nature of the nanocrystalline precursor films is expected to lead to variations in their thermal response. In the first low-pressure heating (step 1 in the scheme in Fig. 5.3), similar phases are observed during heating between 500 ºC and 850 ºC represented through temperature-dependent colour mapping for the cases of the binary and ternary films (Fig. 5.5). However, through the integration of the peaks of interest in the I(2θ) throughout the entire experiment, the temperature-dependent phase evolution for all crystalline precursor phases exhibited in the two films during the heating process is obtained, and shown in Fig. 5.6. Here, striking differences are evidenced. The higher crystallinity of the binary film allows for the following of the CuO peak (1), whereas in the ternary film the peak relative to this phase shows a reduced intensity which makes its integration unfeasible. Moreover, the more amorphous film quality presented by the ternary film results in a crystallization process occurring upon heating: this is reflected clearly in the evolution of the $BaCO_3$ orthorhombic peak, which shows an abrupt increase in its contribution at a temperature of approximately 775 ºC in Fig. 5.6, corresponding to a well defined thermal shift and intensity increase in the temperature dependent colour mapping phase evolution. Contrarily, at this temperature the binary film shows the additional appearance of the monoclinic phase of $BaCO_3$. The contribution of the orthorhombic phase is, however, unaltered, suggesting a possible initial presence of the monoclinic phase in an amorphous state which undergoes crystallization at this elevated temperature. It is absent in the phase evolution of the ternary film supposedly due to its initial generally amorphous character, which instead experiences only crystallization of the orthorhombic phase. Coinciding with these phenomena, the reduction of the copper species from CuO to Cu_2O is found (2). The decrease of the CuO peak concomitant with the increase of the one relative to Cu_2O is only identifiable for the binary film and occurs at 750 ºC approximately, almost 100 ºC higher than what expected from literature data [95].

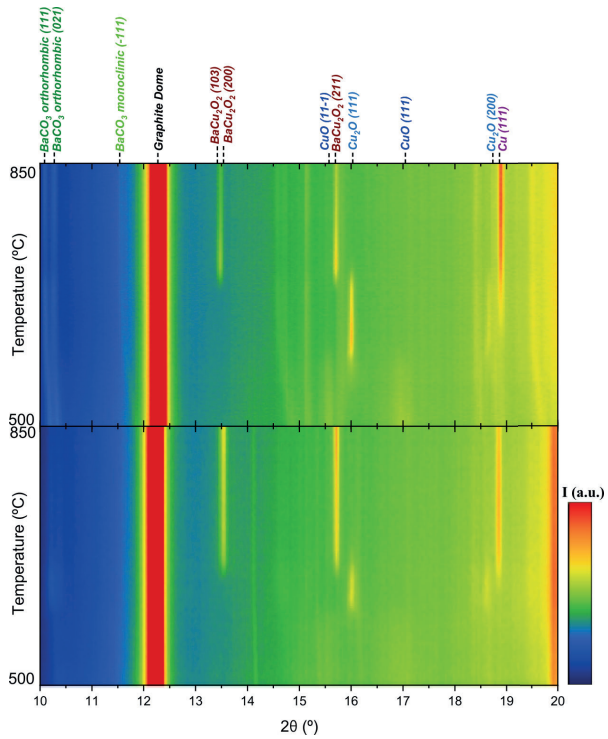


FIGURE 5.5: Phase evolution during the low-pressure heating between 500 ºC and 850 ºC ($dT / dt = 4.5$ ºC s^{-1}) displayed through 2θ-temperature dependent colour mapping, comparing the case of a binary film (upper panel) and a ternary film (lower panel) of (3:7) composition. 2θ positions of the identified phases are labelled at the top.

One must keep in mind the high heating ramp used in this kind of experiments ($dT / dt = 4.5$ ºC s^{-1}); the use of high heating ramps in the out-of-equilibrium TLAG process shift decomposition temperatures to higher values than the ones obtained in equilibrium conditions [101]. Nonetheless, the appearance of Cu_2O in the ternary film at a temperature of only 20 ºC higher suggests similar behaviour, despite the peak of CuO never reaching sufficient crystallinity to be integrated. Above 800 ºC an unexpected phase formation occurs: the further reduction of Cu_2O to Cu(0) with the associated presence of the mixed oxide of $BaCu_2O_2$. According to the phase diagrams of the BaO-Cu-CuO system [95] and to previously established TLAG mechanisms [51, 52, 54], the reaction between $BaCO_3$ and CuO should lead to the formation of the reduced Cu(I) mixed oxide of barium and copper ($BaCu_2O_2$) and Cu_2O (in compositions with copper excess, as would be the case here for films of (3:7) composition) at the selected combination of $P_{TOT} - P_{O_2}$, according to the mechanism in equation 4.1. The phases identified in the low-pressure heating in Fig. 5.6 suggest a variation of that mechanism to the following, with the sole low-pressure heating step described:

$$\begin{aligned} BaCO_{3(s)} + CuO_{(s)} + Y_2O_{3(s)} \rightarrow BaCO_{3(s)} + Cu_2O_{(s)} + Y_2O_{3(s)} \rightarrow \\ \rightarrow BaCO_{3(s)} + BaCu_2O_{2(s)} + Cu(0) + Y_2O_{3(s)} \end{aligned} \tag{5.1}$$

In both of the present films, the appearance of the most reduced phase of copper together with the formation of the mixed oxide $BaCu_2O_2$ suggests a duality in its oxidation state. Additionally, the minor decrease in the contribution of $BaCO_3$ is clearly evidencing its elimination is far from complete. The contemporary presence of these three phases is suggesting the

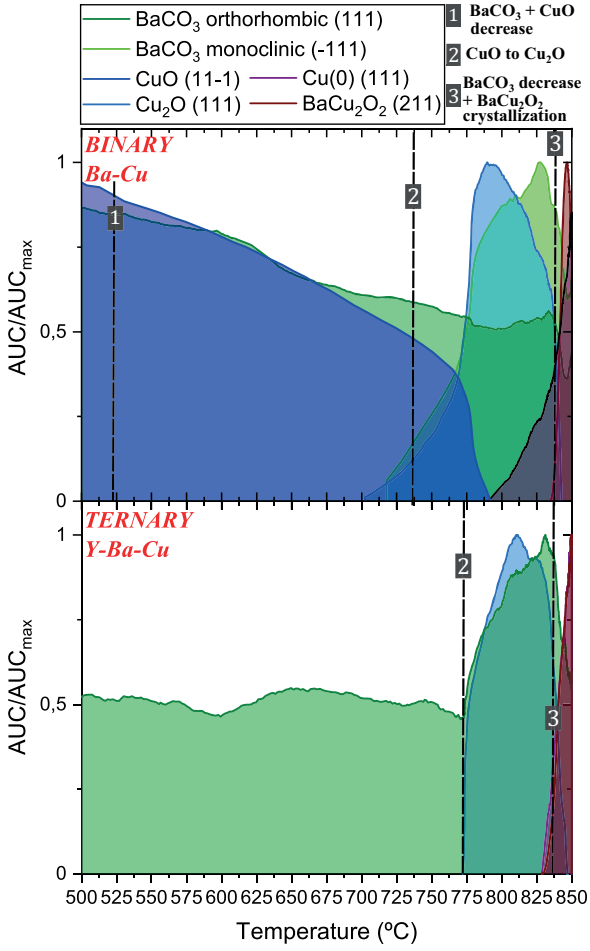


FIGURE 5.6: Temperature dependent phase evolution result of integration of the peaks relative to the precursor phases observed during the low-pressure heating, in the temperature range between 500 ºC and 850 ºC, for a binary and a ternary film. The fundamental steps of the process are identified with enumerated dashed lines, further explained in the legend.

advance of the reaction according to the expected mechanism is hindered. As previously stated, the films developed in this thesis present thickness of approximately 800 nm prior to the growth process and an almost null porosity. In addition, the small size and geometry of the furnace employed for the *in-situ* experiments is presumably causing poor gas flow or, extremely, static flux conditions.

At this point, it is important to remind that the elimination of $BaCO_3$ is solely possible through CO_2 out-diffusion from the film, and the reaction of the carbonate with CuO will proceed to the formation of the desired mixed oxide of $BaCu_2O_2$ in this system. The combination of the low porosity of the films and the insufficient gas evacuation in the sample environment supposedly results in the system reaching an equilibrium between the CO_2 liberated inside the furnace, which cannot be completely removed, and the CO_2 still inside the film. Moreover, the presence of the reduced phase of copper is a further suggestion of the difficult evacuation of CO_2: formation of Cu(0) is not expected and this phase should not be present in the $P_{TOT} - P_{O_2}$ conditions to which the system is subjected. The reduction of Cu_2O to Cu(0) is, thus, the consequence of the presence of a reducing agent. Given that the only gas species result of the process of $BaCO_3$ elimination is CO_2, it is believed that this suffers the reduction to CO in presence of carbon (possibly deriving from the graphite dome, from non-decomposed residues of the solvents contained in the Ag paint used to glue the samples, or any eventual impurities present from the general use of the Anton-Paar furnace) through the mechanism:

$$CO_{2(g)} + C_{(s)} \rightarrow 2CO_{(g)} \tag{5.2}$$

Considering the stagnation of gas to be one of the main reasons for the impossibility of eliminating $BaCO_3$ from the system, which in different furnace conditions has been demonstrated to be undoubtedly achievable in 4.2, the anticipated advantage of the *in-situ* phase transformation process is the gas renewal inside the furnace resulting from the change of pressure. Fig. 5.7 displays the pressure dependent phase evolution ($P_{TOT} - P_{O_2}$) during the pressure jump to $P_{TOT,final} = 35$ mbar and $P_{O_{2,final}} = 0.1$ mbar (below YBCO instability line) for the binary and ternary films whose low-pressure heating process was discussed up to now. Both films display the formation of the same crystalline phases, with the additional presence of $YCuO_2$ for the ternary case, evidently given the presence of Y_2O_3 as yttrium precursor phase. Nonetheless, some differences are to be mentioned. The decrease of the contribution of Cu(0) may be observed to be promptly occurring with the initial pressure increase. The rapid raise in the oxygen partial pressure results in the oxidation of this species to Cu_2O, its Cu(I) oxidation state oxide. Together with the increase in the contribution of $BaCu_2O_2$, the formation of these two solid phases is expected when the final value of $P_{O_{2,final}} = 0.1$ mbar is reached. Nonetheless, the null contribution of $BaCO_3$ orthorhombic is only obtained at elevated pressure values, being

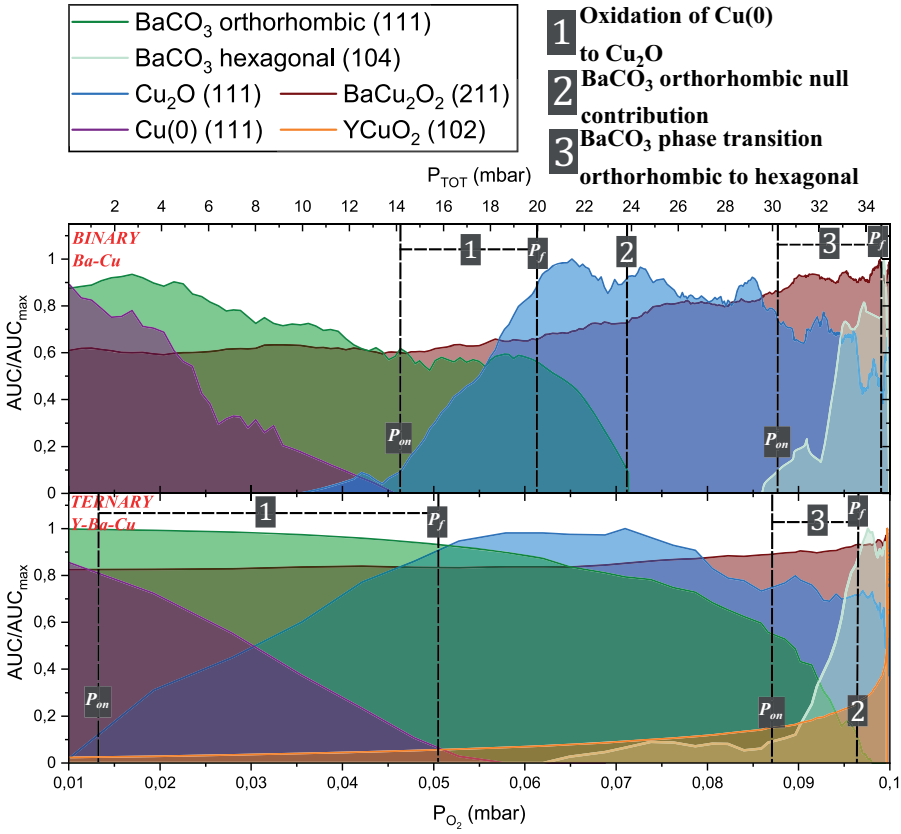


FIGURE 5.7: Pressure ($P_{TOT} - P_{O_2}$) dependent phase evolution result of integration of the peaks relative to the phases observed during the pressure jump to $P_{O_{2,final}} = 0.1$ mbar and $P_{TOT,final} = 35$ mbar at the constant temperature of 850 ºC, for a binary and a ternary film. The fundamental steps of the process are identified with enumerated dashed lines, further explained in the legend. Onset and end of a specific process are determined through the 90%-10% criterion.

$P_{O_2} = 0.07$ mbar and $P_{TOT} = 22$ mbar for the binary film and, even more extremely, $P_{O_2} = 0.096$ mbar and $P_{TOT} = 33.7$ mbar for the ternary one.

Such elevated values are a further proof of how difficult the gas transport inside this particular furnace environment is and what enormous effect the renewal of gas has towards the successful elimination of this precursor phase which is hindering the entire process. In addition, the elimination of $BaCO_3$ orthorhombic seems to be only partially obtained, as the phase transition to $BaCO_3$ hexagonal is observed in the final part of the pressure change. However, from the non-normalized phase evolution relative to the peaks of these two phases of $BaCO_3$ (Fig. E.8, Appendix E), the contribution relative to the $BaCO_3$ hexagonal is evidently low, suggesting the majority of the $BaCO_3$ is, indeed, removed.

During the cooling process, starting at 600 ºC, a phase transition from $BaCO_3$ hexagonal back

to orthorhombic occurs, expected given the hexagonal phase is predominantly stable at elevated temperatures. The thermal stability of these phases was previously described by Arvanitidis *et al.* [92]. Despite this study made use of different processing conditions, such as lower

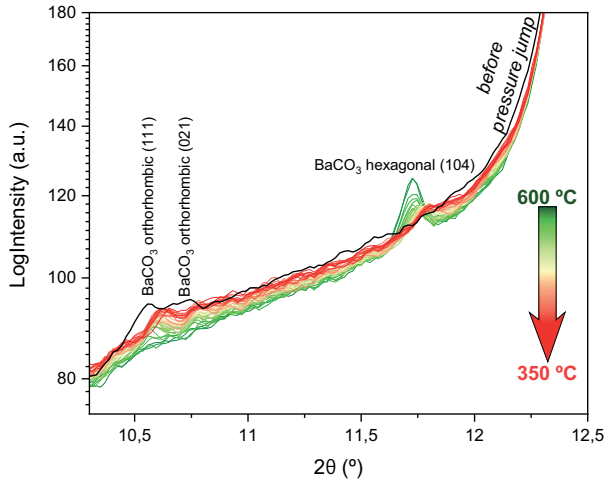


FIGURE 5.8: I(2θ) scans resulting from the integration in χ of the 2D-XRD images acquired during the cooling process of the *in-situ* phase transformation for the ternary film. The I(2θ) corresponding to the 2D-XRD frame acquired prior to the pressure jump is represented (in black) for comparison. Color-graded plots of the I(2θ) scan acquired every 10 scans, between the temperature of 600 ºC (green) and 350 ºC (red). In this temperature range the phase transition from $BaCO_3$ hexagonal to orthorhombic is observed. The contribution from the latter phase appears to be minor if compared to the initial intensity of its peaks prior to the pressure jump (represented as a black line), suggesting the elimination of $BaCO_3$ has almost reached completion through this process.

heating ramps, it demonstrates an interesting point on the importance of the morphology of the sample: both $BaCO_3$ powder and densely compacted spheres were thermally treated in argon, displaying a higher difficulty for the spherical samples towards a complete decomposition. The density of the sphere hinders optimal gas transport, resulting in an unreacted $BaCO_3$ core and decomposition temperature shifting to higher values, supporting the idea behind the hindrance of the elimination of $BaCO_3$ in the films described in this thesis in this particular set-up configuration. Nonetheless, the thermally-driven phase transition yields an extremely low final contribution of $BaCO_3$ orthorhombic, compared to the initial one prior to the *in-situ* phase transformation process. However, a consideration regarding the success of the process must be made. When comparing the I(2θ) scans of the films described in this subsection resulting from the 2D-XRD images acquired at RT following the process, one may determine the binary film to show a higher contribution of $BaCO_3$ orthorhombic remaining after the process. Additionally, a minor contribution from the monoclinic phase of $BaCO_3$ is displayed in the

I(2θ) scan relative to the binary film, absent in the ternary one. This may find an explanation, as for the phase evolution process, in the difference in crystallinity of the initial films. Such behaviour was observed in films quenched ex-situ (described in detail in 4.2), in which ternary nanocrystalline precursor films of higher crystalline nature presented more complications towards a straightforward elimination of the barium precursor phase respect to films with a more amorphous initial character. Therefore, the difference in the contributions of the orthorhombic phase of $BaCO_3$ resulting from the *in-situ* phase transformation process may be ascribed to this phenomenon.

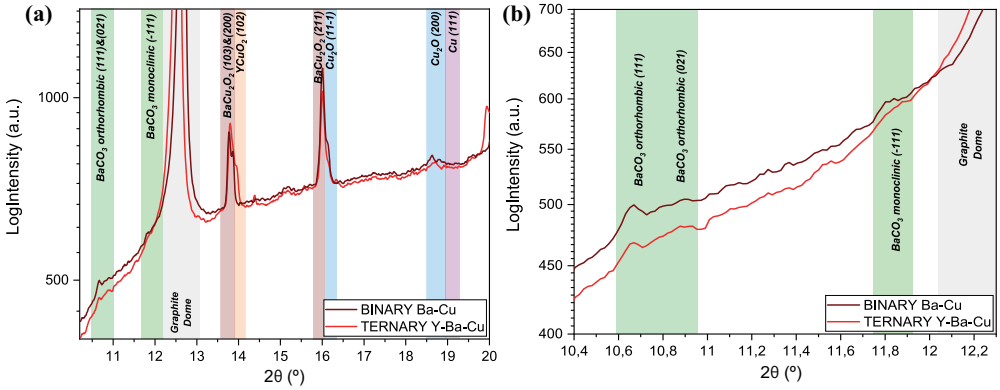


FIGURE 5.9: (a) I(2θ) scans for the binary and ternary films which underwent the *in-situ* phase transformation process, resulting from the integration in χ of the 2D-XRD images acquired at RT following the experiment employing an acquisition time of 1 s. Both films yield in majority $BaCu_2O_2$ and Cu_2O, the expected phases at the value of final P_{O_2} established for this process. (b) Focus on the 2θ range relative to $BaCO_3$ peak positions, showing a higher contribution of this phase in the binary film (burgundy) respect to the case of the ternary one (red).

Nonetheless, the expected phases of $BaCu_2O_2$ and Cu_2O are found in majority, and the absence of peaks relative to Cu(0) demonstrates the entirety of this reduced phase is finally oxidized to Cu_2O, again suggesting the great benefit of the pressure jump towards the gas renewal in the furnace environment.

5.2.1.2 *In-situ* Phase Transformation on ternary films of different liquid composition

Having determined the pathways towards $BaCO_3$ elimination in binary and ternary films of (3:7) composition, this same analysis was widened to films of the four liquid compositions considered in this thesis, subjected to the *in-situ* phase transformation process. Before proceeding with the study of the phase evolution for the four films, the initial microstructural characteristics of the nanocrystalline precursor films of each composition must be taken into consideration. In Chapter 4, the GIXRD of the four films after pyrolysis (Fig. 4.13) display a pronounced difference in the crystalline aspect of the nanocrystalline phases composing the

pyrolyzed films. As the amount of copper in the liquid composition (thus, in the stoichiometry of the metal-organic precursor solution) is increased, the film appears to be more amorphous. This is especially visible for the (111) and (021) reflections of $BaCO_3$ orthorhombic phase (peaks with major intensity relative to this crystalline phase), which show an important decrease in intensity and broader peaks going from (2:3) composition, the least copper-rich, to the (4:11) composition, the one with highest copper content. In Chapter 4, specifically in 4.2.6, it was observed that in the case of *ex-situ* quenches performed in the tubular furnace used for growth processes at ICMAB, a higher crystallinity of the pyrolyzed film would hinder the complete elimination of $BaCO_3$ when the same processing conditions were employed. Films deriving from compositions with copper excess, instead, showed no difficulty in achieving a complete elimination of the barium precursor phase, and this is a consequence of the combination of two effects: the higher amorphous nature of the nanocrystalline precursor film and the catalytic effect of CuO in the elimination of $BaCO_3$ [96], in large excess in films of said compositions.

Films of the four liquid compositions with the aforementioned microstructural differences underwent the *in-situ* phase transformation process, and the phase evolution relative to the low-pressure heating (step 1 in the diagram reported in Fig. 5.3) is shown in Fig. 5.10. As for the ternary film previously described, it is not possible to follow the peak relative to CuO during heating due to the extremely low intensity which makes its integration cumbersome. Therefore, during the initial part of the process, the peak from $BaCO_3$ orthorhombic is the only one to be observed in the four cases considered. No variations in the intensity of this phase occur until approximately 770 ºC, when the the formation of Cu_2O is observed (1), as a result of the reduction of CuO expected when crossing the Cu(II) to Cu(I) reduction line with the increase in temperature. Coinciding with this event, as previously shown in the binary-ternary phase evolution comparison, films of (3:6), (3:7) and (4:11) compositions show an abrupt increase in the contribution of $BaCO_3$, suggesting that a thermally-induced crystallization is occurring. The stoichiometric (2:3) composition is the only one to show no evidence of any crystallization process in this temperature range. The high crystalline character of the initial film microstructure may be the reason for which the intensity of the $BaCO_3$ peak contribution is similar in average throughout the entire heating for this specific liquid composition. The formation of Cu_2O is ranging between 765 ºC and 775 ºC, suggesting a similar thermal behaviour. However, the speed of this particular process is highly enhanced in the films which are richer in copper ((3:7) and (4:11) compositions), which show a rapid growth of the contribution of this phase, respect to the compositions with less copper, in which the increase to saturation is gradual. The unexpected reduction of the Cu(I) phase, Cu_2O, to Cu(0) is also observed in the *in-situ* phase transformation of these films above 820 ºC. Films of (3:6), (3:7) and (4:11) compositions additionally show the concomitant formation of the expected mixed oxide of barium and copper, $BaCu_2O_2$, with a minor decrease in the contribution of $BaCO_3$ (2). Again, the coexistence of these three phases is not ideal, as no complete elimination of $BaCO_3$ is achieved in any of

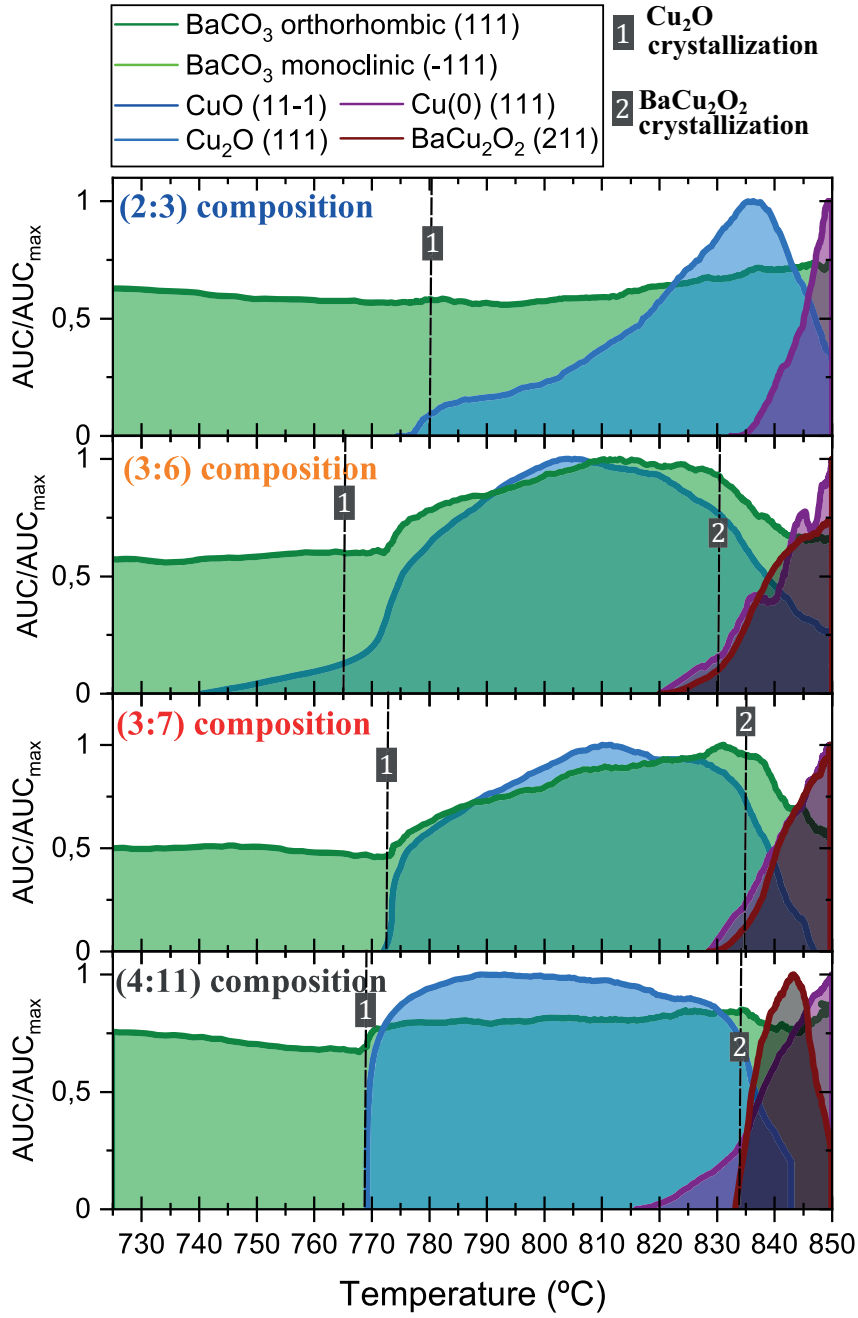


FIGURE 5.10: Temperature dependent phase evolution result of the integration of the peaks relative to the precursor phases observed during the low-pressure heating, normalized to their maximum, in the temperature range between 720 ºC and 850 ºC, for four films of different liquid compositions, from the stoichiometric (2:3) composition increasing the copper content to the (4:11). The fundamental steps of the process are identified with enumerated dashed lines, further explained in the legend. Onset temperatures are determined with the 10% criterion (full details on the method followed for the determination of the onset temperature may be found in E.1.2).

the described cases during the heating. The reduction of oxidation state of copper to zero is a suggestion of a strongly reducing atmosphere, but the contemporary formation of $BaCu_2O_2$ with only partial decrease of the $BaCO_3$ peak intensity is evidence of an initial progress of the process, additionally indicating local atmosphere variations inside the film may be occurring. As previously explained, the poor gas transport and the extremely low porosity presented by the four films considered, ranging between 1% and 2%, are factors hindering the reaction completion. An equilibrium is reached between the evolved gas in the furnace atmosphere and the CO_2 still in the film, blocking the advance of $BaCO_3$ elimination towards the formation of $BaCu_2O_2$. The additional presence of Cu(0) is moreover suggesting the formation of a reducing agent, as identified in the previous subsection possibly due to the presence of C in the furnace environment deriving from several possible causes. The extreme copper excess in the (4:11) composition results in a predominance of the metallic phase of copper and a simultaneous decrease of the $BaCu_2O_2$ contribution, possibly due to Cu(0) grain coalescence phenomena forcing a regression of $BaCu_2O_2$ to $BaCO_3$ (note the rather small increase in the contribution of the latter phase). Contrarily, in the (2:3) composition no $BaCu_2O_2$ formation is observed, and the intensity of the $BaCO_3$ orthorhombic peak remains unaltered until the end of the heating. The sole presence of the reduced Cu(0) and $BaCO_3$ may be implying that the initial highly crystalline microstructure of this film is responsible for an extreme enhancement of the thermal stability of the barium precursor phase which, combined with the insufficient gas evolution, results in a complete obstruction of the progress of $BaCO_3$ elimination in the given conditions.

The time-dependent phase evolution of the pressure jump ($P_{O_{2,final}} = 0.1$ mbar; $P_{TOT,final} =$ 35 mbar) is displayed in Fig. 5.11, in which the raw intensity is represented in order to evaluate the variations associated with each liquid composition during the *in-situ* phase transformation process. In the four cases, during the pressure jump, Cu(0) is promptly oxidized to Cu_2O and the intensity of $BaCu_2O_2$ increases: these are the expected phases to be found in solid form in the specific conditions of pressure and temperature of the process according to the TLAG kinetic phase diagram [101]. In all cases, the phase transition of $BaCO_3$ orthorhombic to hexagonal is occurring during the change in pressure. Nonetheless, the intensity of the latter phase is varying depending on the liquid composition: the stoichiometric (2:3) composition displays the highest contribution of the four cases considered, additionally exhibiting the formation of the expected mixed oxide of $BaCu_2O_2$ only minorly. Moreover, this composition is the sole to present a further formation of Cu(0) when reaching $P_{O_{2,final}} = 0.1$ mbar. A reason for this may be the extreme crystallinity of the initial pyrolyzed film combined with the detrimental coarsening resulting from the low-pressure heating process, also suggested by the presence of a significant amount of $BaCO_3$ prior to the pressure variation. The gas renewal due to the change in pressure seems to be insufficient in this case for the complete progression towards the formation of $BaCu_2O_2$, with the unexpected reduction of Cu_2O to Cu(0) evidencing this. Increasing the copper content in the liquid composition, one may observe a similar

phase evolution in the remaining three cases, with the amount of $BaCO_3$ hexagonal reduced to half when increasing Cu mol% from (3:6) to (3:7) and (4:11) compositions. None of these liquid compositions display further reduction to metallic phase of copper following the jump which, associated to the minor contribution of $BaCO_3$ hexagonal, suggests the *in-situ* phase transformation process to be favourable.

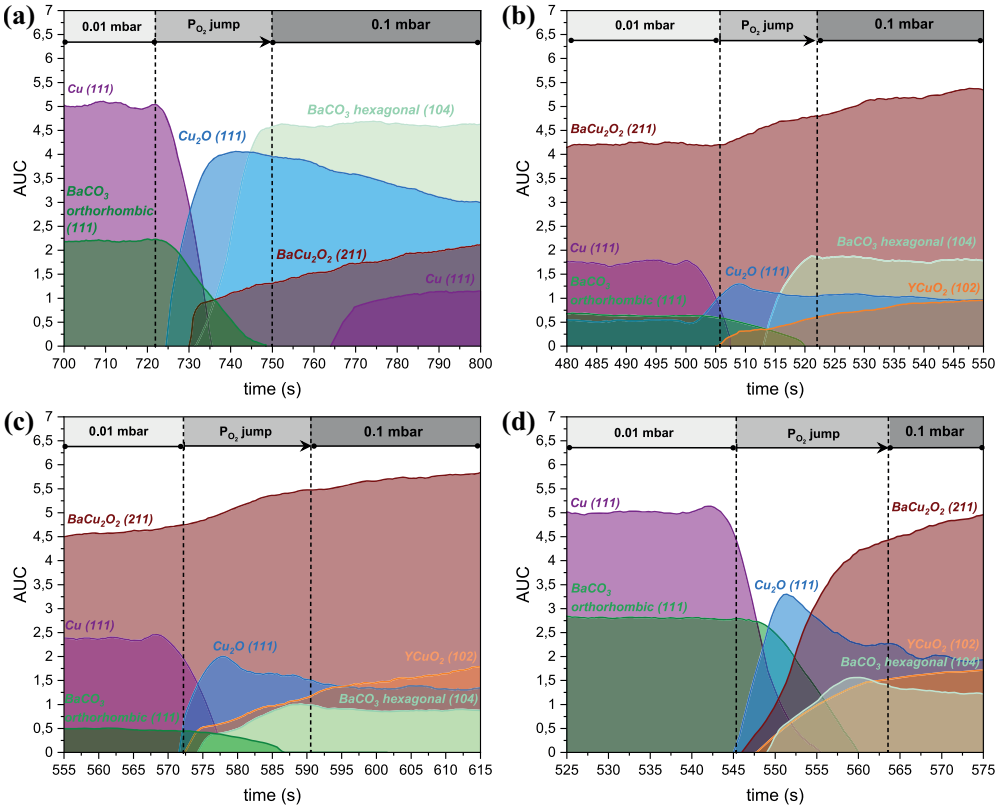


FIGURE 5.11: Time-dependent phase evolution displaying the change in pressure for (a) (2:3), (b) (3:6), (c) (3:7), and (d) (4:11) liquid compositions. Values of P_{O_2} are indicated in the upper part of each plot, indicating the time range in which the pressure jump occurs. The represented time range is varying in each case as it depends on the start of the data acquisition, not always coinciding with the launch of the heating ramp of the furnace. Raw intensity is displayed to fully compare the contributions depending on a specific liquid composition.

The formation of $YCuO_2$ phase is observed, again, only in the films of the (3:6), (3:7), and (4:11) compositions. Stability of this phase at elevated temperatures in the pressure conditions employed is expected [211, 212], given processing conditions to coincide with the Cu(I) oxidation state region in the phase diagram. Moreover, this phase seems to be favoured in the cases of compositions with copper excess, in which the increased amount of copper may easily react partially with the yttria present. As it was previously observed in *ex-situ* growth of films

of Y-rich (4:11) composition, in 4.4, the increased amount of copper and yttrium in this particular liquid composition promoted the formation of Y-Cu mixed oxides, whose augmented presence was demonstrated to be of no hindrance to current percolation.
To summarize, the mechanism observed in the *in-situ* phase transformation process reported up to the moment may be described with the following reaction scheme:

$$\begin{aligned} &\textit{Low Pressure Heating}: \\ &BaCO_{3(s)}(o) + CuO_{(s)} + Y_2O_{3(s)} \rightarrow BaCO_{3(s)}(o) + Cu_2O_{(s)} + Y_2O_{3(s)} \rightarrow \\ &BaCO_{3(s)}(o) + BaCu_2O_{2(s)} + Cu(0)_{(s)} + Y_2O_{3(s)} \rightarrow \\ &\textit{Pressure Jump}: \\ &BaCO_{3(s)}(h) + BaCu_2O_{2(s)} + Cu_2O_{(s)} + Y_2O_{3(s)} + YCuO_{2(s)} \end{aligned} \tag{5.3}$$

To be noted, $BaCO_{3(s)}(o)$ and $BaCO_{3(s)}(h)$ are respectively indicating the orthorhombic and the hexagonal phase of barium carbonate. It is additionally important to specify that this scheme is a general description based on the observation of the phase evolution, and the chemical reactions are thus not balanced. Moreover, $Y_2O_{3(s)}$ and CuO are here listed despite the absence of peaks relative to these phases in the phase evolution, as mentioned before due to their low crystallinity and/or contributions of low intensity.
When analysing the cooling process, an interesting event is worth considering. As previously mentioned for the cases of binary and ternary films described earlier in this chapter, during cooling the phase transition from $BaCO_3$ hexagonal back to orthorhombic could be observed. The exceptionally minor contribution from the resulting $BaCO_3$ orthorhombic is suggesting the complete removal of this phase as a consequence of the *in-situ* phase transformation process. Once more, the microstructure in these films, directly depending on the copper content, is playing a major role, as already observed for the comparison of the phase evolution plots of the heating and pressure jump. Fig. 5.12 shows the cooling process for two exemplary cases, a film of (3:6) and one of (3:7) compositions. In the temperature range between 640 ºC and 350 ºC, the composition with lower copper content shows a phase transition from $BaCO_3$ hexagonal to a majority of its monoclinic phase, and partially, orthorhombic. Contrarily, cooling of a film of composition with higher copper content displays a transition to only an extremely low contribution of the orthorhombic phase, suggesting $BaCO_3$ can be almost entirely eliminated through the use of this process. Again, the important difference between these results may be ascribed to the combined effects of differences in the initial crystalline nature of the films and insufficient CO_2 elimination in the furnace environment. These two features are responsible for an unfavourable elimination of $BaCO_3$ for the films with more crystalline precursor phases (the ones deriving from liquid compositions of lower copper content), thus resulting in a high contribution of $BaCO_3$ remaining after the *in-situ* process. Contrarily, the compositions with

copper excess, which initially show a more amorphous nature of the precursor film, display full elimination of the barium precursor phase successive to the *in-situ* phase transformation process, given the straightforward formation of the expected solid phases of $BaCu_2O_2$ and Cu_2O as the gas renewal during the pressure jump was seen sufficient to eliminate the remaining $BaCO_3$.

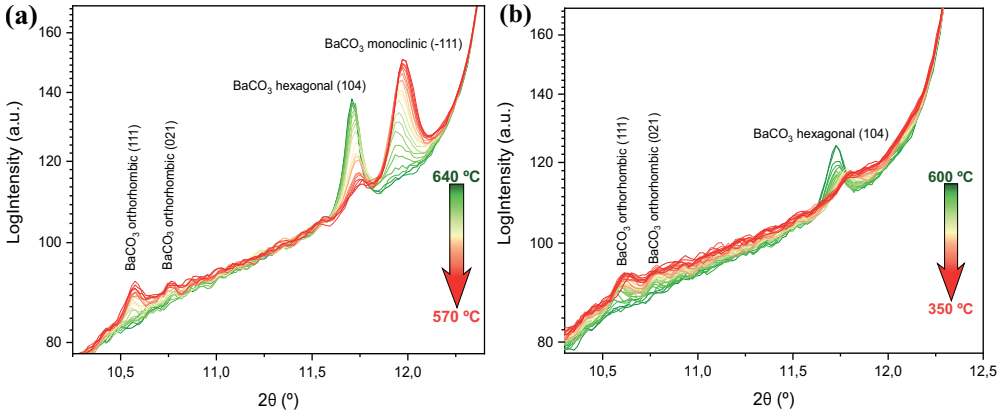


FIGURE 5.12: I(2θ) scans resulting from the integration in χ of the 2D-XRD images acquired during the cooling process of the *in-situ* phase transformation for ternary films of (a) (3:6) and (b) (3:7) compositions. Plots are displaying one of every ten I(2θ) scans in the indicated temperature ranges during the cooling of each film, where the phase transition from $BaCO_3$ hexagonal to orthorhombic is observed. In the case of the liquid composition with low copper content, this phase transition results in the appearance of a strong contribution from the monoclinic phase of $BaCO_3$, and a minor one from the orthorhombic phase, suggesting the elimination of the barium precursor phase to be unsatisfactory.

As above, the phase transformations occurring during cooling may be described as:

$$Cooling: \quad BaCO_{3(s)}(o) + (BaCO_{3(s)}(m)) + BaCu_2O_{2(s)} + Cu_2O_{(s)} + (Cu(0)_{(s)}) + Y_2O_{3(s)} + YCuO_{2(s)} \tag{5.4}$$

where $BaCO_{3(s)}$(o) and $BaCO_{3(s)}$(m) are respectively indicating the orthorhombic and the monoclinic phase of barium carbonate. The phases indicated in brackets are only observed in the exceptional case of films of (2:3) composition, in which the elimination of $BaCO_3$ is facing the most adverse conditions, leading to a strong contribution of monoclinic $BaCO_3$ and further (partial) reduction of $Cu_2O_{(s)}$ to Cu(0).

The I(2θ) scans result of the integration in χ of the 2D-XRD images acquired at RT following the *in-situ* phase transformation process for the films of each liquid composition is displayed in

Fig. 5.13, with an additional focus on the 2θ range where $BaCO_3$ peaks appear. An important difference is evident and a clear separation between compositions with low copper content and the ones with copper excess may be defined. The latter liquid compositions, namely (3:7) and (4:11), display the formation of the expected phases at the conditions chosen for the *in-situ* phase transformation process: the barium and copper mixed oxide $BaCu_2O_2$ and Cu_2O, with contribution of the $YCuO_2$ mixed oxide. Contrarily, in the films of liquid compositions with low copper content, specifically (2:3) and (3:6), elevated contributions of $BaCO_3$ (orthorhombic and monoclinic) may be observed. In the extreme case of the stoichiometric (2:3) composition, the presence of an intense peak belonging to metallic copper combined with only a minor formation of $BaCu_2O_2$ suggests the failure to eliminate the barium precursor phase during the *in-situ* experiment, combined with the coarsening of the most reduced phase of copper. The contrast in the success of the *in-situ* phase transformation process depending on the liquid composition is clearly observed in the focus on the 2θ range characteristic to $BaCO_3$ peaks. The (2:3) and (3:6) compositions yield films with incomplete phase transformation and which, moreover, present a phase transition to the monoclinic phase of the barium precursor, the most unfavourable one towards a positive outcome of the TLAG process due to its elevated thermal stability [91, 93]. The copper-excess liquid compositions exhibit I(2θ) patterns in which the contribution of $BaCO_3$ peaks is only minor or nonexistent, demonstrating the elimination of $BaCO_3$ is possible in this experimental set-up through the phase transformation process.
The evidence presented regarding the *in-situ* phase transformation process on binary and ternary films and on films of various compositions show a similar trend to the one previously observed in *ex-situ* quench processes performed at ICMAB described in 4.2.6. Films which initially exhibit a higher crystalline nature of the nanocrystalline precursor phases (binary films and films of liquid compositions with low copper content) undergo a demanding process towards the elimination of $BaCO_3$. The reaction between $BaCO_3$ and CuO to form the mixed oxide $BaCu_2O_2$ is impeded due to the following factors:

- poor gas transport in the Anton-Paar furnace which hinders CO_2 evacuation, necessary for the reaction to progress (as previously described in 4.2, the elimination of $BaCO_3$ is strictly controlled by CO_2 out-diffusion);
- higher crystallinity of the initial phases obtained from the pyrolysis process, which are prone to have elevated thermal stability.

This effect yields films which present high contributions of $BaCO_3$ and coarsened Cu(0), the latter a consequence of the presence of CO acting as reducing agent. The only minor formation of $BaCu_2O_2$ is a further suggestion of the stalling of the reaction to the side of the precursor phases.

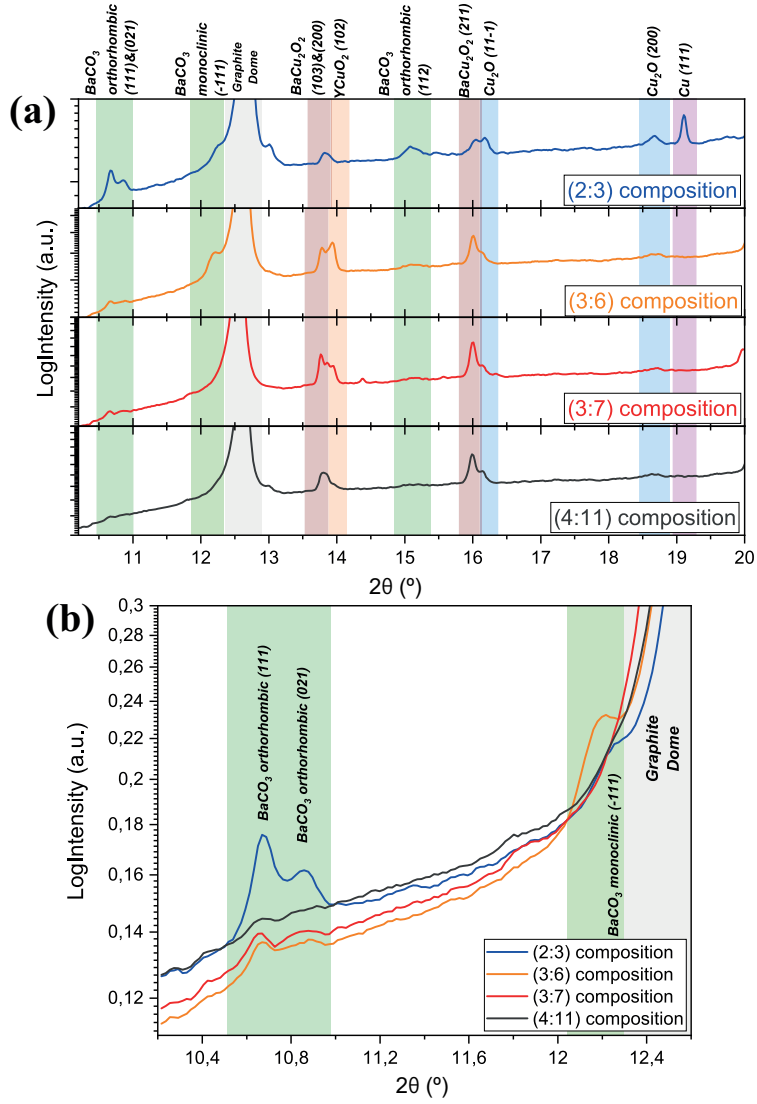


FIGURE 5.13: (a) I(2θ) scans resulting from the acquisition of the 2D-XRD image at RT following the *in-situ* phase transformation process for the four ternary films of various liquid compositions (1 s acquisition time). Films of liquid compositions with higher copper content ((3:7) and (4:11)) yield in majority $BaCu_2O_2$ and Cu_2O, the expected phases at the value of $P_{O_{2,final}}$ established for this process. Liquid compositions with lower copper content ((2:3) and (3:6)) display important contribution of $BaCO_3$. (b) Focus on the 2θ range relative to $BaCO_3$ peak positions, showing a higher contribution of this phase in the films of compositions with low copper content ((2:3) and (3:6), in blue and orange, respectively) respect to the case of the compositions with copper excess ((3:7) and (4:11), in red and black, respectively). The intensity is here normalized to the peak of the graphite dome for correct quantification.

However, the elimination of the barium precursor phase is demonstrated to be possible on films of liquid compositions with higher copper content, again due to a combination of two effects:

- more amorphous nature of the nanocrystalline precursor phases in the films resulting from the pyrolysis;
- catalytic effect of CuO in the elimination of $BaCO_3$, in these compositions found in great excess.

The strategy of using an excess of copper is known to lower the processing temperatures due to the catalytic effect of CuO through its reaction with $BaCO_3$, favouring its elimination and the subsequent formation of the barium and copper mixed oxide [96]. In the films described in this thesis, the additional characteristic of presenting a more amorphous microstructure following the pyrolysis process, thus less coarsened phases, is further seen to aid in the elimination of barium carbonate. In the experimental set-up for the *in-situ* XRD experiments, the limited gas evacuation is an added hindrance to the proceeding of the reaction: in the case of films of compositions with low copper content, the gas renewal in the sample environment resulting from the pressure jump is insufficient to promote the complete CO_2 out-diffusion from films in which the highly coarsened $BaCO_3$ phase is showing significant stability. Conversely, the entrance of gas in the furnace due to the pressure variation is enough to completely remove the CO_2 out-diffused from the more amorphous films of copper-excess compositions, in which the reaction is seen to be favoured considering the lower coarsening of the initial phases. The *in-situ* phase transformation process on the latter films results in the formation of phases expected from the TLAG kinetic phase diagram [101] with a complete elimination of $BaCO_3$, demonstrating the feasibility of the full removal of the barium precursor phase in the set-up employed for *in-situ* XRD experiments.

5.2.2 Elimination of $BaCO_3$ through an *ex-situ* quench process

The second strategy adopted for the elimination of the barium precursor phase, as stated earlier, was to perform an *ex-situ* quench process in the growth furnace at ICMAB. In Chapter 4 it was demonstrated how the optimization of this kind of process led to a successful, complete elimination of $BaCO_3$. This strategy was implemented solely on binary and ternary films of (3:7) composition. The films which underwent such process were then stored in vacuum containers[4] and carried to the synchrotron facility for the *in-situ* XRD experiments. The importance of a correct storage of the *ex-situ* quenched films is explained in detail in D.2.1. An exemplary GIXRD pattern acquired on a Bruker D8 Discover X-ray diffractometer of a ternary

[4]The mixed oxide of barium and copper which is formed through a quench process in the TLAG P_{O_2}*-route*, $BaCu_2O_2$, is unstable in atmospheric conditions and reacts promptly with CO_2 from air to form a superficial layer of $BaCO_3$. The storage in vacuum conditions avoids such reaction to occur.

(3:7) composition film which underwent an *ex-situ* quench process is reported in Fig. 5.14, for reference of the crystalline phases formed during such thermal treatment.

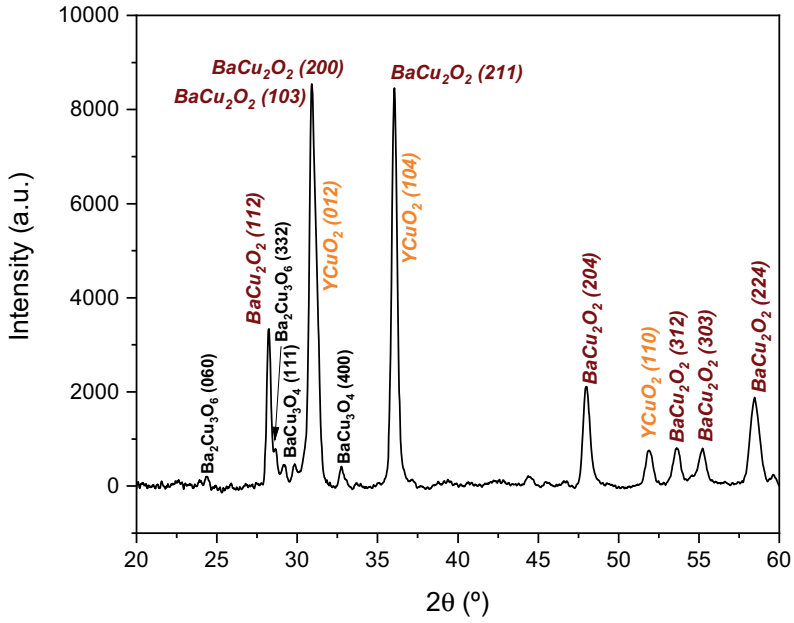


FIGURE 5.14: GIXRD measured on a Bruker D8 Discover X-ray diffractometer of a film of (3:7) composition which was quenched *ex-situ* in the growth furnace at ICMAB (details regarding measurement configurations may be found in D.2.1). The major crystalline contribution is deriving from the mixed oxide of $BaCu_2O_2$. The presence of Cu_2O is also expected, however the peak positions coincide with the ones from $BaCu_2O_2$. No presence of $BaCO_3$ is observed, suggesting the elimination of this phase and its reaction with CuO to form the mixed barium and copper oxide has reached completion.

The process yields majorly $BaCu_2O_2$, with minor contribution from the secondary phase of $YCuO_2$ and other mixed oxides of barium and copper which may be formed during the cooling process. Cu_2O is expected to be present, but the peak positions of the reflections relative to this phase coincide with the ones from the most intense $BaCu_2O_2$. Clearly, the absence of $BaCO_3$ peaks is suggesting its successful removal through the quench process. The reproducibility of the initial conditions was examined on the quenched *ex-situ* films employed for the *in-situ* synchrotron XRD experiments, and I(2θ) scans resulting from the integration in χ of the 2D-image acquired at RT with 1 s acquisition time are displayed in Fig. 5.15. The presence of the aforementioned phases is evidenced, with similar crystallinity and absence of any peaks relative to the $BaCO_3$ precursor phase, both in binary and ternary films.

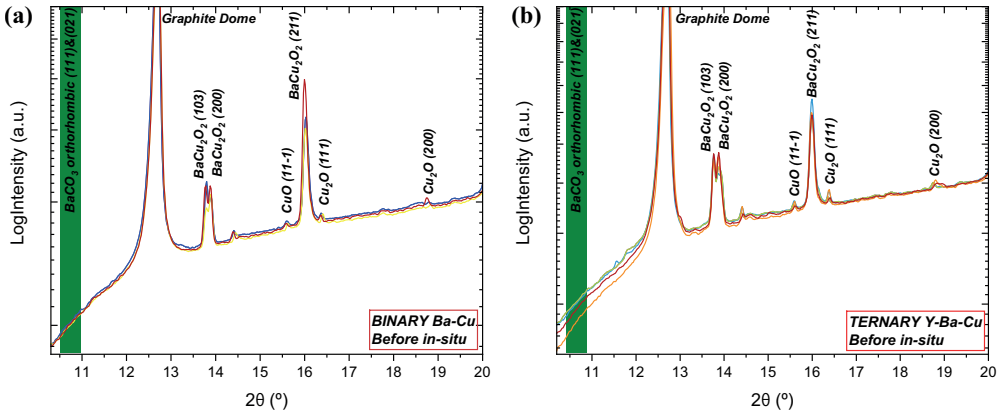


FIGURE 5.15: I(2θ) scans resulting from the integration in χ of the 2D-XRD images acquired prior to the *in-situ* experiment, at RT with 1 s acquisition time for all the (a) binary and (b) ternary films employed in this analysis. Phases present in majority are identified and the 2θ range where peaks from $BaCO_3$ should appear is shaded in dark green, with a clear absence of any contribution in this area.

From this comparison, the reproducibility of the *ex-situ* quench process is further demonstrated and it can be assumed that the films are initiating the *in-situ* XRD experiments from comparable situations. As the current section is devoted to explaining the strategies adopted for $BaCO_3$ elimination in the set-up employed for the *in-situ* XRD experiments, in this subsection the effect of using pre-quenched films on the formation of the phases solely during the low-pressure heating of TLAG P_{O_2}*-route* experiments performed in synchrotron facilities will be assessed. The second step of the process, in which the growth of YBCO from such films occurs, will be described later on.

The low-pressure heating process was performed in identical conditions on three binary films and three ternary films of (3:7) composition and the comparison of the phase evolution of such experiments may be found in Fig. 5.16 and Fig. 5.17, respectively.

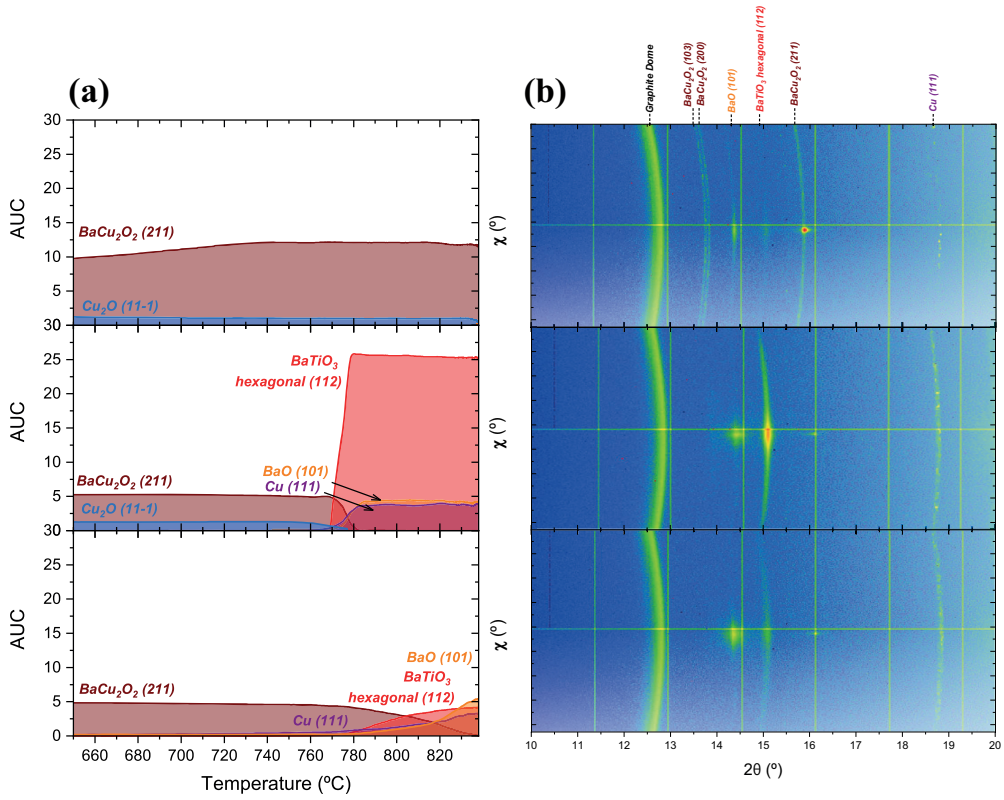


FIGURE 5.16: (a) Temperature-dependent phase evolution plots of three binary films subjected to the same low-pressure heating to T_{set} = 830 ºC with a heating rate of 4.5 ºC s^{-1}. $P_{TOT,base}$ and $P_{O_{2,base}}$ values are set to 0.05 mbar and 0.01 mbar, respectively. (b) 2D-XRD image corresponding to the last frame acquired during the heating process for each binary film in panel (a). Identification of the phases at characteristic 2θ peak positions are indicated in the upper part of the panel.

When observing the temperature-dependent phase evolution plots of both binary and ternary films one striking point is evident: a major issue of irreproducibility in the nucleation temperature and the intensity of the crystalline phases. As previously explained, the starting point is a combination of $BaCu_2O_2$ and Cu_2O. At the temperature and pressure conditions of the process these solid phases are expected to be stable [95]. However, solely in one experiment for both binary and ternary films this occurs and these two phases are the ones present in majority before the pressure jump (respectively in Fig. 5.16(a) and Fig. 5.17(a), upper panels). Contrarily, in the rest of the experiments, at the temperature of 700 ºC or above, the contribution of the mixed oxide of barium and copper decreases abruptly to be substituted by metallic copper and BaO. The reactivity phase with the substrate, $BaTiO_3$ is additionally observed, majorly in the binary films but can be occasionally found also in the ternary ones. In rare cases,

presence of insignificant contributions of $BaCO_3$ has been observed. When this occurs, the high-temperature phase transformation from orthorhombic to hexagonal follows, and the latter phase is transformed to BaO through CO_2 out-diffusion above 800 ºC, as observed in Fig. 5.17(a), lower panel.

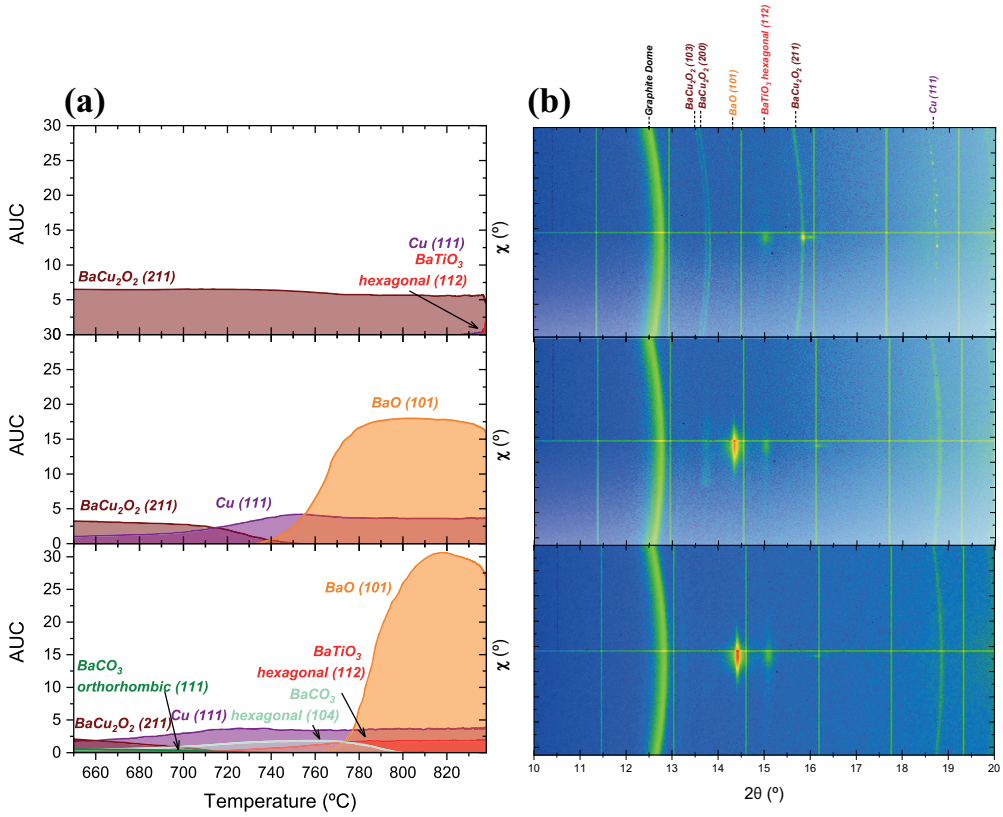


FIGURE 5.17: (a) Temperature-dependent phase evolution plots of three ternary films subjected to the same low-pressure heating to T_{set} = 830 ºC with a heating rate of 4.5 ºC s^{-1}. $P_{TOT,base}$ and $P_{O_{2,base}}$ values are set to 0.05 mbar and 0.01 mbar, respectively. (b) 2D-XRD image corresponding to the last frame acquired during the heating process for each ternary film in panel (a). Identification of the phases at characteristic 2θ peak positions are indicated in the upper part of the panel.

Several points should be considered upon the observation of the unexpected evolution of phases mentioned above:

- No information regarding the microstructure of the films quenched *ex-situ* is available, as the analysis of such films through TEM techniques is very complicated due to their instability at atmospheric temperature and pressure conditions and due to their rough surface, which hinders a successful preparation of the TEM lamellae during the polishing

step. Nonetheless, considering the extremely low porosity of a nanocrystalline precursor film before undergoing a quench process (1-2 %), one may estimate the porosity of the films successive to the *ex-situ* quench process to be below this value, as $BaCO_3$ has been completely eliminated and the film has supposedly been compacted, yielding an even more dense microstructure. This may influence negatively the gas evolution from the inner parts of the films. Difficulties on the gas transport have been demonstrated in the previous subsection to be enhanced in the particular set-up employed for the *in-situ* synchrotron XRD experiments.

- An *ex-situ* quench process means the films have undergone a low-pressure heating process to temperatures above 800 ºC prior to the experiments in the synchrotron facility. Subjecting the films to a second heating is possibly favouring coarsening phenomena, unfavourable towards a fast reaction in the TLAG process, in which small sizes of the nanocrystalline phases are demonstrated to be optimal [53, 54, 101].

Considering the points above, the decomposition of $BaCu_2O_2$ and the formation of phases such as Cu(0) and BaO suggests a strongly reducing atmosphere, generated by the possible aforementioned factors in the text. The initial presence of solely Cu(I) species in the films combined with the formerly described insufficient gas transport in the furnace environment may lead to formation phases which in literature are reported to be formed at lower values of P_{O_2} [95]. The impeded gas evolution may result in the system reaching an equilibrium between the evolved CO_2 inside the furnace environment which cannot be evacuated (due to deficient flux conditions) and the gas which is being evolved from inside the film. The formation of reduced phases, such as Cu(0), are the likely consequence of the reduction of CO_2 to CO in presence of C contamination in the sample environment. Moreover, the irreproducibility of the phase evolution may be enhanced by the unknown initial conditions of microstructural morphology of these films. Despite the I(2θ) scans in Fig. 5.15 corresponding to the 2D-XRD images acquired prior to the *in-situ* experiment show the presence of the same crystalline phases in all films, whether these are distributed homogeneously in all of the films is undefined. Possible inhomogeneous distribution or variations in the grain sizes of the precursor phases may easily lead to the different thermal behaviour, yielding contrasting evolution of the phases. Additionally, when approaching the pressure jump with phases which are not the preferred precursors for the fast formation of the transient liquid (such as Cu(0) and BaO, as observed in the phase evolution of the ternary films, for example), the change in P_{O_2} will force the oxidation of copper when the local pressure resulting from the renewal of gas will be adequate. This will also allow for the nucleation of $BaCu_2O_2$, crystalline or amorphous, and from here, the proceeding of the expected TLAG mechanism: $BaCu_2O_2$ and Cu_2O will form the [Ba-Cu-O] transient liquid during the pressure jump, and the dissolution of the Y_2O_3 nanoparticles in the liquid will result in YBCO nucleation and growth. The oxidation of the copper species occurring during the pressure jump may delay the whole process: this transformation may be occurring

gradually and not simultaneously in the entire film, resulting in major inhomogeneities. An example of the reoxidation of Cu(0) during the jump and the detection of a minor contribution of crystalline $BaCu_2O_2$ is shown in the phase evolution in Fig. 5.18, in which the rapid growth of YBCO may indicate that most of the formed mixed Ba-Cu oxide was amorphous before promptly proceeding to the transient liquid formation. The presence of other oxides of copper is anticipated, but the absence of any relative peaks may be due to either their formation in amorphous form, not detected through XRD, or the extreme rapidity of the process (YBCO growth initiates in a time range below 10 s), which is limited by the acquisition time of the specific experiments. Possible effects of the growth of YBCO through TLAG P_{O_2}*-route* from this kind of films will be presented later on.

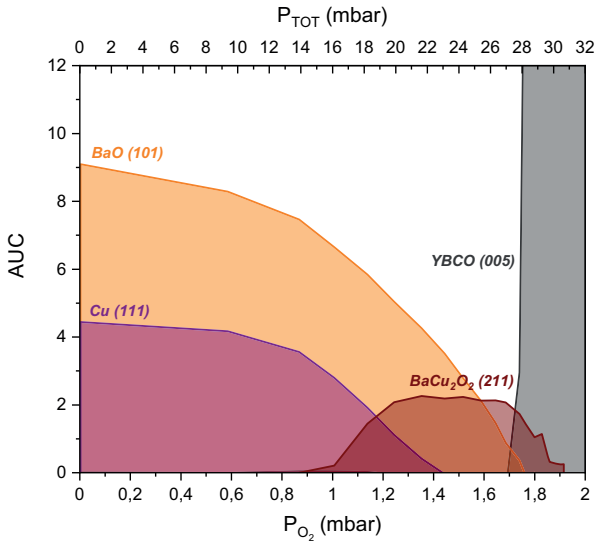


FIGURE 5.18: Pressure-dependent phase evolution during the jump of one of the ternary films previously quenched *ex-situ* and then subjected to the *in-situ* synchrotron XRD experiment. The only crystalline phases present before the pressure jump, Cu(0) and BaO, upon gas renewal and increase of P_{O_2} proceed to the formation of $BaCu_2O_2$, here formed at $P_{O_2} > 1$ mbar. With a further pressure increase this phase reacts with Cu_2O to form the transient liquid and, finally, YBCO. The insignificant contribution of the peak intensity relative to this phase may suggest that a portion of it has proceeded to the formation of the transient liquid from an amorphous form, undetectable through XRD.

As a summary of the results analysed up to now regarding the elimination of $BaCO_3$ in the experimental set-up employed for the *in-situ* XRD experiments, interesting insights could be gained. The two strategies presented for the enhancement of the complicated elimination of $BaCO_3$ in a set-up which suffers from poor gas transport conditions led to the attainment of important knowledge regarding the system employed and the thermal behaviour of the films

in such circumstances. When initiating the low-pressure heating from films composed by nanocrystalline $BaCO_3$, CuO and Y_2O_3, major complications are encountered towards the proceeding of the elimination of the barium precursor phase in the experimental set-up described here: the small volume of the furnace environment combined with the insufficient gas evacuation results in the out-diffusion of CO_2 from the films to reach an equilibrium with the atmosphere inside the furnace, hindering the reaction to reach completion. This is evidenced by the concomitant presence of $BaCO_3$ and $BaCu_2O_2$ whose plateaued intensity suggest no further advancement in the elimination of the former towards the formation of the latter is occurring. Moreover, the CO formed due to possible C impurities in the furnace environment yield the full reduction of copper to the unfavourable Cu(0), renowned to be prone to strong coarsening phenomena. However detrimental these conditions seem to be, the development of the *in-situ* transformation process has demonstrated to produce the complete elimination of $BaCO_3$. In this scenario, the use of films of liquid compositions with copper excess is seen to be preferable, resulting in an easier elimination of the barium precursor phase. The more amorphous microstructure of the initial nanocrystalline precursor films of (3:7) and (4:11) compositions show a more straightforward advancement of the reaction from $BaCO_3$ to the mixed oxide of barium and copper, additionally catalysed by CuO contained in large excess in these compositions. The gas renewal deriving from the pressure jump is, here, sufficient to completely eliminate the remaining $BaCO_3$ through the final CO_2 out-diffusion and yields films of the desired solid precursor phases of $BaCu_2O_2$ and Cu_2O for the transient liquid formation in the successive step of the TLAG process. The microstructure of films of compositions with low copper content, conversely, display highly crystalline initial phases which present elevated thermal stability, hindering the elimination of $BaCO_3$; moreover, these compositions are experiencing a lower catalytic effect of CuO given its reduced presence due to composition stoichiometry. To possibly overcome this complication, films of (2:3) and (3:6) compositions could be subjected to a pressure jump to a $P_{O_{2,final}} > 0.1$ mbar (still maintained below the YBCO instability line), to allow for the entrance of a larger amount of gas in the furnace and, possibly, favour the out-diffusion of the remaining CO_2 which is hindering the complete elimination of barium carbonate. However, this hypothesis has not been tested, but one must consider that the important coarsening effects observed in these films may not change the outcome of the process.

The second strategy is straightforward, as the elimination of $BaCO_3$ is ensured through the use of an optimized quench process in the tubular furnace at ICMAB, in which the complete removal of this phase and the formation of the desired $BaCu_2O_2$ and Cu_2O has been thoroughly demonstrated in 4.2. However, irreproducibility in the temperature dependent phase evolution of *ex-situ* quenched films when employed in the growth process in synchrotron facilities may lead to complications in the analysis of *in-situ* XRD experiments aimed at the study the kinetics of TLAG.

Detailed evaluation of the second step of TLAG P_{O_2}*-route*, in which the transient liquid of

[Ba-Cu-O] is formed and YBCO nucleation and growth occurs, will be presented in the following section, starting from films deriving from both strategies described up to now. Deep understanding of the process was attained considering the initial situation resulting from the various methods employed to eliminate the $BaCO_3$ phase.

5.3 *In-situ* analysis of TLAG kinetic mechanism

Following the detailed analysis regarding the challenging elimination of the limiting phase of the TLAG mechanism, $BaCO_3$, under the unfavourable conditions faced in the set-up employed for *in-situ* synchrotron XRD experiments described earlier in the chapter, this section will be focused on the growth mechanisms and kinetics of YBCO through TLAG. Films which underwent the processes presented in section 5.2 will be employed as precursor films for the *in-situ* analysis of the growth mechanism.

5.3.1 Promoting c-axis nucleation: growth in full-liquid regions

Kinetic phase diagrams have been recently established [101] for the two growth routes possible for YBCO growth through TLAG, namely *T-route* and P_{O_2}*-route*. Considering the sole interest of the latter route for the experimental work described in this thesis, representation and description of the TLAG kinetic phase diagram for P_{O_2}*-route* was provided in Fig. 4.15. Despite several characteristic processing conditions in said diagrams are relative to films of lower thickness deriving from an acetate-based chemical solution, the identification of a large region in which c-axis YBCO nucleation is enhanced was demonstrated to be valid also in the case of the films described in this thesis (see Chapter 4), with only slight variations. The presence of two main full-liquid regions is reported, with the subdivision coinciding with the Cu(II) to Cu(I) reduction line reported in literature [95, 185]. Nonetheless, a well-defined oxidation state of copper close to this line is not expected, and a continuous transition between liquid compositions presenting both cases is possible.

In order to promote c-axis nucleation and obtain highly epitaxial YBCO, several films were grown through TLAG P_{O_2}*-route* in both of the full-liquid regions of the kinetic phase diagram and the process was followed through *in-situ* synchrotron XRD experiments. All films described in this section are (3:7) liquid composition presenting same thickness (400 ± 50 nm of final YBCO). The main difference which will be analyzed here is the effect of growth from films which were subjected to an *ex-situ* quench prior to the growth in the *in-situ* synchrotron set-up (consequences on the phase evolution during the low-pressure heating in this set-up were previously described in 5.2.2) and films which are grown with no previous thermal treatment to formerly eliminate $BaCO_3$ (here denominated as "growth from single heating", given that *ex-situ* quenched films are subjected to a second heating when employed in the *in-situ* synchrotron XRD experiment). Despite these films displayed major difficulty towards $BaCO_3$

elimination during the low-pressure heating step, the analysis of the full growth process led to particularly interesting considerations. Given the highly corrosive and reactive nature of the transient liquid and the rapid pressure variation during the jump (with corresponding gas renewal inside the furnace), $BaCO_3$ is seen to finally react and proceed towards the expected TLAG mechanism. However, the detrimental conditions of the crystalline phases deriving from the low-pressure heating step are seen to complicate the growth process, as will be described in the following part of the text.

Fig. 5.19 shows the analysis of the randomly-oriented contribution normalized to the epitaxial YBCO (005) reflection in a total of 27 films grown in *in-situ* conditions, exhibited as a colour map with the position of each symbol corresponding to the growth temperature and $P_{O_{2,final}}$ conditions[5]. As explained at the beginning of this chapter, complications towards the precise control of the desired thermal profile at the moment of the pressure jump were encountered, with important variations between the experiments in the different beamtime runs. The final temperature reported here is, thus, not the T_{set} selected when initiating the growth process, but the real temperature registered in correspondence to the saturation of the YBCO (005) peak. Considering the large deviations from the desired T_{set}, it was believed that following this method a realistic representation of the experimental results could be provided.

A noticeable distinction is observed. *Ex-situ* quenched films result in generally higher epitaxy, with a maximum contribution of the randomly-oriented YBCO of 20%. Over half of all the considered *ex-situ* quenched films (specifically, 54%) result in a contribution of (103) grains of 5% or below, and in only two cases the contribution of this phase is reaching values of 20% (maximum value obtained for such films), demonstrating that the majority of this type of films in all of the conditions tested led to preferentially epitaxial YBCO nucleation and growth. Contrarily, films which are grown without a previous thermal process to remove $BaCO_3$ display more inconsistent results: a wider distribution of the contribution of randomly-oriented nuclei is observed, with maximum values reaching 55% corresponding to 20% of the this kind of grown films. Moreover, various samples grown using similar processing conditions yield discrepant results. An explanation may be found in the presence of $BaCO_3$ in the latter films at the moment of the pressure jump, given the inconceivability of its complete elimination during the low-pressure heating process, as established in 5.2.1. In the previous chapter, it was demonstrated how several parameters are strictly affecting the straightforward formation of the transient liquid. The effect of slow heating ramps on coarsening of precursor phases shows the detrimental delay in the dissolution of these and, thus, their participation in the homogeneous formation of the transient liquid. A large amount of remaining $BaCO_3$ is seen to favour the homogeneous nucleation of YBCO due to this phase needing to react towards the formation of $BaCu_2O_2$ (crystalline or amorphous) during the time of the pressure jump, when the transient liquid is being generated. This results in an inhomogeneous transient liquid along the film and

[5]The procedure followed for the integration of the peaks relative to each reflection is the same as the one described in D.2.2 employed for the analysis presented in Chapter 4.

a mixed nucleation, with final YBCO films of misoriented texture.

In both of the types of films considered in this subsection, it is clear how highly epitaxial YBCO can be obtained with the correct tuning of the processing parameters. Considerations regarding the supersaturation of the transient liquid as a function of the $P_{O_{2,final}}$ increase observed in the optimization of TLAG on (3:7) composition YBCO films described in the previous chapter, together with several testing in the *in-situ* synchrotron experimental set-up, have led to the understanding that c-axis nucleation is favoured, for this composition and in this set-up, when higher values of $P_{O_{2,final}}$ and $P_{TOT,final}$ are employed. Targeting the growth of YBCO in the area of the phase diagram ranging between 830 ºC and 870 ºC of T_{set} and a value of $P_{O_{2,final}}$ between 6 mbar and 7 mbar (with corresponding $P_{TOT,final}$ of 32 mbar or 100 mbar), yields highly epitaxial YBCO films with contribution of (103) grains below 5% independently of the initial microstructure of the precursor film. Nonetheless, some considerations must be made. In this high c-axis window, ultrafast growth rates can be obtained for both types of films with values well above the state-of-the-art 100 nm s^{-1} [53], yielding an unprecedented maximum value of 2207 nm s^{-1} for 400 nm thick YBCO films.

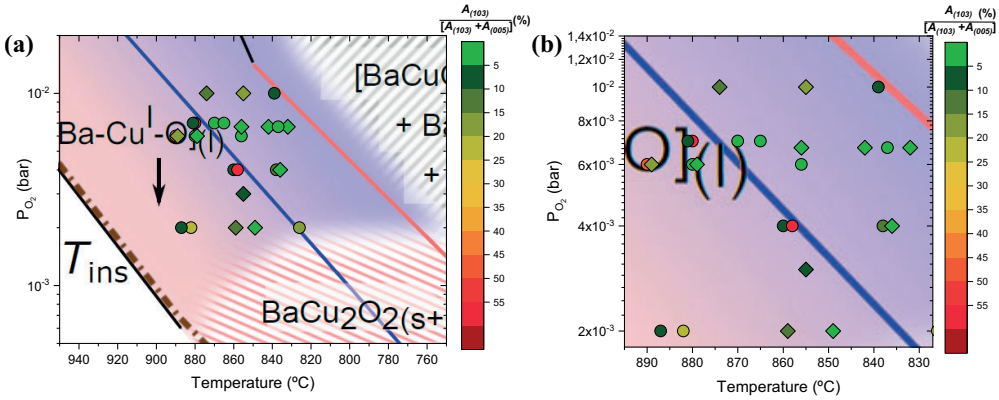


FIGURE 5.19: Colour map relative to the contribution of randomly-oriented YBCO grains in films grown *in-situ* in the full-liquid regions of the pre-established TLAG P_{O_2}*-route* kinetic phase diagrams [101]. Films subjected to an *ex-situ* quench process prior to the growth in the *in-situ* synchrotron XRD experiment are shown as solid rhombi, whereas films grown with no previous thermal treatment to eliminate $BaCO_3$ are represented with solid circles.

However, films deriving from an *ex-situ* quench process prior to their employment in *in-situ* synchrotron XRD experiments, result in majorly higher growth rate values, as is shown in Fig. 5.20(a), where the growth rates exhibited by this kind of films through the use of three different processing conditions led to the achievement of 400 nm of highly epitaxial YBCO grown between 500 nm s^{-1} and 2207 nm s^{-1}. Conversely, three highly epitaxial YBCO films resulting from the growth without any previous thermal treatment to eliminate $BaCO_3$ (thus, through a single heating in the *in-situ* synchrotron XRD experiment) are ranging from the low

value of merely 32 nm s^{-1} up to the ultrafast growth rate of 1433 nm s^{-1}.
Undoubtedly, these films are demonstrating how ultrafast growth rates are possible and characteristic to TLAG P_{O_2}-*route*, boosting the possibilities of industrial implementation of this innovative growth method towards more environmentally friendly and energetically efficient CCs fabrication. Nonetheless, an interpretation of the reasons behind the observed differences is considered necessary at this point. Solely judging by the growth rates obtained, one may be prone to believe that the use of films which have undergone an *ex-situ* quench prior to their implementation in the beamtime experiments is preferable, as high c-axis YBCO orientation is obtained with the highest growth rate values. However, in 5.2.2 it was thoroughly demonstrated that a major issue is encountered with the reproducibility of the phase evolution during the low-pressure heating of these films. Despite the elimination of $BaCO_3$ to be fundamental, given it limits the progression of the TLAG mechanism, the formation of phases differing from the ones expected in the established reaction pathway during the low-pressure heating is undesirable. In contrast, the generally slower growth rates of films grown directly in the

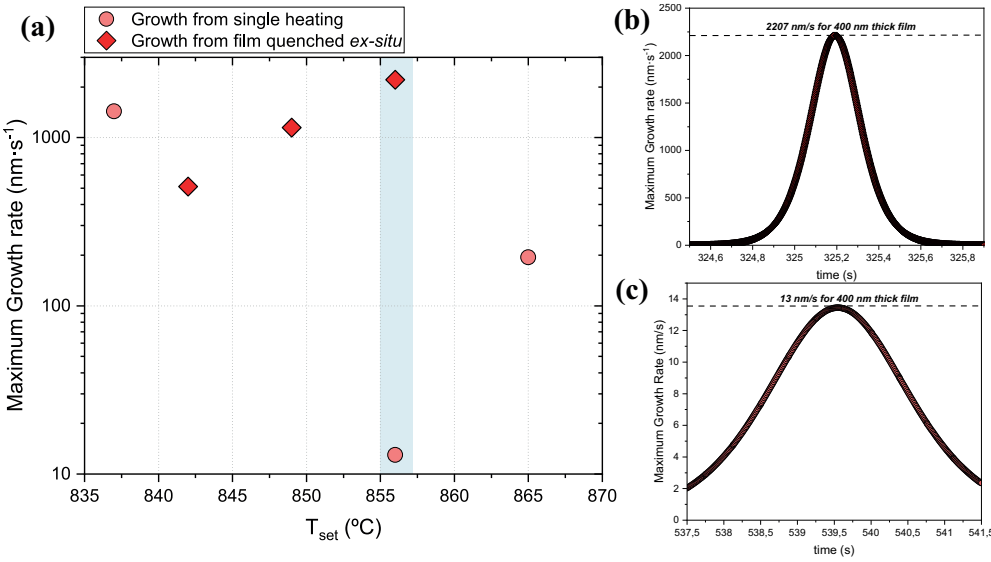


FIGURE 5.20: (a) Growth rate values obtained from selected experiments comparing the case of films quenched *ex-situ* prior to the experiment (red rhombi) and films grown *in-situ* with no previous thermal treatment (single heating, light coral circles). The represented growth rate values are deriving from films grown in similar conditions of P_{O_2} (between 6 mbar and 7 mbar). The two results highlighted through a light blue shading are evidencing the great difference between these two cases, and the growth rate value for these films is shown in (b) and (c), for a film quenched *ex-situ* and one grown directly *in-situ*, respectively.

set-up used for *in-situ* XRD experiments through one single heating may find an explanation in the fact that these are displaying the presence of unreacted $BaCO_3$ prior to the pressure

jump. Considering that the heating rate and the pressure configurations are identical for all experiments regarding the low-pressure heating step, differences in the microstructure may depend strictly on the level of coarsening deriving from the selected T_{set} and the degree of CO_2 out-diffusion reached: as films of the same (3:7) composition are considered in this analysis, only slight variations between the amount of remaining $BaCO_3$ following the low-pressure heating should be observed. However, the microstructural situation prior to the pressure jump is unknown, and there might be significant differences between the phases formed during the low-pressure heating in their grain size and distribution. Initiating a pressure jump, during which the precursor phases are expected to promptly melt to generate the [Ba-Cu-O] transient liquid, with large amount of $BaCO_3$ may retard the liquid formation. In fact, the remaining $BaCO_3$ is expected to react to yield $BaCu_2O_2$ in either crystalline or amorphous form, which will then progress in the TLAG mechanism towards the transient liquid. Moreover, one must remember that in these kind of experiments, as observed in the previous section 5.2, there is the simultaneous presence of the three phases of $BaCO_3$, $BaCu_2O_2$, and the reduced phase of Cu(0). The latter must additionally be oxidized during the pressure jump to be able to take part in the transient liquid generation. The ensemble of these factors are believed to be at the origin of the wider variety of growth rate values obtained for such films. The formation of the transient liquid will suffer from higher degree of inhomogeneities which are difficult to predict. Unreacted and crystallized $BaCO_3$ is far from preferable, and further strategies to enhance its elimination prior to the pressure jump must be found, possibly in the direction of a modification of the set-up to favour gas evacuation: renewal of gas in the furnace during the low-pressure heating will remove the out-diffused CO_2 and allow for the progression of the elimination of this phase, promoting the formation of the expected precursor phases of $BaCu_2O_2$ and Cu_2O prior to the jump.

At this point, an assessment of the outcome of each strategy developed aiming for an improved epitaxial growth of YBCO in the experimental set-up employed for *in-situ* XRD experiments is due. Fig. 5.21 reports the I(2θ) scans result of the integration in χ of the 2D-XRD images (shown in correspondence) acquired at RT following the *in-situ* TLAG process for films deriving from the three strategies described in this chapter. This comparison is carried out solely on ternary (3:7) composition films of same thickness (400 nm of final YBCO), and grown through the use of the same processing parameters, therefore with expected similar supersaturation conditions, as the analysis of the growth from films of different liquid composition will be object of the following section.

The case of a film grown from a single heating in the set-up employed for *in-situ* XRD experiments with no prior thermal treatment and the film previously subjected to the *in-situ* phase transformation process both display a mixture of epitaxial and random nucleation (respectively, Fig. 5.21 upper and central panels). The former film results in a higher contribution

of the randomly-oriented phase and a general polycrystalline character of YBCO, as it can be evinced by the ring-like aspect of the YBCO (005) reflection in the corresponding 2D-XRD image. In the latter film, despite the presence of (103) grains, the lower intensity of this phase and higher epitaxy suggests an improvement towards a higher c-axis orientation when employing the *in-situ* phase transformation process. The final case of a film which underwent an *ex-situ* quench prior to the growth in the set-up for *in-situ* XRD experiments displays optimal epitaxy, exhibiting an intense epitaxial orientation and the complete absence of any randomly-oriented grains. One must remember that, among the three cases considered, the complete

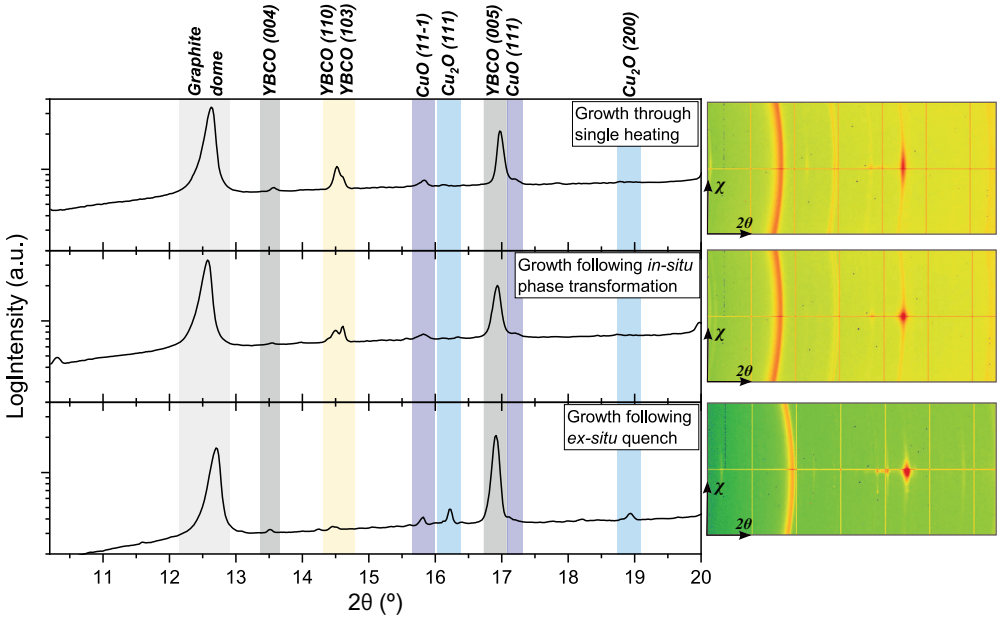


FIGURE 5.21: I(2θ) scans (left) and corresponding 2D-XRD images (right) obtained with 1s acquisition time following the *in-situ* TLAG process of ternary films of (3:7) composition deriving from the three strategies explained in this chapter. Displayed from upper to lower panels, respectively, a film grown *in-situ* without any previous thermal treatment to eliminate $BaCO_3$, a film deriving from the *in-situ* phase transformation process, and a film which underwent an *ex-situ* quench prior to the experiment. The films were grown in the TLAG P_{O_2} - route with a $T_s$et = 850 ºC, base pressure conditions of P_{TOT} = 0.05 mbar/P_{O_2} = 0.01 mbar, final pressure conditions of P_{TOT} = 100 mbar/P_{O_2} = 7 mbar.

elimination of $BaCO_3$ is achieved principally in the case of the *ex-situ* quenched films. Considering the supersaturation conditions expected to be similar, the differences in the homogeneity of formation of the transient liquid are here fundamentally influencing the outcome. Despite the irreproducibility in the phase evolution during the low-pressure heating exhibited from the latter type of films (reported in 5.2.2), it is believed that the absence of the barium precursor phase at the moment of the jump is allowing for a rapid and more consistent transient liquid

formation compared to the cases of the other two kinds of films analysed here. Possibly, in the films deriving from the *in-situ* phase transformation process, the highly coarsened crystalline phases due to the two consecutive heating processes are delaying the reaction of the precursor phases towards the liquid formation, regardless of the possible elimination of $BaCO_3$ through this strategy in (3:7) composition films. The fact that $BaCO_3$ is eliminated during the pressure jump to $P_{O_{2,final}} = 0.1$ mbar may result in the formation of $BaCu_2O_2$ and Cu_2O grains of different size and distribution respect to the case of a film in which these solid phases are formed at a P_{O_2} one order of magnitude lower during the heating process (and in a different furnace configuration). Considering the generally higher epitaxy of the films obtained from an *ex-situ* quench displayed in Fig. 5.19, this strategy seemed to be, at the moment of this thesis work, the most suitable option to overcome the complications encountered for the TLAG process in the set-up employed for the *in-situ* synchrotron XRD experiments. Nonetheless, despite being able to overcome the complicated elimination of $BaCO_3$ in the particular set-up described in this chapter and obtaining highly epitaxial YBCO films through three different film preparation methodologies, it must be considered that the ideal case for a detailed analysis of the TLAG mechanism through *in-situ* XRD experiments would require the efficient elimination of the barium precursor phase during the low-pressure heating process through one single heating, as in the cases of films of lower thickness and different microstructure analyzed in previous studies preformed at synchrotron facilities [53, 54, 101]. To achieve this, major modifications of the experimental set-up are believed to be necessary, and the ongoing work continued in the group towards that direction has yielded the first promising results on a more straightforward elimination of $BaCO_3$.

5.3.2 Variations of the TLAG kinetic mechanism due to differences in transient liquid supersaturation

Growth of YBCO films of the four liquid compositions considered in this thesis through TLAG P_{O_2}*-route* has been analyzed employing *in-situ* XRD synchrotron radiation. Similarly to the description in the previous chapter, the optimization of the processing conditions through the use of the sole (3:7) composition has availed the achievement of optimal *T-P* ranges in which high epitaxy is favoured. Employing these predetermined conditions to the growth of films of different liquid compositions allowed for a detailed evaluation of the influence of the liquid supersaturation on the epitaxial nucleation of YBCO, here deriving from the varying copper content in the solution stoichiometry. As aforementioned in this chapter, the additional hindrance to the elimination of $BaCO_3$ encountered in the set-up employed for *in-situ* XRD experiments has led to the development of several strategies to overcome this. In the case of films of different liquid compositions, the solution to enhance the difficult removal of $BaCO_3$ has been the development of the *in-situ* phase transformation process, described in detail in 5.2.1.2. Following the latter analysis, a detailed evaluation of the growth from ternary films

of various compositions which have undergone such process compared to films which faced no additional thermal treatment to eliminate $BaCO_3$ (as denominated earlier, "growth from single heating") will be conducted here. Two main objectives will be the focus of this subsection. Firstly, the determination of whether the microstructure resulting from the *in-situ* phase transformation process is adequate to be employed as precursor films for the following growth through TLAG in the set-up employed for *in-situ* synchrotron XRD experiments, or whether the use of pyrolyzed films is the optimal alternative, despite the difficulties encountered in $BaCO_3$ elimination in these set-up conditions. Secondly, to evaluate the influences of the variation of supersaturation characteristic to the transient liquid of each composition and how these may affect the nucleation of epitaxial YBCO in TLAG.

5.3.2.1 Coarsening phenomena as a consequence of the *in-situ* phase transformation process

A concerning effect which must be analyzed when studying the TLAG mechanism is whether films which have undergone the *in-situ* phase transformation process present coarsening of the crystalline phases when subjected to the thermal treatment during their growth (step 3 in the schematic overview in Fig. 5.3). For clarification, films of such type will be referred to as undergoing a second heating, whereas pyrolyzed films which are being grown without any previous thermal treatment to remove $BaCO_3$ will be referred to as subjected to a single heating. The difficulty of eliminating $BaCO_3$ on ternary films of different composition in this particular set-up is evident and fully explained in 5.2.1.2. This is reflected in the temperature-dependent phase evolution of the low-pressure heating in Fig. 5.22, in which the presence of $BaCO_3$ orthorhombic is observed in the single heating of the films of all compositions until reaching the set temperature of 850 ºC (lower panels). As explained in the previous subsections, the poor gas transport in the furnace environment hinders the removal of the evolved gases, reaching an equilibrium which impedes the progression of the reaction between $BaCO_3$ and CuO to form the mixed oxide of $BaCu_2O_2$. Corroborating this hypothesis, this phase is only formed above 800 ºC and exhibits minor contributions, with the intensity of $BaCO_3$ showing no important decrease. A different situation is presented by the films undergoing a second heating, given the elimination of $BaCO_3$ (full or partial, depending on the specific liquid composition) was performed in the previous *in-situ* phase transformation process. As explained in the section devoted to the latter process, the elimination of $BaCO_3$ displayed a higher success rate for the compositions with copper excess, specifically (3:7) and (4:11) compositions. The compositions with lower copper content, (2:3) and (3:6), resulted in major complications which led to the phase transition and crystallization of the monoclinic phase of $BaCO_3$ as an addition to the irremovable orthorhombic one. This was a consequence of the combination of the higher crystallinity of the pyrolyzed films of these compositions, resulting in higher thermal stability of the barium precursor phase, and the low copper content, reducing the catalytic role of CuO

in its reaction with $BaCO_3$ towards its elimination to form the mixed Ba-Cu oxide, $BaCu_2O_2$. In the second heating of the films of the latter compositions, shown in the upper panel in Fig. 5.22, the presence of the thermally stable monoclinic $BaCO_3$ together with the most reduced phase of copper are resulting in an intricate mechanism which yields only minor contribution from the expected $BaCu_2O_2$ phase. As for previously explained cases, the stoichiometric (2:3) composition displays the most adverse situation, as the coarsening of Cu(0) is presumably limiting the amount of copper participating in the necessary reaction with $BaCO_3$ to form the desired mixed oxide. Despite the (3:6) composition is also displaying an important contribution from monoclinic $BaCO_3$, none of the other liquid compositions display a further reduction to metallic copper in this thermal process. Moreover, the intensity relative to $BaCu_2O_2$ phase is increasing with the increase of the copper content in the liquid composition, combined with a factor-two decrease of the $BaCO_3$ contribution moving from (2:3) to (3:6) to (3:7), and finally with complete absence of this phase in the (4:11) composition.

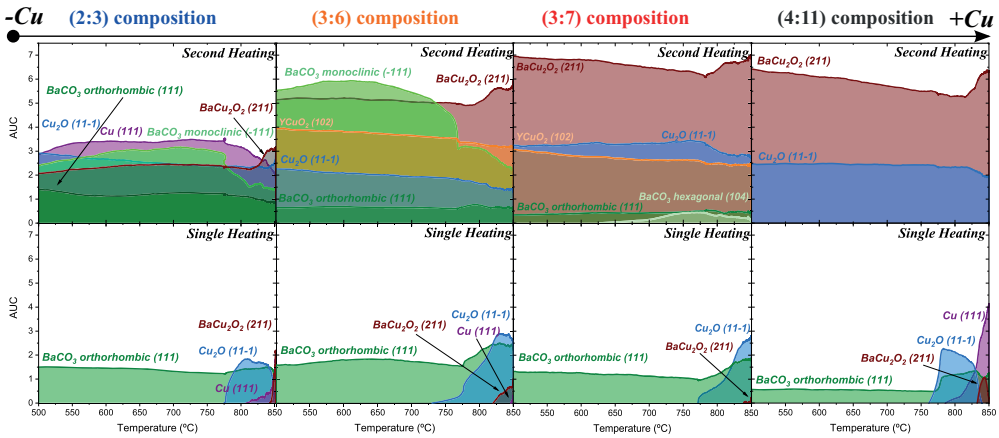


FIGURE 5.22: Temperature-dependent phase evolution for films of varying liquid composition which are undergoing a second heating following the *in-situ* phase transformation process (upper panels) and films which are being grown without any previous thermal treatment aimed to the elimination of $BaCO_3$ (single heating, lower panels). Phases are identified in each plot. The low-pressure heating is at $P_{O_{2,base}} = 0.01$ mbar and a corresponding $P_{TOT,base} = 0.05$ mbar (air) and the displayed temperature range is between 500 °C and 850 °C ($dT / dt = 4.5$ °C s^{-1}).

Despite the successful elimination of the barium precursor phase for copper-rich compositions through the *in-situ* phase transformation process and thus initiating the pressure jump from complete absence or insignificant contribution of $BaCO_3$, the effect of a second, consecutive thermal treatment on the grain size of the crystalline phases must not be disregarded. In Fig. 5.23, the Debye-Scherrer crystallite size for the precursor phases of $BaCO_3$ orthorhombic, Cu_2O, $BaCu_2O_2$ and Cu(0) are displayed. The unmistakable trend of grain size increase from films of single heating and films subjected to two consecutive thermal treatments is evidenced

in all of the analyzed crystalline phases. TLAG is a non-equilibrium, ultrafast growth process in which crystalline phases of reduced sizes are optimal to enhance the fast reaction and the atomic mobility to the YBCO nucleation front [53, 101]. Surely, enlarged grains of the precursor phases are unideal: the formation of the transient liquid will be slowed down given the prolonged dissolution of large grains, delaying the YBCO nucleation and possibly favouring nuclei of other solid secondary phases to form.

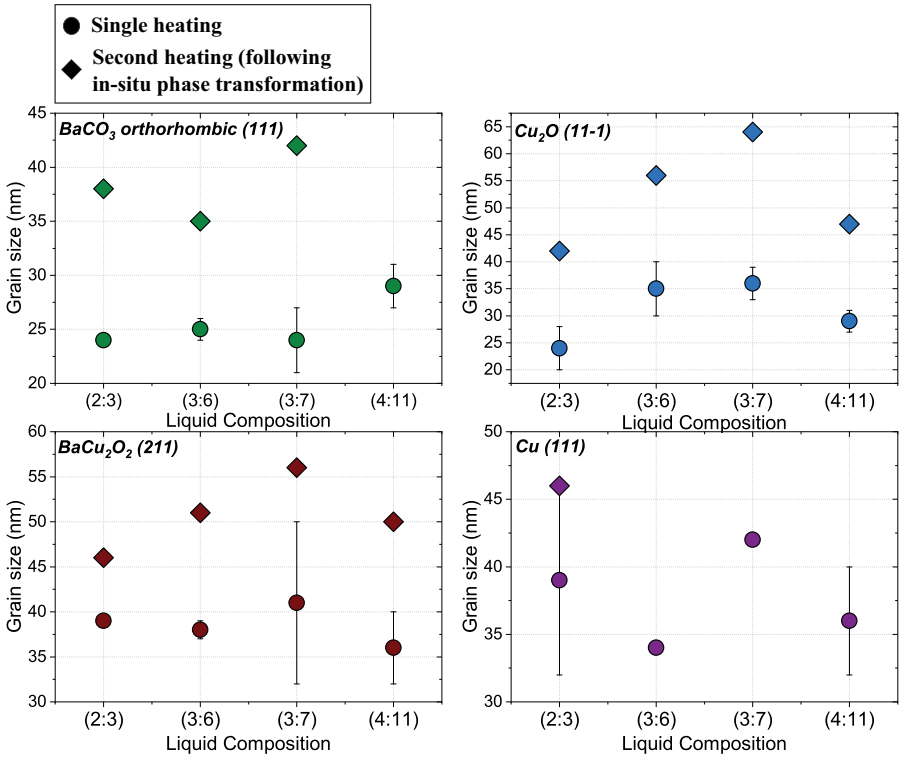


FIGURE 5.23: Debye-Scherrer crystallite size for the major precursor phases observed during the heating process. Relation between the grain sizes of a single heating process (solid circles) and films undergoing two successive thermal treatments (such as the growth after an *in-situ* phase transformation process, shown as solid rhombi) depending on each liquid composition considered. The increase in the grain size of all crystalline phases analyzed is evidencing, as expected, a strong coarsening phenomenon occurring for films which are subjected to two consecutive heating processes. Error bars are not shown for films subjected to a second heating given the fact that only one process of such type was performed for each liquid composition.

Nonetheless, the presence of $BaCO_3$ during the jump is an additional hindrance to a fast growth, given its necessary reaction to form the mixed oxide of $BaCu_2O_2$ first, which only then may form the transient liquid and progress with the nucleation of YBCO following the established TLAG mechanism. Therefore, a compromise between highly coarsened crystalline

phases in films in which no $BaCO_3$ is present or films displaying this phase but with smaller grains must be reached. The effects of this on the formation of YBCO during the pressure jump in TLAG P_{O_2}-*route* will be analyzed next.

5.3.2.2 YBCO nucleation from films of different composition varying in the state of nanocrystalline precursor phases

The second step of the TLAG P_{O_2}-*route* process for films of various liquid compositions is performed, and films deriving from either a single heating or two consecutive ones, with the aforementioned consequences, are subjected to a rapid change in the pressure conditions to nucleate and grow YBCO with the assistance of the [Ba-Cu-O] transient liquid. Two main effects will be analyzed here: the outcome on the epitaxy of YBCO starting from different microstructural scenarios of the two types of films considered, and the influence of the variations of supersaturation linked to each specific liquid composition. Studies on the solubility of RE in [Ba-Cu-O] melts of different (Ba:Cu) molar ratio have evidenced an important increase in this parameter when the copper content of the melt is increased, thus leading to lowering the supersaturation [74, 78–80]. Moreover, given the enhanced solubility of RE in melts of higher copper content, a reduction of the processing temperatures is possible, fundamental towards the widespread of more energetically efficient CCs fabrication processes. In Chapter 4, specifically in 4.4, the increase of the supersaturation of the transient liquid when decreasing copper content from the (4:11) to the (2:3) composition were demonstrated to have detrimental effects towards a high c-axis nucleation of YBCO when the same processing conditions are employed, resulting in films of (2:3) and (3:6) compositions to show mixed nucleation in all of the conditions tested.

The pressure-dependent phase evolution plots resulting from the analysis of the growth process employing *in-situ* synchrotron XRD radiation are shown in Fig. 5.24 for the cases of single and second heating on films of the four liquid compositions. The implementation of a fast acquisition rate (2 ms/frame) enabled the following of the ultrafast formation of YBCO nuclei through the transient liquid. Details regarding data acquisition may be found in E.1.2. Due to the high acquisition rate, the intensity of the phases is reduced, an effect especially significant when observing the peaks of the precursor phases. Raw intensity of the evolution of each peak are represented to be able to quantitatively compare between the different cases. Substantial differences may be evidenced and the use of the fast acquisition has led to a detailed observation of the transformations occurring during the pressure jump. Following the same trend observed in the previous chapter regarding the nucleation of c-axis oriented YBCO, a division between liquid compositions with low copper content and the ones with copper excess may be defined, with the (3:7) and (4:11) compositions generally favouring epitaxial orientation given the lower supersaturation conditions at the moment of transient liquid formation. This is in contrast to the situations exhibited by the compositions with lower copper content, (2:3) and

(3:6), which are displaying a reduction in the intensity of the (005) reflection of YBCO of half or more, simultaneously to a significant increase in the contribution of the randomly-oriented grains. Now that this differentiation has been determined, a further subdivision can be noted with regards to the growth of the two types of films of each individual liquid composition. Again, starting the evaluation from the most favourable case of the compositions with higher copper content ((3:7) and (4:11) compositions), the films deriving from the *in-situ* phase transformation process (upper panels in Fig. 5.24 (c) and (d)) promote the nucleation of a highly epitaxial orientation of YBCO, with only a minor contribution of the randomly-oriented phase present. The only precursor phases in these two cases are, effectively, the expected ones following the thermal treatment aimed at $BaCO_3$ elimination: the mixed oxide of $BaCu_2O_2$ and Cu_2O. Conversely, films of the same liquid compositions which have been grown without any previous thermal treatment to remove $BaCO_3$ (lower panels in Fig. 5.24 (c) and (d)) show the presence of this crystalline phase until extremely elevated pressure values during the pressure jump ($P_{O_{2,final}} = 6.5$ mbar and $P_{O_{2,final}} = 5$ mbar, for the (3:7) and (4:11) compositions, respectively), almost reaching the final P_{O_2} selected for the experiment. In the case of films of (3:7) composition, there is an additional phase transformation from orthorhombic to monoclinic during the pressure jump, and a higher contribution of the YBCO (103) orientation compared to the desired (00l) is obtained. The phase evolution displayed by this film clearly evidences that, even in optimal supersaturation conditions, the presence of undesired solid phases may vary detrimentally the formation of the transient liquid in sufficient amount and/or homogeneously along the entire film. As a result, a loss in epitaxy is obtained. This effect is not as crucial if the copper content of the liquid composition is further increased, lowering even more the supersaturation conditions. This is the case of a (4:11) liquid composition film grown through single heating, which despite showing the presence of crystalline $BaCO_3$ during the pressure jump, displays a predominance of epitaxial growth compared to the undesired (103) grains. Possibly the enhancement of the Y solubility in this liquid is accelerating the formation of YBCO nuclei and the presence of insignificant amounts of $BaCO_3$ are promptly dissolved in the transient liquid. Shifting the focus to the compositions with lower copper content, namely (2:3) and (3:6) compositions, a different trend is observed. The (2:3) composition is showing the most adverse conditions towards the success of the experiment given the intrinsically higher supersaturation conditions presented in these films. Moreover, the coarsening of the crystalline phases deriving from the *in-situ* phase transformation process (Fig. 5.24(a), upper panel) results in the disappearance of contributions relative to $BaCu_2O_2$ and Cu_2O at $P_{O_2} =$ 2 mbar and the simultaneous presence of crystalline $BaCO_3$ monoclinic until $P_{O_2} > 5$ mbar: this is a clear evidence of how inhomogeneous the transient liquid formation is in films of this case, where the dissolution of highly coarsened solid grains of $BaCO_3$ is slowly progressing to their inclusion in the transient liquid. This will cause the already high supersaturation of this

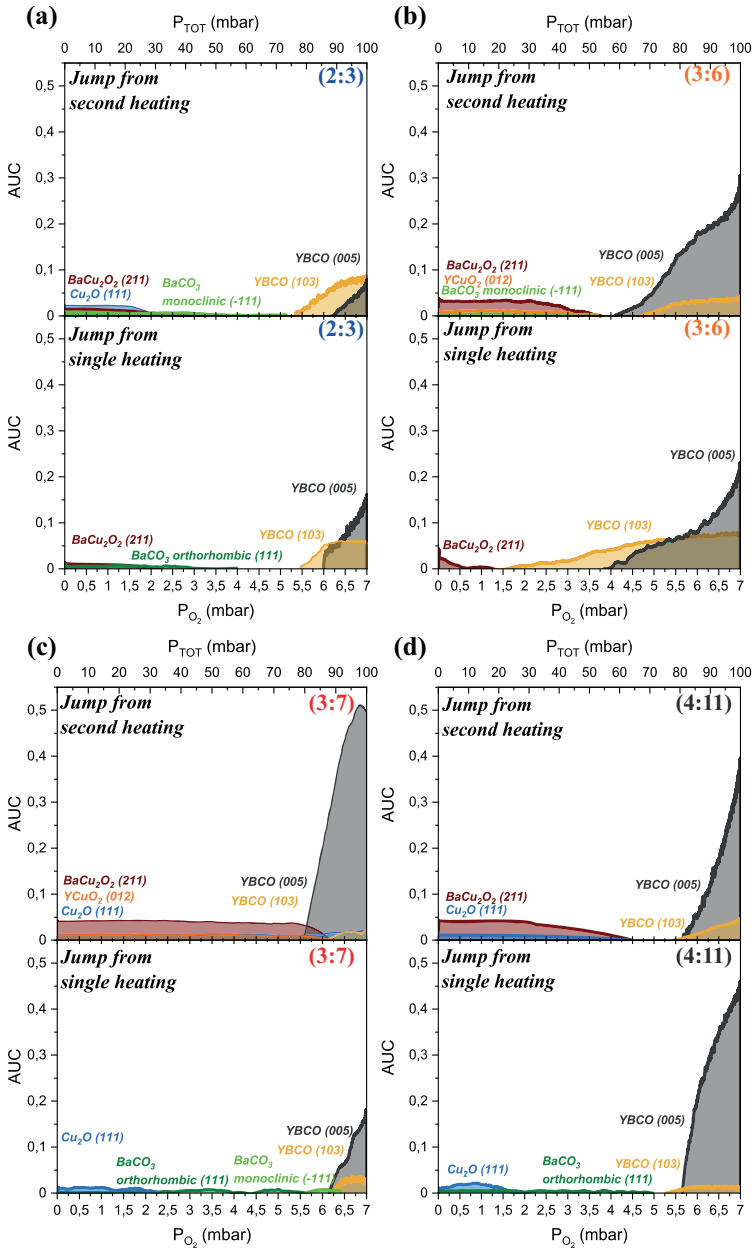


FIGURE 5.24: Pressure-dependent phase evolution plots relative to the pressure jump of films of (a) (2:3), (b) (3:6), (c) (3:7), and (d) (4:11) liquid compositions comparing the case of films deriving from two consecutive thermal treatments (following the *in-situ* phase transformation process, upper panels) and from a single heating (lower panels). Identification of the crystalline phases is shown in each single plot for clarification. Raw peak area is displayed with the same scale for all plots to evince differences on epitaxy due to each liquid composition.

specific transient liquid to be increased even more, given the fact that a lower amount of liquid will be formed until the remaining $BaCO_3$ reacts. As a consequence, the nucleation of majorly randomly-oriented YBCO is obtained. The case of a film of this composition subjected to a single heating displays a more favourable outcome, possibly given the lower degree of coarsening of the precursor phases which, despite also presenting the contribution of $BaCO_3$ during the pressure jump, results in its inclusion in the transient liquid at lower P_{O_2} values, leading to an ideally improved transient liquid formation and higher epitaxy compared to the latter film. Nonetheless, the unfavourably high supersaturation conditions of this specific transient liquid composition in the selected processing conditions are resulting in both films of (2:3) composition to show the lowest epitaxial nucleation of all of the cases considered. It is believed that an enhancement of the epitaxial nucleation in films of this composition could be obtained, as previously proposed in Chapter 4, with the use of higher processing temperatures. Nonetheless, with a slight increase of the copper content to the (3:6) composition, the effect of the *in-situ* phase transformation process appears to be beneficial towards the final epitaxy of the film, despite $BaCO_3$ monoclinic being present during the pressure jump. Possibly, a combination of the partial removal of the barium precursor phase and the minor lowering of the supersaturation compared to the (2:3) composition may favour the formation of a more homogneneous transient liquid in this case, however resulting in a mixed nucleation of YBCO (005) and (103), and a final epitaxial contribution of half if compared to the compositions of higher copper content. Conversely, the growth of a film of (3:6) composition from a single heating shows the initial nucleation of exclusively misoriented grains, then overruled by the (005) orientation. The final contribution of (103) is double than the case of a film of this composition grown following the *in-situ* phase transformation process, suggesting the formation of the transient liquid may thus be improved despite the supersaturation conditions not to be optimal in these specific processing conditions.

A general consideration may be made at this point. As observed during the analysis of the *in-situ* phase transformation, the films of liquid compositions with lower copper content, which are the ones with higher initial crystalline microstructure, display a more difficult elimination of $BaCO_3$ in this process, making the resulting coarsening effects due to the two consecutive heat treatments detrimental towards the formation of epitaxial YBCO in the TLAG process. Nonetheless, the growth of films of these compositions in which no previous elimination of $BaCO_3$ is performed, are also showing major impediments towards the nucleation of fully epitaxial YBCO, given the intrinsically higher supersaturation of the transient liquids of these compositions. It is believed, as evidenced from the results in 4.4, that these films would profit from higher processing temperatures than the ones employed in the experiments described, given that the solubility of RE in [Ba-Cu-O] melts decreases with the decrease of the copper content of a composition, but can be improved through an increase in temperature when considering the same (Ba:Cu) molar ratio [78].

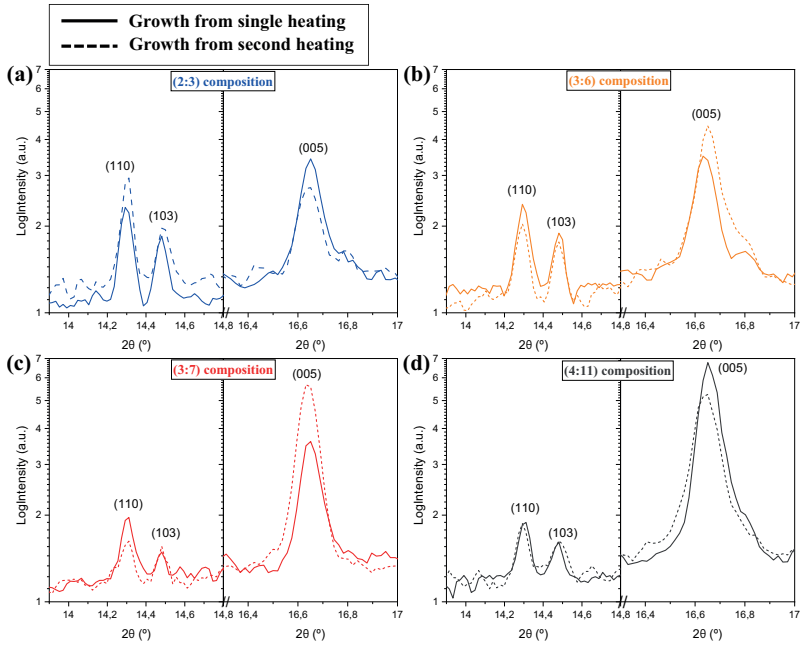


FIGURE 5.25: Integrated I(2θ) corresponding to the 2D-XRD frame acquired at RT following the *in-situ* growth process for the films of (a) (2:3), (b) (3:6), (c) (3:7), and (d) (4:11) liquid compositions, comparing the case of a film grown following a single heating (solid lines) and a film grown following the second heating after the *in-situ* phase transformation process (dashed lines).

Nonetheless, the global pursue towards greater energetic efficiency of the industrial processes implies a general preference of selecting lower processing temperatures [7]. On this regard, the excess of copper in the (3:7) and (4:11) compositions is aiding in decreasing the processing conditions to lower temperatures and this effect is observed in the more favourable outcome of the *in-situ* phase transformation process. The disadvantage of coarsening due to the second thermal treatment has no detrimental effect in these cases, and it outweighs the complication residing in $BaCO_3$ elimination during the pressure jump, resulting in higher epitaxy. This effect is a possible consequence of the optimal supersaturation conditions of the transient liquid formed for these compositions: the higher solubility of Y in these liquids is thought to be favouring the fast reactivity of the process. An evidence of this is the fact that films of (4:11) composition seem to be unaffected by the microstructural differences of the initial film, considering this liquid composition to be presenting the highest solubility of Y, thus lowest supersaturation, of the four cases analyzed in this thesis. Despite the minor presence of $BaCO_3$ in the films of this composition grown with a single heating, the generation of the liquid with optimal supersaturation conditions is promoting the dissolution and reactivity of the latter phase and the proceeding of the mechanism similarly to the case in which no $BaCO_3$

is present at the moment of the jump. Through the use of the fast acquisition, as previously mentioned implemented to follow the ultrafast evolution of the phases throughout the pressure jump, the formation of the transient liquid in a film of (4:11) composition could be unprecedentedly detected. Fig. 5.26 displays the time-dependent phase evolution colour map of the time range relative to the YBCO formation during the pressure jump. In this experiment, the contribution of the crystalline precursor phases of $BaCu_2O_2$ and Cu_2O are visibly disappearing

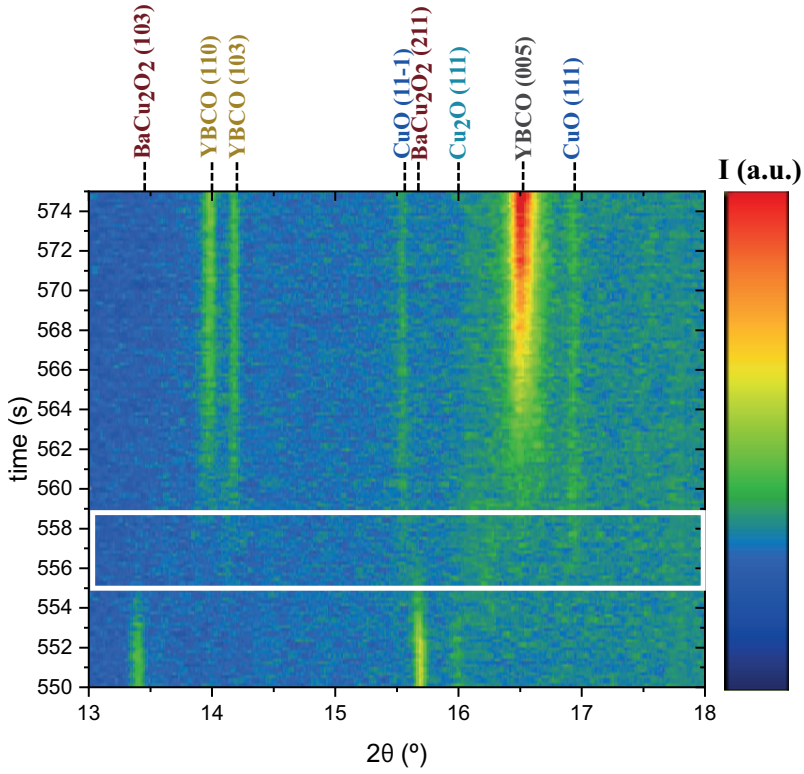


FIGURE 5.26: Time-dependent phase evolution colour map showing the time range corresponding to the pressure jump for a (4:11) composition film grown through TLAG which was previously subjected to the *in-situ* phase transformation process. Identification of the phases according to their 2θ peak positions is specified in the upper part of the graph. The time-range in which no peaks deriving from crystalline phases are visible is indicated through a light grey rectangle.

towards the formation of the final YBCO, majorly (005) with only a minor contribution of the (110) and (103) orientations, and CuO due to the copper excess in this specific liquid composition. The fact that during 3.8 seconds no contribution relative to any crystalline phase is visible is thought to be correspondent to the formation of the transient liquid, followed by the nucleation and successive growth of YBCO, clearly evidenced from the high intensity of the peak of the epitaxial phase. This exceptional identification has been possible through the

use of the fast acquisition of 2 ms per frame implemented at SOLEIL Synchrotron, which allows to follow the TLAG process in its ultrafast mechanism. The complete elimination of $BaCO_3$ through the use of the *in-situ* phase transformation together with the correct tuning of the transient liquid supersaturation conditions through stoichiometry of the initial precursor solution is ensuring the formation of the necessary precursor phases for a homogeneous and complete formation of the transient liquid and ideal epitaxial nucleation of YBCO.

5.4 Challenges of growing thick films in *in-situ* conditions

As evinced in the previous sections, the greatest challenge of the epitaxial growth of YBCO through TLAG in the experimental set-up employed for the *in-situ* XRD experiment was the elimination of $BaCO_3$, demanding due to the various reasons explained in detail. Clearly, with a thickness increase, the difficulty towards the complete removal of the barium precursor phase is also enhanced. Therefore, the growth of YBCO through TLAG P_{O_2}*-route* in *in-situ* conditions applied to thick films was implemented solely adopting the two strategies described in section 5.2, and an analysis of their application on ternary films of (3:7) composition of six and eight layers (2.2 μm and 2.7 μm after the pyrolysis, respectively) is carried out here.
The six-layered film has been subjected to the *in-situ* phase transformation process described in 5.2.1 to evaluate the possibility of eliminating $BaCO_3$ on films of elevated thickness in the set-up employed for the *in-situ* XRD experiments. Analysis of the evolution of phases relative to the low-pressure heating and to the pressure jump to $P_{O_{2,final}} = 0.1$ mbar (steps 1 and 2 of the schematic overview shown in Fig. 5.3) are displayed in Fig. 5.27. The phase evolution during the low-pressure heating exhibits the same pathway as for the case of a film of two layers of this liquid composition (shown in Fig. 5.10): $BaCO_3$ is not eliminated during the thermal treatment, and its crystallization above 800 ºC coincides with the reduction of CuO[6] to Cu_2O. The reaction between $BaCO_3$ and CuO leads to the formation of $BaCu_2O_2$, nonetheless only with a minor contribution due to the simultaneous reduction of Cu_2O to metallic copper. As previously observed for ternary films, the low porosity of the initial microstructure combined with the insufficient gas flow inside the furnace leads to the attainment of an equilibrium between the gas evolved from the film and the gas stagnating in the furnace environment. This results in only a partial elimination of $BaCO_3$ and the presence of unexpected phases, specifically Cu(0), which is fully reduced given the presence of C contamination (as mentioned before, possibly deriving from the graphite dome, residues of the organic solvents from the Ag paint employed to glue the samples in place, or other unknown impurities) which lead to the formation of CO in the furnace atmosphere.

[6] As for the case of ternary films of lower thickness, the insufficient intensity of the CuO peak due to its low crystalline nature impedes its integration.

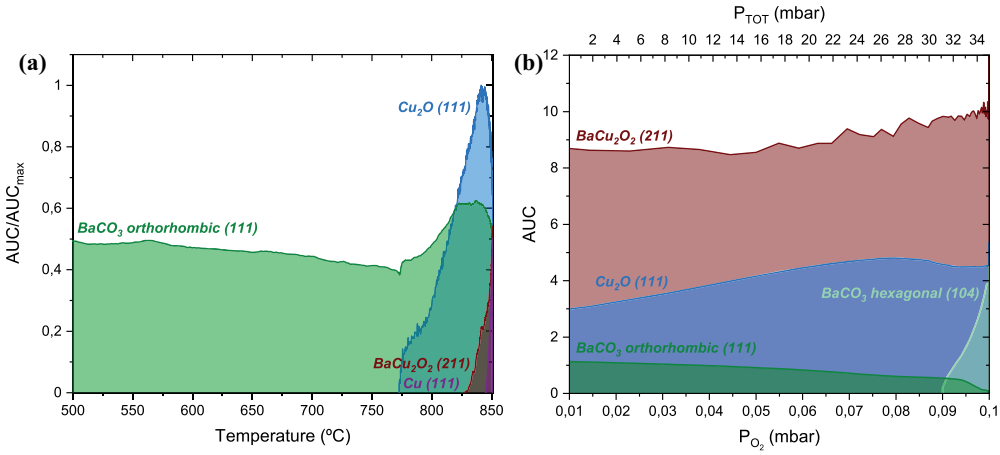


FIGURE 5.27: (a) Temperature-dependent phase evolution relative to the low-pressure heating of the *in-situ* phase transformation process in the temperature range between 500 ºC and 850 ºC for a six-layered ternary film of (3:7) composition. (b) Pressure-dependent phase evolution relative to the pressure jump below the YBCO instability line ($P_{O_{2,final}} = 0.1$ mbar and $P_{TOT,final} = 35$ mbar) aimed at the elimination of the barium precursor phase in the same six-layered film shown in (a).

The renewal of gas inside the furnace due to the pressure jump to the area of the kinetic phase diagram below the YBCO instability line is clearly promoting the formation of the desired crystalline phases of $BaCu_2O_2$ and Cu_2O. Nonetheless, the thickness of the film is such that a complete elimination of $BaCO_3$ is unattainable, and the phase transition from orthorhombic to hexagonal is observed with a significant contribution in the final part of the pressure jump. The cooling process confirms the disadvantage of an incomplete removal of the barium precursor phase. Similarly to the films of lower thickness displaying a more troublesome elimination of this phase (specifically, the ones of (2:3) and (3:6) compositions for the reasons presented before), the high amount of $BaCO_3$ hexagonal is transformed to a mixture of the orthorhombic and, majorly, the monoclinic phase with the decrease of temperature, as clearly evidenced in Fig. 5.28. The formation and coarsening of the monoclinic phase of $BaCO_3$ resulting from this process is evidencing the disastrous outcome of the *in-situ* phase transformation process when applied to the case of thick films in the unfavourable conditions of the current set-up. Furthermore, the inadequate formation of $BaCu_2O_2$, consequence of the hindrance towards the removal of the barium precursor phase, is setting the initial conditions for the TLAG process to be particularly disadvantageous, given the renowned elevated thermal stability of $BaCO_3$ monoclinic [91, 93]. Fig. 5.29 displays the I(2θ) deriving from the integration in χ of the 2D-XRD image acquired at RT following the *in-situ* phase transformation process, evincing the presence of strong contributions of $BaCO_3$ orthorhombic and monoclinic.

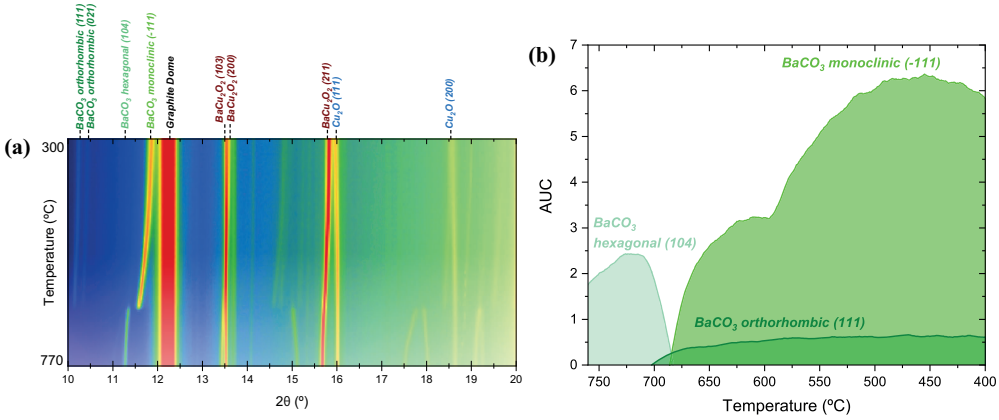


FIGURE 5.28: (a) Temperature-dependent phase evolution colour map showing phases present during the cooling of the *in-situ* phase evolution process of the six-layered film. (b) Temperature-dependent phase evolution relative to the phase transition of $BaCO_3$ from hexagonal to the mixture of orthorhombic and monoclinic observed during cooling, with a major contribution of the latter phase.

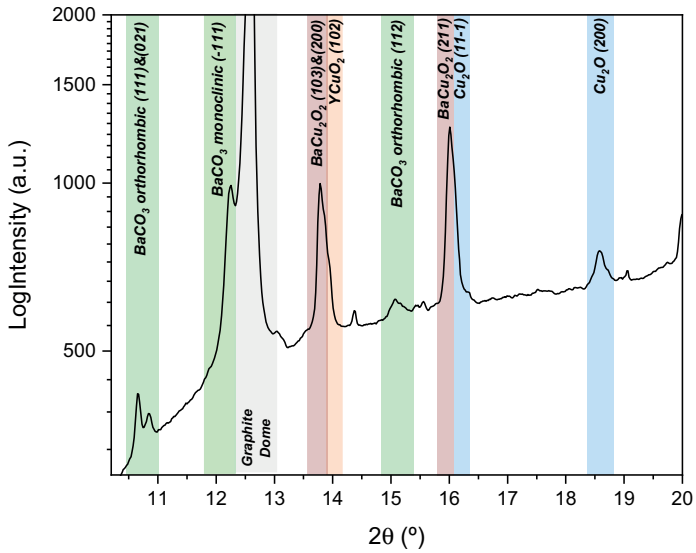


FIGURE 5.29: I(2θ) scan resulting from the integration in χ of the 2D-XRD image acquired at RT following the *in-situ* phase transformation process for the six-layered ternary film of (3:7) composition, demonstrating the unsuccessful outcome of the thermal treatment towards the elimination of $BaCO_3$ and additionally resulting in coarsening of the monoclinic phase.

The second type of film considered in this section was the case of an eight-layered ternary

film of (3:7) composition previously subjected to an *ex-situ* quench process to ensure the elimination of $BaCO_3$ prior to the growth in the set-up of the *in-situ* XRD experiments. Despite the result of such quench process shows the presence of only a minor contribution of $BaCO_3$, possibly due to the imprecise adjustment of the processing conditions for such an elevated thickness, the major contribution of $BaCu_2O_2$ suggests the elimination of the barium precursor phase had almost reached completion (Fig. 5.30).

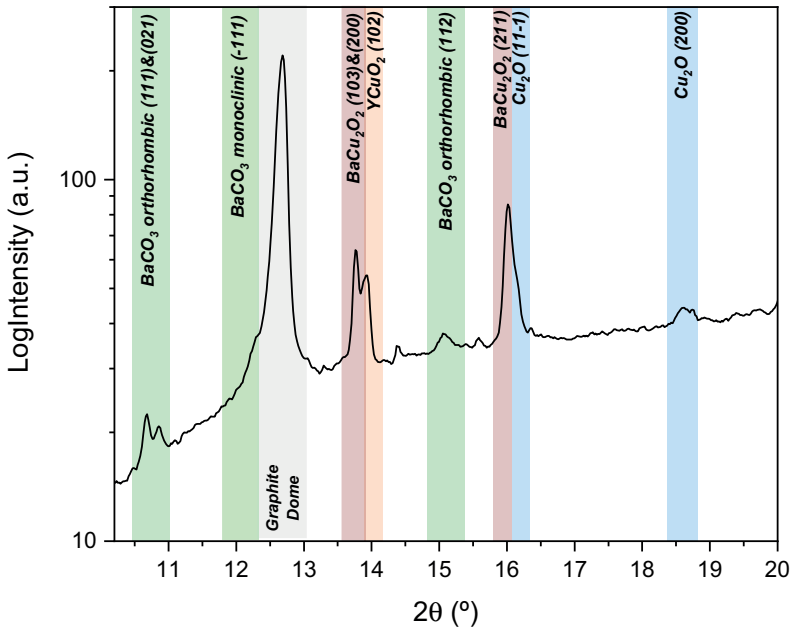


FIGURE 5.30: I(2θ) result of the integration in χ of the 2D-XRD image acquired at RT prior to the growth process process on an eight-layered ternary film of (3:7) composition which was subjected to a previous *ex-situ* quench process. The minor contribution of $BaCO_3$ orthorhombic is supposedly due to inadequate processing conditions for a film of such a thickness. Nonetheless, the major formation of $BaCu_2O_2$ displays the favourable precursor phases for the *in-situ* growth.

Now that the microstructural conditions of both thick precursor films for the growth process have been described, the analysis of TLAG on these films will be conducted through *in-situ* XRD experiments. The initial focus will be set solely on the first step of the growth process, the low-pressure heating, and the temperature-dependent phase evolution colour map is shown in Fig. 5.31. Both films exhibit high intensity of the peaks relative to $BaCu_2O_2$, suggesting both processes have advanced towards the elimination of $BaCO_3$ and the formation of the mixed barium and copper oxide. Nonetheless, if the focus is set to the 2θ range between 10º and 12º, corresponding to the peak positions of $BaCO_3$ phases, an immediate difference is clear: the $BaCO_3$ contribution in the *ex-situ* quenched film is scarce and the phase transition from the initial mixture of orthorhombic and monoclinic to only hexagonal induced by the temperature

increase occurs. Contrarily, the film which underwent the *in-situ* phase transformation process presents a strong contribution deriving from the $BaCO_3$ monoclinic peak throughout the entire heating process, consequence of its coarsening during the previous thermal treatment. The

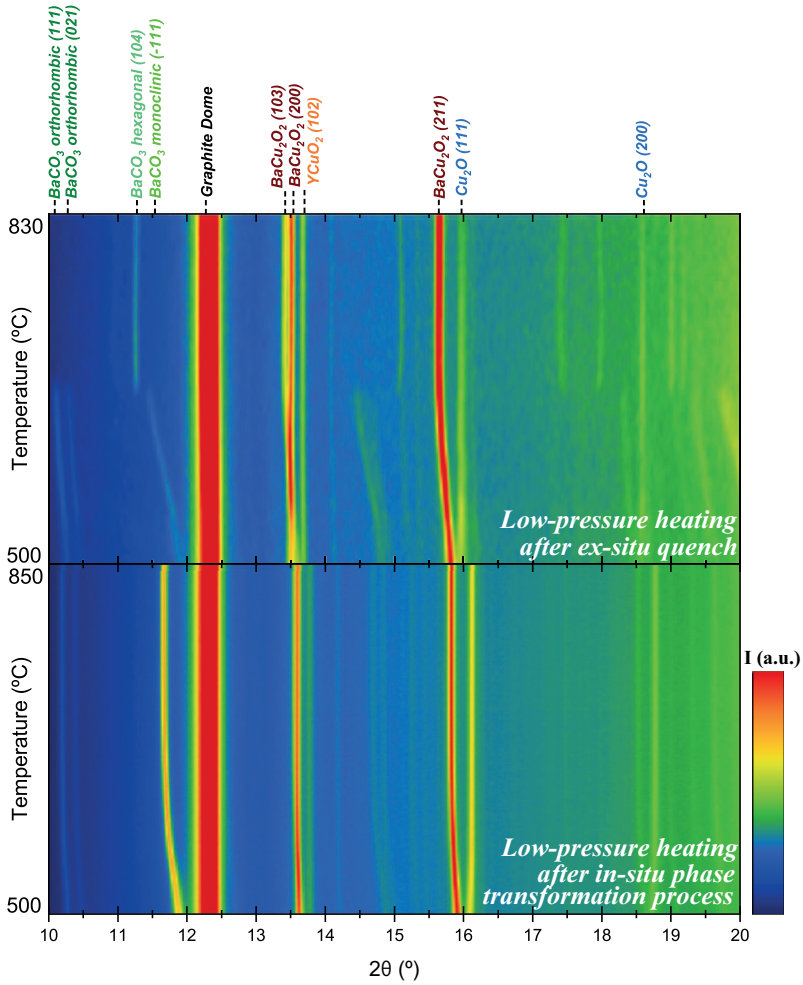


FIGURE 5.31: Temperature-dependent phase evolution colour map relative to the low-pressure heating of the *in-situ* growth process for the cases of the two thick films considered in this section. Identification of the phases according to their 2θ position is labelled in the top part. Small variations in the 2θ positions of the phases are deriving from slight beam energy fluctuations.

combination of higher intensity of the $BaCu_2O_2$ phase and lower intensity of the peaks relative to $BaCO_3$ reflections in the former film suggest that, on such thickness, the success of the *in-situ* phase transformation process is reduced if compared to the *ex-situ* quench process. To enhance the elimination of the barium precursor phase in the experimental set-up used for

in-situ XRD experiments, modifications must be made in order to enhance gas evacuation, already demonstrated to hinder the process on films of two layers, now clearly more crucial with the thickness increase.

When performing the second step of TLAG, the pressure jump, on thick films of such discrepant initial microstructural situation, the analysis reveals different consequences on the epitaxial nucleation of YBCO. A consideration on the processing conditions must be made at this point: the films were grown in different beamtime runs, in which the variations to the set-up resulted in different control of the thermal profile, as explained at the beginning of this chapter. Moreover, the pressure jump was performed at different pressure values, being $P_{O_{2,final}} = 6.7$ mbar, $P_{TOT,final} = 32$ mbar for the *ex-situ* quenched film and $P_{O_{2,final}} = 7$ mbar, $P_{TOT,final} = 100$ mbar for the film subjected to the *in-situ* phase transformation process, as the higher total pressure in the latter case was believed to aid in favouring the epitaxial nucleation of YBCO. The temperature during the pressure jump exhibited an overshoot to 871 ºC in the former case and an oscillation in the latter one, dropping almost 50 ºC while reaching the final pressure (Fig. 5.32). Therefore, to fully evaluate the consequences of these two cases, a strict control of the thermal process should be implemented, and is object of current improvements to the set-up in the ongoing work in the group. Nonetheless, a comparison is provided here as preliminary results on the growth of thick films analysed through *in-situ* XRD radiation, as this had not been previously studied in the group.

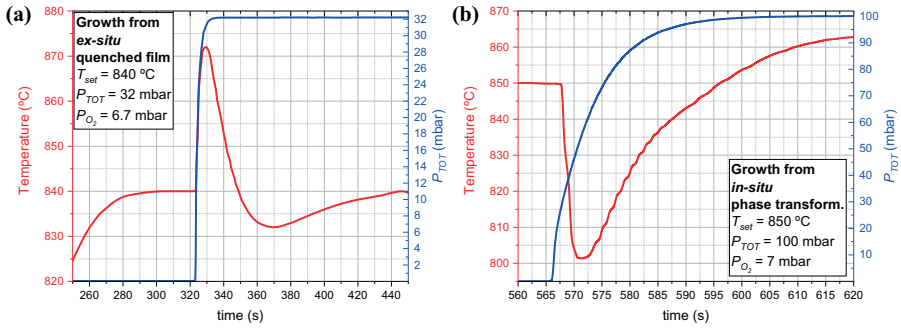


FIGURE 5.32: Temperature (red) and P_{TOT} (blue) profiles as functions of time during the pressure jump for (a) a film of eight layers which was quenched *ex-situ* and (b) a film of six layers which was subjected to the *in-situ* phase transformation process, both prior to the growth process. Variations of the experimental set-up result in variations of the thermal response of the Anton-Paar inductive furnace when the entrance of gas due to the pressure jump occurs.

Fig. 5.33 displays the I(2θ) scans resulting from the integration in χ of the 2D-XRD image acquired at RT following the growth process in the *in-situ* experimental set-up, comparing the resulting epitaxy. The film which was subjected to the *in-situ* phase transformation process (upper panel) and initiated the growth with the presence of unfavourable crystalline phases

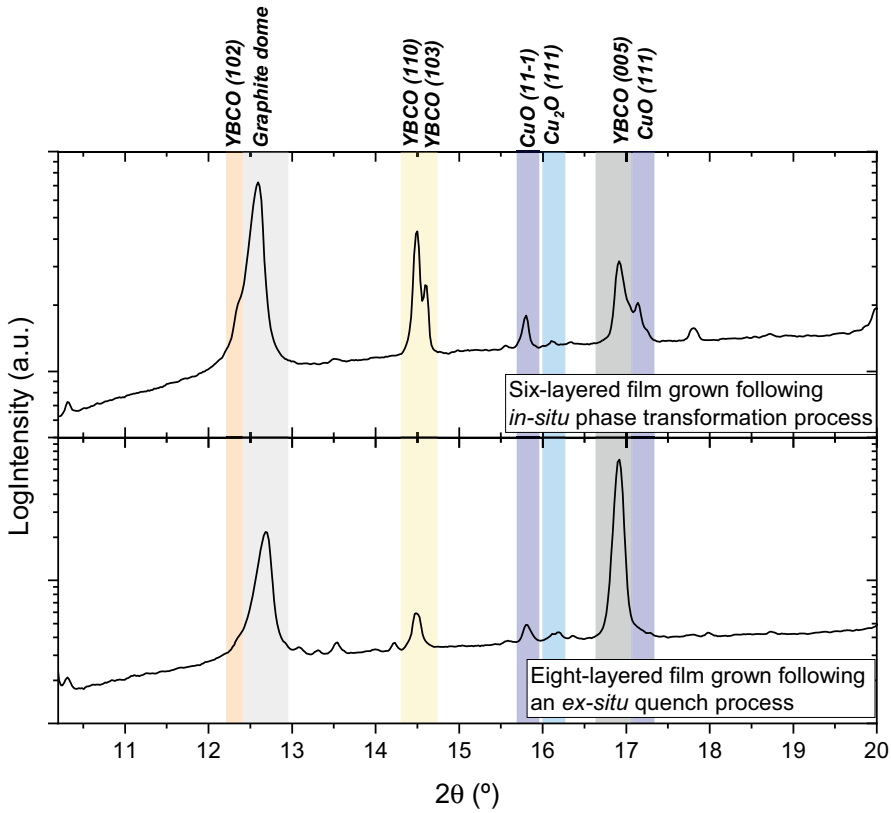


FIGURE 5.33: I(2θ) scans resulting from the integration in χ of the 2D-XRD image acquired at RT after the growth process for the thick films deriving from the two processing conditions described in this section. Identification of the crystalline phases according to their 2θ position is displayed in the upper part and with shaded areas in both plots.

results in a mixture of majorly random and heterogeneous nucleation combined with, less importantly, the homogeneous one. The high amount of $BaCO_3$ still present at the moment of the pressure jump is possibly influencing the transient liquid formation, yielding its inhomogeneous generation and varying detrimentally the supersaturation conditions. This is believed to be hindering the fast reaction of the process and the necessary inclusion of barium of the $BaCO_3$ in the liquid is delaying its formation and competing with YBCO nucleation, which as a result leads to YBCO nuclei to be formed in orientations different than the desired c-axis one. Especially concerning is the case of $BaCO_3$ monoclinic which, presumably, is found in the form of highly coarsened grains due to the two consecutive thermal treatments that this film underwent. This phase is known to have high thermal stability and its presence in the precursor films was previously linked to nucleation of majorly misoriented YBCO [91].
Contrarily, the film deriving from the *ex-situ* quench process (lower panel) yields a highly epitaxial YBCO orientation, with only a mere contribution of randomly-oriented grains. The

time-dependent phase evolution of the time range relative to the pressure jump is represented in Fig. 5.34. It is evident how the growth of c-axis YBCO is not hindered by the initial minor presence of $BaCO_3$ hexagonal, as the majority of the crystalline contribution is deriving from the desired $BaCu_2O_2$.

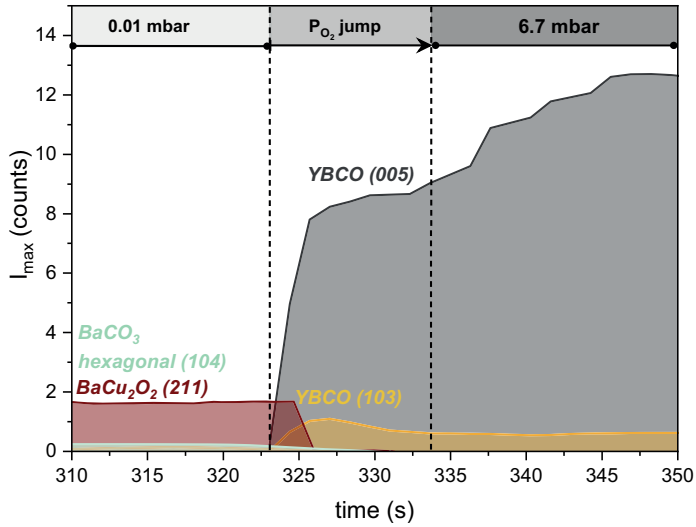


FIGURE 5.34: Time-dependent phase evolution of the time range relative to the pressure jump from the growth process of an eight-layered film which was previously subjected to an *ex-situ* quench process. The P_{O_2} values of the correspondent time-dependent pressure jump are indicated at the top of the graph and extended with dashed lines.

During the initial section of the pressure jump (< 4 seconds), the contributions relative to the precursor phases promptly disappear and YBCO nucleation and growth occurs, demonstrating the ultrafast nature of the transient liquid assisted process. Less than 1% of YBCO is present in the (103) orientation, showing the supersaturation conditions at the selected processing conditions in this specific liquid composition are optimal for the formation and growth of epitaxial nuclei. The ω-scan acquired on this film following the growth process in the *in-situ* experimental set-up reveals a $\Delta\omega$ value of 0.30º, further demonstration of a high c-axis orientation. Considering the elevated thickness of this film, estimated to be 1400 nm of final YBCO, these promising results are demonstrating that no limitation deriving from high film thickness to the epitaxial nucleation of YBCO is observed in the experimental set-up used for *in-situ* XRD experiments. Nonetheless, a further optimization of the set-up must be implemented to enhance the elimination of $BaCO_3$ in films of such thickness, given the difficulty already encountered in two-layered films. The strategy of employing a previously *ex-situ* quench process in the case of films of high thickness is crucial, as the incomplete elimination of $BaCO_3$ is limiting a homogeneous formation of the transient liquid and resulting in mixed homogeneous and

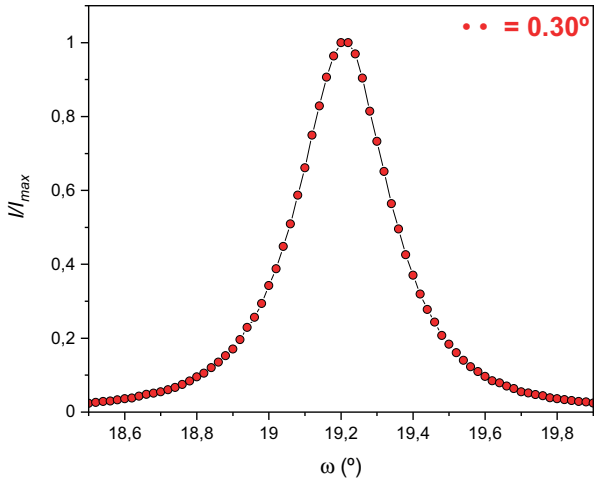


FIGURE 5.35: Rocking curve (ω-scan) acquired on a Bruker D8 Discover X-ray diffractometer at ICMAB, for an eight-layered film following the growth process through TLAG in the *in-situ* XRD synchrotron experiment. This film underwent an *ex-situ* quench prior to the growth. Value of $\Delta\omega$ is indicated in the graph.

heterogeneous nucleation, as observed for the film which underwent the *in-situ* transformation process. This approach, which showed important improvement to the epitaxial orientation of the final YBCO in two-layered films, is here unsuccessful due to the excessive thickness and critical coarsening of $BaCO_3$ in its monoclinic phase. However, once the initial step of the process is controlled through set-up modifications, TLAG mechanism can be thoroughly analysed also in the case of thick films through the essential tool that is the analysis of the growth process through *in-situ* XRD experiments performed in synchrotron facilities.

5.5 Conclusions

An overview on the TLAG kinetic mechanism on a wide range of films has been presented in this chapter. The initial analysis of a binary (Ba-Cu-O) and a ternary (Y-Ba-Cu-O) film has evinced the implications that a different initial microstructure has on the process. The elimination of the $BaCO_3$ phase, identified as the limiting step of TLAG, was effectively a great challenge faced in the *in-situ* XRD experiments. The characteristics of the set-up employed, especially the small size and geometry of the Anton-Paar furnace, result in insufficient gas flow or, possibly, static flux conditions. This feature, in combination with the extremely low porosity of the microstructure of the films developed in this thesis work, are detrimentally hindering the elimination of the barium precursor phase in this particular set-up configuration. An equilibrium is reached between the evolved CO_2 resulting from the elimination of $BaCO_3$ in the furnace environment, and is blocking the progression of the entire process, impeding the

expected reactions to occur and, additionally, favouring the formation of undesired and adverse crystalline phases. To overcome this difficulty, two strategies have been implemented, given that, at the time of the experimental work described here, no major modifications to the set up could be implemented. The advantages and main drawbacks of both approaches have been thoroughly analyzed on ternary films of the four liquid compositions and on ternary films of high thickness, exclusively for the (3:7) composition case. Evaluation of the several effects of the implementation of these strategies on the final YBCO epitaxy was carried out. This yielded interesting considerations on both the identification of the most beneficial circumstances of precursor phases and on the directly linked mechanisms of transient liquid formation, YBCO nucleation and epitaxial growth. However difficult the elimination of the barium precursor phase could be, highly epitaxial YBCO could be obtained in several cases, both for films of different liquid composition and on films of (3:7) composition of a final YBCO thickness of 1400 nm. This evidences how fundamental a correct control of the liquid supersaturation conditions is to the success of the process. In this chapter, in line with results presented in the previous one, the use of transient liquid of high copper content, namely (3:7) and (4:11) compositions, resulted in a significant enhancement of the Y solubility in the liquid. Consequently, the supersaturation is reduced if compared to liquids of lower copper contents (specifically, (2:3) and (3:6) compositions) in the same processing conditions. The growth of films of the latter compositions solely resulted in mixed homogeneous and heterogeneous nucleation due to the intrinsically high supersaturation conditions, unideal for a predominantly c-axis growth. An increase in temperature may aid in shifting the window of processing conditions to a situation of more favourable epitaxial nucleation in these cases. Finally, the growth on thick films in the experimental set-up employed for the *in-situ* XRD experiments is hindered by the difficult elimination of $BaCO_3$: despite considering a film of (3:7) composition, the extreme thickness resulted in an incomplete removal of this phase in the otherwise effective *in-situ* phase transformation process on films of the same composition presenting lower thickness. However, the use of an *ex-situ* quenched film, in which the $BaCO_3$ was eliminated prior to the growth process, led to the attainment of a highly epitaxial YBCO film of a thickness of almost 1.5 μm. This is demonstrating the high thickness is not a limitation towards the growth of c-axis oriented YBCO in the set-up employed for *in-situ* XRD experiments, once an improved control of the first step of the process is obtained. In regards to this, the determination of the kinetic mechanisms of TLAG P_{O_2}*-route* is preferably identified from experiments in which the expected mechanism is followed, where $BaCO_3$ is eliminated during the low-pressure heating. During the beamtime runs and the experiments that are described in this thesis, given that the straightforward elimination of this phase could not be obtained for the several reasons explained in the chapter, different solutions were implemented to be able to study nonetheless the TLAG mechanism through the *in-situ* XRD experiments. However, as mentioned, towards the end of this thesis, through the collaboration with ALBA Synchrotron, a movable rack containing the entire vacuum system necessary for the P_{O_2}*-route* experiments could be developed. The

possibility of an *ex-situ* optimization of this set-up allows for a strict control of the processing parameters when the *in-situ* XRD experiments are then performed, leading to the possibility of the analysis of the TLAG mechanism with higher precision and without the necessity of overcoming problems occurring during the beamtime run. The ongoing work is showing promising results, and modifications to the initial set-up have demonstrated an improvement in the step of elimination of $BaCO_3$, undoubtedly facilitating the success of the entire process and the precise analysis of the TLAG mechanism and kinetics. Moreover, successful optimization of the thermal profile could be attained, leading to the feasible growth of YBCO (and other REBCO systems) through TLAG with great rigour and control over the temperature during the delicate step of the pressure jump.

6

General Conclusions

With the major objective being the development and progress of novel growth approaches for the fabrication of $REBa_2Cu_3O_{7-\delta}$ (REBCO) superconducting films, inexpensive chemical solution deposition (CSD) based methodologies were coupled with the kinetically-driven out-of-equilibrium transient liquid assisted growth (TLAG) process. The nanocrystalline precursor phases of $BaCO_3$, CuO and RE_2O_3 resulting from the pyrolysis of the previously deposited metal-organic chemical solutions are observed to kinetically react, upon heating, towards the formation of a transient liquid of [Ba-Cu-O], not predicted by the equilibrium ternary phase diagram. The RE_2O_3 is here present in the form of dispersed solid nanoparticles. Following their dissolution in the highly corrosive melt, the incorporation of RE in the liquid results in its supersaturation, subsequently promoting the generation of stable REBCO nuclei when the crystallization conditions are adequate. For the application proposed in this thesis, an accurate tuning of the supersaturation is pivotal to favour the nucleation of c-axis oriented REBCO. The complex correlation between the correct supersaturation conditions of the liquid and surpassing the free energy of nucleation barrier for the desired heterogeneous nucleation (here, c-axis orientation) is strictly controlled by several parameters. Processing conditions, such as temperature and oxygen partial pressure (P_{O_2}), but also choice of liquid composition, with the possible variation of the Ba:Cu molar ratio, and selection of the RE, are fundamental factors for the delicate modulation of supersaturation. With only limited knowledge on this intricate topic available in literature, and no data ever reported in the range of processing conditions where TLAG occurs, the work conducted in this thesis is seeking to provide insights into the observed trends of transient liquid supersaturation and the parameters which are governing the kinetic growth of REBCO through TLAG.

Previous studies on TLAG have demonstrated the feasibility of high-performance films displaying critical current density (J_c) values of 5 MAcm^{-2} obtained with ultrafast growth rates in the range of 100 nms^{-1}. Nonetheless, the limitations on the thickness of the films of 100 nm, mainly due to low metal-organic precursor solubility in the chosen solvents, was found as a major drawback to be overcome. Envisioning the future industrial application of TLAG-CSD, the development of a novel metal-organic chemical solution was a necessity, especially considering the requirement of elevated film thickness in the CCs fabrication framework. The widespread use of commercial metal acetates of RE, Ba and Cu as precursors for the metal-organic chemical solution was disregarded, given the incomplete conversion of acetates into propionates when dissolved in the mixture of propionic acid and methanol, commonly employed as solvents. The presence of undesired mixed species or chemical compounds deriving from secondary reactions in solution are especially detrimental to the decomposition pathways followed during the first thermal annealing (pyrolysis), where the organic matter deriving from the aliphatic chains of the ligands must be fully decomposed. For this reason, the optimization of synthetic routes for the preparation of propionate salts of the metals of interest for the formation of REBCO (in this thesis, copper ($Cu(Prop)_2$), yttrium ($Y(Prop)_3$), barium ($Ba(Prop)_2$), samarium ($Sm(Prop)_3$), gadolinium ($Gd(Prop)_2$), and ytterbium ($Y(Prop)_3$), and additionally, cerium ($Ce(Prop)_3$)) have been developed. Thorough characterization and structural investigation revealed the high purity of the powders obtained through facile, cost-effective and one-pot synthetic methods and standard purification procedures. Moreover, complete analysis of the thermal behaviour of all compounds, both in form of powder and in form of films, has been carried out to corroborate their compatibility with the thermal process of pyrolysis employed for TLAG-CSD, with the final confirmation of the formation of the oxides of all the metals and $BaCO_3$.

The implementation of these compounds as precursors resulted in a highly robust chemical solution. Throughout the use of a carefully selected amine additive, monoethanolamine (MEA), substantial enhancement of the solution concentration in total sum of metals could be straightforwardly obtained. Given the bidentate nature of MEA, formation of a complex between the copper propionate and the amine promoted its otherwise difficult solubility in the solvent mixture and, as a consequence, the stability of this complex in solution, resulting in solutions displaying shelf-life of over a year. A detailed rheological, chemical analysis of the precursor solutions led to the observation of the copper-MEA complex through electron paramagnetic resonance (EPR). Additionally, thorough thermogravimetric analysis (TGA) coupled with evolved gas analysis through Fourier-transform infra-red spectroscopy (EGA-FTIR) allowed for the identification of the decomposition pathways these solutions follow during the thermal treatment, evidencing a slower decomposition profile compared to the case of solutions without any additive. The combination of the rheological features and the thermal behaviour are believed to be at the origin of the enhanced viscoelastic properties of the films

towards the strain generated during the pyrolysis thermal treatment, yielding highly homogeneous and defect-free samples. Moreover, with one of the main targets of this thesis being the detailed study of the kinetic mechanism of TLAG from films of different transient liquids, solutions of various stoichiometries were prepared through simple modification of the copper content. Precursor solutions varying from a stoichiometric (2:3) composition, to the slight copper-rich (3:6) composition, the eutectic (3:7) composition and the highest copper excess ones, the (4:11) and its variation Y-rich (4:11) composition, were feasible through the precise fine-tuning of the Cu:MEA molar ratio. Despite an excessive use of MEA is seen to enhance importantly the solubility of the metal propionate precursors and the stability of the solution, the application proposed in this thesis compels for a compromise between solution rheological and chemical properties and its thermal behaviour to yield homogeneous and defect-free films of the desired nanocrystalline phases. Through the use of the metal-organic chemical solution containing optimized amounts of MEA, nanocrystalline precursor films of each of the five stoichiometries were obtained. These display extreme homogeneity, both on the macroscale and on the nanoscale, confirmed by detailed microstructural analysis. X-Ray Diffraction (XRD) and transmission electron microscopy (TEM) studies corroborated the formation of the desired orthorhombic phase of $BaCO_3$, CuO, and RE_2O_3 with reduced grain sizes and homogeneous distribution throughout the films, both required features for a fast reaction in the TLAG process. Following what mentioned above, the example of a solution containing a great excess of MEA is seen to form detrimental phases of $BaCO_3$ monoclinic, undesired due to its elevated thermal stability resulting in its complicated elimination in the successive growth of REBCO through TLAG, and Cu(0), which is known to suffer from strong coarsening phenomena.

Following the optimization of the first step of the process, the homogeneous and reproducible nanocrystalline films obtained from the pyrolysis were then subjected to the TLAG process, in this thesis exclusively employing the TLAG P_{O_2}*-route*. The general advantage of this growth route is the possibility of decoupling the elimination of $BaCO_3$, the limiting step of the process, occurring during a low-pressure heating (generally, at a $P_{O_{2,base}} = 10^{-5}$ bar), from the formation of the transient liquid, generated during the rapid variation of P_{O_2} which, performed at the desired set temperature (T_{set}), leads the system to the T-P_{O_2} conditions of the phase diagram where REBCO is favoured. Considerable efforts were devoted to the analysis of the first step of the process, the elimination of $BaCO_3$, and variation of several processing parameters led to the understanding of the factors controlling its desired, complete removal from the system. Through tuning of heating ramp, T_{set}, dwell time and $P_{O_{2,base}}$, full elimination of the barium carbonate precursor phase was demonstrated on films of thickness up to almost 3 μm. Moreover, the analysis of elimination of this phase on films with varying copper content provided important insight in the fundamental, catalytic role of CuO for the progression of this reaction, and how differences in the crystallinity of the initial films are seen to affect significantly the final outcome.

Through selection of the optimal parameters for the complete elimination of $BaCO_3$ in the first step of the process, the growth of YBCO films through TLAG was performed. An initial optimization carried out exclusively on films of (3:7) composition through the use of a slow and a fast heating ramp, respectively 0.2 ºCs^{-1} and 1.4 ºCs^{-1}, led to the identification of a wide region of the TLAG kinetic phase diagram in which highly epitaxial YBCO is obtained. Nonetheless, the strong coarsening phenomena resulting from the slow heating when the heating rate of 0.2 ºCs^{-1} is employed limit the final physical properties of the films. The implementation of the fast heating ramp led to a general enhancement of the epitaxy and reduction of the formation of secondary phases in all of the conditions tested, followed by the attainment of films of high-performance superconducting properties of up to 2.7 MAcm^{-2} in a reproducible manner, additionally confirming the success of the TLAG-CSD approach. Moreover, preliminary studies on the growth of YBCO thick films through TLAG demonstrated the feasibility of a substantial thickness increase while maintaining high c-axis orientation of the grown YBCO, on thicknesses up to 1.5 μm. These results are an evident manifest of the feasibility of TLAG for a future industrial application, given no substantial complication towards the attainment of epitaxial YBCO on elevated film thickness was encountered, and high-performance is anticipated through fine tuning of the processing conditions.

The growth of YBCO through TLAG from different transient liquids yielded important knowledge regarding the correlation of liquid supersaturation to the c-axis nucleation of YBCO. As previously mentioned, only few works reported on the solubility of Y and other RE in [Ba-Cu-O] melts of different compositions, all of which were performed through melt-textured growth (MTG), liquid phase epitaxy (LPE) or hybrid liquid phase epitaxy (HLPE) among others, and in processing conditions far from the working window of TLAG. Therefore, the results presented in this thesis are believed to be of great interest for the community, given the possibility of a straightforward control of the transient liquid supersaturation through the simple variation of its copper content. Through the use of copper-rich compositions, in this thesis specifically the eutectic (3:7) composition and the copper-excess (4:11) and Y-rich (4:11) compositions, important improvement of the epitaxy was achieved at lower temperatures compared to the compositions with lower copper content (namely, (2:3) and (3:6) compositions). The reason is thought to lie in the higher solubility of Y in transient liquid of higher copper content, as previously displayed in the studies of MTG, LPE, and HPLE, though these were obtained in processing conditions far from the ones employed in TLAG. When the solubility of a RE in a melt increases, its supersaturation decreases, thus if the same processing conditions are selected for several liquid compositions, the copper excess will promote the lowering of this parameter. Decreased supersaturation conditions are demonstrated to be linked to a promotion of the c-axis nucleation, necessary for the resulting YBCO films to display high-performance.

The in-depth analysis of the kinetic growth process of YBCO through TLAG was performed in *in-situ* XRD experiments at two synchrotron facilities, specifically at DiffAbs Beamline of Soleil Synchrotron and NCD-SWEET Beamline of ALBA Synchrotron. The importance of this particular kind of experiments lies in the vital information obtained on the evolution of the phases during the growth of YBCO through TLAG, unattainable through other *ex-situ* techniques. Highly epitaxial YBCO was obtained through the *in-situ* synchrotron XRD experiments, and additional knowledge regarding the kinetic mechanism of TLAG was generated. Throughout the time of this thesis, the additional complexity of a limited control of the experimental set-up when performing the synchrotron experiments resulted in the development of several strategies for the difficult elimination of $BaCO_3$, hindered by the small volume of the Anton-Paar inductive furnace employed and the poor gas transport inside it. Following the overcoming of these difficulties, the use of fast acquisition during the pressure jump, besides allowing for a more accurate tracing of the phase evolution in this step of the process, led to the determination of unprecedented growth rates beyond 2000 mns^{-1}. This is a clear indication of the great industrial interest of TLAG, which surpasses the growth rates presented by the conventional CCs fabrication methods by several orders of magnitude.

Finally, two additional preliminary studies were performed during the work conducted throughout this thesis, the first being the substitution of Y for other RE (here, RE = Sm, Gd, Yb) for the preparation of different REBCO systems, and the second being the development of metal-organic chemical solutions with a variety of different amine additives to modulate solution and film characteristics. The preparation of REBCO films through the simple variation of the RE metal propionate precursor maintaining the optimized solution formulation resulted in solutions of similar rheological properties and films of comparable microstructure and homogeneity. The application of these nanocrystalline precursor films in the TLAG process required tuning of the processing parameters according to RE solubility in the [Ba-Cu-O] melt: again, information regarding this parameter is not available for the TLAG conditions. As the supersaturation is seen to decrease when the solubility is enhanced, supersaturation control is fundamental for the promotion of c-axis nucleation of the final REBCO. The careful selection of the growth temperature resulted in films of high epitaxy for the SmBCO, GdBCO, and YbBCO systems. This study with proof-of-concept objective resulted in competitive physical properties, and fine tuning of the processing parameters is anticipated to yield a further enhancement of the final J_c values in all of the films. The case of solutions of different amine additives opened a new scenario towards the possibility of solution modulation according to requirements of deposition methodology and an important film thickness increase. Several amine compounds were tested, and the complete TLAG-CSD process was performed on films deriving from metal-organic solutions containing ethylenediamine (En) and the mixture of MEA and pyridine (Py). These two systems were found to be the most interesting towards

a substantial enhancement of the film thickness while maintaining the highly homogeneous microstructure following the pyrolysis. Through the use of previously optimized processing conditions for the TLAG process, highly epitaxial YBCO films of high-performance could be obtained, again demonstrating the great versatility of TLAG towards the preparation of competitive superconducting films.

Overall, the work conducted in this thesis provides the community with novel solution formulations, considering the importance of controlling the purity of the precursors employed for its preparation. Moreover, the strict control of the chemical and rheological features of the metal-organic precursor solution is found to be at the origin of the attainment of defect-free films displaying high microstructural homogeneity in a reproducible manner, fundamental for the implementation of the following step of the process. The substantial knowledge acquired on the several parameters controlling the kinetic mechanism of TLAG led to the achievement of high-performance YBCO and REBCO films. Moreover, the demonstration of the formation of YBCO with unprecedented growth rates is a strong confirmation of the great interest of TLAG-CSD as a novel methodology to be introduced in the commercial framework of CCs fabrication.

A

Experimental Methodologies

The experimental procedures regarding each point of the method for the fabrication of YBCO and REBCO superconducting films through the TLAG-CSD approach are reported in detail in the Appendix of each Chapter, as follows:

- **Appendix A** (Experimental Methodologies) will be devoted to the description of the numerous characterization techniques employed throughout the entire thesis in the several steps of the process. Besides giving information regarding each technique, the reason behind its use for the specific point in the experimental process will be provided.
- **Appendix B** (Appendix to Chapter 2) describes the synthetic procedures and full characterization of the synthesized metal propionates employed as powder precursors for the preparation of the YBCO and REBCO precursor solutions.
- **Appendix C** (Appendix to Chapter 3) reports the protocol followed for the preparation of the optimised YBCO precursor solution, then widened to the cases of different amine additives or variation of the RE propionate powder precursor to obtain the different REBCO precursor solutions tested in this thesis.
- **Appendix D** (Appendix to Chapter 4) presents the tubular furnace and vacuum equipment employed for the quench and growth experiments in TLAG P_{O_2}-*route* performed at ICMAB. Moreover, methods used for data treatment and analysis relative to the results presented in the Chapter are fully described.
- **Appendix E** (Appendix to Chapter 5) reports the complexity of the experimental set-up used in the TLAG P_{O_2}-*route* growth experiments performed at synchrotron facilities to

analyse the growth process *in-situ* through the use of synchrotron XRD radiation. Complete description of the data acquisition, data treatment and analysis and the upgrades implemented on the experimental set-up during the years of this PhD thesis are given.

A.1 Characterization techniques for metal propionate powders

The final powder products of all metal propionates are characterized through various techniques.

Fourier Transform Infrared Spectroscopy (FTIR) spectra were measured on a spectrophotometer Jasco 4700 equipped with attenuated total reflectance (ATR) accessory, in the energy range 4000-500 cm^{-1}. This technique allows for identification of the main functional groups present in a molecule. The IR radiation is absorbed by a molecule and transformed into energy of molecular vibration. An FTIR spectrum results from irradiation of a sample (here in form of powder) through the use of a beam of infrared radiation. Following the Fourier transform of the registered signal, the absorbance (or trasmittance) spectrum may be represented. The position of the bands (wavenumber) are correlated to the type of vibrational mode, and allow for the identification of the corresponding functional group present in the molecule.

Elemental Analysis (EA) was measured on a Perkin Elmer 2400 series instrument and the analysis was conducted at the Unitat d'Anàlisi Quimica of the Serveis Tècnics de Recerca of the Universitat de Girona (UdG) through collaboration with the GRMT group of Prof. Dr. Jordi Farjas. This quantitative technique determines the amount of C, H, and N present in each compound, allowing for structural determination of each powder. The powder is dissolved in nitric acid (HNO_3). The element of interest is precipitated and its mass measured, or volatilized and the mass loss is measured.

Structural invesitgation was performed on the metal propionate compounds through two techniques.

Powder X-ray diffraction patterns (PXRD) were measured using a Siemens D-5000 diffractometer, with Cu Kα radiation of $\lambda = 1.5418$ Å and recorded in the range $2\theta = 5^{\circ}$ to 60°, with step scan of 0.02° and acquisition time of 1s per step. This analysis was conducted in the XRD Service Laboratory of ICMAB by the service technician Joan. B. Esquius, following discussion regarding the measurement conditions.

Single Crystal X-Ray Diffraction (SCXRD) was measured for the single crystal of all synthesized compounds obtained through the various crystallization methods reported in Chapter 2, through a collaboration with Prof. Dr. Elies Molins of the Advanced Structural and Functional Crystallography (ASFC) group at ICMAB. Single crystals of all of the compounds

described in 2.2 were selected and mounted for X-ray single crystal diffraction experiments. Crystallographic data was collected on a Bruker APEX-II CCD diffractometer, using a graphite monochromated Mo Kα radiation ($\lambda = 0.71073$ Å). Crystallographic data were collected at 294(2) K. Data reduction was performed using SAINT V6.45A and SORTAV [213] in the diffractometer package. Data were corrected for Lorentz and polarization effects and for absorption by SADABS [214]. The structural resolution procedure was made using SHELXT [215]. Non-hydrogen atoms were refined anisotropically. Hydrogen atoms were introduced in calculated positions and refined riding on their parent atoms, except for those belonging to water molecules which were refined under restrictions of forming the hydrogen bonds expected from a crystallographic perspective [216]. Selected crystal and data collection parameters are reported in the corresponding Table 2.1 and Table 2.2. Complete crystallographic data for the structural analysis have been deposited with the Cambridge Crystallographic Data Centre, CCDC nº 2304806-2304811. Copies of this information may be obtained free of charge from the Director, Cambridge Crystallographic Data Centre, 12 Union Road, Cambridge, CB21EZ, UK. (fax: +44-1223-336033, e-mail: deposit@ccdc.cam.ac.uk or via: www.ccdc.cam.ac.uk). The analysis of the geometry of each Gd(III), Sm(III), Ba(II), Y(III) and Ce(III) center for the six crystal structures has been carried out using the SHAPE software, version 2.155. This uses a low continuous-shape measure (CShM) of the S value [217] to determine the closest geometry. The atomic coordinates for each metal center have been specified from the .cif data.

A.2 YBCO precursor solution rheological and chemical characterization

Comprehensive analysis of the rheological and chemical properties of the YBCO precursor solution involved the use of several characterization techniques, all reported in this section.

A.2.1 Rheological Properties

Rheological properties of optimized solutions were characterized through three techniques.

Viscosity was measured on a HAAKE RheoStress RS600 from Thermo Electron Corp located in the Nanoquim Clean Room Service at ICMAB, using the "controlled stress method". Rheology studies the deformation of a sample (which may be in solid, liquid or gas form) when subjected to stress. In the case described here, the resistance of the solutions (liquid form) to an applied force is determined through the measurement of the shear rate resulting from the liquid placed on a rotating plate, which can be then correlated to its viscosity.
Contact angle was measured on a Drop Shape Analyzer DSA 100 from Krüss located in the Nanoquim Clean Room Service at ICMAB. This technique ensures the quantification of the degree of wettability of a liquid on a specific surface, thus was conducted for all solutions on STO

substrates (the same employed for deposition of films). The analysis of the images collected of the sessile drop employing the Axysimmetric Drop Shape Analysis (ADSA) technique [218] resulted in the angular values of contact angle, θ, as illustrated in Fig. A.1.

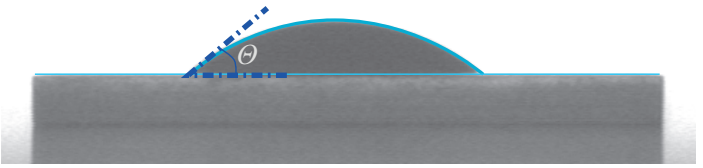


FIGURE A.1: Acquired image of a 2μL sessile drop employed for the analysis of the contact angle, θ, of the YBCO precursor solution on an STO substrate.

Water content of the solutions is crucial, as it may influence the final properties of the REBCO layers; it is thus monitored through the Karl Fischer Titration Method employing a Nittoseiko Analytech, Model CA-310 equipped with VA-200 vaporizer [219] from the Superconducting Materials and Functional Nanoengineered Structures (SUMAN) group at ICMAB. The solutions are generally used until H_2O wt% < 2 wt%, as it was initially believed that more elevated values of this parameter would lead to crack formation during the pyrolysis process or a decrease in the final superconducting properties [51, 91]. However, a detailed analysis on the stability of solutions and the storage method revealed this not to be the case for the optimised solution developed in this thesis (full study reported in 3.2.7).

A.2.2 Chemical Analysis

Electron Paramagnetic Resonance (EPR) measurements were carried out on certain solutions to examine the role of MEA on a Bruker ELEXYS E500 X band EPR spectrometer located at the Spectroscopic Techniques Laboratory at ICMAB. The measurements were performed by EPR technician Vega Lloveras.

EPR measures the absorption spectrum for systems with unpaired electrons, such as organic radicals or paramagnetic transition metals. In the solutions described in this thesis, it is employed to understand the interaction between the Cu^{2+} metal center and its ligands resulting from the formation of the Cu-MEA complex as described in 3.2.5. In an EPR experiment, the frequency, ν, is fixed and a varying magnetic field B_0 is applied, and the energy difference between the molecular states is measured, considering the *Zeeman effect*: the applied magnetic field B_0 will produce two energy levels for the magnetic moment μ of the electron, one aligned with it (lowest energy state) and one aligned against it (highest energy state). The energy of each orientation will be described by the equation:

$$\mu = m_s g_e \beta B_0 \tag{A.1}$$

where β is the Bohr magneton and g_e the spectroscopic g factor for a free electron (a constant). Therefore, considering the energy levels for an electron to be $m_s = \pm 1/2$, and $\mu = \mathrm{m_s g_e} \beta$, the product of μ and B_0 describes the energy difference between the states according to:

$$\Delta E = g \beta B_0 \tag{A.2}$$

where g is defined as g factor and contains information on the nature of the electronic structure of the molecule (generally referred to as the fingerprint of the molecule). In the case of more than one molecule (as in a solution), every paramagnetic molecule will display a principal axis system with principal g factors, namely g_x, g_y, and g_z. Depending on the coordination of the ligands with the paramagnetic metal, the resulting g factor will have a different value for B_0 parallel to z-axis (axial coordination) or for B_0 parallel to the x-y-axes (equatorial coordination).
The interaction between the unpaired electron and the magnetic nucleus will define the *nuclear hyperfine splitting*, resulting in eq. A.2 to be rewritten as:

$$h\nu = g \beta B_0 + h A m_l \tag{A.3}$$

where A is the hyperfine coupling constant and m_l is the magnetic quantum number for the nucleus. Given there are (2l+1) possible values of the latter parameter, the hyperfine interaction splits the Zeeman transition in (2l+1) lines of equal intensity, as illustrated in Fig. A.2. The derivative of the absorption spectrum is represented in order to enhance all the details deriving from the different coordination modes.

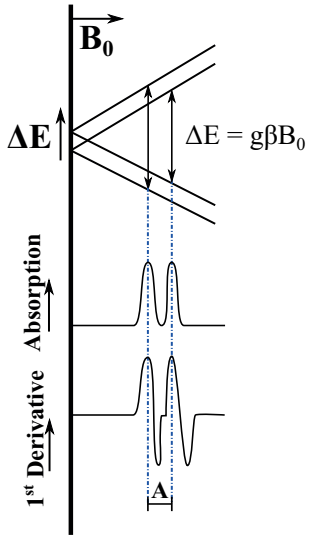


FIGURE A.2: Representation of the energy levels, the acquired absorption curve and representation of the first derivative in an EPR experiment.

A generic EPR spectrum for a Cu^{2+} complex displays a characteristic splitting in four lines (given the nuclear spin for copper isotopes is 3/2). More information is deriving from the in-plane coordination of the ligands, described by the $g_{//}$ factor, if compared to the ligands presenting axial coordination. A possible interaction of the copper metal center with a neighbouring nucleus (such as a N atom from a ligand) will produce a superhyperfine splitting, resulting in more than the expected four lines.
The parameters relative to an EPR spectrum are indicated as an exemplary case in Fig. A.3 on the EPR spectrum of $Cu(Prop)_2$, a well described Cu^{2+} center with four in-plane ligands deriving from the propionate groups.

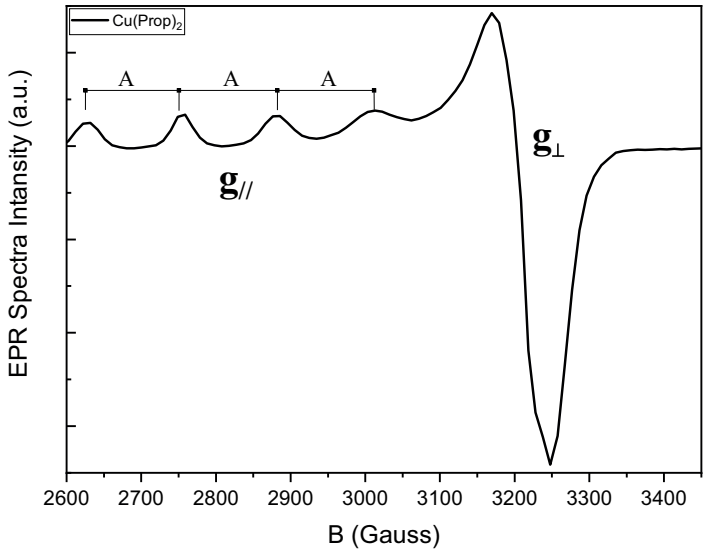


FIGURE A.3: EPR spectrum registered on a solution containing $Cu(Prop)_2$, as an example of a spectrum relative to a Cu^{2+} species. Parameters of hyperfine coupling constant A, g factor for in-plane coordination of the ligands ($g_{//}$) and g factor for axial coordination ($g_{\perp}$) are indicated.

A.3 Thermal Analysis on Powders and Films

Themorgravimetric Analysis (TGA) was conducted on all the metal propionate powders and on films of solutions of the individual metal propionates to determine their decomposition pathway and compatibility with the application in TLAG-CSD (discussion may be found in Chapter 2). Moreover, it was performed on films of the YBCO and REBCO precursor solution to assess differences amongst their thermal behaviours (Chapter 3). TGA allows for the measurement of the thermal evolution of a material (weight loss due to decomposition in powders or films) subjected to different gas atmospheres. TGA and differential thermal analysis (DTA) were registered, and the TGA derivative (dTG) represented in order to clearly identify the main decomposition steps (corresponding to peak maxima in the dTG). Additionally, the evolution

of gases was registered through Evolved Gas Analysis (EGA) coupled to FTIR, which allowed for the identification of the species resulting from the decomposition of the powders or films, and thus the determination of the decomposition mechanism followed. Studies comparing YBCO precursor solutions of different composition with the addition of MEA and without any additive are reported in 3.2.6; evaluation of the thermal behaviour of solutions in which other amine additives other than MEA (specifically En, Py, and the mixture MEA+Py) are discussed in 3.4.3; thermal analysis of REBCO precursor solutions (RE = Sm, Gd, and Yb) are compared to the case of the standard optimised YBCO precursor solution in 3.3.2.
All of the above mentioned TGA experiments have been conducted in collaboration with the GRMT group at Universitat de Girona (UdG) by Prof. Dr. Jordi Farjas and Dr. Daniel Sanchez-Rodriguez on a Mettler-Toledo thermobalance, model TGA/DSC1. The thermal profile employed in the case of films was emulating the pyrolysis process, in order to compare the thermal behaviour in a similar thermal treatment [125, 142, 143, 220, 221]. Heating was performed from 50 to 600 ºC a constant heating rate of 10 ºC/min for powders and 5 ºC/min for films. To identify the evolved gases and understand the decomposition pathways followed by the precursor solutions, *in-situ* EGA-FTIR was obtained by connecting the TGA gas outlet to an ALPHA Bruker FTIR gas analyzer through a 40 cm long steel tube heated to 200 ºC. Powders were placed inside open alumina crucibles and a flowing atmosphere (60 mL/min) of high purity N_2 (Air Liquide, $\geq$ 99.999 %) was established. Films of all solutions were obtained by drop casting on 10x10 mm $LaAlO_3$ (LAO) substrates and were directly placed on the TGA sensor. Preceding the thermal treatment, deposited films are placed on a pre-heated heating plate at 70 ºC for 5 minutes to eliminate solvent excess. A flow (60 mL/min) of high purity dry or humid O_2 (Air Liquide, $\geq$ 99.999 %) was established. Water-saturated flows were obtained by bubbling the carrier gas in deionized water at 25 ºC and atmospheric pressure. EGA-FTIR signals are identified according to [222]. Evolution of the species of interest evolved during the TGA experiments was obtained by tracing the following selected absorption peak frequencies: 1732 cm^{-1} for 3-pentanone, 1780 cm^{-1} for propionic acid, 2180 cm^{-1} for CO, 2355 cm^{-1} for CO_2, 2740 cm^{-1} for acetaldehyde, 3903 cm^{-1} for H_2O, 1508 cm^{-1} for formaldehyde, and 1796 cm^{-1} for acetic acid.

A.4 Thin Film Deposition and Pyrolysis

Before deposition, substrates (in this thesis, only single-crystal (100) SrTiO3 (STO) substrates purchased from CrysTech GmbH or MaTecK GmbH were employed) undergo an annealing process at 900 ºC for 5 h to obtain flat-terraced surfaces, successively cleaned with acetone (Acetone, Multisolvent HPLC grade ACS ISO UV-VIS, Scharlab), and methanol (Methanol, Multisolvent HPLC grade ACS ISO UV-VIS K.F., Scharlab), to eliminate any possible residues.

Precursor solutions of different compositions were deposited via spin coating (SMA 6000 Pro,

Suministro de Materiales y Asistencia, S.L.) in a grade ISO7 clean room designed to be at constant values of 30 % relative humidity (RH) and 21 ºC in the laboratories of SUMAN group at ICMAB, using a spin coating at 10 % RH and a spinning rate of 6000 rpm for 2 min. Following the deposition, the deposited film is placed on a pre-heated heating plate at 70 ºC for 5 min to eliminate all residual solvent. The samples are then placed on an alumina crucible and inserted in a tubular furnace for the thermal treatment (located in the same clean room). Given the size of the furnace employed and its isotherm region, a maximum of three samples could undergo the pyrolysis simultaneously, and were placed along the diagonal of the rectangular crucible. Annealing of the deposited films (pyrolysis) was performed by heating in an oxygen flow (0.12 L/min) up to 110 ºC, subsequently creating a humid oxygen flow by bubbling the carrier gas in deionized water at 25 ºC to promote the hydrolysis and oxidation decomposition mechanism of the propionate ligands (full description in Chapter 2). The thermal profile consisted in heating up to 240 ºC at a rate of of 3 ºC min^{-1}, then switching to a rate of 5 ºC min^{-1} up to 500 ºC, followed by rapid cooling of approximately 30 min (cooling rate of 15 ºC min^{-1}) to room temperature. A slower heating rate is employed in the temperature range where cracks were observed to be favoured. Detailed studies on the viscoelastic behaviour of the films throughout the thermal treatment are required to avoid cracks generated by the extreme strain consequence of the elimination of organic matter and the film being compacted, even more significant when the film thickness is elevated [126]. To obtain thicker precursor films, multideposition processes were carried out repeating the above procedure. A dwell of 5 min is implemented once the final temperature is reached, exclusively performed on every second layer of each sample.

A.5 Thin Film Characterization

Preliminary characterization of nanocrystalline precursor films which underwent the pyrolysis consists of mainly two techniques, specifically optical microscopy (OM) and reflectometry to assess quality and obtain an approximation of the thickness, respectively. Both equipment are located in the clean room in the laboratories of SUMAN group at ICMAB. Subsequently, other characterizations are performed to investigate the film homogeneity and microstructure.

Optical microscopy (OM) was performed on each layer following the pyrolysis to evaluate homogeneity, presence of defects or cracks, and the general quality of the film. Images of the films were acquired on a Leica DM1750 M optical microscope, and an exemplary OM image acquired for a two-layered film after pyrolysis is displayed in Fig. A.4(a).

Reflectometry measurements were carried out on the films after pyrolysis. This rapid and non-destructive measurement ensures an approximation of the film thickness with no special requirements regarding sample preparation. The measurements were performed on a Filmetrics F50 through spectral reflectance, which measures the amount of light reflected from a thin

film over a range of wavelenghts, with the incident beam perpendicular to the film surface. The software allows for the selection of several optical parameters relative to the type of sample (film and substrate) being measured, necessary for correct thickness determination. The measurement consists in a continuous acquisition in several points of the film, covering the entire surface and generating a map of the thickness, as displayed in Fig. A.4. Given the elevated viscosity of the precursor solutions, resulting in films of high thickness which present a certain extent of border effect, the measurement in proximity of the borders is unreliable and the values are, thus, discarded. The thickness values considered for each film will be restricted to a circle defined concentrically to the entire square of the sample.

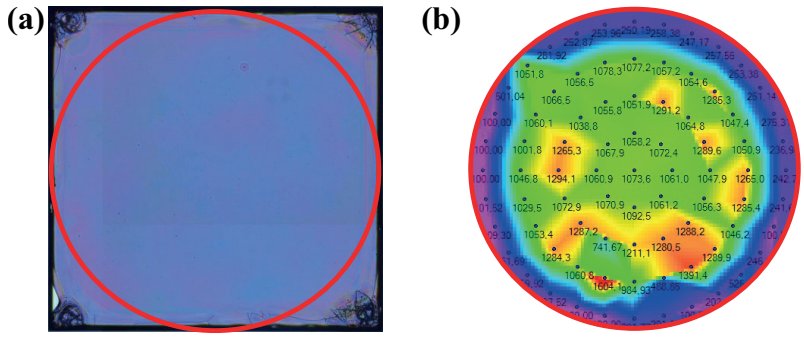


FIGURE A.4: (a) Image of a film following pyrolysis acquired through OM. Red circle defines the area of reliable reflectometry measurement, excluding the corners and borders. (b) Resulting reflectometry measurement, selecting exclusively the data inside the red circle showed in (a).

A.5.1 Structural Characterization

Structural characterization was performed through the use of several X-ray diffraction (XRD) configurations on films following the pyrolysis, to investigate whether the microstructure was optimal for the subsequent growth through TLAG, and on the final YBCO or REBCO films result of the growth process. Full description of the tubular furnace and vacuum system employed for the process of growth through TLAG P_{O_2}*-route* is provided in D, together with information regarding the thermal treatments implemented for the quench or the growth processes, yielding films of, respectively, nanocrystalline precursor phases for the transient liquid formation, and the final films of YBCO or REBCO.

X-ray diffraction (XRD) was performed on two diffractometers: a Bruker-AXS D8 Advance diffractometer (Cu K_α equipped with general area detector diffraction system (GADDS)) and a Bruker D8 Discover system (Cu K_α, X-ray energy = 8.049 keV) equipped with a Lynxeye XE-T energy-dispersive one-dimensional (1D) detector. Both diffractometers are found in the XRD Service Laboratory at ICMAB and are operated by service technicians Anna Crespi and

Francesc Xavier Campos, respectively. This non-destructive technique yields valuable information on the film composition, crystalline structure, texture quality and grain orientation, possible phase and grain size quantification, etc.

An incident beam of X-rays irradiating a crystalline matrix results in the scattering of a monochromatic wave following the constructive interference with its crystallographic planes. This is defined by the renowned law of Bragg [223], which marks the conditions for the constructive interference according to:

$$2d_{hkl}sin\theta = n\lambda \tag{A.4}$$

where d_{hkl} is the interplanar spacing of the crystallographic planes of Miller indices (hkl) and $n\lambda$ the difference of optical path (n is an integer and λ the wavelength of the incident beam). The incident beam forms an angle θ with a family of parallel planes, as illustrated in Fig. A.5. A specific phase will present a diffraction peak at determined values of the angle θ.

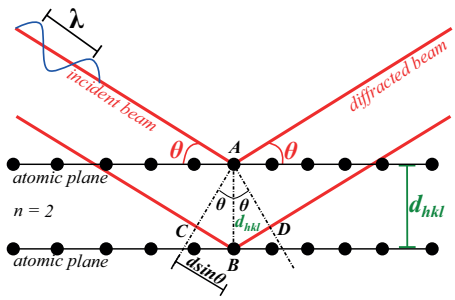


FIGURE A.5: Schematic representation of the constructive interference between incident X-rays on a crystalline matrix.

Generally, the peak positions are straightforwardly derived from the law of Bragg, given that λ is known and the diffraction pattern is the result of the diffracted wave intensity ($I(2\theta)$) collected by the diffractometer detector. In polycrystalline samples (such as powders or films composed by crystalline phases presenting no preferential orientation) the intensity of the scattered waves is constant in all directions, and for the same diffraction angle θ it is distributed along circles, known as Debye rings. In the case of epitaxial films with preferential orientation, exclusively the set of (hkl) planes parallel to the surface plane are resulting in constructive interference, and thus Bragg reflections are acquired as specific points of the reciprocal space representation[1]. A schematic representation of an XRD measurement illustrating the possible rotating angles is displayed in Fig. A.6. Probing the various kind of samples described in this thesis through different, specific configurations led to valuable information regarding the crystal structure of the films.

[1]For a more detailed explanation of the theory behind XRD, refer to [224]

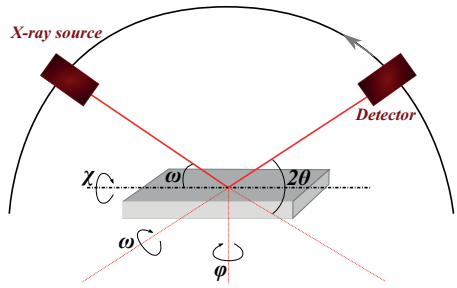


FIGURE A.6: Schematic representation of an XRD measurement performed in Bragg configuration. The XRD source, detector, possible rotating angles are identified.

GADDS was employed for identification of phases and texture quality determination [51, 55, 190], given the possibility of rapid film probing in a large detectable angular volume ($\Delta 2\theta$ = 30º; $\Delta\chi$ = 70º). Measurement configuration for a film resulting from the growth process is set to ensure Bragg conditions with the YBCO (00l) reflections (ω = 10º; 2θ = 35º; χ = 90º) with a previous ω scan (± 15-20 º) in the range of 2θ 10º to 50º to probe the (00l) reflections deriving from the epitaxial REBCO. This results in the acquisition of a 2D-XRD image as displayed in Fig. D.6(a). Integration in the range 15º≤ 2θ ≤52º and -15º≤ χ ≤15º yields the final XRD pattern (Fig. D.6(b)).

The Bruker D8 Discover system was employed for several measurements configurations:

- **Grazing Incidence XRD (GIXRD):** this configuration is selected for polycrystalline films, thus films following pyrolysis and quenched films. The signal deriving from non-oriented phases is enhanced through the implementation of this geometry. To ensure comparability between measurements, a standard measurement consists in, initially, the alignment with the STO (002) peak, then moving to grazing incidence conditions by selecting the incident angle, ω = 1.5º. This guarantees the probed area for different samples is always comparable, and the resulting differences in the XRD patterns may be ascribed to microstructural variations present in the film.

- $\theta - 2\theta$ **scans:** Bragg-Brentano geometry is chosen for this type of measurement, and it is employed in the case of grown films to probe the (00l) peaks of YBCO or REBCO in the 2θ range 7º-100º, selecting a step size of 0.02º and a constant measurement speed of 2s per step. For correct sample alignment, following the determination of the sample position in z, ω scans are acquired in correspondence of the (h00) reflection of the substrate (in the case of the films in this thesis, STO), to ensure the correct alignment with the substrate with the selected values of the χ angle and sample position z. The ϕ angle is then set to zero, and a subsequent ω scan is registered, again on the substrate (h00) reflection in order to obtain the offset on ω. Finally, following a scan in z to validate the

correct sample position, the last scan on the substrate reflection confirms the accurate alignment, prior to moving to the Bragg conditions for the REBCO (00l) reflections. Grain sizes (D) may be straightforwardly calculated from the integral-breadth of the peaks, β, employing the renowned Debye-Scherrer formula:

$$D = \frac{k\lambda}{\beta cos\theta} \tag{A.5}$$

given that k represents the Scherrer constant and λ is the employed wavelength.

- **Rocking curve (ω-scan):** these curves are acquired by probing the out-of-plane orientation of epitaxially aligned grains exclusively in grown films of YBCO or REBCO. As the name of the measurement states, the ω angle is continuously scanned while maintaining 2θ at a fixed position corresponding to the (005) reflection of YBCO (or REBCO). The integration of the curve yields the FWHM which may be directly related to the quality of the texture of the epitaxial film. Previous work conducted in the group correlated high-performance to films displaying $\Delta\omega < 0.2^{o}$ [54].

Full description of how the XRD data is analysed and represented in the case of grown films may be found in Appendix D. Measurement configurations, XRD data acquisition and treatment relative to the *in-situ* XRD experiments performed employing synchrotron radiation at SOLEIL Synchrotron and ALBA Synchrotron facilities may be found in Appendix E.

A.5.2 Microstructural Characterization

Microstructural characterization techniques were employed for the analysis of the crystalline structure of films following pyrolysis and growth processes, and for the evaluation of surface morphology exclusively on grown YBCO and REBCO films.

Scanning electron microscopy (SEM) and Energy-dispersive X-ray (EDX) spectroscopy were employed for the assessment of the quality of the YBCO and REBCO film surface and its composition, respectively. SEM and EDX measurements were conducted on a QUANTA FEI 200 FEG-ESEM, in the Microscopy Service at ICMAB. Film surface is scanned using a focused, energetic electron beam which results in three types of electrons being ejected from the interaction with the superficial layers: X-rays, secondary electrons (SE) and back-scattered electrons (BSE). The SEM detectors collect the SE and BSE, to yield images with specific characteristics depending on each case. The first are low-energy electrons which derive from the inelastic scattering of the ionized atoms relative to the superficial layers (nanometers depth from the surface). The resulting images provide morphological information given the different contrast will depend on the depth of the interaction between incident beam and the atoms composing the film. The second, conversely, are electrons of more elevated energy resulting from the interaction with the nucleus of the atoms, and will thus provide information correlating the

contrast to the composition of the different film areas. The EDX detector collects the scattered X-rays to yield chemical information correlated to the elemental composition of the film. This technique may result in identification of elements on a specific point of the films surface, on a line crossing the entire film, or on a larger surface area, generating an elemental map.
The SEM and EDX measurements were conducted exclusively on oxygenated YBCO and REBCO films, therefore no sample preparation is required given the electrically conductive nature of the films. However, SEM was additionally employed for the analysis of grain size of the synthesized metal propionate powders. Sample preparation consists in placing C tape on a metallic holder and positioning a small amount of the desired powder on it. Image acquisition is not varied for this analysis, and estimation of the size of the grains is performed manually through the SEM software measurement tool. Grain size measurement is carried out for several batches of each powder and the reported value is an average of all measured grains.

Several **transmission electron microscopy (TEM)** techniques were used for an accurate thickness evaluation and comprehensive analysis of the distribution and sizes of nanocrystalline phases in films after pyrolysis, and the assessment of epitaxy or presence of secondary phases of YBCO or REBCO grown films. TEM is characterized by extreme atomic resolution, given the use of a highly collimated electron beam (generally in the order of several hundreds of keV). A filament is responsible of ejecting and accelerating the electron beam which is then exposed to electromagnetic coils serving the purpose of beam aberration. Finally the beam reaches a specimen of reduced thickness which allows the transmission of these charged particles. The electrons interact with the atoms in the specimen to elastically scatter in multiple directions. Annular and circular detectors found at determined angles of the beam gather a different contrast depending on the interaction of the electron beam with the atoms in the specimen. Besides these detectors, an electron energy loss spectroscopy (EELS) may be employed contemporarily to collect the electrons resulting from inelastic scattering, by placing this on the path of the out-coming beam. The differences in energy loss of these electrons allows for compositional identification.
The imaging configurations mostly employed in this thesis for film characterization through STEM are the following:

- **High-resolution transmission electron microscopy (HRTEM):** ensures imaging of the atomic structure in a specimen. It is employed to obtain images of the crystal lattice, in this thesis specifically regarding the epitaxial YBCO or REBCO crystal structure. In this configuration, a wide aperture of the objective is selected to allow the passing of the direct beam. The image contrast is resulting from the phase difference between electron waves scattered from the thin specimen.
- **High-angle annular dark field scanning transmission electron microscopy (STEM-HAADF):** this technique is also known as Z-contrast imaging, given it obtains images

from electrons scattered at high angles which result from interaction with atomic nuclei (sensitivity to Z^2, with Z = atomic number). Elements with elevated Z appear with higher contrast, whereas the elements of low atomic number show reduced contrast. Therefore, this technique allows for a direct identification of the composition of a specimen through correlation with the differences in the image contrast.

- **Electron energy loss spectroscopy (EELS):** by probing excitation of interior shell of the atoms in the specimen, a compositional map may be obtained. The latter is obtained from the differences in the energy the electrons transmit at specific core loss edges, which results in an energy-loss spectrum. Elemental mapping is obtained with a sensitivity of the order of fractions of Å.

Cross-sectional specimens employed for the aforementioned TEM analytical techniques were prepared by the following conventional methods: cutting, gluing the slices face-to-face, thinning down by tripod mechanical polishing, followed by Ar+ ion milling using Gatan PIPS, until electron transparency was attained. In some cases, focused ion beam (FIB) was employed, as FIB etching ensures selection of specific areas of the film (previously identified through SEM) and the achievement of precise electron-transparent lamellae of thickness below 100 nm. The microstructural analysis was conducted by Dr. Kapil Gupta on equipment located in the Electron Microscopy Division at Institut Català de Nanociència i Nanotecnologia (ICN2) and, upon previous discussion, by service technicians of the Laboratorio de Microscopías Avanzadas of Universidad de Zaragoza. An FEI Tecnai F20 (S)TEM operated in both TEM and STEM mode at 200 kV, equipped with a Gatan quantum electron energy-loss spectrometer for EELS analyses, was used.

Pore density was evaluated from the cross-sectional STEM-HAADF micrographs and successively processed through the use of ImageJ [225], a software for image analysis. The well-defined dark contrast areas are identified as pores employing the threshold tool and estimated through the 'analyse particle function'. Histograms of the measured pore areas led to the calculation of the average pore sizes, through consideration of round pores.

EELS data processing made use of the principal component analysis (PCA) to diminish the statistical noise in EELS spectrum images. A reconstruction using the first 10 principal components was performed using the weighted-PCA multivariate statistical analysis (MSA) Plugin [226] within Gatan Digital Micrograph software.

Studies regarding the microstructure, atomic-defect structure, and phase composition of grown YBCO or REBCO films were carried out employing FEI Tecnai F20 (S)TEM operated at 200 kV, as well as, FEI Titan with a X-FEG gun, a CESCOR Cs-probe corrector and a Gatan TRIDIEM 866 ERS energy filter with a monochromator, operated in STEM mode at 300 kV.

A.5.3 Electrical Characterization

Evaluation of the physical performance of the grown and oxygenated YBCO and REBCO films was carried out through measurements conducted in the Low-Temperatures and Magnetometry Service at ICMAB by service technicians Dr. Bernat Bozzo and Dr. Ferrán Vallès.

Inductive measurements were employed for the determination of the electromagnetic response of the YBCO and REBCO films to assess their superconducting performance. Magnetic moment of the films are measured through a non-destructive technique employing a commercial Quantum Design MPMS XL SQUID DC magnetometer equipped with a 7 T magnet. The SQUID sensor has a sensitivity in the order of 10^{-6} emu and is placed in a vacuum-based helium cryostat, allowing for measurements at temperatures ranging between 5K to RT.
The self-field critical current density (J_c) values were obtained from out-of-plane inductive measurements. The film is cooled to 5 K while applying a magnetic field of 3 T. The magnetization of the film is then measured with the temperature increase and J_c self-field (at 5 K and 77 K) was deduced using the Bean critical state model for a thin disk [227] through the equation:

$$J_c = \frac{3m}{\pi r^3 t} \tag{A.6}$$

where t is the thickness of the film and r is the radius, here approximated to 2.5 mm considering the squared STO substrates employed display length of the side of 5 mm. Critical temperature (T_c) measurements through SQUID are performed by cooling the film to typically 20-50 K followed by the application of a small DC magnetic field of approximately 200 mT. The film reaches the Meissner state with the use of fields of such values, and a sufficiently high magnetic moment is generated and detected by the pick-up coils. The superconducting film thus is in a perfect diamagnetic state, displaying full repulsion of the external magnetic field. Consequently, the film is heated above its transition temperature at a rate of 0.5 ºC min^{-1} while simultaneously acquiring its diamagnetic response. T_c is thus defined as the onset where the diamagnetic response is completely suppressed and the material enters its normal state, as displayed in Fig. A.7. Moreover, the transition width, namely ΔT_c, is determined as the range in which the magnetic moment (m) drops from 90% to 10%.

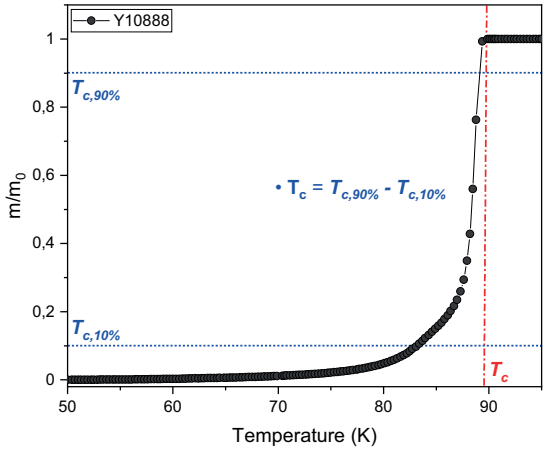


FIGURE A.7: Critical temperature (T_c) curve resulting from the measurement through a SQUID device, as explained in the text. Onset of the loss of diamagnetic response in the Meissner state is defined as T_c, and indicated through a dashed red line. Values of T_c at 90% and 10% are employed for the determination of ΔT_c, as evinced by the dashed blue lines.

Electrical transport measurements are carried out to determine the critical temperature (T_c) (in Van der Pauw configuration) and critical current density (J_c) using a Quantum Design Physical Property Measurement System (PPMS). These measurements were performed by the PhD student Aiswarya Kethamkuzhi in the Low-Temperatures and Magnetometry Service at ICMAB. As described in detail in [54], films are previously prepared through two methods: for T_c measurements only, non-destructive connection through Ag wires of the four corners of the film to the conducting pads of a PUCK were made, whereas for electrical transport measurement of J_c, destructive micropatterning of the film was performed. The magnetic field dependence of the transport critical current density (J_c) up to 9 T was determined from the I(V) characteristics, with a 10 μV/cm criterium in bridges of width of tenths of μm and length around 200 μm. A maxium Lorentz force configuration was applied between the used magnetic field and the transport current.

B

Appendix to Chapter 2

B.1 Experimental Section

B.1.1 Materials and General Details

Propionic acid, ≥ 99.5 % (HProp), cerium(III) carbonate hydrate 99.9 % trace metals basis ($Ce_2(CO_3)_3$), ytterbium(III) acetate hydrate 99.95 % trace metals basis ($Yb(OAc)_3$), and barium acetate ($Ba(OAc)_2$) ACS reagent ≥ 99.5 % were purchased from Sigma-Aldrich. Barium (II) carbonate, 99.95 % trace metals basis ($BaCO_3$), copper(II) oxide, Puratronic, 99.7 % metals basis (CuO), yttrium(III) oxide, REacton, 99.99 % (REO) (Y_2O_3), gadolinium(III) oxide, REacton, 99.99 % (REO) (Gd_2O_3), and samarium(III) acetate, REacton, 99.9 % (REO) ($Sm(OAc)_3$), were purchased from Alfa Aesar. Acetic acid glacial, 99.5 % was purchased from Panreac Sintesis. Diethyl Ether, AGR, ACS, ISO, stabilized with BHT (Et_2O) was purchased from Labbox. Acetone, Multisolvent HPLC grade ACS ISO UV-VIS was purchased from Scharlab. Methanol 99.9 %, anhydrous (max. 0.003 % H_2O) (MeOH) used in the preparation of the solutions of individual metal propionates for film deposition was purchased from Scharlab. All of the above reagents and solvents were used without further purification.

As explained in Experimental Methodologies in A, the annealing (pyrolysis) that yields the films of individual metal propionate was performed by heating the samples in a tubular furnace in a humid oxygen flow (0.12 L min^{-1}) up to 240 ºC at a rate of 3 ºC min^{-1} and up to 500 ºC with a rate of 5ºC min^{-1}, followed by cooling to room temperature.

B.1.2 Synthesis of metal propionates

Synthesis of M(Prop)$_x$ with M = Cu, Y, Ce, Sm, Gd, Yb). Metal propionate precursors (M = CuO, Y_2O_3, $Ce_2(CO_3)_3$, $Sm(OAc)_3$, Gd_2O_3, or $Yb(OAc)_3$) were added individually to HProp to reach a total concentration of $[M^{+x}] = 0.5$ M (where x = 2 when M = Cu, and x = 3 in the cases in which M = Ce, Y, Gd, Yb, or Sm). The reaction is carried out overnight at 140 ºC under vigorous stirring, with only exception being the synthesis of $Ce(Prop)_3$ in which the reaction temperature is 60 ºC. Solvent excess is removed employing a rotary evaporator to obtain a solid, with only exception being the case of $Y(Prop)_3$ in which a solid is obtained through precipitation upon cooling. Purification to eliminate residual solvent is carried out by washing the solid three times with acetone and three times with Et_2O with a Büchner Funnel filtration system, except in the case of Cu in which only purification with Et_2O is necessary.

[Cu(Prop)$_2$]$_n$ (Cu(Prop)$_2$). Blue powder, grain size > 100 μm after manual crushing, average of 30 μm after mechanical grinding (1 min, 650 rpm). Suitable crystals were obtained by recrystallization in MeOH for 5 days. Yield: 29.88 g (95%). Anal. Calcd. for $C_6H_{10}CuO_4$ (209.688 g·mol^{-1}): C, 34.36; H, 4.81. Found: C, 34.24; H, 4.73. FTIR-ATR (wavenumber, cm^{-1}): 2972 [$\nu_{as}(CH_3)$], 2940 [$\nu_s(CH_3)$], 2919 [$\nu_s(CH_3)$], 2876 [$\nu_{as}(CH_2)$], 1583 [$\nu_{as}(COO^-)$], 1510 [$\delta_{as}(CH_3)$], 1472, 1458, 1417 [$\nu_s(COO^-)$], 1370 [$\delta_{as}(CH_3)$], 1298 [$\omega(CH_2)$], 1242 [tw(CH_2)], 1079 [$\nu(CC_\alpha)$], 1006 [$\gamma(CH_3)$], 992 [ν_as(CC_α)], 892 [$\nu_s(C_\alpha CO)$], 810 [$\gamma(C_\alpha H_2)$], 753 [$\gamma(CH_2)$], 696, 662 [$\delta(COO^-)$], 595 [$\gamma(COO^-)$] (Fig. B.1).
$\Delta\nu = \nu_{as}(COO^-) - \nu_s(COO^-) = 166$ cm^{-1}, suggesting a bridging coordination of the propionate ligands [143].

[Y(Prop)$_3$·(OH$_2$)]$_n$ (Y(Prop)$_3$). White powder, average grain size 10 μm after manual crushing. Suitable crystals were obtained by recrystallization in MeOH for 8 days. Yield: 26.62 g (96%). Anal. Calcd. for $C_9H_{15}YO_6 \cdot H_2O$ (326.12 g·mol^{-1}): C, 33.1; H, 5.2. Found: C, 32.99; H, 5.01. FTIR-ATR (wavenumber, cm^{-1}): 3365-3160 [ν(OH)], 2977 [$\nu_{as}(CH_3)$], 2939 [$\nu_s(CH_3)$], 2879 [$\nu_{as}(CH_2)$], 1661, 1558, 1556 [$\nu_{as}(COO^-)$], 1536, 1466 [$\delta_{as}(CH_3)$], 1412 [$\nu_s(COO^-)$], 1375 [$\delta_{as}(CH_3)$], 1287 [$\omega(CH_2)$], 1258 [tw(CH_2)], 1077 [$\nu(CC_\alpha)$], 1013 [$\nu_{as}(CC_\alpha)$], 899 [$\nu_s(C_\alpha CO)$], 810 [$\gamma(C_\alpha H_2)$], 766 [$\gamma(CH_2)$], 698, 584 (Fig. B.2).
$\Delta\nu = \nu_{as}(COO^-) - \nu_s(COO^-) = 146$ cm^{-1}, indicating a mixed case of bidentate chelating and bridging of the propionate ligands.

[Ce(Prop)$_3$(OH$_2$)$_3$]$_n$ (Ce(Prop)$_3$). White powder, grain size between 5 μm and 100 μm after manual crushing. Suitable crystals were obtained by recrystallization in MeOH for 6 days. Yield: 7.40 g (68%). Anal. Calcd. for $C_9H_{15}CeO_6$ (359.33 g·mol^{-1}): C, 30.08; H, 4.20. Found: C, 30.47; H, 4.05. FTIR-ATR (wavenumber, cm^{-1}): 3375 [ν(OH)], 2977 [$\nu_{as}(CH_3)$], 2936 [$\nu_s(CH_3)$], 2874 [$\nu_{as}(CH_2)$], 1708 [$\nu_{as}(C=O)$], 1686, 1538 [$\nu_{as}(COO^-)$]],

1468 [$\delta_{as}(CH_3)$], 1416 [$\nu_s(COO^-)$], 1369 [$\delta_{as}(CH_3)$], 1285 [$\omega(CH_2)$], 1240 [tw(CH_2)], 1116, 1074 [$\nu(CC_\alpha)$], 1008 [$\nu_{as}(CC_\alpha)$], 893 [$\nu_s(C_\alpha CO)$], 813 [$\gamma(C_\alpha H_2)$], 671, 626, 591 (Fig. B.4).
$\Delta\nu = \nu_{as}(COO^-) - \nu_s(COO^-) = 122\ cm^{-1}$, indicating a mixed case of bidentate chelating and bridging of the propionate ligands.

[Sm_2(Prop)$_6$(OH_2)$_2$]$_n$ (Sm(Prop)$_3$). Pale yellow powder, grain size between 5 μm and 60 μm after manual crushing. Suitable crystals were obtained by vapour diffusion of acetone in a solution of (Sm(Prop)$_3$) in HProp after 10 days. Yield: 1.72 g (93%). Anal. Calcd. for $C_{21}H_{39}Sm_2O_{16}$ (848.28 $g \cdot mol^{-1}$): C, 29.73; H, 4.6. Found: C, 30.00; H, 4.54. FTIR-ATR (wavenumber, cm^{-1}): 3346 [ν(OH)], 2973 [$\nu_{as}(CH_3)$], 2946 [$\nu_s(CH_3)$], 2879 [$\nu_{as}(CH_2)$], 1688, 1536 [$\nu_{as}(COO^-)$]], 1464 [$\delta_{as}(CH_3)$], 1410 [$\nu_s(COO^-)$], 1379 [$\delta_{as}(CH_3)$], 1281 [$\omega(CH_2)$], 1245 [tw(CH_2)], 1074 [$\nu(CC_\alpha)$], 1008 [$\nu_{as}(CC_\alpha)$], 894 [$\nu_s(C_\alpha CO)$], 813 [$\gamma(C_\alpha H_2)$], 764 [$\gamma(CH_2)$], 674, 639 (Fig. B.5).
$\Delta\nu = \nu_{as}(COO^-) - \nu_s(COO^-) = 121\ cm^{-1}$, indicating a mixed case of bidentate chelating and bridging of the propionate ligands.

[Gd_2(Prop)$_6 \cdot$ 2HProp]$_n$ (Gd(Prop)$_3$). White powder, grain size between 10 μm and 100 μm after manual crushing. Suitable crystals were obtained both by recrystallization in MeOH after 5 days and by vapor diffusion of acetone in HProp after 8 days. Yield: 9.76 g (86%). Anal. Calcd. for $C_{21}H_{38}Gd_2O_{15}$ (845.0 $g \cdot mol^{-1}$): C, 29.86; H, 4.53. Found: C, 29.25; H, 4.1. FTIR-ATR (wavenumber, cm^{-1}): 3585-3389 [ν(OH)], 2984 [$\nu_{as}(CH_3)$], 2944 [$\nu_s(CH_3)$], 2874 [$\nu_{as}(CH_2)$], 1534 [$\nu_{as}(COO^-)$]], 1465 [$\delta_{as}(CH_3)$], 1417 [$\nu_s(COO^-)$], 1373 [$\delta_{as}(CH_3)$], 1293 [$\omega(CH_2)$], 1240 [tw(CH_2)], 1081 [$\nu(CC_\alpha)$], 1016 [$\nu_{as}(CC_\alpha)$], 897 [$\nu_s(C_\alpha CO)$], 812 [$\gamma(C_\alpha H_2)$], 765 [$\gamma(CH_2)$], 680, 641 (Fig. B.6).
$\Delta\nu = \nu_{as}(COO^-) - \nu_s(COO^-) = 125\ cm^{-1}$, indicating a mixed case of bidentate chelating and bridging of the propionate ligands.

[Yb(Prop)$_3 \cdot$ (OH_2)]$_n$ (Yb(Prop)$_3$). White powder, grain size between 1 μm and 10 μm after manual crushing. Suitable crystals were obtained by vapour diffusion of acetone in a solution of Yb(Prop)$_3$ in HProp after 14 days. Yield: 1.76 g (79%). Anal. Calcd. for $C_9H_{15}YbO_6 \cdot H_2O$ (410.26 $g \cdot mol^{-1}$): C, 26.3; H, 4.1. Found: C, 25.33; H, 3.89. FTIR-ATR (wavenumber, cm^{-1}): 3366-3187 [ν(OH)], 2980 [$\nu_{as}(CH_3)$], 2942 [$\nu_s(CH_3)$], 2879 [$\nu_{as}(CH_2)$], 1662, 1636, 1555, 1534 [$\nu_{as}(COO^-)$]], 1471 [$\delta_{as}(CH_3)$], 1412 [$\nu_s(COO^-)$], 1376 [$\delta_{as}(CH_3)$], 1284 [$\omega(CH_2)$], 1245 [tw(CH_2)], 1078 [$\nu(CC_\alpha)$], 1014 [$\nu_{as}(CC_\alpha)$], 910 [$\nu_s(C_\alpha CO)$], 903 [$\gamma(C_\alpha H_2)$], 810 [$\gamma(CH_2)$], 771, 676, 614 (Fig. B.7).
$\Delta\nu = \nu_{as}(COO^-) - \nu_s(COO^-) = 124\ cm^{-1}$, indicating a mixed case of bidentate chelating and bridging of the propionate ligands.

Synthesis of $[\mathbf{Ba_7(Prop)_{14}(OH_2)_8}]_\mathbf{n}$ ($\mathbf{Ba(Prop)_2}$). $BaCO_3$ is added to deionized water followed by the dropwise addition of HProp under vigorous stirring. HProp and deionized water are in a ratio of 1.125:1, and total $[Ba^{2+}] = 0.5$ M. The reaction starts as a highly foamy, white solution upon the addition of HProp and is stirred vigorously during 24h at RT to yield a transparent, clear solution. Solvent excess was eliminated using a rotary evaporator, to obtain a transparent gel. No solid could be obtained from the evaporation of the solvent, therefore, to induce crystallization, the product was placed in an ice bath for several hours. A white solid was then obtained, and its purification, as in the previous case using the Büchner funnel filtration system, needed a first washing of the product three times with acetone, followed by three times with Et_2O. Yields of up to 88% were obtained following this procedure. In the case of only employing Et2O during purification, yields of only 20% were obtained. The average grain size for the final powder product after manual crushing was 6 μm. Suitable crystals were obtained by recrystallization in MeOH for 14 days. Yield: 25.28 g (88%). Anal. Calcd. for $C_9H_{17}BaO_7$ (359.5474 $g \cdot mol^{-1}$): C, 30.06; H, 4.76. Found: C, 30.00; H, 4.54. FTIR-ATR (wavenumber, cm^{-1}): 3530-3208 [ν(OH)], 2974 [$\nu_{as}(CH_3)$], 2941 [$\nu_s(CH_3)$], 2879 [$\nu_{as}(CH_2)$], 1707 [$\nu_{as}(C=O)$], 1650, 1529 [$\nu_{as}(COO^-)$]], 1462 [$\delta_{as}(CH_3)$], 1413 [$\nu_s(COO^-)$], 1370 [$\delta_{as}(CH_3)$], 1290 [$\omega(CH_2)$], 1246 [tw(CH_2)], 1074 [$\nu(CC_\alpha)$], 1009 [$\gamma(CH_3)$], 880 [$\nu_{as}(CC_\alpha)$], 812 [$\nu_s(C_\alpha CO)$], 606.
$\Delta\nu = \nu_{as}(COO^-)$ - $\nu_s(COO^-) = 116\ cm^{-1}$, indicating a mixed case of bidentate chelating and bridging of the propionate ligands.

Solutions of individual metal propionate. To evaluate the decomposition of M(Prop)x in films, solutions of the individual metal propionates were prepared by simply dissolving the metal propionate in a mixture of HProp and MeOH (1:1) under stirring at 30 ºC, until complete dissolution was obtained (30 minutes approximately). To maximize the EGA-FTIR signal in the TGA experiments, the solutions were saturated; however, due to different solubility of the precursors, the final concentrations were 1.5 M for a solution of $Ba(Prop)_2$, 1 M for the solutions of $Gd(Prop)_3$ and $Ce(Prop)_3$, 0.5 M for a solution of $Cu(Prop)_2$, and 0.25 M for the solutions of $Y(Prop)_3$, $Sm(Prop)_3$ and $Yb(Prop)_3$.

B.1.3 Characterization of initial products

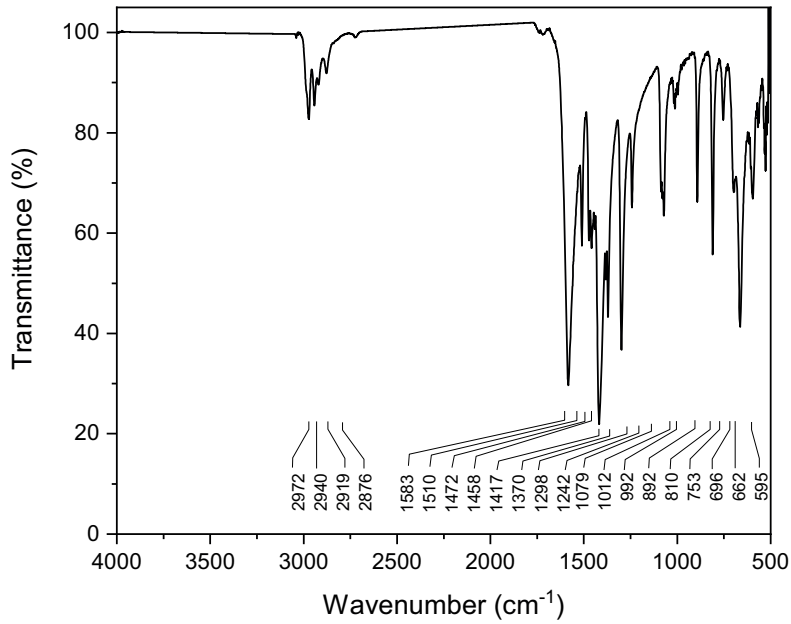


FIGURE B.1: FTIR-ATR spectrum acquired for $Cu(Prop)_2$. Identification of the bands is indicated in the previous subsection.

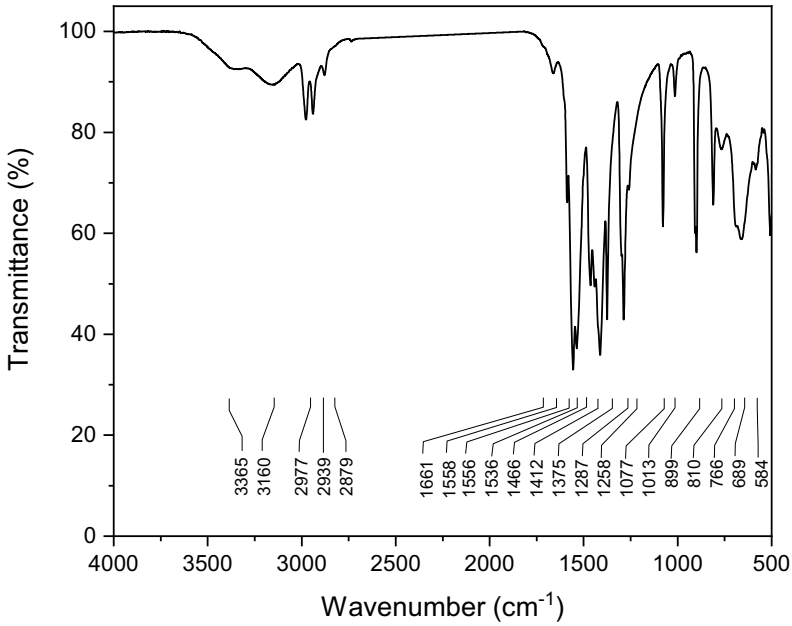


FIGURE B.2: FTIR-ATR spectrum acquired for $Y(Prop)_3$. Identification of the bands is indicated in the previous subsection.

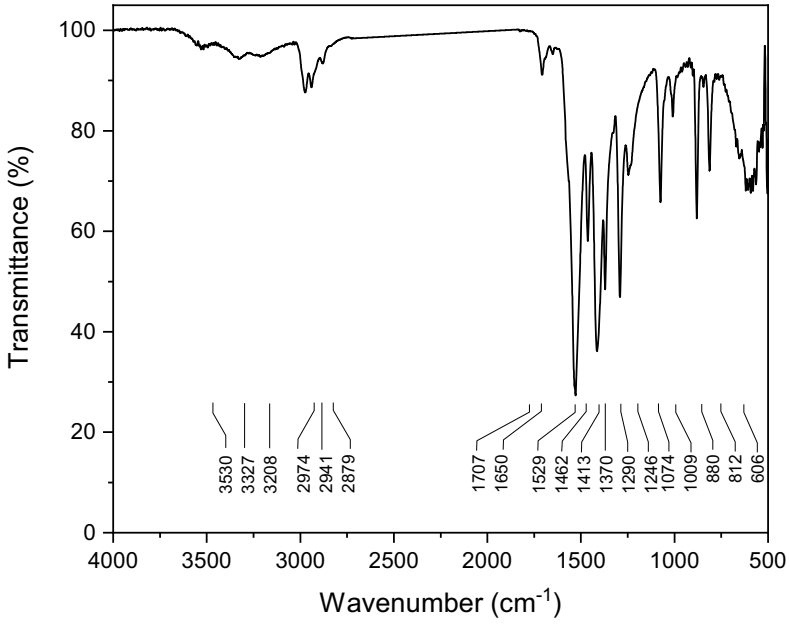


FIGURE B.3: FTIR-ATR spectrum acquired for $Ba(Prop)_2$. Identification of the bands is indicated in the previous subsection.

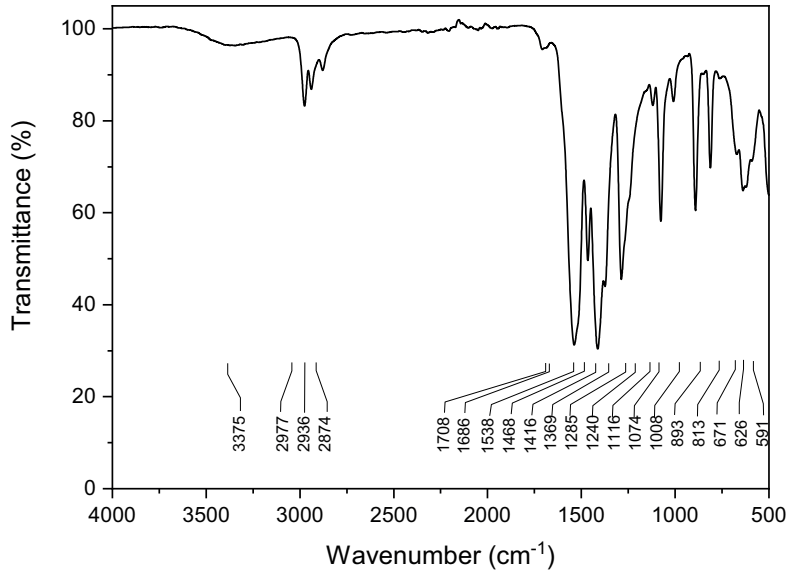


FIGURE B.4: FTIR-ATR spectrum acquired for $Ce(Prop)_3$. Identification of the bands is indicated in the previous subsection.

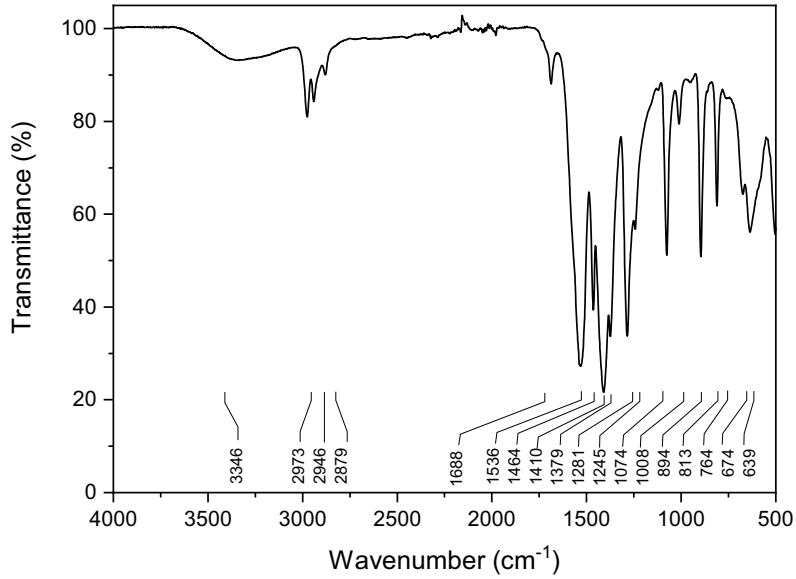


FIGURE B.5: FTIR-ATR spectrum acquired for $Sm(Prop)_3$. Identification of the bands is indicated in the previous subsection.

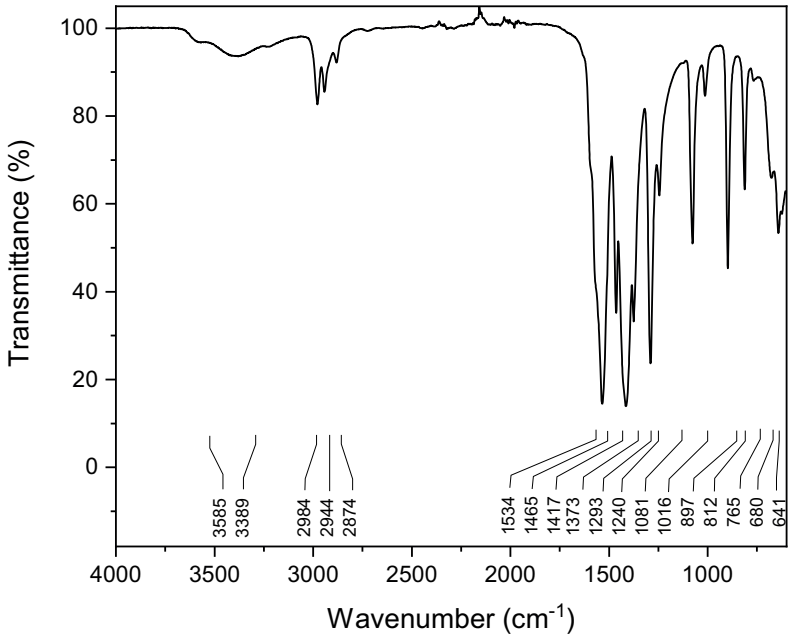


FIGURE B.6: FTIR-ATR spectrum acquired for $Gd(Prop)_3$. Identification of the bands is indicated in the previous subsection.

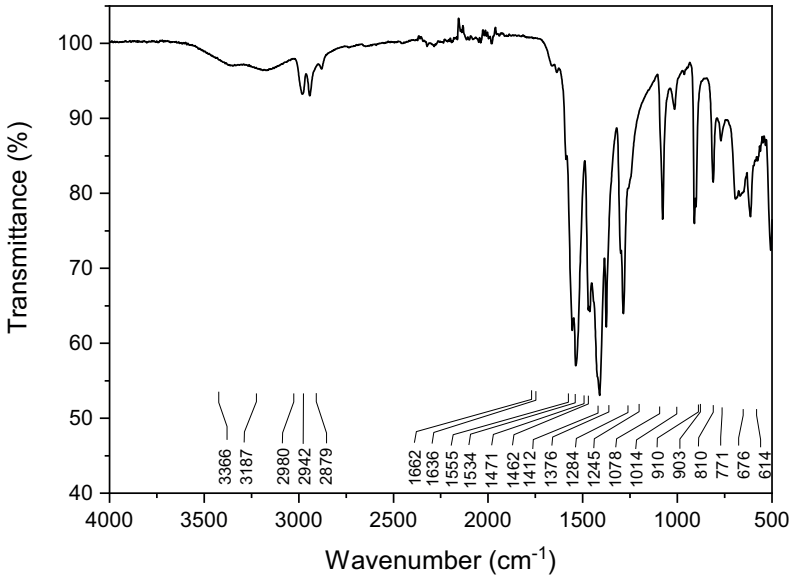


FIGURE B.7: FTIR-ATR spectrum acquired for $Yb(Prop)_3$. Identification of the bands is indicated in the previous subsection.

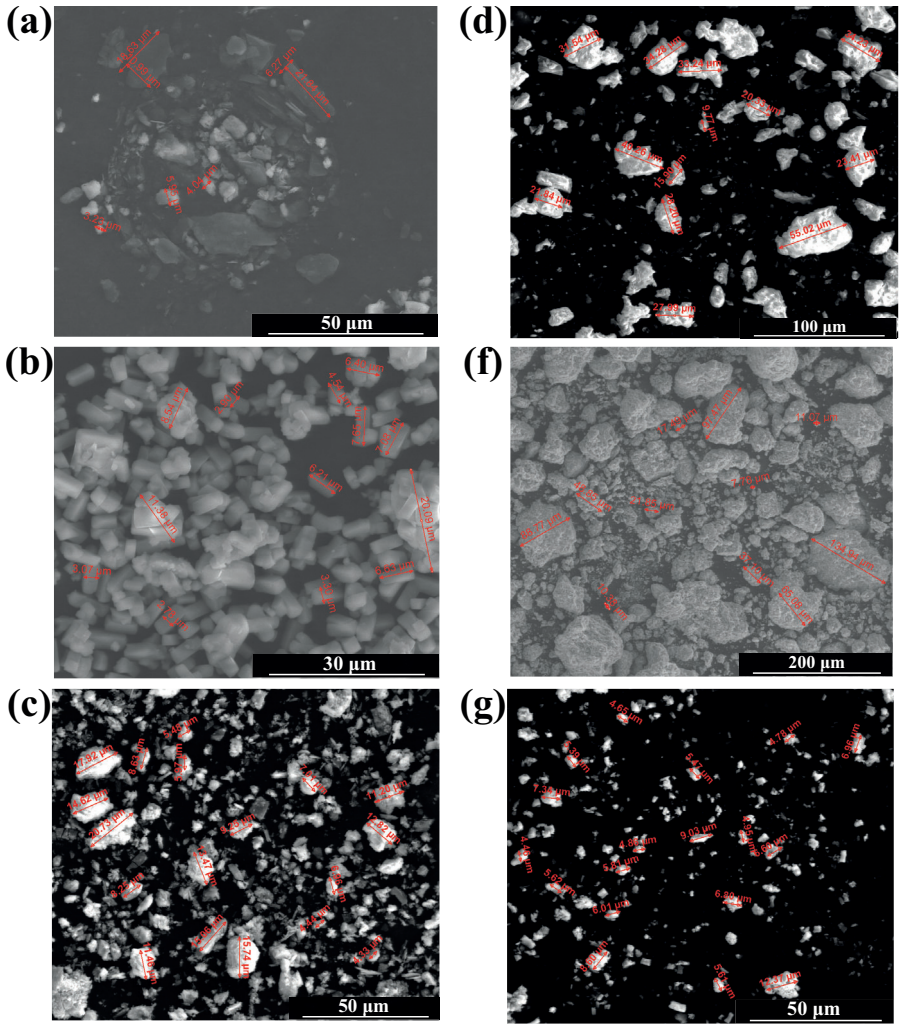


FIGURE B.8: SEM images from the powder precursors with respective grain size measurement of (a) $Y(Prop)_3$; (b) $Ba(Prop)_2$; (c) $Ce(Prop)_3$; (d) $Sm(Prop)_3$; (e) $Gd(Prop)_3$; (f) $Yb(Prop)_3$.

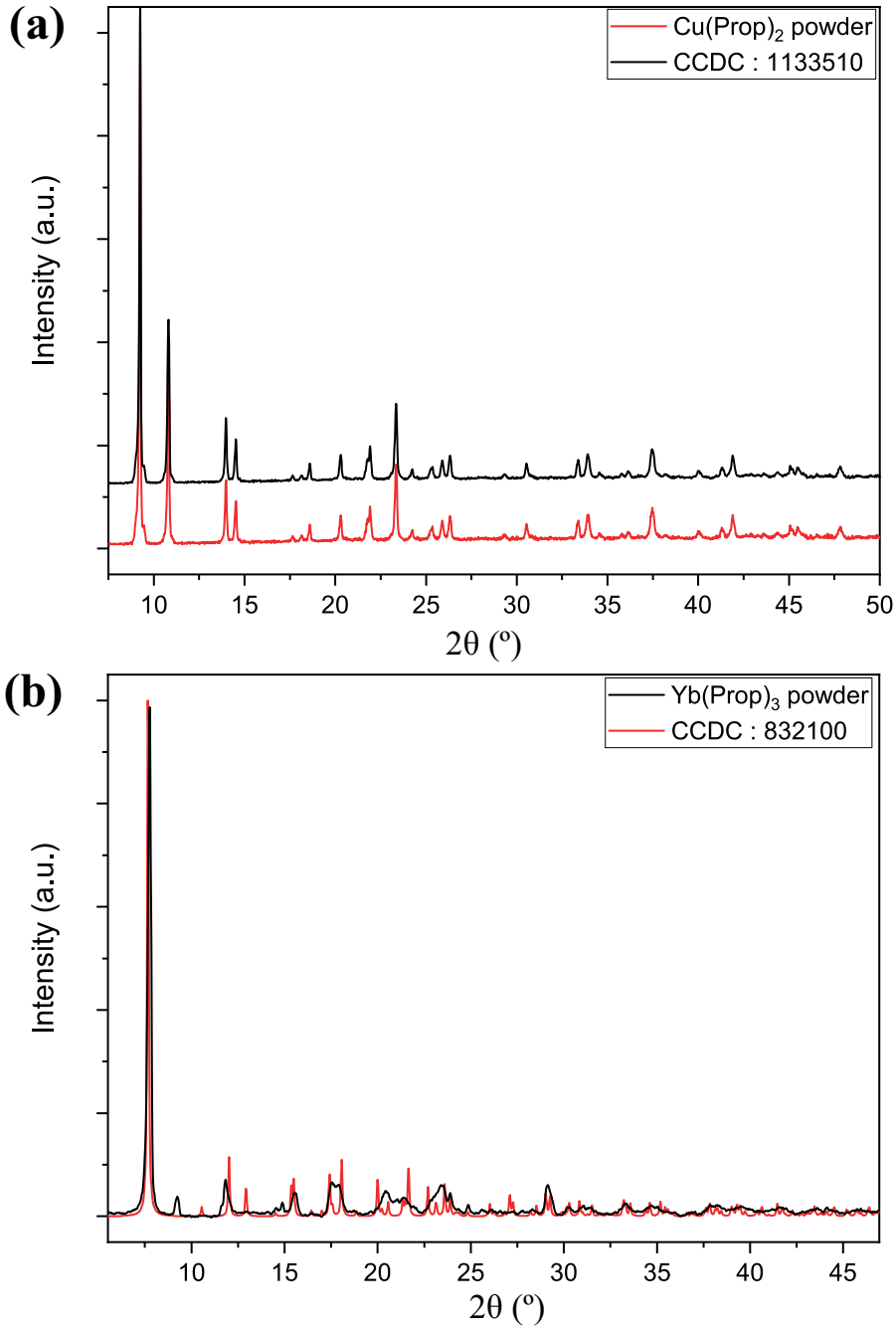


FIGURE B.9: (a) Comparison between XRD of $Cu(Prop)_2$ powder and the one from [132], CCDC: 1133510. (b) Comparison between XRD of $Yb(Prop)_3$ powder and the one from [133], CCDC: 832100.

Table B1. Bond lengths and torsion angles of $Gd(Prop)_3$.

bond lengths (Å)			
	Gd(1)		
Gd(1)-O(7)	2.293(10)	Gd(1)-O(2)	2.436(10)
Gd(1)-O(3)	2.306(9)	Gd(1)-O(26)#1	2.445(11)
Gd(1)-O(9)	2.358(9)	Gd(1)-O(1)	2.494(8)
Gd(1)-O(5)	2.392(10)	Gd(1)-O(25)#1	2.496(8)
	Gd(2)		
Gd(2)-O(4)	2.300(10)	Gd(2)-O(17)	2.447(9)
Gd(2)-O(13)	2.379(8)	Gd(2)-O(6)	2.456(11)
Gd(2)-O(11)	2.390(8)	Gd(2)-O(16)	2.525(9)
Gd(2)-O(1)	2.398(8)	Gd(2)-O(5)	2.609(10)
Gd(2)-O(15)	2.437(9)		
	Gd(3)		
Gd(3)-O(21)	2.303(9)	Gd(3)-O(14)	2.402(10)
Gd(3)-O(18)	2.321(10)	Gd(3)-O(19)	2.424(11)
Gd(3)-O(16)	2.350(9)	Gd(3)-O(20)	2.483(8)
Gd(3)-O(23)	2.371(10)	Gd(3)-O(13)	2.500(8)
	Gd(4)		
Gd(4)-O(22)	2.329(11)	Gd(4)-O(24)	2.456(11)
Gd(4)-O(27)	2.384(9)	Gd(4)-O(9)#2	2.539(9)
Gd(4)-O(20)	2.392(8)	Gd(4)-O(23)	2.648(11)
Gd(4)-O(25)	2.400(8)		
Gd(4)-O(10)#2	2.429(10)		
Gd(4)-O(8)#2	2.449(8)		

bond angles (deg)			
	Gd(1)		
O(7)-Gd(1)-O(3)	87.6(4)	O(2)-Gd(1)-O(26)#1	79.2(4)
O(7)-Gd(1)-O(9)	79.3(4)	O(7)-Gd(1)-O(1)	147.2(3)
O(3)-Gd(1)-O(9)	85.5(3)	O(3)-Gd(1)-O(1)	77.9(3)
O(7)-Gd(1)-O(5)	82.5(4)	O(9)-Gd(1)-O(1)	127.7(3)
O(3)-Gd(1)-O(5)	86.0(3)	O(5)-Gd(1)-O(1)	67.4(3)
O(9)-Gd(1)-O(5)	160.2(3)	O(2)-Gd(1)-O(1)	53.0(3)
O(7)-Gd(1)-O(2)	158.6(4)	O(26)#1-Gd(1)-O(1)	79.7(3)
O(3)-Gd(1)-O(2)	93.4(4)	O(7)-Gd(1)-O(25)#1	75.0(3)
O(9)-Gd(1)-O(2)	79.5(3)	O(3)-Gd(1)-O(25)#1	152.4(3)
O(5)-Gd(1)-O(2)	118.9(3)	O(9)-Gd(1)-O(25)#1	70.4(3)
O(7)-Gd(1)-O(26)#1	107.5(4)	O(5)-Gd(1)-O(25)#1	112.2(3)

O(3)-Gd(1)-O(26)#1	156.3(3)	O(2)-Gd(1)-O(25)#1	95.3(3)
O(9)-Gd(1)-O(26)#1	114.8(4)	O(26)#1-Gd(1)-O(25)#1	51.4(3)
O(5)-Gd(1)-O(26)#1	78.2(4)	O(1)-Gd(1)-O(25)#1	127.6(3)

Gd(2)

O(4)-Gd(2)-O(13)	74.0(3)	O(1)-Gd(2)-O(6)	98.3(3)
O(4)-Gd(2)-O(11)	144.5(3)	O(15)-Gd(2)-O(6)	149.7(3)
O(13)-Gd(2)-O(11)	141.0(3)	O(17)-Gd(2)-O(6)	72.8(3)
O(4)-Gd(2)-O(1)	73.0(3)	O(4)-Gd(2)-O(16)	73.9(3)
O(13)-Gd(2)-O(1)	138.3(3)	O(13)-Gd(2)-O(16)	69.3(3)
O(11)-Gd(2)-O(1)	73.1(3)	O(11)-Gd(2)-O(16)	117.8(3)
O(4)-Gd(2)-O(15)	83.8(4)	O(1)-Gd(2)-O(16)	123.4(3)
O(13)-Gd(2)-O(15)	120.9(3)	O(15)-Gd(2)-O(16)	51.9(3)
O(11)-Gd(2)-O(15)	80.2(3)	O(17)-Gd(2)-O(16)	72.5(3)
O(1)-Gd(2)-O(15)	79.9(3)	O(6)-Gd(2)-O(16)	138.3(3)
O(4)-Gd(2)-O(17)	141.0(3)	O(4)-Gd(2)-O(5)	78.7(3)
O(13)-Gd(2)-O(17)	76.0(3)	O(13)-Gd(2)-O(5)	83.7(3)
O(11)-Gd(2)-O(17)	71.0(3)	O(11)-Gd(2)-O(5)	96.5(3)
O(1)-Gd(2)-O(17)	143.9(3)	O(1)-Gd(2)-O(5)	65.4(3)
O(15)-Gd(2)-O(17)	90.8(3)	O(15)-Gd(2)-O(5)	144.4(3)
O(4)-Gd(2)-O(6)	124.9(4)	O(17)-Gd(2)-O(5)	122.0(3)
O(13)-Gd(2)-O(6)	80.5(3)	O(6)-Gd(2)-O(5)	50.3(3)
O(11)-Gd(2)-O(6)	70.5(4)	O(16)-Gd(2)-O(5)	145.7(3)

Gd(3)

O(21)-Gd(3)-O(18)	86.3(4)	O(14)-Gd(3)-O(19)	80.5(5)
O(21)-Gd(3)-O(16)	85.6(3)	O(21)-Gd(3)-O(20)	77.6(3)
O(18)-Gd(3)-O(16)	77.2(4)	O(18)-Gd(3)-O(20)	146.3(3)
O(21)-Gd(3)-O(23)	87.1(4)	O(16)-Gd(3)-O(20)	129.8(3)
O(18)-Gd(3)-O(23)	81.9(4)	O(23)-Gd(3)-O(20)	68.1(3)
O(16)-Gd(3)-O(23)	158.2(4)	O(14)-Gd(3)-O(20)	80.1(3)
O(21)-Gd(3)-O(14)	157.2(3)	O(19)-Gd(3)-O(20)	52.9(3)
O(18)-Gd(3)-O(14)	110.4(4)	O(21)-Gd(3)-O(13)	151.7(3)
O(16)-Gd(3)-O(14)	112.6(3)	O(18)-Gd(3)-O(13)	74.5(3)
O(23)-Gd(3)-O(14)	80.4(4)	O(16)-Gd(3)-O(13)	70.1(3)
O(21)-Gd(3)-O(19)	89.7(4)	O(23)-Gd(3)-O(13)	110.0(3)
O(18)-Gd(3)-O(19)	157.5(4)	O(14)-Gd(3)-O(13)	51.0(3)
O(16)-Gd(3)-O(19)	80.4(3)	O(19)-Gd(3)-O(13)	100.1(3)
O(23)-Gd(3)-O(19)	120.1(4)	O(20)-Gd(3)-O(13)	129.2(3)

Gd(4)

O(22)-Gd(4)-O(27)	144.5(4)	O(10)#2-Gd(4)-O(24)	147.7(4)
O(22)-Gd(4)-O(20)	72.2(3)	O(8)#2-Gd(4)-O(24)	73.6(3)

O(27)-Gd(4)-O(20)	73.6(3)	O(22)-Gd(4)-O(9)#2	73.1(3)
O(22)-Gd(4)-O(25)	74.2(4)	O(27)-Gd(4)-O(9)#2	119.2(3)
O(27)-Gd(4)-O(25)	140.7(4)	O(20)-Gd(4)-O(9)#2	122.2(3)
O(20)-Gd(4)-O(25)	138.1(3)	O(25)-Gd(4)-O(9)#2	69.1(3)
O(22)-Gd(4)-O(10)#2	87.0(4)	O(10)#2-Gd(4)-O(9)#2	52.1(3)
O(27)-Gd(4)-O(10)#2	78.6(4)	O(8)#2-Gd(4)-O(9)#2	73.0(3)
O(20)-Gd(4)-O(10)#2	81.4(3)	O(24)-Gd(4)-O(9)#2	138.7(3)
O(25)-Gd(4)-O(10)#2	121.2(3)	O(22)-Gd(4)-O(23)	79.3(4)
O(22)-Gd(4)-O(8)#2	140.8(3)	O(27)-Gd(4)-O(23)	94.9(3)
O(27)-Gd(4)-O(8)#2	71.4(3)	O(20)-Gd(4)-O(23)	65.1(3)
O(20)-Gd(4)-O(8)#2	144.6(3)	O(25)-Gd(4)-O(23)	84.7(3)
O(25)-Gd(4)-O(8)#2	75.8(3)	O(10)#2-Gd(4)-O(23)	146.2(3)
O(10)#2-Gd(4)-O(8)#2	87.4(3)	O(8)#2-Gd(4)-O(23)	122.3(3)
O(22)-Gd(4)-O(24)	124.1(4)	O(24)-Gd(4)-O(23)	49.5(3)
O(27)-Gd(4)-O(24)	70.8(4)	O(9)#2-Gd(4)-O(23)	145.9(3)
O(20)-Gd(4)-O(24)	99.1(3)		
O(25)-Gd(4)-O(24)	79.7(4)		

Symmetry transformations used to generate equivalent atoms:
#1 x-1,y+1,z #2 x+1,y-1,z

Table B2. Bond lengths and torsion angles of $Ba(Prop)_2$.

bond lengths (Å)			
Ba(1)			
Ba(1)-O(3)	2.688(17)	Ba(1)-O(2)	2.844(19)
Ba(1)-O(1)	2.708(18)	Ba(1)-O(19)	2.937(17)
Ba(1)-O(16)#1	2.761(17)	Ba(1)-O(17)#1	2.939(19)
Ba(1)-O(20)	2.820(15)	Ba(1)-O(6)	3.029(18)
Ba(1)-O(7)	2.825(15)		
Ba(2)			
Ba(2)-O(21)	2.634(18)	Ba(2)-O(6)	2.830(18)
Ba(2)-O(7W)	2.779(15)	Ba(2)-O(7)	2.932(15)
Ba(2)-O(19)	2.791(16)	Ba(2)-O(8)	2.936(18)
Ba(2)-O(9)	2.799(18)	Ba(2)-O(10)	2.977(18)
Ba(2)-O(11)	2.802(17)	Ba(2)-O(5)	3.039(18)
Ba(3)			
Ba(3)-O(4)	2.702(19)	Ba(3)-O(6)	2.812(17)
Ba(3)-O(24)	2.710(18)	Ba(3)-O(3)	2.815(18)
Ba(3)-O(4)#2	2.760(18)	Ba(3)-O(10)	2.837(19)

Ba(3)-O(6W)	2.769(16)	Ba(3)-O(4W)	2.968(18)
Ba(3)-O(7)	2.795(15)		

Ba(4)

Ba(4)-O(8)	2.65(2)	Ba(4)-O(12)	2.916(17)
Ba(4)-O(25)	2.697(18)	Ba(4)-O(13)	2.919(19)
Ba(4)-O(15)	2.720(19)	Ba(4)-O(10)	2.924(18)
Ba(4)-O(23)	2.856(19)	Ba(4)-O(24)	3.036(18)
Ba(4)-O(11)	2.897(18)		

Ba(5)

Ba(5)-O(12)	2.513(18)	Ba(5)-O(14)	2.870(19)
Ba(5)-O(20)#3	2.618(15)	Ba(5)-O(16)	2.889(19)
Ba(5)-O(5W)	2.798(15)	Ba(5)-O(17)	2.907(19)
Ba(5)-O(18)	2.84(2)	Ba(5)-O(15)	3.138(18)
Ba(5)-O(13)	2.846(19)		

Ba(6)

Ba(6)-O(26)	2.627(19)	Ba(6)-O(1W)	2.880(18)
Ba(6)-O(13)	2.750(18)	Ba(6)-O(26)#4	2.886(19)
Ba(6)-O(3W)	2.788(16)	Ba(6)-O(15)	3.029(18)
Ba(6)-O(2)#3	2.812(19)	Ba(6)-O(25)	3.029(18)
Ba(6)-O(17)	2.843(19)		

Ba(7)

Ba(7)-O(5)	2.664(19)	Ba(7)-O(2W)	2.816(19)
Ba(7)-O(14)#5	2.67(2)	Ba(7)-O(22)	2.82(2)
Ba(7)-O(9)	2.675(18)	Ba(7)-O(21)	2.88(2)
Ba(7)-O(18)#5	2.80(2)	Ba(7)-O(5W)#5	2.928(19)

bond angles (deg)

Ba(1)

O(3)-Ba(1)-O(1)	73.7(6)	O(20)-Ba(1)-O(19)	43.9(4)
O(3)-Ba(1)-O(16)#1	94.9(5)	O(7)-Ba(1)-O(19)	66.8(4)
O(1)-Ba(1)-O(16)#1	115.0(6)	O(2)-Ba(1)-O(19)	136.2(6)
O(3)-Ba(1)-O(20)	133.0(5)	O(3)-Ba(1)-O(17)#1	157.3(6)
O(1)-Ba(1)-O(20)	153.0(6)	O(1)-Ba(1)-O(17)#1	93.8(6)
O(16)#1-Ba(1)-O(20)	65.6(5)	O(16)#1-Ba(1)-O(17)#1	72.9(5)
O(3)-Ba(1)-O(7)	78.6(5)	O(20)-Ba(1)-O(17)#1	59.9(5)
O(1)-Ba(1)-O(7)	76.3(5)	O(7)-Ba(1)-O(17)#1	117.5(5)
O(16)#1-Ba(1)-O(7)	165.1(5)	O(2)-Ba(1)-O(17)#1	67.6(5)
O(20)-Ba(1)-O(7)	109.2(4)	O(19)-Ba(1)-O(17)#1	72.5(5)

O(3)-Ba(1)-O(2)	91.0(6)	O(3)-Ba(1)-O(6)	64.9(5)
O(1)-Ba(1)-O(2)	42.3(5)	O(1)-Ba(1)-O(6)	120.9(5)
O(16)#1-Ba(1)-O(2)	75.5(6)	O(16)#1-Ba(1)-O(6)	108.9(5)
O(20)-Ba(1)-O(2)	121.1(5)	O(20)-Ba(1)-O(6)	81.1(5)
O(7)-Ba(1)-O(2)	117.6(5)	O(7)-Ba(1)-O(6)	56.2(4)
O(3)-Ba(1)-O(19)	130.2(5)	O(2)-Ba(1)-O(6)	155.6(5)
O(1)-Ba(1)-O(19)	126.7(5)	O(19)-Ba(1)-O(6)	66.3(5)
O(16)#1-Ba(1)-O(19)	109.5(5)	O(17)#1-Ba(1)-O(6)	136.8(5)

Ba(2)

O(21)-Ba(2)-O(7W)	85.3(6)	O(19)-Ba(2)-O(8)	92.8(5)
O(21)-Ba(2)-O(19)	101.3(6)	O(9)-Ba(2)-O(8)	112.0(5)
O(7W)-Ba(2)-O(19)	74.5(5)	O(11)-Ba(2)-O(8)	61.3(5)
O(21)-Ba(2)-O(9)	68.5(6)	O(6)-Ba(2)-O(8)	99.9(5)
O(7W)-Ba(2)-O(9)	133.6(6)	O(7)-Ba(2)-O(8)	44.8(5)
O(19)-Ba(2)-O(9)	145.9(5)	O(21)-Ba(2)-O(10)	113.2(6)
O(21)-Ba(2)-O(11)	90.9(6)	O(7W)-Ba(2)-O(10)	129.8(5)
O(7W)-Ba(2)-O(11)	62.0(5)	O(19)-Ba(2)-O(10)	137.8(5)
O(19)-Ba(2)-O(11)	133.6(5)	O(9)-Ba(2)-O(10)	45.6(5)
O(9)-Ba(2)-O(11)	80.1(5)	O(11)-Ba(2)-O(10)	71.1(5)
O(21)-Ba(2)-O(6)	109.1(6)	O(6)-Ba(2)-O(10)	75.3(5)
O(7W)-Ba(2)-O(6)	144.5(5)	O(7)-Ba(2)-O(10)	73.6(4)
O(19)-Ba(2)-O(6)	71.0(5)	O(8)-Ba(2)-O(10)	68.8(5)
O(9)-Ba(2)-O(6)	81.6(6)	O(21)-Ba(2)-O(5)	66.4(6)
O(11)-Ba(2)-O(6)	145.6(5)	O(7W)-Ba(2)-O(5)	136.7(5)
O(21)-Ba(2)-O(7)	163.9(5)	O(19)-Ba(2)-O(5)	79.5(5)
O(7W)-Ba(2)-O(7)	101.6(5)	O(9)-Ba(2)-O(5)	66.5(5)
O(19)-Ba(2)-O(7)	67.3(5)	O(11)-Ba(2)-O(5)	144.5(5)
O(9)-Ba(2)-O(7)	114.2(5)	O(6)-Ba(2)-O(5)	42.7(5)
O(11)-Ba(2)-O(7)	105.2(5)	O(7)-Ba(2)-O(5)	99.5(5)
O(6)-Ba(2)-O(7)	57.3(5)	O(8)-Ba(2)-O(5)	142.3(5)
O(21)-Ba(2)-O(8)	150.6(6)	O(10)-Ba(2)-O(5)	92.4(5)
O(7W)-Ba(2)-O(8)	73.6(5)		

Ba(3)

O(4)-Ba(3)-O(24)	124.5(6)	O(6W)-Ba(3)-O(3)	102.0(5)
O(4)-Ba(3)-O(4)#2	65.9(7)	O(7)-Ba(3)-O(3)	77.0(5)
O(24)-Ba(3)-O(4)#2	79.6(6)	O(6)-Ba(3)-O(3)	66.4(5)
O(4)-Ba(3)-O(6W)	77.8(6)	O(4)-Ba(3)-O(10)	155.3(6)
O(24)-Ba(3)-O(6W)	131.3(5)	O(24)-Ba(3)-O(10)	72.9(5)
O(4)#2-Ba(3)-O(6W)	71.9(6)	O(4)#2-Ba(3)-O(10)	105.3(6)
O(4)-Ba(3)-O(7)	121.2(5)	O(6W)-Ba(3)-O(10)	77.6(5)
O(24)-Ba(3)-O(7)	75.2(5)	O(7)-Ba(3)-O(10)	77.8(5)
O(4)#2-Ba(3)-O(7)	152.4(5)	O(6)-Ba(3)-O(10)	77.8(5)

O(6W)-Ba(3)-O(7)	134.3(5)	O(3)-Ba(3)-O(10)	143.3(5)
O(4)-Ba(3)-O(6)	98.0(5)	O(4)-Ba(3)-O(4W)	71.7(6)
O(24)-Ba(3)-O(6)	129.8(5)	O(24)-Ba(3)-O(4W)	62.4(5)
O(4)#2-Ba(3)-O(6)	148.4(6)	O(4)#2-Ba(3)-O(4W)	83.8(6)
O(6W)-Ba(3)-O(6)	78.4(5)	O(6W)-Ba(3)-O(4W)	146.8(5)
O(7)-Ba(3)-O(6)	59.1(5)	O(7)-Ba(3)-O(4W)	74.8(5)
O(4)-Ba(3)-O(3)	45.2(5)	O(6)-Ba(3)-O(4W)	118.0(5)
O(24)-Ba(3)-O(3)	124.7(6)	O(3)-Ba(3)-O(4W)	64.7(5)
O(4)#2-Ba(3)-O(3)	109.4(6)	O(10)-Ba(3)-O(4W)	132.0(5)

Ba(4)

O(8)-Ba(4)-O(25)	88.8(6)	O(23)-Ba(4)-O(13)	117.0(5)
O(8)-Ba(4)-O(15)	171.6(5)	O(11)-Ba(4)-O(13)	74.8(5)
O(25)-Ba(4)-O(15)	86.7(6)	O(12)-Ba(4)-O(13)	57.8(5)
O(8)-Ba(4)-O(23)	115.5(6)	O(8)-Ba(4)-O(10)	73.4(5)
O(25)-Ba(4)-O(23)	73.1(6)	O(25)-Ba(4)-O(10)	152.7(5)
O(15)-Ba(4)-O(23)	69.9(6)	O(15)-Ba(4)-O(10)	113.2(5)
O(8)-Ba(4)-O(11)	63.5(5)	O(23)-Ba(4)-O(10)	95.6(6)
O(25)-Ba(4)-O(11)	120.2(6)	O(11)-Ba(4)-O(10)	70.6(5)
O(15)-Ba(4)-O(11)	113.1(5)	O(12)-Ba(4)-O(10)	82.0(5)
O(23)-Ba(4)-O(11)	166.0(6)	O(13)-Ba(4)-O(10)	139.0(5)
O(8)-Ba(4)-O(12)	108.9(5)	O(8)-Ba(4)-O(24)	70.4(5)
O(25)-Ba(4)-O(12)	124.1(6)	O(25)-Ba(4)-O(24)	87.6(5)
O(15)-Ba(4)-O(12)	68.2(5)	O(15)-Ba(4)-O(24)	116.4(5)
O(23)-Ba(4)-O(12)	132.8(6)	O(23)-Ba(4)-O(24)	48.1(5)
O(11)-Ba(4)-O(12)	45.5(5)	O(11)-Ba(4)-O(24)	124.0(5)
O(8)-Ba(4)-O(13)	109.6(5)	O(12)-Ba(4)-O(24)	148.2(5)
O(25)-Ba(4)-O(13)	66.3(5)	O(13)-Ba(4)-O(24)	153.7(5)
O(15)-Ba(4)-O(13)	62.0(5)	O(10)-Ba(4)-O(24)	67.2(5)

Ba(5)

O(12)-Ba(5)-O(20)#3	152.1(5)	O(18)-Ba(5)-O(16)	112.5(6)
O(12)-Ba(5)-O(5W)	98.3(5)	O(13)-Ba(5)-O(16)	98.0(5)
O(20)#3-Ba(5)-O(5W)	87.6(5)	O(14)-Ba(5)-O(16)	145.0(6)
O(12)-Ba(5)-O(18)	139.2(6)	O(12)-Ba(5)-O(17)	135.8(5)
O(20)#3-Ba(5)-O(18)	68.5(6)	O(20)#3-Ba(5)-O(17)	62.5(5)
O(5W)-Ba(5)-O(18)	71.5(5)	O(5W)-Ba(5)-O(17)	114.0(5)
O(12)-Ba(5)-O(13)	63.2(5)	O(18)-Ba(5)-O(17)	43.6(6)
O(20)#3-Ba(5)-O(13)	138.3(5)	O(13)-Ba(5)-O(17)	76.0(5)
O(5W)-Ba(5)-O(13)	114.2(5)	O(14)-Ba(5)-O(17)	94.9(6)
O(18)-Ba(5)-O(13)	84.7(6)	O(16)-Ba(5)-O(17)	71.6(5)
O(12)-Ba(5)-O(14)	69.8(6)	O(12)-Ba(5)-O(15)	67.0(5)
O(20)#3-Ba(5)-O(14)	136.4(6)	O(20)#3-Ba(5)-O(15)	106.6(5)
O(5W)-Ba(5)-O(14)	67.3(5)	O(5W)-Ba(5)-O(15)	165.1(5)

O(18)-Ba(5)-O(14)	69.9(6)	O(18)-Ba(5)-O(15)	117.7(5)
O(13)-Ba(5)-O(14)	47.0(5)	O(13)-Ba(5)-O(15)	57.9(5)
O(12)-Ba(5)-O(16)	97.1(5)	O(14)-Ba(5)-O(15)	103.7(5)
O(20)#3-Ba(5)-O(16)	66.4(5)	O(16)-Ba(5)-O(15)	42.7(5)
O(5W)-Ba(5)-O(16)	147.7(5)	O(17)-Ba(5)-O(15)	77.7(5)

Ba(6)

O(26)-Ba(6)-O(13)	149.7(6)	O(2)#3-Ba(6)-O(26)#4	125.9(6)
O(26)-Ba(6)-O(3W)	69.6(6)	O(17)-Ba(6)-O(26)#4	156.7(6)
O(13)-Ba(6)-O(3W)	81.3(6)	O(1W)-Ba(6)-O(26)#4	72.7(6)
O(26)-Ba(6)-O(2)#3	77.2(6)	O(26)-Ba(6)-O(15)	150.1(6)
O(13)-Ba(6)-O(2)#3	129.3(6)	O(13)-Ba(6)-O(15)	60.2(5)
O(3W)-Ba(6)-O(2)#3	126.2(6)	O(3W)-Ba(6)-O(15)	138.9(5)
O(26)-Ba(6)-O(17)	102.5(6)	O(2)#3-Ba(6)-O(15)	76.1(6)
O(13)-Ba(6)-O(17)	78.6(5)	O(17)-Ba(6)-O(15)	80.5(5)
O(3W)-Ba(6)-O(17)	77.9(6)	O(1W)-Ba(6)-O(15)	67.9(5)
O(2)#3-Ba(6)-O(17)	69.4(5)	O(26)#4-Ba(6)-O(15)	118.4(5)
O(26)-Ba(6)-O(1W)	88.8(6)	O(26)-Ba(6)-O(25)	112.8(5)
O(13)-Ba(6)-O(1W)	114.1(5)	O(13)-Ba(6)-O(25)	64.1(5)
O(3W)-Ba(6)-O(1W)	149.2(6)	O(3W)-Ba(6)-O(25)	101.5(6)
O(2)#3-Ba(6)-O(1W)	65.8(5)	O(2)#3-Ba(6)-O(25)	130.4(6)
O(17)-Ba(6)-O(1W)	129.8(5)	O(17)-Ba(6)-O(25)	142.2(5)
O(26)-Ba(6)-O(26)#4	68.5(6)	O(1W)-Ba(6)-O(25)	66.0(5)
O(13)-Ba(6)-O(26)#4	98.4(6)	O(26)#4-Ba(6)-O(25)	45.1(5)
O(3W)-Ba(6)-O(26)#4	78.8(6)	O(15)-Ba(6)-O(25)	75.7(5)

Ba(7)

O(5)-Ba(7)-O(14)#5	176.3(7)	O(2W)-Ba(7)-O(22)	176.8(7)
O(5)-Ba(7)-O(9)	73.9(5)	O(5)-Ba(7)-O(21)	68.5(6)
O(14)#5-Ba(7)-O(9)	107.9(6)	O(14)#5-Ba(7)-O(21)	115.2(6)
O(5)-Ba(7)-O(18)#5	105.0(6)	O(9)-Ba(7)-O(21)	66.7(5)
O(14)#5-Ba(7)-O(18)#5	73.4(6)	O(18)#5-Ba(7)-O(21)	111.8(6)
O(9)-Ba(7)-O(18)#5	178.3(7)	O(2W)-Ba(7)-O(21)	136.6(6)
O(5)-Ba(7)-O(2W)	77.5(6)	O(22)-Ba(7)-O(21)	46.5(6)
O(14)#5-Ba(7)-O(2W)	99.6(6)	O(5)-Ba(7)-O(5W)#5	108.4(5)
O(9)-Ba(7)-O(2W)	78.8(6)	O(14)#5-Ba(7)-O(5W)#5	68.0(5)
O(18)#5-Ba(7)-O(2W)	102.3(6)	O(9)-Ba(7)-O(5W)#5	111.3(5)
O(5)-Ba(7)-O(22)	104.4(7)	O(18)#5-Ba(7)-O(5W)#5	70.2(5)
O(14)#5-Ba(7)-O(22)	78.5(7)	O(2W)-Ba(7)-O(5W)#5	40.1(5)
O(9)-Ba(7)-O(22)	104.2(7)	O(22)-Ba(7)-O(5W)#5	136.8(5)
O(18)#5-Ba(7)-O(22)	74.8(7)	O(21)-Ba(7)-O(5W)#5	176.5(5)

Symmetry transformations used to generate equivalent atoms:

#1 x+1,y,z #2 -x+1,-y,-z #3 x-1,y,z #4 -x,-y+1,-z
#5 -x+1/2,y-1/2,-z+1/2 #6 -x+1/2,y+1/2,-z+1/2

Table B3. Bond lengths and torsion angles of $Y(Prop)_3$.

bond lengths (Å)			
	Y(1)		
Y(1)-O(8)	2.319(4)	Y(1)-O(3)	2.418(4)
Y(1)-O(1)	2.342(3)	Y(1)-O(5)	2.459(4)
Y(1)-O(7)	2.351(4)	Y(1)-O(2)#1	2.489(4)
Y(1)-O(6)	2.392(4)	Y(1)-O(1)#1	2.502(4)
Y(1)-O(4)	2.394(5)		

bond angles (deg)			
	Y(1)		
O(8)-Y(1)-O(1)	154.06(12)	O(6)-Y(1)-O(5)	53.45(12)
O(8)-Y(1)-O(7)	82.38(15)	O(4)-Y(1)-O(5)	77.53(16)
O(1)-Y(1)-O(7)	79.22(13)	O(3)-Y(1)-O(5)	126.73(16)
O(8)-Y(1)-O(6)	129.47(14)	O(8)-Y(1)-O(2)#1	75.78(15)
O(1)-Y(1)-O(6)	73.58(12)	O(1)-Y(1)-O(2)#1	116.24(13)
O(7)-Y(1)-O(6)	145.80(13)	O(7)-Y(1)-O(2)#1	74.99(15)
O(8)-Y(1)-O(4)	81.72(17)	O(6)-Y(1)-O(2)#1	98.78(14)
O(1)-Y(1)-O(4)	95.24(15)	O(4)-Y(1)-O(2)#1	145.48(15)
O(7)-Y(1)-O(4)	127.70(15)	O(3)-Y(1)-O(2)#	140.43(14)
O(6)-Y(1)-O(4)	75.83(15)	O(5)-Y(1)-O(2)#1	72.42(16)
O(8)-Y(1)-O(3)	75.87(14)	O(8)-Y(1)-O(1)#1	126.05(15)
O(1)-Y(1)-O(3)	81.65(12)	O(1)-Y(1)-O(1)#1	65.29(13)
O(7)-Y(1)-O(3)	74.38(15)	O(7)-Y(1)-O(1)#1	73.57(13)
O(6)-Y(1)-O(3)	120.57(14)	O(6)-Y(1)-O(1)#1	76.40(12)
O(4)-Y(1)-O(3)	53.46(15)	O(4)-Y(1)-O(1)#1	149.72(13)
O(8)-Y(1)-O(5)	77.89(13)	O(3)-Y(1)-O(1)#1	137.32(13)
O(1)-Y(1)-O(5)	126.83(12)	O(5)-Y(1)-O(1)#1	95.35(14)
O(7)-Y(1)-O(5)	145.11(15)	O(2)#1-Y(1)-O(1)#1	51.78(11)

Symmetry transformations used to generate equivalent atoms:
#1 -x+1,-y+1,-z+1

Table B4. Bond lengths and torsion angles of $Sm(Prop)_3$.

bond lengths (Å)

Sm(1)

Sm(1)-O(5)	2.338(10)	Sm(1)-O(4)#2	2.475(11)
Sm(1)-O(3)	2.379(10)	Sm(1)-O(3)#2	2.485(10)
Sm(1)-O(1)	2.400(10)	Sm(1)-O(13)	2.501(10)
Sm(1)-O(14)	2.437(9)	Sm(1)-O(11)#1	2.573(10)
Sm(1)-O(12)#1	2.448(12)		

Sm(2)

Sm(2)-O(9)	2.369(9)	Sm(2)-O(2)#1	2.471(11)
Sm(2)-O(11)	2.369(10)	Sm(2)-O(1)#1	2.516(10)
Sm(2)-O(8)	2.401(10)	Sm(2)-O(7)	2.537(10)
Sm(2)-O(6)	2.416(9)	Sm(2)-O(9)#3	2.618(10)
Sm(2)-O(10)#3	2.417(11)		

bond angles (deg)

Sm(1)

O(5)-Sm(1)-O(3)	75.6(4)	O(14)-Sm(1)-O(3)#2	74.8(3)
O(5)-Sm(1)-O(1)	79.8(3)	O(12)#1-Sm(1)-O(3)#2	116.1(4)
O(3)-Sm(1)-O(1)	148.7(3)	O(4)#2-Sm(1)-O(3)#2	51.2(3)
O(5)-Sm(1)-O(14)	145.8(4)	O(5)-Sm(1)-O(13)	72.6(3)
O(3)-Sm(1)-O(14)	110.3(4)	O(3)-Sm(1)-O(13)	79.0(3)
O(1)-Sm(1)-O(14)	101.0(4)	O(1)-Sm(1)-O(13)	75.3(3)
O(5)-Sm(1)-O(12)#1	138.8(4)	O(14)-Sm(1)-O(13)	141.2(3)
O(3)-Sm(1)-O(12)#1	75.4(3)	O(12)#1-Sm(1)-O(13)	73.7(4)
O(1)-Sm(1)-O(12)#1	113.4(3)	O(4)#2-Sm(1)-O(13)	140.0(4)
O(14)-Sm(1)-O(12)#1	72.7(4)	O(3)#2-Sm(1)-O(13)	139.0(3)
O(5)-Sm(1)-O(4)#2	75.5(4)	O(5)-Sm(1)-O(11)#1	134.9(3)
O(3)-Sm(1)-O(4)#2	115.5(3)	O(3)-Sm(1)-O(11)#1	124.0(3)
O(1)-Sm(1)-O(4)#2	75.8(3)	O(1)-Sm(1)-O(11)#1	64.2(3)
O(14)-Sm(1)-O(4)#2	71.7(4)	O(14)-Sm(1)-O(11)#1	71.1(3)
O(12)#1-Sm(1)-O(4)#2	144.3(4)	O(12)#1-Sm(1)-O(11)#1	50.8(3)
O(5)-Sm(1)-O(3)#2	77.4(3)	O(4)#2-Sm(1)-O(11)#1	117.3(3)
O(3)-Sm(1)-O(3)#2	66.8(4)	O(3)#2-Sm(1)-O(11)#1	145.8(3)
O(1)-Sm(1)-O(3)#2	125.9(3)	O(13)-Sm(1)-O(11)#1	72.8(3)

Sm(2)

O(9)-Sm(2)-O(11)	82.9(3)	O(2)#1-Sm(2)-O(1)#1	51.1(3)
O(9)-Sm(2)-O(8)	78.9(3)	O(9)-Sm(2)-O(7)	128.5(4)
O(11)-Sm(2)-O(8)	156.6(3)	O(11)-Sm(2)-O(7)	148.6(3)
O(9)-Sm(2)-O(6)	152.5(3)	O(8)-Sm(2)-O(7)	52.0(3)
O(11)-Sm(2)-O(6)	78.4(3)	O(6)-Sm(2)-O(7)	71.5(3)
O(8)-Sm(2)-O(6)	123.5(3)	O(10)#3-Sm(2)-O(7)	82.1(4)

O(9)-Sm(2)-O(10)#3	115.5(3)	O(2)#1-Sm(2)-O(7)	71.3(3)
O(11)-Sm(2)-O(10)#3	85.3(4)	O(1)#1-Sm(2)-O(7)	113.9(3)
O(8)-Sm(2)-O(10)#3	89.3(4)	O(9)-Sm(2)-O(9)#3	65.0(4)
O(6)-Sm(2)-O(10)#3	83.0(3)	O(11)-Sm(2)-O(9)#3	81.6(3)
O(9)-Sm(2)-O(2)#1	83.8(4)	O(8)-Sm(2)-O(9)#3	77.4(3)
O(11)-Sm(2)-O(2)#1	116.6(3)	O(6)-Sm(2)-O(9)#3	130.6(3)
O(8)-Sm(2)-O(2)#1	76.0(3)	O(10)#3-Sm(2)-O(9)#3	50.6(3)
O(6)-Sm(2)-O(2)#1	86.8(4)	O(2)#1-Sm(2)-O(9)#3	142.2(3)
O(10)#3-Sm(2)-O(2)#1	153.3(3)	O(1)#1-Sm(2)-O(9)#3	133.6(3)
O(9)-Sm(2)-O(1)#1	78.7(3)	O(7)-Sm(2)-O(9)#3	111.2(3)
O(11)-Sm(2)-O(1)#1	65.5(3)		
O(8)-Sm(2)-O(1)#1	124.1(4)		
O(6)-Sm(2)-O(1)#1	75.3(3)		
O(10)#3-Sm(2)-O(1)#1	146.4(4)		

Symmetry transformations used to generate equivalent atoms:

#1 -x+1,-y+1,-z+1 #2 -x,-y+1,-z+1 #3 -x+1,-y,-z+1

Compound	Geometry[a]	S-value
$Gd(Prop)_3$ Gd(1)	HBPY-8	13.364
	CU-8	8.846
	SAPR-8	3.859
	TDD-8	**3.067**
	JGBF-8	12.797
	JETBPY-8	25.967
	JBTP-8	3.896
	BTPR-8	3.389
	JSD-8	5.822
	ETBPY-8	22.140
	TT-8	9.598
$Gd(Prop)_3$ Gd(3)	HBPY-8	13.367
	CU-8	9.903
	SAPR-8	4.602
	TDD-8	**2.966**
	JGBF-8	12.949
	JETBPY-8	25.628
	JBTP-8	4.182
	BTPR-8	3.640
	JSD-8	6.247
	ETBPY-8	21.996
	TT-8	9.828
$Gd(Prop)_3$ Gd(2)	EP-9	34.216
	HH-9	8.255
	MFF-9	**1.497**
$Gd(Prop)_3$ Gd(4)	EP-9	34.459
	HH-9	8.671
	MFF-9	**1.508**

TABLE B.5: Geometry distortion analysis for $Gd(Prop)_3$ using S-parameter [217] calculated with SHAPE [228]. Closer values for the geometry of each metal center are reported in bold. [a]HBPY-8 = Hexagonal bipyramid; CU-8 = Cube, SAPR-8 = Square antiprism; TDD-8 = Triangular dodecahedron; JGBF-8 = Johnson – Gyrobifastigium; JETBPY-8 = Johnson - Elongated triangular bipyramid; JBTP-8 = Biaugmented trigonal prism; BTPR-8 = Biaugmented trigonal prism; JSD-8 = Snub disphenoid; ETBPY-8 = Elongated trigonal bipyramid; TT-8 = Triakis tetrahedron, EP-9 = Enneagon; HH-9 = Hula-hoop; MFF-9 = Muffin.

Compound	Geometry[a]	S-value
$Ba(Prop)_2$ Ba(1)	EP-9	21.609
	HH-9	**6.884**
	MFF-9	8.229
$Ba(Prop)_2$ Ba(3)	EP-9	35.273
	HH-9	10.485
	MFF-9	**2.404**
$Ba(Prop)_2$ Ba(4)	EP-9	22.666
	HH-9	**4.264**
	MFF-9	9.636
$Ba(Prop)_2$ Ba(5)	EP-9	23.872
	HH-9	**7.274**
	MFF-9	8.584
$Ba(Prop)_2$ Ba(6)	EP-9	36.979
	HH-9	9.55
	MFF-9	**2.120**
$Ba(Prop)_2$ Ba(2)	HD-10	10.795
	JATDI-10	16.233
	JBCSAPR-10	7.693
	JMBIC-10	7.595
	JSPC-10	6.042
	SDD-10	5.000
	TD-10	**4.334**
$Ba(Prop)_2$ Ba(7)	**HBPY-8**	**6.819**
	CU-8	7.764
	SAPR-8	17.301
	TDD-8	14.617
	JGBF-8	13.258
	JETBPY-8	19.496
	JBTP-8	15.575
	BTPR-8	15.295
	JSD-8	14.326
	ETBPY-8	16.862
	TT-8	8.575

TABLE B.6: Geometry distortion analysis for $Ba(Prop)_2$ using S-parameter [217] calculated with SHAPE [228]. Closer values for the geometry of each metal center are reported in bold. [a]HBPY-8 = Hexagonal bipyramid; CU-8 = Cube, SAPR-8 = Square antiprism; TDD-8 = Triangular dodecahedron; JGBF-8 = Johnson – Gyrobifastigium; JETBPY-8 = Johnson - Elongated triangular bipyramid; JBTP-8 = Biaugmented trigonal prism; BTPR-8 = Biaugmented trigonal prism; JSD-8 = Snub disphenoid; ETBPY-8 = Elongated trigonal bipyramid; TT-8 = Triakis tetrahedron, EP-9 = Enneagon; HH-9 = Hula-hoop; MFF-9 = Muffin; HD-10 = Hexadecahedron; JADTI-10 = Augmented tridiminished icosahedron; JBCSAPR-10 = Bicapped square antiprism; JMBIC-10 = Metabidiminished icosahedron; JSPC = Sphenocorona; SDD-10 = Staggered dodecahedron; TD-10 = Tetradecahedron.

Compound	Geometry[a]	S-value
$Y(Prop)_3$ Y(1)	EP-9	34.539
	HH-9	9.831
	MFF-9	**1.973**

TABLE B.7: Geometry distortion analysis for $Y(Prop)_3$ using S-parameter [217] calculated with SHAPE [228]. Closer values for the geometry of each metal center are reported in bold. [a]EP-9 = Enneagon, HH-9 = Hula-hoop, MFF-9 = Muffin.

Compound	Geometry[a]	S-value
$Sm(Prop)_3$ Sm(1)	EP-9	31.488
	HH-9	7.099
	MFF-9	**2.772**
$Sm(Prop)_3$ Sm(2)	EP-9	31.554
	HH-9	10.261
	MFF-9	**3.388**

TABLE B.8: Geometry distortion analysis for $Sm(Prop)_3$ using S-parameter [217] calculated with SHAPE [228]. Closer values for the geometry of each metal center are reported in bold. [a]EP-9 = Enneagon, HH-9 = Hula-hoop, MFF-9 = Muffin.

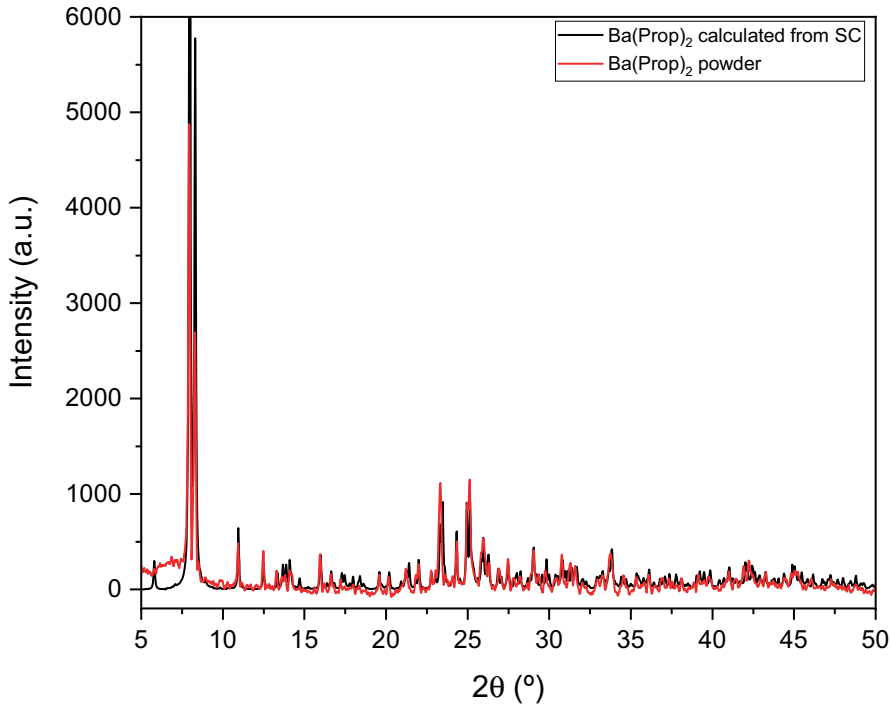


FIGURE B.10: Comparison of the measured PXRD and the pattern calculated from the single crystal (SC) structure for $Ba(Prop)_2$.

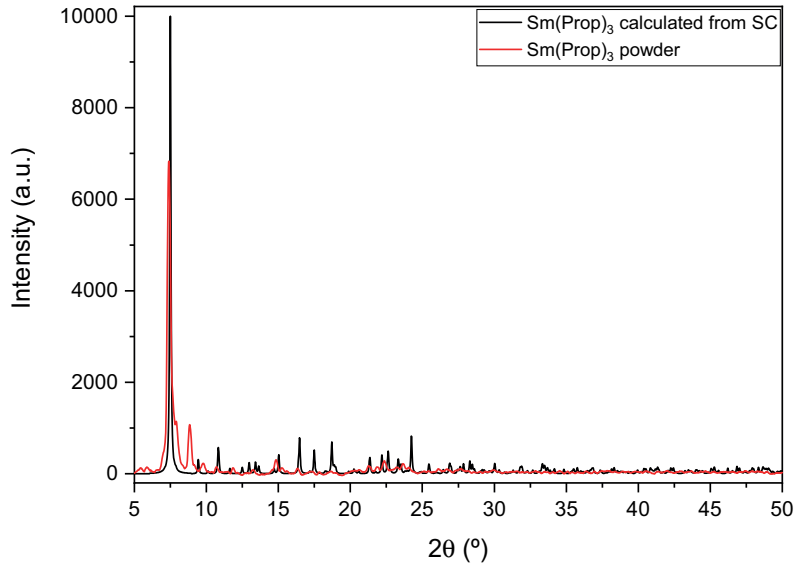


FIGURE B.11: Comparison of the measured PXRD and the pattern calculated from the single crystal (SC) structure for $Sm(Prop)_3$.

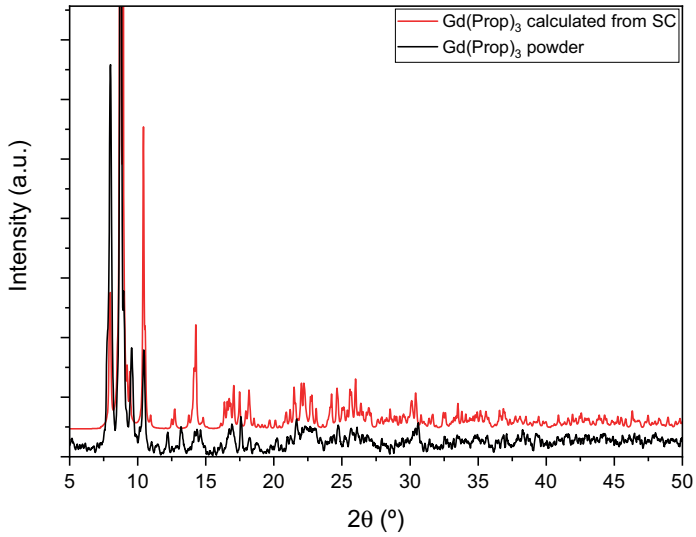


FIGURE B.12: Comparison of the measured PXRD and the pattern calculated from the single crystal (SC) structure for $Gd(Prop)_3$.

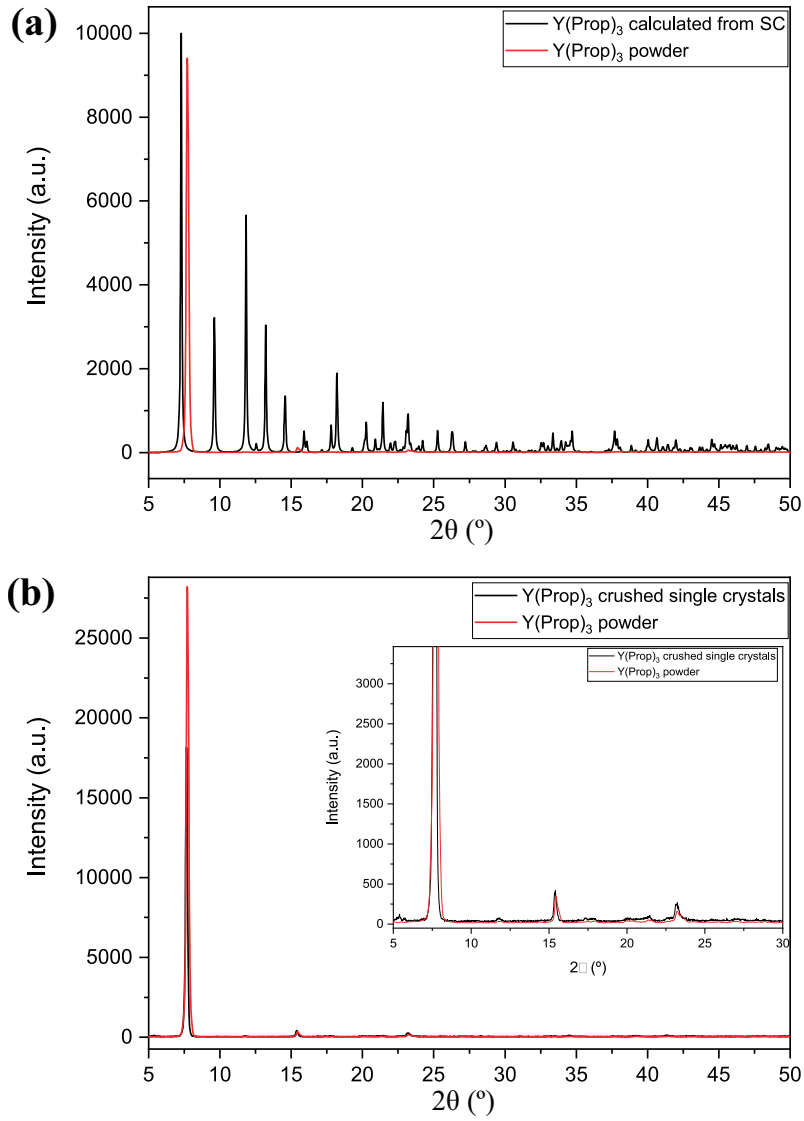


FIGURE B.13: (a) Unmatching PXRD and the pattern calculated from the single crystal (SC) structure for $Y(Prop)_3$. (b) XRD comparison between a sample of the crushed SC from (a) and the synthesized $Y(Prop)_3$ powder. The matching between the two is suggesting the possibility of the existence of various types of SC in the same crystallization vessel, with a preferential orientation exhibited by the measured SC.

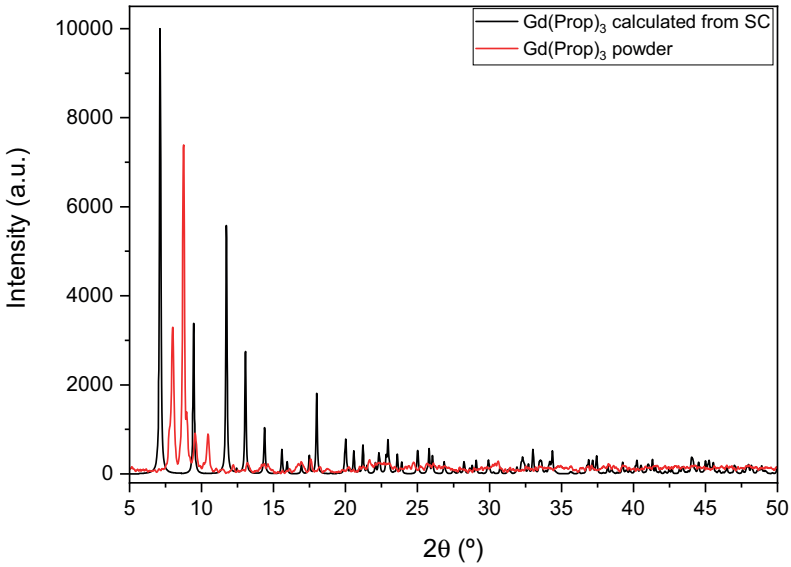


FIGURE B.14: Comparison between PXRD and the pattern calculated from the single crystal (SC) structure for $Gd(Prop)_3$ obtained through recrystallization through slow evaporation in MeOH, exhibiting an unmatching pattern.

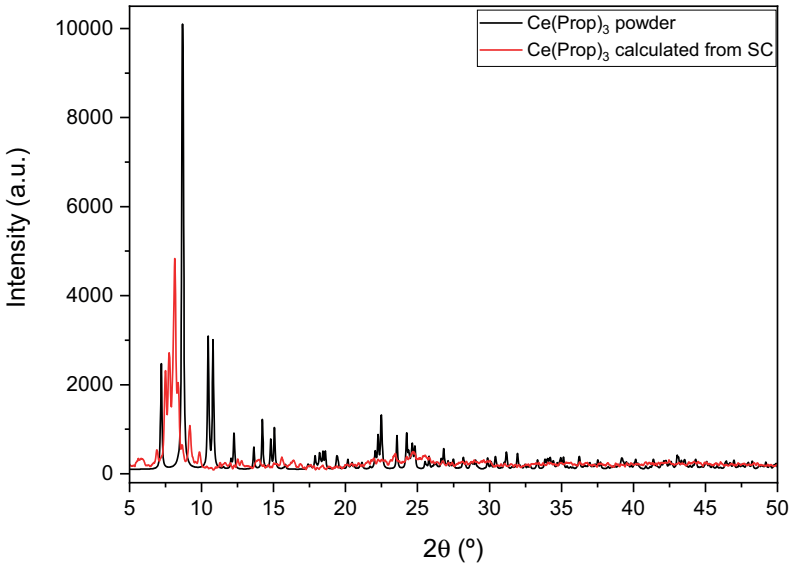


FIGURE B.15: Comparison between PXRD and the pattern calculated from the single crystal (SC) structure for $Ce(Prop)_3$ obtained through recrystallization through slow evaporation in MeOH, exhibiting an unmatching pattern.

Table B9. Bond lengths and torsion angles of $Gd(Prop)_3$ obtained by recrystallization in MeOH.

bond lengths (Å)			
	Gd(1)		
Gd(1)-O(7)	2.293(11)	Gd(1)-O(2)	2.476(9)
Gd(1)-O(3)	2.398(8)	Gd(1)-O(6)	2.493(10)
Gd(1)-O(8)	2.414(9)	Gd(1)-O(4)#1	2.522(10)
Gd(1)-O(1)	2.434(13)	Gd(1)-O(3)#1	2.556(9)
Gd(1)-O(5)	2.441(9)		

bond angles (deg)			
	Gd(1)		
O(7)-Gd(1)-O(3)	153.3(3)	O(1)-Gd(1)-O(6)	78.6(4)
O(7)-Gd(1)-O(8)	83.7(3)	O(5)-Gd(1)-O(6)	52.8(3)
O(3)-Gd(1)-O(8)	79.3(3)	O(2)-Gd(1)-O(6)	128.2(4)
O(7)-Gd(1)-O(1)	78.9(5)	O(7)-Gd(1)-O(4)#1	78.6(4)
O(3)-Gd(1)-O(1)	95.3(4)	O(3)-Gd(1)-O(4)#1	115.9(3)
O(8)-Gd(1)-O(1)	127.4(4)	O(8)-Gd(1)-O(4)#1	74.6(4)
O(7)-Gd(1)-O(5)	129.6(3)	O(1)-Gd(1)-O(4)#1	145.9(4)
O(3)-Gd(1)-O(5)	72.8(3)	O(5)-Gd(1)-O(4)#1	98.3(4)
O(8)-Gd(1)-O(5)	144.7(3)	O(2)-Gd(1)-O(4)#1	140.4(4)
O(1)-Gd(1)-O(5)	77.3(4)	O(6)-Gd(1)-O(4)#1	72.4(4)
O(7)-Gd(1)-O(2)	74.1(4)	O(7)-Gd(1)-O(3)#1	127.8(4)
O(3)-Gd(1)-O(2)	81.5(3)	O(3)-Gd(1)-O(3)#1	66.1(3)
O(8)-Gd(1)-O(2)	74.3(4)	O(8)-Gd(1)-O(3)#1	73.1(3)
O(1)-Gd(1)-O(2)	53.3(4)	O(1)-Gd(1)-O(3)#1	150.9(4)
O(5)-Gd(1)-O(2)	121.3(4)	O(5)-Gd(1)-O(3)#1	75.9(3)
O(7)-Gd(1)-O(6)	79.3(3)	O(2)-Gd(1)-O(3)#1	137.4(3)
O(3)-Gd(1)-O(6)	125.4(3)	O(6)-Gd(1)-O(3)#1	93.9(3)
O(8)-Gd(1)-O(6)	145.2(4)	O(4)#1-Gd(1)-O(3)#1	50.6(3)

Symmetry transformations used to generate equivalent atoms:
#1 -x+1,-y+1,-z+1

Table B10. Bond lengths and torsion angles of $Ce(Prop)_3$ obtained by recrystallization in MeOH.

bond lengths (Å)			
Ce(1)			
Ce(1)-O(9)	2.497(9)	Ce(1)-O(6)	2.574(8)
Ce(1)-O(3)	2.518(9)	Ce(1)-O(5)	2.612(8)
Ce(1)-O(12)#1	2.524(9)	Ce(1)-O(8)	2.656(9)
Ce(1)-O(2)	2.527(8)	Ce(1)-O(1)	2.731(8)
Ce(1)-O(7)	2.555(9)	Ce(1)-O(11)#1	2.749(8)
Ce(2)			
Ce(2)-O(1)	2.455(10)	Ce(2)-O(2W)	2.536(9)
Ce(2)-O(11)	2.473(9)	Ce(2)-O(4)	2.591(9)
Ce(2)-O(3W)	2.499(8)	Ce(2)-O(3)	2.650(8)
Ce(2)-O(1W)	2.504(10)	Ce(2)-O(9)#2	2.678(7)
Ce(2)-O(10)#2	2.524(9)		

bond angles (deg)			
Ce(1)			
O(9)-Ce(1)-O(3)	78.5(3)	O(2)-Ce(1)-O(8)	73.4(3)
O(9)-Ce(1)-O(12)#1	113.3(3)	O(7)-Ce(1)-O(8)	50.4(3)
O(3)-Ce(1)-O(12)#1	152.0(3)	O(6)-Ce(1)-O(8)	139.3(3)
O(9)-Ce(1)-O(2)	148.5(3)	O(5)-Ce(1)-O(8)	154.0(3)
O(3)-Ce(1)-O(2)	113.1(3)	O(9)-Ce(1)-O(1)	135.4(3)
O(12)#1-Ce(1)-O(2)	70.9(3)	O(3)-Ce(1)-O(1)	63.8(3)
O(9)-Ce(1)-O(7)	80.4(3)	O(12)#1-Ce(1)-O(1)	111.2(3)
O(3)-Ce(1)-O(7)	76.9(3)	O(2)-Ce(1)-O(1)	49.6(3)
O(12)#1-Ce(1)-O(7)	128.8(3)	O(7)-Ce(1)-O(1)	69.0(3)
O(2)-Ce(1)-O(7)	74.5(3)	O(6)-Ce(1)-O(1)	114.7(3)
O(9)-Ce(1)-O(6)	80.7(3)	O(5)-Ce(1)-O(1)	67.8(3)
O(3)-Ce(1)-O(6)	82.2(3)	O(8)-Ce(1)-O(1)	105.3(3)
O(12)#1-Ce(1)-O(6)	75.3(3)	O(9)-Ce(1)-O(11)#1	64.1(3)
O(2)-Ce(1)-O(6)	128.6(3)	O(3)-Ce(1)-O(11)#1	136.6(3)
O(7)-Ce(1)-O(6)	154.1(3)	O(12)#1-Ce(1)-O(11)#1	49.3(3)
O(9)-Ce(1)-O(5)	127.2(3)	O(2)-Ce(1)-O(11)#1	110.4(3)
O(3)-Ce(1)-O(5)	76.7(3)	O(7)-Ce(1)-O(11)#1	115.3(3)
O(12)#1-Ce(1)-O(5)	76.1(3)	O(6)-Ce(1)-O(11)#1	71.1(3)
O(2)-Ce(1)-O(5)	84.3(3)	O(5)-Ce(1)-O(11)#1	108.2(3)
O(7)-Ce(1)-O(5)	135.9(3)	O(8)-Ce(1)-O(11)#1	68.9(3)

O(6)-Ce(1)-O(5)	50.3(3)	O(1)-Ce(1)-O(11)#1	159.1(3)
O(9)-Ce(1)-O(8)	76.1(3)		
O(3)-Ce(1)-O(8)	124.1(3)		
O(12)#1-Ce(1)-O(8)	83.9(3)		

Ce(2)

O(1)-Ce(2)-O(11)	141.8(3)	O(2W)-Ce(2)-O(4)	77.9(3)
O(1)-Ce(2)-O(3W)	74.0(3)	O(1)-Ce(2)-O(3)	65.9(3)
O(11)-Ce(2)-O(3W)	141.2(3)	O(11)-Ce(2)-O(3)	101.8(3)
O(1)-Ce(2)-O(1W)	69.8(3)	O(3W)-Ce(2)-O(3)	77.7(3)
O(11)-Ce(2)-O(1W)	72.4(3)	O(1W)-Ce(2)-O(3)	78.7(3)
O(3W)-Ce(2)-O(1W)	142.5(3)	O(10)#2-Ce(2)-O(3)	141.9(3)
O(1)-Ce(2)-O(10)#2	78.4(3)	O(2W)-Ce(2)-O(3)	125.5(3)
O(11)-Ce(2)-O(10)#2	114.8(3)	O(4)-Ce(2)-O(3)	49.7(3)
O(3W)-Ce(2)-O(10)#2	80.2(3)	O(1)-Ce(2)-O(9)#2	110.2(3)
O(1W)-Ce(2)-O(10)#2	101.7(4)	O(11)-Ce(2)-O(9)#2	65.6(3)
O(1)-Ce(2)-O(2W)	144.0(3)	O(3W)-Ce(2)-O(9)#2	125.7(3)
O(11)-Ce(2)-O(2W)	73.3(3)	O(1W)-Ce(2)-O(9)#2	77.4(3)
O(3W)-Ce(2)-O(2W)	75.9(3)	O(10)#2-Ce(2)-O(9)#2	50.4(3)
O(1W)-Ce(2)-O(2W)	141.5(3)	O(2W)-Ce(2)-O(9)#2	72.9(3)
O(10)#2-Ce(2)-O(2W)	77.4(3)	O(4)-Ce(2)-O(9)#2	135.9(3)
O(1)-Ce(2)-O(4)	112.9(3)	O(3)-Ce(2)-O(9)#2	155.5(3)
O(11)-Ce(2)-O(4)			
O(3W)-Ce(2)-O(4)	76.1(3)		
O(1W)-Ce(2)-O(4)	109.1(4)		
O(10)#2-Ce(2)-O(4)	149.2(3)		

Symmetry transformations used to generate equivalent atoms:

#1 -x+1,y+1/2,-z+3/2 #2 -x+1,y-1/2,-z+3/2

Compound	Geometry[a]	S-value
$Gd(Prop)_3$ Gd(1)	EP-9	33.989
	HH-9	10.049
	MFF-9	**2.007**

TABLE B.11: Geometry distortion analysis for $Gd(Prop)_3$ obtained by recrystallization in MeOH using S-parameter [217] calculated with SHAPE [228]. Closer values for the geometry of each metal center are reported in bold. [a]EP-9 = Enneagon, HH-9 = Hula-hoop, MFF-9 = Muffin.

Compound	Geometry[a]	S-value
$Ce(Prop)_3$ Ce(1)	HD-10	6.249
	JATDI-10	18.047
	JBCSAPR-10	3.932
	JMBIC-10	7.661
	JSPC-10	**3.344**
	SDD-10	5.606
	TD-10	4.621
$Ce(Prop)_3$ Ce(2)	EP-9	33.286
	HH-9	6.928
	MFF-9	**2.282**

TABLE B.12: Geometry distortion analysis for $Ce(Prop)_3$ obtained by recrystallization in MeOH using S-parameter [217] calculated with SHAPE [228]. Closer values for the geometry of each metal center are reported in bold. [a]EP-9 = Enneagon; HH-9 = Hula-hoop; MFF-9 = Muffin; HD-10 = Hexadecahedron; JADTI-10 = Augmented tridiminished icosahedron; JBCSAPR-10 = Bicapped square antiprism; JMBIC-10 = Metabidiminished icosahedron; JSPC = Sphenocorona; SDD-10 = Staggered dodecahedron; TD-10 = Tetradecahedron.

C

Appendix to Chapter 3

C.1 Solution preparation procedure

C.1.1 Optimized YBCO solution

The preparation of YBCO precursor solutions follows the same procedure independently of the stoichiometries or concentration. The solvents of choice are a mixture in the ratio (1:1) of Propionic Acid (HProp) and Methanol (MeOH) (Methanol, 99.9 %, anhydrous (max. 0.003 $\%H_2O$), Scharlab) in which metal propionate precursors of yttrium, barium and copper are dissolved. Synthetic procedures and characterization of the latter compounds may be found in Appendix B. The optimized solution sees the addition of different $\%_{v/v}$ of Monoethanolamine (MEA) (Monoethanolamine, purified by redistillation, $\geq$ 99.5 %, Sigma Aldrich). In this thesis, optimized solutions of two concentrations for spin-coating deposition were used: 1.75 M and 1.5 M in sum of metal salts. These concentrations were only possible with the employment of MEA: as explained in Chapter 3, MEA aids complete precursors dissolution, increases the stability of solutions and the homogeneity and thickness of the final precursor films. Solutions of 1.75M are the highest concentration possible with the optimized (Cu:MEA) molar ratio. If higher concentrations are desired, this ratio should be increased, but as seen in 3.2.4, an amine excess is yielding an unfavourable outcome of the nanocrystalline precursor films. Solutions of this concentration are stable during several months, ranging between two months average for the most Cu-rich compositions and over four months for the (2:3) composition, the least Cu-rich[1]. The 1.5 M concentration is a more versatile solution, which yields

[1] $Cu(Prop)_2$ is the precursor which shows major easiness to precipitation, thus the stability is highest for the composition with less copper.

nanocrystalline precursor films of similar thickness and displays endured stability of over a year: for this reason, this solution concentration was widely employed. It must be specified that any desired concentration lower than the 1.75 M is possible, but the optimized (Cu:MEA) ratio must be maintained such for each composition in order to obtain highly homogeneous nanocrystalline precursor films. If no amine additive is used, only a maximum total concentration of 1 M in sum of salts is possible due to solubility limitations of the metal propionates precursors.

The procedure for the preparation of an optimized solution, despite of concentration and composition, starts with the process of weighing the MEA in the round-bottom flask used for solution preparation. This step is crucial as a precise control of the addition of MEA is needed: the high density of MEA is impeding the use of classical micropipettes and standard syringes are lacking accuracy. As MEA suffers from rapid evaporation, this step is performed rapidly, but never overlooking high precision. When the desired amount of MEA is reached, an oval-shaped magnetic stirrer is added[2] and the flask is placed on a heating plate. The highly hygroscopic nature of anhydrous MeOH implies the use of a flux of Argon (Ar) to maintain inert conditions during the reaction time. The first solvent to be added is HProp, done while starting the magnetic stirring (450 rpm on a Sartorius Analytical Balance). MeOH is successively added under stirring and complete homogenization is awaited. The first metal propionate precursor to be added is $Ba(Prop)_2$, which shows a prompt dissolution. $Cu(Prop)_2$ is the following one, while the heating plate is set to 30 ºC. Once the temperature is reached, the system is left in these conditions during 30 min, time needed for the complete dissolution of this precursor. Consequently, $Y(Prop)_3$ is added and the system is allowed to reach complete dissolution during 30 min more. Finally, the solution is cooled down, brought to volume in a volumetric flask and filtered: considering the high viscosity of these kind of solutions, special filters for highly viscous solutions are needed (Millex Syringe Filter, Hydrophilic PTFE, HPF, Non-sterile, 0.20 µm pore size, 25 mm diameter, Millex-LCR hydrophilic PTFE membrane with glass fiber prefilter, domed housing). The obtained solution is stored in a vial with screw cap under Ar atmosphere. How the solution is stored has been observed to have deep effects on its rheological properties and stability, and is discussed in 3.2.7.

C.1.1.1 Rheological characterization

Rheological properties for optimized solutions of the two concentrations for each composition employed are shown in the following Table C.1. The evolution of H_2Owt% over time (during the first month) for each composition is displayed in the graph in Fig. C.1. It may be noted how all solutions follow a similar trend. The compositions more rich in copper exhibit a lower

[2]The magnetic stirrer should not be added to the flask before weighing the MEA as it might interfere with the analytical balance's measurement system (based on the principle of "magnetic force restoration", through the use of an electromagnet).

Composition	Concentration (M)	Water content (wt%)	Viscosity (mPa·s)	Contact Angle (°)
(2:3)	1.5M + 3.86%$_{v/v}$ MEA	0.77% ± 0.06	11.91 ± 0.05	17 ± 0.1
(2:3)	1.75M + 4.3%$_{v/v}$ MEA	0.89% ± 0.06	17.4 ± 0.05	18.1 ± 0.1
(3:6)	1.5M + 3.4%$_{v/v}$ MEA	0.76% ± 0.06	10.46 ± 0.05	16 ± 0.1
(3:6)	1.75M + 4%$_{v/v}$ MEA	0.79% ± 0.06	13.1 ± 0.05	18 ± 0.1
(3:7)	1.5M + 3.4%$_{v/v}$ MEA	0.61% ± 0.06	8.5 ± 0.05	17 ± 0.1
(3:7)	1.75M + 4%$_{v/v}$ MEA	0.77% ± 0.06	13.42 ± 0.05	18 ± 0.1
(4:11)	1.5M + 3.5%$_{v/v}$ MEA	0.65% ± 0.06	6.93 ± 0.05	15.9 ± 0.1
(4:11)	1.75M + 4.1%$_{v/v}$ MEA	0.82% ± 0.06	9.78 ± 0.05	17.5 ± 0.1
Y-rich (4:11)	1.5M + 3.51%$_{v/v}$ MEA	0.64% ± 0.06	7.6 ± 0.05	16.9 ± 0.1
Y-rich (4:11)	1.75M + 4.1%$_{v/v}$ MEA	0.80% ± 0.06	10.1 ± 0.05	18 ± 0.1

TABLE C.1: Rheological properties of optimized YBCO precursor solutions for the five compositions and two concentrations considered in this thesis. Water content, viscosity and contact angle reported here are measured on the day of the preparation of the solution to confirm reproducibility of the rheological properties, but also of the measurements.

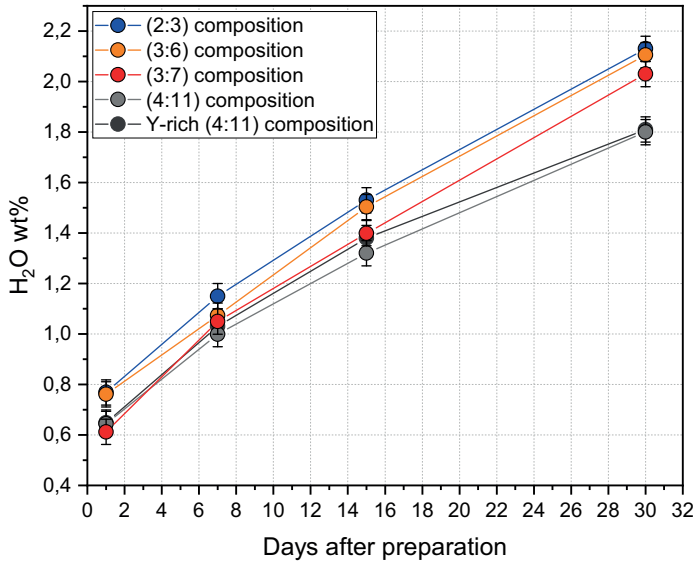


FIGURE C.1: Evolution of H_2Owt% for solutions of each composition during the first month after their preparation.

H_2Owt%, generally due to the stoichiometry: the initial values are majorly dictated by the coordination H_2O in the metal propionate precursors, thus Cu-rich solutions have lower starting value of H_2Owt% as this precursor is the only anhydrous one of the three used. The increase

in H_2Owt%, as explained in 3.2.5 is governed by Fischer Esterification reaction: as the reaction conditions are the same for all the solutions, slight differences may be ascribed to catalytic behaviour of the solution components (especially, metal cations may have a catalytic effect for this reaction [164]).

C.1.1.2 Supplementary Information

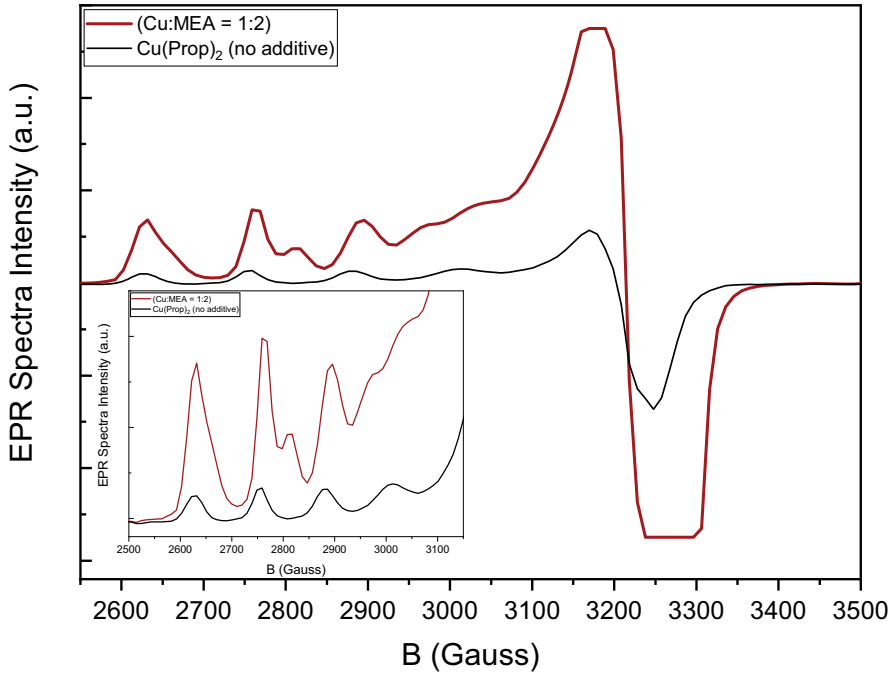


FIGURE C.2: EPR spectra of a mixture of HProp and MeOH (1:1) and $Cu(Prop)_2$ without MEA (black), and with an excess of MEA (8%$_{v/v}$ MEA) (dark red). Inset shows the magnification of the main bands.

C.1.2 Optimized REBCO solution

The preparation of optimized solutions for REBCO films follows the same procedure explained in C.1.1 for the YBCO precursor solution, with the only difference being the replacement of $Y(Prop)_3$ for $Sm(Prop)_3$, $Gd(Prop)_3$ or $Yb(Prop)_3$ in the final powder precursor addition. The reaction time is maintained the same, as these powder precursors show similar solubility in the solvent mixture used. As specified in 3.3, only (3:7) composition solutions were tested and the concentration was, for all REBCO precursor solutions, 1.5 M with the addition of the optimized %$_{v/v}$ MEA. The resulting solutions presented similar stability as for the case of the YBCO one.

C.1.3 Solutions with different amine additives

The preparation of solutions with different amine additives consisted in, generally, the same preparation procedure as for the optimized case with MEA. Nonetheless, several of the tested amines are added dropwise to the HProp under stirring, followed by the addition of MeOH. The total volume, order of addition of precursors, temperature of heating, reaction time and storage of these solutions are not varied, in order to ensure reproducibility of the process and a proper comparison to the case of MEA. However, some additives presented almost instantaneous dissolution of the precursors after addition, especially evident for en (when the optimal (Cu:en) molar ratio is reached) and pyridine, suggesting shorter possible reaction times may be implemented in a future continuation of this study. The resulting solutions present variable stability, ranging from a week or less for amines such as Et_3N, TEA, and 2,6-Lutidine, to more than a month for Py and MEA-Py mixture, 2-(Methylamino)pyridine, 4-Formylpyridine and 2-Acetylpyridine[3]. The difference in stability is possibly due to the goodness of the Cu-amine complex formed.

[3]The colour of the solution with 2-Acetylpyridine changed during ageing from bright blue to dark brownish-black, suggesting a reaction is occurring with time. If this amine is employed in further studies, this aspect must not be ignored.

C.1.3.1 Supplementary Information

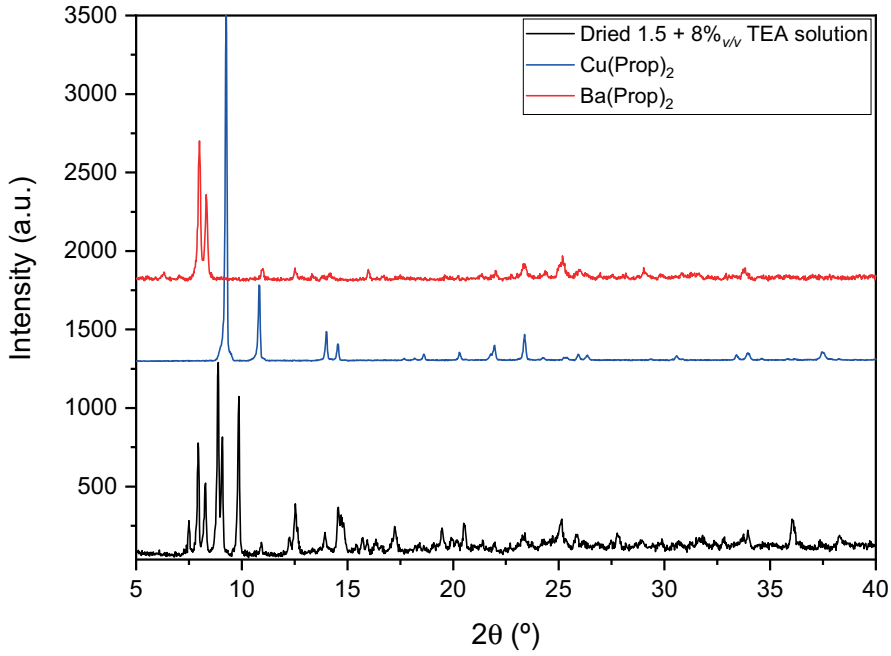


FIGURE C.3: Comparison of XRD pattern of the dried solution of 1.5 M with 8%$_{v/v}$ TEA (black) with the XRD patterns of the powders of $Cu(Prop)_2$ and $Ba(Prop)_2$, the only precursors present when the detrimental precipitation occurred.

D

Appendix to Chapter 4

D.1 Experimental set-up for TLAG P_{O_2}-*route* experiments

The experimental set-up for the growth of YBCO films through TLAG P_{O_2}-*route* was designed and developed within the group. A schematic representation may be found in Fig. D.1. As explained in the Chapter, the great advantage of the P_{O_2}-*route* is the possibility of decoupling the elimination of $BaCO_3$ from the nucleation and growth of YBCO, as these occur in two different steps:

1. **Low-P_{O_2} heating:** the sample is heated to reach the desired T_{set} at a constant $P_{O_{2,base}}$ below the YBCO instability line (for the experiments described in this thesis, $P_{O_2,base}$ values of 10^{-5} bar and 10^{-6} bar have been employed). The impossibility of YBCO crystallization at given conditions allows for accurate control of the elimination of $BaCO_3$ through its reaction with CuO to form the crystalline precursor phases for the transient liquid formation: the mixed oxide $BaCu_2O_2$ and Cu_2O.

2. **P_{O_2} jump:** rapid variation of P_{O_2} at constant temperature to reach the desired $P_{O_2,final}$ of the process. During the pressure jump the [Ba-Cu-O] transient liquid is formed, followed by the dissolution of the yttria nanoparticles in the liquid, the migration of the Y atoms to the nucleation front and, consequently, the formation of stable YBCO nuclei, resulting in the growth of the YBCO film.

The rapidity of the pressure variation is key to the success of the process as the growth of YBCO through TLAG experiences ultrafast growth rates. A slow P_{O_2} change would favour

the nucleation of undesired crystalline phases when crossing their regions of thermodynamical stability in the phase diagram, hindering the formation of the transient liquid. To perform such rapid changes in pressure, the tubular furnace where the sample is placed is connected to a vacuum system divided in two independent circuits, accessible individually through remotely controlled electrovavles (EV1 and EV2). Through the high-vacuum circuit (C1), the initial low-P_{O_2} heating is performed employing a turbomolecular pump in series with a rotary pump to reach the required low pressures. In this system, contrarily from the one used in *in-situ* experiments described in Appendix E, the desired pressure values is obtained through inlet of pure O_2 ($\geq 99.995\%$) and therefore, the total pressure (P_{TOT}) is equals to P_{O_2} in this system. The exact P_{O_2} value is adjusted through fine regulation with the use of the needle valve (NV1). Once the predetermined temperature is reached, switching from the high-vacuum circuit (C1) to the low-vacuum circuit (C2) using the remote control of the elecrtrovalves EV1 and EV2 allows to perform the P_{O_2} jump: the final pressure is adjusted precisely through the needle valve (NV2) prior to the process, and pressure values of both circuits are continuously monitored and registered through the pressure meters throughout the entire experiment. Given the large volume of the sample environment, a gas reservoir was installed in C2: when switching from C1 to C2, the pressure is believed to reach an equilibrium to the final value of P_{O_2} more rapidly with the aid of a large quantity of gas introduced in the system previously accumulated in the reservoir.

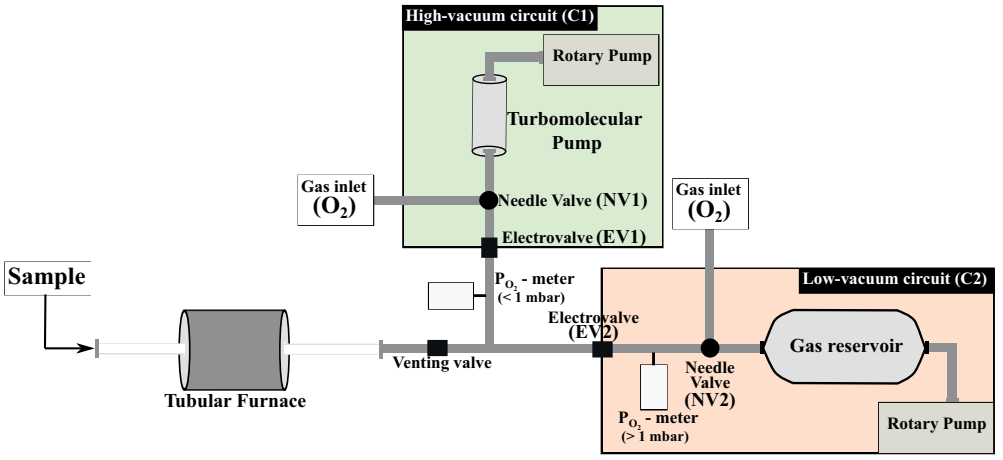


FIGURE D.1: Schematic representation of the experimental set-up employed for TLAG P_{O_2}-*route* experiments performed at ICMAB. The tubular furnace is connected to two independent vacuum circuits, operable individually through the use of remotely-controlled electrovalves. Components of each circuit are named.

As reported in Fig. D.1, the sample is inserted in a tubular furnace where it is heated to the desired processing temperature. A schematic representation of the sample holder is displayed

in Fig. D.2. An alumina crucible is placed in proximity of a type-K thermocouple at the end of a long alumina thermocouple protection tube, held in place with a stainless steel support system. Up to three samples can be employed in a growth process without any significant differences to be noticed in the epitaxy or performance of the individual films (when optimal processing conditions are selected). As the process is conducted in vacuum, to hold in place the samples throughout the growth process, these are stuck to the alumina crucible prior to the experiment through the use of 62000007 (L200N) Conductive Silver Lacquer (CDS Electronique, acquired from Ferro GmbH) and let dry completely according to specifications of the lacquer.

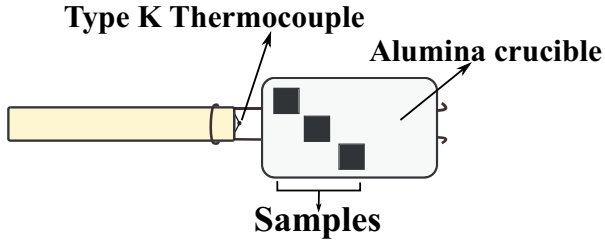


FIGURE D.2: Schematic overview of the sample holder.

As specified in the text, two different heating ramps have been implemented for the optimization of TLAG P_{O_2}*-route*: a slow heating ramp, with average heating rate $\mathrm{d}T\,/\,\mathrm{d}t = 0.2$ ºC s^{-1}, and a fast heating ramp which increased the average heating rate up to $\mathrm{d}T\,/\,\mathrm{d}t = 1.4$ ºC s^{-1}. The first case was achieved through the simple introduction of the sample on the holder in the furnace, coinciding with the isotherm region. Once the vacuum conditions for the experiment were set, the furnace was set to the desired temperature and heated at the maximum heating rate possible from furnace specifications. As reported in 4.2.1, this method was detrimental for the process due to the long heating and cooling times, which were demonstrated to promote importantly coarsening of the crystalline phases. In order to be able to heat the sample with increased heating rates, a remotely controlled set of motorized rails were installed at the base of the furnace. In this way, the furnace could be moved at controlled speed along the direction of the entire quartz tube corresponding to the sample environment. A schematic representation of the heating in a growth process following the installation of the motorized rails can be found in Fig. D.3. The sample is placed in the quartz tube with the furnace positioned away from it. While the independent vacuum systems are set to the required P_{O_2} values for the experiment, the furnace can be preheated to the T_{set} without affecting the sample (panel (1) in the scheme). When desired, the predetermined set of programmed movements of the furnace can be launched, and the furnace will follow the selected sequence finally reaching the position in which the sample coincides with the isotherm of the furnace (panel (2)). The optimisation of this sequence led to the selection of the following parameters for furnace movement: speed

of the furnace was set to 1 mm s^{-1} (533 Hz), and it was moved in sequential steps of 1 cm with a pause of 20 seconds after completing each step. At this point, a standard, optimised thermalisation time is awaited before performing the pressure jump [1]. Eventual dwell at high temperature is performed and, successively, the furnace is moved at a speed of 1.1 mm s^{-1} (600 Hz) to the initial position, with the sample experiencing a fast cooling as a consequence.

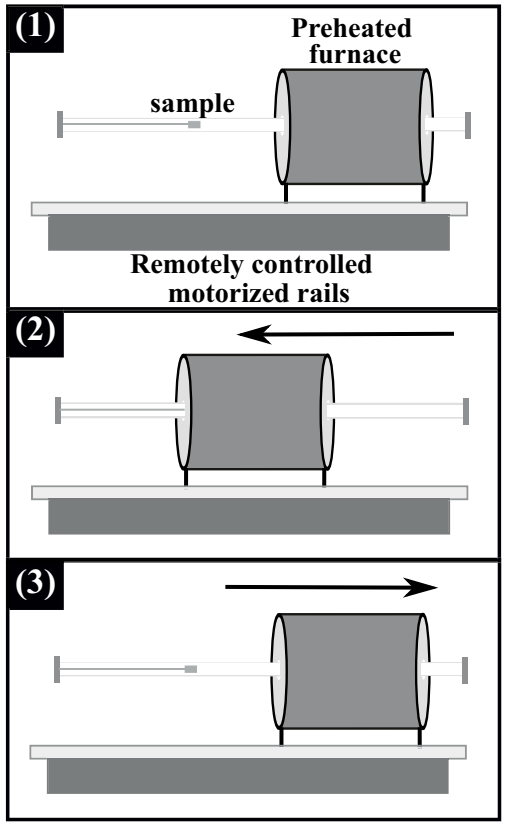


FIGURE D.3: Schematic representation of the furnace movement through the remotely controlled motorized rails during a growth process. This strategy was employed to be able to tune the heating rate by preheating the furnace to the desired temperature in a position far from the sample (panel (1)) and then move it to a position where the sample coincides with the isotherm of the furnace (panel (2)) to perform the pressure jump. Finally, a rapid cooling can be implemented by simply moving the furnace back to the initial position away from the sample (panel (3).

Besides the upgrade to the experimental set-up allowed for important tunability of the heating rate of the growth process, it additionally increased its efficiency: given the slow heating

[1] The thermalisation time (6'30") was the result of several experiments aimed at the optimisation of the optimal sequence of movements performed by the furnace, corresponding to the ideal heating ramp experienced by the sample. The selected thermalisation time was observed to be the best compromise between reaching the desired T_{set} in a short time while avoiding detrimental coarsening of the crystalline phases prior to the jump.

and cooling rate of the previously employed set-up, it was only possible to perform one growth process per day. The introduction of the motorized rails enables for several processes to be performed, as each one lasts less than one hour.
Following the growth process YBCO is present in its tetragonal crystalline phase. A further, final heat treatment is necessary in order to incorporate oxygen in the structure and yield the orthorhombic crystalline phase responsible for superconducting properties. Oxygen doping is obtained through exposure of the grown films to an elevated oxygen flow (0.6 mL/min) heating at a rate of 10 ºCmin^{-1} up to high temperatures (450 ºC), and performing a dwell of 210 min before cooling to room temperature with the same rate of 10 ºCmin^{-1}. This process is required to induce in-diffusion of O_2 in the crystalline structure and reach the optimally doped state of YBCO.

D.2 Data Acquisition and Treatment

The films analysed in Chapter 4 can be mainly divided in two types: quenched films, thoroughly described in 4.2, and grown YBCO or REBCO films, object of the rest of the chapter. Different characterization techniques were employed according to the nature of the film, and a detailed explanation of how the data retrieved from each technique for the different kind of film is acquired and treated will follow.

D.2.1 Quenched Films

As explained in the chapter, films which underwent a quench process are expected to be composed by the solid crystalline phases of $BaCu_2O_2$ and Cu_2O in majority, identified through GIXRD on a Bruker D8 Discover X-ray diffractometer. Details regarding the diffractometer and the possible scanning geometries may be found in Experimental Methodologies (Appendix A). These phases are formed at high temperatures and low-P_{O_2} during the first step of the TLAG P_{O_2}-*route* experiment: as stated in the text, in a quench process, a rapid cooling of the system is performed instead of carrying out the P_{O_2} jump in order to obtain information regarding the microstructure of the film before the transient liquid formation. However, the phases of $BaCu_2O_2$ and Cu_2O are not thermodynamically stable at atmospheric pressure and RT, and the mixed oxide of barium and copper is known to readily react with CO_2 in air to form $BaCO_3$. This information must be taken into account for a correct characterization of the films. The optimal procedure for the acquisition of the GIXRD of these films was, thus, to perform the quench process in accordance with the XRD service at ICMAB, where a measurement slot was reserved and the GIXRD of the film was promptly acquired immediately following the end of the process. GIXRD configuration is chosen in the case of quenched films given the polycrystalline nature of the film at this point of the process: the signal deriving from non-oriented phases is greatly amplified through the XRD measurements in this

specific geometry. To ensure comparability between measurements, alignment with the STO (002) peak was performed prior to moving to grazing incidence conditions, following by the selection of the incident angle (ω), always maintained at 1.5º[2]. In this way, the area scanned for each sample is equivalent and any variations of the resulting XRD pattern are attributable to differences in the microstructure of the films. Generally, the hour-long duration of the measurement is short enough to avoid any changes in the crystalline phases formed during the quench. Nonetheless, if the film has to be further employed in an eventual subsequent experiment[3], storage conditions must be carefully selected. Fig. D.4 displays the consequences of two storage conditions for quenched films. In the first case, a quenched film was stored in a sealed container under vacuum for 40 days, after which a second GIXRD measurement was performed, showing no evident change in the reflections relative to the crystalline phases present in the film. Contrarily, a quenched film which was stored in air (atmospheric pressure and at RT) shows the appearance of peaks relative to $BaCO_3$ upon remeasurement after only 9 days, and a general variation of the intensity of the reflections corresponding to the rest of the crystalline phases.

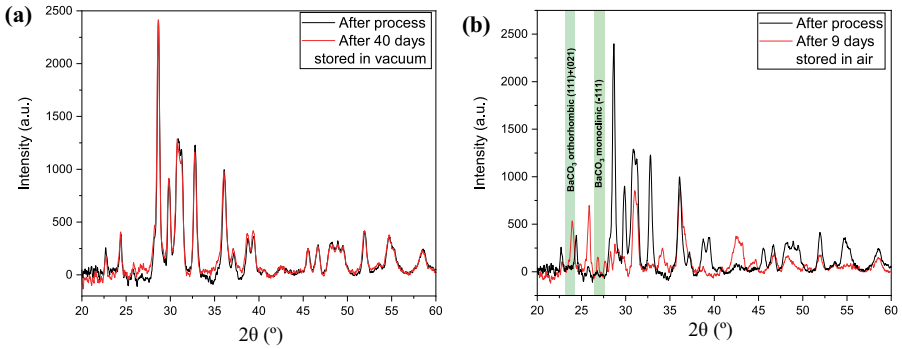
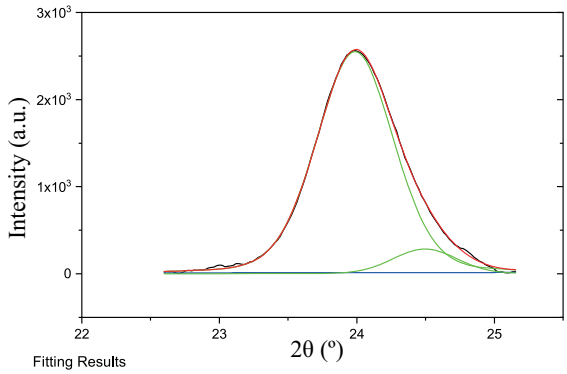


FIGURE D.4: Evaluation of storage methodology for quenched films. Both films were quenched using the same processing conditions: $P_{O_2,base} = 10^{-}5$ bar, heating to $T_{set} = 835$ ºC with a heating rate of 0.2 ºC s^{-1}. (a) Comparison between the GIXRD of the same (3:7) composition film measured after the quench process (black line) and following 40 days of storage in a sealed container under vacuum conditions (red line), showing no change in the intensity of the reflections or any difference in the crystalline contributions. (b) GIXRD patterns of a film after quench (black line) and measured again after 9 days of storage in air (atmospheric pressure and RT), showing the appearance of contributions attributable to $BaCO_3$, highlighted in dark green (orthorhombic phase) and light green (monoclinic phase).

[2] As described in Experimental Methodologies (Appendix A), this is the standard scanning geometry for the GIXRD measurements carried out in the films of this entire thesis.

[3] In Chapter 5, the use of previously quenched films for their use in TLAG P_{O_2}*-route* experiments performed at synchrotron facilities for in-situ XRD characterization of the growth process will be reported. Said films underwent a quench process at ICMAB in the furnace described in the previous section weeks before the beamtime run, as part of the sample preparation process.

Grain sizes referred to in 4.2.1 were obtained through measurement of the films in θ-2θ configuration in the same Bruker D8 Discover diffractometer, and the Scherrer equation was used for crystallite size determination following the procedure explained in A.5.1.
For what concerns the quantification of the contributions of $BaCO_3$ phases employed in the determination of the optimal processing parameters for the quench processes described in section 4.2, the analysis was carried out on the GIXRD patterns of the films acquired after the process. Simple integration of the peaks of interest using a Pseudo-Voigt 1 function[4], specifically the combination of the $BaCO_3$ orthorhombic (111) and (021) peaks and the $BaCO_3$ monoclinic (-111) peak, led to the determination of the area of each peak. This value was then used as a function of dwell time (Fig. 4.4(c)), T_{set} (Fig. 4.8(c)) or copper content in the liquid composition of the film (Fig. 4.14) for evaluation of the elimination of the barium precursor phase in these specific cases. As an example, the fitting of the $BaCO_3$ orthorhombic (111) and (021) peaks in a film is shown in Fig. D.5.



Fitting Results

Peak Index	Peak Type	Area Intg	FWHM	Max Height	Center Grvty
1	PsdVoigt1	1869,65548	0,65939	2546,08867	23,98755
2	PsdVoigt1	161,78392	0,5445	279,73407	24,49537

FIGURE D.5: Peak fitting of the $BaCO_3$ orthorhombic (111) and (021) using the Pseudo-Voigt function in a film measured by GIXRD. Resulting parameters are reported in the Table below the plot, and the value of "Area Intg" is employed as Peak Area in the plots referred to in the text.

This same procedure was used to obtain the values employed in the plots in which the percentile of reduction of the $BaCO_3$ contribution is estimated following the quench process, specifically in Fig. 4.4(b), Fig. 4.8(b) and Fig. 4.12(b). In these cases, the peaks of $BaCO_3$ phases obtained from the GIXRD measured after the pyrolysis process are integrated first, following the same method mentioned above. Consequently, the value of the resulting peak areas are considered the 100% for each phase of $BaCO_3$, and the respective values after quench are normalized to this.

[4]The Pseudo-Voigt function is an approximation for the more general Voigt function, which is a combination of Gaussian and Lorentzian functions. It finds general use as a peak profile in XRD analysis in specific cases where pure Gaussian or Lorentzian functions fail to describe a peak appropriately.

Microstructural characterization through TEM analysis on quenched films was not possible due to the brittle nature of the film. TEM sample preparation led to the loss of part of the film in the step of mechanical polishing.

D.2.2 Grown Films of YBCO and other REBCO

Grown films of YBCO and the other REBCO systems studied in this thesis were characterized mainly through the use of various XRD techniques, SEM, TEM, and measurements of physical properties. More details on each one of these techniques and the specific conditions used for each measurement are explained in Experimental Methodologies, Appendix A, specifically A.5.1. The objective of this subsection is the description of the data treatment methods used to construct the graphs reported in Chapter 4, specifically the cases of plots analysing the contribution of secondary phases and the determination of quality of surface morphology.

D.2.2.1 Determination of secondary phase contribution

The determination of the contribution of each secondary phase to the epitaxy of a YBCO film was obtained from the XRD pattern acquired employing a Bruker-AXS D8 Advance diffractometer equipped with general area detector diffraction system (GADDS). This measurement technique was widely used in the group as a rapid evaluation of texture quality of the epitaxial film [51, 55, 190]. An example of the 2D-XRD image resulting from the measurement of an epitaxial YBCO film in GADDS and the corresponding integration in χ is displayed in Fig. D.6.

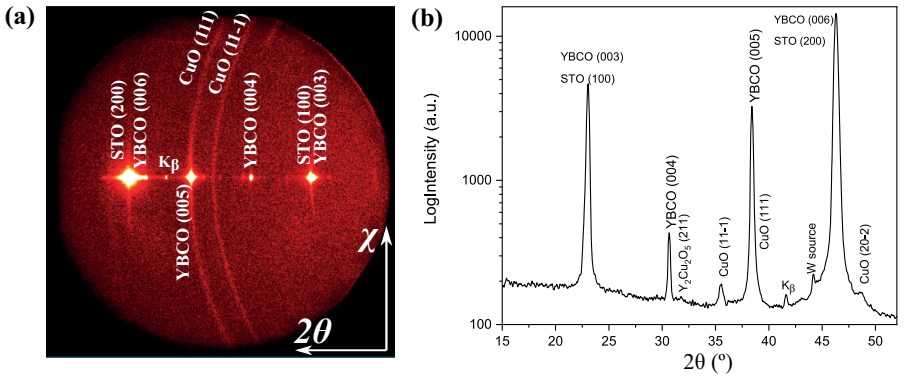


FIGURE D.6: (a) 2D-XRD image obtained from the measurement of an epitaxial YBCO film through GADDS. (b) Integration in χ of the 2D-XRD in (a), with identification of the phases shown in both cases.

As reported in the structural characterization section of Experimental Methodologies, the range for the integration of the 2D-XRD is 15º$\leq 2\theta \leq$52º and -15º$\leq \chi \leq$15º. This range must

be maintained the same for the analysis of contributions of secondary phases to avoid over- or under-estimating polycrystalline contributions to the epitaxy of the film. From the integrated 2D-XRD, one can follow the same fitting procedure previously explained in D.2.1 to obtain the peak area of all the reflections present in the XRD pattern. However, some considerations must be made at this point.

- The CuO (111) reflection is contained in the peak relative to the YBCO (005) reflection, given the proximity in 2θ positions. In order to avoid overestimating the latter and correctly determining its peak area, a deconvolution of the two peaks must be carried out. To do so, the fitting of the CuO (11-1) reflection is performed first to determine the FWHM of this peak. Considering the relative intensity of the CuO (11-1) and the CuO (111) reflections is, respectively, 100% and 99%, the approximation of both peaks having similar FWHM may be made with sufficient certainty. Therefore, when fitting the combined peaks of YBCO (005) and CuO (111), one may specify the FWHM value as a bound to the fitting process of the copper oxide peak. In this way, the deconvolution will yield the correct area of the two peaks and the YBCO (005) contribution alone can be selected, without overestimating it by considering the additional area of the CuO (111) reflection.
- Fitting of the peaks relative to all secondary phases is performed and the following formula is employed to determine the contribution (as a percentage) of each specific secondary phase to the epitaxy of the film:

$$\frac{\mathrm{PeakArea}_{(\mathrm{SecondaryPhase})}}{[\mathrm{PeakArea}_{(\mathrm{SecondaryPhase})} + \mathrm{PeakArea}_{(\mathrm{YBCO(005)})}]} \cdot 100 \tag{D.1}$$

It must be specified that this formula provides a percentage of the contribution of each phase to the epitaxy of the film which cannot be considered as a volume fraction. It is, however, an extremely useful ratio employed for a general quantification and a direct comparison regarding the presence of undesired or secondary phases in the films.

D.2.2.2 Surface morphology quality analysis

The construction of the plots regarding the quality of surface morphology for grown films required a previous analysis of the images acquired through SEM for each sample. As explained in the text, a set of numerical variables were assigned to the presence or the absence of a specific feature, respectively 1 and 0. This approach is particularly useful to quantify surface characteristics, which are solely qualitative after image collection. Moreover, the set of data resulting from this analysis can be later on employed to build plots as functions of processing conditions to observe eventual tendencies or in the development of machine learning algorithms.

A visual definition of the specific features from the surface morphology analysis can be found in the following images, and is provided for the reader in order to have an easier understanding of the parameters chosen during the qualitative analysis.

- **Flat surface:** a highly epitaxial YBCO film displays a porous-free, continuous layer with possible presence of terraces commonly resulting from liquid-mediated techniques. In the specific case of copper-excess compositions described in this thesis, CuO precipitates are found expelled on the surface, result of the high c-axis nucleation which allows for strong pushing phenomena to occur.

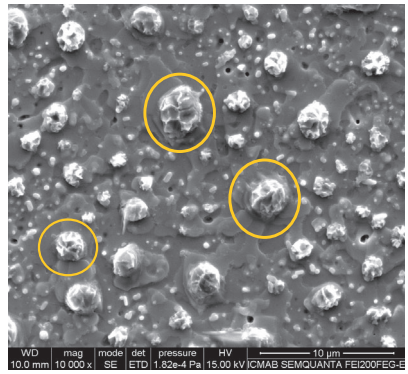


FIGURE D.7: YBCO film which is assigned with the feature of "flat surface". As this specific sample deriving from a (3:7) liquid composition was grown in optimal conditions for high epitaxy, the excess of copper is pushed to the surface and is found in form of CuO particles (confirmed by EDX). Some of said particles are identified with a yellow circle, to provide an example.

- **Granular morphology:** generally correlated to high misorientation of YBCO deriving from growth of the film in conditions of mixed homogeneous and heterogeneous nucleation.

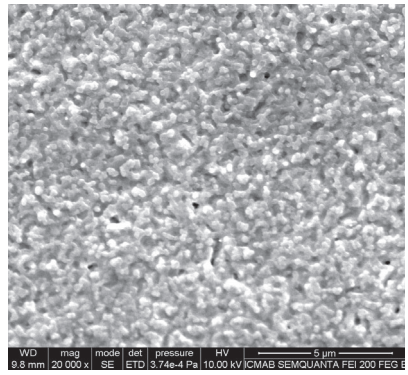


FIGURE D.8: YBCO film showing granular surface morphology.

- **Dewetting:** incomplete formation of the film, leaving areas in which the underlying substrate is visible. This phenomenon may be caused by a combination of the high supersaturation of the liquid during the growth (promoting formation of misoriented grains or secondary phases) and the ultrafast growth rates of TLAG which result in a lack of complete coverage of the liquid and growth of a continuous film.

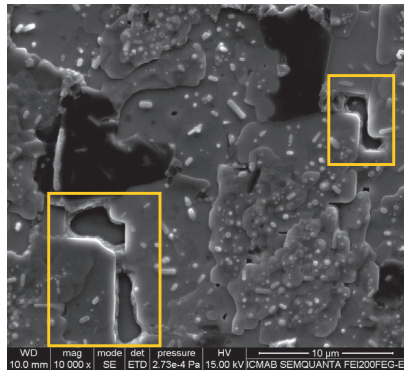


FIGURE D.9: YBCO film showing presence of areas in which no full coverage of the substrate is obtained (marked by yellow rectangles), exposing the STO (confirmed by EDX).

- **a/b-grains:** typically visible due to the orientation of 90º respect to the epitaxial film surface, deriving from the preferential growth YBCO in homogeneous nucleation conditions.

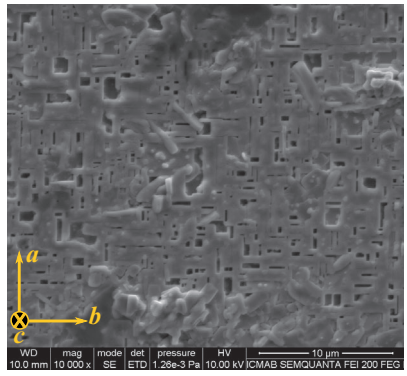


FIGURE D.10: YBCO film grown in conditions where the a/b nucleation is favoured.

- **Reactivity with the substrate:** the transient liquid of [Ba-Cu-O] is highly corrosive and may generate reactivity with the substrate when excessive temperature is reached. In the case of the films described in this thesis, given the substrates employed are STO single crystals, the formation of barium titanate ($BaTiO_3$) reactivity phase is observed

when extremely elevated T_{set} are selected. Usually, these phases have a needle-like appearance.

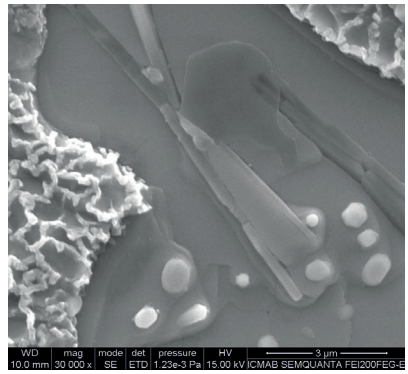


FIGURE D.11: Needle-like grain deriving from the $BaTiO_3$ reactivity phase between the [Ba-Cu-O] transient liquid and the STO substrate.

As explained in the text, apart from a film exhibiting a flat surface, the remaining surface morphology features described in this list are all contributing to major current percolation impediment. Control of the processing conditions in order to avoid the appearance of these features is fundamental.

D.3 Supporting Information

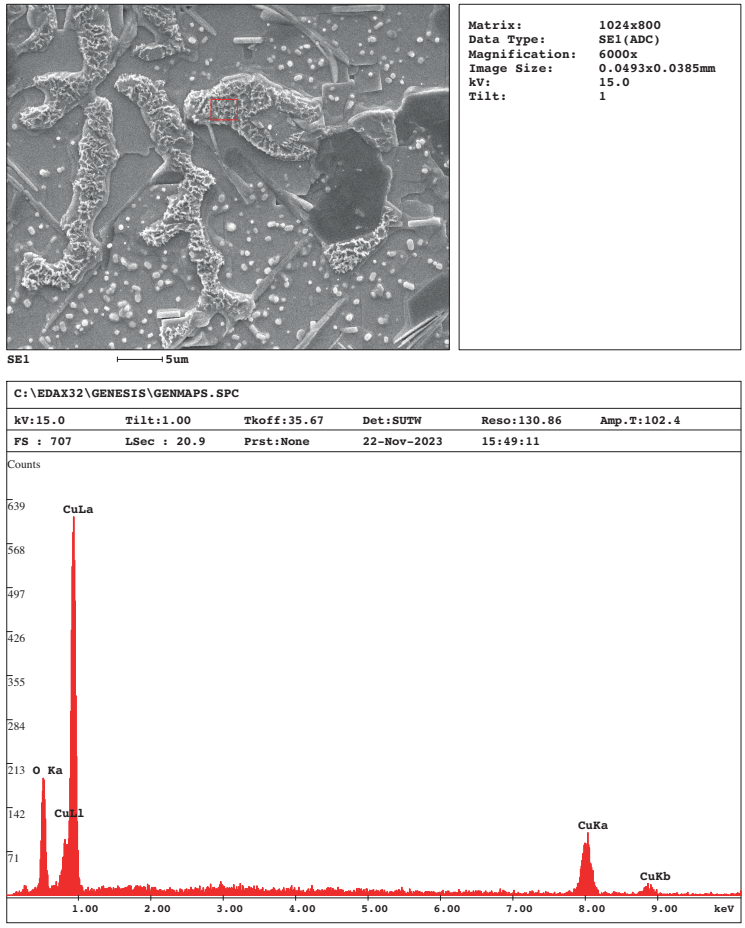


FIGURE D.12: EDX acquired on a 6-layered film indicating the composition of the dendritic-like structure to be copper oxide oxide (measurement conducted on the area depicted by a red rectangle).

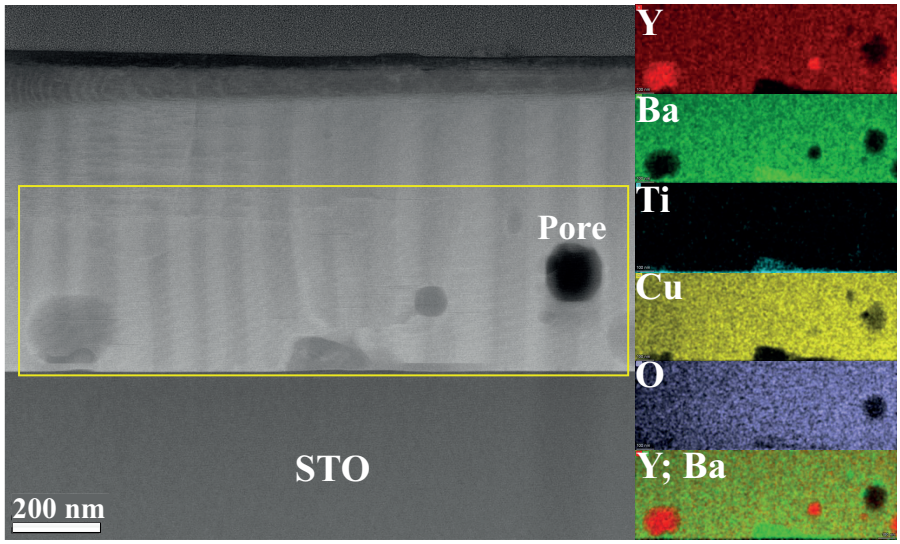


FIGURE D.13: STEM-EDX elemental maps allowing for the identification of the secondary phases present in the grown film of four layers. The maps for Y K-edge, Ba L-edge, Ti L-edge, Cu K-edge, O K-edge, and the combination of Y K-edge and Ba L-edge are acquired in the region of the film marked by a yellow rectangle.

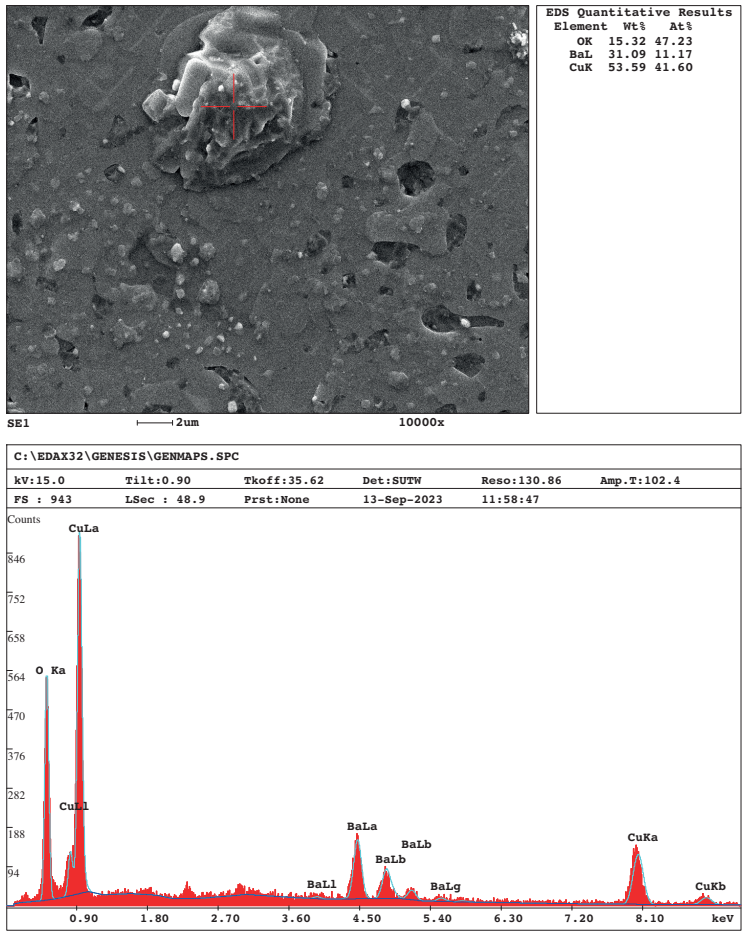


FIGURE D.14: EDX acquired on a grown film of SmBCO, specifically on a large grain found at the surface. It can be identified as a barium- and copper-mixed phase (measurement conducted on the area depicted by a red cross).

E

Appendix to Chapter 5

E.1 Experimental methodologies for *in-situ* synchrotron XRD experiments

In-situ XRD experiments were carried out in five beamtime runs, each one of approximate duration of one week, throughout the time of this thesis in collaboration with two synchrotron facilities: Soleil Synchrotron, working at the DiffAbs (**Diff**raction and **Abs**orption) Beamline with the guidance of beamline scientist Dr. Cristian Mocuta, and ALBA Synchrotron, at the **N**on-**C**rystalline **D**iffraction - **S**AXS **W**AXS **E**xp**E**rimental **T**echniques (NCD-SWEET) with the help of beamline scientist Dr. Eduardo Solano.

E.1.1 Technical specifications and experimental set-up at DiffAbs and NCD-SWEET beamlines

Technical information relative to the experimental specifications and the equipment employed in the two beamlines is reported in Table E.1.

At DiffAbs beamline, the analysis of fast crystalline phase transitions is possible through the use of hard X-ray photons in the energy range 3-23 keV. The 6-axis diffractometer allows for multiple measurement configurations and the two detectors (0D point detector and XPAD 2D area detector) enable ultra-fast data aquisition in the order of tenths of milliseconds. The optimization of the set-up and corresponding angular opening to cover the entire range of interest, in addition to a sufficient signal-to-noise ratio for high acquisition rates was implemented in beamtime runs during previous PhD theses carried out in the group with the collaboration of

Dr. Cristian Mocuta.
NCD-SWEET beamline uses Small and Wide Angle X-ray Scattering in transmission (SAXS and WAXS)and Grazing Incidence Small and Wide Angle X-ray Scattering (GISAXS and GIWAXS) for the analysis of a broad variety of nanostructured materials through several measurement configurations, with beam energy in the range 6.5-20 keV. In the case of the measurements described in this thesis, the detector selected was the one used for WAXS measurements, provided by Rayonix (LX255-HS). Appropriate sample-to-detector distance was adjusted through the guidance of beamline scientist Dr. Eduardo Solano to cover the 2θ and χ range of interest for the *in-situ* experiments (for these experiments, sample-to-detector distance was 300 mm).

	DiffAbs	**NCD-SWEET**
Energy (E)	18 keV	18 keV
Energy Resolution ($^{\Delta E}/_{E}$)	10^{-4}	$2.7 \cdot 10^{-4}$ at 10.0 keV
Flux (f)	$4 \cdot 10^{13}$ ph/s/0.1%bw at 20 keV / 500mA ring current	$1.5 \cdot 10^{12}$ ph/s at 12.4 keV / 150mA ring current
Beam size (HxW)	250x300μm^2 (FWHM)	130 μm x 130 μm
Beam divergence	0.24 x 3.5 mrad^2	-
Data Acquisition	0D point detector XPAD 2D area detector	CDD WAXS Detector by Rayonix (LX255-HS)
Sample Environment	Anton Paar conductive-type furnace (DHS1100)	Anton Paar conductive-type furnace (DHS1100)

TABLE E.1: Technical configuration used in the *in-situ* XRD experiments regarding beamline specifications and equipment used for data acquisition.

The sample environment for both beamlines was the same, employing a commercially available domed conductive-type heating stage provided by Anton Paar (model DHS1100). This allowed for the use of fast heating ramps (maximum of 4.5 ºC s^{-1}) up to 1100 ºC and compatibility with operating in vacuum and controlled gas conditions. In Fig. E.1, the exemplary situation of the set-up used at DiffAbs beamline is represented, identifying incoming beam, diffraction angles, detectors used, and sample stage. The sample is positioned on a silicon wafer through the use of clamps or employing silver paint (CDS Electronique, Ag Pâte L200N) and fixed on the heating stage. The silicon wafer is used to avoid strong contributions deriving from the aluminum nitride of the heating plate. In order to work in vacuum conditions and simultaneously record XRD data, an X-ray transparent dome made of graphite is screwed in

place, covering the heating stage. A precise set of motors control the detectors and the sample stage and allow movements within an error of 0.001°.

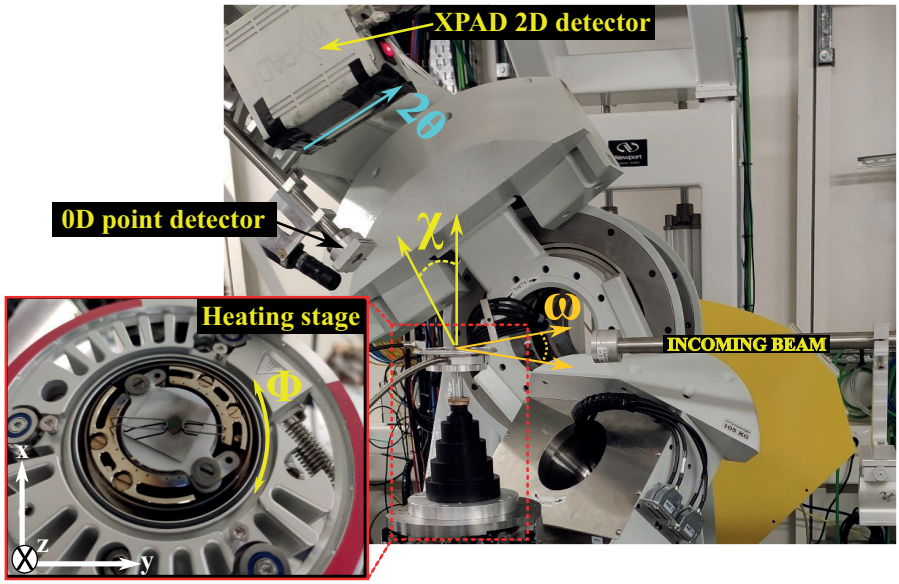


FIGURE E.1: Experimental set-up of the sample stage and detectors at DiffAbs beamline, Soleil Synchrotron, showing the angles with possible movement relative to sample stage, detector and incoming beam. Inset shows a top-view of the heating stage and sample positioning.

The Eulerian coordinates that may be adjusted through the movement of the several motors at the DiffAbs Beamline at Soleil Synchrotron are represented in Fig. E.1. 2θ is the detector angle relative to the XPAD 2D area detector. Coordinates of the sample stage are indicating the possible translation in the x, y and z directions, combined with the potential movement of the sample azimuth (ϕ). χ and ω are, respectively, the elevation angle of the sample stage and the incidence angle of the incoming beam. In the case of NCD-SWEET Beamline at ALBA Synchrotron, conversely, the detector is fixed and the possible movement of the sample stage in x, z, χ and ω allows for the fulfillment of the law of Bragg with the incoming beam.
An overview of the vacuum system experimental set-up is represented in Fig. E.2. As explained in Chapter 4, TLAG P_{O_2}*-route* allows to decouple the $BaCO_3$ elimination (limiting step of the process), occurring during the low-pressure heating, and the actual nucleation and growth of YBCO through the assistance of the transient liquid, happening in the pressure jump. The description of the tubular furnace used for TLAG processes in *ex-situ* conditions is reported in D.1. In *in-situ* conditions, an in-house designed vacuum system that emulates the same experimental configuration was developed, and a scheme of the system is displayed in Fig. E.2(a). Two independent vacuum circuits are connected to the conductive-type furnace

equipped with the domed housing, and can be operated independently through the use of remotely controlled electrovalves (EV1 and EV2). The high-vacuum circuit (C1) is used to perform the initial step of the process, specifically the low-pressure heating, with the low pressures achieved through the use of a turbomolecular pump. To reach the desired values of P_{O_2}, high-purity (< 10 ppm) synthetic air is introduced in the system. Due to safety regulations, no pure O_2 could be used in *in-situ* conditions. Therefore, considering the content of O_2 to be 20 % of air, the value of base pressure for the experiment would be adjusted as $P_{TOT} = 1/5 P_{O_2}$. In the experiments described in this thesis, the respective values of $P_{TOT,base}$ and $P_{O_{2,base}}$ were 0.05 mbar and 0.01 mbar. The low-vacuum circuit (C2) is responsible for the final pressure of the experiment, reached through the use of a rotary pump. To achieve the desired $P_{TOT,final}$ and $P_{O_{2,final}}$ values, in this case, three mass-flows were connected to high-purity (< 10 ppm) synthetic air and N_2 inlets. A wide variety of air/N_2 mixtures were available to achieve several conditions of $P_{TOT,final}$ and $P_{O_{2,final}}$, with $P_{TOT,final}$ ranging from 12 mbar to 100 mbar, allowing for final $P_{O_{2,final}}$ values up to 10 mbar. The exact pressure value would be adjusted through high-precision needle valves (NV1 and NV2) located between the gas inlet and its connection to the vacuum system, with the value of $P_{TOT,final}$ continuously measured through pressure meters and recorded throughout the entire experiment. The pressure jump is obtained by switching from C1 to C2 through the remote control of the electrovalves EV1 and EV2. An accessory of the EV2 was added to the system, namely the move valve. This valve allows for a fine tuning of the opening of the circuit towards the entrance of the gas flow, with the possibility of selecting a specific opening percentage. Its use may be interesting for an accurate analysis of the processes occurring during the jump if the speed of the pressure transition is varied. Due to time constraints, only preliminary testing with the use of this valve was carried out during the time of this thesis work. During the initial beamtime runs, the entire vacuum system would be mounted on-site prior to the experiments, as shown in Fig. E.2(b). One would have to keep in mind a considerable time consumption required to mount the system and test it on valuable beamtime. During this PhD thesis, in the framework of a collaboration with ALBA Synchrotron through the PTI+TransEner CSIC programme for Spanish NGEU project, an important upgrade to the system was implemented, displayed in Fig. E.2(c). The entire experimental set-up, containing the vacuum system, pressure-meters, mass-flows, heater controller unit and a controlling Moxa unit was fitted through an adjustable skeleton to a movable rack. This may be transported to the beamline and simply connected to the heating stage through a vacuum connection and to the gas connections provided by the facility, with no additional mounting required. Moreover, the system may be tested *ex-situ* for a careful optimization of the desired processing conditions, allowing for high precision of the *in-situ* experiments.

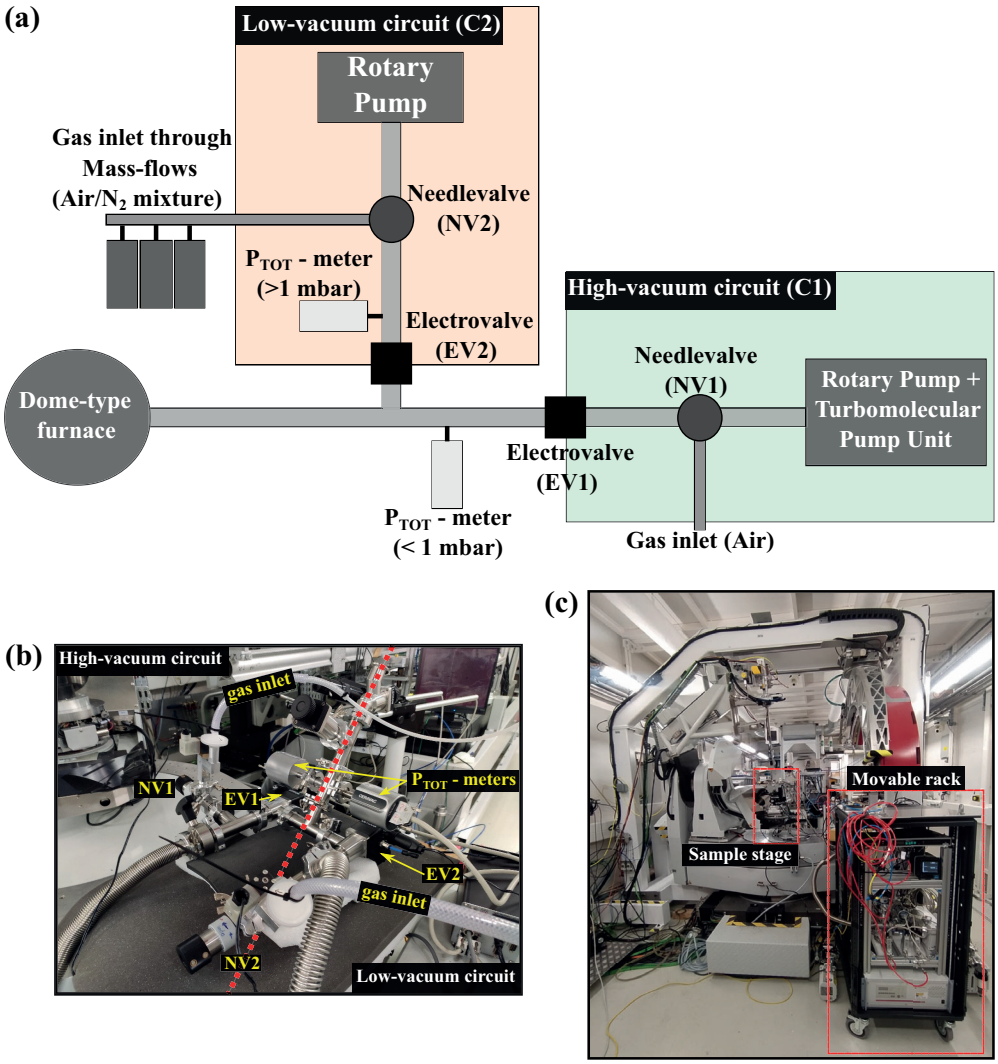


FIGURE E.2: (a) Schematic representation of the vacuum system experimental set-up employed for *in-situ* XRD experiments. (b) Vacuum system mounted on-site at DiffAbs beamline during the initial beamtime runs. (c) Upgraded system developed in the final years of this PhD thesis, in which the entire set-up is contained in a movable rack which can be carried to the beamline and simply connected to the heating stage and gas connections.

E.1.2 Data acquisition and data treatment

At both beamlines, the alignment of the sample employing a beam energy of 18 keV was carried out using, as a reference, the STO single crystal (substrate employed for sample preparation) (200) peak. The range of 2θ and χ angles adequate for the clear identification of all the precursor and final crystalline phases without overlapping of significant peaks was set to

2θ=10º-20º and χ=-9º-9º. Two configurations were used to record the evolution of the phases during the *in-situ* experiments:

- **ω=4º and χ=0º:** lowering the incidence angle (ω) to increase the irradiated surface area (as in a grazing incidence XRD measurement), to enhance the intensity of polycrystalline precursor and secondary phases.
- **ω=8.1º and χ=0º:** alignment with the Bragg reflection of the (005) peak of YBCO. The value of ω is slightly shifted out of the exact Bragg conditions to avoid saturating the detector when the YBCO peak appears during the TLAG process, given the ultrafast conditions and the extreme intensity obtained.

Standard experiments were recorded at a rate of 100 ms per frame (total time between frames was 250 ms, with 100 ms being acquisition rate and 150 ms needed to send the data to the main server), to enhance the usually low intensity of the initial precursor phases. Nonetheless, during the pressure jump, when the transient liquid is formed and YBCO nucleation occurs, valuable information was being lost due to the ultrafast nature of this particular process. With the support of Dr. Cristian Mocuta, an ultrafast acquisition was implemented at DiffAbs beamline, which allowed acquiring a frame every 2 ms (7 ms must be added due to storage time, resulting in a total time between frames of 9 ms). This type of data acquisition was solely focused on the pressure jump due to the enormous amount of data generated[1].
Pre-established temperature profiles would be launched once the data acquisition was started, following the manual adjustment of the initial and final pressure values and the sample alignment in the desired configuration. Temperature and pressure profiles could be later synchronized to the corresponding acquired frames through machine times saved in each log file. The acquired images are obtained in raw format and correspond to (2θ, χ, Intensity) matrices. Further data processing must be conducted to extract the I(2θ) patterns through an integration in χ of the corresponding 2D-XRD image. An example of an acquired 2D-XRD image and its integration in χ to obtain the I(2θ) pattern is displayed in Fig. E.3.

[1]The maximum limit of acquired frames for an experiment with ultrafast acquisition time is 9999. If this limit is surpassed, a new acquisition must be launched. The low-pressure heating generally lasts in the order of minutes (depending on the heating ramp employed), forcing for several new acquisitions to be launched. Therefore, the following synchronization of machine time and actual experiment time when switching to a new acquisition, despite it being relative to the same experiment, would be extremely difficult.

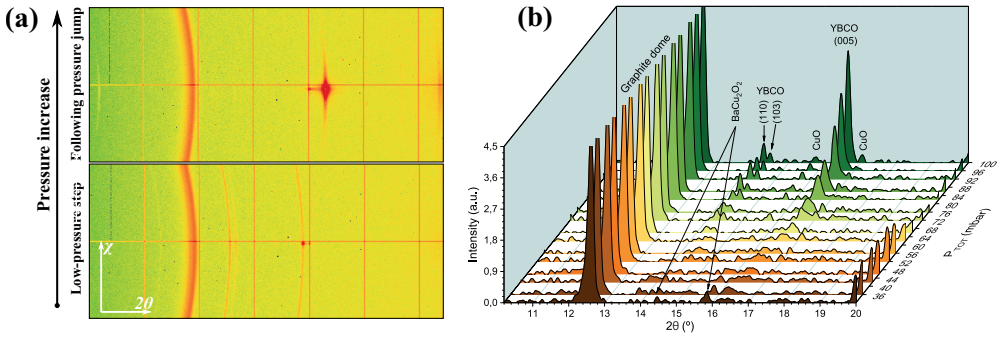


FIGURE E.3: (a) Exemplary 2D-XRD images acquired with the 2D detector during an *in-situ* synchrotron XRD experiment of TLAG P_{O_2}*-route* with the increase of pressure, showing one frame acquired prior to the pressure jump, and one following it. (b) Integrated intensity in χ as an evolution of the P_{O_2} during the pressure jump.

Each experiment generates a large volume of data, ranging between 1000 to 10000 frames depending on acquisition time and processing conditions, especially considering the length of the thermal treatment when varying the heating ramp. To facilitate the analysis of such experiments, a graphical user interface was developed to visualize straightforwardly such amount of data, and screenshots of an exemplary visualization of the experiment are displayed in Fig. E.4. It allows the simultaneous visualization of the temperature and pressure profile (upper right panel), the integrated I(2θ) patterns (upper left panel), the corresponding 2D-XRD images acquired (lower left panel) and the time-dependent colour mapping (lower right panel), evolving throughout the experiment by moving the cursor from start to end of the *T-P* profiles. Polycrystalline phases, such as $BaCO_3$, Cu_2O or homogeneously nucleated YBCO, are showing constant intensity along χ corresponding to a specific 2θ position in the 2D-XRD images (as the rings shown in Fig. E.3(a), lower panel). Contrarily, the epitaxial YBCO shows broadened diffraction spots in the determined 2θ peak positions corresponding to the (00l) indices (diffraction spot in Fig. E.3(a), upper panel, relative to the (005) reflection of YBCO).

To analyze the evolution of the crystalline phases during the *in-situ* experiment, an additional application developed in Python is used for the peak fitting. Through a previous identification of the 2θ range of the peak with the aid of the graphical interface, a least-square fitting is possible for single or multiple Gaussian profiles, through the use of a built-in fitting model (here, GaussianModel). The baseline is removed through the use of a specific function applied to the entire pattern (IModPoly: improved multi-polynomial fit).

Both the graphical user interface and the program used for the fitting of the peaks were developed by Jordi Aguilar during the upgrade of the experimental set-up, together with additional programs which aided in the remote control of several experimental tools (i.e. heating stage and its thermal profile, switching of the electrovalves to perform the pressure jump, control of the mass-flows).

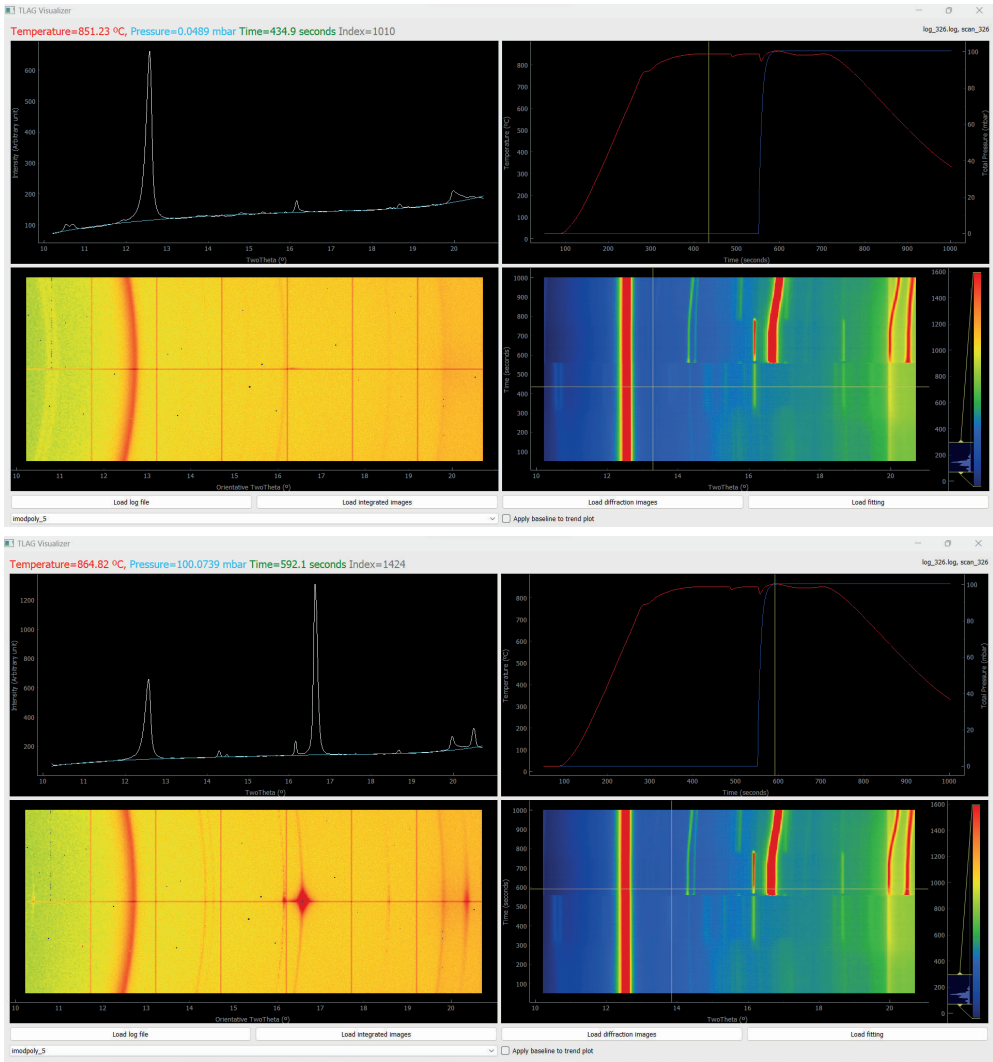


FIGURE E.4: Graphical user interface employed for the simultaneous visualization of the temperature and pressure profile (upper right panel), the integrated I(2θ) patterns (upper left panel), the 2D-XRD images (lower left panel) and the time-dependent colour mapping (lower right panel) for the *in-situ* experiments. To visualize the evolution of phases, one must simply move the cursor from start to end of the temperature profile, observing the continuous change of the four windows corresponding to each time-dependent frame. Upper screenshot shows the example of polycrystalline precursor phases observed during heating, whereas the lower one is displaying the situation of grown YBCO. Corresponding information of time, temperature, pressure and image index are continuously displayed in the upper left part of the window.

Through an initial visual analysis using the visualizer, one may select the range of frames in which the relative crystalline phase in question is showing contribution. Fitting of the 2θ of the

peak (or peaks) deriving from that phase(s) in the I(2θ) patterns related to the selected range of frames is carried out employing the Python peak fitting program, which automatically exports the results according to the experiment scan number, combining the information of time, temperature and pressure conditions for each integration. Through this method, time-dependent, temperature-dependent or pressure-dependent evolution of each phase may be promptly represented. Examples of the representation of a time-dependent fitted curve generated from this integration is displayed in Fig. E.5. From the fitting of all the contributions visible during an experiment, one may construct phase evolution plots, corresponding to the specific time, temperature or pressure range of interest in the experiment, as the ones displayed in the chapter. As visible in Fig. E.5, the generated fitting is represented as fitted peak area (AUC), in this case as a function of time. Depending on the intensity of the peak in the initial moments of the formation of the crystalline phase, the error on the fitting is too elevated for the model to give a valid output and the curve is cut where the intensity is insufficient for the fit to converge. Therefore, an extrapolation is made considering the frame (with corresponding time,

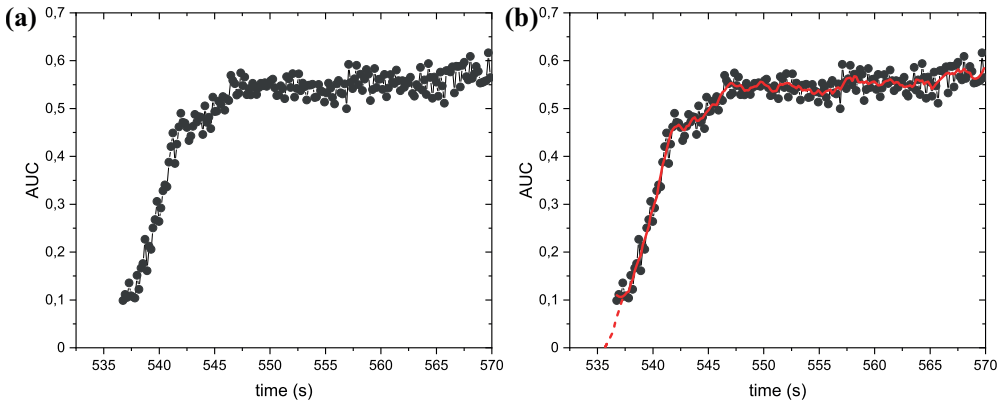


FIGURE E.5: (a) Time dependent phase evolution of a peak relative to the (005) reflection obtained from the integration in χ of the 2D-XRD images acquired during a TLAG *in-situ* XRD experiment, subsequently fitted in the indicated time range through the use of the aforementioned Python peak fitting program. (b) Smoothing of the phase evolution curve shown in (a). Extrapolation of the missing initial data (shown as a red dashed line) due to insufficient signal intensity which results in a non-converging fit.

temperature and pressure values observed in the visualizer) to represent the missing data (red dashed line in Fig. E.5(b)). Moreover, smoothing of the resulting curves is performed through a Stravinsky-Golay model, for a better representation. To determine the onset or final characteristic temperature or pressure values (T_{on} and T_f or P_{on} and P_f), the 90% and 10% criterion is employed, with an error on the determined value of $\pm$5%. The onset is corresponding to the value at 90% of the curve intensity, whereas the end is the value relative to the intensity at 10%, as illustrated in Fig. E.6.

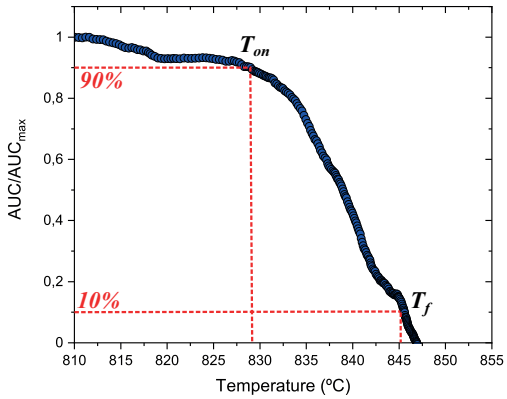


FIGURE E.6: Example of the determination of onset and final temperature values through the 90% and 10% criterion for a phase evolution curve of a peak relative to, here, the disappearance of Cu_2O phase.

Finally, the analysis of the YBCO growth rates, as described in 5.3.1, was strictly performed exclusively on films which displayed a total contribution of the (103) misoriented grains normalized to the (005) peak of 5% or below, to avoid overestimating the growth rate value due to the contribution of non-epitaxial growth[2]. The YBCO (005) time dependent phase evolution curve is normalized to the thickness of the film (in the analysis in the chapter, all films are in average 400 nm thick), and it is fitted employing a sigmoidal model (Boltzmann fit). The first derivative of the latter curve will result in the growth rate, as displayed in the following Fig. E.7.

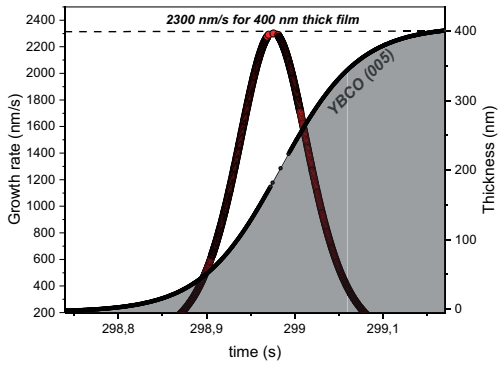


FIGURE E.7: Growth rate determination as first derivative (red) of the sigmoidal fit of the time-dependent phase evolution curve of YBCO (005) reflection normalized to the film thickness (grey). Film thickness in this case if 400 nm.

[2]The procedure employed for the fitting of the peaks and the calculation of the (103) contribution to the epitaxy of the film is described in D.2.2

E.2 Supplementary Information

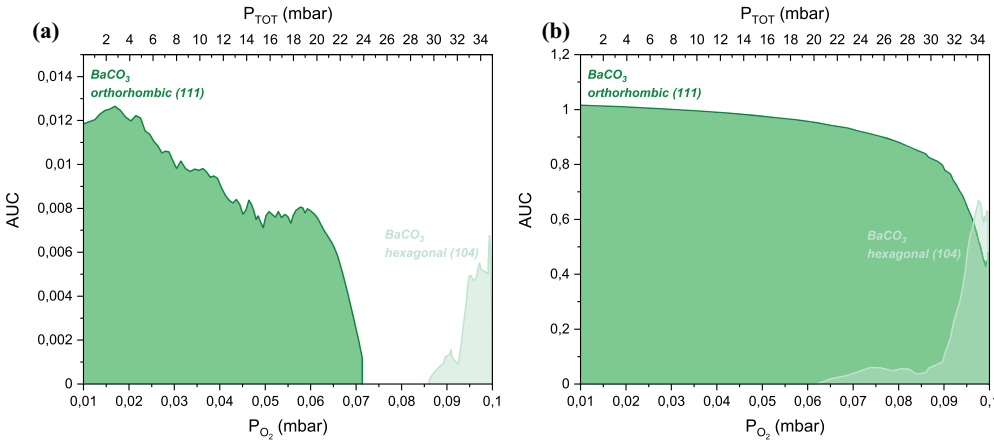


FIGURE E.8: Pressure ($P_{TOT} - P_{O_2}$) dependent phase evolution result of integration of the peaks relative to $BaCO_3$ observed during the pressure jump to $P_{O_{2,final}} = 0.1mbar$ and $P_{TOT,final} = 35$ mbar at the constant temperature of 850 ºC, for (a) a binary and (b) a ternary film. The variations in integrated area derives from the difference in the acquisition time of the two experiments, resulting in lower intensity for the binary film.

Bibliography

(1) Kunzler, J. E.; Buehler, E.; Hsu, F.; Wernick, J. H. *Physical review letters* **1961**, *6*, 89, DOI: 10.1103/PhysRevLett.6.89.

(2) Gavaler, J. *Applied Physics Letters* **1973**, *23*, 480–482, DOI: 10.1063/1.1654966.

(3) Bednorz, J. G.; Müller, K. A. *Zeitschrift für Physik B Condensed Matter* **1986**, *64*, 189–193, DOI: 10.1007/BF01303701.

(4) Wu, M.-K.; Ashburn, J. R.; Torng, C.; Hor, P.-H.; Meng, R. L.; Gao, L.; Huang, Z. J.; Wang, Y.; Chu, a. *Physical review letters* **1987**, *58*, 908, DOI: 10.1103/PhysRevLett.58.908.

(5) Schilling, A.; Cantoni, M; Guo, J.; Ott, H. *Nature* **1993**, *363*, 56–58, DOI: 10.1038/363056a0.

(6) Rogalla, H.; Kes, P. H., *100 years of superconductivity*; Taylor & Francis: 2011, DOI: 10.1201/b11312.

(7) Larbalestier, D.; Gurevich, A.; Feldmann, D. M.; Polyanskii, A. *Nature* **2001**, *414*, 368–377, DOI: 10.1038/35104654.

(8) Obradors, X.; Puig, T. *Superconductor Science and Technology* **2014**, *27*, 044003, DOI: 10.1088/0953-2048/27/4/044003.

(9) Molodyk, A.; Larbalestier, D. C. *Science* **2023**, *380*, 1220–1222, DOI: 10.1126/science.abq4137.

(10) Glowacki, B.; Majoros, M; Vickers, M; Evetts, J.; Shi, Y; McDougall, I *Superconductor Science and Technology* **2001**, *14*, 193, DOI: 10.1088/0953-2048/14/4/304.

(11) Shiohara, Y.; Taneda, T.; Yoshizumi, M. *Japanese Journal of Applied Physics* **2011**, *51*, 010007, DOI: 10.1143/JJAP.51.010007.

(12) Malozemoff, A. *Annual review of materials research* **2012**, *42*, 373–397, DOI: 10.1146/annurev-matsci-100511-100240.

(13) Shiohara, Y.; Yoshizumi, M.; Takagi, Y.; Izumi, T. *Physica C: Superconductivity* **2013**, *484*, 1–5, DOI: 10.1016/j.physc.2012.03.058.

(14) Obradors, X.; Puig, T; Pomar, A; Sandiumenge, F; Mestres, N; Coll, M; Cavallaro, A; Roma, N; Gazquez, J; Gonzalez, J., et al. *Superconductor Science and Technology* **2006**, *19*, S13, DOI: 10.1088/0953-2048/19/3/003.

(15) Rupich, M. W.; Li, X.; Thieme, C.; Sathyamurthy, S.; Fleshler, S.; Tucker, D.; Thompson, E.; Schreiber, J.; Lynch, J.; Buczek, D., et al. *Superconductor Science and Technology* **2009**, *23*, 014015, DOI: 10.1088/0953-2048/23/1/014015.

(16) Selvamanickam, V; Chen, Y; Shi, T; Liu, Y; Khatri, N.; Liu, J; Yao, Y; Xiong, X; Lei, C; Soloveichik, S, et al. *Superconductor Science and Technology* **2013**, *26*, 035006, DOI: 10.1088/0953-2048/26/3/035006.

(17) MacManus-Driscoll, J. L.; Wimbush, S. C. *Nature Reviews Materials* **2021**, *6*, 587–604, DOI: 10.1038/s41578-021-00290-3.

(18) Molodyk, A; Samoilenkov, S; Markelov, A; Degtyarenko, P; Lee, S; Petrykin, V; Gaifullin, M; Mankevich, A; Vavilov, A; Sorbom, B, et al. *Scientific reports* **2021**, *11*, 2084, DOI: 10.1038/s41598-021-81559-z.

(19) Wee, S. H.; Gao, Y.; Zuev, Y. L.; More, K. L.; Meng, J.; Zhong, J.; Stocks, G. M.; Goyal, A. *Advanced Functional Materials* **2013**, *23*, 1912–1918, DOI: 10.1002/adfm.201202101.

(20) Wu, J.; Shi, J. *Superconductor Science and Technology* **2017**, *30*, 103002, DOI: 10.1088/1361-6668/aa8288.

(21) Thomas, O; Hudner, J; Östling, M; Mossang, E; Chenevier, B; Weiss, F; Boursier, D; Senateur, J. *Journal of alloys and compounds* **1993**, *195*, 287–290, DOI: 10.1016/0925-8388(93)90741-5.

(22) Selvamanickam, V; Chen, Y; Kesgin, I; Guevara, A; Shi, T; Yao, Y; Qiao, Y; Zhang, Y; Majkic, G; Carota, G, et al. *IEEE transactions on applied superconductivity* **2011**, *21*, 3049–3054, DOI: 10.1109/TASC.2011.2107310.

(23) Majkic, G.; Galstyan, E.; Selvamanickam, V. *IEEE Transactions on Applied Superconductivity* **2014**, *25*, 1–4, DOI: 10.1109/TASC.2014.2372902.

(24) Bauer, M; Semerad, R; Kinder, H *IEEE transactions on applied superconductivity* **1999**, *9*, 1502–1505, DOI: 10.1109/77.784678.

(25) Nemetschek, R; Prusseit, W; Holzapfel, B; Eickemeyer, J; Miller, U; Maher, E *IEEE transactions on applied superconductivity* **2003**, *13*, 2477–2480, DOI: 10.1109/TASC.2003.811825.

(26) Prusseit, W; Nemetschek, R; Hoffmann, C; Sigl, G; Lümkemann, A; Kinder, H *Physica C: Superconductivity and its applications* **2005**, *426*, 866–871, DOI: 10.1016/j.physc.2005.01.054.

(27) Matias, V.; Rowley, E. J.; Coulter, Y.; Maiorov, B; Holesinger, T.; Yung, C.; Glyantsev, V.; Moeckly, B. *Superconductor Science and Technology* **2009**, *23*, 014018, DOI: 10.1088/0953-2048/23/1/014018.

(28) Hung, C.-Y.; Van Scyoc, J.; Schlesingera, T.; Johnson, J.; Brewer, J.; Migliuolo, M *Materials Science and Engineering: B* **1995**, *33*, 85–90, DOI: 10.1016/0921-5107(94)01179-6.

(29) Wördenweber, R *Superconductor Science and Technology* **1999**, *12*, R86, DOI: 10.1088/0953-2048/12/6/202.

(30) Fujita, S.; Muto, S.; Hirata, W.; Yoshida, T.; Kakimoto, K.; Iijima, Y.; Daibo, M.; Kiss, T.; Okada, T.; Awaji, S. *IEEE Transactions on Applied Superconductivity* **2019**, *29*, 1–5, DOI: 10.1109/TASC.2019.2896535.

(31) Zhao, Y; Zhu, J.; Jiang, G.; Chen, C.; Wu, W; Zhang, Z.; Chen, S.; Hong, Y.; Hong, Z.; Jin, Z., et al. *Superconductor Science and Technology* **2019**, *32*, 044004, DOI: 10.1088/1361-6668/aafea5.

(32) Wu, Y.; Jiang, G.; Zhu, J.; Wu, D.; Quan, X.; Shi, J.; Suo, H.; Zhao, Y. *Superconductor Science and Technology* **2021**, *34*, 05LT01, DOI: 10.1088/1361-6668/abece6.

(33) Wu, Y.; Shi, J.; Guo, C.; Jiang, G.; Suo, H.; Wu, W.; Li, X.; Wang, Y.; Zhao, Y. *Materials & Design* **2022**, *224*, 111406, DOI: 10.1016/j.matdes.2022.111406.

(34) Feighan, J.; Lai, M.; Kursumovic, A; Zhang, D; Wang, H; Lee, J.; Moon, S; MacManus-Driscoll, J. *Superconductor Science and Technology* **2021**, *34*, 045012, DOI: 10.1088/1361-6668/abe18d.

(35) Puig, T.; Gutierrez, J.; Obradors, X. *Nature Reviews Physics* **2023**, 1–17, DOI: 10.1038/s42254-023-00663-3.

(36) Gupta, A.; Jagannathan, R; Cooper, E. I.; Giess, E.; Landman, J.; Hussey, B. *Applied Physics Letters* **1988**, *52*, 2077–2079, DOI: 10.1063/1.99752.

(37) McIntyre, P. C.; Cima, M. J.; Ng, M. F. *Journal of applied physics* **1990**, *68*, 4183–4187, DOI: 10.1063/1.346233.

(38) Rupich, M. W.; Verebelyi, D. T.; Zhang, W.; Kodenkandath, T.; Li, X. *MRS bulletin* **2004**, *29*, 572–578, DOI: 10.1557/mrs2004.163.

(39) Teranishi, R.; Honjo, T.; Tokunaga, Y.; Fuji, H.; Matsuda, J.; Izumi, T.; Yajima, A.; Shiohara, Y. *Physica C: Superconductivity* **2004**, *412*, 920–925, DOI: 10.1016/j.physc.2004.01.117.

(40) Gutierrez, J; Llordes, A; Gazquez, J; Gibert, M; Roma, N; Ricart, S; Pomar, A; Sandiumenge, F; Mestres, N; Puig, T, et al. *Nature materials* **2007**, *6*, 367–373, DOI: 10.1038/nmat1893.

(41) Solovyov, V.; Dimitrov, I. K.; Li, Q. *Superconductor Science and Technology* **2012**, *26*, 013001, DOI: 10.1088/0953-2048/26/1/013001.

(42) Obradors, X.; Puig, T; Ricart, S; Coll, M; Gazquez, J; Palau, A; Granados, X *Superconductor Science and Technology* **2012**, *25*, 123001, DOI: 10.1088/0953-2048/25/12/123001.

(43) Palmer, X; Pop, C.; Eloussifi, H.; Villarejo, B; Roura, P; Farjas, J; Calleja, A; Palau, A; Obradors, X; Puig, T, et al. *Superconductor Science and Technology* **2015**, *29*, 024002, DOI: 10.1088/0953-2048/29/2/024002.

(44) Miura, M.; Maiorov, B.; Sato, M.; Kanai, M.; Kato, T.; Kato, T.; Izumi, T.; Awaji, S.; Mele, P.; Kiuchi, M., et al. *NPG Asia Materials* **2017**, *9*, e447–e447, DOI: 10.1038/am.2017.197.

(45) Li, Z.; Coll, M.; Mundet, B.; Chamorro, N.; Vallès, F.; Palau, A.; Gazquez, J.; Ricart, S.; Puig, T.; Obradors, X. *Scientific reports* **2019**, *9*, 5828, DOI: 10.1038/s41598-019-42291-x.

(46) Manabe, T; Sohma, M; Yamaguchi, I; Kondo, W; Tsukada, K; Kamiya, K; Mizuta, S; Kumagai, T *IEEE transactions on applied superconductivity* **2005**, *15*, 2923–2926, DOI: 10.1109/TASC.2005.848635.

(47) Schoofs, B.; Cloet, V.; Vermeir, P.; Schaubroeck, J.; Hoste, S.; Van Driessche, I. *Superconductor Science and Technology* **2006**, *19*, 1178, DOI: 10.1088/0953-2048/19/11/015.

(48) Lei, L.; Zhao, G.; Zhao, J.; Xu, H. *IEEE transactions on applied superconductivity* **2010**, *20*, 2286–2293, DOI: 10.1109/TASC.2010.2050589.

(49) Zhao, Y.; Torres, P.; Tang, X.; Norby, P.; Grivel, J.-C. *Inorganic chemistry* **2015**, *54*, 10232–10238, DOI: 10.1021/acs.inorgchem.5b01486.

(50) Chu, J.; Zhao, Y.; Khan, M. Z.; Tang, X.; Wu, W.; Shi, J.; Wu, Y.; Huhtinen, H.; Suo, H.; Jin, Z. *Crystal Growth & Design* **2019**, *19*, 6752–6762, DOI: 10.1021/acs.cgd.9b01120.

(51) Soler Bru, L. Liquid-assisted ultrafast growth of superconducting films derived from chemical solutions, Ph.D. Thesis, Univeristat Autònoma de Barcelona, 2019.

(52) Rasi, S. Advanced Thermal Analysis of REBCO Superconducting Precursor Films and Functional Oxides, Ph.D. Thesis, Univeristat de Girona, 2019.

(53) Soler, L.; Jareño, J.; Banchewski, J.; Rasi, S.; Chamorro, N.; Guzman, R.; Yáñez, R.; Mocuta, C.; Ricart, S.; Farjas, J., et al. *Nature communications* **2020**, *11*, 344, DOI: 10.1038/s41467-019-13791-1.

(54) Banchewski, J. Transient Liquid Assisted Growth of YBCO Superconducting Films: Growth Kinetics, Physical Properties and Vortex Pinning, Ph.D. Thesis, Univeristat Autònoma de Barcelona, 2020.

(55) Jareño Cerulla, J. Transient liquid assisted growth of superconducting nanocomposite films, Ph.D. Thesis, Univeristat Autònoma de Barcelona, 2020.

(56) Haran, K. S.; Kalsi, S.; Arndt, T.; Karmaker, H.; Badcock, R.; Buckley, B.; Haugan, T.; Izumi, M.; Loder, D.; Bray, J. W., et al. *Superconductor Science and Technology* **2017**, *30*, 123002, DOI: 10.1088/1361-6668/aa833e.

(57) Rodriguez, J. *physica status solidi (c)* **2005**, *2*, 3605–3608, DOI: 10.1002/pssc.200461769.

(58) Meissner, W.; Ochsenfeld, R. *Naturwissenschaften* **1933**, *21*, 787–788, DOI: 10.1007/BF01504252.

(59) Gurevich, A. *Annu. Rev. Condens. Matter Phys.* **2014**, *5*, 35–56, DOI: 10.1146/annurev-conmatphys-031113-133822.

(60) Waldram, J. R., *Superconductivity of metals and cuprates*; Taylor & Francis: 1996, DOI: 10.1201/9780203737934.

(61) Jorgensen, J.; Veal, B.; Kwok, W.; Crabtree, G.; Umezawa, A; Nowicki, L.; Paulikas, A. *Phys. Rev. B: Condens. Matter;(United States)* **1987**, *36*, DOI: 10.1103/PhysRevB.41.1863.

(62) Breit, V; Schweiss, P; Hauff, R; Wühl, H; Claus, H; Rietschel, H; Erb, A; Müller-Vogt, G *Physical Review B* **1995**, *52*, R15727, DOI: 10.1103/PhysRevB.52.R15727.

(63) Graser, S; Hirschfeld, P.; Kopp, T; Gutser, R; Andersen, B.; Mannhart, J *arXiv preprint arXiv:0912.4191* **2009**, DOI: 10.1038/nphys1687.

(64) International Centre for Diffraction Database (ICDD), https://www.icdd.com/.

(65) Foltyn, S.; Civale, L; MacManus-Driscoll, J.; Jia, Q.; Maiorov, B; Wang, H; Maley, M *Nature materials* **2007**, *6*, 631–642, DOI: 10.1038/nmat1989.

(66) Iijima, Y.; Kakimoto, K.; Kimura, M.; Takeda, K.; Saitoh, T. *IEEE Transactions on Applied Superconductivity* **2001**, *11*, 2816–2821, DOI: 10.1109/77.919649.

(67) Goyal, A; Ren, S.; Specht, E.; Kroeger, D.; Feenstra, R; Norton, D; Paranthaman, M; Lee, D.; Christen, D. *Micron* **1999**, *30*, 463–478, DOI: 10.1016/S0968-4328(99)00047-5.

(68) MacManus-Driscoll, J.; Bianchetti, M; Kursumovic, A; Kim, G; Jo, W; Wang, H; Lee, J.; Hong, G.; Moon, S. *APL Materials* **2014**, *2*, DOI: 10.1063/1.4893339.

(69) Lee, J.-H.; Lee, H.; Lee, J.-W.; Choi, S.-M.; Yoo, S.-I.; Moon, S.-H. *Superconductor Science and Technology* **2014**, *27*, 044018, DOI: 10.1088/0953-2048/27/4/044018.

(70) Stadel, O; Schmidt, J; Wahl, G; Weiss, F; Selbmann, D; Eickemeyer, J; Gorbenko, O. Y.; Kaul, A.; Jimenez, C *Physica C: Superconductivity* **2002**, *372*, 751–754, DOI: 10.1016/S0921-4534(02)00898-5.

(71) Sánchez-Valdés, C.; Puig, T; Obradors, X *Superconductor Science and Technology* **2015**, *28*, 024006, DOI: 10.1088/0953-2048/28/2/024006.

(72) Chepikov, V; Mineev, N; Degtyarenko, P; Lee, S; Petrykin, V; Ovcharov, A; Vasiliev, A; Kaul, A; Amelichev, V; Kamenev, A, et al. *Superconductor Science and Technology* **2017**, *30*, 124001, DOI: 10.1088/1361-6668/aa9412.

(73) Mao, S. S.; Zhang, X. *Engineering* **2015**, *1*, 367–371, DOI: 10.15302/J-ENG-2015065.

(74) Krauns, C.; Sumida, M; Tagami, M; Yamada, Y; Shiohara, Y *Zeitschrift für Physik B Condensed Matter* **1994**, *96*, 207–212, DOI: 10.1007/BF01313285.

(75) Nakamura, M.; Krauns, C.; Shiohara, Y. *Journal of materials research* **1996**, *11*, 1076–1081, DOI: 10.1557/JMR.1996.0136.

(76) Yao, X; Shiohara, Y *Materials Science and Engineering: B* **1998**, *53*, 11–17, DOI: 10.1016/S0921-5107(97)00294-8.

(77) Kuršumović, A; Cheng, Y.; Glowacki, B.; Madsen, J; Evetts, J. *Journal of crystal growth* **2000**, *218*, 45–56, DOI: 10.1016/S0022-0248(00)00519-4.

(78) Kuznetsov, M.; Krauns, C.; Nakamura, Y.; Izumi, T.; Shiohara, Y. *Physica C: Superconductivity* **2001**, *357*, 1068–1072, DOI: 10.1016/S0921-4534(01)00556-1.

(79) Qi, X; MacManus-Driscoll, J. *Current Opinion in Solid State and Materials Science* **2001**, *5*, 291–300, DOI: 10.1016/S1359-0286(00)00040-1.

(80) Kursumovic, A; Evetts, J.; MacManus-Driscoll, J.; Maiorov, B; Civale, L; Wang, H; Jia, Q.; Foltyn, S. *Applied physics letters* **2005**, *87*, DOI: 10.1063/1.2149975.

(81) Shiohara, Y.; Endo, A. *Materials Science and Engineering: R: Reports* **1997**, *19*, 1–86, DOI: 10.1016/S0927-796X(96)00198-2.

(82) Cima, M. J.; Flemings, M. C.; Figueredo, A. M.; Nakade, M.; Ishii, H.; Brody, H. D.; Haggerty, J. S. *Journal of applied physics* **1992**, *72*, 179–190, DOI: 10.1063/1.352155.

(83) Yamada, Y *Superconductor Science and Technology* **2000**, *13*, 82, DOI: 10.1088/0953-2048/13/1/311.

(84) Kursumovic, A; Tomov, R.; Hühne, R; MacManus-Driscoll, J.; Glowacki, B.; Evetts, J. *Superconductor Science and Technology* **2004**, *17*, 1215, DOI: 10.1088/0953-2048/17/10/024.

(85) Yun, K.; Choi, B.; Matsumoto, Y; Song, J.; Kanda, N; Itoh, T; Kawasaki, M; Chikyow, T; Ahmet, P; Koinuma, H *Applied physics letters* **2002**, *80*, 61–63, DOI: 10.1063/1.1432111.

(86) Ohnishi, T; Huh, J.-U.; Hammond, R.; Jo, W *Journal of materials research* **2004**, *19*, 977–981, DOI: 10.1557/JMR.2004.0127.

(87) Ichino, Y.; Matsuo, H.; Yoshida, Y.; Takai, Y.; Matsumoto, K.; Mukaida, M.; Ichinose, A.; Horii, S. *Japanese journal of applied physics* **2006**, *45*, 758, DOI: 10.1143/JJAP.45.758.

(88) Lu, F; Kametani, F; Hellstrom, E. *Superconductor Science and Technology* **2011**, *25*, 015011, DOI: 10.1088/0953-2048/25/1/015011.

(89) Parmigiani, F.; Chiarello, G.; Ripamonti, N; Goretzki, H; Roll, U *Physical Review B* **1987**, *36*, 7148, DOI: 10.1103/PhysRevB.36.7148.

(90) Hirano, S.-i.; Hayashi, T.; Miura, M. *Journal of the American Ceramic Society* **1990**, *73*, 885–888, DOI: 10.1111/j.1151-2916.1990.tb05130.x.

(91) Rasi, S.; Soler, L.; Jareño, J.; Banchewski, J.; Guzman, R.; Mocuta, C.; Kreuzer, M.; Ricart, S.; Roura-Grabulosa, P.; Farjas, J., et al. *The Journal of Physical Chemistry C* **2020**, *124*, 15574–15584, DOI: 10.1021/acs.jpcc.0c03859.

(92) Arvanitidis, I; Siche, D.; Seetharaman, S *Metallurgical and materials transactions B* **1996**, *27*, 409–416, DOI: doi.org/10.1007/BF02914905.

(93) Vermeir, P.; Cardinael, I.; Schaubroeck, J.; Verbeken, K.; Bäcker, M.; Lommens, P.; Knaepen, W.; D'haen, J.; De Buysser, K.; Van Driessche, I. *Inorganic Chemistry* **2010**, *49*, 4471–4477, DOI: 10.1021/ic9021799.

(94) Nevřiva, M; Pollert, E; Matějková, L; Tříska, A *Journal of crystal growth* **1988**, *91*, 434–438, DOI: 10.1016/0022-0248(88)90265-5.

(95) Lindemer, T.; Specht, E. *Physica C: Superconductivity* **1995**, *255*, 81–94, DOI: 10.1016/0921-4534(95)00460-2.

(96) Itoh, T *Journal of materials science letters* **2003**, *22*, 185–189, DOI: 10.1023/A:1022293724698.

(97) Sobolik, J. L.; Wang, H.; Thomson, W. J. *Journal of the American Ceramic Society* **1994**, *77*, 2738–2746, DOI: 10.1111/j.1151-2916.1994.tb04669.x.

(98) Lindemer, T.; Washburn, F.; MacDougall, C.; Cavin, O. *Physica C: Superconductivity* **1991**, *174*, 135–143, DOI: 10.1016/0921-4534(91)90429-3.

(99) Chu, P.-Y.; Buchanan, R. C. *Journal of materials research* **1994**, *9*, 844–851, DOI: 10.1557/JMR.1994.0844.

(100) Gamalski, A.; Tersoff, J; Sharma, R; Ducati, C; Hofmann, S *Nano letters* **2010**, *10*, 2972–2976, DOI: 10.1021/nl101349e.

(101) Rasi, S.; Queraltó, A.; Banchewski, J.; Saltarelli, L.; Garcia, D.; Pacheco, A.; Gupta, K.; Kethamkuzhi, A.; Soler, L.; Jareño, J., et al. *Advanced Science* **2022**, *9*, 2203834, DOI: 10.1002/advs.202203834.

(102) Dash, J. *Reviews of Modern Physics* **1999**, *71*, 1737, DOI: 10.1103/RevModPhys.71.1737.

(103) Mei, Q.; Lu, K *Progress in Materials Science* **2007**, *52*, 1175–1262, DOI: 10.1016/j.pmatsci.2007.01.001.

(104) Frenken, J. W.; Van der Veen, J. *Physical review letters* **1985**, *54*, 134, DOI: 10.1103/PhysRevLett.54.134.

(105) Teraoka, Y *Surface science* **1993**, *281*, 317–322, DOI: 0.1016/0039-6028(93)90644-Y.

(106) Pawlow, P *Zeitschrift für Physikalische Chemie* **1909**, *68*, 316–322, DOI: 10.1515/zpch-1909-6824.

(107) Kofman, R; Cheyssac, P; Aouaj, A; Lereah, Y; Deutscher, G; Ben-David, T; Penisson, J.; Bourret, A *Surface science* **1994**, *303*, 231–246, DOI: 10.1016/0039-6028(94)90635-1.

(108) Lu, K; Jin, Z. *Current Opinion in Solid State and Materials Science* **2001**, *5*, 39–44, DOI: 10.1016/S1359-0286(00)00027-9.

(109) Zhong, J; Zhang, L.; Jin, Z.; Sui, M.; Lu, K *Acta materialia* **2001**, *49*, 2897–2904, DOI: 10.1016/S1359-6454(01)00212-9.

(110) Sheng, H.; Lu, K; Ma, E *Acta materialia* **1998**, *46*, 5195–5205, DOI: 10.1016/S1359-6454(98)00108-6.

(111) Benz, K.-W.; Neumann, W., *Introduction to crystal growth and characterization*; John Wiley & Sons: 2014, DOI: 10.1002/9783527689248.

(112) Sosso, G. C.; Chen, J.; Cox, S. J.; Fitzner, M.; Pedevilla, P.; Zen, A.; Michaelides, A. *Chemical reviews* **2016**, *116*, 7078–7116, DOI: 10.1021/acs.chemrev.5b00744.

(113) Ichino, Y.; Sudoh, K.; Miyachi, K.; Yoshida, Y.; Takai, Y. *IEEE transactions on applied superconductivity* **2003**, *13*, 2735–2738, DOI: 10.1109/TASC.2003.811972.

(114) Markov, I. V., *Crystal growth for beginners: fundamentals of nucleation, crystal growth and epitaxy*; World scientific: 2016.

(115) Aselage, T.; Keefer, K. *Journal of Materials Research* **1988**, *3*, 1279–1291, DOI: 10.1557/JMR.1988.1279.

(116) Jha, A. K.; Matsumoto, K. *Frontiers in Physics* **2019**, *7*, 82, DOI: 10.3389/fphy.2019.00082.

(117) Armenio, A. A.; Augieri, A; Ciontea, L; Contini, G; Davoli, I; Galluzzi, V; Mancini, A; Rufoloni, A; Petrisor, T; Vannozzi, A, et al. *Superconductor Science and Technology* **2008**, *21*, 125015, DOI: 10.1088/0953-2048/21/12/125015.

(118) Rijckaert, H.; Pollefeyt, G.; Sieger, M.; Hänisch, J.; Bennewitz, J.; De Keukeleere, K.; De Roo, J.; Hühne, R.; Bäcker, M.; Paturi, P., et al. *Chemistry of materials* **2017**, *29*, 6104–6113, DOI: 10.1021/acs.chemmater.7b02116.

(119) Pop, C.; Villarejo, B.; Pino, F.; Mundet, B.; Ricart, S.; De Palau, M; Puig, T; Obradors, X. *Superconductor Science and Technology* **2018**, *32*, 015004, DOI: 10.1088/1361-6668/aaea4e.

(120) Miura, M.; Tsuchiya, G.; Harada, T.; Sakuma, K.; Kurokawa, H.; Sekiya, N.; Kato, Y.; Yoshida, R.; Kato, T.; Nakaoka, K., et al. *NPG Asia Materials* **2022**, *14*, 85, DOI: 10.1038/s41427-022-00432-1.

(121) Obradors, X.; Puig, T.; Ricart, S.; Palau, A.; Coll Bau, M.; Gutierrez, J.; Farjas, J; Bartolomé, E. *Superconductor Science and Technology* **2024**, DOI: 10.1088/1361-6668/ad36eb.

(122) Lu, Y. M.; Cai, C. B.; Liu, Z. Y.; Guo, Y. Q.; Jiang, H. B.; Zhang, Y. J.; Li, M. J.; Fan, F.; Bai, C. Y.; Lu, Q., et al. *IEEE Transactions on Applied Superconductivity* **2019**, *29*, 1–5, DOI: doi.org/10.1109/TASC.2019.2910021.

(123) List, F.; Clem, P.; Heatherly, L; Dawley, J.; Leonard, K. J.; Lee, D. F.; Goyal, A. *IEEE transactions on applied superconductivity* **2005**, *15*, 2656–2658, DOI: 10.1109/TASC.2005.847760.

(124) Mos, R.; Nasui, M; Petrisor Jr, T; Gabor, M.; Varga, R; Ciontea, L; Petrisor, T *Journal of Analytical and Applied Pyrolysis* **2011**, *92*, 445–449, DOI: 10.1016/j.jaap.2011.08.007.

(125) Rasi, S.; Ricart, S.; Obradors, X.; Puig, T.; Roura-Grabulosa, P.; Farjas, J. *Journal of Analytical and Applied Pyrolysis* **2019**, *141*, 104640, DOI: 10.1016/j.jaap.2019.104640.

(126) Villarejo, B.; Pop, C.; Ricart, S.; Mundet, B.; Palau, A.; Roura-Grabulosa, P.; Farjas, J.; Puig, T.; Obradors, X. *Journal of Materials Chemistry C* **2020**, *8*, 10266–10282, DOI: 10.1039/d0tc01846e.

(127) Zhang, S.; Xu, S.; Fan, Z.; Jiang, P.; Han, Z.; Yang, G.; Chen, Y. *Superconductor Science and Technology* **2018**, *31*, 125006, DOI: 10.1088/1361-6668/aae460.

(128) Majkic, G.; Pratap, R.; Xu, A.; Galstyan, E.; Higley, H. C.; Prestemon, S. O.; Wang, X.; Abraimov, D.; Jaroszynski, J.; Selvamanickam, V. *Superconductor Science and Technology* **2018**, *31*, 10LT01, DOI: 10.1088/1361-6668/aad844.

(129) Namburi, D. K.; Shi, Y.; Cardwell, D. A. *Superconductor Science and Technology* **2021**, *34*, 053002, DOI: 10.1088/1361-6668/abde88.

(130) Sohma, M; Yamaguchi, I; Tsukada, K; Kondo, W; Mizuta, S; Manabe, T; Kumagai, T *Physica C: Superconductivity* **2004**, *412*, 1326–1330, DOI: 10.1016/j.physc.2004.01.164.

(131) Zhao, Y; Ma, L; Wu, W; Suo, H.-L.; Grivel, J.-C. *Journal of Materials Chemistry A* **2015**, *3*, 13275–13282, DOI: 10.1039/c5ta00153f.

(132) Chung, Y.; Wei, H.; Liu, Y.; Lee, G.; Wang, Y. *Polyhedron* **1998**, *17*, 449–455, DOI: 10.1016/S0277-5387(97)00367-7.

(133) Bierke, T. Experimental Crystal Structure Determination, Ph.D. Thesis, CCDC: 832100, 2013, DOI: https://doi.org/10.5517/ccwxvyk.

(134) Nasui, M; Petrisor Jr, T; Mos, R.; Mesaros, A; Varga, R.; Vasile, B.; Ristoiu, T; Ciontea, L; Petrisor, T *Journal of Analytical and Applied Pyrolysis* **2014**, *106*, 92–98, DOI: 10.1016/j.jaap.2014.01.004.

(135) Bierke, T. Experimental Crystal Structure Determination, Ph.D. Thesis, CCDC: 843672, 2013, DOI: https://doi.org/10.5517/ccx9x7b.

(136) Barnes, P.; Stephenson, G; Warrington, S. *Journal of Thermal Analysis and Calorimetry* **1982**, *25*, 299–311, DOI: 10.1007/bf01912955.

(137) Grivel, J.-C. *Journal of thermal analysis and calorimetry* **2012**, *109*, 81–88, DOI: 10.1007/s10973-011-1745-9.

(138) Akanni, M. S.; Burrows, H. D.; Begun, P. B. *Thermochimica acta* **1984**, *81*, 45–58, DOI: 10.1016/0040-6031(84)85109-6.

(139) Akanni, M. S.; Okoh, E. K.; Burrows, H. D.; Ellis, H. A. *Thermochimica acta* **1992**, *208*, 1–41, DOI: 10.1016/0040-6031(92)80150-U.

(140) Kim, M.; R. Hinklin, T.; Laine, R. M. *Chemistry of Materials* **2008**, *20*, 5154–5162, DOI: 10.1021/cm703382x.

(141) Roura, P; Farjas, J; Camps, J; Ricart, S; Arbiol, J; Puig, T; Obradors, X *Journal of Nanoparticle Research* **2011**, *13*, 4085–4096, DOI: 10.1007/s11051-011-0352-9.

(142) Rasi, S.; Ricart, S.; Obradors, X.; Puig, T.; Roura, P.; Farjas, J. *Journal of Analytical and Applied Pyrolysis* **2018**, *133*, 225–233, DOI: 10.1016/j.jaap.2018.03.021.

(143) Rasi, S.; Silveri, F.; Ricart, S.; Obradors, X.; Puig, T.; Roura-Grabulosa, P.; Farjas, J. *Journal of Analytical and Applied Pyrolysis* **2019**, *140*, 312–320, DOI: 10.1016/j.jaap.2019.04.008.

(144) Foltyn, S.; Jia, Q.; Arendt, P.; Kinder, L; Fan, Y; Smith, J. *Applied Physics Letters* **1999**, *75*, 3692–3694, DOI: 10.1063/1.125431.

(145) Izumi, T; Yoshizumi, M; Miura, M; Sutoh, Y; Nakanishi, T; Nakai, A; Ichikawa, Y; Yamada, Y; Goto, T; Yajima, A, et al. *Physica C: Superconductivity* **2008**, *468*, 1527–1530, DOI: 10.1016/j.physc.2008.05.270.

(146) Pop, C; Barusco, P; Vlad, R; Queralto, A; Gupta, K; Almog, B; Saraf, A; Deutscher, G; Granados, X; Puig, T, et al. *Superconductor Science and Technology* **2022**, *35*, 054007, DOI: 10.1088/1361-6668/ac5be9.

(147) Solovyov, M.; Pardo, E.; Šouc, J.; Gömöry, F.; Skarba, M.; Konopka, P.; Pekarčíková, M.; Janovec, J. *Superconductor Science and Technology* **2013**, *26*, 115013, DOI: 10.1088/0953-2048/26/11/115013.

(148) Saltarelli, L.; Gupta, K.; Rasi, S.; Kethamkuzhi, A.; Queraltó, A.; Garcia, D.; Gutierrez, J.; Farjas, J.; Roura-Grabulosa, P.; Ricart, S., et al. *ACS applied materials & interfaces* **2022**, *14*, 48582–48597, DOI: 10.1021/acsami.2c11414.

(149) Tafto, J; Suenaga, M.; Wang, T; Sabatini, R.; Moodenbaugh, A.; Levine, S *MRS Online Proceedings Library (OPL)* **1987**, *99*, 511, DOI: 10.1557/PROC-99-511.

(150) Kato, M.; Jonassen, H. B.; Fanning, J. C. *Chemical Reviews* **1964**, *64*, 99–128, DOI: 10.1021/cr60228a003.

(151) Li, M.; Cayado, P.; Erbe, M.; Jung, A.; Hänisch, J.; Holzapfel, B.; Liu, Z.; Cai, C. *Coatings* **2020**, *10*, 31, DOI: 10.3390/coatings10010031.

(152) Villarejo, B.; Pino, F.; Pop, C.; Ricart, S.; Valles, F.; Mundet, B.; Palau, A.; Roura-Grabulosa, P.; Farjas, J.; Chamorro, N., et al. *ACS Applied Electronic Materials* **2021**, *3*, 3948–3961, DOI: 10.1021/acsaelm.1c00513.

(153) Pacheco, A. Use of Inkjet Printing to Obtain YBa2Cu3O7-x Thick Films by TLAG-CSD Process, Ph.D. Thesis, Univeristat Autònoma de Barcelona, 2023.

(154) Queraltó, A.; Banchewski, J.; Pacheco, A.; Gupta, K.; Saltarelli, L.; Garcia, D.; Alcalde, N.; Mocuta, C.; Ricart, S.; Pino, F., et al. *ACS Applied Materials & Interfaces* **2021**, *13*, 9101–9112, DOI: 10.1021/acsami.0c18014.

(155) Rijckaert, H.; Cayado, P.; Hänisch, J.; Billet, J.; Erbe, M.; Holzapfel, B.; Van Driessche, I. *The Journal of Physical Chemistry Letters* **2021**, *12*, 2118–2125, DOI: 10.1021/acs.jpclett.1c00135.

(156) Queraltó, A.; Pacheco, A.; Jiménez, N.; Ricart, S.; Obradors, X.; Puig, T. *Journal of Materials Chemistry C* **2022**, *10*, 6885–6895, DOI: 10.1039/D1TC05913K.

(157) Fick, A. *Annalen der Physik* **1855**, *170*, 59–86, DOI: 10.1002/andp.18551700105.

(158) Roma, N; Morlens, S; Ricart, S; Zalamova, K; Moreto, J.; Pomar, A; Puig, T; Obradors, X *Superconductor Science and Technology* **2006**, *19*, 521, DOI: 10.1088/0953-2048/19/6/019.

(159) Cayado, P.; De Keukeleere, K.; Garzón, A; Perez-Mirabet, L; Meledin, A; De Roo, J.; Vallés, F; Mundet, B; Rijckaert, H.; Pollefeyt, G., et al. *Superconductor Science and Technology* **2015**, *28*, 124007, DOI: 10.1088/0953-2048/28/12/124007.

(160) Cayado, P.; Mundet, B.; Eloussifi, H.; Vallés, F.; Coll, M.; Ricart, S.; Gázquez, J.; Palau, A.; Roura, P.; Farjas, J., et al. *Superconductor Science and Technology* **2017**, *30*, 125010, DOI: 10.1088/1361-6668/aa8ffe.

(161) Calleja, A; Ricart, S; Palmer, X; Luccas, R.; Puig, T; Obradors, X *Journal of sol-gel science and technology* **2010**, *53*, 347–352, DOI: 10.1007/s10971-009-2100-5.

(162) Fischer, E.; Fischer, E.; Speier, A. *Untersuchungen aus Verschiedenen Gebieten: Vorträge und Abhandlungen Allgemeinen Inhalts* **1924**, 285–291, DOI: 10.1007/978-3-642-51364-0_52.

(163) Bender, M. L. *Chemical Reviews* **1960**, *60*, 53–113, DOI: 10.1021/cr60203a005.

(164) Luo, F.; Pan, C.; Cheng, J. *Synlett* **2012**, *2012*, 357–366, DOI: 10.1055/s-0031-1290101.

(165) Rasia, R. M.; Bertoncini, C. W.; Marsh, D.; Hoyer, W.; Cherny, D.; Zweckstetter, M.; Griesinger, C.; Jovin, T. M.; Fernández, C. O. *Proceedings of the National Academy of Sciences* **2005**, *102*, 4294–4299, DOI: 10.1073/pnas.040788110.

(166) Sakaguchi, U.; Addison, A. W. *Journal of the Chemical Society, Dalton Transactions* **1979**, 600–608, DOI: 10.1039/DT9790000600.

(167) Peisach, J; Blumberg, W. *Archives of biochemistry and biophysics* **1974**, *165*, 691–708, DOI: 10.1016/0003-9861(74)90298-7.

(168) Saladino, A. C.; Larsen, S. C. *Catalysis today* **2005**, *105*, 122–133, DOI: 10.1016/j.cattod.2005.04.018.

(169) Eloussifi, H.; Farjas, J; Roura, P; Ricart, S.; Puig, T.; Obradors, X.; Dammak, M. *Thermochimica Acta* **2013**, *556*, 58–62, DOI: 10.1016/j.tca.2013.01.022.

(170) Eloussifi, H.; Farjas, J; Roura, P; Ricart, S.; Puig, T.; Obradors, X.; Dammak, M. *Thin Solid Films* **2013**, *545*, 200–204, DOI: 10.1016/j.tsf.2013.07.082.

(171) De Ávila, S. G.; Logli, M. A.; Matos, J. R. *International Journal of Greenhouse Gas Control* **2015**, *42*, 666–671, DOI: 10.1016/j.ijggc.2015.10.001.

(172) Cayado, P.; Grünewald, L.; Erbe, M.; Hänisch, J.; Gerthsen, D.; Holzapfel, B. *RSC advances* **2022**, *12*, 28831–28842, DOI: 10.1039/d2ra03807b.

(173) Erbe, M; Cayado, P; Freitag, W; Ackermann, K; Langer, M; Meledin, A; Hänisch, J; Holzapfel, B *Superconductor Science and Technology* **2020**, *33*, 094002, DOI: 10.1088/1361-6668/ab9aa0.

(174) Miura, M.; Itoh, M.; Ichino, Y.; Yoshida, Y.; Takai, Y.; Matsumoto, K.; Ichinose, A.; Horii, S.; Mukaida, M. *IEEE transactions on applied superconductivity* **2005**, *15*, 3078–3081, DOI: 10.1109/TASC.2005.848962.

(175) Matsushima, K; Taka, C; Nishida, A In *Journal of Physics: Conference Series*, 2018; Vol. 969, p 012059, DOI: 10.1088/1742-6596/969/1/012059.

(176) Karabach, Y. Y.; Kirillov, A. M.; Haukka, M.; Kopylovich, M. N.; Pombeiro, A. J. *Journal of inorganic biochemistry* **2008**, *102*, 1190–1194, DOI: 10.1016/j.jinorgbio.2007.11.007.

(177) Safarifard, V.; Morsali, A. *Coordination Chemistry Reviews* **2015**, *292*, 1–14, DOI: 10.1016/j.ccr.2015.02.014.

(178) Anslyn, E. V.; Dougherty, D. A., *Modern physical organic chemistry*; University science books: 2006.

(179) Tsukada, K.; Yamaguchi, I.; Sohma, M.; Kondo, W.; Kamiya, K.; Kumagai, T.; Manabe, T. *Physica C: Superconductivity* **2007**, *458*, 29–33, DOI: 10.1016/j.physc.2007.03.026.

(180) Benzi, P.; Bottizzo, E.; Demaria, C.; Rizzi, N. *Journal of Chemical Sciences* **2007**, *119*, 631–635, DOI: 10.1007/s12039-007-0079-4.

(181) Kato, M.; Muto, Y. *Coordination chemistry reviews* **1988**, *92*, 45–83, DOI: 10.1016/0010-8545(88)85005-7.

(182) Layer, R. W. *Chemical reviews* **1963**, *63*, 489–510.

(183) Herlem, G.; Reybier, K.; Trokourey, A.; Fahys, B. *Journal of The Electrochemical Society* **2000**, *147*, 597, DOI: 10.1149/1.1393239.

(184) Machado, A.; Jardim, R. *Materials Letters* **1994**, *19*, 177–183, DOI: 10.1016/0167-577X(94)90065-5.

(185) Ellingham, H. *Journal of the Society of Chemical Industry* **1944**, *63*, 125–160, DOI: 10.1002/jctb.5000630501.

(186) Lindemer, T.; Washburn, F.; MacDougall, C. *Physica C: Superconductivity* **1992**, *196*, 390–398, DOI: 10.1016/0921-4534(92)90462-L.

(187) MacManus-Driscoll, J.; Bravman, J.; Beyers, R. *Physica C: Superconductivity* **1995**, *241*, 401–413, DOI: 10.1016/0921-4534(94)02369-7.

(188) Taïr, F.; Carreras, L.; Camps, J.; Farjas, J.; Roura, P.; Calleja, A.; Puig, T.; Obradors, X. *Journal of Alloys and Compounds* **2017**, *692*, 787–792, DOI: 10.1016/j.jallcom.2016.08.072.

(189) Engel, S; Thersleff, T; Hühne, R; Schultz, L; Holzapfel, B *Applied physics letters* **2007**, *90*, DOI: 10.1063/1.2711761.

(190) Llordes, A.; Palau, A; Gázquez, J; Coll, M; Vlad, R; Pomar, A; Arbiol, J.; Guzman, R.; Ye, S; Rouco, V, et al. *Nature materials* **2012**, *11*, 329–336, DOI: 10.1038/nmat3247.

(191) Erbe, M; Hänisch, J; Hühne, R; Freudenberg, T; Kirchner, A; Molina-Luna, L; Damm, C; Van Tendeloo, G; Kaskel, S; Schultz, L, et al. *Superconductor Science and Technology* **2015**, *28*, 114002, DOI: 10.1088/0953-2048/28/11/114002.

(192) Hidaka, Y.; Enomoto, Y.; Suzuki, M.; Oda, M.; Murakami, T. *Journal of Crystal Growth* **1987**, *85*, 581–584, DOI: 10.1016/0022-0248(87)90025-X.

(193) Bykov, A.; Demianets, L.; Zibrov, I.; Kanunnikov, G.; Melnikov, O.; Stishov, S. *J. Cryst. Growth;(Netherlands)* **1988**, *91*, DOI: 10.1016/0022-0248(88)90242-4.

(194) Zhang, W.; Osamura, K.; Ochiai, S. *Journal of the American Ceramic Society* **1990**, *73*, 1958–1964, DOI: 10.1111/j.1151-2916.1990.tb05252.x.

(195) Vermeir, P.; Feys, J.; Schaubroeck, J.; Verbeken, K.; Lommens, P.; Van Driessche, I. *Materials Research Bulletin* **2012**, *47*, 4376–4382, DOI: 10.1016/j.materresbull.2012.09.033.

(196) Murakami, M; Fujimoto, H; Gotoh, S; Yamaguchi, K; Koshizuka, N; Tanaka, S *Physica C: Superconductivity* **1991**, *185*, 321–326, DOI: 10.1016/0921-4534(91)91993-E.

(197) Sandiumenge, F.; Piñol, S.; Obradors, X.; Snoeck, E.; Roucau, C. *Physical Review B* **1994**, *50*, 7032, DOI: 10.1103/PhysRevB.50.7032.

(198) Sandiumenge, F; Vilalta, N; Obradors, X; Piñol, S; Bassas, J; Maniette, Y *Journal of applied physics* **1996**, *79*, 8847–8849, DOI: 10.1063/1.362476.

(199) Sandiumenge, F; Martinez, B; Obradors, X *Superconductor Science and Technology* **1997**, *10*, A93, DOI: 10.1088/0953-2048/10/7A/008.

(200) Kim, C.-J.; Kim, K.-B.; Park, H.-W.; Kuk, I.-H.; Hong, G.-W. *Journal of materials science* **1997**, *32*, 4701–4709, DOI: 10.1023/A:1018614527118.

(201) Kim, C.-J.; Kim, K.-B.; Kuk, I.-H.; Hong, G.-W.; Lee, Y.-S.; Park, H.-S. *Superconductor Science and Technology* **1997**, *10*, 947, DOI: 10.1088/0953-2048/10/12/019.

(202) Di Uccio, U. S.; Granozio, F. M.; Di Chiara, A; Tafuri, F.; Lebedev, O.; Verbist, K; Van Tendeloo, G *Physica C: Superconductivity* **1999**, *321*, 162–176, DOI: 10.1016/S0921-4534(99)00350-0.

(203) Shi, D.; Krishnan, H; Hong, J.; Miller, D; McGinn, P.; Chen, W.; Xu, M.; Chen, J.; Fang, M.; Welp, U, et al. *Journal of applied physics* **1990**, *68*, 228–232, DOI: 10.1063/1.347122.

(204) McGinn, P; Zhu, N; Chen, W; Sengupta, S; Li, T *Physica C: Superconductivity* **1991**, *176*, 203–208, DOI: 10.1016/0921-4534(91)90714-A.

(205) Shi, Y.; Bergamo-Andreis, G.; Dennis, A. R.; Durrell, J. H.; Cardwell, D. A. *Superconductor Science and Technology* **2020**, *33*, 035003, DOI: 10.1088/1361-6668/ab6ee4.

(206) Muralidhar, M; Sunsanee, P; Takemura, K; Srikanth, A. S.; Jirsa, M; Rao, M. R.; Oka, T; Sakai, N; Murakami, M. *Superconductor Science and Technology* **2020**, *33*, 074002, DOI: 10.1088/1361-6668/ab877a.

(207) Stangl, A.; Palau, A.; Deutscher, G.; Obradors, X.; Puig, T. *Scientific Reports* **2021**, *11*, 8176, DOI: 10.1038/s41598-021-87639-4.

(208) Cayado, P.; Hauck, D.; Barthlott, D.; Erbe, M.; Hänisch, J.; Holzapfel, B. *ACS Applied Electronic Materials* **2021**, *3*, 5374–5382, DOI: 10.1021/acsaelm.1c00861.

(209) Cayado, P.; Bonura, M.; Lucas, C.; Saule, E.; Rijckaert, H.; Bagni, T.; Konstantopoulou, K.; Alessandrini, M.; Senatore, C. *Scientific Reports* **2023**, *13*, 16917, DOI: 10.1038/s41598-023-44086-7.

(210) Queraltó, A.; Sieger, M.; Gupta, K.; Meledin, A.; Barusco, P.; Saltarelli, L.; de Palau, M.; Granados, X.; Obradors, X.; Puig, T. *Superconductor Science and Technology* **2022**, *36*, 025003, DOI: 10.1088/1361-6668/acaad3.

(211) Wiesner, U; Krabbes, G; Ritschel, M *Materials research bulletin* **1989**, *24*, 1261–1266, DOI: 10.1016/0025-5408(89)90201-8.

(212) Suzuki, R. O.; Okada, S.; Oishi, T.; Ono, K. *Materials Transactions, JIM* **1990**, *31*, 1078–1084, DOI: 10.2320/matertrans1989.31.1078.

(213) Blessing, R. *Acta Cryst. A* **1995**, *51*, 33.

(214) A.X.S, B., *Inc. SAINT*; Madison, Wisconsin, USA.

(215) Sheldrick, G. M. *Acta Crystallographica Section A: Foundations and Advances* **2015**, *71*, 3–8.

(216) Nardelli, M. *Journal of applied crystallography* **1999**, *32*, 563–571, DOI: 10.1107/S0021889899002666.

(217) Pinsky, M.; Avnir, D. *Inorganic chemistry* **1998**, *37*, 5575–5582, DOI: 10.1021/ic9804925.

(218) Ström, G.; Fredriksson, M.; Stenius, P. *Journal of colloid and interface science* **1987**, *119*, 352–361, DOI: 10.1016/0021-9797(87)90280-3.

(219) Karl Fischer reagents—technical manual, Mitsubishi Chemical Corporation, Tokyo, http://www.mcckf.com/english/scope.html.

(220) Sanchez-Rodriguez, D.; Farjas, J.; Roura, P.; Ricart, S.; Mestres, N.; Obradors, X.; Puig, T. *The Journal of Physical Chemistry C* **2013**, *117*, 20133–20138, DOI: 10.1021/jp4049742.

(221) Roura, P; Farjas, J; Eloussifi, H; Carreras, L; Ricart, S; Puig, T; Obradors, X *Thermochimica acta* **2015**, *601*, 1–8, DOI: 10.1016/j.tca.2014.12.016.

(222) Linstrom, P. J.; Mallard, W. G. *Journal of Chemical & Engineering Data* **2001**, *46*, 1059–1063, DOI: 10.1021/je000236i.

(223) Bragg, W. H.; Bragg, W. L. *Proceedings of the Royal Society of London. Series A, Containing Papers of a Mathematical and Physical Character* **1913**, *88*, 428–438, DOI: 10.1098/rspa.1913.0040.

(224) Warren, B. E., *X-ray Diffraction*; Courier Corporation: 1990.

(225) ImageJ, Rasband, W.S. 1997.

(226) Bosman, M; Watanabe, M; Alexander, D.; Keast, V. *Ultramicroscopy* **2006**, *106*, 1024–1032, DOI: 10.1016/j.ultramic.2006.04.016.

(227) Bean, C. P. *Physical review letters* **1962**, *8*, 250, DOI: 10.1103/PhysRevLett.8.250.

(228) Llunell, M. e. a., *SHAPE*; Universitat de Barcelona and Hebrew University of Jerusalem: 2013.